Variability and Rotation of Young Low Mass Stars:

The case of the Cygnus OB2 Association

Julia Maria Torres Roquette

Abril 2017

Universidade Federal de Minas Gerais - UFMG
Instituto de Ciências Exatas - ICEx
Programa de Pós Graduação em Física

Variability and Rotation of Young Low Mass Stars: The Case of the Cygnus OB2 Association

Tese apresentada ao Departamento de Física da Universidade Federal de Minas Gerais como requisito para obtençao do grau de Doutora em Física

Orientadora: Profa. Dra. Sílvia Helena Paixão Alencar
Co-Orientador (Sanduíche): Dr. Jérôme Bouvier
Co-Orientador: Prof. Dr. Luiz Paulo Ribeiro Vaz

Área de Concentração: Astrofísica

Abril, 2017

Abstract

Photometric variability is one of the main characteristics of young stellar objects and explore its particularities in different wavelengths may provide insights on the ongoing physical processes at work in such objects. The most common source of photometric variability in young stars is the brightness modulation, caused by the rotation of a spotted stellar surface. This type of variability allows to measure rotation periods in young stars.

In the last decades, the early evolution of pre-main sequence stellar rotational picture has been constrained by studies targeting different young regions at a variety of ages. Observational studies suggest a dependence of rotation with mass, and for some mass ranges a connection between rotation and the presence of a circumstellar disc. Not still fully explored, though, is the role of environmental conditions on the stellar rotational regulation.

In this thesis, we explored the occurrence and main characteristics of near-infrared variability for young stars of the massive OB association Cygnus OB2, which is 1.4 kpc away from the Sun. For objects with periodic variability that could be associated with stellar rotation, we investigated the rotational properties of Cygnus OB2 members. For the sample of rotational periods evaluated, we addressed questions regarding the effect of environment properties on the pre-main sequence rotational evolution.

We investigated JHK-band variability of 5083 candidate members (24% of which are disc-bearing stars), using data observed with the wide-field camera (WFCAM) of the UK Infrared Telescope (UKIRT) on Mauna Kea, Hawaii. A total of 112 nights were observed, spanning 217 days. The sample studied is spread over a field of 0.78 squared degrees.

The selection of variable stars was done by using Stetson variability index, and 60% of the stars in the sample were found to be variable according to this criterion. We investigated the light-curve morphology, and the variations in the colour-colour and colour-magnitude diagrams for JHK-bands, and when the variability was highly correlated in different bands and colours, the slopes produced by the variations inside such diagrams were estimated. These slopes were compared to the slopes expected from the models explaining physical mechanisms responsible by the variability in young stars, and the causes of variability were investigated.

Period search was performed using Lomb-Scargle periodogram for periods between 0.83-45 days. Period detection quality was verified by using False Alarm Probability levels, the Saunders statistics, string/rope length method, and visual verification of folded light curves. We identified 1224 periodic variable stars. Monte Carlo simulations were performed in order to evaluate completeness and contamination of the periodic sample, out of which 894 measured periods were considered as reliable. Our study was considered reasonably complete for periods between 2 and 30 days.

The general scenario for the rotational evolution of young stars seen in other regions is confirmed by Cygnus OB2 period distributions, with disc-bearing stars rotating on average slower than stars without discs. A mass-rotation dependence was also verified, but as in NGC 6530, very low mass stars ($M < 0.4\mathrm{M}_{\odot}$) are rotating on average slower than higher mass stars ($0.4\mathrm{M}_{\odot} < M < 1.4\mathrm{M}_{\odot}$). We observed an excess of slow rotators among the lower mass population. The disc and mass-rotation connection was also analysed by taking into account the incident UV radiation arising from O stars in the association. Results compatible with the disc-locking scenario were verified for stars with low UV incidence, but no statistical significant relation between rotation and disc presence was verified for stars with high UV incidence, suggesting that massive stars can have an important role on regulating the nearby low mass stars rotation.

Keywords: Star Formation, Young Stellar Objects, Star Rotation, Angular Momentum, Photometric Variability

Resumo

Variabilidade fotométrica é uma das principais características de objetos estelares jovens, e entender suas particularidades em diferentes comprimentos de onda pode ajudar a entender os processos físicos em ação em tais objetos. A causa da variabilidade fotométrica mais comum em estrelas jovens é a modulação do brilho estelar pela rotação de uma superfície estelar com manchas. Esse tipo de variabilidade nos permite medir períodos de rotação em estas estrelas jovens.

Nas últimas décadas, a evolução da rotação estelar durante o princípio da pré sequência principal foi o assunto de diversos estudos, focados em diferentes regiões jovens com diferentes idades. Estudos observacionais sugerem uma dependência da rotação com a massa da estrela, e para estrelas em certo intervalo de massa, uma dependência da rotação com a presença de um disco circunstelar também é esperada. Por outro lado, o papel das condições ambientais na regulação da rotação estelar ainda não é bem entendido.

Nesta tese, nós exploramos a ocorrência e principais características da variabilidade fotométrica no infravermelho próximo em estrelas jovens, situadas na massiva associação Cygnus OB2, a qual está localizada a 1.4 kpc distante do Sol. Para objetos com variabilidade periódica associada com a rotação estelar, investigamos as propriedades rotacionais de membros de Cygnus OB2. Para a amostra de períodos de rotação, investigamos questões relacionadas ao efeito das propriedades ambientais na evolução rotacional durante a fase pré sequência principal.

Investigamos variabilidade em 5083 candidatos a membros da associação (24% deles possuem disco circunstelar) nas bandas JHK do infravermelho próximo, usando dados observados com a Câmera Wide-field (WFCAM) instalada no UK Infrared Telescope (UKIRT), no Mauna Kea, Havaí. Um total de 112 noites foi observado, compreendendo 217 dias. A amostra estudada está distribuída em um campo de 0.78 graus quadrados.

A seleção de variáveis foi feita usando o índice de variabilidade de Stetson, e 60% das estrelas da amostra foram consideradas variáveis. Investigamos a morfologia das curvas de luz, e as variações de cores e magnitudes JHK dentro de diagramas cor-magnitude e cor-cor. Nos casos em que a variação em cor e magnitude eram altamente correlacionadas, as

inclinações produzidas pela variação foram medidas. Tais inclinações foram comparadas com as inclinações esperadas a partir de modelos explicando os mecanismos físicos responsáveis por variabilidade fotométrica em estrelas jovens.

A busca por períodos foi feita usando-se periodogramas de Lomb-Scargle para períodos entre 0.83-45 dias. As detecções de períodos foram verificadas utilizando-se os níveis de Probabilidade de Falso Alarme, a estatística de Saunders, os métodos de comprimento de string/rope, e a inspeção visual das curvas de luz. Simulações de Monte Carlo foram realizadas para estimar a completeza e os níveis de contaminação na amostra de estrelas periódicas. A partir das simulações, 894 períodos foram considerados confiáveis. O presente estudo foi considerado completo para períodos entre 2 e 30 dias.

O cenário geral para a evolução da rotação de estrelas jovens visto em outras regiões foi confirmado pelas distribuições de período para estrelas em Cygnus OB2. Estrelas com disco giram em média mais devagar do que estrelas sem disco. A dependência da rotação com a massa estelar também foi verificada, mas como é o caso de NGC 6530, estrelas de massa muito pequena ($M < 0.4\mathrm{M}_{\odot}$) giram mais devagar que estrelas mais massivas ($0.4\mathrm{M}_{\odot} < M < 1.4\mathrm{M}_{\odot}$). Observamos um excesso de rotores lentos entre a população de menor massa. A dependência da rotação com a presença de disco foi investigada considerando-se o nível de radiação UV ambiente, provindo das estrelas do tipo O na associação. Resultados compatíveis com o fenômeno de trancamento pelo disco foram verificados para estrelas em regiões com baixa incidência de radiação UV, mas nenhuma relação com significância estatística foi verificada entre a rotação e a presença de disco para estrelas em regiões com alta incidência de radiação UV. Isso sugere que estrelas de massa muito grande podem ter um importante papel na regulação das propriedades rotacionais de estrelas pouco massivas em sua vizinhança.

Palavras-chave: Formação de Estrelas, Objetos Estelares Jovens, Rotação de Estrelas, Momento Angular, Variabilidade Fotométrica

We thank Dr. Bo Reipurth for kindly providing us with the WFCAM/UKIRT dataset used in this work.

This study has made use of NASA's Astrophysics Data System Bibliographic Services. This research did extensive use of TOPCAT software (Taylor 2005), of Python 2.7 and Python Libraries such as Numpy, Astropy, and Scypy, and of IDL 7.

The analysis and results presented in Chapters 3.4, 4 and 6 have been accepted for publication in the Astronomy and Astrophysics (A&A). The preliminary results presented in Section 2.3.4 and Chapter 5, will be the subject of a second paper in preparation.

This thesis was granted by the Conselho Nacional de Desenvolvimento Científico e Tecnológico (CNPq) and by the Coordenação de Aperfeiçoamento de Pessoal de Nível Superior (CAPES).

Acknowledgements

Agradeço a todas as pessoas que de alguma forma fizeram parte da minha rotina nos últimos 4 anos. Em especial, agradeço à minha família: minha mãe, Maria, minha irmã, Flávia e à Sônia, pelo apoio às minhas escolhas que me trouxeram até aqui. Je remercie Joan, pour sa complicité, son encouragement et pour completer ma vie d'une façon si unique.

Aos meus orientadores: Agradeço à Sílvia pela orientação e pela paciência, por todo o aprendizado que me proporcionou, e pelo grande exemplo que ela é, como mulher e cientista. Agradeço ao Luiz Paulo, por tudo o que me ensinou e principalmente pela ajuda nas partes mais maçantes deste trabalho. I also thank Jerome, for receiving me at IPAG, for his valuable advices that were fundamental for the development of this work, and for the opportunity to be hosted by the Odyssey group during my stays in France.

Agradeço à Bonnie, Alana e Tati, pela amizade e pelas infinitas discussões sobre o sexo dos anjos, sobre de onde vem o momento angular do universo, sobre extraterrestres e o Acre, sobre o quão ineficiente é pegar o interno pra fazer o caminho da Avenida Antônio Carlos até o ICEx ou sobre alguma fruta ou erva que a Alana jura que é comestível, mas que todo mundo acha que ela inventou.

Agradeço ao querido Mário Sérgio, pela sua amizade e companheirismo e à Famiglia. Ao Saulo pela amizade e pelas tantas vezes em que calorosamente me recebeu em Paris. Ao Guilherme por ser um porto seguro fora do mundo dos físicos.

Agradeço também aos colegas de laboratório e depertamento por todos os momentos divididos durante os dez anos em que fui parte do Departamento de Física. À Stela, Francisco, Nathália, Amanda, Gustavo, João, Guga, Fábio, e todos que fizeram parte da minha história no Laboratório de Astrofísica. À Bárbara, Cobra, Ana, Gabriel e Luiz. À Shirley, responsável por tornar a biblioteca do departamento um lugar tão querido.

To all the friends I made at IPAG and Grenoble: Victor, Isadora, Susmita, Ritam, Laura, Kike, Ricardo, Aline, and Riccardo. Obrigada! Dhonyobad! Gracias! Grazie! Merci! Thank you all for the multicultural cousine nights (and for the weird food you made me eat), and for enriching my horizons with random knowledge from different cultures. Also, merci Simon, de m'avoir montré que si j'étais capable de réussir des mortelles randonnées, toutes proches d'abimes de plus de mille metres de profondeur, finir mon doctorat serait une tâche facile.

Contents

List of Figures

List of Tables

List of Abbreviations

2MASS	Two Micron All Sky Survey
BD	Brown Dwarf
CASU	Cambridge Astronomy Survey Unit
CC diagram	Colour-colour diagram
CygOB2	Cygnus OB2
DR8	Data Release 8
EUV	Extreme ultraviolet
far-IR	Far-infrared
FUV	Far ultraviolet
GDW15	Guarcello et al. (2015)
GTC	Gran Telescopio Canarias
IPHAS	Isaac Newton Telescope Photometric Halpha Survey of the Northern Galactic Plane
IRAC	The Infrared Array Camera
ISM	Interstellar medium
LM	Low Mass
mid-IR	mid infrared
MS	Main Sequence
OIR	Optical and Infrared
OSIRIS	Optical System for Imaging and low-Intermediate-Resolution Integrated
PSC	Point Source Catalogue
RL-statistics	Rope-Length statistics
SDSS	Sloan Digital Sky Survey
AM	Angular Momentum
CTTS	Classical T Tauri Star
CCD	Charge-coupled device
CM diagram	Colour-magnitude diagram
DM	Distance Modulus
DANCe	Dynamical Analysis of Nearby Clusters
FAP	False Alarm Probability
FOV	Field of View
GDW13	Guarcello et al. (2013)
GMC	Giant Molecular Clouds
HR diagram	Hertzprung-Russel diagram
IR-excess	Infrared excess
KS	Kolmogorov-Smirnov
LSP	Lomb-Scargle Periodogram
MIPS	Multi-Band Imaging Photometer
near-IR	near infrared
ONC	Orion Nebulae Cluster
PMS	Pre Main Sequence
ptp	peak to peak
rms	root main square
SED	Spectral energy distribution

SL-statistics	String-Length statistics
TTS	T Tauri star
UKIRT	United Kingdom Infrared Telescope
VLM	Very Low Mass
WTTS	Weak-line T Tauri Star
ZAMS	Zero age main sequence
S-statistics	Saunders-Statistics
UKIDSS	UKIRT Infrared Deep Sky Survey
UV	Ultra Violet
WFCAM	Wide Field Camera
YSO	Young Stellar Object

Chapter 1

The early evolution of low mass stars

1.1 Introduction

The angular momentum evolution along the early stages of the life of a star, is a fundamental question currently under debate (e.g., Bodenheimer 1995; Jappsen & Klessen 2004; Bouvier et al. 2014) in stellar astrophysics. The angular momentum is a fundamental stellar parameter and together with the stellar mass and initial composition, it influences directly the stellar structure and its subsequent evolution. The instantaneous rotation rate of a star is connected with its magnetic activity, with mixing and convection inside the star, and it is also related to stellar winds. Several physical processes, as the origins of ultraviolet excesses, of X-ray excess, and the formation of surface spots are also related to the stellar rotation. Understanding the angular momentum evolution of low mass stars may also give us clues about the formation of solar analogues (stars with the same fundamental properties to the Sun), and of planets around them.

At the end of the protostellar phase, the young stellar object formed is composed by a young central star and a circumstellar disc. During the first million years of pre main sequence evolution, the young low mass star and its disc interact through the stellar magnetic field. As a consequence of this interaction, the mass accretion process occurs, and the star acquires mass initially stored in the disc. After the mass accretion phase is over, the disc dissipates in a process thought to include the formation of planets. All these processes are responsible for modifying the stellar angular momentum. These processes also produce light variations in all parts of the spectra, from radio to X-ray, in time-scales from hours to years. Since the first studies about young stars (e.g., Joy 1945), this variability was recognized as one of the main characteristics of stars in the pre main sequence. Mapping the stellar variability in different spectral ranges is a powerful tool to understand the ongoing physics in such young stars and in their environments.

In this doctoral thesis we investigated some aspects related to the near-infra-red photometric variability of young stars in the Cygnus OB2 association. The questions we investigated are: What are the main near-infra-red variability properties of young stellar objects in the Cygnus OB2 association? What can we learn about the physical processes in action from the variability analysis? Are there variability properties correlated to the disc presence? How is the rotational scenario for low mass stars in the Cygnus OB2

association?

In this first Chapter we review the main physical concepts involved in the early evolution of low mass stars. In Chapter 2 we bridge theory and observational astrophysics, and discuss the main observational tools to be used and what is the physics we can access by using such tools. In the same chapter, we also present the observational scenario for the Cygnus OB2 association, which is our observational target.

The Cygnus OB2 association is a very massive young association ($\sim$ 5 Myr), 1.33 kpc distant from the Sun (Kiminki et al. 2015). Due to its rich massive population, the association is a valuable target for studying the environmental conditions effect during the pre main sequence phase. The observational dataset analysed is presented in Chapter 3. A 0.78 squared degrees field, comprising a large fraction of the Cygnus OB2 association was surveyed for variability using 1 day cadence near-infra-red light curves. The JHK ($\sim$1.2 - 2.2 μm) light curves were obtained using the Wide Field Camera (WFCAM) installed at the United Kingdom Infra-red Telescope (UKIRT), in Manua Kea, Hawaii. The main target of the analysis was a list of 5083 Cygnus OB2 candidate members, extracted from previous studies in the literature. Data from public photometric surveys in several wavelengths were also considered in the study, and at the end of Chapter 3 they were used to estimate stellar parameters for the candidate members.

The time series analysis techniques applied to the observed light curves are presented in Chapter 4. A series of Monte Carlo simulations were performed in order to evaluate the limitations of the dataset and techniques used. In Chapter 5 the main results of the variability survey are presented, and the possible physical processes producing the variability are discussed. In Chapter 6, a sub sample of variable stars which present periodic variability that may be reflecting the stellar rotation is analysed. The rotational scenario for the Cygnus OB2 association is presented, and put in context. The rotational properties are then compared to environmental conditions, as the local ultraviolet radiation level, and the question: "Can environmental conditions shape the rotational evolution?" is investigated.

Conclusions and perspectives are presented in Chapter 7.

1.2 Nomenclature: low mass stars

The timescales and physical processes involved in the star formation and stellar evolution are quite dependent on the stellar mass. Accounting for that, the study of such topics is usually divided in three mass ranges: High mass stars (M$>$ 10 M$_\odot$), intermediate mass stars (2 M$_\odot$ $< M <$ 10 M$_\odot$), and low mass stars (M$<$ 2 M$_\odot$). Those mass ranges are not exact because the effective temperature, and thus spectral type, slightly varies along the stellar life. The present study focus on low mass stars (LM-stars), and all the subsequent discussion comprises only stars in this mass range.

Inside the LM-stars mass range, it is pertinent to define three mass sub-ranges. First there are the Solar-type stars (or Solar-like stars), which are stars that when reaching the main sequence (MS) will have common structural characteristics with our Sun (*i.e.* MS stars composed of a radiative core surrounded by a convective envelope). Roughly speaking, those are stars with 0.3 M$_\odot$ $< M <$ 1.4 M$_\odot$. Second, there are the very low mass stars (VLM-stars), which are stars with masses bellow the fully convective boundary

(~ 0.3 $M_\odot$), which therefore will never develop a radiative core. They have masses in the range $0.08-0.3$ $M_\odot$. Third, there are the Brow Dwarf (BDs), which are objects without enough mass to allow stable hydrogen burning. They have masses smaller than ~ 0.08 $M_\odot$, and are outside the detection limits of the observational dataset used in this study.

1.3 A brief summary of star formation

Stars are formed from molecular gas - mainly hydrogen - available in the interstellar medium (ISM). Most of such gas is concentrated in molecular clouds, which are the densest regions in the ISM, and are localized mainly in the Galaxy spiral arms. Giant complexes of gas, the Giant Molecular Clouds (GMC), have masses around $\sim 10^6$ solar masses ($M_\odot$), sizes of 100 parsecs (pc), and highly hierarchical structures that go from the cloud size to the Jeans length[1](Hartmann 1998). GMC are cold ($\sim$10 K) and have a typical column density of $\sim$100 $M_\odot pc^{-2}$. The gas density inside a GMC can vary several orders of magnitude, with median values of 20 molecules of H_2 per cm^3 for the whole cloud, but it can reach up to 10^5 H_2 molecules per cm^3 for pre-stellar cores (Williams et al. 2000; Larson 2003; McKee & Ostriker 2007, and references therein). The cooling of such clouds is mainly due to the emission of radiation in the far-infrared (far-IR) from molecules like CO (McKee et al. 1982; Gilden 1984). Because of that, one of the way those clouds can be observed is by using emission lines from CO and its isotopes.

Since star formation itself is not the scope of this thesis, the subject will be only briefly summarized here. The focus will be the main physical processes involved in star formation, and we will not explore the research being developed around it. If the reader is interested in a deeper description of the star formation observational scenario and in the models proposed to explain it, or in the many open issues regarding star formation (for example, the particularities of the cloud collapse and fragmentation), we refer to some more specialized literature (e.g. Hartmann 1998; Williams et al. 2000; Larson 2003; McKee & Ostriker 2007; Maeder 2009; Stahler & Palla 2005, and references therein).

Star formation starts when the self-gravity of some parts of the cloud overcomes the cloud magnetic fields, turbulence and the thermal forces and the cloud enters gravitational collapse. What triggers this gravitational collapse is not yet fully understood, but some possible triggers could be a shock wave from a nearby supernova, or a collision with another cloud. The condition for a cloud to collapse can be expressed in terms of the Jeans mass, which behaves as $M_J \sim T^{\frac{3}{2}}\rho^{-\frac{1}{2}}$. When the collapse starts, according to the virial theorem, gravitational potential energy is converted in thermal energy. At this stage, the contracting cloud is still optically thin, and the thermal energy generated in the collapse can be radiated efficiently, and hence the collapse is initially isothermal. As the density in the contracting cloud increases, the Jeans mass diminishes, and some cloud fragments start collapsing by themselves. Initially, this collapse is very non-uniform, which causes the rapidly growing of a denser core in the centre of the collapse (e.g., Larson 1969). Fragmentation continues as long as the energy from the cloud contraction can be radiated away. When the core becomes

[1]Jeans length is the minimal size for a cloud, of given temperature and density, starting from which the thermal forces are overcome by gravity resulting in the cloud's gravitational collapse.

dense enough, the material becomes opaque, and the thermal radiation produced in the contraction is kept in the core, increasing the central temperature. The fragment contraction then becomes adiabatic and both pressure and temperature in the central part start increasing (Maeder 2009). All this process happens in a timescale of 0.1 Myr (Garcia et al. 2011), and after that the protostellar phase begins.

Due to the existence of some fossil angular momentum (AM) in the progenitor cloud, only the low AM material will collapse towards the centre of the collapse. The majority of the cloud mass, by having high AM, is prevented from collapsing towards the centre unless it loses several orders of AM in the process. Instead, the material goes first to centrifugally supported disc: Assuming that the contracting material is spherically symmetric, and making its rotation axisymmetric, then the momentum flux of the infalling material (perpendicular to the equatorial plane) on each side of the equator will have the same magnitude, but will be opposite in direction. The result is that the infalling material will suffer a shock when it reaches the equatorial plane, dissipating kinetic energy of motion perpendicular to this plane. If the shock of material is cooled quickly, the result is an accumulation of material in a thin structure in the equatorial plane, *i.e.*, a circumstellar disc (Hartmann 1998).

When the protostellar phase begins, the system is composed of a central protostar surrounded by a keplerian circumstellar disc, immerse in a residual envelope of material. At this point, a star that will have ~ 1 $M_\odot$ when it reaches the MS, has a protostellar mass of $\sim 1\%$ of its final mass (Larson 2003). The rest of the mass that will be acquired is at the circumstellar disc. The study of the protostellar accretion phase can be divided into two problems: the evolution of the protostellar interior for a known mass accretion rate, and the problem of modelling and understanding what determines the mass accretion rate (e.g., Stahler et al. 1980a,b, 1981).

With the modest initial mass, the protostar does not have central temperatures high enough to ignite nuclear reactions. At the beginning of the protostellar phase, the inner part of the envelope is still very opaque, and only the outer part radiates in the far-IR and submillimeter. Afterwards, and during almost the whole protostellar accretion phase, the radiation of the central object heats the dust in the envelope, and the radiation is re-emitted in the far-IR. When the star reaches ~ 0.2 $M_\odot$ (Larson 2003), the central temperatures are high enough to allow deuterium burning. The deuterium burning produces too much energy to be transported through radiation in an opaque medium, hence convection begins at the stellar interior (Stahler & Palla 2005).

During the protostellar accretion phase, which has a duration of a $\sim$1 Myr, the star accretes mass from the envelope and from the disc at a typical rate of $\sim 10^{-6}$ $M_\odot$/yr (Hartmann 2009). As the material available to be accreted becomes scarce, this mass accretion rate drops drastically. By the end of the protostellar accretion phase, most of the material around the star was accreted or ejected, and emission from the forming star is shifted towards shorter wavelengths. At this point, the object is denominated as a pre main sequence star (PMS) and it can be placed in the Hertzprung-Russel diagram (HR-diagram) - which is a plot of luminosity as a function of effective temperature - in a region named *birthline*[2]. The birthline, the zero age main sequence (ZAMS), and the pre and post MS evolutionary track for a $1M_\odot$ star are shown in

[2]Birthline is the region in the HR-diagram a star occupy when it first became optically visible.

Figure 1.1, which was extracted from Stahler (1983).

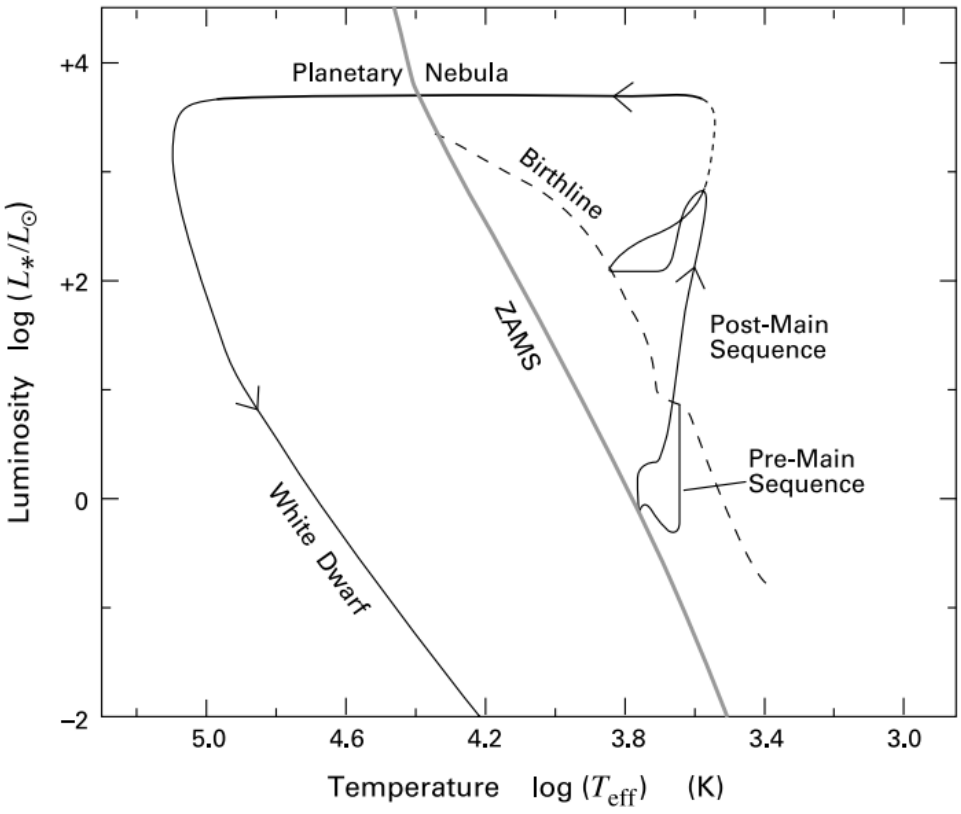

Figure 1.1: Theoretical HR-diagram showing the evolutionary track of a $1M_\odot$ star (continuous black line). The birthline is shown as a dashed line, and the ZAMS is shown as a grey line. The grey solid line. Figure extracted from Stahler & Palla (2005).

Because protostars are highly extincted at the optical and IR wavelengths, it is very difficult to study the accretion process in this phase. Because of that, most of what we know about accretion is based on observations of the accretion process during the PMS.

1.4 Pre Main Sequence evolution

PMS stars are objects in hydrostatic equilibrium, slowly contracting towards the zero age main sequence (ZAMS). The maximum radius a PMS star will have is the radius it has at the end of the protostellar phase, hence the birthline can be seen simply as the locus in HR-digram occupied by PMS stars with a protostellar radius. Starting on the birthline, PMS LM-stars contract in a nearly homologous way, with almost constant effective temperature (Stahler & Palla 2005). As they are contracting, their luminosity diminish, and because of that, they initially evolve in the HR-diagram describing nearly vertical lines for constant temperature and varying luminosity. These vertical lines are called Hayashi tracks (Hayashi 1970), and they are the location of the fully convective stars in a HR-diagram. The specific location of this line in the HR-diagram will depend on the mass of the star, but it is always above the location of the MS (see Section 2.3.1).

In the case of Solar-type stars, when the interior opacity diminishes to the point that radiation becomes an efficient way of transporting energy, a radiative core develops, the effective temperature starts increasing

and the star leaves the Hayashi track and starts describing a more horizontal path in the HR-diagram (Stahler & Palla 2005). In the case of VLM-stars, conditions for the development of a radiative core can not be achieved, and the star will spend its whole PMS phase in a Hayashi track. The PMS star contraction continues until the central temperatures are high enough to ignite hydrogen (via p - p chains). After that, the star thermal forces can finally balance the gravitational forces, braking the contraction, and the star becomes a zero age main sequence (ZAMS) star.

At the beginning of the PMS phase, even though the major accretion phase is over, a circumstellar disc made of dust and gas still exists, and episodic mass accretion is still observed. The most accepted models explaining the mass accretion from the disc to the star are the magnetospheric accretion models (e.g. Koenigl 1991a; Collier Cameron & Campbell 1993; Shu et al. 1994). In such models, a star-disc interaction happens through the stellar magnetic field lines that intercept the disc, and the mass accretion from the disc to the star is a by-product of such interaction.

Observational studies (e.g. Johns-Krull 2007) suggest that most classical T Tauri stars (young low mass stars with a disc, see Section 1.4.1 for a formal definition) are covered by few kilogauss magnetic fields. These strong magnetic fields are able to truncate the disc at a distance from the stellar surface where the magnetic pressure balances the gas pressure. The radius where the truncation happens is denominated truncation radius (r_T), and it is localized at a few stellar radii from the star.

The stellar magnetic field reach regions in the disc farther away from r_T, and interact with material in the inner part of disc. The material in the inner disc is partially ionized, and the ions couple to the magnetic field, carrying with them some neutral material. In the innermost parts of the disc, the temperatures are too high for dust to survive, and dust grains are sublimated up to a radius called dust destruction radius. At the edge of this radius, there is a wall of dust capable of radiating the energy it absorbs, an this radiation accounts for much of the near-IR excess observed in young stars.

As the field lines are rooted into the star, they rotate with the same rotational velocity as the star itself. Another important distance parameter in this context is the co-rotation radius (r_C), which is the radius at which the rotational velocity of the material in the disc is the same as at the stellar surface. As the disc is in Keplerian rotation, inside r_C, the disc material rotates faster than the star, and outside of it, it rotates slower. For material inside the co-rotation radius to be accreted, it must loose AM. The material in the disc can loose AM through some mechanism of transference of AM to the ISM, or through AM transport inside the disc. Some of these mechanisms will be discussed in Section 1.5.

The idea behind the AM transport inside the disc can be understood with a very simple model. One can assume that the disc is composed of several concentric rings. Since each ring describes keplerian rotation, material in the inner rings rotates faster than material in the outer rings. Due to friction, the inner rings will tend to spin up the outer rings by transferring AM to them, while the inner rings themselves spin down. The decelerated material will therefore move inward, and accelerated material will move outward. As friction is required for the AM transfer to occur, and as friction dissipates energy, the net gravitational energy must decrease, producing an inward net motion of mass in the disc (Hartmann 1998). As friction is required for this process to occur, models explaining accretion based on AM transport in the disc require the existence

of viscosity in the disc (e.g., α-model of viscous accretion disc such as Ghosh & Lamb 1979).

Mechanisms of transference of AM out of the star-disc system include stellar and disc winds and jets, and models for such process will be discussed in details in Section 1.5.

Another condition for accretion to occur is the relative position of r_T and r_C. If $r_T < r_C$, the inner disc rotates faster than the stellar magnetosphere, then when the inner disc interacts with the magnetosphere it loses a bit of AM, and accretes into the star. If $r_C < r_T$, then the star would rotate faster than the inner disc, and the star-disc coupling would transfer AM from the star to the disc. With the extra AM and the centrifugal forces, the material would be propelled outward (Details about stable accretion and propeller regimes can be found in the recent review by Romanova & Owocki 2016). When the conditions in the disc favour accretion, ionized material from the inner disc can couple to the field lines and be accreted into the star through funnel flows along the magnetic field lines. The structure of such funnel flows can be very complex, and it is dependent upon the mass accretion rate, the magnetic field topology, and on the inclination of the magnetic field axis compared to the stellar rotational axis (e.g. Romanova et al. 2004; Johnstone et al. 2014). The accreting material reaches the stellar surface at essentially free-fall velocities, creating a shock region in the stellar surface. In these shock regions, the gas reaches very high temperatures and strongly emits soft X-ray radiation. Most of this X-ray radiation is absorbed by the accretion columns and re-emitted as UV radiation. The shock region at the base of the accreting funnel is observationally seen as a hot spot, or hot annulus. The size and shape of these hot spots will depend on the tilt of the magnetic axis compared to the rotation axis (Romanova et al. 2004). When the material reaches the inner disc, some of the incoming matter may be caught in the rotating field lines and ejected perpendicular to the disc, forming bipolar jets of outflowing material and AM (e.g. Lovelace & Romanova 2004), while the rest is funnelled to the stellar surface.

Figure 1.2 was adapted from Romanova & Owocki (2016) review on the subject of accretion process, outflows and winds, and it sketches the main features of the magnotospheric accretion models that we mentioned.

As the material available in the disc is finite, discs eventually dissipate, and the accretion process and the star-disc interaction cease. Even though the star-disc interaction is very important for disc evolution, it is not the only important physical process dictating the disc dispersal. Other important mechanisms contributing to disc dispersal are the effects of stellar winds, the close encounters inside a dense cluster environment, the gas and dust acquired by planets in formation, and the photoevaporation by high energy radiation such as UV and X-ray. Hence, it is important to notice that the timescales for the duration of the star-disc interaction and that for disc dissipation are not the same. While the first one is important for understanding the stellar AM evolution (Section 1.5), the second one is fundamental for constraining planet formation theories. There is a known spread in both star-disc interaction and disc-dispersal timescales. Herbst & Mundt (2005), for example, by studying the rotational evolution of PMS stars, suggested that the star-disc interaction has a duration of 1 to 5 Myr. Other author suggest larger values, Fedele et al. (2010), for example, suggest that the inner disc dissipates, and the accretion process ceases in timescales of 1 to 10 Myr. Observationally, discs lifetimes are commonly studied by investigating the disc fraction in a coeval population. When studying

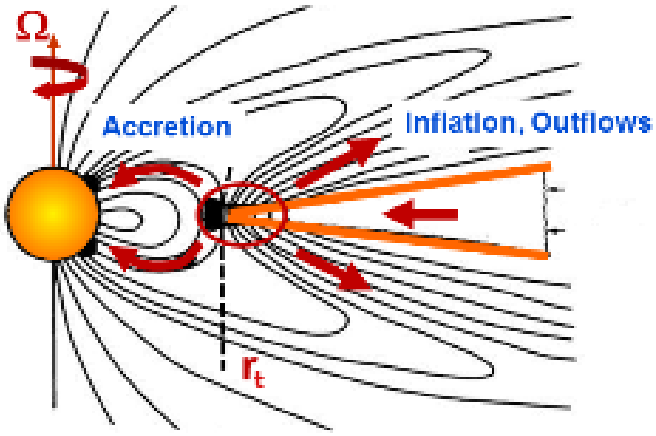

Figure 1.2: Sketch showing the star-disc magnetosphere interaction. Matter of the inner disc is accreted into the star through closed magnetic field lines forming funnel streams. Field lines of the external layers are twisted, due to differential rotation between the star and some parts of the disc, and they inflate and even disconnect, allowing material outflow and winds. Figure adapted from Romanova & Owocki (2016).

coeval populations with ages in the range 0.5 - 30 Myr, Haisch et al. (2001) found that one-half of the stars in a cluster population kept their discs until about 3 Myr, and that with ∼6 Myr the majority of the stars had lost their discs. (Fedele et al. 2010). Long-lived discs also exist, and can have a maximum lifetime of about 10 - 20 Myr (Bell et al. 2013).

Disc erosion due to high energy radiation can happen due to radiation generated by the parent star itself (e.g. Clarke et al. 2001; Hollenbach & Gorti 2005; Gorti et al. 2009), and Clarke et al. (2001) suggested that this phenomenon can erode a disc in a timescale of ∼ 10 Myr. Disc photoevaporation can also happen due to the radiation field generated by high mass stars in the vicinity of the disc-bearing star (e.g. Johnstone et al. 1998; Adams et al. 2004). For example, Guarcello et al. (2016) found in their observational study for the Cygnus OB2 association that the disc-fraction decreases up to 20% in the vicinity of high mass stars in the association. As the Cygnus OB2 association is the observational target of this thesis, the disc photoevaporation due to the radiation field of massive stars will be discussed again later in the text (Section 6.3.2).

1.4.1 T Tauri stars

When a LM-star becomes visible, it is identified as a T Tauri star (TTS). This class of stars were first observationally studied by Joy (1945), who recognized on the prototype star, T Tauri, a new class of variable stars. TTS have spectral types between F and M (effective temperatures in the range 3000 - 7000 K), low optical luminosity (∼0.01 - 10 $L_\odot$), and are usually found in association with dark or bright nebulosities. They also have Hα emission lines, and can present highly irregular short term variability of several magnitudes. Their variability can have timescales from seconds to decades (e.g. Kurosawa & Romanova 2013).

Walter (1986) divided TTS into two groups: the "classical" T Tauri stars (CTTs), and Naked T Tauri stars, that were later called "weak-line" T Tauri stars (WTTs) by Ménard & Bertout (1999) who spectro-

scopically characterized this class of stars. CTTs are still accreting from their circumstellar discs. Due to the shock of the accreting material in the stellar surface, they have large UV excess with respect to the photosphere and continuum veiling. The circumstellar discs are still optically thick, hence CTTs also have large infrared (IR) excess (e.g., Lada & Wilking 1984). They have strong Hα emission lines originated in the accretion funnels, stellar winds and chromospheric emission (e.g., Kurosawa et al. 2006), they present moderate hard X-ray emission arising from their coronal activity (e.g., Favata et al. 2005), and starspot modulation (e.g., Vrba et al. 1988). WTTs are no longer accreting. Even so, a thin disc in process of dissipation is still present, and it produces small infrared excess (e.g., Lada & Wilking 1984). Strong X-ray emission (e.g., Favata et al. 2005) is also observed, and it is thought to come from magnetic field lines reconnection events, and from coronal flares (Section 2.2.1.5). They have moderate Hα emission, arising from the chromospheric emission.

Initially, the distinction between CTTs and WTTs was based in the equivalent width of the Hα emission line such that if the equivalent width was lower than 10 Å, then the star was classified as an WTTS, otherwise it was a CTTS (e.g. Ménard & Bertout 1999). Modern classification schemes consider that the Hα equivalent width threshold increases with spectral type due to the decrease of the photospheric continuum level close to the Hα line in cooler stars, and different threshold are considered for different spectral type ranges (e.g., White & Basri 2003; Fang et al. 2009).

There is a general belief that WTTs are evolved CTTs, after the accretion and the star-disc magnetic interaction has ceased. This does not mean, however, that WTTs will always be older than CTTs, as the transition from CTTs to WTTs depends on the disc evolution timescale, and this timescale varies from star to star. Accordingly, in a coeval population one should expect to find both CTTs and WTTs with similar ages as a result from the spread in the disc evolution timescale.

1.5 Angular momentum evolution

In the early evolution of a LM star, the mass acquired during the mass accretion phase and the gravitational contraction are responsible by changes in the inertia momentum of the star. If AM conservation was the sole responsible for the early rotational evolution, PMS stars should reach their first few Myr with spin rates close to critical values (when the centrifugal forces balance gravity). On the other hand, observations mapping rotational velocities of TTS found that their typical rotational velocities are only a fraction of their critical velocities (e.g. Vogel & Kuhi 1981; Bouvier et al. 1986a, and Section 2.5). This suggests that there must exist ongoing physical mechanisms on such stars that counteract the spin-up expected from stellar contraction and accretion.

1.5.1 Physical processes modifying the stellar angular momentum

The AM of a forming star is determined both by internal and external physical processes. Internal processes determine how AM is transported in the stellar interior. External processes are responsible for the AM exchange with the stellar surface, and models for such processes include the magnetic star-disc

interaction, accretion-powered stellar winds, and mass ejections.

To constrain the physical models, recent studies have been looking for correlations between stellar rotation rates and other stellar parameters, such as the stellar mass. A summary of the main observational results in the field will be presented in Section 2.5.

1.5.1.1 Star-disc interaction

The "disc-locking" scenario is based on the observational evidence that accreting stars are on average slower rotators than non-accreting stars (e.g. Rebull et al. 2004; Cieza & Baliber 2007). Inside this context, PMS stars still magnetically interacting with their discs would be prevented from spinning-up via star-disc interaction, despite the fact that they are contracting towards the ZAMS and accreting. Consequently, they would remain with almost constant rotational velocity during their first few Myr.

Following the pioneer work by Koenigl (1991b), models for rotational evolution of young stars prior the 2000s rely on the star-disc magnetic interaction to explain the disc-locking state. Most of the so called "disc-locking models" (as is the case of Koenigl 1991b) are based on the Ghosh & Lamb (1979) paradigm of a dipolar magnetic field interacting with a circumstellar disc. In such models, the field lines of a kilogauss magnetic field would be anchored to the disc: the field lines around r_C would act on braking the star that should be spinning up due to mass accretion and contraction. As regions in the disc outside r_C rotate slower than the star, the field lines anchored outside r_C would act on spinning-down the star. In the other hand, as regions in the disc inside r_C rotate faster than the star, they would act on spinning-up the star. The torque produced by the magnetic interaction with fast rotating parts of the disc would be counteracted by the torque produced by the interaction with slow rotating parts of the disc, and the net torque into the star would be null.

One of the modern critics to the disc-locking models is that in a rotating magnetic star, due to differential rotation between the star and regions of the disc outside r_C, the magnetic field lines become highly twisted in the azimuthal direction (This is illustrated in Figure 1.2), which causes an inflation and opening (disconnection) of the field lines. This effect prevents the star to get anchored in a large region of the disc, reducing the spin-down torque from the disc into the star (e.g. Matt & Pudritz 2005; Matt et al. 2010).

Recently, with the observational studies on the magnetic field topology by Donati (2011) and Gregory et al. (2012), it was shown that the dipolar component of the surface magnetic fields in CTTs were not as intense as required by disc-locking models to brake the star, and that the magnetic field of such stars is dominated by multipoles components of higher order.

A second class of disc-locking models, initially proposed by Ostriker & Shu (1995) for a dipolar field, is the X-wind model. In such models, material accreted from a small region in the disc denominated X-region, and localized at $r_C > r > r_T$, is in an equilibrium state such that no torque is felt by the accreting star.

Matt et al. (2010) developed a AM evolution model for a solar-type star and considered the torques expected according to disc-locking models. Their results suggested that the disc-locking process is not sufficient to explain alone the observed spin rates in young stars, and that other phenomena such as magnetic winds should be considered as additional physical phenomena draining AM during the PMS.

1.5.1.2 Stellar winds and magnetospheric ejections

The spinning up expected from stellar contraction and mass accretion can be efficiently counteracted if there are strong stellar magnetized winds able to carrying AM out (e.g. Hartmann & Stauffer 1989; Matt et al. 2012). The amount of AM released by stellar winds will increase with the mass loss rate and with the magnetic field strength, and in principle these models can overcome the weak dipole component problem by having higher mass loss rates. However, such higher mass lot rates would require very strong large-scale magnetic fields (Zanni & Ferreira 2011) and the observed values (Donati 2011; Gregory et al. 2012) are only close to the minimum required.

AM can also be extracted through magnetic ejections (e.g. Romanova et al. 2009; Zanni & Ferreira 2013), which are caused by the expansion and reconnection of field lines that connect the star to the disc (the same phenomenon that reduces the effect of the disc-locking). This phenomenon contributes to regulate the star rotational period in two ways (Zanni & Ferreira 2013): First, AM is extracted from the disc, close to r_T, reducing the accretion torques (which would spin-up the star). Second, if the ejected plasma rotates slower than the star, then the ejections efficiently extract AM directly from the star. Magnetic ejection models such as the one presented by Romanova et al. (2009) suggest that the outflow of matter happens in two components: one that originates close to the inner edge of the disc and has a conical shape, called "conical"-wind, and a second one called jet which is a magnetic driven ejection from an extended disc region flowing along the magnetic field lines.

In the already mentioned X-wind models, outside the X-region ($r > r_C$), material carrying AM is sent away via magnetically driven winds, called X-winds (the X-winds are shown in the sketch of Figure 1.3). Given the observational evidence that the magnetic field of young stars may not be dominated by the dipolar component, Mohanty & Shu (2008) generalized the X-wind model for multipole fields.

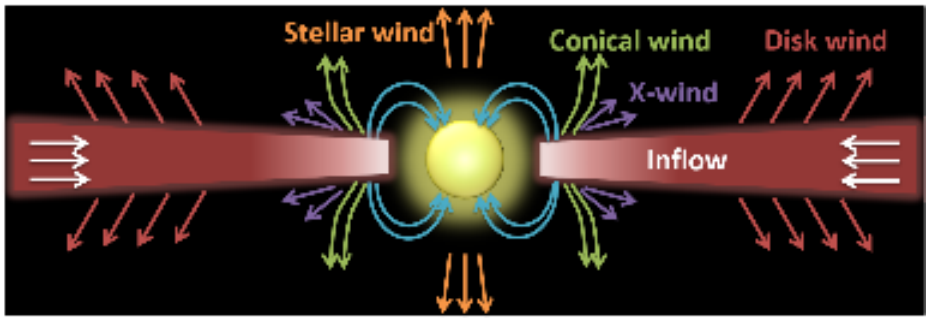

Figure 1.3: Sketch showing the physical processes influencing the AM evolution of accreting magnetized stars. Accretion funnels are show as blue arrows; the conical winds are shown as green arrows; the X-wind, as purple arrows; the disc winds, as red arrows; and the stellar winds as orange arrows. The inward flow of matter expected in a keplerian viscous disc is shown as white arrows. Figure extracted from Romanova & Owocki (2016).

While none of such models are capable of explaining alone the slow rotational velocities observed in PMS stars, the real scenario may be a combination of the contribution of the physical processes proposed in several models, and the formation of binary stars and planets. Figure 1.3, extracted from the Romanova & Owocki (2016), sketches the several physical processes influencing the AM of accreting magnetized stars.

1.5.1.3 Angular momentum transport in the stellar interior

Models describing the AM evolution of LM stars usually adopt two main classes of AM redistribution models in the stellar interior. The first one, which is adequate for describing fully convective stars (VLM-stars and Solar-type stars while they are still on Hayashi track), assumes that the redistribution is instantaneous, which is the same as assuming that the star is a rigid body. The second one is adequate for describing solar-type stars after a radiative core developed. It assumes that the stellar interior is composed by two rigid bodies: a spherical one in the core, and a shell surrounding it. The rotation of two rigid bodies can evolve independently, and large velocity gradients can develop in the layer between the two zones.

1.5.2 Angular momentum evolution models

In order to explain the observational results regarding the AM evolution of LM-stars, AM evolution models must account for the star-disc interaction during the PMS phase, for the wind braking during the early MS, and for the effect of AM redistribution in the stellar interior. They must also consider the spread on the timescale of disc evolution, which gives rise to the spread in observed rotational periods in young clusters (Section 2.5)

1.5.2.1 Solar-type stars

The Figure 1.4 shows the results for an AM evolution parametric model for solar-type stars from Gallet & Bouvier (2013). The results are for stars in the mass interval 0.9 - 1.0 $M_{\odot}$, from the beginning of the PMS ($\sim$1 Myr) until the age of the Sun (4.5 Gyr). More details about the model can be found in the original paper by Gallet & Bouvier (2013).

The models assume constant angular velocity during the phase of star-disc interaction at the beginning of the PMS. After that they use the model of magnetized wind braking proposed by Matt et al. (2012), and a model of structure with decoupling between the radiative core and the convective envelope (meaning that after a coupling timescale is passed, the two zones in the stellar interior are free to rotationally evolve independently). The period distributions for several clusters and associations were used as contour condition in these models. Models for three rotational regimes are shown: slow rotators (red), with median starting period of 10 days; medium rotators (green), with starting period of 7 days; and fast rotators (blue), with starting period of 1.4 days. The evolution model has as free parameters: the initial period, which is adjusted according to observational data from the youngest clusters; the time scale of star-disc interaction, τ_d, during which the rotational velocity is kept constant; the coupling timescale (τ_{rc}) between radiative core and convective envelope; and a calibration constant, K_1, related to the model of AM lost through stellar winds, which is fixed so the star rotational velocity is regulated to the Sun when it reaches 4.56 Gyr (age of the Sun). All the parameters are varied until the best agreement with observations is reached. The models shown in Figure 1.4 are adjusted according to the 90-th percentile of the observational period distributions for slow rotators, median percentile for medium rotators, and 25-th percentile for fast rotators.

In these models, star-disc interaction ceases at 2.5 Myr for fast rotators, and around 5 Myr for slow rotators. With the earlier release of fast rotators from their discs, by 5 Myr the lower envelope of the period

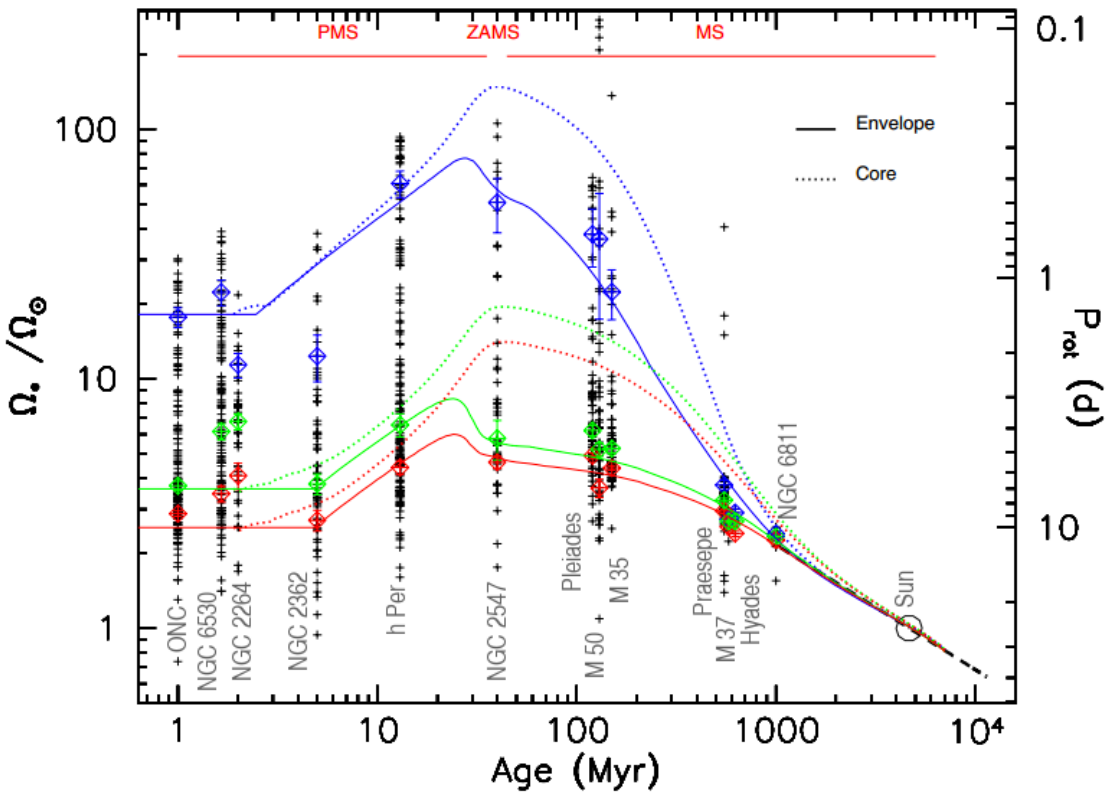

Figure 1.4: Results from the AM evolution models by Gallet & Bouvier (2013) for Solar-type stars. The rotational velocity, given in both angular velocity and rotational period, is plotted as a function of age. Period distributions for several clusters and associations are shown as black crosses. Models for fast rotators are shown in blue, medium rotators in green, and slow rotators in red. Continuous lines show the rotational evolution of the convective envelope, and dashed lines show the rotational evolution of the radiative core. The Sun is shown as an open circle, and the Skumanich relationship is shown as a dashed black line. The 90-th, 50-th and 25-th percentiles of the observational period distributions are shown as blue, green and red diamonds respectively. The name of each cluster used as contour conditions in their models is shown in grey along the cluster data.

distributions (upper envelope of rotational angular velocity distributions) has significantly spin-up. The core-envelope coupling time scales are longer for slow rotators ($\sim$ 30 Myr) than for fast rotators ($\sim$ 12 Myr). Before the core-envelope decoupling, all types of rotators behave as rigid bodies and AM is instantaneously redistributed from the stellar surface to the stellar interior. After decoupling, the star is composed of core and envelope, and while the two evolve independently, each of them behaves like rigid bodies, and the envelope rotational evolution is the same as the surface rotational evolution. As they are contracting, all types of rotators spin-up until they reach the ZAMS, after that, they start spinning down. There is a dependence on the braking rate with angular velocity, hence fast rotators are more efficiently braked than slow rotators. After the core-envelope decoupling, the radiative core keeps most of the initial AM, while the outer envelope is spun-down. This AM stored in the core, will resurface at some point. In slow and medium rotators, as the resurface of AM hidden in the core is slow, the curve of rotational evolution after the ZAMS for such objects is way flatter than for the fast rotators. Early in the MS, there is still a large spread in angular velocity,

but around 1 Gyr, all types of rotators converge to the same rotational regime, that can be described by the Skumanich relation for a star being broken by a magnetized wind, ($\Omega_* \propto t^{\frac{-1}{2}}$ Skumanich 1972).

Gallet & Bouvier (2015) extended the Gallet & Bouvier (2013) models to lower mass stars down to 0.5 $M_\odot$. They used Baraffe et al. (1998) models to study the evolution of the internal structure of Solar-type stars for different masses, and verified that the stellar radius, the stellar moment of inertia, the core moment of inertia, the core radius and the core mass increase with increasing mass, while the envelope moment of inertia decreases for higher masses. They presented models for 1.0, 0.8 and 0.5 $M_\odot$, which were computed using the same initial conditions and constraints as the models presented by Gallet & Bouvier (2013). The AM evolution for 1.0 and 0.8 $M_\odot$ are qualitatively similar. For the 0.5 $M_\odot$ model, even though the main trends in the rotational evolution are the same, the timescales of evolution are longer than for higher masses. While the disc lifetimes and initial rotation periods only slightly vary with mass, the core-envelope decoupling timescale, and the wind braking efficiency strongly increase with mass.

One of the constrains imposed by the observations to the AM evolution models is that the models must account for the dispersion in the rotation period distributions for regions with different ages. In Figure 1.4, all but two clusters have only rotational periods measured from ground-based telescopes. Affer et al. (2013) measured rotation periods in NGC 2264 using the space telescope CoRoT[3], and Meibom et al. (2011) measured rotation periods in NGC 6811 using the Kepler space telescope[4]. Note that in Figure 1.4, those are the cluster presenting the shortest rotation period dispersion among the PMS clusters, in the case of NGC 2264, and among the MS clusters in the case of NGC 6811. This suggest that large dispersions in the rotation period distribution may be a consequence of the measurement of rotation periods performed using ground-based telescopes. Due to the sparsity of space-based rotation period measurements current available in the literature, it is not possible, nowadays, to evaluate whether the dispersion in the rotation period distributions is introduced by the nature of ground-based observations or not. However, in the coming years, ongoing missions as the Kepler K2 (Howell et al. 2014), and the TESS (Ricker et al. 2014) Open Cluster Survey (TOCS) will help increasing the availability of space-based measurements of rotation periods in cluster of all ages, and the questions regarding the reliability of the dispersion in the distributions of ground-based rotation periods may be re-addressed.

1.5.2.2 Very low mass stars

Figure 1.5 shows the results for an AM evolution model for VLM-stars (0.1 - 0.34 $M_\odot$) from Irwin et al. (2011). In order to make the comparison with the models for Solar-type stars easier, we coloured the original plot from Irwin et al. (2011).

Irwin et al. (2011) model assumes initial rotational velocities constrained to the observations of ONC, the youngest population in their observational sample. As the modelled stars are fully convective, they are considered rigid bodies. A standard wind prescription is used, which assumes the saturation of AM loss at high angular rotational velocities. There are therefore two free parameter in such models: K_W and $\omega_{\rm sat}$

[3]sci.esa.int/corot/

[4]https://www.nasa.gov/mission_pages/kepler/main/index.html

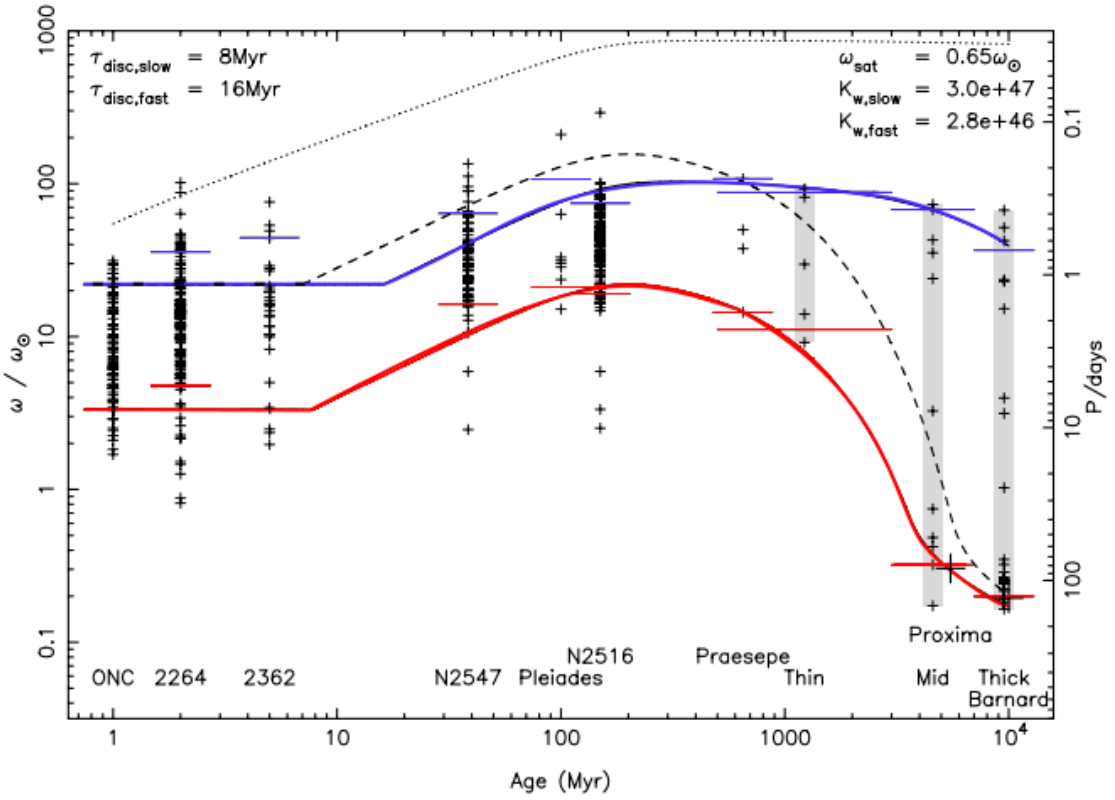

Figure 1.5: Results from the AM evolution models from Irwin et al. (2011) for VLM-stars. The rotational velocity, given in both angular velocity and rotational period, is plotted as a function of age. Period distributions for several clusters and associations are shown as black crosses (The name of each cluster used is marked in the bottom of the plot). Models for slow rotators are shown in blue, and fast rotators in red. The dotted line shows the break-up limit, and dashed lines show the rotational evolution of fast rotators in the case the K_W is assumed to be fixed as the same as in the case of slow rotators. The 90-th, and 10-th percentiles of the observational period distributions are shown as blue, and red horizontal line-segments respectively. Large bold crosses show the position of Proxima Centauri and Bernard's stars. The stars in the grey regions are field M-type stars studied by Irwin et al. (2011).

which are related to the wind model and to the saturation rate respectively. Slow and fast rotators have different initial rotational velocities and these velocities are held constant during a time $\tau_{\rm disc}$ to account for the disc-locking phenomenon. Even though observational evidence for disc-locking in VLM stars is still controversial (Section 2.5), the authors argued that disc-locking seems to be required in order to explain their slow rotation during the PMS phase. Also, the authors argued that the only way they found to fit the observational data to the models was to assume that slow rotators are released from their discs earlier than fast rotators. This is a counter-intuitive assumption, as it is in the contrary sense from what is assumed for solar-type stars, and it highlights the need for better observational constraints and physical models for the AM evolutions of VLM-stars.

The plot presented in Figure 1.5 is for a low $\omega_{\rm sat}$ model, which Irwin et al. (2011) considered to be the model that better fitted the observations.

Contrary to the Solar-type stars, in the VLM-star there is not a reference star like the Sun, with well

known mass, age, and rotational period, and the constraint of the models in the MS has to rely on field M-type stars. This constraint is problematic because there is a large distribution of periods among the field M-type stars, with periods going from 0.2-150 days (Irwin et al. 2011). This observational feature can not be explained by their models if one uses the same K_W value for slow and fast rotator models.

1.5.2.3 Models based on Monte Carlo simulations

Vasconcelos & Bouvier (2015) used semi-empirical Monte Carlo simulations to investigate the effect of the disc-locking hypothesis on the period distributions of groups of coeval stars of solar-type. They adopted a very simple evolutionary model in which accreting stars have constant rotational periods (disc-locking), and non-accreting stars conserve AM. For each model they simulated 280000 stars, and for each star they randomly assigned a mass, mass accretion rate and initial period. A mass accretion rate evolution according to an evolution equation from Hartmann (1998) was assumed, and they defined a mass accretion rate threshold for the star to be considered released from its disc. Finally, the sample of stars was evolved each from 1 to 12.1 Myr in steps of 0.1 Myr, and the results were compared to observational studies for several clusters and associations available in the literature. The comparison with observational results was done for the period distributions, for disc-fraction as a function of period, and for mass vs. period distributions. They succeeded in reproducing the scenario observed in young clusters of several ages when they started their simulations with a bimodal distribution of periods at the age of 1 Myr: disc-bearing stars rotating with periods of 8±6 days, and stars without disc rotating with periods of 3±2 days.

Following the same idea, Vasconcelos & Bouvier (2016) applied similar semi-empirical Monte Carlo simulations for groups of coeval VLM-stars. In all the observational studies they used for comparison, VLM stars rotate faster than the Solar-type stars. They considered models with and without bi-modality in the period distribution at the age of 1 Myr, but none of the models were able to reproduce all the observational constraints simultaneously.

Chapter 2

Linking observation and theory

In the last Chapter the main physical concepts involved in the early stellar evolution were discussed. We also gave a special attention to the physical mechanisms proposed as responsible for modifying the stellar AM during the early stellar evolution. In this Chapter, more practical issues are examined: Where and how does one find young stars? What it is observationally known about Cygnus OB2, the young massive association targeted by this thesis? What it is and how can one use the Hertzsprung-Russell Diagram for studying the main properties and ongoing physical processes in young stars? What is the physics behind the photometric variability in young stars?

It has been suggested that the vast majority of stars form within clusters and associations (Krumholz 2015), but while most stars are observed to be clustered at a young age, only 10% of stars are found in bound clusters by 10 Myr (Lada & Lada 2003). It is therefore a common practice to search for young stars in clusters and associations. The time-scales involved in the evolution of high mass stars are quite different from those involved in the evolution of LM-stars: A 20 $M_{\odot}$ star leaves the MS after $\sim$10 Myr of evolution (Stahler & Palla 2005), while a 1 $M_{\odot}$ spend $\sim$40 Myr in the PMS before reaching the ZAMS. Hence, finding clusters and associations harbouring high mass stars is a powerful way of identifying young regions. Given also the fact that high mass stars are very bright, and consequently easier to study than the fainter LM counterparts, their characterization can help determining clusters properties such as age and distance.

As the time-scales involved in the cloud collapse and fragmentation are very short compared to the evolutionary time-scales, it is reasonable to assume in principle that LM-stars and high mass stars that are members from the same cluster will be coeval. Studying statistical properties of a coeval populations in different evolutionary phases can help us understanding stellar properties that vary with age, as the rotational periods and the disc presence.

The observational target of this thesis is an OB association called Cygnus OB2. It harbours hundreds of O stars, and we know it is also the nursery of LM-stars, containing the largest group of young stars in the Sun's vicinity (within 2kpc) . Before switching to the subject of how to select and observationally study LM-stars, the next Section presents a general picture of the Cygnus OB2 association.

2.1 Cygnus OB2 association: the observational picture

Cygnus OB2 (hereafter CygOB2) is a very massive OB association ($\sim 1-3\times10^4$ $M_\odot$, Drew et al. 2008; Wright et al. 2010, 2015) localized in the Cygnus X complex (see Reipurth & Schneider 2008, for a review on the Cygnus X complex). When we look in the direction of the Cygnus X complex, which is at the galactic longitude $\sim 80^o$, we see projected in the sky a mix of stars and structures located in the Local Arm (∼1-2 kpc), in the Perseus Arm (∼5 kpc), and in the outer Outer Arm (∼10 kpc Rygl et al. 2012). CygOB2 would be a naked-eye cluster if it was not localized behind the Cygnus Rift, which is responsible for a visual extinction from 2^m to 5^m in the line of sight (Schneider et al. 2007; Sale et al. 2009).

The association was first discovered by Münch & Morgan (1953), who reported a possible clustering of giant blue stars in the direction of the Cygnus constellation. The first study investigating the association's morphology was made by Reddish et al. (1966), who suggested the association had an ellipsoidal shape and estimated a population of 3000 stars with 10% of OB-type stars. Later, Knödlseder (2000) used 2MASS data (Two Micron All Sky Survey; Cutri et al. 2003)[1] to compose colour-magnitude diagrams to select the association population, counting 8600±1300 members with spectral type later than F3V, and 2600±400 OB-type members, among which 120±20 should be O-type stars. He also suggested that CygOB2 was a young globular cluster, due to its huge mass, density and shape (he suggested a spherically symmetric cluster with a 2 degrees radius). This classification, however, was reviewed by Knödlseder (2003) after finding observational evidences that the association was bigger than previously thought.

CygOB2 is the closest young massive association to the Sun, and it is known for harbouring some of the brightest stars in the Galaxy. Among its rich population, there are two O3If-type stars (#7 and 22-A from Walborn et al. 2002), the peculiar B-type supergiant CygOB2#12 which is one of the most extinguished stars in our Galaxy (M_V=-10,A_V $\sim10^m$ Massey & Thompson 1991), and some Wolf- Rayet stars (e.g., WR 142a from Pasquali et al. 2002). Kiminki et al. (2015) recently reviewed its distance by studying four double-lined eclipsing binaries within the association, analysed using both photometry and spectroscopy. They found an average distance of 1.33±0.06 kpc to the association. Distances as high as 1.75 kpc (e.g., Massey & Thompson 1991) have been suggested, but the most recent distance estimated by Kiminki et al. (2015) is in accordance with the parallax distance of 1.4±0.08 kpc estimated by Rygl et al. (2012) for the Cygnus X complex, and with the distance of 1.45 kpc derived by Hanson (2003) using spectroscopy of a group of massive stars in the association. In the present work, we adopted the Kiminki et al. (2015) distance.

Wright et al. (2016), as part of the DANCe project (Dynamical Analysis of Nearby Clusters, Bouy et al. 2013)[2], used high-precision proper motions of stars in the association to investigate its kinematic and dynamic. They suggested that CygOB2 formed pretty much as it is today: a highly sub-structured, globally unbound association.

CygOB2 massive population has been extensively studied by photometric and spectroscopic studies in both optical and infra-red (e.g. Reddish et al. 1966; Torres-Dodgen et al. 1991; Knödlseder 2000; Comerón et al. 2002; Hanson 2003; Drew et al. 2008; Rauw et al. 2015; Wright et al. 2015; Kiminki et al. 2015; Wright

[1] http://irsa.ipac.caltech.edu/Missions/2mass.html
[2] http://www.project-dance.com/

et al. 2016). Nowadays, there are 169 confirmed OB-type stars (Wright et al. 2015) among the association members. Given the fact that most of the OB-type stars are still in the MS, Torres-Dodgen et al. (1991) suggest CygOB2 high mass population can not be older than around 3 Myr, and Hanson (2003) argued that the existence of a age dispersion of at least ±1 Myr was necessary to validate the membership of the O3-type star (CygOB2 #7).

CygOB2 intermediate mass population was first studied by Drew et al. (2008) with data from IPHAS (Isaac Newton Telescope Photometric Halpha Survey of the Northern Galactic Plane; Drew et al. 2005)[3], and the authors identified ∼1000 stars with spectral type between A0 and A5 in the association. They found an age of 5 Myr for such stars, adopting the 1.45 kpc distance, which is older than the age estimated for the OB-type stars (2 - 3 Myr, e.g., Hanson 2003), hence they suggest the occurrence of multiple star formation episodes in the association. Vink et al. (2008) used the same IPHAS data to study Hα emission, and together with spectroscopic data they identified 50 stars with characteristics compatible with Herbig Ae/Be, and T Tauri stars in the association.

Beyond its massive population, CygOB2 is also a valuable target for studying the environmental influence on the formation and early evolution of LM-stars and, in particular, to probe LM-star evolution in the vicinity of massive stars. In the last decade, CygOB2 low mass population has been the target of a growing number of studies (e.g., Vink et al. 2008; Wright & Drake 2009; Guarcello et al. 2012, 2013; Wright et al. 2014; Guarcello et al. 2015, 2016). Wright et al. (2010) found an age of $3.5^{+0.75}_{-1.0}$ Myr to stars in CygOB2 central region, and $5.25^{+1.5}_{-1.0}$ Myr to stars in a north-east field, when considering the LM and OB populations. Guarcello et al. (2012) used riz photometry from GTC/OSIRIS[4],to derive an extinction map of the region. Using a 3.5 Myr Siess et al. (2000) isochrone, they found extinctions between $2.64^m < A_V < 5.57^m$ for the association, and a median value of $A_V = 4.33^m$ for members candidates in the central region of CygOB2, and $A_V = 3.21^m$ for member candidates in a field at the northwest part of CygOB2. Guarcello et al. (2013) used wide and deep photometry from r band to 24 μm to unveil its disc-bearing population. As result of the Chandra Cygnus OB2 Legacy Survey[5] (Wright et al. 2014; Guarcello et al. 2015, 2016; Kashyap 2017), thousands of LM-stars that are X-ray emitters have been unveiled.

Guarcello et al. (2016) recently used the disc-bearing and non disc-bearing candidate members in the CygOB2 association to investigate the subject of the dissipation time-scale of protoplanetary discs of low mass stars in the vicinity of massive stars. They analysed the spatial variation of the disc fraction across the association, and its correlation with the local ultraviolet radiation and stellar density. They found evidence that discs are more rapidly dissipated in regions with higher stellar density and more intense UV radiation within the association. They also found that disc dissipation due to close encounters is negligible in the association, and that disc dissipation is dominated by photoevaporation.

Some of the main features of CygOB2 can be seen in the composite image presented in the top of Figure 2.1. In this Figure, Chandra X-ray data is shown in blue, and it shows the X-ray emission that may arise

[3]http://www.iphas.org/

[4]GTC/OSIRIS: Optical System for Imaging and low-Intermediate-Resolution Integrated at the Gran Telescopio Canarias: http://www.gtc.iac.es/instruments/osiris/osiris.php

[5]Chandra Cygnus OB2 Legacy Survey website: http://www.cygob2.org/

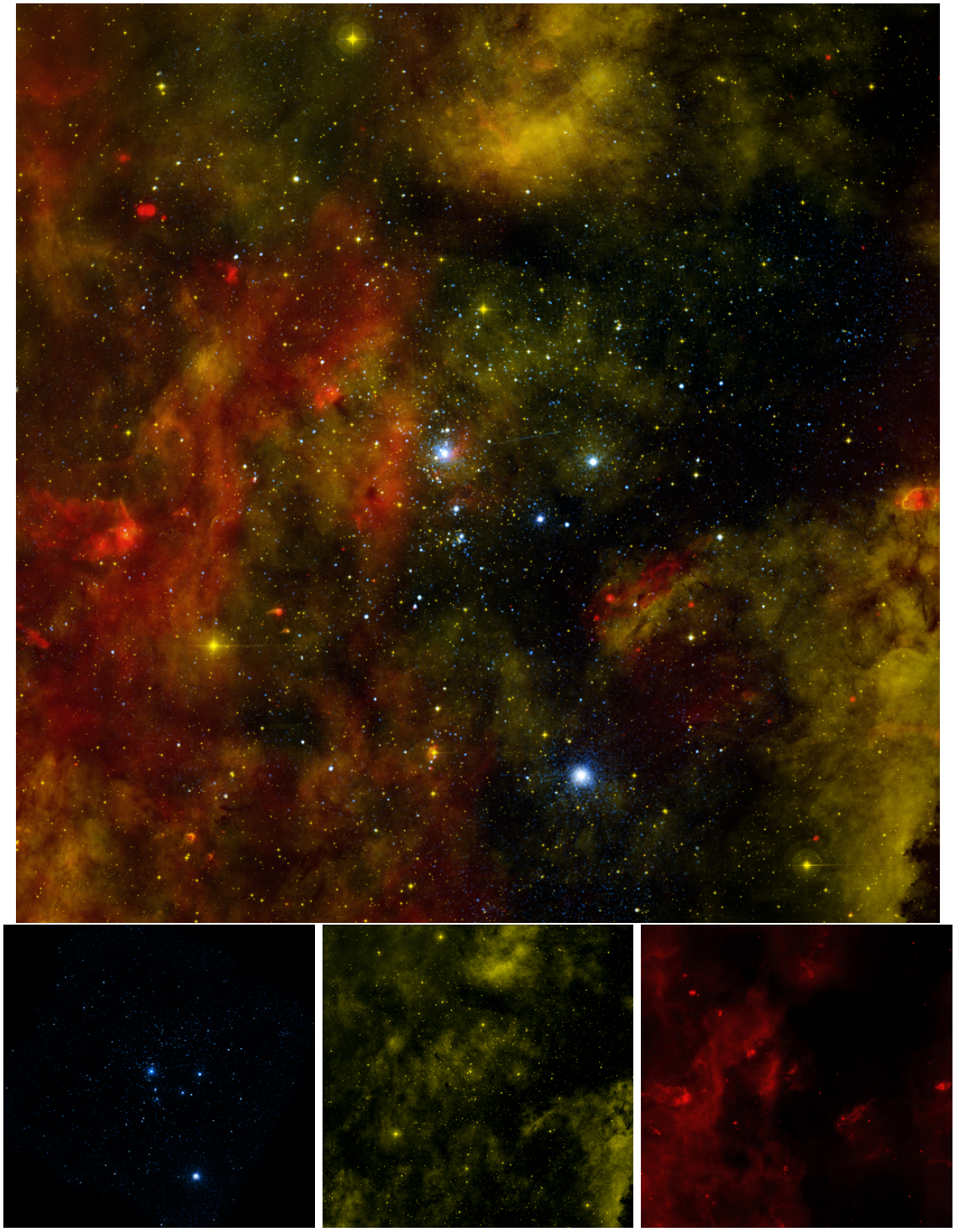

Figure 2.1: Top: composite image of the Cygnus OB2 association. Blue colours correspond to the features of an X-ray Chandra image, orange corresponds to a Hα IPHAS image, and red to a mid-IR Spitzer image. Bottom: individual images used in the composition. The original images were cropped in order to comprise the same field of view displayed in Figure 2.2. The original images were retrieved from Chandra website (CXO) X-ray: NASA/CXC/SAO/J.Drake et al, Optical: Univ. of Hertfordshire/INT/IPHAS, Infrared: NASA/JPL-Caltech.

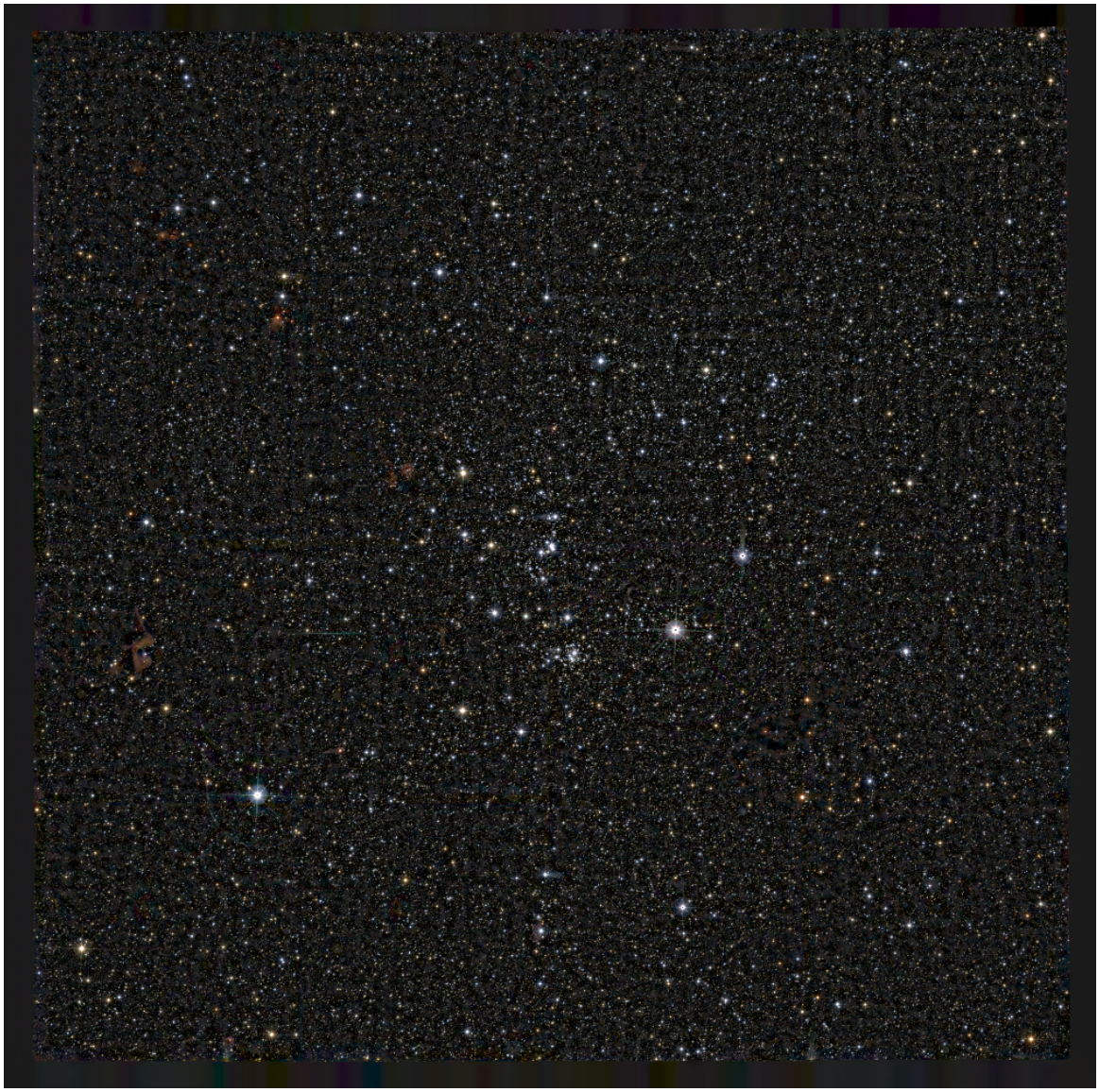

Figure 2.2: Composite image of the CygOB2 association, built from images used in the present work. The J, H, and K filters are shown in blue, green, and red respectively. More than half a million point sources could be identified in these images.

from radiatively-driven winds from massive stars, or from chromospheric emission by PMS LM-stars. The orange colour shows traces of Hα emission, which happen due to the accretion process, and due to the heating of ISM gas by stars. Finally, the red colour shows thermal emission from dust grains in the mid-IR, which is visible in both the ISM and the circumstellar environment. With all those features, this image illustrates the youth of CygOB2. The image also shows the highly variable extinction towards CygOB2, and one can see that more gas and dust are accumulated around the centre, the east and the south of the association, explaining the different median extinctions found by Guarcello et al. (2012) in the central and north-west regions. The individual images used in the composition are shown in smaller plots in the bottom of the Figure. In both Figures 2.1, and 2.2, the north direction is up, and the east is left.

The observational data used in the present study is composed of photometric images in the near-IR filters J, H, and K, taken with the United Kingdom Infra-Red Telescope. The image in Figure 2.2 is composed of J

(blue colours), H (green colours), and K (red colours) images from the observational dataset used. From the near-IR composite image, one can see by the number of resolved point sources that near-IR wavelengths are very efficient for observing stars in young regions, as these wavelengths are less affected by the interaction of the light with dust.

As can be seen from Figure 2.2, when observed in the near-IR filters, thousands of sources can be identified in the same field of view as CygOB2. These sources are composed by CygOB2 members mixed with stars in the background and in the foreground, and even non-stellar objects such as Galaxies very far away. Thereby, to study CygOB2 LM-population using such images, one must know how to identify its member population.

2.2 Identifying young stars

2.2.1 Membership evaluation techniques

Selecting a cluster's coeval population can be a complicated task. When the objects targeted are LM-stars, to evaluate a cluster or association membership is often equivalent to select PMS stars in the field of view, if one can guarantee that there is a unique young stellar population in that line of sight. In this Section, we list the main techniques for evaluating membership of LM-stars in clusters and associations, and we comment on their applicability to select the LM-population of CygOB2.

2.2.1.1 Position in the colour-magnitude diagram - reddening

As will be discussed in Section 2.3.1, PMS stars occupy a different region in the HR-diagram than MS stars, being located above the ZAMS. This can be used to distinguish between PMS population, MS stars, and non-stellar sources inside a colour-magnitude diagram. This method is susceptible to high contamination levels. For example, Barrado y Navascués et al. (2004) used colour-magnitude diagrams for optical and near-IR data to select candidate members in the λ Ori cluster, and by acquiring spectra for part of the candidate member sample, they estimated a 25% level of contamination in the sample selected via colour-magnitude diagrams.

An example of source of contamination in such diagrams is that there exist some degenerescence inside the diagrams regarding the position of young stars, and the position of some MS stars of different mass. Another source of contamination are the age spreads observed in several young regions, and modern versions of colour-magnitude membership evaluation methods try to account for that (e.g. Mayne & Naylor 2008a).

As there are other suitable methods for evaluating membership in CygOB2, this method was not used.

2.2.1.2 Infrared excesses - disc diagnosis

Due to the dusty circumstellar material around some PMS-stars, the IR-excess can be used to identify young stars. The IR-excess a disc-bearing star will present is dependent upon the disc morphology, the system geometry (*i.e.*, the inclination from which the observer sees the disc), and the disc evolutionary

status. Several different techniques for identifying disc-bearing stars are presented in the literature. More details about discs evolutionary status and the IR-excess they produce will be given in Section 2.4. Spitzer Space Telescope[6] and its IRAC[7] and MIPS[8] cameras contributed a great deal to identify disc-bearing stars (e.g. Lada et al. 2006; Hernández et al. 2007), as techniques combining Spitzer colours, and near-IR and optical colours are useful for distinguishing between real disc-bearing stars and background galaxies.

The techniques for evaluating IR-excesses were applied by Guarcello et al. (2013) to select LM-stars with discs in CygOB2. After combining optical and infrared datasets, the authors selected disc-bearing candidates by using Gutermuth et al. (2009) scheme, the Harvey et al. (2007) scheme, J-H vs H-K diagrams, reddening-free colour indices (based on Damiani et al. 2006; Guarcello et al. 2007, 2009), and the [3.6] vs. [3.6]-[4.5] diagram (Rebull et al. 2011). They found an initial list of 2703 possible disc-bearing candidates, and after cleaning it for unreliable excesses, candidate foreground stars, background giants, and extragalactic sources, they presented the final list of 1843 disc-bearing candidate stars.

We used their final list of disc-bearing candidate stars in order to select the CygOB2 disc-bearing population. After discussions with Dr. Mario Guarcello in private communication, 30 more stars were added to the disc-bearing sample. These stars were initially ruled out from Guarcello et al. (2013) disc-bearing stars list as possible contaminants, but were later selected as CygOB2 candidate members by using other criteria.

Since IR-excess is related to circumstellar material presence, this method favours the selection of disc-bearing PMS stars.

2.2.1.3 Hα line

Due to the accretion process, PMS LM-stars may show strong Hα emission (Section 1.4.1). Hα can be studied through spectroscopic or photometric surveys.

In spectroscopic surveys, Hα equivalent widths are measured with respect to the photospheric continuum and an appropriate threshold can be used to distinguish TTs from normal MS stars, and to distinguish between WTTs and CTTs. The usual threshold used is a Hα emission with equivalent width higher than 10 Å for CTTs, and lower than this value for WTTs, but as mentioned in Chapter 1, modern selection schemes consider thresholds that vary with spectral type (e.g., White & Basri 2003; Fang et al. 2009).

As CygOB2 stars suffer from high interstellar extinction (Section 3.4.1), and also due to its large extension, spectroscopic surveys of its LM population are nowadays still difficult to accomplish.

The INT/WFC Photometric Hα Survey of the Northern Galactic plane (IPHAS Drew et al. 2005) was a photometric survey that contained CygOB2 inside its field of view. IPHAS observations were taken in the r' and i' Sloan filters (Figure 2.3), and also in a narrow band filter around the Hα line (central wavelength 6568 Å). With these bands, a colour indicative of the stellar continuum, (r'-i'), can be compared with a colour (r'-Hα) which will be in excess in the case of Hα emission. Hα photometry as performed by IPHAS

[6]http://www.spitzer.caltech.edu/
[7]http://irsa.ipac.caltech.edu/data/SPITZER/docs/irac/
[8]http://irsa.ipac.caltech.edu/data/SPITZER/docs/mips/

is especially good for selecting Hα emitter candidates for follow up study. Vink et al. (2008) and Guarcello et al. (2013) used IPHAS first release to select a total of 52 possible Hα emitters in the CygOB2 field of view. Vink et al. (2008) confirmed the nature of 13 objects, through follow up spectroscopy, inside the same field of view as the present study.

As strong Hα emission is related to the accretion process, this method favours the selection of stars actively accreting from their discs. Also, IPHAS is only available for the brightest LM-stars in the sample, and accreting VLM-stars may be missed by it.

2.2.1.4 Lithium

When some part of the stellar interior reaches temperatures of ~ 2.5 MK (Soderblom 2010), Lithium is quickly depleted. *Where* in the stellar interior this will happen depends upon stellar internal structure and energy transport mechanism: in Solar-type stars this will happen in the base of the convective zone, in the most massive VLM-stars this will happen in their core, and in VLM-stars with masses smaller than about 0.06 $M_{\odot}$, the core will never get hot enough to destroy Li (Soderblom 2010). *When* Li depletion occurs depends upon the star's spectral type. According to Jeffries et al. (2014) empirical approach, the timescale for Li depletion is about $\sim$10 Myr for mid-M stars, $\sim 10^2$ Myr for K-type stars and $\sim 10^3$ Myr for G-type stars. Given those timescales, Li absorption lines give a very efficient way of selecting young M- and K-type stars.

Li is usually observed in stars as an absorption line at 6708 Å (Soderblom 2010). Because this is in the optical part of the stellar spectrum, apart from the few optical spectra obtained by Vink et al. (2008) - that covers the spectral range 4500 - 91000 Å - no membership selection based on Lithium is available for CygOB2 stars.

2.2.1.5 X-ray emission

X-ray emission is a well known marker of youth: PMS LM-stars are typically 10 - 10^4 times more luminous in the X-ray than normal MS stars (Preibisch & Feigelson 2005). The X-ray emission in both WTTs and CTTs is thought to be related to chromospheric activity due to the strong magnetic field of such objects. Observational studies suggest that X-ray emission is stronger in fully convective stars (e.g., ONC, Feigelson et al. 2003) than in stars with a tachocline (Preibisch & Feigelson 2005), but fully understanding the origins of X-ray emission in such objects it is still an open problem in astrophysics.

Since hard X-ray photons can overcome several magnitudes of visual extinction, they are a youth-diagnosis independent of biases due to the accretion process and circumstellar material (Guarcello et al. 2016). The technique also has advantages over optical-based ones since typical contaminants to these samples, as higher mass stars in the field, are not expected to be strong X-ray emitters. On the other hand, methods for selecting PMS stars based on X-ray emission rely on the existence of a strong X-ray source spatially associated with an optical and/or IR counterpart. Hence, this technique may bring a bias against faint VLM-stars.

Also, observational studies suggest that WTTs are more luminous in X-ray than CTTs (e.g. Favata et al.

2005), but the mechanism causing this difference is not yet well understood. Because of this difference in luminosity, surveys of PMS-stars through X-ray emission may favour the detection of WTTs.

CygOB2 has been targeted by the Chandra X-ray Observatory as part of the Chandra Cygnus OB2 Legacy Survey (Wright et al. 2014), which unveiled 7924 X-ray sources in the direction of the association. Guarcello et al. (2015) found that 5703 of such X-ray sources had optical and/or infrared counterparts. Using the optical and infrared photometry merged by Guarcello et al. (2015), Kashyap (in preparation 2017) classified 4864 sources as candidate members.

2.2.1.6 Periodicity and the photometric variability

Since the first studies by Joy (1945), photometric variability has been recognized as one of the main features of TTs. Among the main mechanisms causing photometric variability in TTs (Section 2.3.4) the rotational modulation by hot/cold spots in the stellar surface, and the variable obscuration due to circumstellar material (e.g. Carpenter et al. 2001; Herbst et al. 2004) can result in periodic variability. As the light modulation in such mechanisms is produced by stellar rotation, the timescales of the brightness variations will be of the order of typical rotational periods in young stars, usually from 0.5 to 15 days during the first few Myr (Rebull et al. 2004). Even though some contamination due to binary stars can exist, and if one can guarantee that there is no more than one young region projected in the same line of site, this type of variability could then be used for evaluating candidate members in a cluster or association.

2.2.1.7 Kinematic methods: proper motions and radial velocities

Kinematic methods for selecting members of a coeval population are based on variations in the star position in the sky. There are two complementary techniques for studying stellar kinematics: the study of proper motions, and the study of radial velocities. Proper motions (PM) are measurements of the variations of the star coordinates compared to the fixed background of very distant stars, it can be determined by monitoring the stellar astrometric parameters over time. If the distance to the star is known, a proper motion measurement can be transformed in the stellar transverse velocity (TV) which is the component of the star's 3D velocity in the plane perpendicular to line of sight. Radial velocity (RV) is the velocity with which the star is moving in the observer's direction. It can be determined by studying the redshift/blueshift of spectral lines in the stellar spectrum.

At the end of the process of star formation, a group of stars born from the same cloud is supposed to move together in relation to the centre of the Galaxy, presenting kinematic properties common to the parent cloud. Hence, a group of coeval stars can be distinguished from foreground and background sources due to the fact they will share the same kinematic properties.

Velocity dispersions in open clusters are usually very small. If the angular diameter of the cluster is small, it is a good approximation to say that the stars in the cluster will have the same proper motion. This way, stars with similar proper motions will likely be members of the same group (Jones 1997). In the case of OB associations, even though they are unbound, their velocity dispersions are usually small enough that on average their members will be moving towards a common point (de Zeeuw et al. 1999).

At the end of the 1990s, as part of the satellite HIPPARCOS[9] results, de Zeeuw et al. (1999) found proper motions for several OB associations within 1 kpc of the Sun's vicinity. Recent spectroscopic surveys as GAIA[10] will help cataloguing RVs in galactic clusters. Unfortunately, none of those surveys contemplate CygOB2 low mass stars, as the combination of the association distance (1.33 kpc Kiminki et al. 2015), and high extinction (Section 3.4.1) makes its low mass population too faint for such surveys.

CygOB2 high mass population had RV determined by Kiminki et al. (2007): 120 OB stars present a radial velocity dispersion of $\sigma_{RV} \sim 5 - 10$ km/s.

DANCe is a project that uses well-calibrated ground-based, wide-field exposures, taken from several optical and near-IR telescopes in the last 15 years, in order to determine proper motion for stars in nearby clusters. CygOB2 is one of the DANCe targets, and in their study about the association, Wright et al. (2016) estimated proper motions for 873 stars selected as member candidates in previous spectroscopic studies (in the case of OB stars), or due to X-ray emission (in the case of lower mass stars). They found a transverse velocity dispersion of $1.89^{+0.07}_{-0.06}$ and $1.32^{+0.05}_{-0.04}$ mas/yr in the two proper motion directions. The list of stars with X-ray emission for which they estimated PM was taken from a study of the region prior to the release of the Chandra Cygnus OB2 Legacy Survey, that targeted only the association central region (Wright & Drake 2009). Hence, only candidate members in a small central region in CygOB2 can be evaluated with this technique.

2.2.2 Conclusions: Cygnus OB2 low mass stars membership

	Number	Criteria used	Reference	common
1-	27	Hα/Lithium	Vink et al. (2008)	
2-	1843	Disc-bearing	Guarcello et al. (2013)	27 in 1-
3-	4783	X-ray	Guarcello et al. (2015); Kashyap (2017)	401 in 2-
4-	817	Kinematics	Wright et al. (2016)	817 in 2- and 3-
Total :			6225 candidate members	

Table 2.1: Summary of low mass member candidates listed in the literature. The field common list the amount of objects in common with other catalogues.

For the studies presented in this thesis, a candidate member list was composed based in membership evaluation from the literature. A summary of the list composed is presented in Table 2.1. Using the results of the Chandra Cygnus OB2 Legacy Survey (Section 2.2.1.5), there were 4864 X-ray sources considered as members by Kashyap (2017), spread over a region of 1 squared degree. Among these sources, 81 where identified as OB stars. The remaining 4783 are LM candidate members. The 1843 disc-bearing stars from Guarcello et al. (2013) were also considered as candidate members (Section 2.2.1.2), and there were 401 stars in common between Kashyap (2017) and Guarcello et al. (2013) lists. Only 27 of the objects with Hα emission (Section 2.2.1.3) from Vink et al. (2008) list were inside the field of view considered, and all of them were also in the disc-bearing sources list. From the 873 objects with estimated proper motions by Wright et al. (2016), 817 were not massive stars, but they were already selected as candidate members due to X-ray

[9] http://sci.esa.int/hipparcos/
[10] http://sci.esa.int/gaia/

emission criteria. This adds up 6225 candidate members in the CygOB2 association.

2.3 Basic tools for photometric observations

Stars are studied through measurements of the electromagnetic radiation arising from them. Their radiant flux, captured with a telescope, can be passed through a spectrograph and be discretized in frequency components. In first approximation, the star radiates as a blackbody, and its spectral energy distribution (SED) can be roughly described by the Planck's law. Superimposed to the stellar continuum, there are some darker and brighter spectral lines, which are produced by physical processes in the stellar atmosphere, hence one can learn about the stellar atmosphere by studying such lines. Modern spectra classifications are based on the stellar effective temperature, which is the temperature that a blackbody with the same luminosity per surface area as the star would have. Different temperatures in the stellar atmospheres favour different electronic transitions between bound atomic levels, which correspond to different types and intensities of absorption lines, hence spectral lines are often used for identifying the stellar spectral type.

Another way of studying the star's radiant flux is through photometry, which consists in filtering the radiation, captured by the telescope, by using a filter of known effective wavelength and passband, measuring the filtered radiation with a detector, and then calibrating it to some well studied stars. The set filters+detector is called photometric system. As the stellar SED contains signatures of physical processes in several different scales and wavelengths, different photometric systems can be used to access different physical processes. Modern photometric systems are designed to select regions from the stellar SED where the variations of the stellar atmospheric parameters allow to trace particular characteristics from the star[11]. This is the observational technique used in this work: the observational data we analysed was measured in the near-Infrared (near-IR) filters J (1.25μm), H (1.63μm), and K (2.20μm) and calibrated to the AB system(Oke & Gunn 1983)[12]. Formal specifications about data acquisition and calibration will be given in Chapter 3. We also used additional data available from several public surveys that includes the CygOB2 region in their field of view. The system response function of the available data is shown in Figure 2.3 and it serves as an exemplification of some of the photometric systems currently used in astrophysics.

After corrections for atmospheric extinction and instrumental signature, the radiant fluxes measured with a filter of central wavelength λ are transformed into apparent magnitudes (m_λ)[13,14]. If the distance to the star is known, m_λ can be transformed to absolute magnitude (M_λ), which is defined as the apparent magnitude on the wavelength λ a star would have if it was located at 10 pc from the Earth, corrected by

[11] One example of photometric system that was already mentioned in Section 2.2.1.3 is the IPHAS photometric system (Drew et al. 2005) which is composed of two Sloan filters r' and i' (green curves in Figure 2.3), that can be used to measure a piece of the stellar continuum, and a narrow filter around the Hα line (grey curve in Figure 2.3).

[12] In the AB system, the stars are calibrated such that a hypothetical star with constant flux in all wavelengths would have no colour.

[13] The apparent magnitude in a certain wavelength λ can be written as $m_\lambda - m'_\lambda = -2.5\log_{10}(\frac{f_\lambda}{f'_\lambda})$, where m_λ and f_λ are the stellar magnitude and flux respectively, and m'_λ and f'_λ are the magnitude and flux of a reference star.

[14] The radiant flux, in turn, is related to the stellar luminosity as $f = \frac{L}{4\pi d^2}$, where d is the distance to the star.

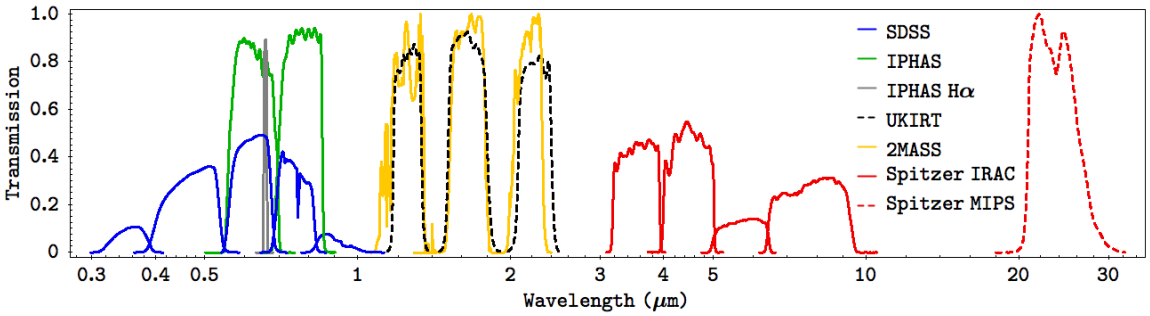

Figure 2.3: System response functions for the analysed survey data. The system response is given as a function of wavelength in μm.

the interstellar extinction in that wavelength[15,16].

Inside this context, a colour is the difference between magnitudes of different wavelengths. For example, for the photometric system used in the present work, one can define the colours J-H and H-K. Since magnitudes are given in a logarithmic scale, a colour is the relative flux for the wavelengths of the two filters. The Wien's displacement law states that the wavelength of the maximum intensity in a perfect blackbody is determined uniquely by its temperature. As stars can be roughly described as blackbodies, a colour is nothing else than a measurement of the slope of the star's SED, which is in turn an indicative of its temperature and can be used as an indicative of its spectral type. Stars with different temperatures will thus have different colour indexes. By convention, a colour is composed by subtracting the longer wavelength magnitude from the shorter.

Using magnitudes and colours to study stars is very practical, but it only discretely samples the SED of the star . If one could find an ideal filter whose passband included the complete stellar SED[17], this filter would measure the stellar bolometric magnitude ($M_{\rm bol}$). $M_{\rm bol}$ is a measurement of the total energy radiated by the star. Transformation between observable magnitudes and bolometric ones can be done by adding up an appropriate bolometric correction to the observed magnitude. Synthetic bolometric corrections are calculated through the study of stellar atmospheric models for different chemical compositions, for a given photometric system (e.g. Casagrande & VandenBerg 2014).

2.3.1 Hertzsprung-Russell diagram

With the determination of spectral class and visual[18] absolute magnitude measurements one can build an empirical Hertzsprung-Russell Diagram (HR-diagram) as the one shown in Figure 2.4. This type of diagram was first developed independently in studies by Enjar Hertzsprung and Henry Russell (Hertzsprung 1909; Russell 1914), and it is nowadays one of the main techniques in astrophysics for comparing observations from

[15]One can relate absolute and apparent magnitude as : $M_\lambda = m_\lambda - 5\log_{10}(\frac{d}{10\ pc}) + 5 - A_\lambda$, where d is the distance in parsec to the star, and A_λ is the interstellar extinction at wavelength λ.

[16]The interstellar extinction is an effect due to the absorption by dust grains in the interstellar medium of the light coming from a star.

[17]And find an ideal detector sensitive to the whole electromagnetic spectrum and an ideal site for observing with no atmosphere influence.

[18]A visual magnitude is a magnitude measured in the V filter of Johnson photometric system(Johnson & Morgan 1953).

stars with theory. When the brightest stars in the Sun's vicinity are placed in an empirical HR-diagram, as shown in Figure 2.4, most of the stars will occupy a diagonal locus in the graph. This diagonal locus is occupied by stars that are currently in hydrostatic equilibrium due to the balance between the thermal energy generated by hydrogen burn in their centre and the gravitational potential energy. This locus is denominated Main Sequence (MS). Giant stars, *i.e.,* stars with larger radii than MS stars are located to the right of the MS. This includes, as mentioned in Chapter 1, the PMS stars. The region of the HR-diagram which is of interest in this thesis is marked as a black box in Figure 2.4, and it comprises the region in the diagram occupied by PMS and MS LM-stars.

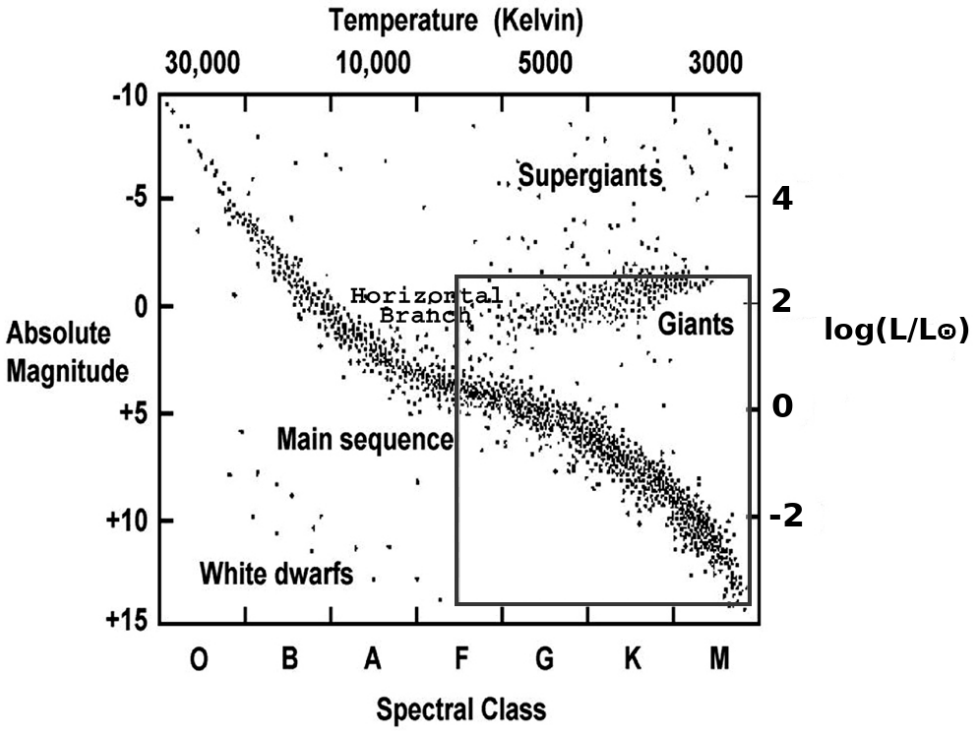

Figure 2.4: HR-diagram for the brightest stars in the Sun's vicinity. Theoretically, the position of stars in this diagram are set according to Equation 2.1. The diagonal locus is the Main Sequence. The locus of post-Main Sequence phases is also shown. The black box shows the region of interest of this thesis. (This Figure was adapted from the original in the CHANDRA-XO website, to show the luminosity axis to appear in a logarithmic scale.)

The bolometric absolute magnitude of a star is related to its luminosity according to $M_{\rm bol} - {\rm M}_{\odot} = -2.5\log_{10}(\frac{L_*}{{\rm L}_{\odot}})$, where L_* is the star's luminosity, and $\rm M_{\odot}$, and $\rm L_{\odot}$ are the Sun's absolute magnitude and luminosity respectively. The luminosity of a star can be described by the Stefan-Boltzmann equation for a blackbody radiating trough a spherical surface :

$$L_* = 4\pi R_*^2 \sigma T_{\rm eff}^4, \tag{2.1}$$

where R_* is the stellar radius, $T_{\rm eff}$ is the star's effective temperature, and σ is the Stefan-Boltzmann constant.

The stellar evolution can be mapped inside an HR-diagram. The luminosity of a star is determined by its instantaneous radius, and effective temperature (Equation 2.1). The physical processes involved in each

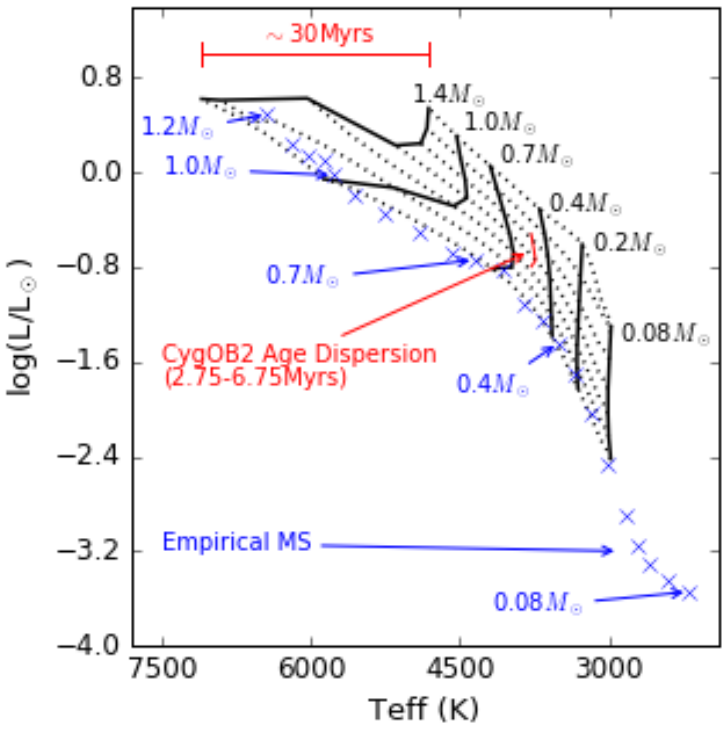

Figure 2.5: Theoretical HR-diagram for LM-stars. Luminosity is shown in terms of solar luminosity and in a log-scale, and temperature is shown in Kelvins. Black solid lines show mass tracks from PISA models (Tognelli et al. 2011, 2012) for PMS ages from 1 to 30 Myr and masses between 0.08 $M_\odot$ and 1.4 $M_\odot$. Dashed lines show isochrones for ages between 1 and 30 Myr with a step of log Age = 0.25. An empirical MS isochrone from Kraus & Hillenbrand (2007) is shown in blue, and some of the MS stellar masses are shown with arrows pointing to the position of the star in the diagram. The effect of CygOB2 age dispersion for a 0.5 $M_\odot$ star is shown in red.

evolutionary phase are responsible by modifying those two quantities. Accordingly, the star will move inside the HR-diagram during its evolution. It happens that this evolution is very slow when compared to the human life. A star of ~ 1 $M_\odot$, for example, takes around 10 billion years to leave the MS. Because of that, it is not possible to observe a single star over its whole lifetime. Instead, stars with the same fundamental parameters (*e.g.*, mass, and metallicity) can be observed at different ages and be assembled in an evolutionary sequence. A sequence of all the positions a star, with a certain mass, will ever occupy in the HR-diagram is called a mass evolutionary track. An example of such evolutionary track for a 1$M_\odot$ stars was already show in Figure 1.1. A sequence with the positions of stars with the same ages and all possible masses is called an isochrone. Nowadays, complex theoretical numerical simulations for stellar evolution are used for generating theoretical isochrones and mass tracks (e.g. Baraffe et al. 1998; Siess et al. 2000; Meynet & Maeder 2005; Dotter et al. 2008; Tognelli et al. 2011; Baraffe et al. 2015). Figure 2.5 shows a theoretical HR-diagram for PMS stars built using mass tracks and isochrones from PISA evolutionary models (Tognelli et al. 2011, 2012) for LM-stars with mass in the range 0.08 - 1.4 $M_\odot$. From the mass tracks (black lines) in Figure 2.5 one can see that, as mentioned in Section 1.4, stars with mass smaller or equal than 0.4 $M_\odot$ spend most of their PMS time in an almost vertical path with almost constant effective temperature, called a Hayashi track.

2.3.2 Colour-magnitude diagrams

As colours are an observational quantity related to the stellar effective temperature, and absolute magnitudes can be related to the stellar luminosity, one can build an observable HR-diagram as shown in Figure 2.6 for the near-IR filters H and K. This kind of observable diagram is called colour-magnitude diagram (CM-diagram).

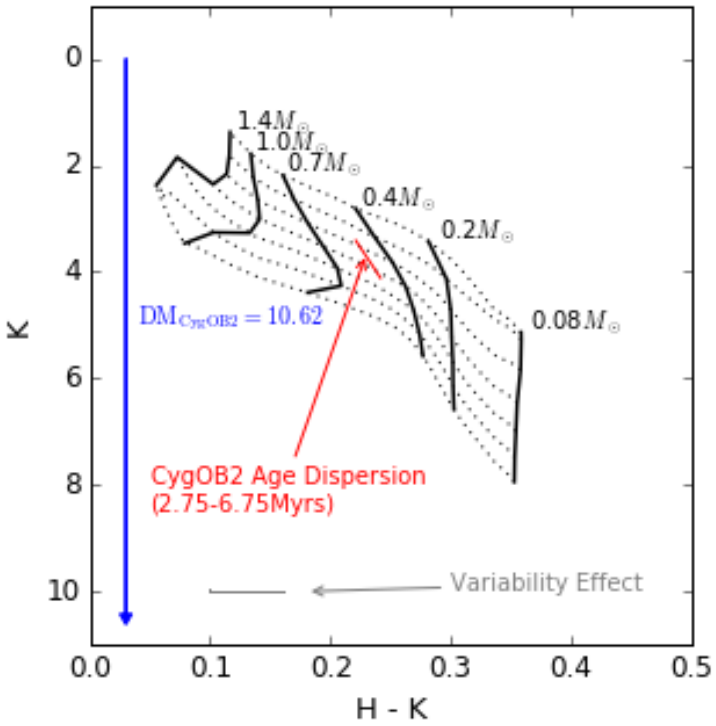

Figure 2.6: Theoretical HR-diagram for LM-stars. K absolute magnitude is shown as a function of the H - K colour. Black lines show mass tracks from PISA models (Tognelli et al. 2011, 2012) for PMS from 0.08 to 1.4 $M_\odot$. Dashed lines show isochrones for ages between 1 and 30 Myr with a step of log Age = 0.25. The effect of CygOB2 age dispersion for a 0.5 $M_\odot$ star is shown in red. The effect of the interstellar reddening is shown as a red arrow for the median visual extinction estimated for the CygOB2 association. The effect of the distance is shown as a blue arrow in terms of the distance modulus for CygOB2. The grey lines show the median effect of photometric variability in the diagram, in terms of median amplitude of variability for CygOB2 data presented in the present thesis.

To compare the theoretical HR-diagram (Figure 2.5) with the observational CM-diagram (Figure 2.6), one must take into account several aspects inherent to the observations. First, we have to consider the effect that the material in the ISM has into the stellar light. The ISM is filled by matter in the form of gas and dust. The so called interstellar reddening is the resultant effect of both absorption and scattering by the material of the ISM. Absorption acts on particles with sizes larger than the wavelength of incidence, the typical size of the interstellar dust is about 10nm, so scattering is efficient for wavelength of the order of the sizes of the particles. This effect is called reddening because blue light (with larger wavelength) is more affected than redder light. Extinction laws depend upon location, since the quantity and type of ISM material varies for different lines of sight. One of the ways of expressing the extinction law is in terms of the absolute extinction

ratio, $\frac{A_\lambda}{A_V}$, where A_λ is the wavelength dependent extinction coefficient and A_V is the extinction coefficient in visual magnitudes. Extinction coefficients in each photometric band analysed in the present study are shown in Table 3.3 in Chapter 3.4.

The effect of interstellar extinction inside the CM-diagram is exemplified in Figure 2.6: the median reddening estimated for CygOB2 stars is $A_V = 4.1^m$ (Section 3.4.1), the effect of extinction in colour H - K (A_{H-K}) and magnitude K (A_K) results in a displacement along the red arrow inside the H-K vs K CM-diagram starting from the position of the reddened star in this diagram.

Next, one must consider the distance to the star. This can be measured as the distance modulus, $\mathrm{DM} = 5 \log d - 5$. Using the adopted distance to CygOB2, $d = 1.33$ kpc (Kiminki et al. 2015), the distance modulus for CygOB2 is DM=10.62, the effect of distance in the CM-diagram is to displacement the star along the blue vector in Figure 2.6, the size of this vector shows the DM of CygOB2.

Even though the age evolution of a single star is not observable inside the CM-diagram, other physical phenomena have time-scales short enough to be visualized in it. The grey line-segments in Figure 2.6 show the median amplitude of variability in CygOB2 stars for the K magnitude and H-K colour estimated in Chapter 5, and one can see that the physical mechanisms causing such variability can significantly change the position of a star inside this diagram. We will discuss the physical mechanisms associated to YSO variability in Section 2.3.4.

There are other physical phenomena that can change the position of a star inside the CM-diagram. Models that consider stars with magnetic fields and/or rotation, for example, due to the effect of them in the stellar internal structure, result in lower effective temperature and luminosity (e.g., Mendes et al. 1999; Mullan & MacDonald 2001). On the other hand, models for lower metallicity result in higher effective temperature and luminosity than higher metallicity models (e.g. Schaller et al. 1992). However, these phenomena will not be explored in this thesis, and the evolutionary models considered here assumes that the stars have solar metallicity (Z=0.013), that they are isolated (do not have a binary companion), and have no discs.

2.3.3 Colour-colour diagrams

Another useful diagram that can be built using the stellar colours is the colour-colour diagram (CC-diagram). Figure 2.7 shows an example of such diagram for the near-IR colours. As colours are independent on the distance to the star, the properties of a star inside this diagram are also distance independent. Accordingly, this diagram is specially good for evaluating the effect of the interstellar extinction, as this will be the major phenomenon shifting the position of stars in the diagram.

An estimative of interstellar reddening for a star in this diagram can be done by displacing the star parallel to the reddening vector, until it reaches the position expected for that type of star in this diagram. The size of the displacement required will give the individual extinction for that star. This method has some limitations as it supposes that the only process affecting the stellar position inside the CC-diagram is the interstellar extinction. As one will see in Section 2.3.4, for PMS stars this is often not the case. Also, the supposed 'original' position of a star in this diagram has to be known from an empirical sequence (as the one shown in Figure 2.7) or from a theoretical isochrone. When it comes to the near-IR CC-diagram, there

are additional problems such as a degenerescence in the location of the stars with mass larger than about 0.6 $M_\odot$, due to the fact that near-IR isochrones for such masses are almost parallel to the reddening vector; also, since discs around young stars produce large IR-excesses (Section 2.4), young stars are often shifted towards redder colours.

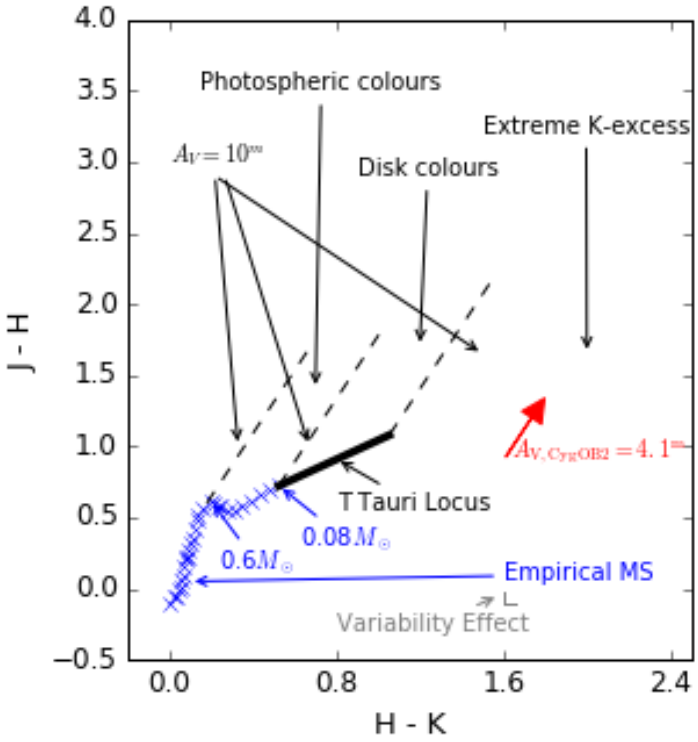

Figure 2.7: Near-IR colour-colour diagram. The effect of the interstellar reddening is shown as a red arrow for the median visual extinction estimated for the CygOB2 association. An empirical MS isochrone is shown in blue. The Meyer et al. (1997) T Tauri locus is shown as a black bold line. Dashed black lines show extinction paths of $A_V = 10^m$ for 0.6 $M_\odot$ and 0.08 $M_\odot$ stars, and for the truncation point of the T Tauri locus. The grey vectors show the effect of photometric variability in the diagram, in terms of the median amplitude of variability for the CygOB2 data presented in the present thesis. The regions in this diagram occupied by reddened stars with photospheric colours, disc colours and extreme K-excess are indicated by black arrows.

There are other colours that are less affected by IR-excess produced by discs, and optical colours may be more adequate for interstellar extinction estimates than IR colours. For example, the median extinction for CygOB2 stars, shown as red arrows in Figures 2.6, and 2.7 was estimated using riz colours (see Figure 2.3 and Section 3.4.1), instead of near-IR ones.

An important locus that can be identified inside the near-IR CC-diagram is the T Tauri Locus, which is the region in the CC-diagram that CTTs are expected to occupy when considering their IR-excesses. This locus was first identified by Meyer et al. (1997), who presented the positioning of the T Tauri locus for the JHK filters in the CIT photometric system. For this thesis, the locus was transformed to the UKIRT photometric system (see Chapter 3 for details about the observational data used) by first transforming it from CIT system to 2MASS using Carpenter (2001) transformations, and then using transformations between

2MASS and UKIRT photometric systems for giant stars from Hewett et al. (2006). Finally, the T Tauri Locus inside a CC-diagram with UKIRT's photometric system near-IR colours is:

$$(J-H)_{\rm CTTS} = 0.551 \times (H-K)_{\rm CTTS} + 0.498 \tag{2.2}$$

The position of this locus is shown in Figure 2.7. Meyer et al. (1997) truncate their locus at $(\text{H-K})_{\rm CIT} = 1^m$. Repeating the transformations for this value, the CC-diagram presented in Figure 2.7 is truncated at (H-K)=1.054^m.

With the T Tauri locus placed inside the CC-diagram in Figure 2.7, three regions can be defined. First, there is the region of the stars with photospheric colours, reddened by the interstellar extinction. In the case of a young LM population, this region will be populated by stars with no significant circumstellar material, and one may expect to find WTTs and/or the Class III YSO (Section 2.4) in this region. Second, there is the region populated by stars with a disc responsible to produce IR-excess, and one may expect to find CTTs and/or Class II YSO in this region. Third, there is the region populated by stars with extreme IR-excess, which is typically occupied by still embedded young stars, as the Class I YSO.

2.3.4 The physics behind photometric variability

Even though the timescale for stellar evolution is too big to be observed inside an HR-diagram, this is not the case for many of the physical processes causing photometric variability during the PMS, with time scales from hours to months.

The most common causes of photometric variability in YSO are cold spots caused by magnetic activity, hot spots due to the accretion process, variable disc emission, and variable extinction. The variability due to hot spots, and disc emission requires the existence of a circumstellar disc. Cold spots and variable extinction may also be present in disc-bearing stars. One may also notice that more than one variability mechanism can be in action at the same time.

A pioneer study towards statistically establishing the characteristics of near-IR YSO variability was presented by Carpenter et al. (2001) for stars near the Trapezium region of the Orion Nebula Cluster observed in the near infrared JHK_s filters with 2MASS. Since then, several authors also contributed to the subject, but if in one hand, some studies provided longer baselines, in the other hand only few studies presented a variable star sample as big and statistically significant as Carpenter et al. (2001). A brief literature review on this topic will be presented in the discussion of Chapter 5. Given the typical photometric error in our dataset (2% as in Section 3.1.3), it was not possible to access variability that could be caused by exoplanets, and such subject will not be discussed in the present thesis.

2.3.4.1 Stellar spots

Stellar spots can be either hotter or colder than the stellar photosphere. They cause variability because the fraction of the stellar surface covered by the spots and seen by the observer changes as the star rotates.

Cold spots are similar to sunspots (e.g. Bouvier et al. 1993), they are colder than the photosphere and

arise from magnetic activity. They are the most common source of photometric variability in LM-stars in all ages (Scholz et al. 2009). In young stars they can cover up to ∼60% of stellar surface (Venuti et al. 2015). Hot spots are formed on regions where the material free-falls onto the star, as a result of the magnetospheric accretion process, and consequently they are confined into high latitudes.

Carpenter et al. (2001), and Scholz et al. (2009) used similar single-temperature blackbody models for estimating the variability amplitude caused by the presence of spots. In such models, the amplitude of variability could be estimated as a function of spot and stellar effective temperatures, and of the fraction of the stellar surface covered with spots, while considering that both star and spot radiate as blackbodies. Effects of limb-darkening, inclination and opacities differences between the spot and the stellar atmosphere are ignored in their model.

Carpenter et al. (2001) applied such models to a 0.5 $M_{\odot}$ 1 Myr star, which is assumed to have an effective temperature of 4000 K. They assumed cold and hot spots temperatures of 2000 and 8000 K respectively, and tested surface coverages from 1 to 30%. They found that spots produce a maximum change in colour of ∼0.03 mag for cold spots, and 0.1 - 0.2 mag for hot spots. Consequently, they suggested that for high spot coverages, the variability amplitude could be used for distinguishing between cold and hot spots. Using a similar model, Scholz et al. (2009) estimated variability amplitudes for stars with effective temperatures of 3000 K and 4000 K, spot temperatures between 5000 - 12000 K, and filling factors between 2 - 40%. They limited their choice of parameters in order to keep J-band amplitude between 0.4 and 1.0 mag (reflecting their observational results).

As the brightness of the star varies in both magnitude and colour, the position of the star changes inside the CM and CC diagrams, and the trajectory the star describes on it can be described by the slope of this trajectory. By comparing simulations with their observational results inside these two diagrams, the authors of both studies inferred that variability due to hot spots produce slopes in the interval: $\frac{\Delta J}{\Delta(J-H)}$ ∼63° - 71°, $\frac{\Delta K}{\Delta(H-K)}$ ∼60° - 80°, and $\frac{\Delta(J-H)}{\Delta(H-K)}$ ∼56° - 63°. Variability due to cold spots produce the slopes: $\frac{\Delta J}{\Delta(J-H)}$ ∼78° - 85°, $\frac{\Delta K}{\Delta(H-K)}$ ∼70° - 85°, and $\frac{\Delta(J-H)}{\Delta(H-K)}$ ∼40° - 56°.

An improved version of the model used by Carpenter et al. (2001) and Scholz et al. (2009) was proposed by Bouvier et al. (1993), in which limb-darkening[19] effects are taken into account. In such models the variation in magnitude caused by a spot of temperature, $T_{\rm spot}$, in the surface of a star of temperature, T_*, can be estimated as:

$$\Delta m = -2.5 \log \left(1 - \frac{f}{1 - \frac{\mu}{3}} [1 - \frac{B_\lambda(T_{\rm spot})}{B_\lambda(T_*)}]\right), \tag{2.3}$$

where f is the fraction of the stellar surface covered by spots, $B_\lambda(T)$ is Plank Law for the radiation of a blackbody of temperature T at the wavelength λ, and μ is the limb-darkening coefficient.

A series of amplitudes produced by spotted stellar surfaces was estimated using Equation 2.3, and using the amplitudes slopes of variability were estimated. Typical young stellar effective temperatures were taken

[19]Limb darkening is an optical effect related to the optical depth of the star, in which the edge of the stellar surface seen by the observer seems to be darker than the central parts.

from Cohen & Kuhi (1979). Limb-darkening coefficients were provided by Dr. Antônio Claret[20] and they were estimated by using a least square method to fit limb darkening coefficients to the specific intensities from ATLAS atmospheric model, using a linear law to describe the limb-darkening coefficients. The methodology applied in the calculation was similar to the one described in Claret & Bloemen (2011). The results were convolved with the WFCAM/UKIRT JHK photometric system. Typical spot temperatures and spot coverage fraction were taken from Venuti et al. (2015). Parameters for stars with the following spectral types were considered: M2, M0, K7, K4, K3, K2, K0, G2, and F2. This set of spectral type covers approximately the mass interval 0.3 $M_{\odot}$ to 1.5 $M_{\odot}$, which contains most of the stars studied in this thesis. Venuti et al. (2015) used a similar model with Equation 2.3 to estimate spot coverages and temperatures for young stars in NGC 2264, and we used their results as reference. For each spectral type, distributions of spot temperatures and spot coverage from the Venuti et al. (2015) were built, and the max/min, median, and 10-th/90-th percentile were taken as typical values for each parameter. The results of the simulations are shown in Table 2.2: max, min and median values for variability amplitude for each band and colour are presented, as well as the slopes inside the CC and CM-diagrams in degrees.

Table 2.2: Results of spot variability simulations. Both amplitudes of variability and slopes produced inside CC and CM-diagrams are shown for both cold and hot spots.

	hot spot			cold spot		
Band	Min	Max	Median	Min	Max	Median
J (mag)	10^{-3}	1.6	0.22	10^{-5}	1.4	0.16
H (mag)	10^{-3}	1.3	0.16	10^{-5}	1.3	0.14
K (mag)	10^{-3}	1.1	0.12	10^{-5}	1.1	0.11
J-H (mag)	10^{-4}	0.3	0.05	10^{-6}	0.2	0.03
H-K (mag)	10^{-4}	0.2	0.03	10^{-6}	0.2	0.03
$\frac{\Delta K}{\Delta(H-K)}$ (°)	67.7	79.0	74.7	74.9	83.6	78.2
$\frac{\Delta J}{\Delta(J-H)}$ (°)	71.8	79.9	77.4	78.3	86.1	80.3
$\frac{\Delta(J-H)}{\Delta(H-K)}$ (°)	51.6	59.4	55.0	35.9	54.6	51.6

From Table 2.2, one can see that even though the extreme values for the slopes and amplitudes are slightly different from those found by Carpenter et al. (2001), and Scholz et al. (2009), the median values are very similar, and therefore the results can be considered qualitatively the same. Figure 2.8 shows the results of the simulations inside the CM and CC diagrams. From the Figure one can see that while the lengths of the vectors (amplitudes) produced by hot spots (red vectors) are systematically longer than those of cold spots (blue vectors), there are sets of spot temperature and spot coverage that result on cold spot variability amplitude as high as those produced by hot spots. Hence, one may consider that it is not possible to differentiate hot spots from cold spots in the near-IR, unless the spot coverage is known in advance. Also, even though hot and cold spots produce vectors in different senses, unless the spot temperature is known it is not possible to identify the sense of variation, but only the direction. It is important to note from Figure 2.8 and in the subsequent similar plots that a positive inclination inside the CM diagrams will produce a line that goes from the down right to the upper left, while a positive inclination inside the CC diagram will produce a

[20]From Instituto de Astrofísica de Andalucía, Granada, Spain

line that goes from the bottom left to the upper right. This positive inclination in the CM-diagrams means that variable stars due to spots get redder as they fade.

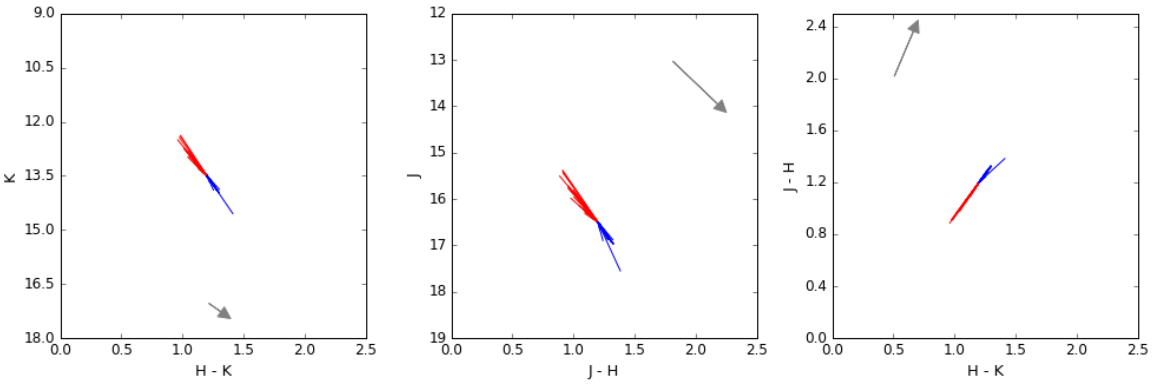

Figure 2.8: Simulation results of the effect of variability induced by spots in the near-IR CM and CC diagrams. H - K vs. K, J - H vs J, and H - K vs. J - H diagrams are shown from left to right. The effect of the interstellar reddening is shown as a grey arrow for the median visual extinction estimated for the CygOB2 association. Blue vectors show the effect of variability induced by cold spots for different spot and star effective temperatures, and spot coverage fractions. Red vectors show the same for hot spots. The central position of the vectors were chosen for visualization purposes.

2.3.4.2 Circumstellar extinction

Variability due to extinction can arise from inhomogeneities in the absorbing material moving across the line of sight. This inhomogeneity can be either in the inner circumstellar environment or in the ambient molecular cloud. The wavelength dependence of extinction in the near-IR and submillimeter can be described as a power law: $A_\lambda \sim \lambda^{-\beta}$ (Scholz et al. 2009). The constant β is the dust opacity index and it represents the efficiency at which dust grains radiate at long wavelengths (Sadavoy et al. 2016). Typical values for the ISM β in the IR are $\beta \sim$1.7 (Mathis 1990). β is not necessarily constant and it can vary even inside the same cloud (Froebrich et al. 2005), as it is a function of the size of the grain producing opacity, and it can evolve with both density and temperature. In circumstellar discs, typical values are $\beta \sim 1$ (Beckwith & Sargent 1991; Miyake & Nakagawa 1993; Williams & Cieza 2011), but it can have values as low as 0.4 and as high as 1.6 (e.g. Rodmann et al. 2006; Garufi et al. 2017).

Slopes produced by variable extinction are presented in Table 2.3 and illustrated in Figure 2.9. The slopes were calculated using the reference values mentioned in the previous paragraph with β in the range 0.4 - 1.6. Ten equally spaced values of β were generated in this range. Due to the nature of this type of variability, it can assume arbitrary amplitudes, but for the purpose of illustration, we used an amplitude value such that $\Delta x^2 + \Delta y^2 = 1$ in each plot, so all the vectors shown will have the same length regardless the value of their slopes.

Carpenter et al. (2001) analysed the timescale of variability in the case the extinction variation is caused by the ambient molecular cloud. In this case, the timescale is set by the size of the inhomogeneity causing the variability and by the velocity field of the molecular gas in this inhomogeneous part of the cloud. In

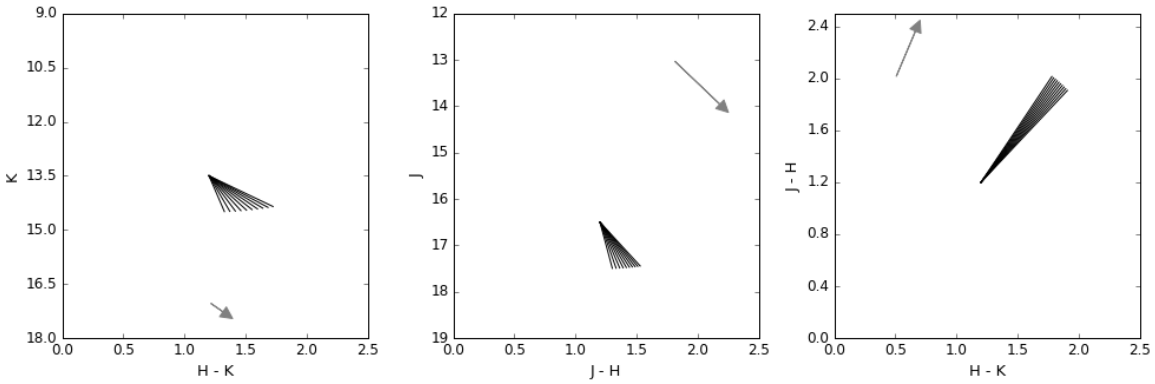

Figure 2.9: Simulation results of the effect of variability due to variable circumstellar extinction in the near-IR CM and CC diagrams. H - K vs. K, J - H vs. J, and H - K vs. J - H diagrams are shown from left to right. The effect of the interstellar reddening is shown as a grey arrow for the median visual extinction estimated for the CygOB2 association. Black vectors show the effect of variability cause by variable circumstellar extinction for different values of dust opacity index. The position and length of the vector were chosen for visualization purposes and the physical meaning of the vectors are limited to their slopes.

the case of their target cluster, ONC, they assumed a typical velocity of the ambient gas of $\sim$2 km s^{-1}, and analysed the timescale for a point source in the cloud that is 3 R$_\odot$ away from a 0.5 M$_\odot$ mass, 1Myr star, to complete a transit, resulting in a timescale of $\sim$12 days.

When the extinction is caused by inhomogeneities in the circumstellar disc, a variety of timescales from hours to years is possible, depending on the position in the disc. There are several star-disc system geometries that can cause this type of variability. For example, in the AA Tauri variable stars, the magnetospheric star-disc interaction, via which accretion occurs, would be responsible to lift some dust above the plane of the disc. This lifted dust would by turn be responsible to create a warp in the inner disc, and as the dust is optically thick, this warp cause extinction occultations of the light arriving from the stellar photosphere. Studies of variable stars of this type (e.g. Bouvier et al. 2007; McGinnis et al. 2015) found timescales of variability of days to weeks producing features in the light curve that can happen in a stable way over a few years. Inhomogeneities in the disc wind (e.g. Tambovtseva & Grinin 2008) could explain this kind of variability as well.

Whatever is the mechanism introducing the inhomogeneity to the line of sight, the overall effect of extinction is to make the object redder as it becomes fainter, and hence the inclinations produced inside the CM and CC diagrams are positive. Looking at Figures 2.8 and 2.9 we see that both spots and extinction produce very similar slopes inside the diagrams, and it may be difficult to distinguish between the two mechanisms by using only near-IR colours.

Table 2.3: Results of extinction variability simulations.

Band	Min	Max	Median
$\frac{\Delta K}{\Delta(H-K)}$ (°)	58.4	82.8	71.0
$\frac{\Delta J}{\Delta(J-H)}$ (°)	70.8	84.2	76.0
$\frac{\Delta(J-H)}{\Delta(H-K)}$ (°)	58.4	84.2	76

2.3.4.3 Disc emission and accretion

Discs contribute to IR emission in two ways (Meyer et al. 1997): first, by absorbing the optical and ultraviolet radiation form the star and re-radiating it at longer wavelengths; and second by releasing energy as the material in the disc is radially transported through a viscous optically thick accretion disc (e.g. Lynden-Bell & Pringle 1974). Those two phenomena result in the IR-excess typically observed in YSOs (Section 2.4).

This IR-excess can occur in several different wavelength from near-IR to far-IR, and the region of the star-disc system producing excess in each wavelength range will depend on the temperature distribution in the star-disc system. When looking to the system radially, the temperature decreases for increasing distance to the central star. As mentioned before, up to the dust destruction radius, the temperatures in the disc are too high for dust to survive. Modern disc models, suggest that localized at the dust destruction radius, there is a thick "wall" of dust, separating the dusty outer regions in the disc from the gaseous inner disc (see Dullemond & Monnier 2010, for a review on the subject of disc structure). The temperature at which dust is sublimated is around 1500 K (Dullemond & Monnier 2010), and as the wall of dusty material is at this temperature, it is supposed to produce a continuum of near-IR emission (a blackbody irradiating with about 1500 K will have the maximum of its SED around $\sim$1.9 μm). Inside the dust destruction radius, the disc opacity is dominated by the gas, and the SEDs of inner discs present emission lines of (e.g. Dullemond & Monnier 2010; Najita et al. 2007): TiO (emission at $\lambda \lesssim 1$ μm), water vapor (excitation temperatures T $\sim$1500 K, producing emission at $1.2 \lesssim \lambda \lesssim 3$ μm) and CO overtone emission (T$\geq$ 2000 K, producing emission in the range 2.3 - 2.4 μm). Hence, the physical phenomena related to the near-IR variability must be acting around and inside the dust destruction radius.

Generally speaking, the shorter wavelength at which the IR-excess can be observed depends on the temperature of the inner disc material and on the inner hole size (e.g. Meyer et al. 1997). The temperature distribution in the inner disc can be affected by changes in the release of energy, for example, due to changes in the accretion rate, or in changes in the inner hole size, which in turn alters the amount of absorbed and reprocessed radiation (Scholz et al. 2009). There are two main mechanisms responsible by dissipating the disc: accretion and disc erosion due to the photoevaporation. During the initial evolution of the disc, the accretion rate dominates over the evaporation rate, and as the star accretes from the inner disc, material is inwardly transported from the outer regions in the viscous disc. Later in the evolution, the material in the outer disc is no longer able to resupply the inner disc material, holes are formed in the disc (Williams & Cieza 2011), and finally the photoevaporation starts dominating the disc dissipation.

All those mechanisms related to the disc dispersal are responsible for altering the amount of near-IR excess observed, and hence they are the responsible for producing variability in the near-IR. Meyer et al. (1997) showed with simulations that the radius of sublimation increases with the mass accretion rate, increasing the emission on the near-IR. On the other hand, the effect of holes in the disc is to diminish the disc contribution to the near-IR flux. As the disc emission becomes stronger at longer wavelengths, one can expect higher amplitude variations in the K band, than in the J band. As a consequence of this, variability related to the disc emission will make the star bluer (approaching the true stellar colour) as it fades, which

is contrary to what happens due to the variable extinction or to the spotted surface. Accordingly, the slopes produced by this type of variability inside the CM-diagrams will be negatives, and slopes inside the CC-diagram will be positives.

Carpenter et al. (2001) used Meyer et al. (1997) to estimate the typical slopes and amplitudes produced by this type of variability. They considered two cases: The case of a variable mass accretion rate, changing from $\dot{M} = 10^{-7}\mathrm{M}_{\odot}\mathrm{yr}^{-1}$ to $\dot{M} = 10^{-8.5}\mathrm{M}_{\odot}\mathrm{yr}^{-1}$, and the case of inner disc edge changing from 1 to $4\mathrm{R}_{\odot}$.

Table 2.4: Slopes of variability related to the inner disc from Carpenter et al. (2001).

	Variable Accretion rate		Changes in the inner disc size	
Band	Min	Max	Min	Max
$\frac{\Delta K}{\Delta(H-K)}$ (°)	-54.46	-75.96	-63.43	-78.69
$\frac{\Delta J}{\Delta(J-H)}$ (°)	-51.34	-78.69	-75.96	-78.69
$\frac{\Delta(J-H)}{\Delta(H-K)}$ (°)	21.8	30.96	23.80[1]	33.47[1]

[1]In this case the slopes are equivalent to the definition of the T Tauri Locus, which gives a slope of 28.86° in the CC-diagram.

They found that this type of variability can produce amplitudes as large as 1 magnitude in K band, and it is is expected to produce slopes between -45° and -90° inside the CM-diagrams, and shallower slopes in the CC-diagram than those produced by extinction or spots, which is consistent with the CTTs locus inside this diagram.

2.4 Observational evidence of the evolution of Young Stellar Objects

The evolutionary stage of a YSO, including PMS stars, can be classified according to measurements of the distribution of material around the forming star. This can be inferred observationally by measuring the inclination of the stellar SED in the IR. This inclination is defined as:

$$\alpha_{\mathrm{IR}} = \frac{d\log(\lambda F_{\lambda})}{d\log\lambda}, \tag{2.4}$$

where F_{λ} is the flux in the wavelength λ.

Lada & Wilking (1984), Lada (1987), Andre et al. (1993), and Greene et al. (1994), proposed the definition of empirical evolutionary classes of YSO based on α_{IR} values. These empirical classes are explained below, together with the main characteristics and the evolutionary stages related to it. The typical bolometric temperatures (T_{bol}; Blackbody temperature inferred from the wavelength of the SED maximum value) for each class were obtained by Chen et al. (1995), who studied the position of YSO inside the $\log(L_{\mathrm{bol}})\times\log(T_{\mathrm{bol}})$ diagram (bolometric temperatures are commonly used in the study of YSO due to the difficulty in obtaining effective temperatures for such objects).

- Class 0: They are only visible in the sub-millimetre $\frac{L_{\mathrm{smm}}}{L_{\mathrm{bol}}} > 0.5\%$, with L_{smm} calculated for $\lambda \geq 350$

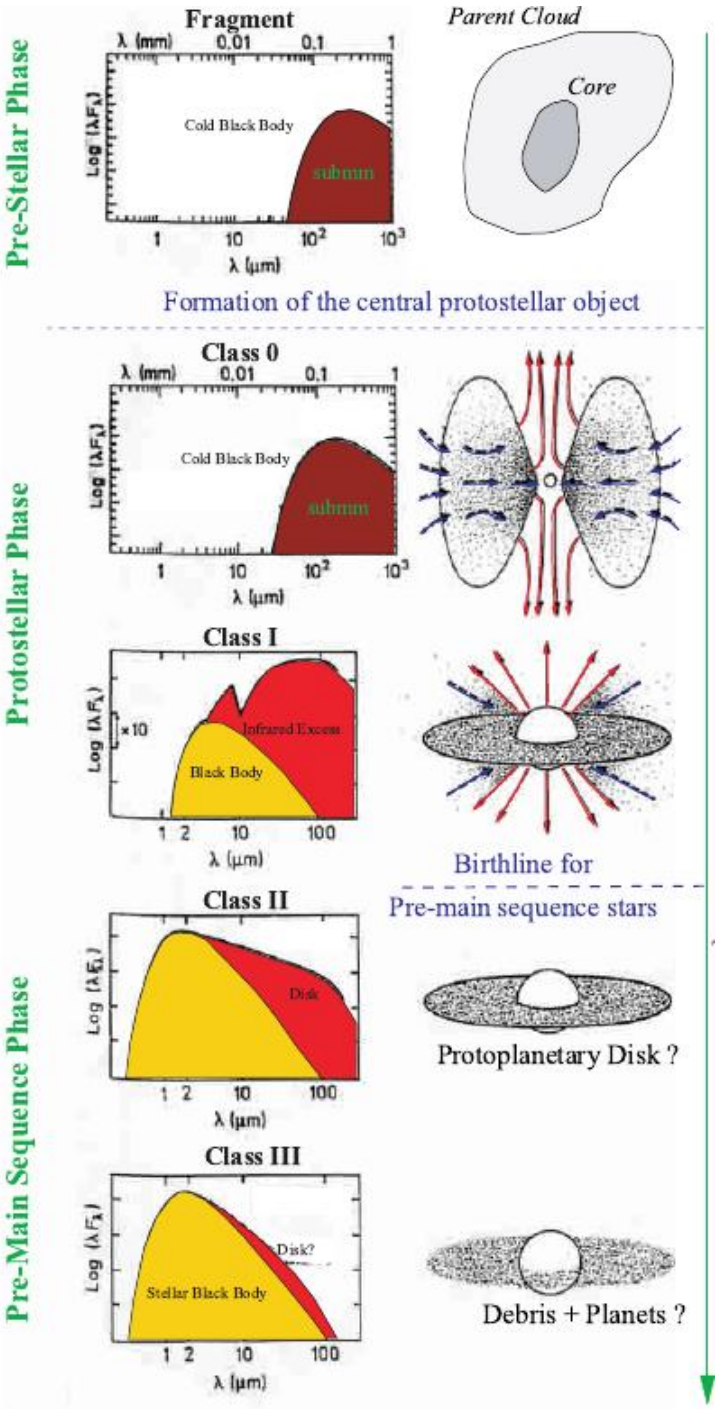

Figure 2.10: Sketch showing the spectral energy distribution of young stellar objects in different empirical evolutionary stages. The left plots show the SED for the star-disc system. The stellar flux contribution to the SED is shown in yellow, and the disc contribution is shown in red (the effect of accretion in the SED is not shown). The drawings in the right sketch the geometry of the YSO in each phase. Figure adapted from André (2002).

μm)[21]., hence it is not possible to classify them according to $\alpha_{\rm IR}$.

They are composed by a central protostar surrounded by an optically thick envelope, in a phase of

[21] $\frac{L_{\rm smm}}{L_{\rm bol}} > 0.5\%$ is the observational criterion to select protostars with $\frac{M_{\rm envelope}}{M_*} > 1$, where $M_{\rm envelope}$ is the mass stored in the envelope.

strong spherically symmetric accretion. Stars are supposed to gain most of their mass during this phase, but initially they have $M_{\rm envelope} >> M_*$. Typical ages for such objects are around 1-3×10^4 yrs. They present $T_{\rm bol}$ between 20 K and 70 K.

- Class I: Objects with $\alpha_{\rm IR} \geq$0.3.

  They are protostars in an advanced stage of accretion. The central star is not optically visible yet, as it is embedded in a massive accretion disc, constantly fed by the falling envelope. They show strong IR emission. The accretion is no longer spherically symmetric, and jets and bipolar outflows are commonly observed, $M_* > M_{\rm envelope}$. Typical ages: $1 - 2 \times 10^5$ years. They have $T_{\rm bol}$ between 70 K and 650 K.

- Flat Spectrum: objects with $-0.3 \leq \alpha_{IR} <$0.3.

  They are considered as transient objects between Class I and II, where the IR excess due to disc emission is added up to the emission due to the material falling into the star.

- Class II: Objects with $-1.6 \leq \alpha_{\rm IR} < -0.3$.

  The central object is already optically visible, and it is usually identified as a CTTs. The accretion disc ($M_{\rm disc} \sim 0.01$ $M_\odot$) is still optically thick and produces an IR excess due to emission at $\lambda \leq 10$ μm. Accretion is still observed. They show $T_{\rm bol}$ between 650 K and 2800 K.

- Class III: Objects with $\alpha_{\rm IR} < -1.6$.

  They are stars contracting toward the MS, with an optically thin residual disc, responsible for weak IR excess ($\lambda \leq 10$ μm). They are usually identified as WTTs. They have $T_{\rm bol} > 2800$ K.

Due to system inclination effects, and asymmetric geometry, ambiguities in the classification of YSO may occur. This classification scheme led to the idea that the classes could be seen as an evolutionary sequence. But this notion has to be taken with caution when applying this scheme to a coeval population. As mentioned before in the text, even though cluster and association populations are often considered coeval, often there are some small effects of age dispersion, also the complexities in the disc dispersal process allow the existence of stars which have the same age, but are in different classes in this classification scheme. Figure 2.10 shows a sketch with the geometry of the star-disc system and its SED during each evolutionary class listed above.

2.5 Pre Main Sequence stellar rotation: observational studies

Determining stellar rotational properties starting from first principles is an impossible task. Because of that, the study of stellar rotation is heavily constrained by the empirical knowledge on the subject acquired form observational studies (Krishnamurthi et al. 1997). The AM of a star can be roughly written as $J \sim M_* R_*^2 \Omega$, where M_* is the stellar mass, R_* is its radius, Ω its angular velocity, and the proportionality constant will be related to the stellar moment of inertia and has to do with how matter is distributed around the rotational axis. Ω can be written in terms of the rotational period, P: $\Omega = \frac{2\pi}{P}$. As P can be a direct product from the observations, and as radii are difficult to measure, it is usual to simply use P as demonstrative of the AM quantity in a star of a given mass.

Because stars with spectral types between F and M are magnetically active, the study of their rotational properties happens through the measurement of rotational periods using the brightness modulation caused by spots at the stellar surface. This technique has been broadly used both because it gives high precision in period measurement (uncertainty down to 1 percent, Herbst et al. 2007) and because photometric surveys are common nowadays.

Constraining physical models that explain the AM evolution, as the ones summarized in Chapter 1, can be done by looking for correlations between the rotational periods and other stellar parameters: the mass-rotation dependence can be investigated by comparing rotational periods of stars in different mass ranges or in different spectral type ranges. The age-rotation dependence can be investigated by comparing the rotational properties of groups of stars with similar masses, but different ages. The magnetic properties-rotation dependence can be investigated by comparing rotational periods with X-ray emission fluxes, for example. The disc-locking scenario can be investigated by correlating rotational properties with indexes indicative of the star-disc interaction such as mass accretion rates and circumstellar disc indicators.

Interpreting period distributions in the light of disc-locking models may be a delicate process. Often, conclusions regarding the statistical significance of the differences between the rotational period distributions of CTTs and WTTs - commonly seen as supportive of disc-locking scenario - are a controversial. The results reported in some studies are often not verified by other studies, even for the same group of stars. This is because external factors can easily introduce ambiguities in the period distribution interpretation. Among the typical observational biases are the 1 day aliasing phenomenon introduced by Earth's rotation in ground-based observations (to be discussed in Chapter 4), sample incompleteness, periodic sample with small statistics numbers, and physical aspects like the fact the rotational scenario is mass dependent, and therefore uncertainties in mass estimation can easily contaminate the results. Another recurrent physical contamination factor is the diagnosis used to identify stars interacting with their discs. Several studies (including the one developed on this thesis) use IR excess as indicative of the disc presence (see Chapter 3.4), and despite being a good diagnosis for a dusty local environment (Section 2.4), interpreted as a disc, it does not tell if there is indeed an active accretion process in the disc, and thus it does not inform whether the star is still magnetically interacting with the disc or not. Even when using Hα as star-disc interaction diagnosis, biases may be introduced due to the fact accretion in CTTs is often episodic, and that our observations of Hα emission arising from accretion is dependent on the system inclination with respect to our line of sight.

The investigation of the mass-rotation relation is often hampered by the difficulty to estimate stellar masses. Most of the surveys of rotational periods uses only photometric data, and the mass determination is based on fitting the star's position in HR-diagrams with theoretical evolutionary models. Mass estimated like that are extremely model dependent, and as different studies adopt different models, the comparison between studies may lead to wrong conclusions.

Even with all those caveats, the best way to date to study AM evolution is still to measure rotational periods of groups of coeval stars in open cluster or associations, and then to assemble the period distributions for clusters of different ages in an evolutionary sequence. In this direction, thousands of rotational periods

of stars in young clusters and associations have been measured during the last decades (for a review see Bouvier et al. 2014).

The period distribution with which stars become visible is quite broad, with periods distributed mainly between 0.7 days to 10 days for stars with mass in the range 0.2 - 1.0 $M_{\odot}$ (Bouvier et al. 2014), but with a smaller population of very slow rotators with periods up to ∼25 days (Cody & Hillenbrand 2010). Explanations for such dispersion of rotational periods are still open. Gallet & Bouvier (2013) suggested that this spread can be related to the star-disc interaction during the protostellar phase and to the mass distribution of protostellar discs, with more massive discs spinning down protostars more efficiently during the embedded phase (e.g. Ferreira et al. 2000). The lower limit in the period distribution is attributed to the critical rotational velocity of those stars. Even though shorter periods than this lower limit are often observed, Henderson & Stassun (2012) suggested that such shorter periods are due to close contact binary stars, and not due to stellar rotation itself.

Since the first studies about rotational periods in Taurus Auriga (Bouvier et al. 1986b) and in the Orion Nebulae (Attridge & Herbst 1992), an observational scenario was established in which solar-type stars with ages of a few Myr present a bi-modal period distribution. Several authors suggested that this bi-modality for solar-type stars would be an observational evidence for the disc-locking phenomenon due to a correlation between the peak of slow rotators and disc presence (e.g. Rebull et al. 2004). This picture is supported by studies in several regions like NGC 2264 (peaks at ∼4.2 days, and ∼7.0 days. Affer et al. 2013), and IC 348 (peaks at ∼2 days and ∼8 days Littlefair et al. 2005). Cieza & Baliber (2007) presented an alternative way of looking for observational evidences for the disc-locking phenomenon by studying the disc-fraction as a function of period. They showed for ONC and NGC 2264 that there is a trend of increasing disc fraction with increasing period with fast rotators presenting significantly smaller disc-fraction than slow rotators. Vasconcelos & Bouvier (2015) examined disc-fractions as a function of rotational period (Section 1.5.2.3) and found that as a coeval sample evolves, because slow rotators spin up after loosing their discs, the disc-fraction as a whole decreases, but the decrease rate is larger for shorter periods with an accumulation of non disc-bearing stars around shorter periods.

A mass-rotation connection was first reported for stars in ONC (2.5-5.2 Myr), where Herbst et al. (2001) found that while stars in the cluster with spectral types between M2 and K presented a bi-modal distribution, stars with spectral type later than M2 presented a unimodal distribution with a single peak around fast rotators (∼2 days). Since then, most studies for VLM-stars have failed in finding evidence for the disc-locking scenario, and the fact that an unimodal distribution for rotational periods of VLM-stars is repeatedly reported led several authors to suggest that there must be a mass-dependent effect at work (e.g., Cieza & Baliber 2007; Cody & Hillenbrand 2010).

Figure 2.11 shows a compilation of rotational periods as a function of mass for several coeval regions with ages ranging from ∼2 Myr to ∼550 Myr, presented in order of age from top to bottom, and from left to right. The data presented were originally compiled by Bouvier et al. (2014), and they include: NGC 6530 (Henderson & Stassun 2012), the Orion Nebulae Cluster (ONC, Irwin & Bouvier 2009; Rodríguez-Ledesma

et al. 2009), NGC 2264 (Lamm et al. 2005; Affer et al. 2013; Venuti et al. 2016)[22], Cep OB3b (Littlefair et al. 2010), NGC 2362, h Per (Moraux et al. 2013), M 35 (Meibom et al. 2009), and M 37 (Hartman et al. 2009).

From the mass vs. period plots in Figure 2.11 one can see a large spread in period for all young ages. The youngest region is NGC 6530 (2 Myr), and it presents rotational periods widely scattered between 0.5 days and 19 days. While in NGC 6530 only 32% of the sample is composed by fast rotators, for h Per (13 Myr) the fast rotators percentage is ∼56%, and this illustrates the spin up towards the ZAMS, after the star is released from its disc, discussed in Chapter 1. ONC, NGC 2264, Cep OB3b, and NGC 2362 seem to present some transitional properties from the rotational state of NGC 6530 to the rotational state of h Per. For some clusters (ONC, Cep OB3b, and NGC 2362), the spin up of the distribution's lower envelope seems to be more efficient for lower mass stars. h Per distribution is quite flat, and one can see very well defined upper and lower envelopes at periods around 0.3 days, and around 15 days. Moraux et al. (2013) interpret the lower envelope as a strong evidence for PMS spin up, as after the accretion phase is over, the stars are free to contract towards the ZAMS. They also suggested that the slow rotators could be seen as evidence for core-decoupling phenomena (Section 1.5.2.1).

As 1 $M_\odot$ star reaches the ZAMS in around ∼40 Myr, and a 0.5 $M_\odot$ star, in around ∼150 Myr (Bouvier 2013), by the age of M 37, the solar-type stars are already in the MS. When a star reaches the ZAMS, it stops contracting and the AM loss via magnetic winds become the dominant mechanism changing its rotation. This MS spin down explains the accumulation of slow rotators in the distributions of M 35 and M 37, when most of the stars already evolved towards the slow rotators sequence. Comparing M 35 and M 37, the development of this slow rotators sequence is gradual and while in M 35 a few fast rotators of all masses are still seen, by the age of M 37 only a few lower mass stars still present fast rotation. The slow rotator sequence is the basis of the gyrochronology technique (e.g. Barnes 2007), which is an empirical tool for measuring ages of MS stars based on the mass-rotation connection.

Turning back to the PMS rotational evolution, most observational studies for VLM stars suggested that there is a pattern of faster rotation for decreasing masses (e.g. Zapatero Osorio et al. 2003; Rodríguez-Ledesma et al. 2009; Cody & Hillenbrand 2010). Artemenko et al. (2012) correlated the rotation of CTTS in the Taurus-Auriga complex with the position of the stars inside the HR-diagram by separating them in fully convective stars, and stars with a radiative core. They found that stars with a radiative core are on average faster rotators than fully convective stars, and they suggested that this could indicate that changes in the stellar magnetic field after a radiative core is formed (e.g. Gregory et al. 2012) would change the role of the magnetospheric interaction in regulating the stellar rotation.

A feature that markedly varies from cluster to cluster during the PMS is the slope of the distribution's upper envelope for VLM stars. Irwin et al. (2008) suggest that this varying slope for masses between 0.1 - 0.5 $M_\odot$ was a result of the cluster evolution with age. Following this suggestion, Henderson & Stassun (2012) used such slope as an age proxy, and suggest that NGC 6530 would be in an earlier evolutionary stage

[22]In the case of NGC 2264 the period sample was complemented with recently released data from Venuti et al. (2016).

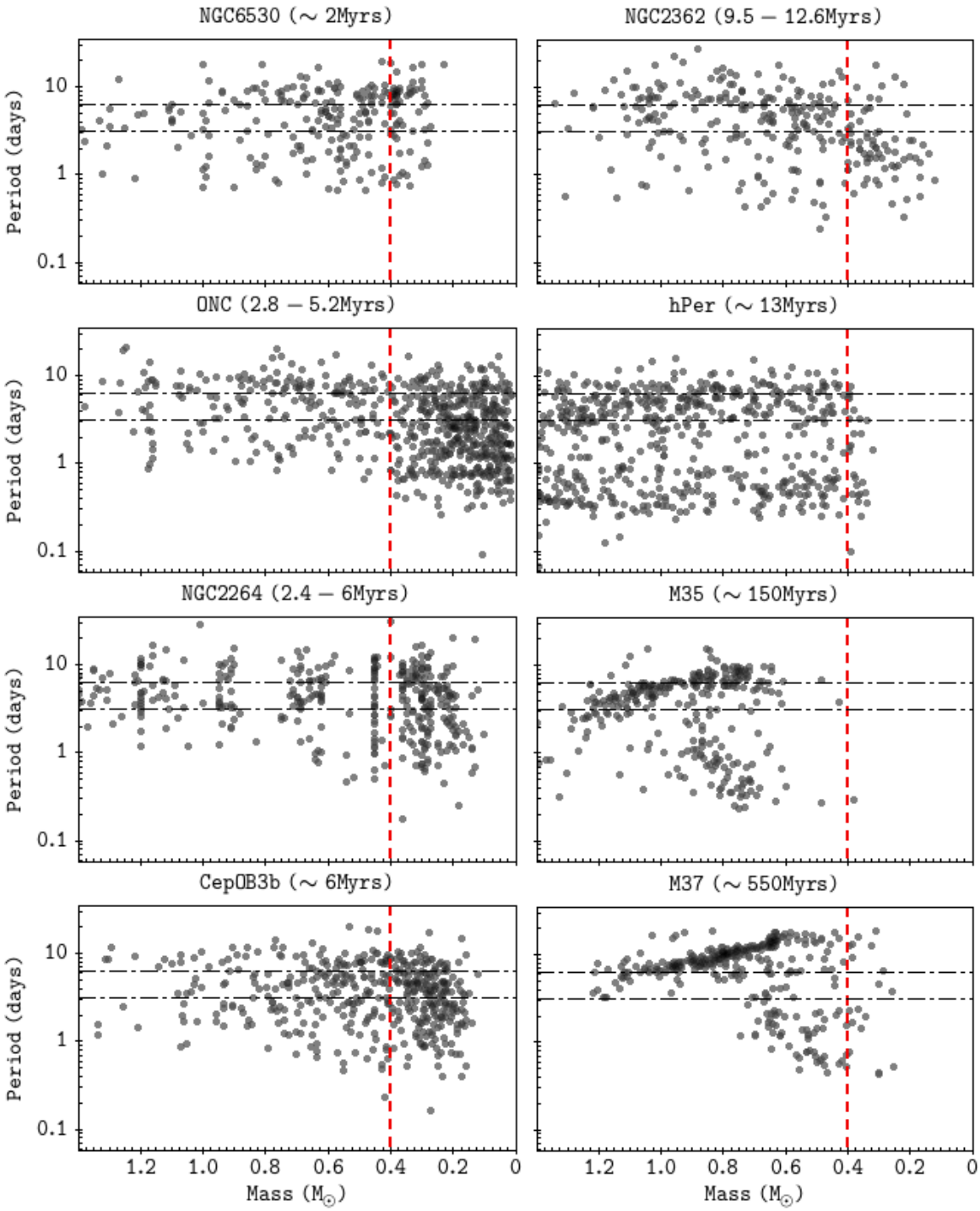

Figure 2.11: Rotational periods as a function of mass for several young regions with ages between 1-550 Myr. Horizontal black lines show the limits between fast rotators and slow rotators. The red dashed line shows the limit between Solar-type stars and VLM-stars. Black dash-dotted lines show the limits between slow/medium and medium/fast rotators.

compared to ONC. They argued that this younger age would justify the remarkable differences between the mass vs. period distributions for NGC 6530 and other clusters. In particular, they found that lower mass stars in NGC 6530 are rotating much slower than the higher mass stars, unlike observed in most other young clusters where lower mass stars rotate faster than higher mass stars. Henderson & Stassun (2012) also argued

that given an younger age, the explanation for the opposite sense in the period-mass relationship, would be that the lowest mass stars in the cluster are currently spinning up, and that in a future step of evolution they would end up rotating faster than the higher mass ones.

NGC 6530 is not the only region with observational results showing a different rotational behaviour for VLM stars. In a study about the Cep OB3b region, Littlefair et al. (2010) reported quite different rotational period distributions at very low mass than Irwin et al. (2008) reported to the supposedly similarly aged NGC 2362. The differences could be partially explained after Bell et al. (2013) reviewed the ages of several young regions, showing that NGC 2362 was actually older than Cep OB3b. However, when comparing it to other clusters of similar age, Littlefair et al. (2010) also found an excess of slow rotators within the VLM stars.

The assumption that each region represents a piece of the same evolutionary process, assumes that global environmental conditions do not play a significant role in the overall rotational evolution. Notwithstanding, the discrepant observational results for regions with similar age mentioned here show that environmental conditions may have an important effect in the evolution of AM during the first million years.

Rodríguez-Ledesma et al. (2009) investigated if the rotational properties were the same in every position inside the ONC cluster. They found that the period distribution for stars in the innermost region of ONC was bi-modal with peaks around $\sim$2.5 days and $\sim$8.0 days for solar-type stars, while in the periphery of the cluster, bi-modality was not evident. Also, they found that stars in the cluster central region were on average slower rotators than stars in the periphery.

As summarized in Section 1.5 and in this section, there are several questions regarding the early rotational evolution of LM-stars that remain open. What determines the period distribution of stars at the birthline? What are the differences one should expect from the rotational evolution of Solar-type stars and VLM-stars? What physical mechanisms regulate the rotation of VLM-stars? What are the environmental conditions influencing the rotational evolution of young stars? Can the environment favour or hamper the disc-locking phenomenon?

Chapter 3

Analysed data

3.1 WFCAM/UKIRT data

The observational dataset used in this thesis, kindly provided by Dr. Bo Reipurth from University of Hawaii, was obtained with the 3.8 m United Kingdom Infra-Red Telescope (UKIRT), at Manua Kea, Hawaii, equipped with the Wide Field Camera (WFCAM, Casali et al. 2007), programs U/07A/H16 and U/07B/H60. The complete dataset is composed of up to 115 nights observed using the J, H and K filters (Hewett et al. 2006). The observations were carried during 2007 in two seasons (Figure 3.1): The first season comprises 43 observed nights between April 1st, and May 21-th; The second season comprises 73 observed nights between August 4th and November 3-nd. The two observational seasons span a total of 217 days. The exposures were short, 2 seconds in each filter.

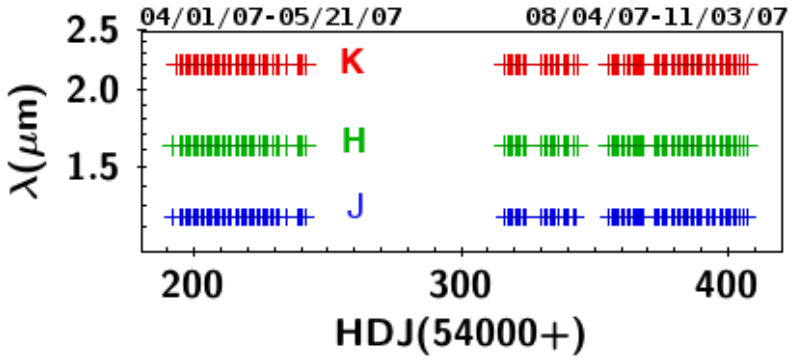

Figure 3.1: Plot showing the nights when observations were taken in the given filters.

The WFCAM is composed of four 2048 × 2048 Rockwell Hawaii-II detectors (Casali et al. 2007, hereafter CCDs W, X, Y, and Z). The detectors are spaced with a separation of 94% of each detector's width, such that four exposures (hereafter exposures A, B, C and D) are required in order to image a contiguous area of 0.87 squared degrees. WFCAM's layout is schematically shown in Figure 3.2. The observed area was centred on $\alpha_{2000} = 20^h33^m$, $\delta_{2000} = +41^o12'$, which comprises approximately the centre of the CygOB2 association.

The data were pipeline-reduced and calibrated at the Cambridge Astronomy Survey Unit (CASU; Irwin

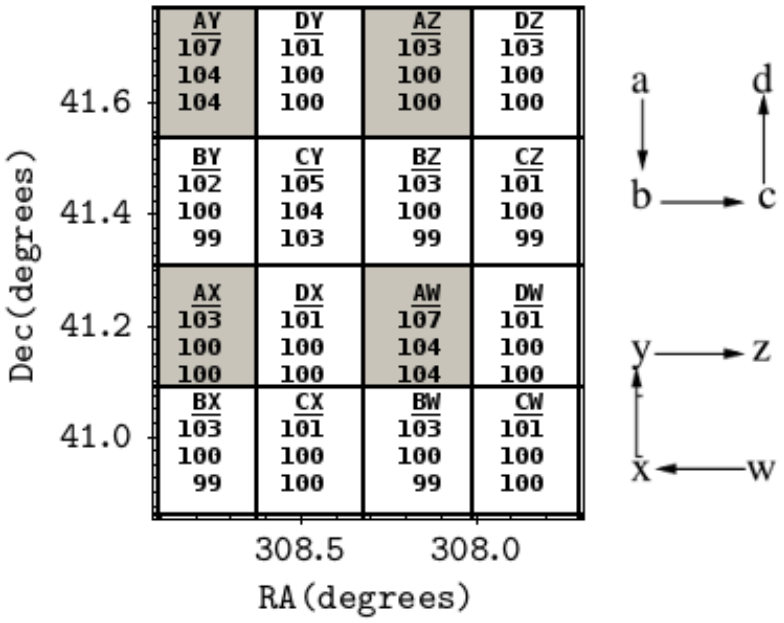

Figure 3.2: Illustration of the WFCAM layout. A sequence of 4 exposures (ABCD) with the 4 CCDs (WXYZ) produces a mosaic of 16 observed regions covering a total area of 0.87 squared degrees in the sky. For each region composing the mosaic, we also show the number of observations in the J, H, and K filters after the data was processed and cleaned.

et al. 2004; Hodgkin et al. 2009), and a source catalogue was provided, displayed in 1388 fits-tables: One for each filter and each exposure. Data calibration was made by CASU's pipeline, using 2MASS sources with extinction-corrected colours 0.0≤J-K≤1.0 and signal-to-noise ratio ≥ 10 in each filter (Hodgkin et al. 2009).

3.1.1 Content of CASU catalogues

The catalogues are in the format of fits-tables. Each fits table has 4 extensions, one for each WFCAM CCD, adding up 5294 tables. Each table is composed of 80 columns, which include a set of fluxes measured with different aperture radii for each source. The content of those columns is detailed on Tables A.1, A.2 and A.3 at Appendix A.

The aperture photometry provided by CASU was used in the present study. As a single number for the flux in all images (in order to link the objects building consistent light curves) was sought, CASU's documentation was followed and an aperture flux number 3 was adopted, which is a soft-edge aperture of 1,″0 radius. In order to convert fluxes into magnitudes and calibrate the photometry, as in the telescope documentation, the following relation was used:

$$m = ZP - 2.5\log_{10}(\frac{f}{t}) - k(\chi - 1) - A - P \tag{3.1}$$

where ZP is the zeropoint for the frame (keyword MAGZPT in the fits header), f is the flux for aperture 3 (APER_FLUX_3), t is the exposure time for each combined integration (EXP_TIME), A is the aperture correction for flux 3 (APCOR3), k is the extinction coefficient (EXTINCTION), χ is the airmass (AMSTART,AMEND), and P is a percentage sky correction (PERCORR). Additionally, the magnitude errors

were derived as:

$$\Delta m = \frac{2.5}{\ln(10)} \frac{\Delta f}{f} \tag{3.2}$$

where Δm is the magnitude error, f is the flux for aperture 3, and Δf is the error in aperture flux 3 (APER_FLUX_3_err).

3.1.2 Linking the stars and producing a light curve catalogue

In order to process the 5294 tables provided by CASU, a semi-automatic IDL procedure was built in order to read, manipulate, and link sources from the tables. This procedure dealt with one (out of 16) exposures/CCD field per time (see Figure 3.2). All sources with a Classification Flag in CASU's catalogues indicating noise, borderline stellar or saturated objects were excluded prior to linking the sources.

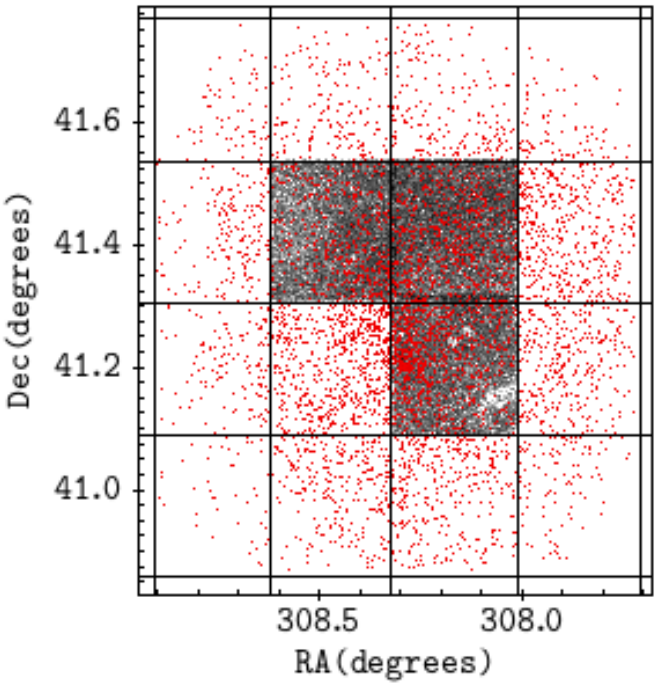

Figure 3.3: Spatial Distribution of the stars with an analysed light curve. Control Sample objects are shown as grey dots, and candidate member stars are shown as red dots.

At first, a control sample was built including all the stars visible in the three central regions (AW, BZ and CY in Figure 3.2) regardless of confirmed membership. This sample was called "control sample", and it was used for statistical purposes in the chapters to come. Second, for the full observed field, member candidates previously identified in the literature were catalogued. This sample was called "member candidates sample". The two samples are shown in a RA versus Dec map in Figure 3.3.

3.1.2.1 Control Sample:

The first approach to deal with the data was to catalogue all the stars in the FOV regardless of confirmed membership for 3 of 16 CCDs (AW, BZ and CY, see Figure 3.2). For each region, the most precise night for

K band in terms of seeing was chosen, and an initial catalogue with the coordinates of all the stars observed on that night was generated. The typical number of detected sources in the central fields was around 25000 sources for nights with good seeing. For each subsequent night or filter exposure for the same region, we used a searching radius of 0.75 arcsec around the position of each object already in the catalogue.

After a complete inspection, the objects in each exposure not matched with the light curve catalogue were added to it as new objects. A human-operator was necessary in the procedure in order to judge parameters and make decisions in how to proceed in case of ambiguities due to:

1. objects in the central fields being too crowded and causing more than one object to be found inside the 0.75 arcsec radius searched;
2. Seeing variations from night to night, causing variations in how many resolved objects were detected from one night to the other.
3. some objects presented proper motion showing varying coordinates;
4. spurious objects inside the source catalogue caused by defects in the data reduction, which were not correctly flagged by CASU processing.

As the goal of this thesis is to study photometric variability, only objects with a minimum amount of 10 valid observations per filter were selected. Table 3.1 shows the numbers of objects catalogued in each region against the number of objects with light curves considered as valid. The 42777 objects with valid light curves composing the control sample are shown in grey in the map of Figure 3.3. Constant stars, selected from the control sample, were used to estimate limit values for the statistical indexes used for evaluating periodic stars, as it will be described in Chapter 4.

Table 3.1: Number of objects detected in the regions AW, BZ, and CY, and number of objects with more than 10 valid points in the light curve for all filters (valid light curves).

Area	Number Objects	Objects with N>10
AW	26774	12963
BZ	28799	15937
CY	25007	13877
Total	80580	42777

3.1.2.2 Member Candidate Sample

As the main goal of this thesis is to determine the variability characteristics and analyse the AM evolution of YSO that belong to the CygOB2 association, the literature was searched for studies that evaluated membership of low mass stars in the CygOB2 association (Sections 2.1 and 2.2). The coordinates of the candidate members were then used to build an input catalogue to cross-match and to merge all CASU tables together in a single multi-band light curve catalogue.

The candidate member catalogues used to compose the input catalogue were already presented in detail in Section 2.2 and Table 2.1, but to summarize they are:

- The list of disc-bearing stars from Guarcello et al. (2013, , hereafter GDW13): 1843 sources;

- The X-ray sources from the Chandra Cygnus OB2 Legacy Survey with optical/infrared counterparts from Guarcello et al. (2015, 2016, hereafter GDW15), considered as members by Kashyap (2017, in preparation): 4864 sources.

Crossing both catalogues, a RA, DEC catalogue containing the 6306 sources was built, and only sources inside the same FOV as the WFCAM/UKIRT data were considered (see Figure 3.4). Each source in the input catalogue was searched inside the CASU tables using a searching radius of 0.75 arcsec. Every time two sources were found inside this search radius, both sources were excluded in order to avoid contaminations to the light curves, and this selection rule accounts for most sources that could not be recovered inside the FOV considered. The catalogue was built by processing region by region (AW, AX, and so on, cf. Figure 3.2). At the end, the 16 light curve catalogues and the sources in the overlapping region between the CCDs were merged into a single identifier.

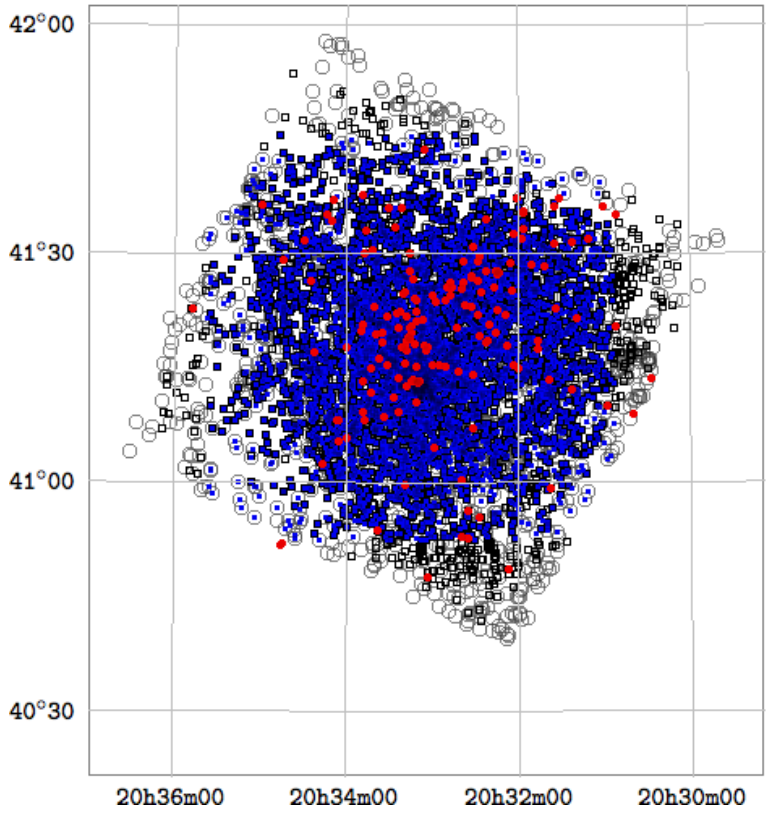

Figure 3.4: Spatial distribution of candidate members. Stars from GDW15 are shown as black squares, and stars from GDW13 are shown as grey circles. Candidate members with valid light curve in the present study are shown as blue dots. OB stars from Wright et al. (2015) are shown as red circles.

There were 100 OB stars on GDW15 (1.99% of GDW15), and all of those stars were saturated in the WFCAM/UKIRT images. GDW15 and GDW13 have 401 low mass stars in common, and 354 of them were also found in the WFCAM/UKIRT catalogues (87.84% of them). We catalogued 1272 stars from the disc-bearing list of GDW13 (69.02% of the disk-bearing input list) and 4165 X-ray sources of GDW15 (85.63% of the X-ray source input list). A total of 5083 sources in the candidate member list were recovered (∼80% of the input catalogue) and these are the sources analysed in this thesis. The spatial distribution of the stars

in the final candidate member light curve catalogue is shown in Figure 3.4.

3.1.3 Evaluating Photometric Errors:

After completing the multi-band light curve catalogues, the empirically derived correction presented by Hodgkin et al. (2009) was applied to the pipeline-estimated photometric errors (equation 3.2).

$$M^2 = cE^2 + s^2, \tag{3.3}$$

where M is the correct measured total error, E is the pipeline-estimated photometric error (from equation 3.2), and $c = 1.082$, and $s = 0.021$ were empirically determined by Hodgkin et al. (2009). With this updated error, the 2% level of night to night variations estimated by Hodgkin et al. (2009) for UKIRT/WFCAM data pipe-line reduced by the CASU was confirmed, as can be verified in Figures 3.5 and 3.6.

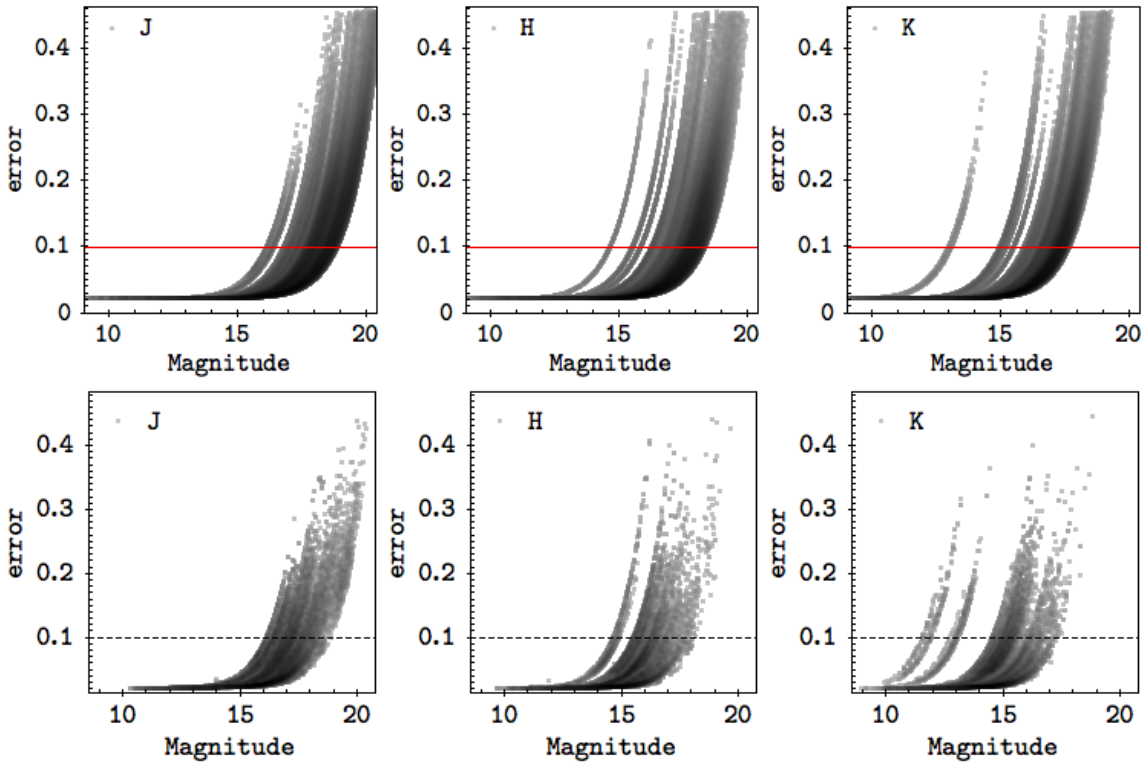

Figure 3.5: Error versus magnitude distributions for all data-points in both control sample catalogue (top) and member candidate catalogue (bottom), for J, H, and K filters. The limit of 0.1 magnitudes for the error, adopted in the present study, is shown as a red line in the top plot, and as a dashed line in the bottom plot.

For each light curve, in order to remove individual points with error unusually higher than the light curve's mean error, a two iterations 2σ-clipping was done in the error distribution around the mean error. After cleaning the complete candidate member sample, the outlier points were analysed and the nights suffering from systematic errors (those for which more than 40% of the valid points in a certain filter were removed) were identified and removed. Eight observed nights were removed from the light curves by this criterion. Excluded nights are listed in Table 3.2 together with the percentage of nights that were excluded

by the cleaning process described. Figure 3.5 shows the error versus magnitude distribution for each filter in each sample before removing those points, and Figure 3.6 shows the same distribution after removing those points. For the purposes of the present study, only data points with error smaller than 0.1 magnitude were used.

Table 3.2: Nights (HDJ 54000+) with more than 40% of valid points excluded and the percentages of excluded objects on each filter.

Night (HDJ)	Filter J (%)	Filter H (%)	Filter K (%)
54191.6+	99.74	99.74	99.74
54193.6+	-	67.83	67.83
54355.38+	46.42	33.04	33.04
54358.2+	88.30	61.58	61.58
54360.4+	97.70	92.30	92.30
54365.2+	-	55.55	55.56
54388.20+	86.04	64.96	64.96
54388.23+	93.34	32.21	25.49

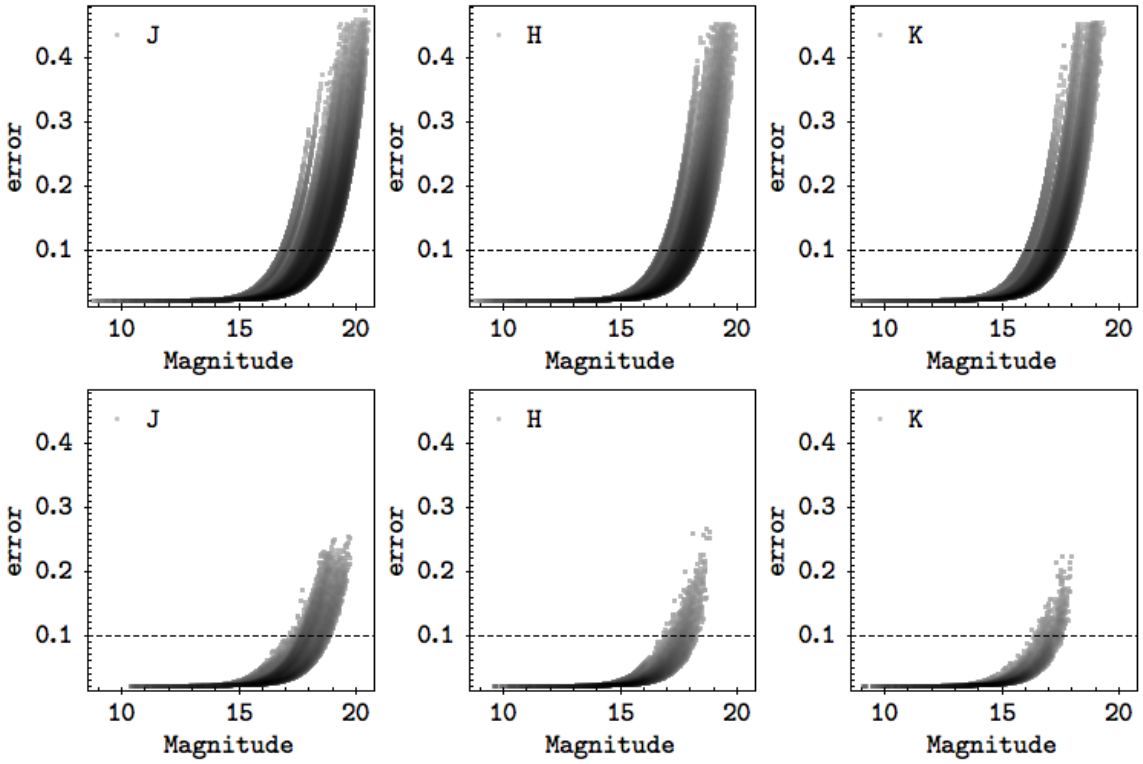

Figure 3.6: Error distributions for filter J (blue), H (green) and K (red) for all observed points (top) and for cleaned data (bottom).

3.2 Literature data

GDW13 composed an optical-infrared (OIR) catalogue using wide and deep photometry, from r band to 24μm, extracted from other surveys of CygOB2 available in the literature. Their OIR catalogue is composed of 328540 sources in the field of CygOB2. The surveys used by the authors to build their catalogue were:

GTC/OSIRIS Catalogue (hereafter GDW12; Guarcello et al. 2012). r, i and z bands, 65349 sources. For sources with good photometry, as defined by GDW12, the catalogue reaches r = 25^{m}; for objects at the distance of 1400 pc, and using a 3.5 Myr isochrone (Wright et al. 2010), with the average extinction $A_V = 4^{m}.3$ (from GDW12), this limit corresponds to a 0.16 $M_{\odot}$ star (Guarcello et al. 2013). There are 3874 objects (76%) in the candidate member catalogue with valid available GTC/OSIRIS photometry.

WFC/IPHAS catalogue in r' , i' , and Hα filters, 24072 sources. First release (Drew et al. 2005) for GDW13 and second release (Barentsen et al. 2014) for GDW15. The limit for good photometry is around $r'=21^{m}.5$ (Guarcello et al. 2013). There are 2364 objects (47%) with at least one valid WFC/IPHAS filter in the candidate member catalogue (2042 with valid Hα).

SDSS DR8 catalogue (Aihara et al. 2011). u, g, r, i, and z bands, 27531 sources. The limit for good photometry is at r=22^{m} ($\sim$0.4$M_{\odot}$) but with a higher limit of saturation than GTC/OSIRIS catalogue, allowing the study of stars up to r=16^{m} ($\sim$ 2.5$M_{\odot}$ Guarcello et al. 2013). There are 1695 objects (33%) with valid riz SDSS photometry in the candidate member catalogue.

UKIDSS/GPS Catalogue J, H, and K bands, 273473 sources. The original UKIDSS (Lucas et al. 2008) photometry extraction was redone by Guarcello et al. (2013), and reaches J=21^{m} corresponding to a mass limit of $\sim$0.1$M_{\odot}$ at the distance of Cygnus OB2. There are 4737 objects (93%) in the candidate member catalogue with valid JHK UKIDSS photometry.

2MASS/PSC (Cutri et al. 2003). J, H, and K_s filters, 43485 sources. According to Guarcello et al. (2013), it was used because it has a higher limit of saturation than UKIDSS. There are 3291 objects (65%) in the candidate member catalogue with valid 2MASS photometry.

Spitzer Legacy Survey of the Cygnus X region (Beerer et al. 2010). IRAC 3.6, 4.5, 5.8, 8.0 μm, and MIPS 24 μm (149381 sources) bands with sources detected down to 0.5$M_{\odot}$ (Guarcello et al. 2013). There are 3294 objects (65%) with at least one valid IRAC observation in the candidate member catalogue.

As part of the Chandra Cygnus OB2 Legacy Survey (Wright et al. 2014), a region of 1 square degree was covered using 36 Chandra/ACIS-I overlapping fields, and the authors detected and verified 7924 X-ray point sources in the observed region. GDW15 cross matched those X-ray sources with GDW13 OIR catalogue and found 5703 X-ray sources with OIR counterpart. X-ray fluxes are available for such objects.

Access to the OIR catalogue composed by GDW13 was provided by Dr. Mario Guarcello, from Osservatorio Astronomico di Palermo, and it was used for estimating several stellar parameters, as presented later in this Chapter.

3.3 Completeness of the analysed data

The completeness of the analysed data was estimated based on the drop in the number of detected objects in the magnitude distribution histograms for J, H, and K filters, which are shown in Figure 3.7 for the control and member candidate samples.

For the control sample (left plots), the limit magnitude detected in each band was $J_{max} \sim 20.2$ mag, $H_{max} \sim$19.4 mag, and $K_{max} \sim$19.0 mag. The samples are complete up to magnitudes $J_{complete} \sim 19.2$ mag,

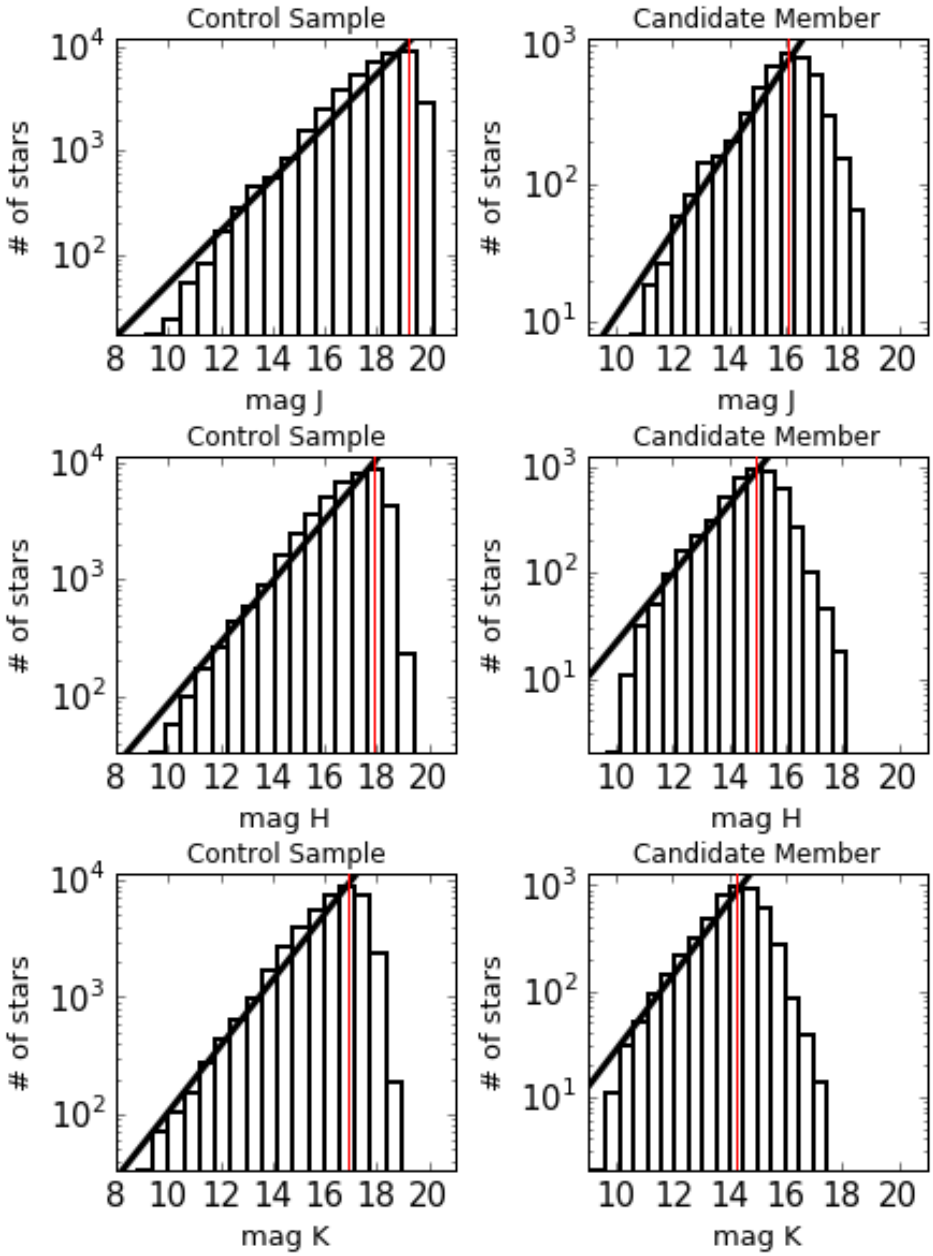

Figure 3.7: Magnitude distributions for the control sample (left) and candidate member sample (right), for J, H, and K filters. The red vertical line shows the completeness limit. The black bold line shows the straight line fitted to the distribution and used for estimating completeness.

$H_{complete}$ ∼17.9 mag, and $K_{complete}$ ∼16.9 mag. For the candidate member sample (right plots), the limit magnitude detected in each band was J_{max} ∼ 18.8 mag, H_{max} ∼18.2 mag, and K_{max} ∼17.4 mag. The samples are complete up to magnitudes $J_{complete}$ ∼ 16.1 mag, $H_{complete}$ ∼14.9 mag, and $K_{complete}$ ∼14.3 mag.

From Figure 3.7 one can estimate the completeness based on the slope of the distribution. With the '# of stars' axis in log-scale, the distribution can be approximated by a straight line. The slope of such line was estimated by considering the central bin values vs the number of counts in each bin. Because the brighter stars in the sample are saturated in the vicinity of the OB stars, no bin with magnitude smaller than about 12 was considered when calculating this slope. Accordingly, the straight line was fitted considering bins larger

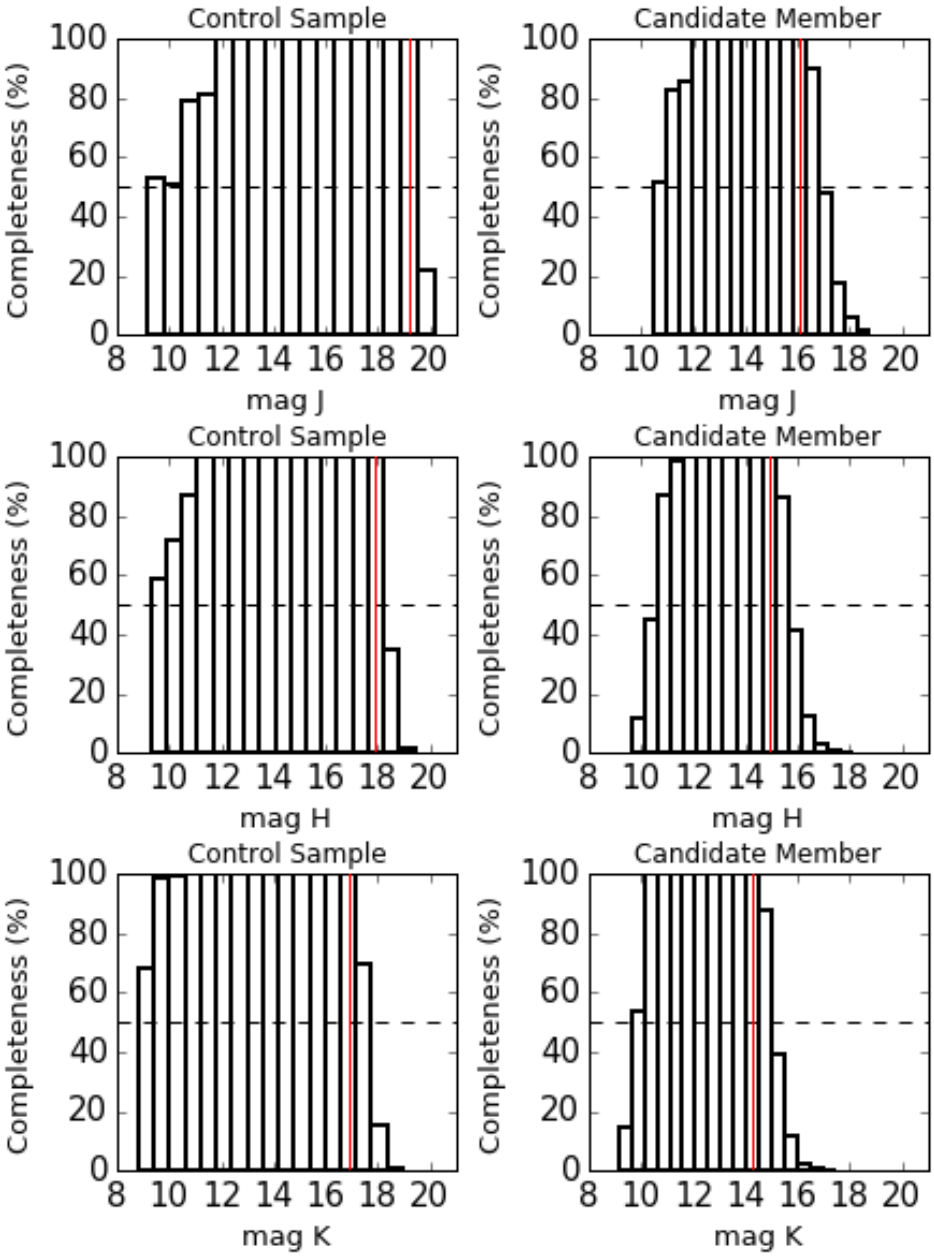

Figure 3.8: Completeness as a function of magnitude for the analysed data for the control sample (left) and candidate member sample (right), for J, H, and K filters. The red vertical line shows the completeness limit. The horizontal dashed line shows the 50% completeness level.

than 12 mag, up to the bin before the drop in the distribution. The fitted line was then plotted against the magnitude distribution, and the incompleteness can be estimated as the missing amount of counts until the straight line in each bin. Completeness plots as a function of magnitude are shown in Figure 3.8, where one can see that the control sample goes deeper than the candidate member sample. This is due to the lower completeness limits in the studies used to compose the candidate member sample. Also, there is a incompleteness toward the brighter stars in both samples. This is due to the fact that the OB stars are highly saturated in the WFCAM/UKIRT images used, raising the sky counts around them and causing the saturation of some relatively bright stars in their vicinity.

3.4 Deriving stellar parameters

3.4.1 Interstellar reddening

In order to estimate masses for the candidate member sample it would be necessary the knowledge of individual extinctions, which in turn would require the knowledge of spectral types for individual stars. Since there is no available information about the spectral type coming from spectroscopic studies in the literature (Section 2.2), individual extinction for stars in the candidate member sample could not be formally determined. An alternative for that was to look for optical counterparts in other surveys (Section 3.2), and to use optical colours to estimate the extrinsic reddening for each object in the sample. As colours are not affected by the distance, a distance independent individual A_V can be estimated for each star by measuring the displacement of a star inside the CC-diagrams in relation to an isochrone, as it was described in Section 2.3.3.

The i-z vs r-i colour-colour diagram was used in order to estimate individual extinctions for the candidate member sample. As described in Chapter 3, *riz* photometry is available from Guarcello et al. (2012) and from SDSS. There were 4073 stars in the candidate member sample wit *riz* counterparts with error smaller than 0.2 magnitudes in every filter: 3690 from GTC/OSIRIS observations, and 383 from SDSS DR8.

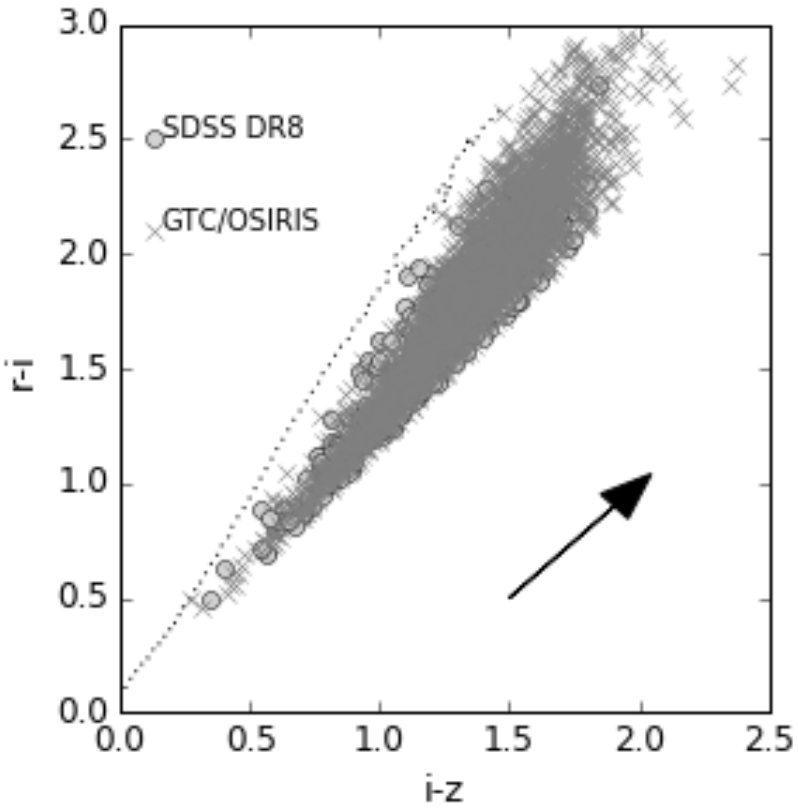

Figure 3.9: Colour-colour diagram for *riz* colours. Stars with data from Guarcello et al. (2012) are shown as grey Xs, stars with data from SDSS are shown as grey circles. The Covey et al. (2007) empirical dwarf sequence is shown as a dashed line. A reference reddening vector for $A_V = 2^m$ is shown in black.

The approach adopted by Guarcello et al. (2012) to evaluate individual extinctions was to use a 3.5

Myr isochrone from Siess et al. (2000) with relative extinctions from O'Donnell (1994). As Siess isochrones were calculated for the Johnson-Cousin filters, Guarcello et al. (2012) had to perform several transformations between photometric systems, which can introduce systematic errors to the reddening estimations. We used instead an empirical dwarf sequence from Covey et al. (2007), which is already in the same photometric system as the *riz* data. We adopted relative extinctions for *riz* bands from Schlegel et al. (1998), with a R_V=3.1 extinction law from Cardelli et al. (1989), transformed from *u'g'r'i'z'* (USNO 40 in) to *ugriz* (SDSS 2.5m) according to SDSS documentation[1]. Table 3.3 shows the relative extinctions for each filter. Because CC-diagrams for JHK colours were used in other moments in this thesis, we also list their relative extinction, extracted from Hanson (2003) and transformed to WFCAM/UKIRT photometric system using the transformations of Hewett et al. (2006).

Figure 3.9 shows the *riz* CC-diagram. For estimating the extinctions, each star was shifted parallel to the reddening vector in the opposite direction as it points, until it reached the Covey et al. (2007) empirical dwarf sequence. Using this technique, it was possible to estimate A_V for 3818 member candidate stars, 3459 using GTC/OSIRIS data, and 359 using SDSS DR8 data. The distribution of individual extinction values obtained is shown in the plot of Figure 3.10. The median A_V obtained for the periodic sample was 4.0^m, which is in good accordance with the 4.33^m value obtained by Guarcello et al. (2012) for stars in CygOB2 centre. The bottom plot in Figure 3.10 shows the A_V distribution for the sample of stars with reliable period (Chapter 6).

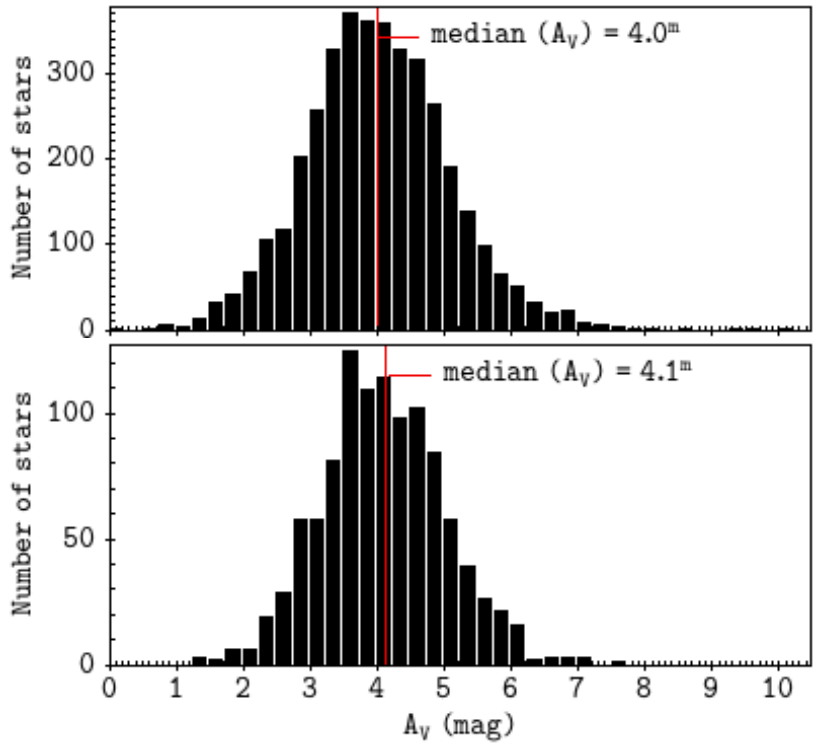

Figure 3.10: Individual extinction distribution estimated using *riz* colours. Top: For all stars in the candidate member catalogue. Bottom: For all stars with reliable periods measured.

[1] http://classic.sdss.org/dr7/algorithms/jeg_photometric_eq_dr1.html

JHK		riz	
Filter	A_λ/A_V (mag)	Filter	A_λ/A_V (mag)
J	0.285	r	0.850
H	0.172	i	0.647
K	0.121	z	0.447

Table 3.3: Relative extinction coefficients in terms of visual magnitude extinction for JHK filters extracted from Hanson (2003), and for *riz* filters from Schlegel et al. (1998).

3.5 Mass estimation

Next, the estimations of individual extinction values can be used, together with the r vs. r-i CM-diagram, to estimate masses. The distance modulus for CygOB2 is DM=10.62 (d=1.33 kpc Kiminki et al. 2015). Each star with estimated extinction was de-reddened for its individual A_V, and the distance modulus was applied. Masses were then estimated given the position of the de-redden and distance-corrected star inside the CM-diagram in relation to a grid of PMS semi-empirical isochrones from Bell et al. (2014), with PISA models (Tognelli et al. 2011, 2012) for solar metallicity ($Z_\odot$=0.013), and ages in the range 0.1-30 Myr. The grid of semi-empirical isochrones was built by using the CMDfit software[2], and the bolometric corrections applied were calculated by the software's authors by folding spectra with opacities from BT-Settl (Allard et al. 2011) through the desired filter response and applying empirical corrections from Bell et al. (2014). The isochrones used here were convolved to SDSS filters (Doi et al. 2010) with an AB zero point. The isochrones used in the grid comprise masses in the range 0.1-8 $M_\odot$. It was possible to successfully estimate masses for 3818 candidate member stars. The top plot in Figure 3.11 shows a histogram with the distribution of estimated masses for all member candidate stars. The bottom plot shows the same, but for stars with reliable period measured. The plot in Figure 3.12 shows a r-i vs. r CM-diagram for de-redden periodic stars and mass tracks from 0.1 to 1.4 $M_\odot$.

From Figures 3.11 and 3.12 one can notice a lack of stars with masses larger than $\sim$0.9 $M_\odot$, which is mainly due to the fact that most of the stars with masses larger than this value are very close to the saturation limit in our WFCAM/UKIRT observations. One may also notice that the shape of the distribution does not change significantly after the selection of periodic stars, which points out that the techniques applied to identify periodic stars (to be presented in Chapter 4) does not favour the identification of periodic stars with any specific mass. Finally, one may also note that there are fewer stars with masses under $\sim$0.5 $M_\odot$, and this is explained by the fact the studies used to select members and the dataset used to evaluate the masses are incomplete for VLM-stars.

A caveat on using optical colours for estimating masses is that stars with discs may be affected by accretion, scattering, or obscuration by the inner disc. Only 65 stars in the sample analysed are periodic (Chapter 4), have discs (Section 3.6) and had masses estimated as described in this section. It was verified that only 3 of those stars had evolutionary status from GDW13 compatible with some ongoing phenomena that could affect their optical colours: 1 star has Hα emission, 1 star has colours compatible with scattering,

[2]CMDfit software, author: Tim Naylor: `http://www.astro.ex.ac.uk/people/timn/tau-squared/software.html`

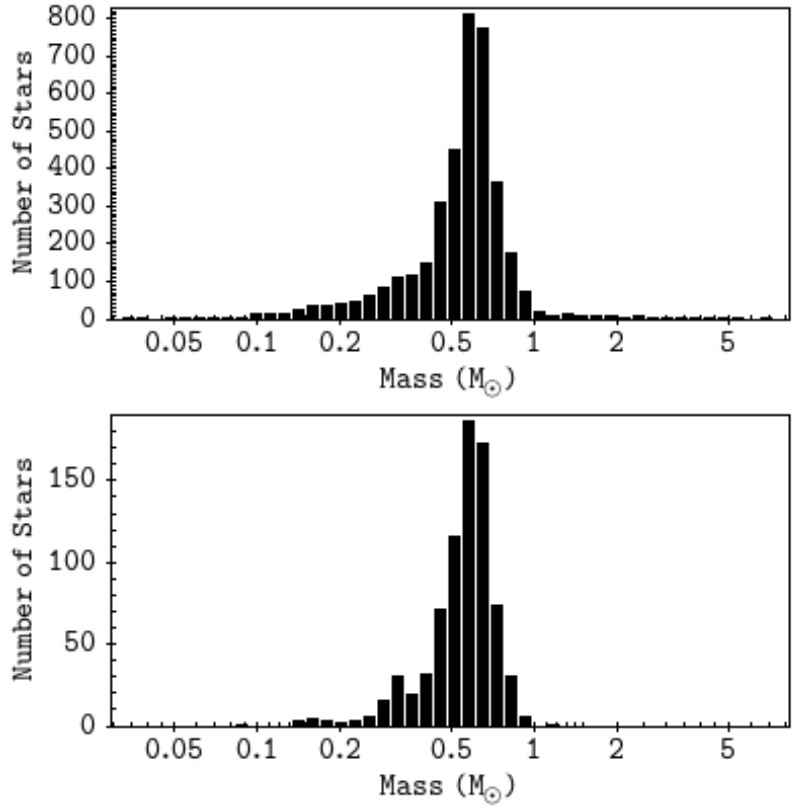

Figure 3.11: Mass distribution for (top) candidate members and (bottom) reliable periodic stars.

and 1 star has a disc at high inclination. As they correspond to a very small fraction of our sample, we considered, for general purposes, that these effects do not influence the mass estimations we performed.

The choice of Pisa isochrones with empirical corrections instead of other models commonly used in the literature is justified as follows. Bell et al. (2012) critically analysed the most used isochrones for estimating PMS stellar masses in the literature. As there are sources of opacity missing in the models for atmospheres of cool stars ($T_{\rm eff}$<3700 K), in the optical regime of the spectrum, Bell et al. (2012) commented that the use of MS isochrones for estimating PMS masses is problematic because MS isochrones do not fit well the PMS lower mass stars. Additionally, in MS models, photometric calibration is done for dwarf stars, what can introduce even more uncertainties when dealing with giant PMS stars. Bell et al. (2014) used Ks-band magnitudes to define a $T_{\rm eff}$ scale for young stars, and used this new scale to quantify the differences between the observed sequence and theoretical pre-MS model isochrones as a function of $T_{\rm eff}$ in individual photometric bandpasses. The results were used to empirically recalibrate the Bolometric Corrections - $T_{\rm eff}$ tables. Using the existent stellar interior models together with this new recalibrated Bolometric Corrections - $T_{\rm eff}$ table, they generated semi-empirical isochrones for PMS stars.

To test the influence of the choice of the model in the derived masses, masses were also calculated using Baraffe et al. (1998) with Bell et al. (2014) empirical corrections, Siess et al. (2000), and Baraffe et al. (2015) models. A comparison of the mass distribution for each model is shown in Figure 3.13. The masses calculated with each of these three models as a function of masses estimated with Pisa+empirical corrections

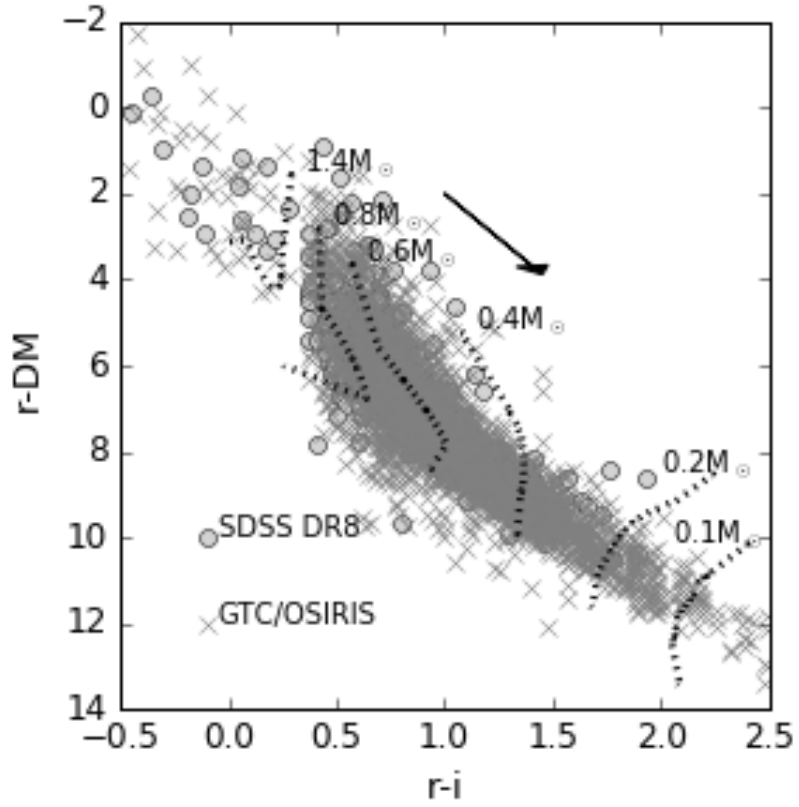

Figure 3.12: CM-diagram for *riz* photometric system. Stars with data from Guarcello et al. (2012) are shown as grey Xs, stars with data from SDSS are shown as grey circles. A reference reddening vector for $A_V = 2^m$ is shown in black. Mass tracks from Bell et al. (2014) for Pisa models (Tognelli et al. 2012) with semi-empirical corrections are show as dotted lines.

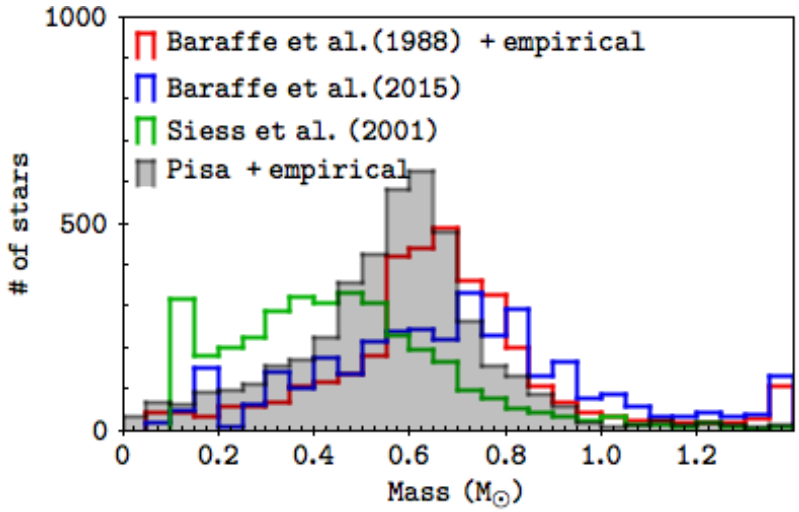

Figure 3.13: Mass distribution for masses estimated using different evolutionary models.

are shown in Figure 3.14. From the two figures one can see that Siess masses are systematically smaller than the masses from the other models. One can also see that for masses around $0.5M_\odot$ and smaller, Siess masses are about half of the Pisa masses. Baraffe et al. (1998) with empirical corrections result in mass estimations that are the closest to the Pisa model, but both Baraffe et al. (1998) and Baraffe et al. (2015) result in

masses systematically larger than Pisa ones.

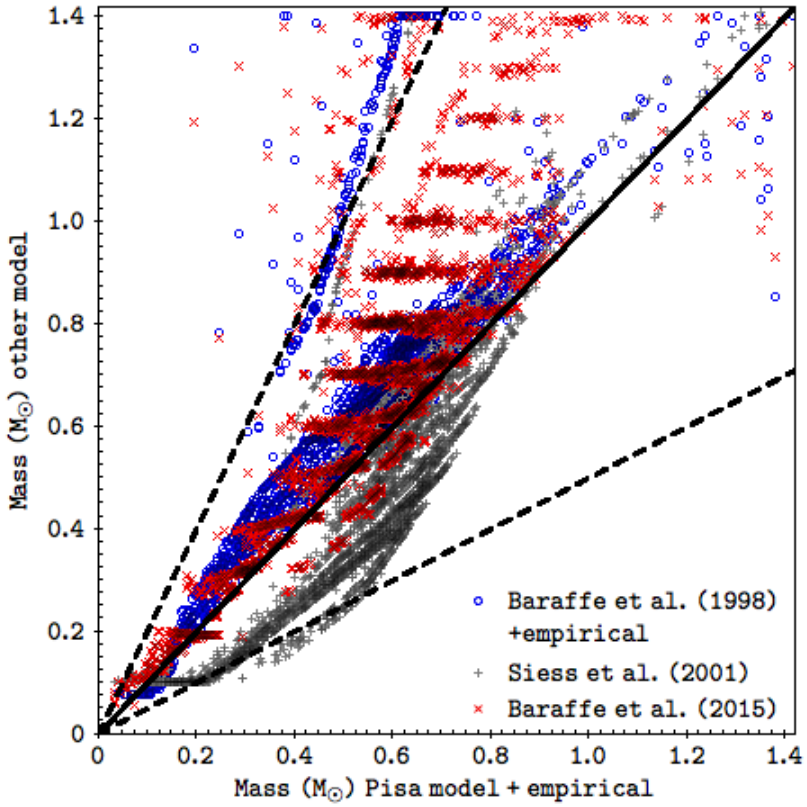

Figure 3.14: Comparison between masses estimated with different models. Masses estimated using Baraffe et al. (1998) with Bell et al. (2014) empirical corrections, Siess et al. (2000), and Baraffe et al. (2015) models are shown as a function of masses estimated with Pisa models. The black solid line shows the equality line for both models. Dashed black lines show the path for masses that are the double, and the half of masses estimated with Pisa models.

3.6 Disc-bearing stars and their discs evolutionary status

In Guarcello et al. (2013), the authors investigated the evolutionary status of the disc-bearing sources, identified in their study, using the infrared spectral index, $\alpha_{\rm IR}$, presented earlier in Equation 2.4. For doing so, they converted K, IRAC, and [24] magnitudes into flux units, and applied a linear fit to the infrared SED. Guarcello et al. (2013) call attention to the fact that they do not de-redden the stars before calculating the α index. To attribute evolutionary classes to the 30 extra sources added to the disc-bearing candidate list (Section 2.2.1.2), the same scheme used by Guarcello et al. (2013) was followed. The flux of a star, F_λ, in a certain filter of wavelength λ, is $F_\lambda = F_0 10^{\frac{-m}{2.5}}$, where F_0 is the zero point flux for that filter, and m is the magnitude in the same filter. The zero point fluxes and $\lambda_{\rm eff}$ for the infrared data used are presented in Table 3.4. WFCAM/UKIRT JHK information was extracted from Hewett et al. (2006), and IRAC and MIPS from IRAC and MIPS Instrument Handbook. To convert F_ν to F_λ, the relation $F_{\lambda,\rm eff}[\frac{\rm J}{\rm s}{\rm m}^2{\rm Hz}] = \frac{c}{\lambda^2} F_\nu \times 10^{-26}$ was used.

It was possible to calculate $\alpha_{\rm IR}$ for 29 of the 30 extra disc-bearing sources. Figure 3.15 presents the $\alpha_{\rm IR}$

Filter	$\lambda_{\rm eff}$ (μm)	F_ν (Jy)	Filter	$\lambda_{\rm eff}$ (μm)	F_ν (Jy)
UKIRT			MIPS		
J	1.2483	1530	[3.6]	3.550	280.9 ± 4.1
H	1.6313	1019	[4.5]	4.493	179.7 ± 2.6
K	2.2010	631	[5.8]	5.731	115.0 ± 1.7
IRAC			[8.0]	7.872	64.9 ± 0.9
[24]	23.68	7.15±0.11			

Table 3.4: $\lambda_{\rm eff}$ and zero point fluxes for WFCAM/UKIRT JHK filters, and IRAC and MIPS filters.

distribution for the 1301 disc-bearing stars with valid $\alpha_{\rm IR}$ estimated in the present work or by Guarcello et al. (2013). According to the classification scheme presented in Section 2.2.1.2, and according to the classification previously attributed by Guarcello et al. (2013), the candidate member sample is composed of: 58 Class I YSO, 154 Flat Spectrum YSO, 1084 Class II YSO. We considered as Class III sources all the stars in the candidate member list that were X-ray emitters and that were not listed as disc-bearing stars by Guarcello et al. (2013) or by us. Hence, there were 3887 Class III YSO in our sample. The additional Class III that were not listed by Guarcello et al. (2013) are not shown in the distribution of Figure 3.15.

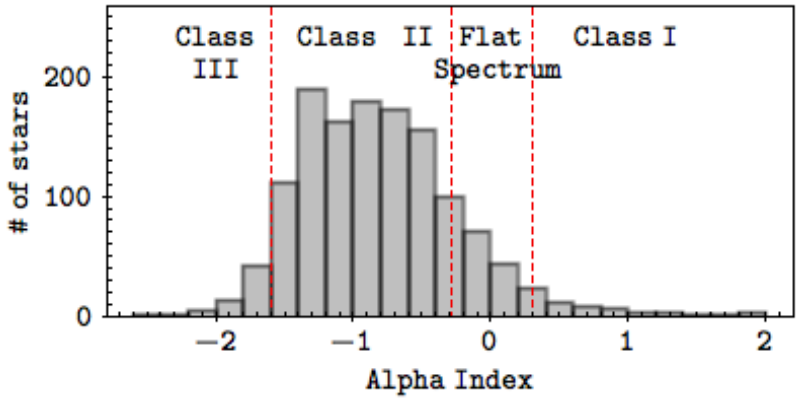

Figure 3.15: Distribution of $\alpha_{\rm IR}$ for stars in the candidate member sample. Red dashed lines show the limits between the evolutionary classes.

Chapter 4

Time series analysis

4.1 Light curve morphology

The first step towards the variability characterization of our sample was the visual inspection of the light curves and their classification according to the main features in their morphology. Initially the objects were classified with the following nomenclature:

0 - Non-variable: If no coherent signal was visually identified neither in the light curve, nor in the cross-correlation-function, and also if the Stetson Index (Section 4.2) was close to zero.

1 - Possibly Periodic: At least one significant peak was found in the Periodogram and the same peak was present in each other filter's periodogram; a periodic signal was found in the cross-correlation-curve; Stetson Index was at least equal to 0.25.

2 - Other variables: Stars with Stetson variability Index larger than 0.25, but that did not fit in any other variability category.

3 - Eclipse-like variations: Stars presenting Stetson Index at least equal to 0.25; the morphology in the light curve, and cross-correlation-curve was compatible with an eclipse-like variation: the stars spend most of their time in a maximum of brightness, but suffer occasionally quick diminishing in bright; Periodicity occurrence was observed, but was not used as a selection criterion.

Table 4.1 shows the number of stars per listed group.

Type	Number of Stars
Non-Variable	2006
Possibly Periodic	1679
Other Variables	1288
Eclipse-like	110

Table 4.1: Number of stars flagged with each morphological type.

4.2 Stetson variability index

The Stetson variability index (hereafter S, Stetson 1996) provides a very efficient way of selecting variable stars. The multi-band Stetson Index is defined as:

$$S = \frac{\sum_{i=1}^{p} w_i \mathrm{sgn}(P_i)\sqrt{|P_i|}}{\sum_{j=1}^{p} w_i} \tag{4.1}$$

where i is a pair of observations, which has a weight w_i, and p is the total number of pairs of observations. P_i is defined as the product of the normalized residuals of two observations j and k that constitute the i-th pair, $P_i = \delta_{j(i)}\delta_{k(i)}$, and as $P_i{=}\delta^2_{j(i)} - 1$ when there is only one valid observation ($j = k$). If one night has valid observations in all J, H and K filters, then there are three pairs of observations for that night. Following Carpenter et al. (2001), if the star has valid J, H, and K, then each pair of observation has weight $w_k{=}\frac{2}{3}$ (total weight of 2 for the whole set), when there was a missing point, *i. e.*, non-existent observation in one or two filters, then a weight $w_k{=}1$ was assigned. The normalized residuals are defined as:

$$\delta_k = \sqrt{\frac{n}{n-1}}\frac{m_k - \bar{m}}{\sigma_k}, \tag{4.2}$$

for a given filter, where n is the number of measurements used for determining the mean magnitude, $\bar{m}$, and σ_k is the photometric uncertainty for the k-th measurement .

Designed this way, the Stetson Index sets uncorrelated non-variable stars with values of $S \sim 0$, and significantly variables with $S \geq 1$. Different authors adopt different Stetson index limits to account for low-amplitude variable stars. For example, Carpenter et al. (2001) adopts $S \geq 0.55$, and Plavchan et al. (2008) found periodic variables down to $S \sim 0.2$. For the purposes of the present work a selection limit of $S \geq 0.25$ was adopted for selecting variable stars. From the candidate member sample, 4079 (80%) stars met the Stetson variability criterion. There were 1002 stars (20%) that met the Stetson variability index criteria, but were not considered as variables after light curve morphology inspection.

Figure 4.1 presents a histogram with the S distribution for the control sample (top) and for the candidate member sample (bottom). Figure 4.2 shows a S versus H-K colour distribution for the control sample, member candidate sample, periodic stars, and non periodic variable stars. In all the plots the $S = 0.25$ level chosen for selecting variable stars is shown as a black dashed line. In the four plots in Figure 4.2 darker colours show a higher concentration of points. This artefact of darker colours marking higher density of points allows the identification of a locus in each distribution. The top left plot, which contains the S distribution for all stars in the field, shows a S locus centred under the $S = 0.25$ limit used for selecting variable stars, which indicates that variability is not a dominant characteristic when the population considered is the whole field of view. On the contrary, when considering only member candidate stars (the other three plots) the locus of S distribution is located above the S limit. This corroborate the idea that variability is an important characteristic of young stellar objects.

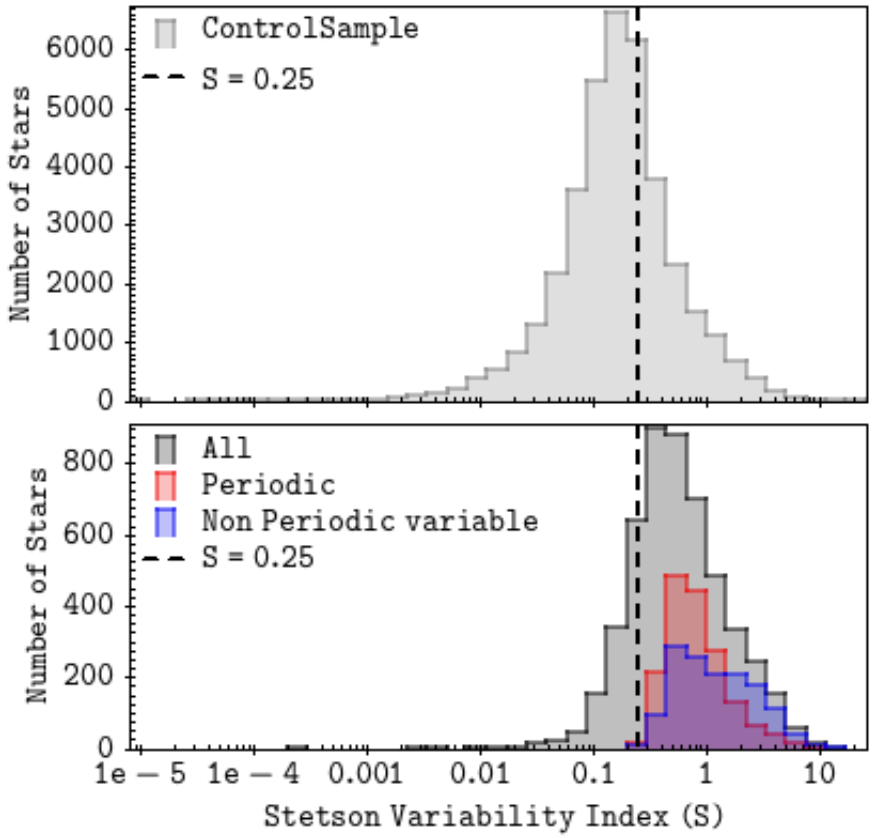

Figure 4.1: Histogram showing the Stetson variability index distribution. Top: all stars in the field of view (Control Sample). Bottom: all member candidates (Black/grey), periodic variable stars (red), and non periodic variable stars (blue).

4.3 Periodicity analysis

The main technique used for identifying periodic stars and determining their periods was the Lomb-Scargle Normalized Periodogram (hereafter LSP, Lomb 1976; Scargle 1982), a widely used modified version of the classical periodogram based on fast Fourier transforms, that can be applied to unevenly spaced datasets. The LSP algorithm used here was implemented according to Press et al. (1992) and Horne & Baliunas (1986), and it was normalized by the total variance of the data. This normalization guarantees that the power of a certain frequency's peak in the periodogram (z) is related to the false alarm probability (FAP) for that frequency as:

$$\mathrm{FAP} = 1 - (1 - e^{-z})^{N_i}, \tag{4.3}$$

were N_i is the number of independent frequencies used to compose the periodogram.

To apply the LSP algorithm to the sample, an oversampling factor of 260, and a scale factor of 5 for the Nyquist Frequency were used, a choice that sets the lower limit in the period search as ∼0.83 day and that will be discussed in more details in Section 4.4.6. For evenly spaced data, the higher limit in the frequency search would be given by $f_{\mathrm{Nyquist}} = \frac{1}{2\Delta t}$, were Δt is the time between consecutive data points. For unevenly spaced data, the Nyquist frequency, calculated with Δt being the mean time between two

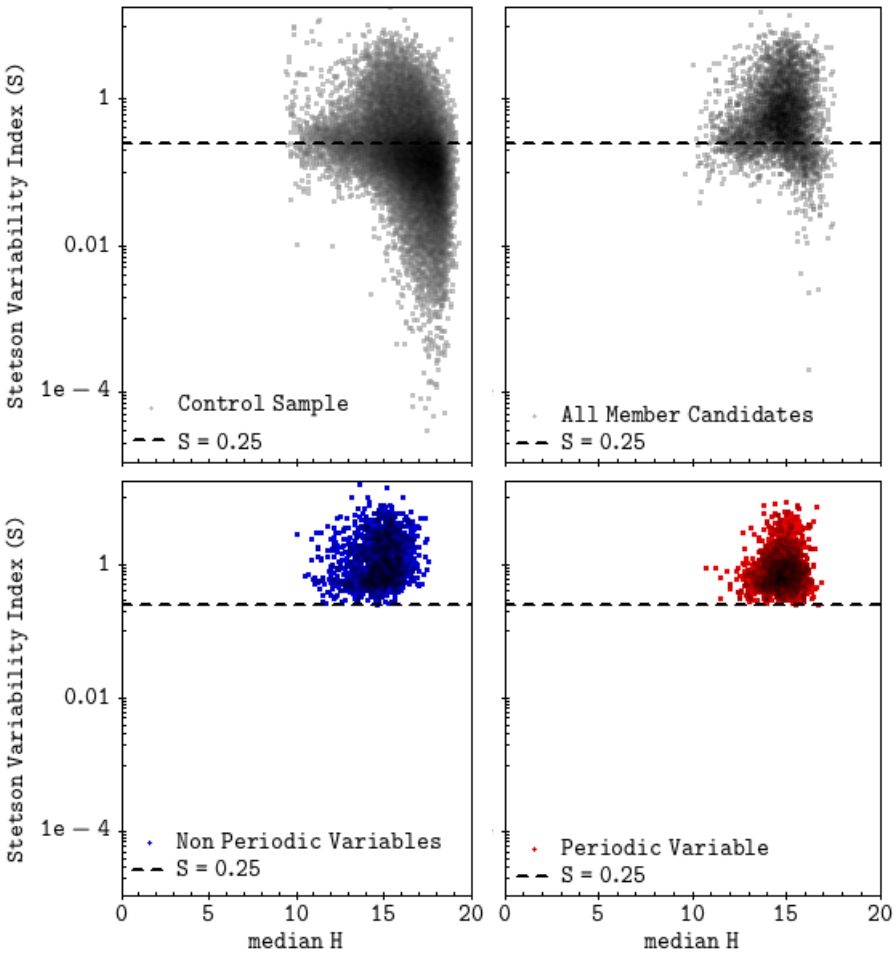

Figure 4.2: Stetson Index distribution versus median H magnitude. Top left: All stars in the field of view (control sample). Top right: candidate members regardless of variability. Bottom left: non periodic variable stars. Bottom right: periodic variable stars.

consecutive measurements, gives only a rough estimation for the higher limit in the frequency search (Scholz & Eislöffel 2004). As the dataset in the present study is unevenly spaced, the search for periodic signals is extended over higher frequencies than the limit imposed by the Nyquist frequency (which is around 2 days for our dataset). Potential contamination due to this choice will be discussed in Section 4.4. The dataset is composed by two observational seasons of ∼45 days and ∼75 days, respectively. For the lower limit in the frequency search, the resolution of the smaller season was adopted, i.e. $\frac{1}{45\ \mathrm{days}}$. Hence, we searched for periodic signals in the period range 0.83-45 days.

The search for periodic signals via LSP consists in studying the highest peaks in the periodogram, and determining their significance. Judging a certain frequency's power peak significance can be a tricky task and it is until nowadays one of the main limitations in studies regarding periodic stars. First, there is the 1 day aliasing phenomenon that can be written as:

$$P_{\mathrm{measured}} = \frac{1}{n + \frac{1}{P_{\mathrm{True}}}} \tag{4.4}$$

with n integer, and it is caused by the limitations in the observations imposed by the Earth's rotation (cf.,

Tanner 1948). Second, we are here dealing with young stars and they typically show irregular variability that may be mixed with the periodic signal. The combination of irregular variability with discrete and uneven sampling may cause the occurrence of spurious periodogram power peaks, that despite being high peaks, are not truly associated to a periodic signal.

Horne & Baliunas (1986) False alarm probability: Horne & Baliunas (1986) reduced the problem of estimating the FAP (FAP_h when referring to their concept of FAP) to the problem of finding the number of independent frequencies adequate to be applied in Equation 4.3. They used Monte Carlo simulations to generate a large number of datasets with pseudo-Gaussian noise, and different time-samplings. From the simulated data, they estimated N_i for a set of uneven and non clumped data, as N_i=$-6.3+1.2N+0.00098N^2$, where N is the number of valid data points.

Despite being largely used in the literature, this method for estimating FAP_h may not always be adequate. As pointed out by Littlefair et al. (2010), FAP_h calculations via Monte Carlo simulations with gaussian noise are not reliable, as they can only account for variability due to photometric errors, while often there is also some intrinsic variability characteristic of young stellar objects. Littlefair et al. (2010) propose, as an alternative, to use the light curves themselves as a mean of estimating the height of spurious peaks due their intrinsic variability. When using the light curves themselves, spurious peaks introduced into the periodogram by all factors affecting the dataset - like imperfect photometry, intrinsic variability, a finite S/N and sampling windows problems - are accounted for. Monte Carlo simulations were not used for estimating FAP_h in the present work, but this idea was applied for performing simulations used to estimate the completeness and contamination levels of the periodic sample, as will be discussed later in Section 4.4.

False alarm probability from a control sample: When studying the sample of member candidates of CygOB2, one may expect to be dealing with a sample of young stars, and possibly with a high fraction of periodic stars. On the contrary, when studying the sample of all objects in CygOB2 FOV, one may expect instead a sample rich in field stars, and a lower fraction of periodic stars. This difference gives an alternative method for estimating the FAP, that consists in studying known constant stars in the field of view and estimating the recurrence and typical height of spurious periodogram peaks for their light curves.

FAP was estimated by using data from the control sample, with 42777 catalogued stars with more than 10 valid observed nights per filter. LSPs were calculated for all the objects in the sample, and the power of the highest peak in the periodogram for each object was recorded. A sample of objects with frequency of the highest peak in the range $0.3 < f < 0.5$ day^{-1} was selected. We chose this interval based on the frequency vs. periodogram power peak plots in Figure 4.3: this frequency interval is outside the bulk produced by the 1 day alias, and also outside the bulk of longer periods (lower frequencies). From this sample, a sub-sample of stars with Stetson Variability Index smaller than $S = 0.15$ was selected, building this way a constant star sample, composed by 3999, 3077 and 3064 objects in J, H and K filters respectively. Cumulative distribution for the values of highest power peak in the periodogram of each filter's sample were built. From the cumulative distribution plots, the false alarm probability, FAP_c, was estimated as the power peak bin that contains a 99.99% percentage of the constant stars data. The 0.01% FAP_c level for J, H, and K filters estimated are

presented in Table 4.2. Figure 4.3 shows both the frequency versus periodogram highest power peak, and the cumulative distributions for each filter.

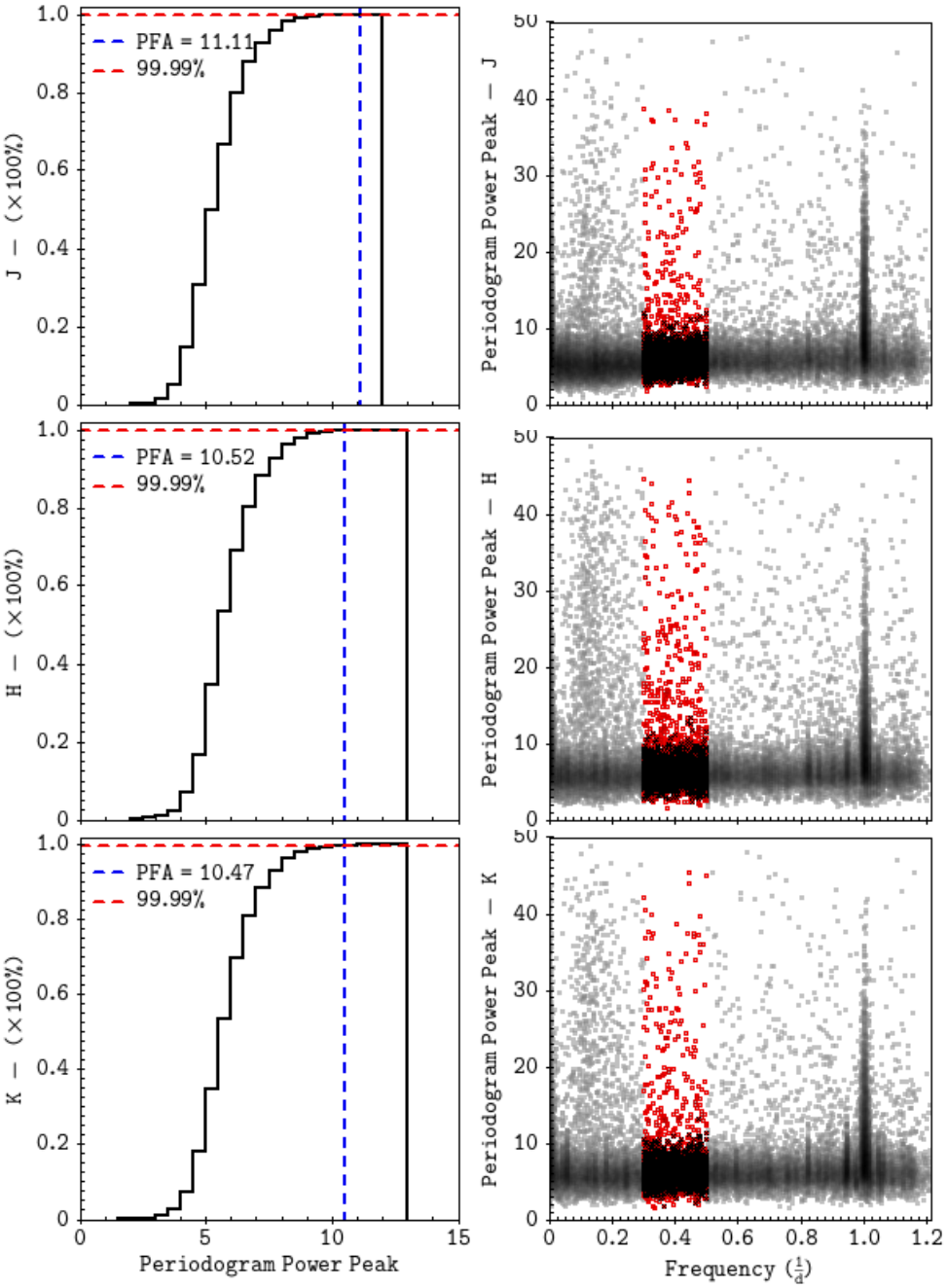

Figure 4.3: Right panels: frequency versus periodogram power peak for the highest periodogram power peak in each filter. All the stars in the central area complete catalogue are shown in grey; stars in with the frequency of the highest peak in the range $0.3 < f < 0.5$ day^{-1} are shown as red circles; stars in the frequency range cited before, that also have Stetson variability index smaller than 0.25 are shown as black X. Left panels: cumulative distributions for each filter; dashed red line shows the 99.99% level, and blue dashed line shows the estimated value for FAP_c.

Despite being a more accurate FAP estimator than analytical estimates or Monte Carlos simulations as derived by Horne & Baliunas (1986), FAP_c gives only a reference value for the FAP. Using it alone as a cut

Filter	J	H	K
$FAP_c(0.01\%)$	11.11	10.52	10.47

Table 4.2: Periodogram Power Peak levels for 0.01% False Alarm Probability estimated from a control sample composed by constant stars in the CygOB2 field of view.

for selecting periodic stars may minimize spurious detections, but will not be enough for rejecting all of them. When composing a sample of constant stars to estimate FAP_c, all stars with $S > 0.15$ were rejected. This cut means that the detection of periodic variable stars with $S < 0.15$ is not expected, but it does not mean that all the stars with $S > 0.15$ will be periodic variable stars. Actually, for the candidate member sample, only ∼50% of the stars with $S > 0.25$ were selected as possibly periodic stars after the initial morphological inspection in Section 4.1. As discussed by Littlefair et al. (2010), very irregular variables and stars with poor rotational phase coverage are two common sources of contaminants in such analysis. Looking for a sample with the least contamination possible, the periodic search also relied on the comparison of the periodograms in each of the three observed bands, and in two complementary statistical analysis, independent from the LSP.

There are more robust methods for estimating FAP like the bootstrap technique (Kuerster et al. 1997), but they consume too much computational time for a sample as big as ours to have a practical application. Hence other complementary statistical analysis, independent on the LSP, were used to improve the alias cleaning.

4.3.1 Phase dispersion methods

String/Rope length methods (Clarke 2002; Lafler & Kinman 1965) are non-parametric period search methods based on Lafler-Kinman statistics (Lafler & Kinman 1965). For each trial period, P, the original data is folded in phase, i.e., for each observation, m_i, a phase is given as:

$$\phi_i = \frac{t_i}{P} - [\frac{t_i}{P}], \tag{4.5}$$

where t_i is the time in which the observation was taken, and $[\frac{t_i}{P}]$ is the integer part of $\frac{t_i}{P}$, and $0 \leq \phi_i \leq 1$. The data is then re-ordered for ascending phases, and the "String-Length" statistics (hereafter SL-statistics) is calculated as the summation of the squares of the differences between the consecutive measurement values. A periodic signal will give a minimum value for:

$$T(P) = \frac{\sum_{i=1}^{N}(m_{i+1} - m_i)^2}{\sum_{i=1}^{N}(m_i - \bar{m})^2} \times \frac{(N-1)}{2N}, \tag{4.6}$$

where m_i is the i-th observation in order of ascending phase, N is the total number of observations, and $m_{N+1} = m_1$. The normalization by the variance guarantees that the statistics value is independent of the measurement noise.

The SL-statistics can be extended for the case of multi-band data. Given Z sets of data ($Z = 3$ for the present study since we are working with J, H and K filters.), the contribution of each filter, k, to the Rope-Length Statistics (RL-Statistic) is:

$$T(k,P) = \frac{\sum_{i=1}^{N[k]}(m[k]_{i+1} - m[k]_i)^2}{\sum_{i=1}^{N[k]}(m[k]_i - \bar{m[k]})^2} \times \frac{(N[k]-1)}{2N[k]}, \tag{4.7}$$

where $N[k]$ is the number of measurements in filter k, and $m[k]_i$ is the i-th measurement in the same filter. Finally the RL-statistics can be written as:

$$T(Z,P) = \frac{1}{Z}\sum_{k=1}^{Z} T(k,P). \tag{4.8}$$

As presented by Clarke (2002), $T(P)$ and $T(Z,P)$ can be calculated for a set of trial periods, and used to compose a periodogram. We did not compose a periodogram using this method. Instead, $T(P_0)$ (SL-statistics for the period P_0 estimated through LSP) and $T(3,P_0)$ (RL-statistics for the period P_0 estimated through LSP) were calculated for P_0s, were P_0s are the periods found using LSP. Thus the RL-statistics was not used for determining periods, but instead as a test for aliasing.

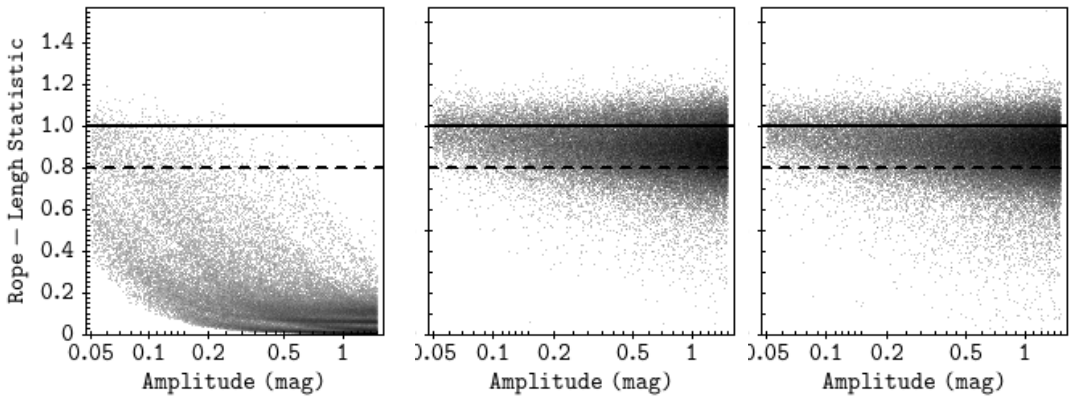

Figure 4.4: RL-Statistics versus amplitude distributions for periodic synthetic light curves. Left panel: light curves with true period; middle and right panels: light curves with an alias as period.

With the normalization in Equations 4.6, 4.7 and 4.8, proposed by Clarke (2002), SL- and RL-statistics values will fluctuate around unity, with periodic stars presenting minimum values. For choosing a limit value, a set of simulations was performed: 78000 synthetic periodic light curves were generated by following the procedure that will be described in Section 4.4. Each synthetic light curve has a random period between 0.83 - 45 days, a random amplitude between 0.05 - 1.5 magnitudes, using a constant star light curve as template. For each synthetic light curve, RL-statistics was calculated for the true period, P, and for the two aliases $P_{\rm alias} = \frac{1}{1 \pm \frac{1}{P}}$. The results are presented in Figure 4.4. One may note that the true period and the alias distributions have significantly different shapes. For true periods, most of the light curves have small values of RL-statistics, while for the alias periods, points are distributed around a value close to unity. Based on the visual inspection of these distributions, the value $T(3,P_0) = 0.8$ was adopted as a limit value for selecting periodic stars. The effect of such selection is shown in the periodogram power peak as a function of frequency plots in Figure 4.5. For each observed band, grey points show stars with SL-statistics$<$0.8 and yellow points show filtered objects with SL-statistics$<$0.8. The position of the yellow points in theses plots show that this technique is especially appropriate for eliminating low amplitude signals that may bring biases to the sample.

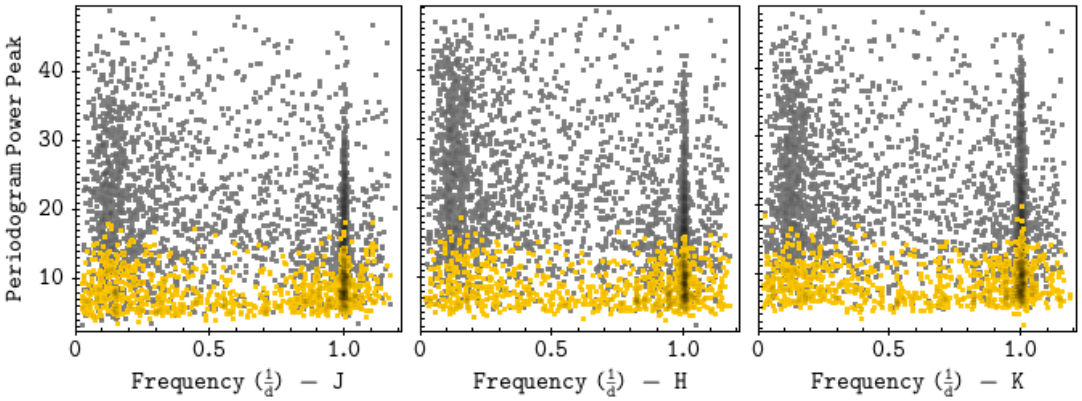

Figure 4.5: Frequency of the highest peak in the periodogram versus periodogram power peak for stars in the candidate members catalogue with valid periodogram. For each filter, light curves with SL-statistics$>$ 0.8 are shown in yellow, and light-curves with SL-statistics$<$ 0.8 are shown in grey.

4.3.2 Saunders statistics

The Saunders statistics (hereafter S-statistics, or S_s; Saunders et al. 2006)[1] is a technique that may be used for investigating the aliasing effect of sampling. As defined by Saunders et al. (2006), S_s is a normalized phase coverage metric and it is defined as the sum of the squares of the distances between two consecutive points in the folded in phase light curve, ordered for ascending phases, normalised by the value of the sum for an ideal spacing of equally spaced observations across the phase space.

Given a light curve composed by N observations, the ideal spacing would be $g_I = \frac{1}{N}$, from which follows the ideal metric:

$$S_I = \sum_{n=1}^{N} g_{I,n}^2 = N(\frac{1}{N})^2 = \frac{1}{N}. \tag{4.9}$$

For a periodic light curve with P as period, and with ϕ_n as in Equation 4.5, the S-statistics is:

$$S_s = \frac{S_u}{S_I} = N(\phi_n - 1 - \phi_1)^2 + N\sum_{n=1}^{N} N(\phi_n - \phi_{n-1})^2. \tag{4.10}$$

The normalization by S_I guarantees that an uniform phase coverage will give a S-statistics of order unity. Growing irregular phase coverage makes S-statistics increase. The S-statistics is especially good for removing the spurious periods arising from the 1 day^{-1} natural frequency introduced by the Earth's rotation (e.g. Littlefair et al. 2010).

Figure 4.6 shows the S-Statistics distribution as a function of period for both control sample, and candidate member catalogue, and for each filter. In this Figure, a high value of S-Statistics indicate a poor phase coverage, and hence periods measured in light curves of stars with high values of S have a big chance of being an alias. The Figure also shows that the sample is not adequate for detecting periods larger than $\sim$100 days.

Monte Carlo simulations were also done in order to obtain a limit value for S-statistics. For each synthetic

[1]Not to be confused with the Stetson Variability Index, S.

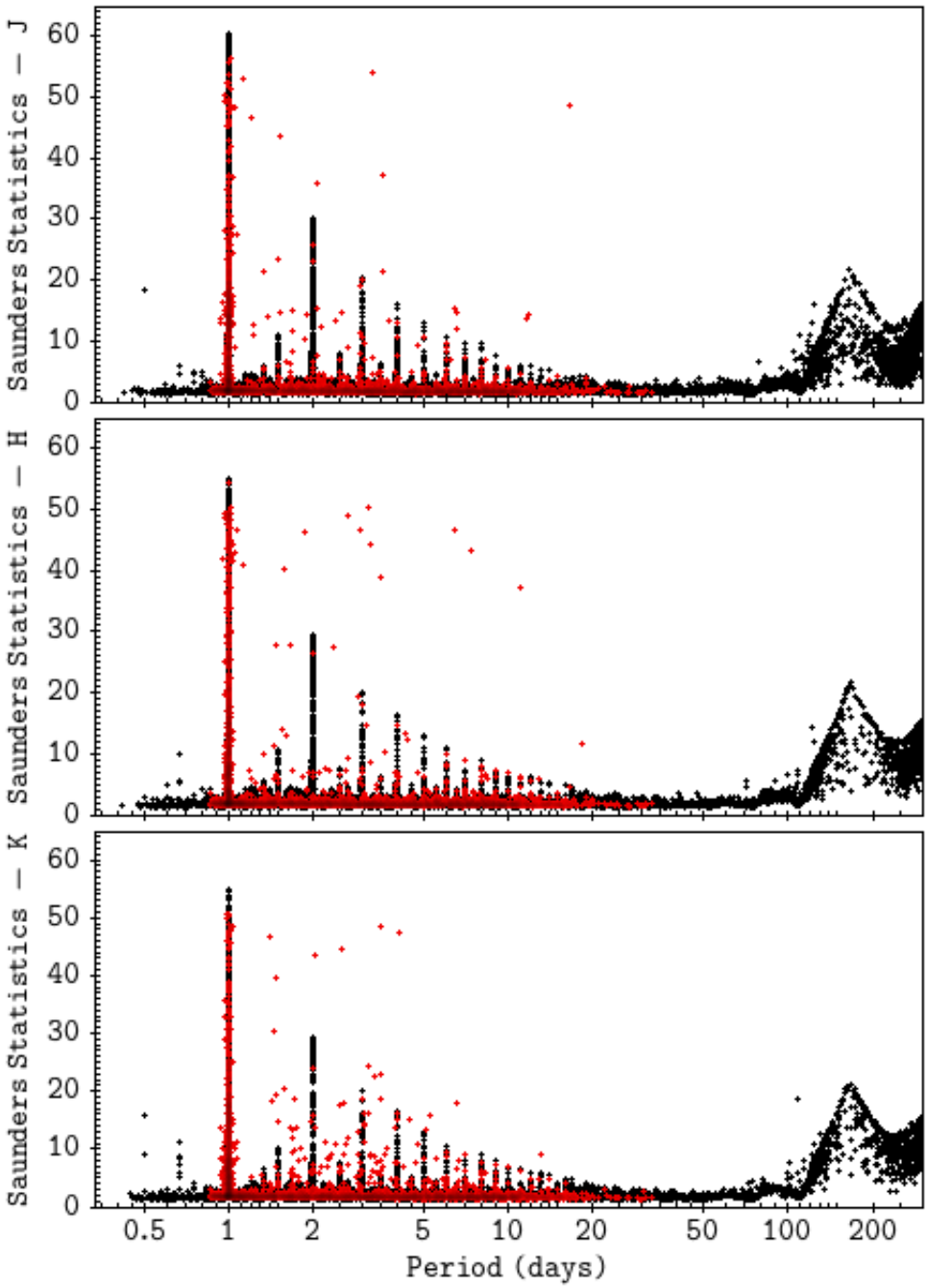

Figure 4.6: S-Statistics versus period distributions for J, H and K filters for observed data. Each period corresponds to the highest peak in the periodogram. Stars from the control sample are shown in black, and stars from candidate member list are shown in red.

light curve in the sample, LSP analysis was applied, and the highest peak in the periodogram was recorded. In light curves in which the difference between the LSP period and the input period was smaller than 10%, the input period was selected, resulting in a sub-sample of 64102 synthetic light curves for which S-Statistics was calculated. A cumulative distribution was built for this sub-sample and it is presented in Figure 4.7. In each band plot in Figure 4.7 the distribution for that filter is shown in black, and the 99% level is shown as a red dashed line. From the intersection of the 99% with the cumulative distribution the value S_s=5 was chosen a limit for non-aliased periodic stars.

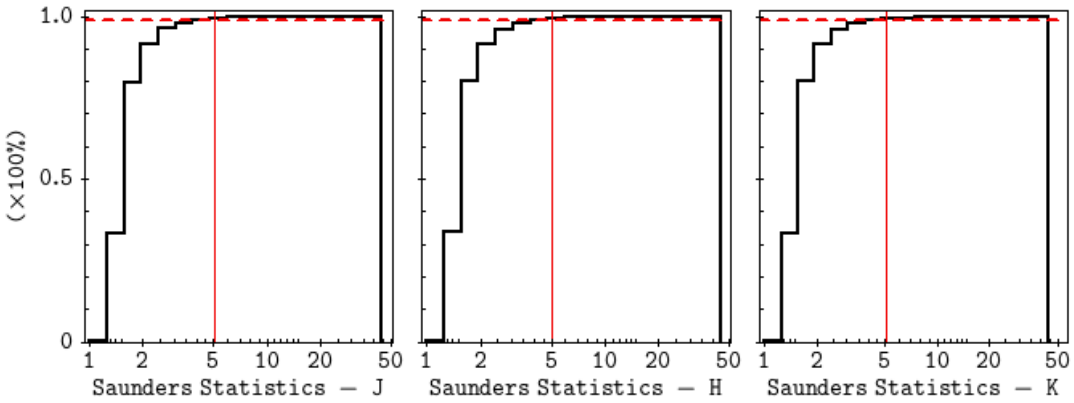

Figure 4.7: Cumulative distribution for S-statistics from non-aliased synthetic periodic light curves. Filters J (left), H (middle), and K (right) are shown. The 99% level is shown as a red dashed line and the chosen limited level of S_s=5 is shown as a red continuous line.

The effect of the chosen S-statistics selection limit is shown inside the frequency versus highest periodogram power peak distribution in Figure 4.8. From Figure 4.8 it is possible to verify that the S-Statistics filtering is specially suited for cleaning the distribution for the 1 day alias.

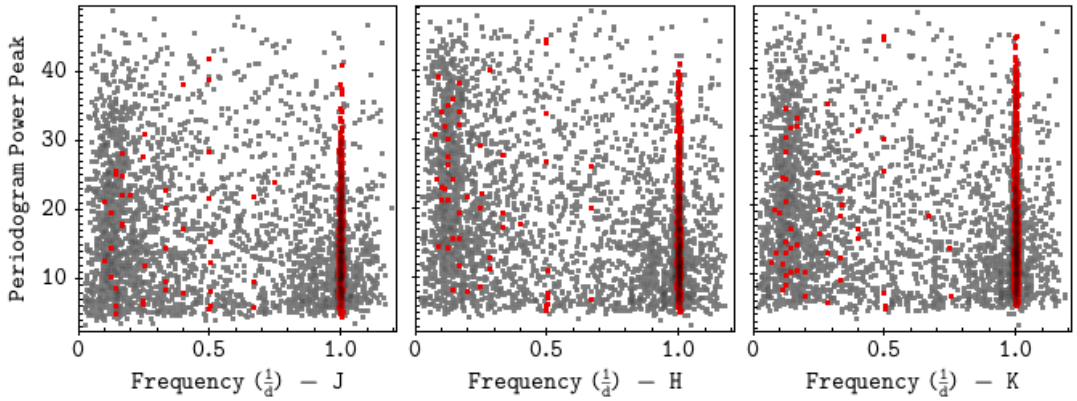

Figure 4.8: Periodogram highest power peak versus frequency of the highest peak for stars in the candidate members catalogue with valid periodogram. Light curves with $S_s > 5$ are shown in red, and light-curves with $S_s < 5$ are shown in grey.

4.3.3 Automatic period search among candidate members

Given the techniques for time-series analysis and variability search presented in the previous Sections, an automatic procedure to select periodic stars among the candidate member sample was built. During the procedure, a series of flags were attributed to each star according to each selection criterion.

First, stars were filtered according to their Stetson Variability Index (Section 4.2).

1. `Stet` - Stetson Variability Index: S >0.25: 1 if true. Otherwise: 0.

Next, the existence of significant peaks in each of the J, H, and K periodograms was evaluated. Given the oversampling factor and the Nyquist frequency scale factor adopted when building LSPs, each periodic signal will produce up to 3 significant peaks in the periodogram, following the rule of 1 day aliasing $P_{\rm measured}$ =

$\frac{1}{n \pm \frac{1}{P_{\text{True}}}}$ day (with n integer). For most periodic stars, the highest peak in the periodogram was the same for the three bands, and when that happens, that frequency was recorded as a possible valid periodic signal. An example of such case is shown in Figure 4.9 where the JHK periodograms for the periodic star CygOB2-000066 ($P = 5.13$ days) are shown. For convenience, the periodograms are shown as a function of frequency $f = \frac{1}{P}$. An important information here is that the frequency of a certain couple of peaks for two filters i and j was considered the same if the absolute value of their equivalent periods difference was smaller than 10% of one of the periods, i.e., $|P_i - P_j| \leq 10\% \times P_i$.

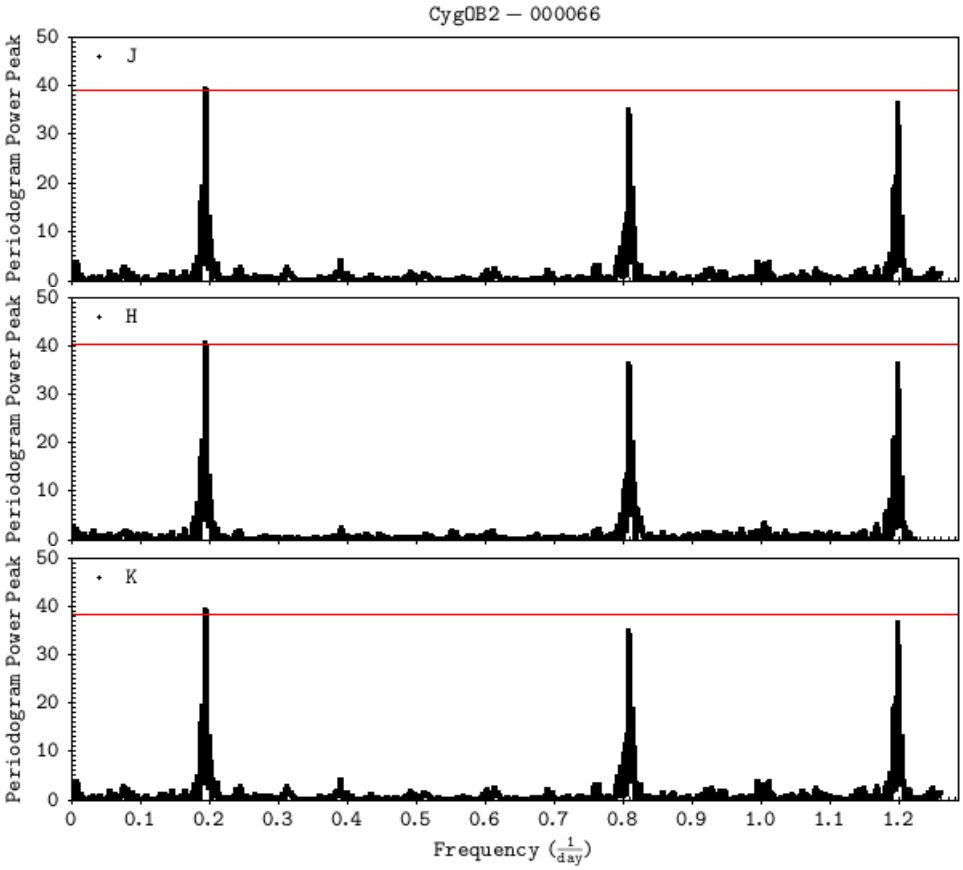

Figure 4.9: JHK periodograms for the star CygOB2-000066, which has been considered a periodic star with period $P = 5.13$ days. Red horizontal lines show the highest peak in each periodogram. The same highest peak was found in each band.

For some other stars, due to missing points, to differences in photometric errors and in amplitudes, sometimes, the same periodic signal produced different values of maximum power peak for each band. In particular, some missing points may favour the detection of an alias instead of the true period. Thus, when the highest peak frequency was not the same for each of the three periodograms, we compared the power for highest peak in each other band periodogram and chose the one with the highest power among the three bands. The other two bands periodograms were then checked to verify if the same frequency was responsible for one of the three highest peaks. If it was the case, that frequency and its power peak in each filter were recorded. If the same frequency was not found within the three highest peaks in each filter's periodogram, or if its power was smaller than the FAP_c of 0.01%, the light curve was rejected as periodic. Figure 4.10

shows an example of this case for the periodic star CygOB2-093169. In this example, the periodograms for J and H bands have the same highest peak, while the periodogram for K bands has different highest peak. Since the J band has the highest periodogram power peak, its highest peak was adopted as indicative of the true period, and since this peak is significant in all the other bands, the star was selected as periodic.

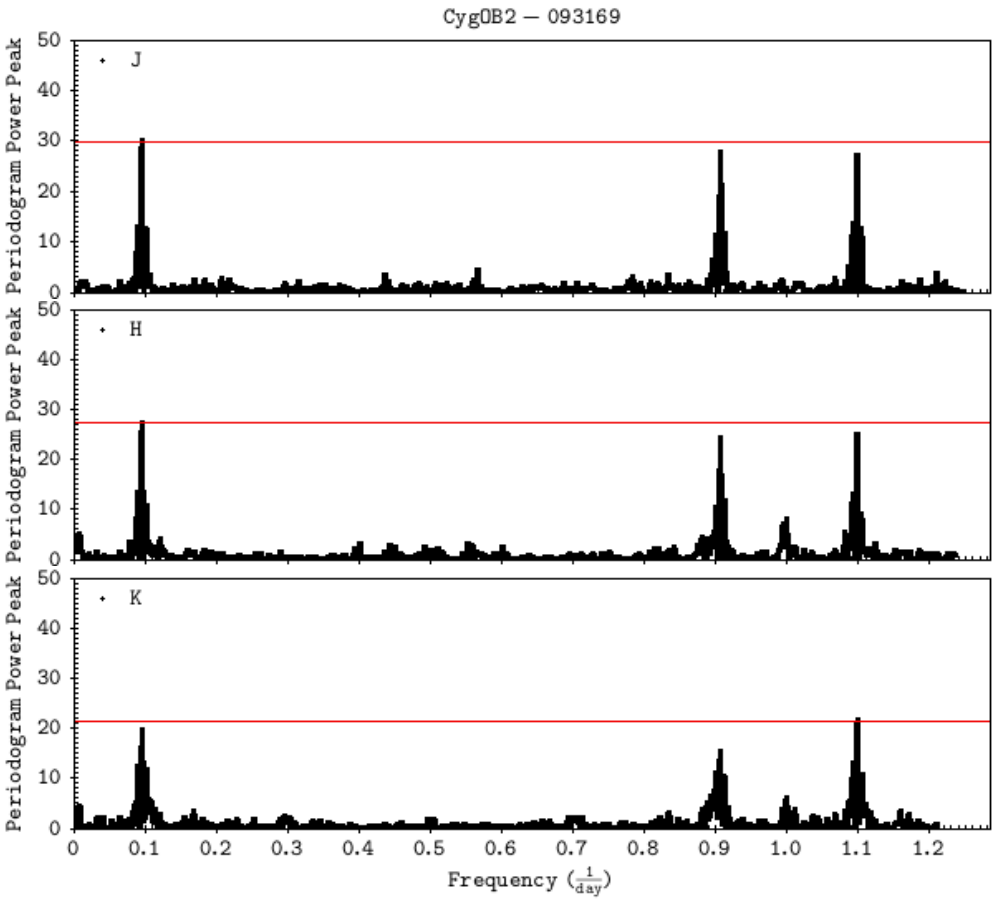

Figure 4.10: JHK periodograms for the star CygOB2-093169, which has been considered a periodic star with period $P = 10.43$ days. Red horizontal lines show the highest peak in each periodogram.

Summarizing, this second step tests if the periods measured are the same in each band's periodogram. The following flag is attributed:

2. `Peq` - equal 1 if the highest peak for each band periodogram has the same frequency; -1 if the highest peak is different for each band, but the highest power peak among the three bands exists in every other band periodogram. Otherwise: 0.

Given the results in the two previous steps, each star will receive two flags according to the selected peak FAP (Section 4.3):

3. `FAP99` - False Alarm Probability: FAP<0.01%: 1 if true for all filters. Otherwise: 0;
4. `FAP95` - False Alarm Probability: FAP<5.00%: 1 if true for all filters. Otherwise: 0.

The Saunders-Statistics and Rope-Length Statistics were verified according to the limit values established on Sections 4.3.2 and 4.3.1 respectively.

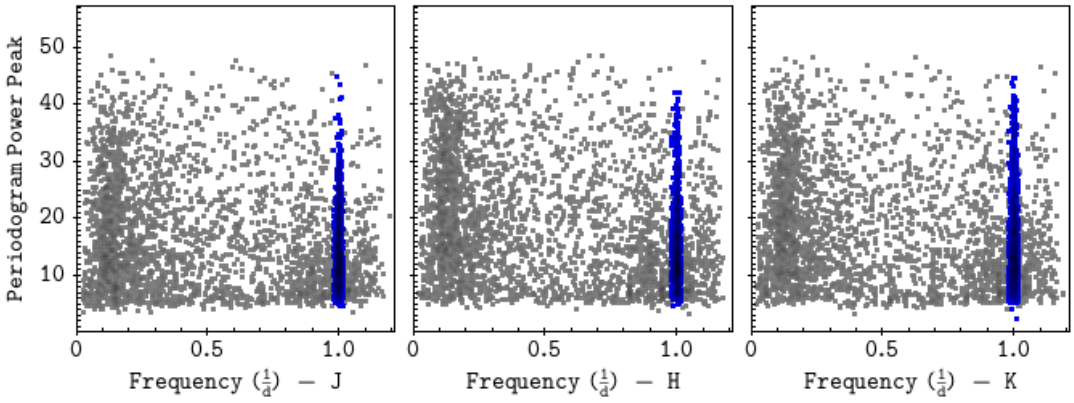

Figure 4.11: Selected frequencies vs. periodogram power peak for all stars with valid periodograms for JHK filters. Stars with frequency $\sim 1 \frac{1}{day}$ excluded from periodic selection are shown in blue.

5. `Saund` - Saunders-Statistics<=5 : 1 if true, 0 otherwise;

6. `RL` - Rope-Length Statistics <= 0.8 : 1 if true, 0 otherwise.

Even though the filter for Saunders-Statistics significantly reduces the ∼1 day excess in the power peak versus frequency distribution (*cf.* Figure 4.8), it is not enough to completely account for such aliasing effect. This conclusion was achieved after visually inspecting the light curves and folded in phase light curves for stars with detected period very close to 1 day that were not filtered by S-statistics limits: in their majority, those stars were long term non periodic variables, and not truly periodic stars. To deal with the remaining contamination, a filter for frequencies in the range 0.98 - 1.02 $\frac{1}{d}$ was added. This choice will be justified later in Section 4.4.6, when the effect of contamination due to periodic stars with periods outside the observations resolution will be investigated. For now, the effect of this ∼ 1 day filtering is shown in the frequency vs. power of the highest peak plot in Figure 4.11. Stars in this frequency interval were flagged as:

6. `1d` - Filter for stars in the range 0.98-1.02 $\frac{1}{d}$: -1 if true; 0 otherwise.

Finally, a star was considered as periodic if all the 5 first flags were different from zero, and the last one was equal to zero. For each star, a 6 digits flag explaining it's periodicity status was attributed. Some examples are: the star CygOB2-000066 (Figure 4.9) has periodicity flag 1111110 meaning it was selected as periodic with good confidence, and the star CygOB2-093169 (Figure 4.10) has periodicity flag 1-111110, meaning that even though the selected period was not present as the highest peak in every filter's periodogram, the same peak was present as a significant one in each periodogram and fulfill all the remaining conditions for a periodic star. Another example is the star CygOB2-000064 that was found to have a 0.99 day period, and has a flag 111111-1, and thus it was not selected as a confident periodic star.

4.3.4 Periodicity analysis results

Using the procedure described in the previous Section, 1291 periodic stars were selected, which correspond to 25.4% of the candidate members sample. From the periodic stars selected, 25 were eclipse-like, 1256 were in the candidate periodic variables list, 2 were non-periodic variables (stars selected as periodic stars,

but with no visible periodic signal in the light curve), and 8 were non-variable stars (stars not considered as variable according to visual selection). Also, 64 of them were stars listed as candidate member only by GWD13, 1177 stars were listed only by GWD15, and 50 were listed in both. After applying the filtering shown in Figures 4.5, 4.8, and 4.11, Figure 4.12 shows the selected stars inside the frequency versus power peak distribution for each filter. Figure 4.13 shows the resultant period distribution in both normal and log-scale.

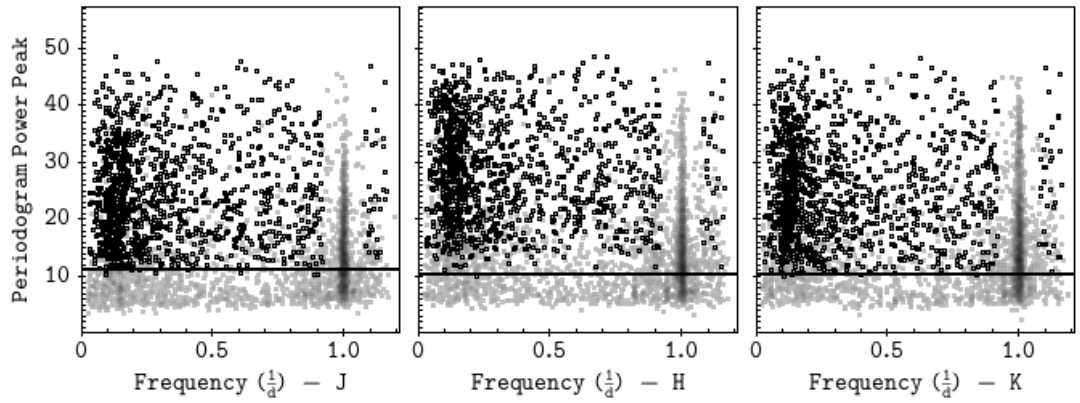

Figure 4.12: Selected frequency versus periodogram power peak for all candidate members in JHK bands. Stars selected as periodic are shown in black. The 0.1% FAP level for each band is shown as a black line.

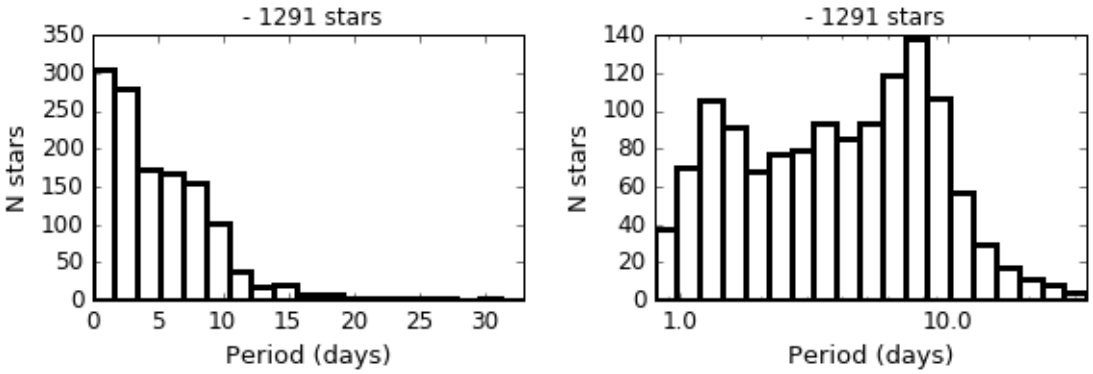

Figure 4.13: Period distribution for stars selected as periodic in linear scale (left) and log-scale (right).

4.3.4.1 Variability amplitudes

Peak to peak (ptp) and root main square (rms) variability amplitudes were evaluated for the candidate members using the techniques to be described on Section 4.4.3. Figures 4.14 and 4.15 show the ptp and rms distributions for candidate members, periodic stars, and non periodic variable stars in each band. In each distribution, the vertical lines show the median value for each sample, these values are also listed in Table 4.3. From these plots, one can see that all three amplitude distributions go to zero before $A_{\rm ptp}$ =1.5 mag. This justifies the superior limit in the amplitude interval 0.015 - 1.5 mag that was set as the amplitude range in the simulations presented in next Section. Also, one can see from the periodic stars distribution

(red distributions in Figures 4.14 and 4.15) that the majority of such stars have amplitudes smaller than 0.2 magnitudes in all filters.

Table 4.3: Peak-to-peak and rms amplitudes for periodic stars in the candidate member catalogue.

	All Members		Periodic		Non Periodic Variable	
band	ptp (mag)	rms (mag)	ptp (mag)	rms (mag)	ptp (mag)	rms (mag)
J	0.068	0.094	0.073	0.101	0.098	0.134
H	0.055	0.075	0.062	0.086	0.084	0.114
K	0.054	0.074	0.057	0.079	0.090	0.123

4.3.5 Visual light curve cross-check

Finally, the folded light curves for periodic stars selected in Section 4.3.3 were visually cross-checked, and it was verified if a periodic signal was indeed present on them. The 23 stars (1.8% of the periodic sample) that were selected as periodic but that did not show a visible periodic signal in the folded light curve were considered as contaminants. The light curves for the stars selected as periodic, but classified during de visual inspection as non-variable were also visually checked, and it was verified that 4 (0.3%) of them did not show a periodic signal in the folded light curve, being considered as extra contaminations to the periodic sample.

4.4 Monte Carlo simulations

Monte Carlo simulations were run on synthetic light-curves in order to estimate the efficiency and limitations of the techniques employed in the period search. Variations of the same simulations were also used to study the uncertainties in the estimated periods, and to investigate the origins of aliasing. The basis of our simulations is a modified version of the Monte Carlo simulation commonly presented in the literature for completeness analysis (e.g., Littlefair et al. 2010; Moraux et al. 2013): instead of field stars with constant light curves, candidate members with the most constant light curves were used for building synthetic light curves.

The basic idea behind the simulations was: for each constant light-curve (Section 4.4.1), the time sampling, magnitude and error values were kept, and a periodic signal with random waveform (Section 4.4.2), period (P_{in}, given the period search range in Section 4.3), amplitude (Section 4.4.3), and phase was added to it. A total of 2000 synthetic light curves were generated per constant star, totalling 78000 synthetic light curves. Random periods, amplitudes and phases were generated from a uniform distribution. Each synthetic light curve was then analysed and the input and output parameters were recorded for further analysis.

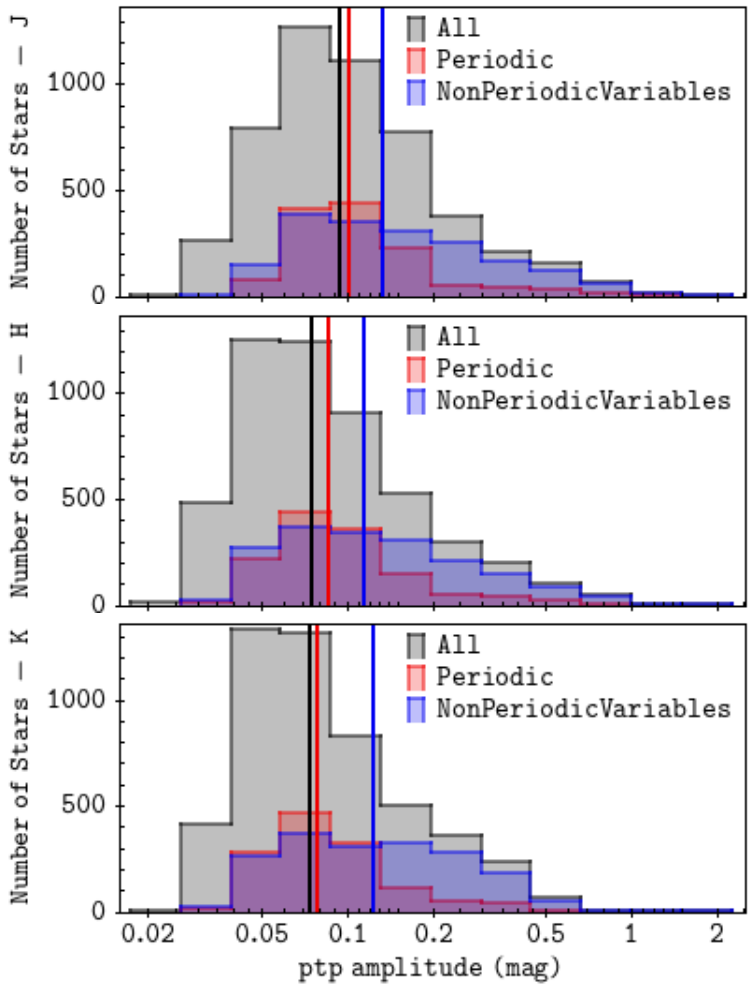

Figure 4.14: Peak to peak amplitude distributions in the J (top), H (middle) and K (bottom) bands for all candidate members (black/grey), for periodic stars (red), and for non periodic variable stars (blue). Continuous lines show the median value for each sample.

4.4.1 Input: constant stars

The constant stars used to build synthetic light curves were selected from the candidate member sample using the following criteria:

- Stars with small values of Stetson Variability Index ($S < 0.15$);
- stars with more than 60 valid observations in each filter;
- Stars classified as non variable during the morphological inspection (which means they present only very small and uncorrelated variability);
- For each filter, using magnitude bins of size one for magnitudes between 10 and 18, stars in the minimum outlier of peak to peak (max - min) amplitude distribution were randomly selected. One or, whenever possible, two stars were selected per magnitude bin.

The 39 stars selected this way were considered the most constant stars in the candidate member catalogue, and their light curves reflect the fingerprints of the dataset, including the window of observations

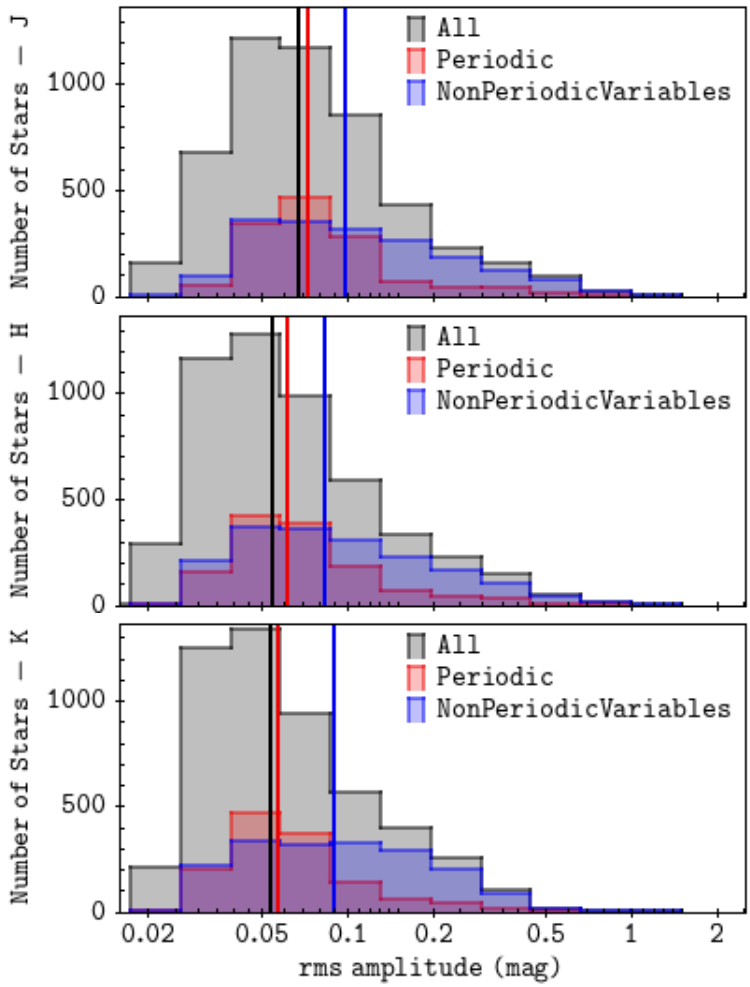

Figure 4.15: Root main square amplitude distributions in the J (top), H (middle) and K (bottom) bands for all candidate members (black/grey), for periodic stars (red), and for non periodic variable stars (blue). Continuous lines show the median value for each sample.

and the typical photometric and instrumental error contained on the light curves. Each light curve in this constant stars sample was then used as a template for building synthetic light curves.

4.4.2 Simulated waveforms

From the morphological inspection phase in the light curve analysis, it was noticed that even though periodic behaviour was quite often observed, it was usually not a perfect sinusoidal signal. This may have direct consequences in the period analysis performed, since certain waveforms may favour the detection of aliases or harmonics in the LSP, instead of the true frequency.

To improve our understanding of the period recovering rate, the Monte Carlo simulations were performed using a mixture of periodic signals with different waveforms, inserted in true light curves of constant stars. Figure 4.16 shows synthetic light curves produced for each waveform considered, using, as example, an amplitude of 0.2 magnitudes and an 8 days period.

The waveforms plotted in Figure 4.16 can be written as:

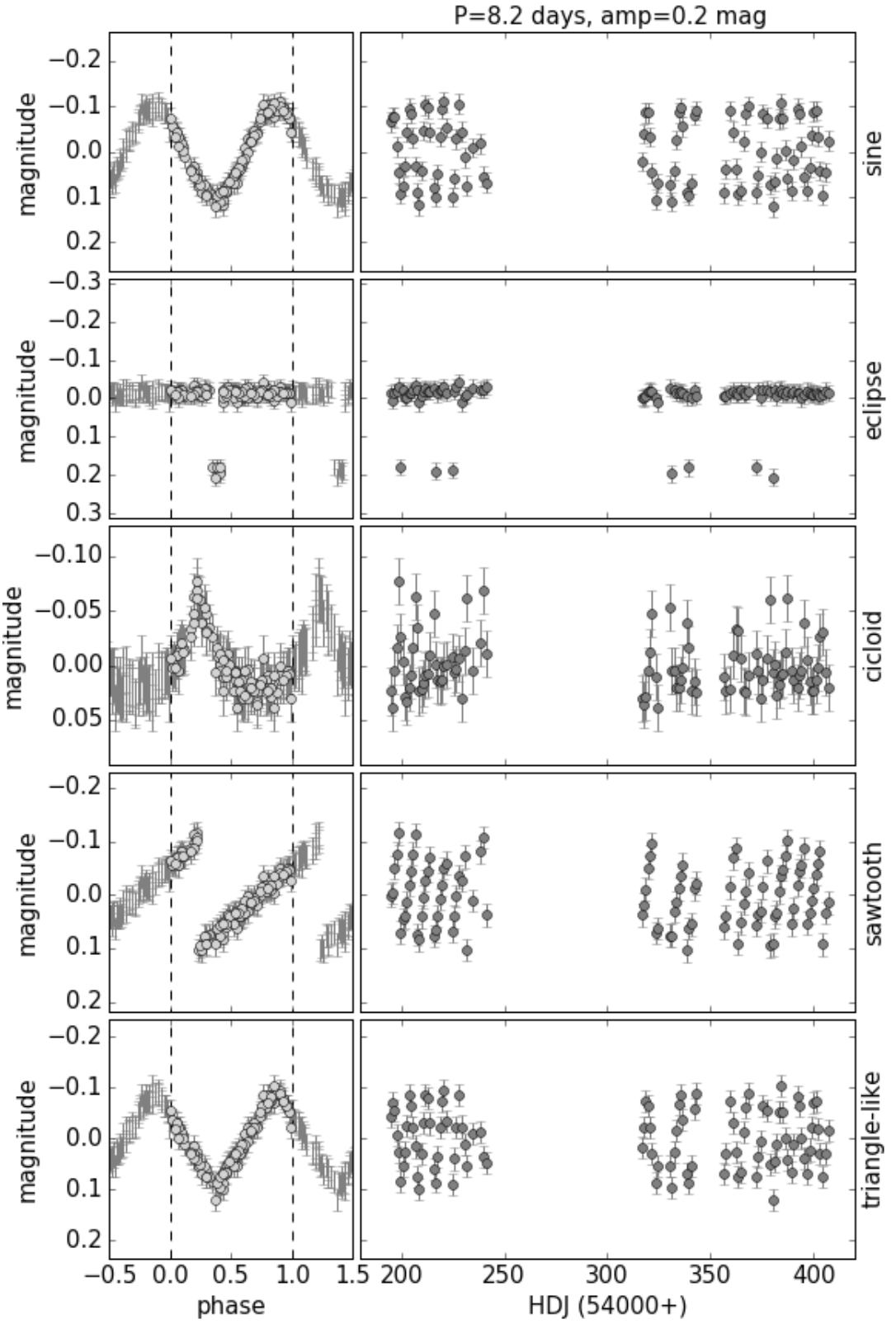

Figure 4.16: Synthetic light curves containing a periodic signal of 8.2 days period, and 0.2 ptp amplitude for each waveform used in the simulations. Left panels: synthetic light curves; right panels: folded in phase light curves.

Sinusoidal-wave: $m(t) = \frac{a}{2}\sin(\frac{2\pi t}{P} + \phi)$;

Sawtooth-wave: $m(t) = \frac{a}{\pi}\arctan(\tan^{-1}(\frac{2\pi t}{P} + \phi))$;

cycloid-wave $m(t) = -a\sqrt{|\sin(\frac{2\pi t}{P} + \phi)|}$;

Triangle-wave: $m(t) = \frac{a}{\pi}\arcsin(\sin(\frac{2\pi t}{P} + \phi))$;

eclipse-wave: $m(t) = \begin{cases} a & \text{if } \{\frac{t}{P}\} \geq 0.1, \\ 0 & \text{if } \{\frac{t}{P}\} > 0.1; \end{cases}$ where $\{\frac{t}{P}\}$is the fractional part of $\frac{t}{P}$;

where P is the period, a is the ptp amplitude, ϕ is the phase, and t is the date of the observation.

4.4.3 Measuring amplitudes

The Monte Carlo simulations were used to test three techniques for measuring amplitudes. A sixth waveform (shown in Figure 4.17) was added to those described on Section 4.4.2, in order to account for variable stars with non-periodic long-term variability. This waveform is a straight line defined as $m(t) = \frac{a}{N} \times (t - t_{\min})$, where a is the ptp amplitude, N is the number of observations, t is the date of the observation, and $t_{\min}$ is the date of the first observation. A total of 2000 synthetic light curves were generated per input constant start (Section 4.4.1), totalling 78000 synthetic light curves. For each one, a random period between 0.5 and 40 days, and a random amplitude between 0.015 and 2.5 were attributed. For each set of parameters, a random waveform was chosen and applied. The amplitude of each synthetic light-curve was then measured using each of the three techniques. Finally, the measured amplitudes were plotted against the input amplitudes for each waveform. The $A_{\text{in}} \times A_{\text{out}}$ plots are shown in Figure 4.18.

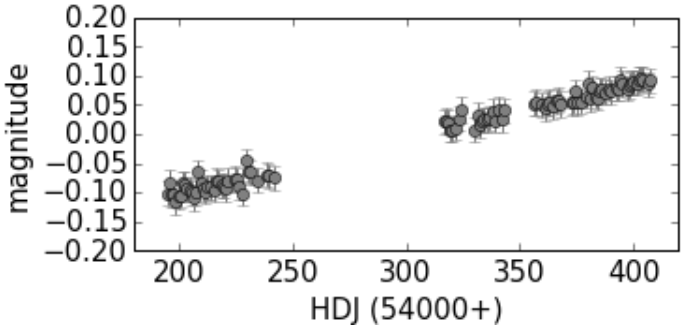

Figure 4.17: Synthetic light curve containing a long term non-periodic variability signal.

The first technique used was the standard deviation measurement $A_{\text{out}} = \sigma = \sqrt{\frac{\sum_{i=1}^{N}(m_i - \bar{m})^2}{N-1}}$, or simply the root main square (rms). As can be seen in the top plots in Figure 4.18, this technique always underestimates the input amplitude by a factor larger than 2. Next, a peak-to-peak (ptp) measurement for amplitude was applied to the data. The first try was to measure ptp amplitudes simply as the difference between maximum and minimum value, *i.e.,* $A_{\text{out}} = \texttt{max}[m(t)] - \texttt{min}[m(t)]$. The results for this measurement are shown in the middle plots of Figure 4.18 for each waveform considered. From those plots it is possible to verify that even though this method improves the precision in the measurements for sine-waves, it is not as much efficient for the other waveforms. Finally, still focussing on the ptp amplitude, a more robust measurement was built using data's percentiles. A_{out} was defined as the difference between the mean value

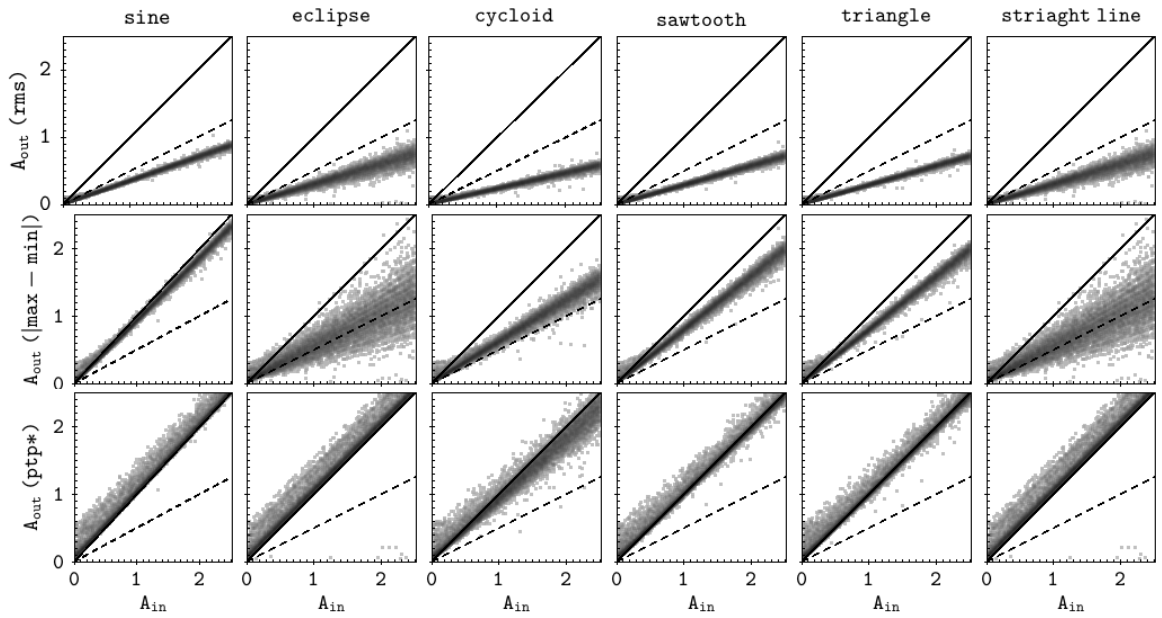

Figure 4.18: Input amplitude versus output amplitudes measured as rms (top), max/min (middle) and using a robust ptp measurement (bottom) for synthetic light-curves with the waveforms: sine-wave, eclipse-like, cycloid, saw-tooth, triangle-wave and straight line. The bold black line shows the path for $A_{\rm in} = A_{\rm out}$ and the black dashed line shows the path for $A_{\rm in} = 2 \times A_{\rm out}$.

of all data with values larger than a percentile X, and the mean value of all data with values shorter than a $100 - X$ percentile. This measurement was tested for the several percentile values, and the percentile 80% was chosen as the one that best measured the true ptp amplitude. The results for the 80% percentile are thus shown on the bottom plots in Figure 4.18. From the plots, one can verify that this is so far the most efficient method for measuring ptp amplitude for the group of wave-forms analysed.

Using as criterion the minimum dispersion of the data around the path of $\mathrm{A}_{out} = A_{in}$, the percentile 80% (Figure 4.18) was adopted as the main technique for measurement of amplitudes in this study. From now on, this technique will be referred simple as percentile ptp amplitude. Since most of the literature studies adopt the rms measurement as amplitude measurement, this measurement will also be kept as a characteristic of each star studied.

4.4.4 Uncertainties in the periods obtained

Each period is measured as the inverse of a frequency obtained via LSP, P=$\frac{1}{f}$. Thence, the rms error for each period is $\delta P = \delta f \times P^2$. Simulations were also used for estimating the resolution δf for each filter. For each synthetic periodic light curve, LSP was calculated and the highest periodogram power peak frequency's full width at half maximum was estimated as FWHM=$f_{\rm l} - f_{\rm r}$, where $f_{\rm l}$ and $f_{\rm r}$ are the frequency values for which the periodogram first assumes the value $PP(f) = \frac{PP(f_{\rm hp})}{2}$ in the vicinity to the left, and to the right of $\mathrm{f_{hp}}$, respectively; and where $f_{\rm hp}$ is the frequency of the highest peak in the periodogram. Given the FWHM versus period distributions, shown in Figure 4.19 for filters J, H, and K, δf was measured as the 1% quantile in the distributions. As P is measured as the mean value of P_J, P_H, and P_K, the estimated δP_J,

δP_H, and δP_K where propagated, and the following error estimate for the measured periods was obtained:

$$\delta P = 0.002 \times P^2, \tag{4.11}$$

which gives a 4.8 hours error for a 10 day period.

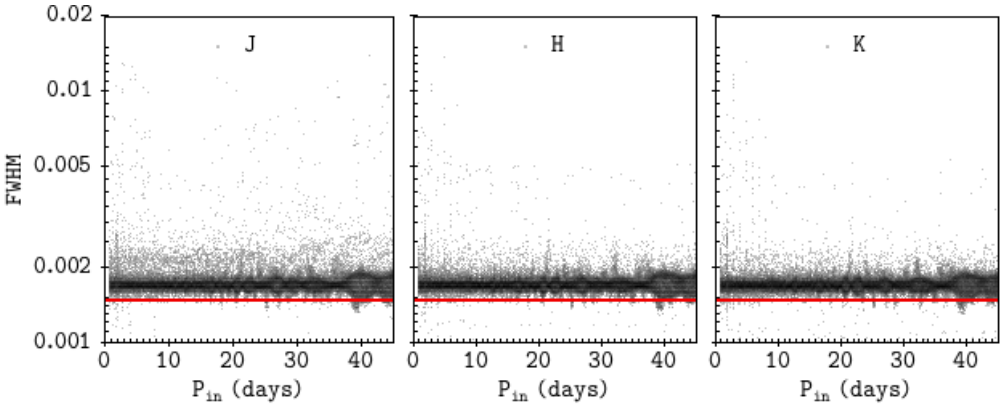

Figure 4.19: Period versus FHM from the highest peak distributions for synthetic periodic light curves. The red line shows the lower envelope defined as the 1% quantile.

4.4.5 Period recover rate and sample completeness

To estimate the completeness and investigate the level of contamination in our periodic sample, two series of simulations were performed. The first one considers periods as large as the maximum period searched (45 days, c.f., Section 4.3), and as short as 0.2 days, which is about the minimum rotational periods verified in other young regions (e.g., Irwin et al. 2008; Littlefair et al. 2010; Moraux et al. 2013). It also considers a large range of amplitudes from 0.015-1.5 magnitudes. As the goal of this set of simulations was to investigate the reliability of the measured periods, supposing one is dealing with a sample of stars with periodic modulation in their light curve caused by the rotation of a spotted surface, the eclipse-like and straight line waveforms were kept out of the simulations. Again, a total of 78000 synthetic light curves were generated, and one of the following waveforms was randomly chosen for each synthetic light-curve: sine, cycloid, saw-tooth and triangle. Random ptp amplitudes were generated for the J filter, and amplitudes for H and K bands were set according to the ratio between the median amplitude value for each band's ptp amplitude distribution for periodic stars (Table 4.3): $\frac{A_J}{A_H} = 1.17$, and $\frac{A_J}{A_K} = 1.28$.

We repeated, for the synthetic light-curve sample, the same analysis done for the candidate members catalogue: we evaluated the LSPs, compared the highest peaks in each filter, filtered the results according to RL- and S-statistics, and for frequencies close to 1day^{-1}. Synthetic light curves considered as periodic, given the same criteria used for real data, were flagged, and both input and output periods were recorded. From the results, two samples were defined: the synthetic light curves which were flagged as periodic were called the "selected"-sample, and the synthetic light curves with the same input and output periods were called the "recovered"-sample. To be considered the same, the deviation between input and output period has to be smaller than 10% of the input period ($(|P_{\rm in} - P_{\rm out}|) \leq 0.1 P_{\rm in}$)). The results for J band are shown

in Figure 4.20, and the upper left plot in Figure 4.20 shows the $P_{\rm in} \times P_{\rm out}$ distribution.

For the completeness analysis, a period in a synthetic light curve was considered successfully recovered if it was present in both selected and recovered samples. The completeness (*i.e.,* successfully recovered periods divided by the number of input periods) for the first series of simulations is presented as a function of magnitude, amplitude and period in the right plots in Figure 4.20, where one can see that the completeness decreases slightly for increasing magnitude (upper right plot), going from ∼69% for magnitudes around 12, to 47% for magnitudes larger than 18. The completeness of the sample is quite uniform, and around ∼67% for amplitudes between 0.18 and 1.5 mag, having a significant drop between 0.015 and 0.18 mag, reaching only 37% (middle right plot). It is also quite uniform, and around ∼87%, for periods between 1.2 and 24 days (bottom right plot); but it drops to ∼12% for periods smaller than ∼1 day, and to ∼12% for periods larger than 36 days. These drops in completeness for the extreme values can be explained by strong aliasing factors at the very long, and very short period extremes.

Figure 4.20 also shows the contamination analysis for the selected-sample. In the left middle and bottom panels, 100% means the complete selected-sample, empty bars show the percentage of light-curves in this sample with successfully recovered periods per period or amplitude bins, and filled grey bars show the percentage of light-curves in the selected-sample, but that do not have ($|P_{\rm in} - P_{\rm out}|$) $\leq 0.1 P_{\rm in}$) and, thus, are contaminants to the sample. The reader is advised to keep in mind what are the samples used to build each histogram in Figure 4.20 and 4.21: while the completeness analysis takes into account the total number of periods available to be measured (*i.e.*, every grey dot inside the $P_{in} \times P_{out}$), the contamination analysis accounts only for periods which were measured by the process described in the previous section (*i.e.* blue and grey points inside the $P_{in} \times P_{out}$). From the amplitude vs. contamination fraction histogram (middle left plot) one can see that the contamination level is quite small for a given amplitude, going from a maximum of about 16% for the smallest amplitude bin, and reaching only 5% for the highest amplitude bin. The period vs. contamination fraction histogram (top left plot) shows that the contamination level is insignificant (∼1%) for periods longer than 6 days, and that it increases significantly up to 70% for measured periods shorter than ∼1 day.

Even though the simulations presented in Figure 4.20 comprise the whole amplitude and period ranges measured for our periodic sample, they assume uniform distributions for the ranges considered, which is unrealistic if we consider the real distributions of periods and amplitudes. Only ∼1% of the periodic sample had measured periods longer than 20 days, and Figure 6.3 shows that the measured amplitudes are mostly low amplitudes up to 0.2 magnitudes, which corresponds to the first bin of amplitude in Figure 4.20. Therefore, a second set of simulations was run in order to consider in more details a sample dominated by low amplitude light-curves with periods shorter than 20 days.

The second set of simulations considers amplitudes in the range 0.015 - 0.2 mag, and periods in the range 0.2 - 20.0 days. The results for the second set of simulations are presented in Figure 4.21. The completeness vs. amplitude panel shows that the sample's completeness increases from merely 4% for amplitudes smaller than 0.035 (which is very close to the data's 2% error level), to ∼78% for amplitudes larger than 0.18 mag in J filter. The completeness for a given period is quite homogeneous, and about 57% for periods larger than

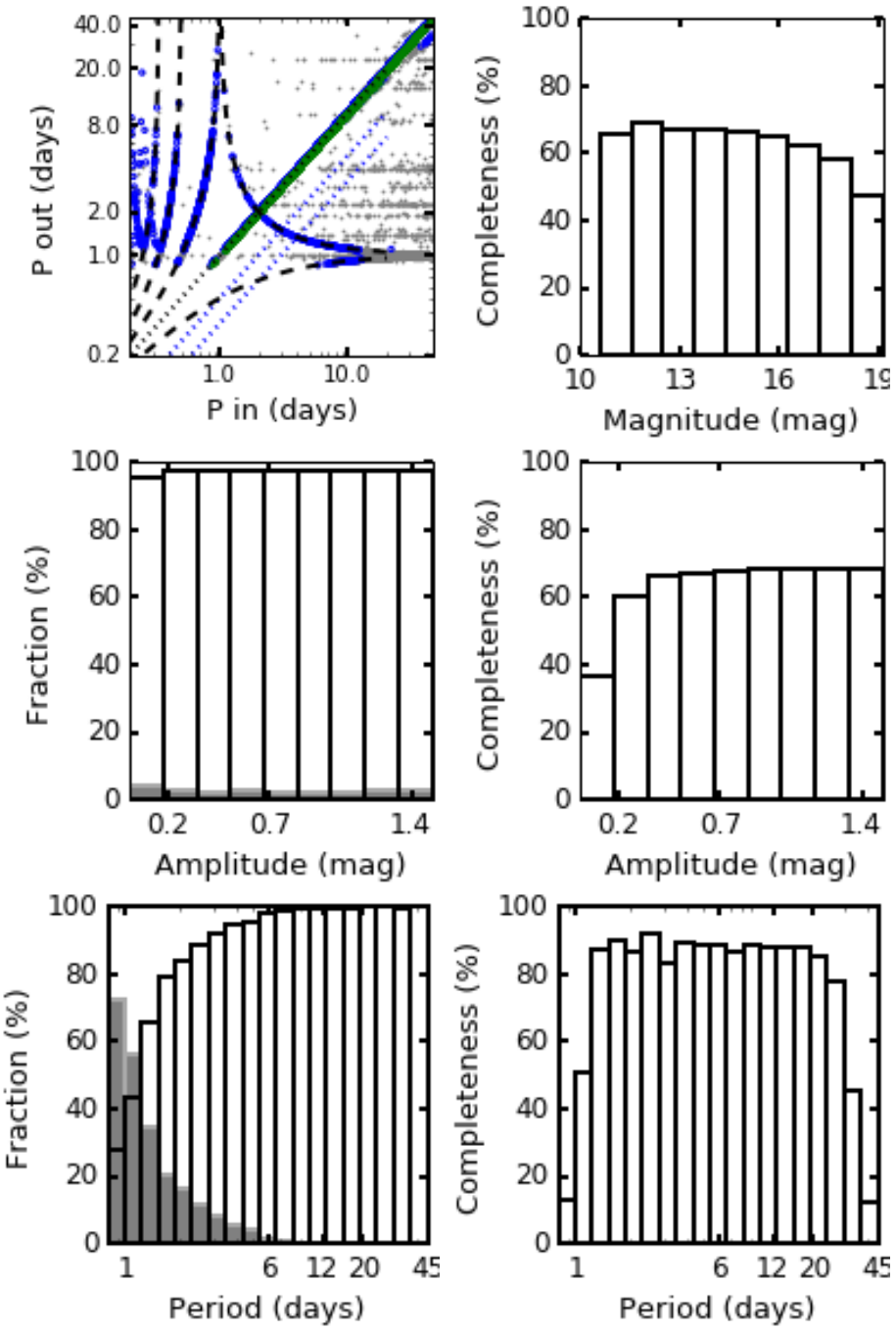

Figure 4.20: Period detection completeness and contamination levels for a mix of periodic synthetic light curves, with periods between 0.2 and 45 days, and amplitudes between 0.015 and 1.5 magnitudes. Upper left panel shows $P_{\rm in} \times P_{\rm out}$ diagram, with every synthetic light curve shown as a grey dot, recovered sample's periods shown in green, and selected sample's periods shown in blue. Harmonic paths are shown as blue dotted lines, and 1 day aliasing (cf. Equation 4.4) paths are shown as dashed black lines. Right plots: Completeness distributions per magnitude (top), amplitude (middle) and period (bottom) bins. Left middle and bottom plots: Given the selected sample, contamination levels are shown per amplitude (middle), and period (bottom) bins. Fraction of true recovers are shown as empty bars, and fraction of contaminants are shown as filled grey bars.

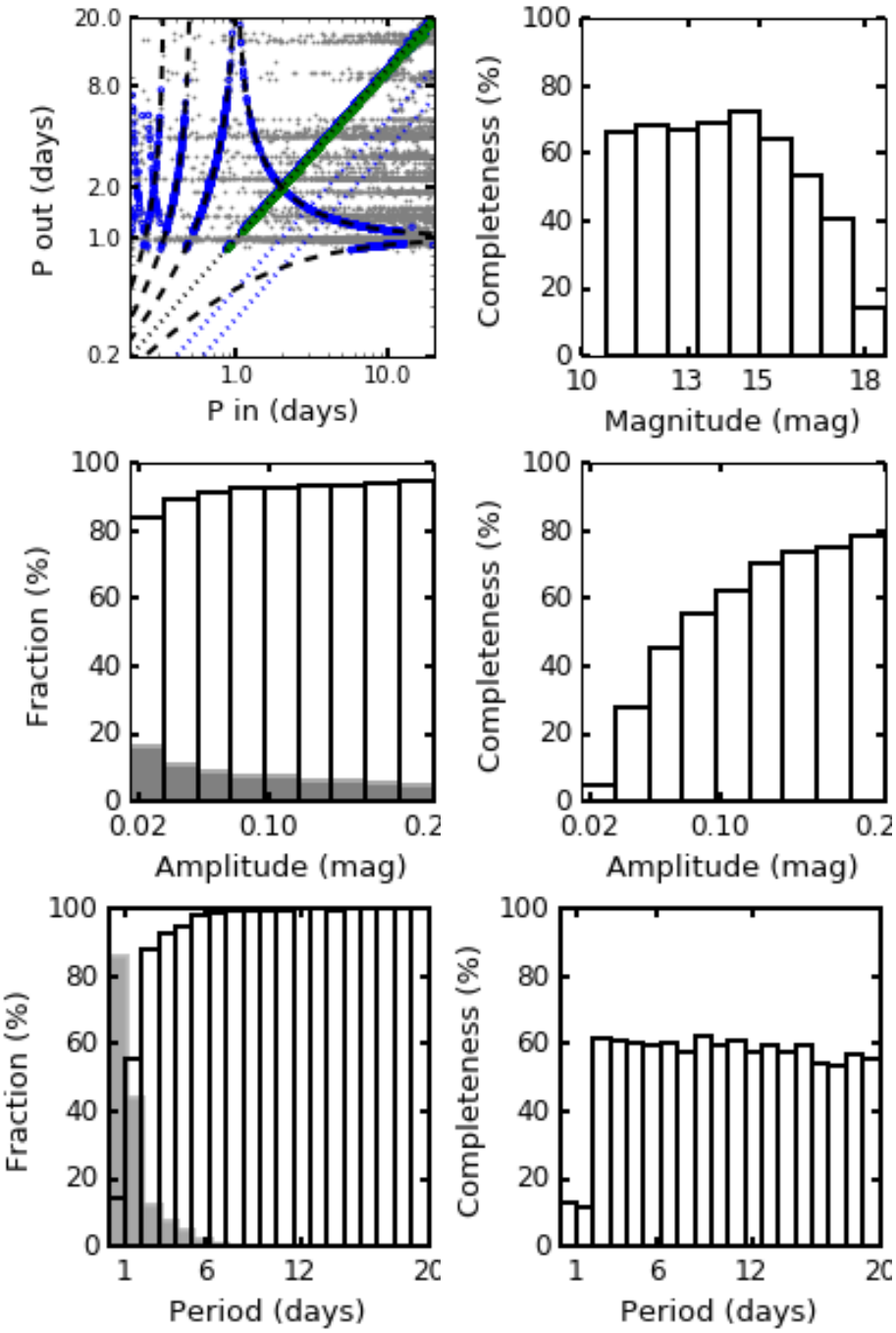

Figure 4.21: Same as Figure 4.20, but for a mix of periodic synthetic light curves, with periods between 0.2 and 20 days, and amplitudes between 0.015 and 0.2 magnitudes.

2 days, and as small as about 12% for periods smaller than 2 days. The completeness as a function of J magnitude distribution is quite flat, and it is about 67% until magnitude 15, but it decreases toward larger magnitudes down to ∼14% for magnitudes larger than 18. The completeness increase with amplitude can be explained by the fact that higher amplitudes result in higher signal to noise ratio, making the periodic signal easier to detect. The decrease with magnitude can be explained by the error distributions in Figure 3.5, as larger magnitudes have larger errors, they also have smaller signal to noise ratio and hence are more difficult to detect.

The contamination level decreases from ∼16% to ∼5% with increasing amplitude. For the period range considered, no significant contamination was verified for periods measured between 7 and 20 days, but for periods smaller than 7 days there is an increasing contamination level for decreasing period, reaching ∼44% for periods between 1.0 and 2.0 days, and ∼86% for periods smaller than 1 day. This contamination is partially a consequence of our choice to search for periods under the Nyquist frequency (Section 4.3).

4.4.6 Contamination by periods outside the observations resolution

Given the evidence of high contamination in the shorter periods bins (Figures 4.20 and 4.21), some extra simulations were performed, this time focussing on periods outside the period range considered for period search.

We first looked for possible contamination due to periods longer than 20 days. The simulation described in Section 4.4 was repeated, but this time considering periods ($P_{\rm in}$) between 20 and 100 days with amplitudes between 0.015 and 0.5 mag. For those specific simulations, the filtering for FAP, RL- and S-statistics was kept, but no further cleaning for periods around 1day was performed. The recovery success on this range is only ∼12% in a sample of 78000 synthetic periodic light curves, for the amplitude range considered. For the 680 (9%) synthetic light curves in the contaminant sample (*i.e.*, synthetic light curves selected as periodic, but with $P_{\rm out} \neq P_{\rm in}$), the distribution of measured periods ($P_{\rm out}$) was analysed and it is shown in the left plot in Figure 4.22. It was verified that ∼98% of the contaminant sample had $P_{\rm out}$ around 1±0.2 days, showing that for our data sampling, the majority of such periods appears aliased around 1 day. This justifies the filtering for periods in the range 0.92 - 1.08 days applied in Section 4.3.

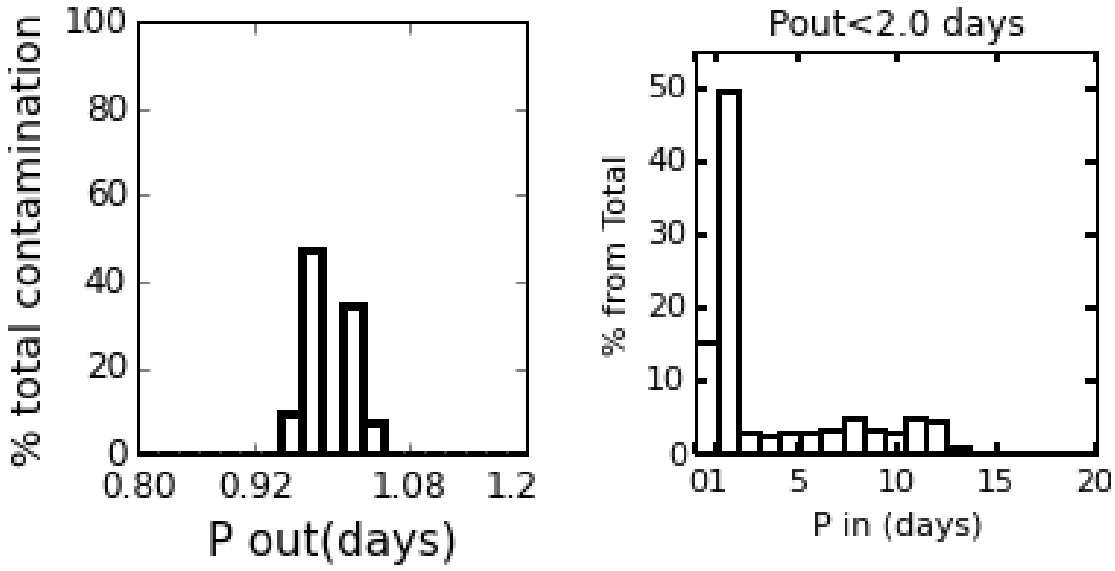

Figure 4.22: Left: Histogram showing the period distribution for output periods for synthetic light curves generated with long periods ($P_{\rm in}$ >20.0 days), and that were considered contaminants ($P_{\rm out} \neq P_{\rm in}$). Right: Period distribution histogram for the input periods for synthetic light curves with measured period smaller than 2 days ($P_{\rm out}$ <2.0 days), which are the 2 shorter period bins in Figure 4.21.

Second, the contamination due to periods shorter than our data-sampling is capable of resolving was

considered. For the set of simulations presented in Figure 4.21, the input characteristics of the synthetic light curves generated for the simulations were analysed. The right plot in Figure 4.22 shows the input period ($P_{\rm in}$) distribution for the synthetic light curves with $P_{\rm out} < 2.0$ days, which comprises the two shortest period bins in Figure 4.21. The y-axis shows the fraction of contaminants with $P_{\rm out} < 2$ days. From this plot, one can estimate that ∼15% of the contamination arises from aliased periods smaller than 1 day, and ∼49% of the contamination arises from unresolved periods between 1 and 2 days. Despite the fact that these short period aliases account for ∼64% of the contamination, there is a lower level contamination arising from all period bins larger than 2 days up to ∼15 days, which adds up ∼36% of contamination. As it is not possible to untangle the two contaminant sources, it was concluded that the periodic sample with $P < 2.0$ days suffers from strong contamination, and it should not be used in the further analysis.

4.4.7 Contamination due to non-periodic variability

We performed additional Monte Carlo simulation for non-periodic waveforms and applied the automatized period search to the non-periodic sample. For each synthetic light curve, a random amplitude was generated and two possible waveforms were randomly assigned. The first waveform assumes that the light-curve is a straight line with slope defined as the ratio between the randomly selected amplitude and the total number of observations. The second waveform was composed of random numbers generated between 0.015 and the amplitude value.

A total of 78000 synthetic light curves were generated this way, with amplitudes between 0.015 and 1.5 mag. While ∼ 49% of the sample presented periodogram power peaks in the three bands with a power higher enough to be automatically selected as periodic, they were however not wrongly selected as periodic, since most of them are distributed around 1 day, and were ruled out from the periodic selection. The few objects with periods outside this range were ruled out by the RL-statistics or Saunders-Statistics filters. Finally, after applying the automatized period search procedure to this sample, we concluded that the procedure is robust enough to avoid any contamination due to these non-periodic waveforms in our periodic sample.

4.4.8 Eclipse-like waveforms

Figure 4.23 shows a $P_{in} \times P_{out}$ plot for a set of simulations considering only synthetic light curves with eclipse-like waveforms. From the plot, it is possible to notice a favouring for the detection of harmonics, instead of the true period. A comparison with the $P_{in} \times P_{out}$ plot for a mix of sine, cycloid, saw-tooth, and triangle waveforms (Figure 4.20 and 4.21), where almost no contamination due to harmonics happened, shows that our data-sampling is not appropriate for measuring periods for eclipse-like variables. Because of this harmonic contamination issue for eclipse-like waveforms, periods measured for stars flagged as eclipse-like during the morphological classification were not considered as reliable.

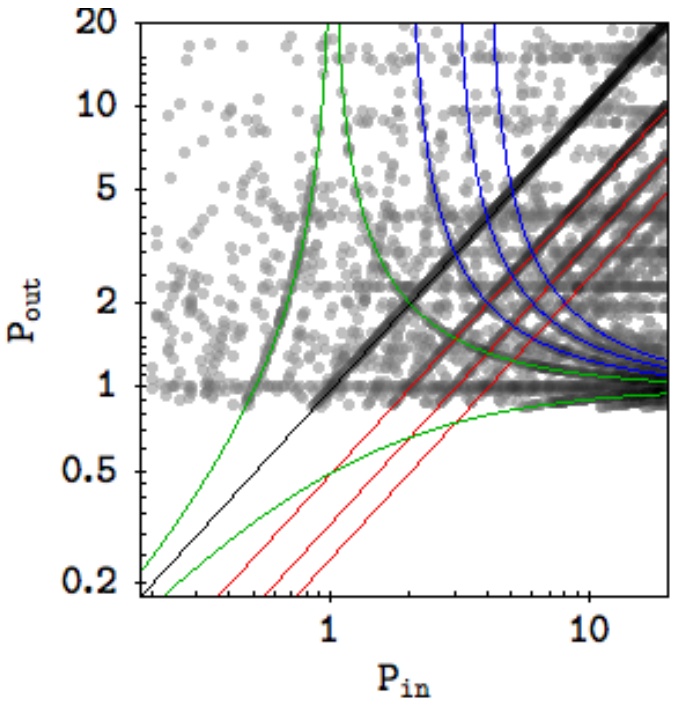

Figure 4.23: $P_{in} \times P_{out}$ distribution for eclipse-like waveforms. Every synthetic light curve shown as a grey dot, a black line shows the recovered sample's path, the first three harmonics paths are shown as red lines, 1 day aliasing (cf. Equation 4.4) paths are shown in green and paths for the harmonics of the aliased periods are shown in blue.

4.5 Comparison with periods in the literature and binary stars contamination

Henderson et al. (2011) observed CygOB2 in two seasons of 19 and 18 nights, with a few observations per night. They presented 121 stars variable in the R and I bands, 95 of which had measured periods. With a searching radius of $0,''45$ we found 79 of their variable stars in our candidate member sample: 7 of them were classified by the present study as non-variable stars; 9 were eclipse-like variables; 17 were classified as non-periodic variable stars; and 46 were periodic candidates. Figure 4.24 shows a comparison between the periods measured by Henderson et al. (2011), and the ones measured in the present study. Both studies measured periods of 32 stars in common, and the same period for 14 of them. As we are mainly interested in periodic behaviour that may be reflecting stellar rotation, all the variables presented by Henderson et al. (2011) as eclipsing binary candidates (10 stars) were excluded from the periodic stars list. Taking out the eclipsing binary candidates from the plot in Figure 4.24, all remaining stars with different periods measured in the two studies fall on the aliasing paths, and the 8 objects in this situation were also ruled out from our periodic list.

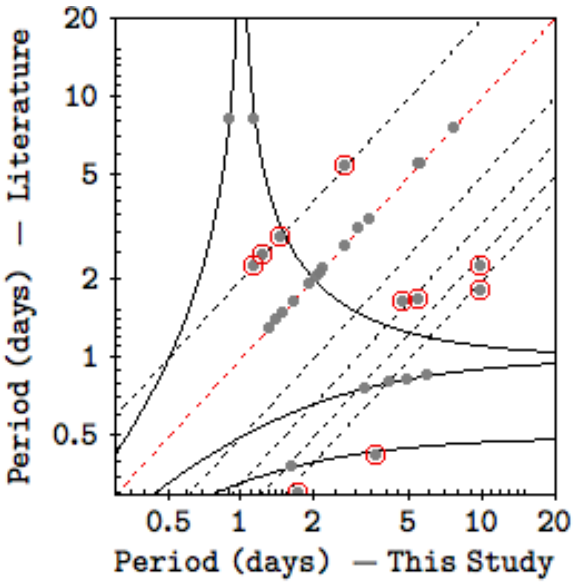

Figure 4.24: Comparison between periods measured in the present work, and in Henderson et al. (2011). Grey circles show the periodic stars in common between the two works. Stars with the same period measured in both works fall over the red dashed line. Red circles show the eclipsing binaries candidates from Henderson et al. (2011). Continuous black lines show 1 day aliasing paths, and dashed black lines shows the path for harmonics.

4.6 Visual light-curve cross-check

Finally, the folded in phase light curves for periodic stars selected in Section 4.3 were visually cross-checked, and it was verified if a periodic signal was indeed present on them. The stars that were selected as periodic but that did not show a visible periodic signal in the folded light curve were considered as contaminants. There were 23 (1.8% of the periodic sample) identified as contaminant by this process. The light curves for the stars selected as periodic, but classified during de morphological inspection as non-variable were also visually checked, and it was verified that 4 of them did not show a periodic signal in the folded light curve, and they were considered as extra contaminants to the periodic sample. The periodic stars folded in phase light curves are presented in the Appendix D.

This visual cross-check process was necessary in addition to the one described in Section 4.1, because it verifies the reliability of the periods measured inside the folded light curves.

Chapter 5

Variability of disc-bearing stars

Recalling Section 2.3.3, and Figure 2.7, due to the near-IR excess produced by the disc, disc-bearing stars are expected to occupy different regions in the CC-diagram than stars without disc. This can be verified in the plots of Figure 5.1, in which CC-diagrams with disc-bearing and non disc-bearing candidate members of CygOB2 are shown.

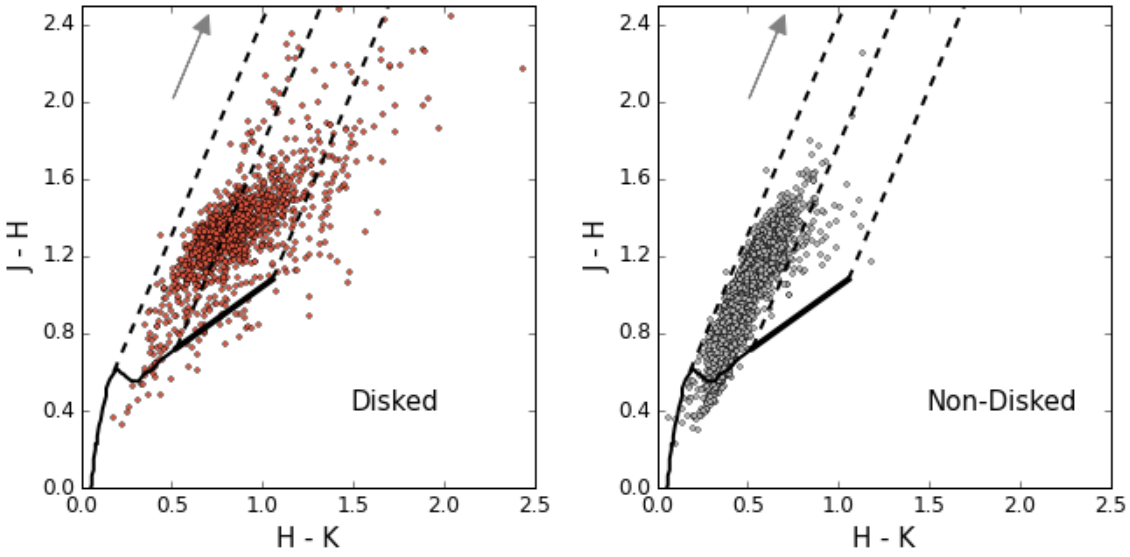

Figure 5.1: Colour-colour diagrams for disc-bearing and non disc-bearing candidate members. Disc-bearing stars are shown in red in the left plot, and non-disc bearing stars are shown in grey in the right plot. The effect of the interstellar reddening is shown as a grey arrow for the median visual extinction expected for the CygOB2 association. The Meyer et al. (1997) T Tauri locus and the regions defined by it are shown as in Figure 2.7.

In Section 2.3.4 the physical mechanisms proposed to explain near-IR variability were discussed. Disc-bearing stars can present variability due to cold or hot spots, variable extinction, variable accretion and changes in the inner disc. Non disc-bearing stars are expected to present near-IR variability due to cold spots or variable extinction. Except in extreme cases, cold spots produce lower variability amplitudes than the other physical phenomena discussed, hence one may expect disc-bearing stars to be *more* variable than

stars without disc. This assertion can be verified in Figure 5.2, in which the same plots from Figure 5.1 are presented, but this time each star is plotted as a line segment centred on the median colour values, with its ptp amplitude in each colour is represented as the length of the line segment.

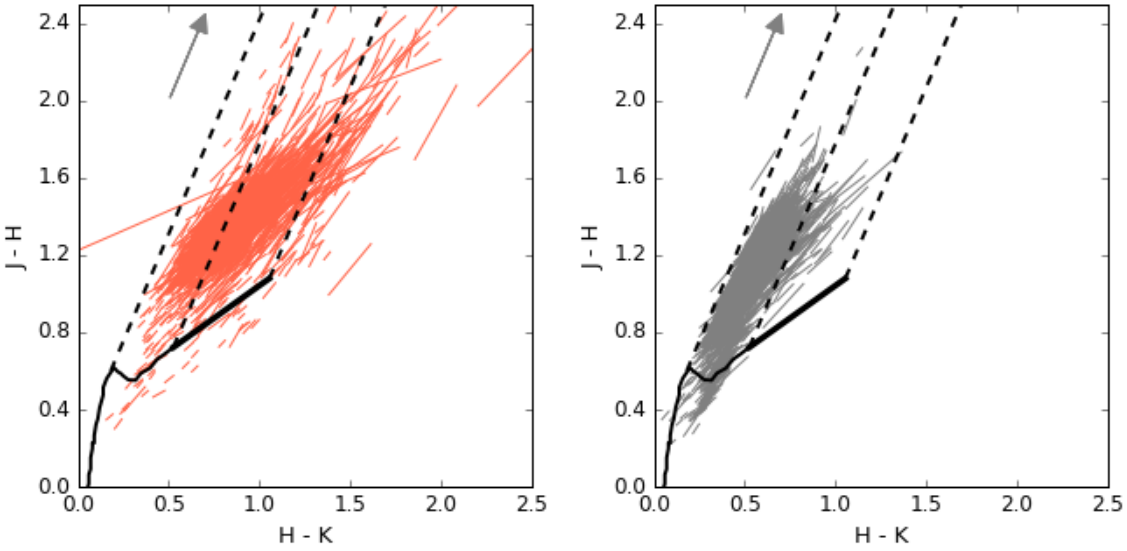

Figure 5.2: Colour-colour diagrams for disc-bearing (left, red) and non disc-bearing (right, grey) candidate members. Each star is shown as a line-segment with the length of its variability peak-to-peak amplitudes.

In this Chapter we investigate the characteristics of the variable stars in the CygOB2 candidate member sample.

5.1 General variable properties

Following Section 4.2, initial variable selection was done by using the Stetson variability index as selection criterion. The sample of all candidate members has $S(\mu, \sigma, \nu)$=0.9, 1.1, 0.5 (mean, standard deviation and median value), the sample of disc-bearing stars has $S(\mu, \sigma, \nu)$=1.8, 1.7, 1.3, and the sample of non disc-bearing stars has $S(\mu, \sigma, \nu)$=0.6, 0.6, 0.4. The 90-th quantile of the disc-bearing stars is at S(90th quantile) = 17.7, and of non disc-bearing stars at S(90th quantile) = 1.2. These results corroborate the idea that disc bearing stars are more variable in the near-IR than non disc-bearing stars.

Figure 5.3 shows the Stetson variability index as a function of J magnitude and colours for the samples of member candidate, non disc-bearing stars, and disc-bearing stars. As the distributions of Stetson index as a function of J and H magnitude were qualitatively the same as for K magnitude, we only show plots for the last one. From these plots, one can verify that for magnitudes and colours, the bulk of the distribution is different for each sample, and disc-bearing stars have its distribution's bulk located at higher values of the Stetson variability index than non disc-bearing stars. From Figure 5.3 one can also notice a tendency of higher Stetson index for redder colours, which is in accordance with the CC-diagrams shown in Figure 5.2 in which there was a tendency of higher observed ptp amplitudes for stars with increasing near-IR excess. The difference is also supported by a KS-test between the samples of Stetson index for disc-bearing and non

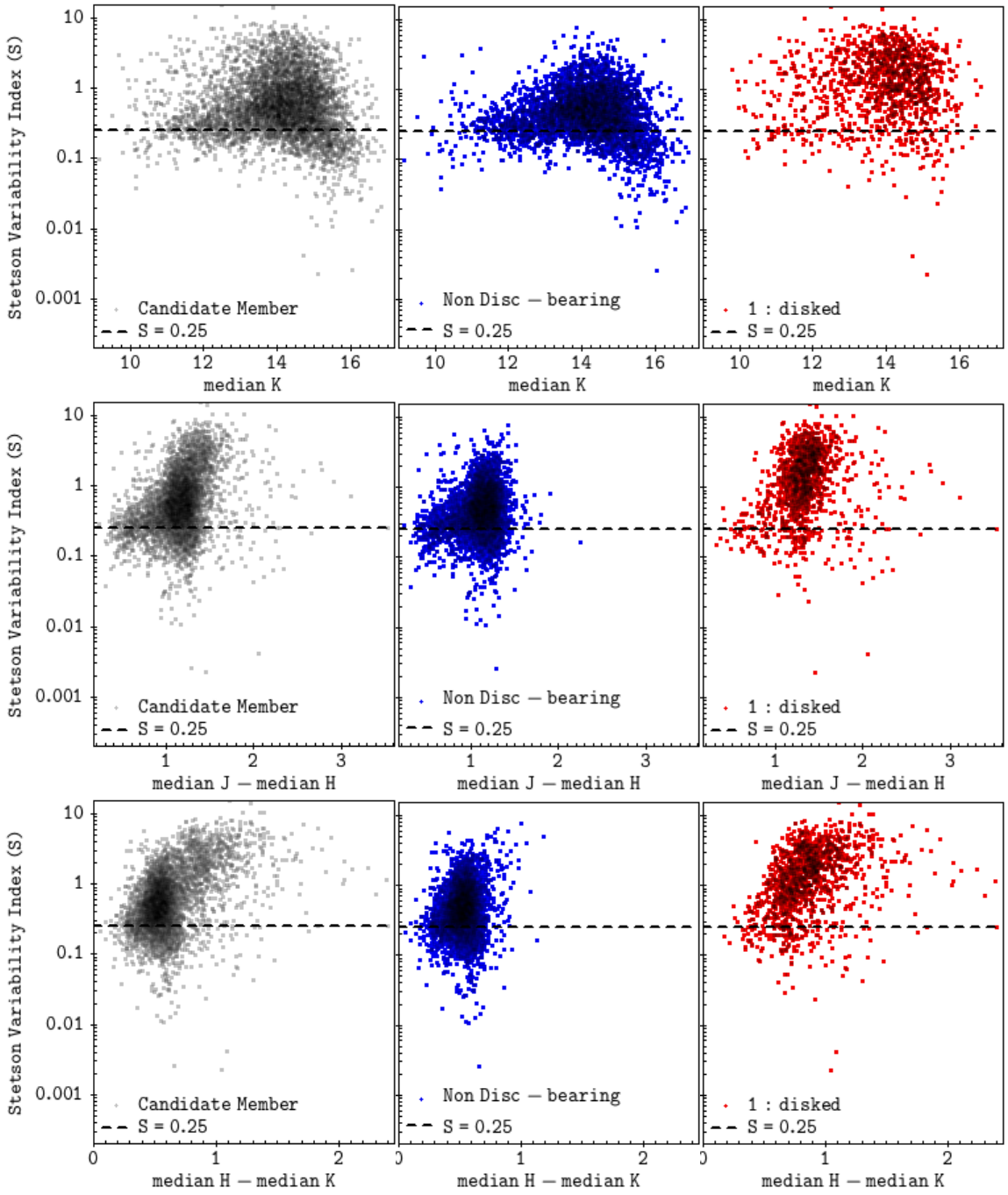

Figure 5.3: Stetson variability index as a function of J magnitude, J-H, and H-K colours for candidate members (left), non disc-bearing stars (middle), and disc-bearing stars (right).

disc-bearing stars, which yields a null chance that the two samples came from the same parent distribution.

The differences between the variability in disc-bearing and non disc-bearing stars can also be verified in Table 5.1, which shows in numbers what was seen in the plots in Figure 5.2. The max, mean, median and standard deviation values for the ptp and rms amplitudes are presented for each sample. The disc-bearing variable stars show median ptp amplitudes higher than about 0.1 mag for all colours and magnitudes. On the other hand, variable stars without discs presents median ptp amplitude of ∼0.07 mag. For reference, we also show in the amplitudes of the complete candidate member sample.

Table 5.1: Amplitudes for all Member Candidates, disc-bearing stars, and stars without discs.

All Candidate Members

	ptp				rms			
Band	Max	Mean	Median	stdev	Max	Mean	Median	stdev
J	1.79	0.14	0.09	0.14	1.29	0.10	0.07	0.1
H	1.84	0.12	0.08	0.13	1.32	0.09	0.06	0.09
K	1.61	0.11	0.07	0.10	1.14	0.06	0.05	0.08
J-H	0.72	0.09	0.07	0.06	0.27	0.03	0.03	0.02
J-K	1.08	0.11	0.08	0.10	0.39	0.04	0.03	0.04
H-K	0.97	0.08	0.06	0.07	0.35	0.03	0.02	0.03

Disc-bearing Stars

	ptp				rms			
Band	Max	Mean	Median	stdev	Max	Mean	Median	stdev
J	1.79	0.27	0.20	0.22	1.29	0.20	0.15	0.17
H	1.84	0.24	0.17	0.20	1.32	0.18	0.13	0.15
K	1.61	0.22	0.18	0.15	1.14	0.16	0.14	0.11
J-H	0.72	0.13	0.11	0.09	0.27	0.05	0.04	0.03
J-K	1.08	0.21	0.18	0.15	0.4	0.08	0.07	0.05
H-K	0.97	0.14	0.11	0.10	0.35	0.05	0.04	0.04

Non Disc-bearing Stars

	ptp				rms			
Band	Max	Mean	Median	stdev	Max	Mean	Median	stdev
J	0.94	0.10	0.09	0.07	0.67	0.08	0.06	0.05
H	0.78	0.09	0.07	0.06	0.56	0.06	0.05	0.04
K	1.08	0.08	0.07	0.05	0.75	0.06	0.05	0.04
J-H	0.33	0.07	0.06	0.04	0.13	0.03	0.03	0.02
J-K	0.58	0.08	0.07	0.05	0.21	0.03	0.02	0.02
H-K	0.41	0.06	0.05	0.04	0.15	0.02	0.02	0.01

Figure 5.4 shows CC-diagrams for stars selected as variables according to Stetson index in different ptp amplitude ranges in the K band. Table 5.2 shows the disc fraction for each K ptp amplitude range presented in Figure 5.4. As one can see from both plots and Table, there is an increase in the disc fraction with higher variability amplitude.

Table 5.2: Disc fraction as a function of ptp amplitude in the K band.

K ptp Amplitude (mag)	< 0.08	0.08 - 0.1	0.1 - 0.15	0.15 - 0.2	0.2 - 0.5	>0.5
Disc Fraction (%)	8.66	15.60	28.88	60.31	79.21	90.39

5.2 Variability morphologies

Even though Figure 5.2 gives a good notion of the level of variability in terms of variability amplitudes, it is not realistic in describing the shapes of the variability inside the CC-diagram. As mentioned in the previous Chapter, not all stars selected via Stetson variability index presented well defined light-curves. While 80% (4079 stars) of the candidate members were considered variable according to Stetson variability index, only 61% (3077 stars) were selected for variability analysis after light curve morphological inspection. There were 110 eclipse like variables, 1288 non periodic-variables, and 1679 possibly periodic variables. These numbers

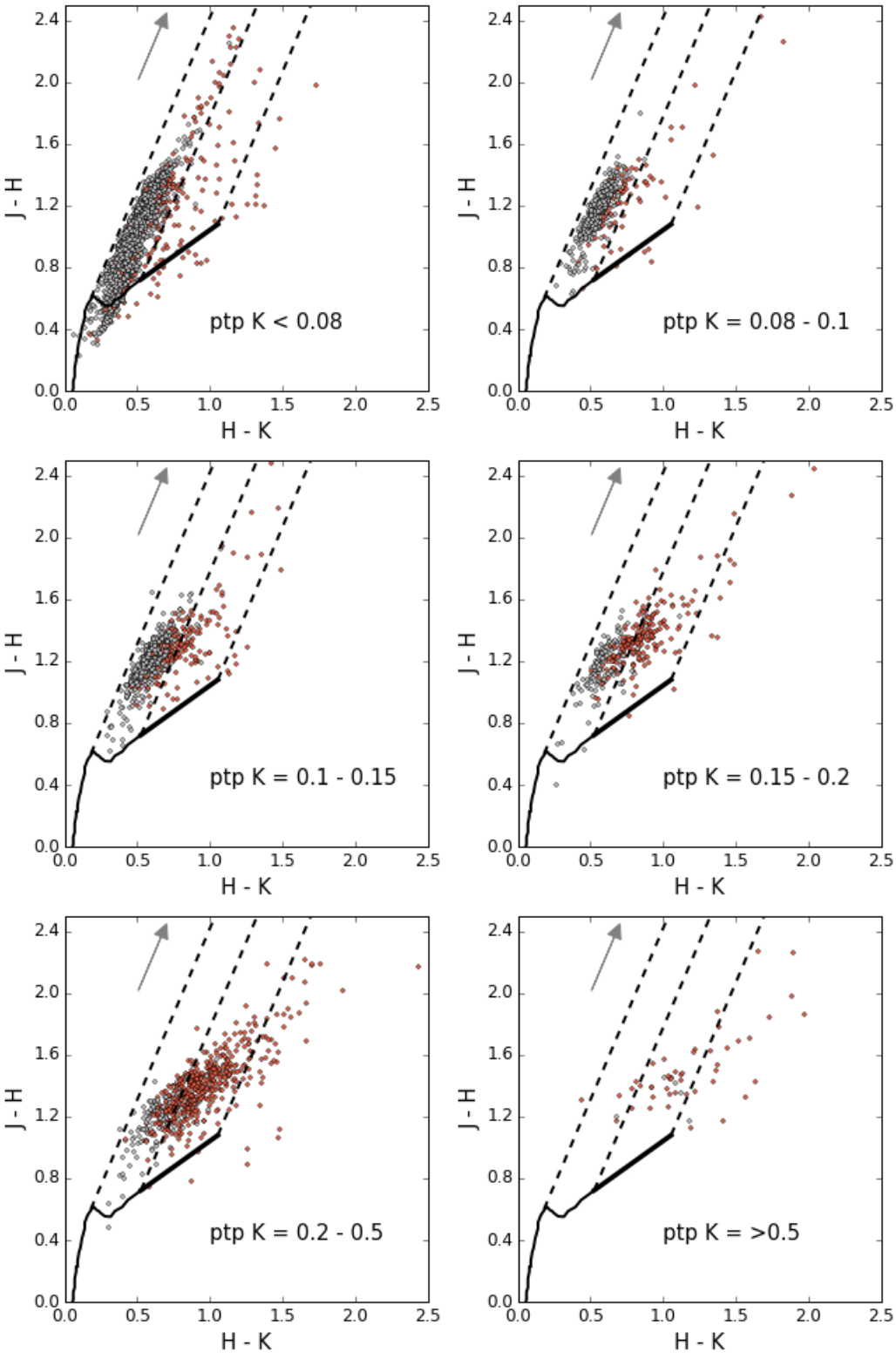

Figure 5.4: Colour-colour diagram for stars with different peak-to-peak variability amplitude in the K filter. Disc-bearing stars are shown in red, and non disc-bearing stars are shown in grey.

do not imply that the 1002 stars discarded after morphological inspection should be ruled out as variable stars, but as they presented only stochastic variations in their light curves, they were out of the type of variability we are looking forward to identify (Section 2.3.4).

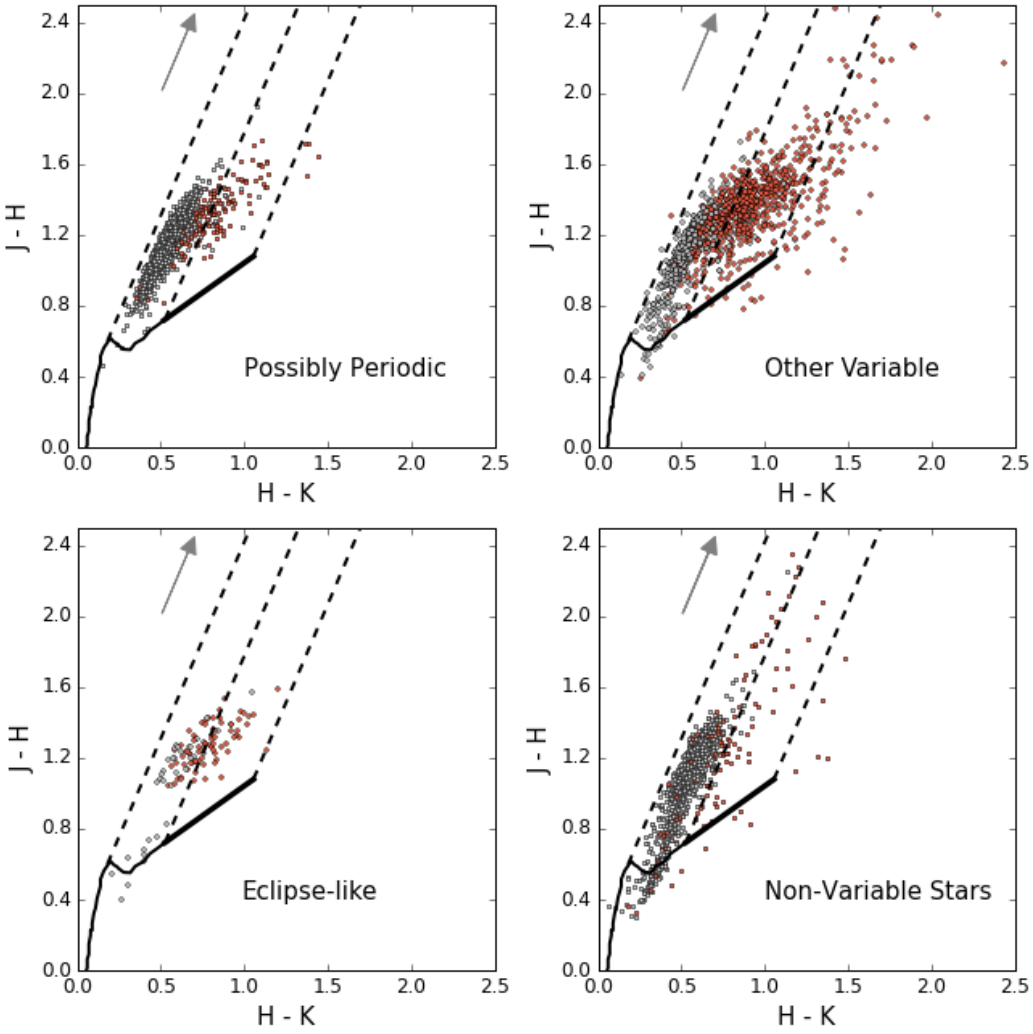

Figure 5.5: Samples of stars with different light curve morphological class inside the CC-diagram. In all the plots, disc-bearing stars are shown in red, and non disc-bearing stars are shown in grey.

Figure 5.5 shows the position of stars in each morphological class inside the CC-diagram. This Figure also shows the position of the non-variable stars inside the same diagram. By comparing the regions occupied by different types of variable stars in the CC-diagram, one can see that periodicity is more common among stars without disc (the disc fraction in the possibly periodic sample is 7%), and such variables are mainly distributed in the region of normal photospheric colours. On the other hand, the disc fraction is 59% for non periodic variable stars, and 68% for eclipse-like variables, and most of the stars in these two sample occupy regions in the CC-diagram associated with near-IR excess typically associated with the disc presence, hence these two types of variability are more common among stars with discs.

For each star in the sample of variable stars we generated a series of plots as exemplified in Figure 5.6 with the star CygOB2-000348. The figure contains plots of H-K, and J-H colour-curves, J and K band light-curves,

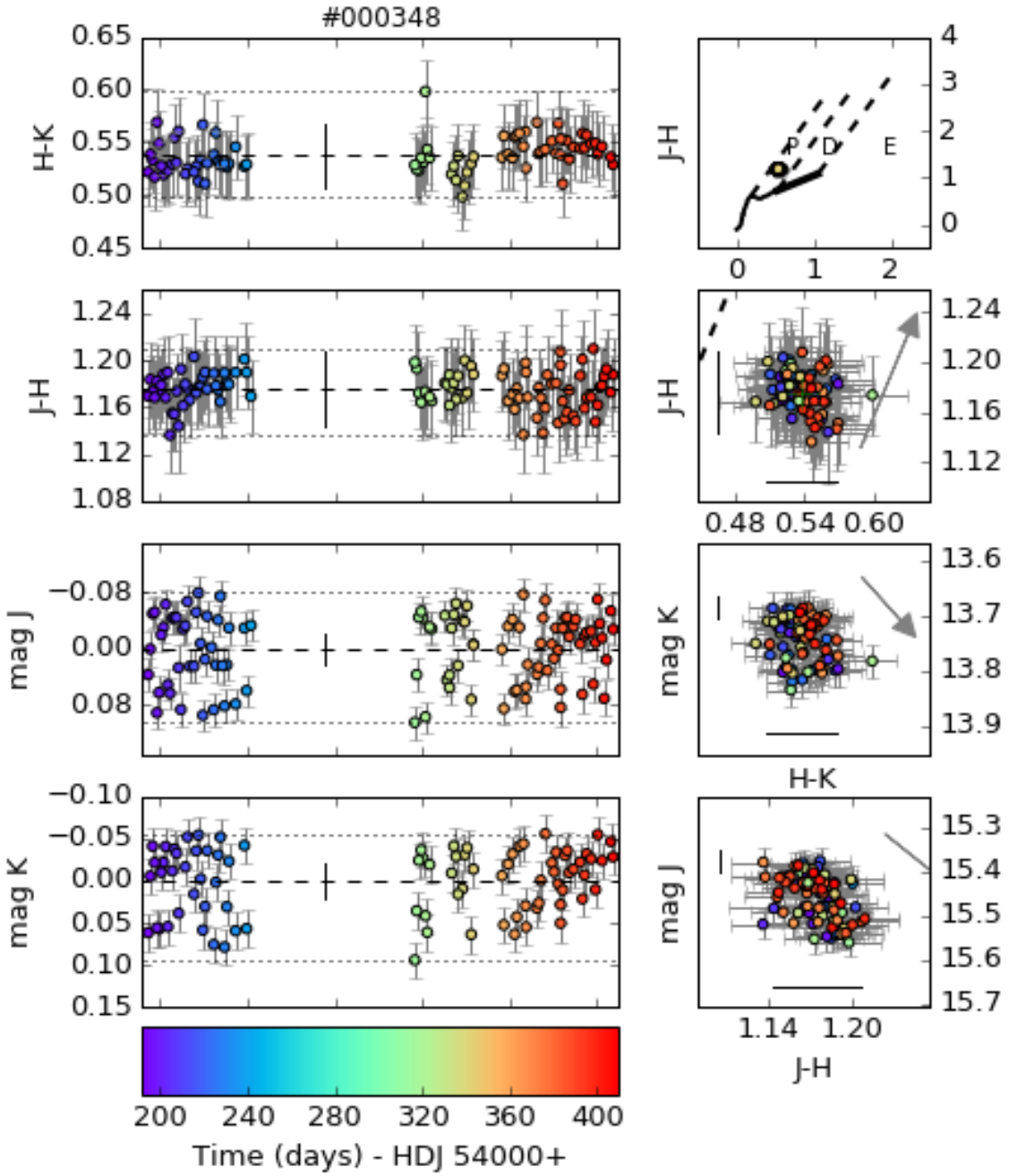

Figure 5.6: Light and colour curves, and colour-colour and colour-magnitude diagrams for the star CygOB2-000348, a periodic variable star with $P = 5.11$ days and $S = 1.62$. Left, from top to bottom: H-K colour-curve, J-H colour-curve, J, and K magnitude light-curves, and a colour table showing the colour attributed for each observation date. The dotted lines show maximum and minimum values in the light curves, and dashed line shows the median value. Right, from top to bottom: Colour-colour diagram with P, D, and E regions (Photospheric colours, disc colours, extreme near IR-excess colours, see Section 2.7), CC-diagram zoomed around the data points, K vs. H-K CM-diagram, and J vs. J-H CMD-diagram both zoomed around the stellar data points. In the CM and CC diagrams, grey arrows show the effect of an interstellar reddening of $A_V = 1^m$. The vertical and horizontal black line segments show the median error in each axis. In each plot, error bars are shown in grey.

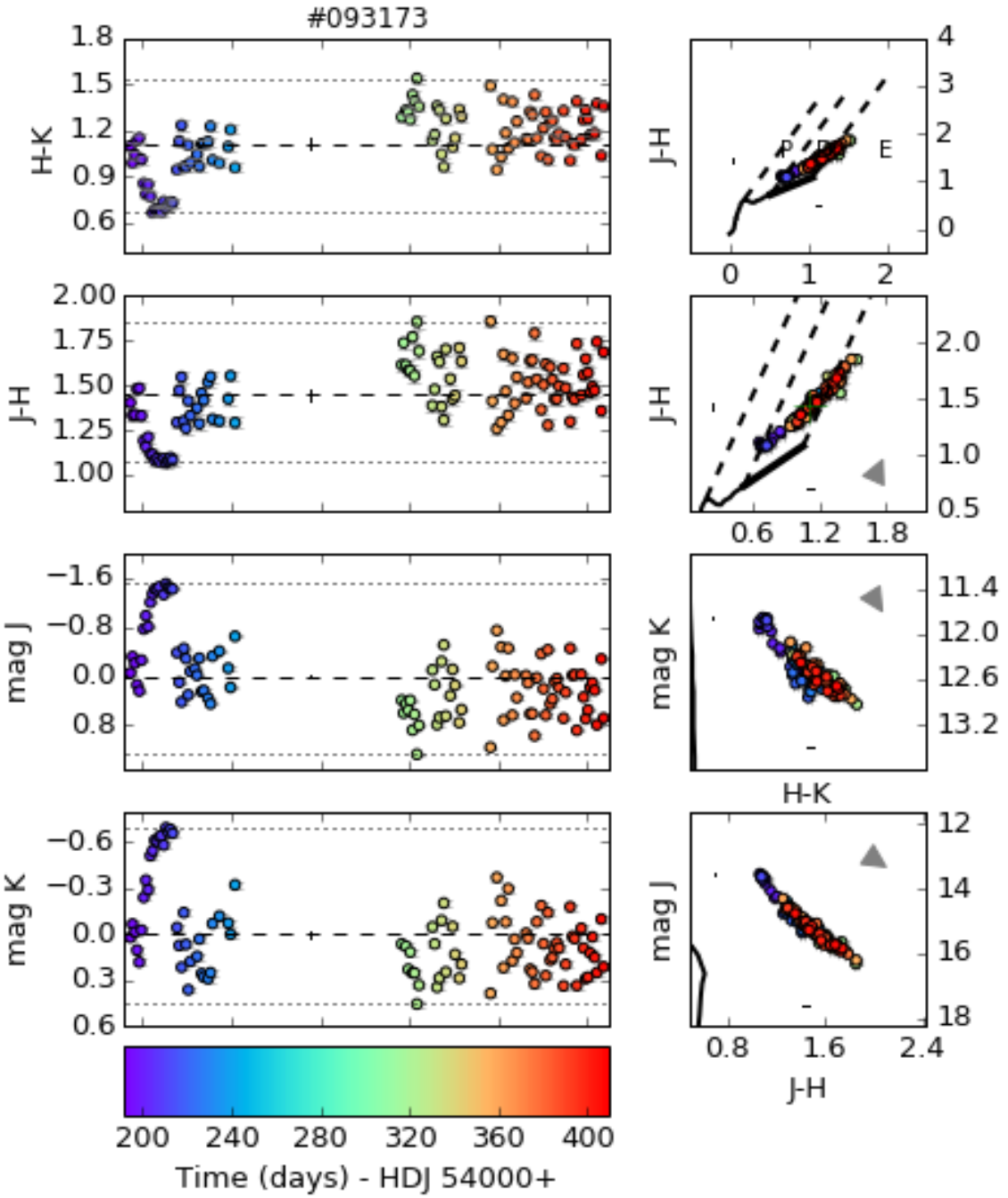

Figure 5.7: Light and colour curves, and colour-colour and colour-magnitude diagrams for the star CygOB2-093173, a short term non periodic variable star with $S = 15.64$, and with correlated variability in CC and CM-diagrams (Slopes presented in Table 5.3). The star gets redder as it gets fainter. The colours and symbols are the same as in Figure 5.6.

CC and CM-diagrams, and inside each plot, to each data point is attributed a colour according to the date the data was measured. For each variable star, we examined a plot similar to the one given as example, and examined the morphology of the light curve, the morphology of the colour curve, the trajectories described by the star inside the CC-diagram and CM-diagrams, and in the case of variability correlated in colour and magnitudes, the slopes of these trajectories were also investigated.

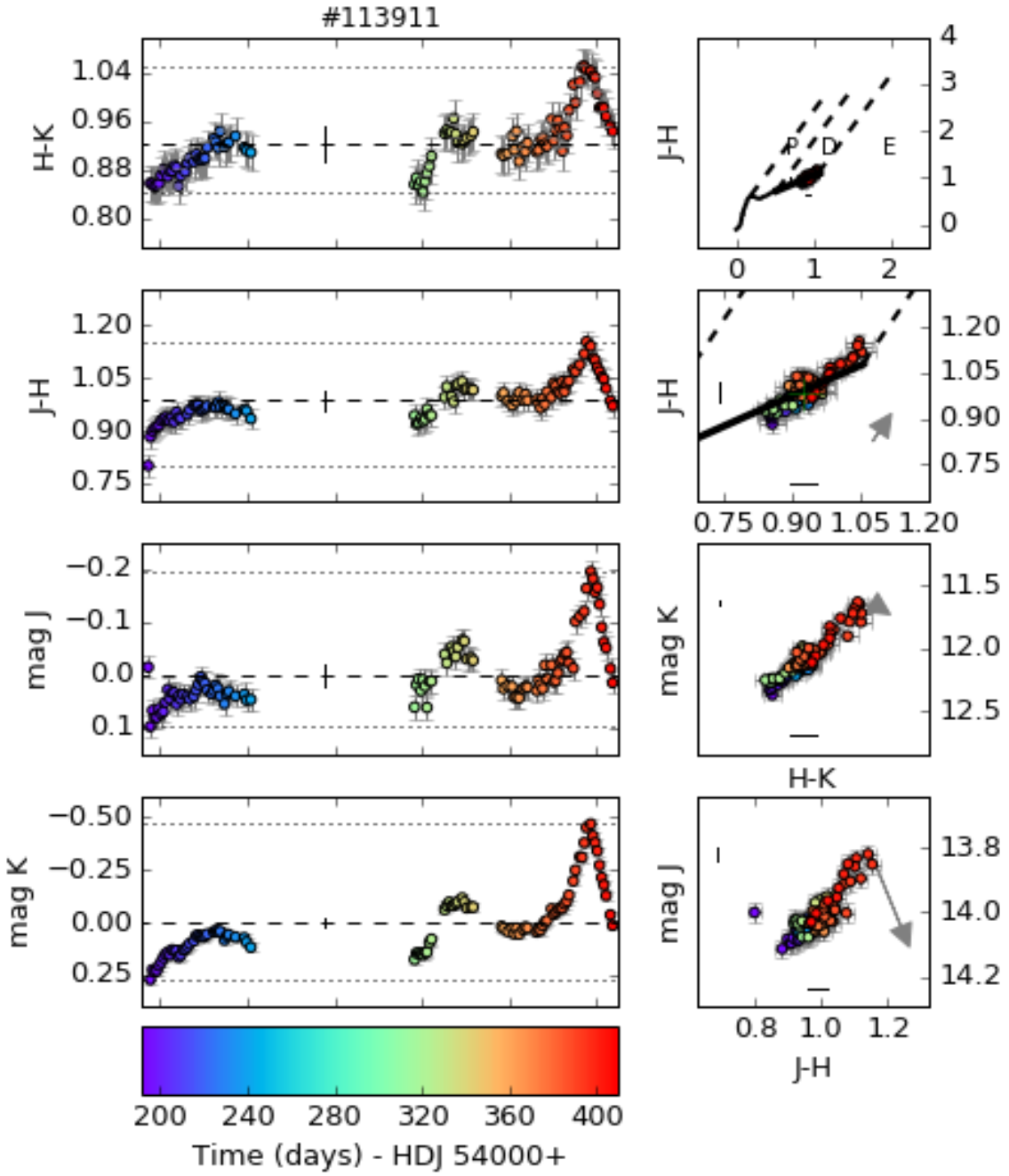

Figure 5.8: Light and colour curves, and colour-colour and colour-magnitude diagrams for the star CygOB2-113911, a non periodic long term variable star with $S = 3.67$, and with correlated variability in CC and CM-diagrams (Slopes presented in Table 5.3). The star gets bluer as it gets fainter. The colours and symbols are the same as in Figure 5.6.

Figures 5.6, 5.7, 5.8 5.9 exemplify the light curve morphological classes. Figure 5.6 shows the periodic star CygOB2-000348, which has $P = 5.11$ days, and $S = 1.62$. Figures 5.7, and 5.8 show other types of variables: CygOB2-093173 is a short term non periodic variable star with $S = 15.64$, and CygOB2-113911 is a long term non periodic variable star with $S = 3.67$. Finally, Figure 5.9 shows the star CygOB2-041510, an eclipse-like variable star, which is also periodic, with $P = 4.68$ days, and $S = 3.06$.

The variable stars may also differ due to their behaviour in colour compared to their behaviour in

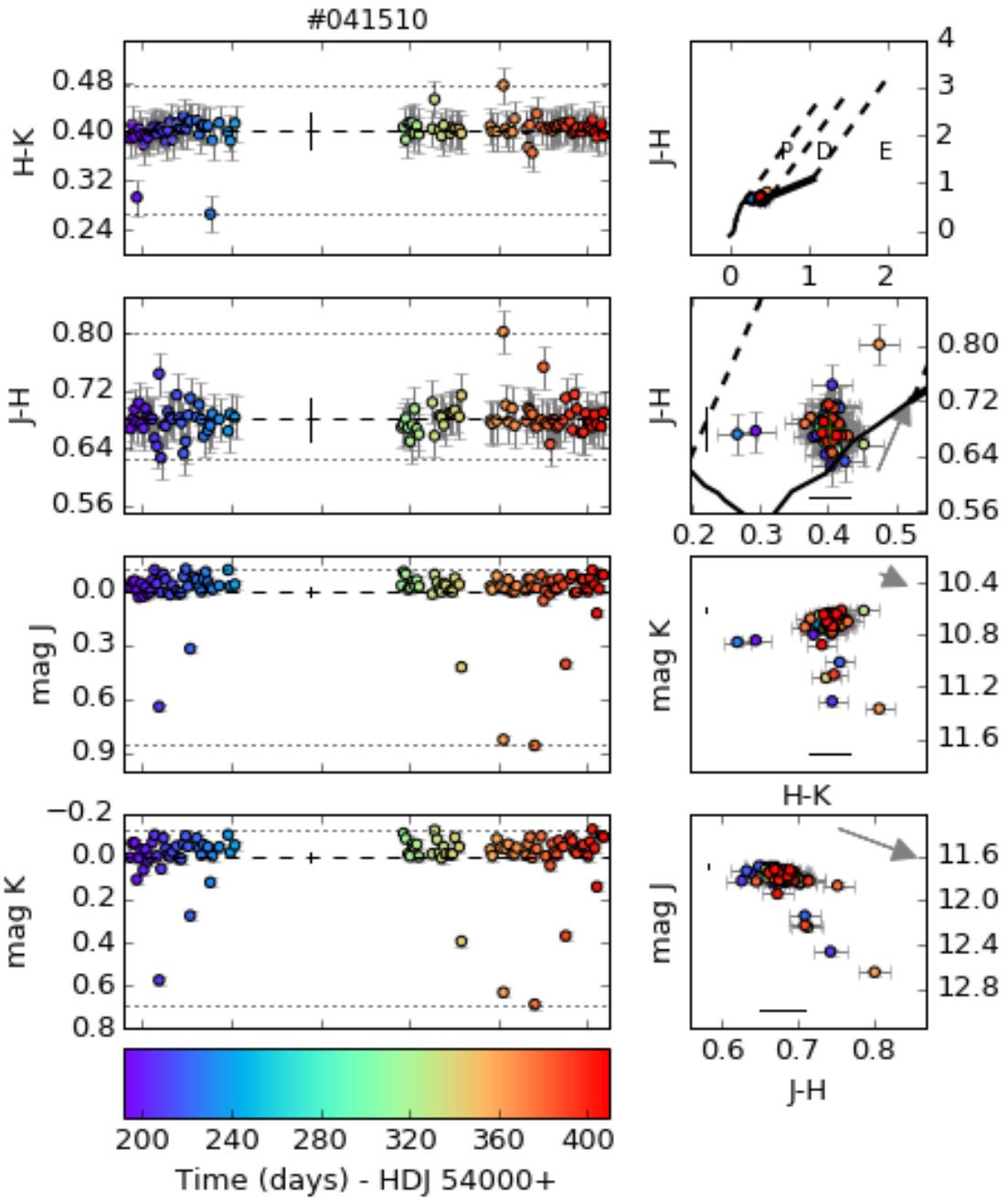

Figure 5.9: Light and colour curves, and colour-colour and colour-magnitude diagrams for the star CygOB2-041510, an eclipse-like periodic variable star with $P = 4.68$ days, and $S = 3.06$. The colours and symbols are the same as in Figure 5.6.

magnitude. Three main behaviours were identified: 1- Stars with no visible trend in colour variability (Colourless Variables); 2- stars that get redder when they get fainter; and 3- stars that get bluer when they get fainter. As discussed in Section 2.3.4, behaviour 2- can be associated with spots (hot or cold) and with variable extinction, and behaviour 3- can be associated to variability due to variable mass accretion rate, or changes in the inner disc. Before discussing examples of each case, one may notice that due to effects of error propagation, the signal-to-noise ratio is lower in the colour-curves than in the light-curves. Because of that, low amplitude variations in colour are not detectable within our data sampling. As cold spots produce

low amplitude variability (Section 2.3.4.1), except in extreme cases, one may expect that cold spot driven variability in our dataset will not show any variability in colour. The variable star CygOB2-000348 (Figure 5.6) shows no IR-excess indicative of a disc, and the probable explanation for its periodicity is therefore the rotational modulation of a cold spot. Stars CygOB2-093173 (Figure 5.7), and CygOB2-000807 (Figure 5.11) are examples of the behaviour 2-, and star CygOB2-113911 (Figure 5.8) is an example of behaviour 3-. Some stars, were difficult to classify, the star CygOB2-041510 (Figure 5.9) is an example of it, but as it did not show a definite tendency in colour, it was also considered as 1-.

5.2.1 Periodicity in colour

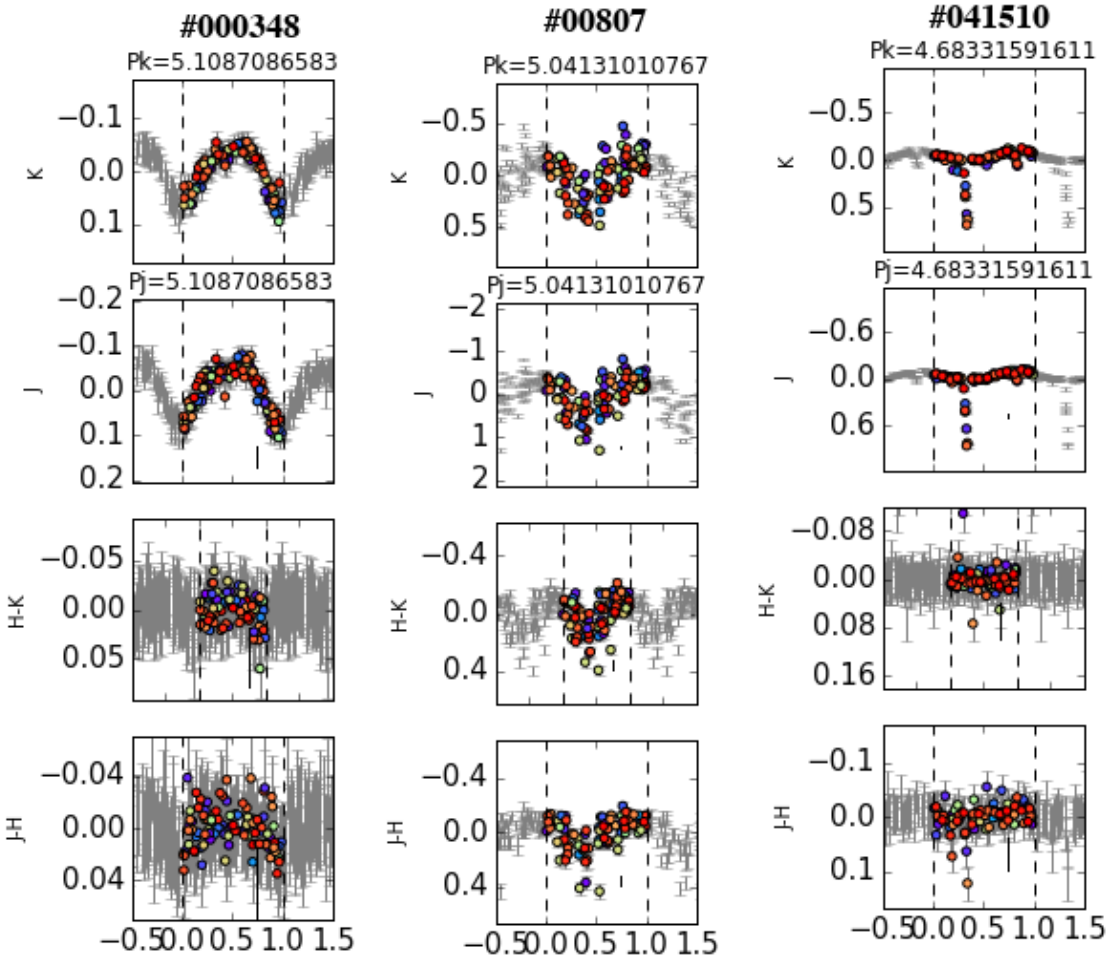

Figure 5.10: Examples of periodic behaviour in colour. Left column: The periodic star CygOB2-000348 (Figure 5.6) is not periodic in colour. Middle column: the periodic star CygOB2-000807 (Figure 5.11) is also periodic in colour. Right column: the eclipse-like star CygOB2-041510 (Figure 5.6) has a colourless eclipse feature.

Even though our data sampling was not appropriate for determining reliable periods shorter than 2 days, periodic signals were often visually verified in the light curves, and periodic variability is so far the most common variability type in the Cygnus OB2 candidate member sample ($\sim$ 54% of the variable sample was

possibly periodic).

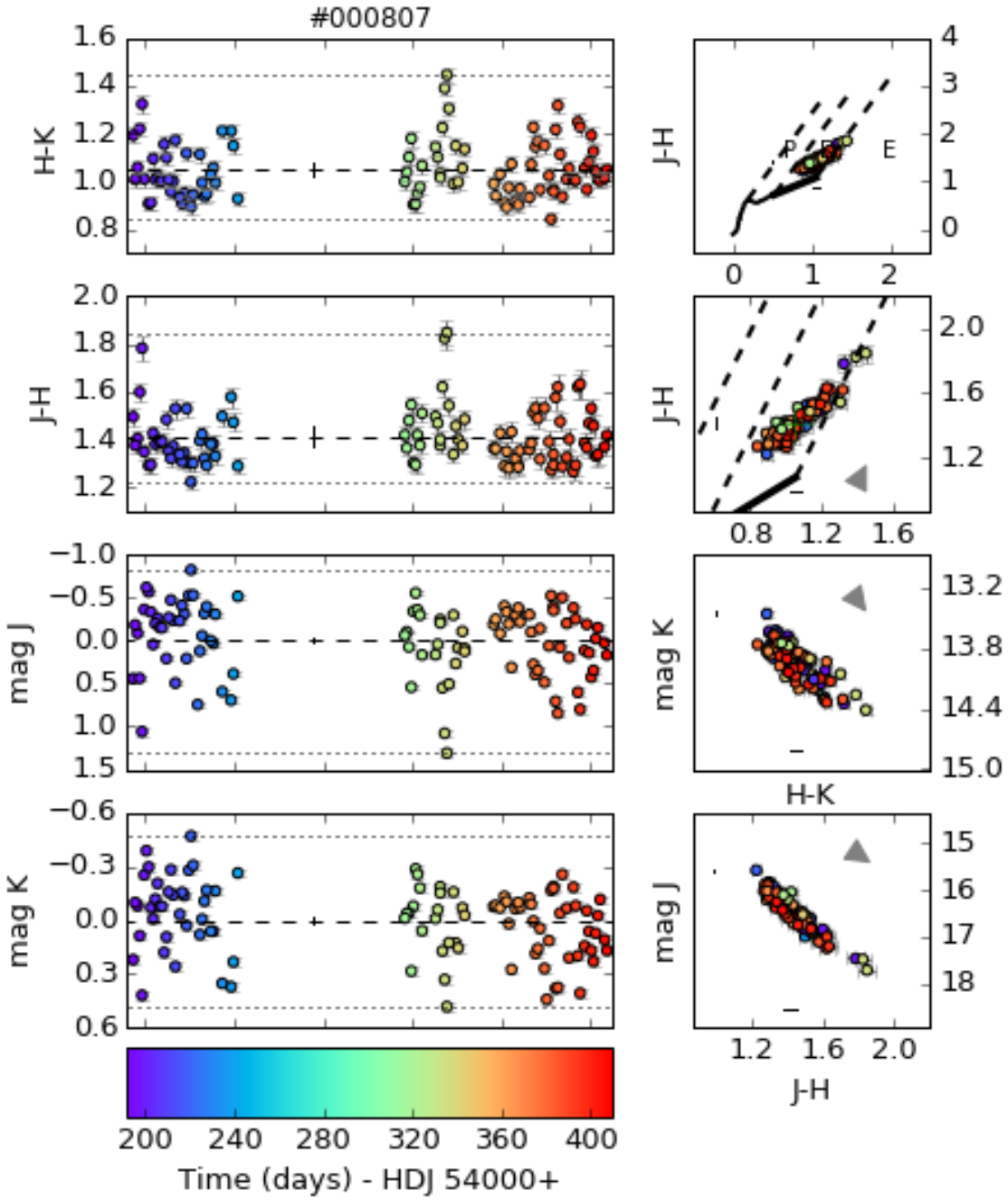

Figure 5.11: Light and colour curves, and colour-colour and colour-magnitude diagrams for the star CygOB2-000807, a disc-bearing (Class 2) periodic variable star with $P = 5.04$ days, $S = 8.75$, and with correlated variability in CC and CM-diagrams (Slopes presented in Table 5.3). The star gets redder as it gets fainter. The colours and symbols are the same as in Figure 5.6.

We present in the Appendix D, the folded light curves for the 894 reliable periodic stars identified in the previous Chapter. For each of them, we also folded the colour-curves in phase for the period detected in the light-curve, and we investigated whether a periodic signal was also present in colour plot or not. Some examples are shown in Figure 5.10. In the first column, the phased colour and light curves for the periodic

variable star CygOB2-000348 (Figure 5.6) are shown. While a very well defined periodic signal of 5.11 days is verified in the J and K light curves, no coherent signal is visible in the colour phased light curves. In the middle column, the phased colour and light curves for the disc-bearing periodic variable star CygOB2-000807 (Figure 5.11) are shown, and in this case the 5.04 days periodic signal was also verified in the colour phased curves. Finally, in the right column the same type of plots are shown for the eclipse-like variable star CygOB2-041510 (Figure 5.9). In the phased light curves an eclipse-like feature is present with a 4.68 days period, but the eclipse is colourless, and it is not visible in the phased colour curves. There were 20 periodic variables which were also periodic in colour, but all the other periodic stars were colourless within our data precision.

5.2.2 Colour slopes

Variable stars may show strong correlations between their variability in different bands, which causes the star to produce colour trajectories in the colour space. Mapping these trajectories may help understanding the physical mechanisms causing variability and their origins. Correlation in the near-IR bands have been studied in the literature by estimating and comparing the slopes of the trajectories in the CM diagrams, $\frac{\Delta K}{\Delta(H-K)}$ and $\frac{\Delta J}{\Delta(J-H)}$, and in the CC-diagram, $\frac{\Delta(J-H)}{\Delta(H-K)}$ (e.g, Carpenter et al. 2001; Rice et al. 2015; Alves de Oliveira & Casali 2008; Rice et al. 2012). The physical mechanisms behind these trajectories were already discussed in Section 2.3.4.

As weak correlations may be a bias caused by uncertainties in the dataset, before estimating the slopes it is mandatory to first investigate how strong is the correlation between the two variables in question. Spearmans non-parametric rank correlation test (Press et al. 1992) was used to test the statistical significance of the correlations in the CC and CM diagrams. Spearmans correlation measures how well the relation between two variables can be described by a monotonic function. It can assume values between -1 and 1 with the extremes occurring when the relationship between the variables is perfectly monotonic.

For stars with Spearman correlation larger than 0.7, the orthogonal distance regression method[1] was used to estimate the slopes in the CC and CM-diagrams and their uncertainties. This method takes the uncertainty of each data point into account while estimating the linear fit. Finally, only the slopes of stars that have signal to noise ratio larger than 2.0, and more than 10 valid observations in each filter were considered. Only a few percent of the candidate member stars satisfied these criteria, and all of them have higher ptp amplitudes than the median values for the whole sample, hence the analysis of variability slopes is restricted to high amplitude stars. Out of the 178 stars with slope measured in at least one of the diagrams, only 8 stars were not in the disc-bearing stars list. There were 43 stars with measured $\frac{\Delta K}{\Delta(H-K)}$ slopes, 122 with measured $\frac{\Delta J}{\Delta(J-H)}$ slopes, an 168 with measured $\frac{\Delta J-H}{\Delta(H-K)}$ slopes. Before describing the results, it is important to understand how the slopes are defined: in the case of CM-diagrams, a positive slope is defined as a positive change in colour, and a positive change in magnitude, which results in a vector pointed towards the bottom-right of the CM-diagram due to the inverted scale of magnitude, and the slope grows clockwise.

[1]Both Spearmans non-parametric rank correlation and Orthogonal Distance Regression are in the SciPy package for Python 2.7

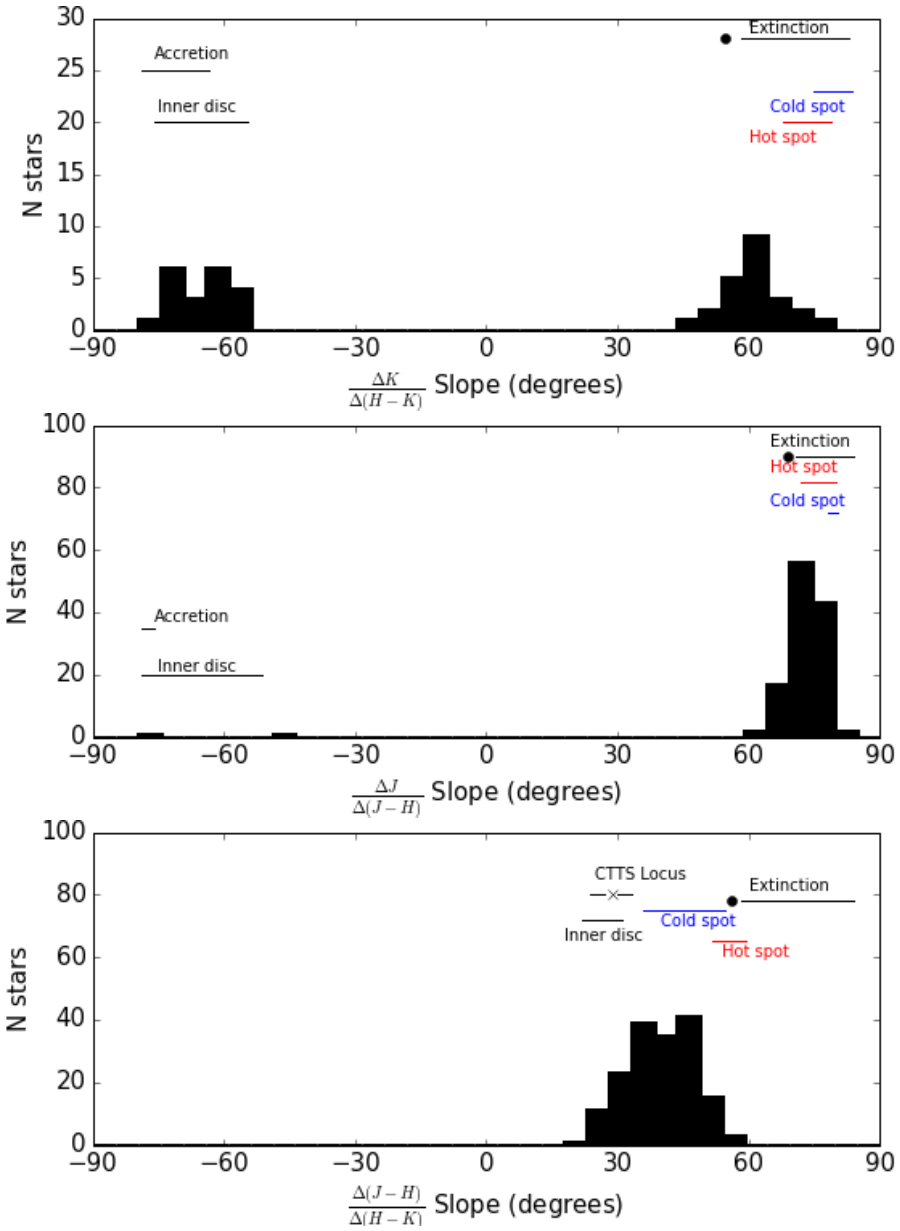

Figure 5.12: Histograms of slopes measured in the colour-colour and colour-magnitude diagrams. Slopes for K vs. H-K (top), J vs. J-H (middle), and J-H vs. H-K (bottom) diagrams are shown. The predicted slopes based on models for cold and hot spot, variable extinction, and changes in the accretion rate or inner disc, described in Section 2.3.4 are also shown for each diagram. The X mark shows the exact position of the T Tauri Locus. The black circle shows the slope expected for the typical dust opacity index in the ISM, $\beta = 1.8$ (Mathis 1990).

In the case of the CC-diagram, a positive slope is defined as positive changes in both colours, the resultant vector points to the top right, and the slope grows counter-clockwise. The distributions of measured slopes are shown in the histogram presented in Figure 5.12. The range of slopes expected to be produced by each physical mechanism responsible for near-IR variability, discussed in Section 2.3.4, are also shown in Figure 5.12. The measured slopes are shown inside CM and CC-diagram, in Figure 5.13, and they are listed in Table 5.3.

The distributions of slopes $\frac{\Delta J}{\Delta(J-H)}$, and $\frac{\Delta J-H}{\Delta(H-K)}$, shown in Figure 5.12 are very similar to the ones presented by Carpenter et al. (2001), and by Rice et al. (2015) for the ONC. In the case of the $\frac{\Delta K}{\Delta(H-K)}$ slopes, as it was also the case for the sample of variable stars with measured slopes presented by Rice et al. (2015), the relative fraction of variable accretion/changes in the inner disc variability vs. spot/variable extinction variables is higher than in the sample presented by Carpenter et al. (2001). In the $\frac{\Delta K}{\Delta(H-K)}$ slope distribution, 23 stars presented slopes between 63° and 77°, compatible with variability due to spots or variable extinction, and 20 stars presented slopes between -24° and -79°, compatible with variability due to variable accretion rate, or changes in the inner disc. In the $\frac{\Delta J}{\Delta(J-H)}$ slope distribution, 120 stars presented positive slopes between 62° and 82° compatible with spot/variable extinction variability, while only 2 stars presented negative slopes between -47° and -77°, compatible with variable accretion or changes in the inner disc variability. In the $\frac{\Delta J-H}{\Delta(H-K)}$ slope distribution the distinction between types of variability is more complicated, as all types of variability investigated produce positive slopes inside the CC-diagram. And even though variable accretion and changes in the inner disc are expected to produce shallower slopes, there may be a significant overlap between the slopes produced by different physical mechanisms. There were 168 stars with slopes between 21° and 58°. The 178 stars with measured slopes are listed in Table 5.3, which presents: their ID inside our catalogue, their ID in the GDW13 and GDW15 catalogues, their coordinates, their variability type, periodicity and Stetson variability index, and their slopes and uncertainties in the CC and CM-diagrams. A full version of this table is shown in Appendix D.

The fact that less stars presented $\frac{\Delta J}{\Delta(J-H)}$ slopes compatible with variable accretion rate or changes in the inner disc is related to the nature of the near-IR excesses in disc-bearing stars. The amount of light re-emitted by the disc in the near-IR is larger for larger wavelengths. The same is true for the variability amplitudes produced by physical mechanisms acting in the same region of the disc where the near-IR radiation in excess comes from. Because of that, one may expect that the amplitudes of variability due to variable accretion rate and changes in the inner disc will be larger for the magnitude K and colour H-K, than for magnitude J and colour J-H. These lower amplitudes make the trajectories in the CC and J vs. J-H CM diagrams less evident and difficult to measure, hence explaining the lack of negative slopes in this CM diagram.

Some of the stars presented as example in the previous figure had slopes measured. The variable star CygOB2-093173 (Figure 5.7) had slopes measured in all diagrams: a slope of 42.87° was measured in the J-H vs. H-K diagram, 53.39° in the K vs. H-K diagram, and 74.14° in the J vs. J-H diagram. This set of slopes together with the short term variability in the light curve indicates the star has variability due to a hot spotted surface or variable extinction.

The variable star CygOB2-113911 (Figure 5.8), also had slopes measured in all diagrams: a slope of 47.87° was measured in the J-H vs. H-K diagram, -73.41° in the K vs. H-K diagram, and -47.6° in the J vs. J-H diagram. This set of slopes might indicate that the variability is caused by variable accretion or changes in the inner disc. The fact that the $\frac{\Delta J-H}{\Delta(H-K)}$ slope measured is very close to the one measured for the star CygOB2-093173 shows that there is an overlap in the distributions of slopes in the CC-diagram.

Figure 5.12 also show the rage of slopes expected for each physical mechanism studied. In some cases, specially when more than one of the three slopes were measured for the same star, it was possible to infer

								Slopes (°)					
ID	RA (h:m:s)	Dec (d:m:s)	GDW13	GWD15	Type[1]	Periodic?[2]	Stetson	$\frac{\Delta J-H}{\Delta(H-K)}$	err	$\frac{\Delta K}{\Delta(H-K)}$	err	$\frac{\Delta J}{\Delta(J-H)}$	err
CygOB2-000064	20:32:15	+41:11:10	11704	1269	2		5.79	42.61	0.05			73.11	0.14
CygOB2-000116	20:32:25	+41:17:22	29903	1482	2		2.04	41.23	0.1				
CygOB2-000133	20:32:27	+41:15:16	67478	1531	2		4.52	35.51	0.05			73.74	0.19
CygOB2-000217	20:32:38	+41:12:01	308405	1822	2		4.1	32.72	0.06				
CygOB2-000284	20:32:46	+41:16:47	31382	2006	1	1	3.33	44.49	0.15			75.75	0.47
CygOB2-000291	20:32:46	+41:10:42	10284	2016	2		2.97	35.67	0.05			74.25	0.19
CygOB2-000334	20:32:50	+41:14:59	67108	2124	2		5.91	38.93	0.09	65.6	0.26	77.32	1.24
CygOB2-000381	20:32:54	+41:10:07	73793	2249	2		5.48	31.61	0.05			73.41	0.27
CygOB2-000392	20:32:55	+41:09:02	73721	2266	2		4.97	26.8	0.04			80.01	0.65
CygOB2-000432	20:32:58	+41:17:35		2355	2		7.8	34.5	0.04			77.12	0.89
CygOB2-000576	20:33:06	+41:16:35	66361	2652	2		7.12	49.37	0.16			77.32	1.0
CygOB2-000744	20:33:13	+41:11:33	312145	2972	1		3.02	31.46	0.04	-67.83	0.13		
CygOB2-000762	20:33:14	+41:13:46	65768	3009	1	1	7.91	36.69	0.08			77.79	4.82
CygOB2-000771	20:33:14	+41:12:22	292858	3029	1	1	7.65	40.88	0.06	70.78	0.25	78.06	11.98
CygOB2-000772	20:33:14	+41:12:24		3032	1	1	5.65	47.42	0.17			74.77	0.2
CygOB2-000795	20:33:16	+41:08:28	72761	3083	1	1	2.53	43.23	0.07			69.2	0.17
CygOB2-000804	20:32:06	+41:12:24	10595		2		3.82	46.61	0.08			70.21	0.16
CygOB2-000807	20:32:14	+41:16:05	11995		1	1	8.75	41.38	0.06	63.73	0.35	75.99	0.26
CygOB2-000845	20:32:07	+41:18:14	68446		2		1.51	27.13	0.05	-60.66	0.72		
CygOB2-000860	20:33:07	+41:07:51	73267		2		4.04	35.37	0.07			74.76	0.38
CygOB2-000869	20:32:49	+41:10:32	73827		2		3.76	43.24	0.08			70.32	0.15
CygOB2-000871	20:32:38	+41:06:00	73946		3		4.1	34.26	0.06				
CygOB2-000878	20:32:41	+41:09:47	74085		2		5.17	43.81	0.1	58.44	1.72	74.36	0.18
CygOB2-000881	20:32:35	+41:06:36	74147		2		2.36	31.24	0.05	-69.66	0.25		
CygOB2-000898	20:33:14	+41:13:04	101288		2		10.19	44.48	0.13	55.71	0.92	74.18	0.25
CygOB2-000908	20:32:52	+41:17:42	112350		2		4.66	28.76	0.07			72.03	0.25
CygOB2-000920	20:33:12	+41:11:40	312016		3		5.89	38.09	0.06			77.73	2.3
CygOB2-010953	20:34:34	+41:15:41	92649	4831	1	1	4.46	45.59	0.11			73.14	0.29
CygOB2-011072	20:34:27	+41:11:31	16491		2		2.52	54.91	0.49			67.19	0.16
CygOB2-011076	20:34:52	+41:14:07	18989		2		7.07	57.55	16.44			66.5	0.08
CygOB2-011083	20:34:28	+41:17:36	63764		1		7.1	46.44	0.18	69.35	0.18	76.33	0.39
CygOB2-011091	20:35:03	+41:10:01	98617		1	1	5.39	42.76	0.08	62.07	0.29	75.48	0.23
CygOB2-011098	20:34:59	+41:12:02	102105		2		1.84	42.34	0.11				
CygOB2-021182	20:34:47	+41:41:59	93709		1		5.87	44.12	0.1			71.78	0.15
CygOB2-021183	20:35:24	+41:34:38	94590		2		2.63	45.14	0.17			70.9	0.32
CygOB2-021185	20:34:53	+41:40:18	95624		2		3.82	32.04	0.05			70.56	0.11
CygOB2-021188	20:35:06	+41:39:32	96834		2		0.99	38.16	0.06	-55.69	0.92		
CygOB2-021190	20:35:14	+41:34:00	97877		1	1	3.24	33.94	0.09				

Table 5.3: Stars with measured slopes in the colour-colour diagram or colour-magnitude diagrams. A complete version of the table containing all the 178 stars with measured slope is available in the Appendix B.

[1]Periodic? equal to 1 means the star had reliable period measured.

[2]Variability type according to the morphological of the light curves. 1- Possibly Periodic; 2- Other type of variables; 3- Eclipse-like variables.

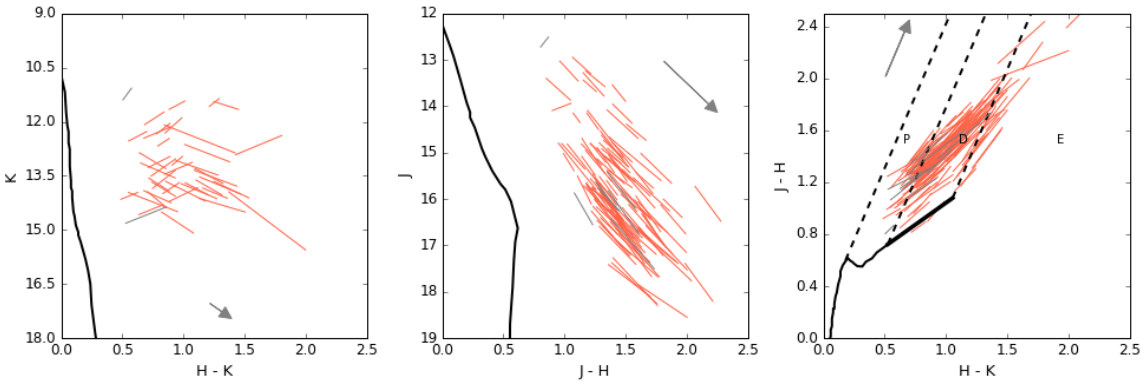

Figure 5.13: Measured variability slopes inside colour-colour and colour-magnitude diagrams. K vs. H - K, J vs. J - H, and J - H vs. H - K diagrams are shown from left to right. Disc-bearing stars are shown in red, and stars without discs are shown in grey. The grey arrow shows the median interstellar extinction towards CygOB2.

the dominant physical mechanism in the light curve. There were 116 (∼65.2%) stars with two or more slopes compatible with variability due to hot spot; 20 stars (∼11.3%) were compatible with changes in the inner disc or variable accretion; 4 stars (∼2.5%) could be either spot or variable extinction, and 38 stars (∼21.4%) did not have enough slopes measured to unambiguously indicate a physical mechanism.

In both (Carpenter et al. 2001) and (Rice et al. 2015) the authors distinguish only between stars that get redder when fainter (reddening), that could be explained either by spots or variable extinction, and stars that get bluer when fainter (blueing type), that could be explained either by changes in the inner disc or variable accretion. (Carpenter et al. 2001) found 6 times more reddening type variables than blueing type variables, while (Rice et al. 2015) found 1.5 times more reddening than blueing types. When considering only the $\frac{\Delta K}{\Delta(H-K)}$ slope, or dataset present similar results to Rice et al. (2015), with generally speaking as many blueing variables as reddening variables, but when considering also the $\frac{\Delta J}{\Delta(J-H)}$ slopes, we found 6 times more reddening type variables than blueing variable, similarly to Carpenter et al. (2001).

5.2.3 Compound variables

Rice et al. (2015) identified among their sample of variable stars in the ONC, stars that presented compound colour behaviour, *i.e.*, stars which trajectories inside the CC and CM-diagrams are not confined into a single positive or negative slope behaviour. Some stars with compound variability were also identified in our sample. One example is the disc-bearing non periodic long term variable star CygOB2-021188 (Figure 5.14) which describes a negative $\frac{\Delta K}{\Delta(H-K)}$ slope during the first 100 days of observation, but has a positive $\frac{\Delta J}{\Delta(J-H)}$ slope in the last 100 days of observations. Compound variables like this one highlight the fact the physical mechanisms proposed to explain variability are not mutually exclusive.

While compound variables show that the dominant physical mechanism causing variability may change with time, it may also be the case that multiple physical mechanisms are acting at the same time, producing light curves and colour trajectories too complex to be identified.

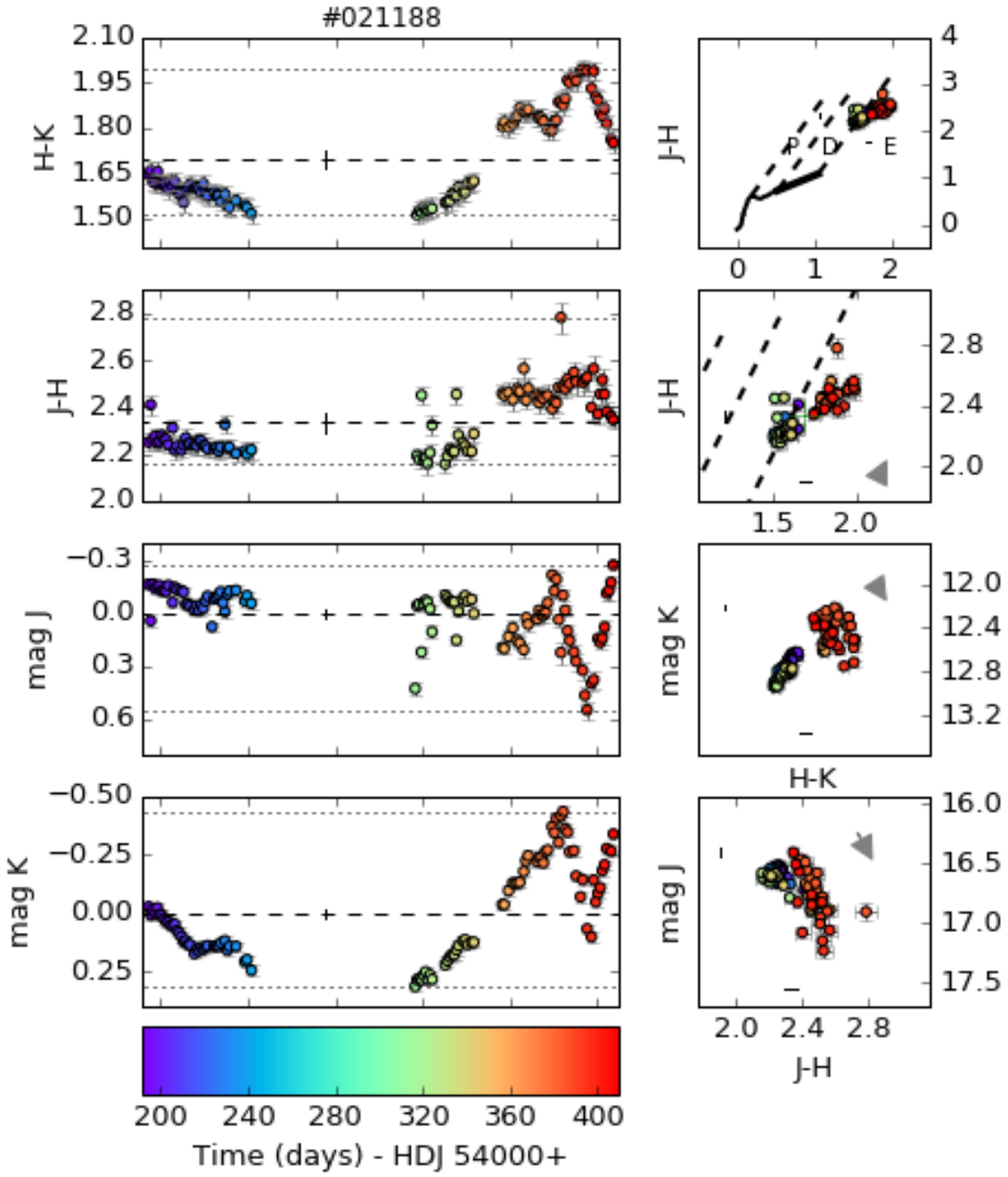

Figure 5.14: Light and colour curves, and colour-colour and colour-magnitude diagrams for the star CygOB2-021188, which is a disc-bearing (Class 2) non periodic, long term variable star with compound behaviour in the CM-diagrams, and $S = 1.00$. The colours and symbols are the same as in Figure 5.6.

5.2.4 Transient near infrared excesses

Rice et al. (2012), in their study about WFCAM/UKIRT JHK variability of stars in the Cygnus OB7 association, named as stars with "transient near-IR excesses" those stars that vary in colour space such that they spend part of their time in the photospheric colours region of the CC-diagram (P) and part of their time in the disc colours region (D). From the CC-diagram plot in Figure 5.13 (first and second top right plots), one can see that several stars in our sample have this kind of behaviour.

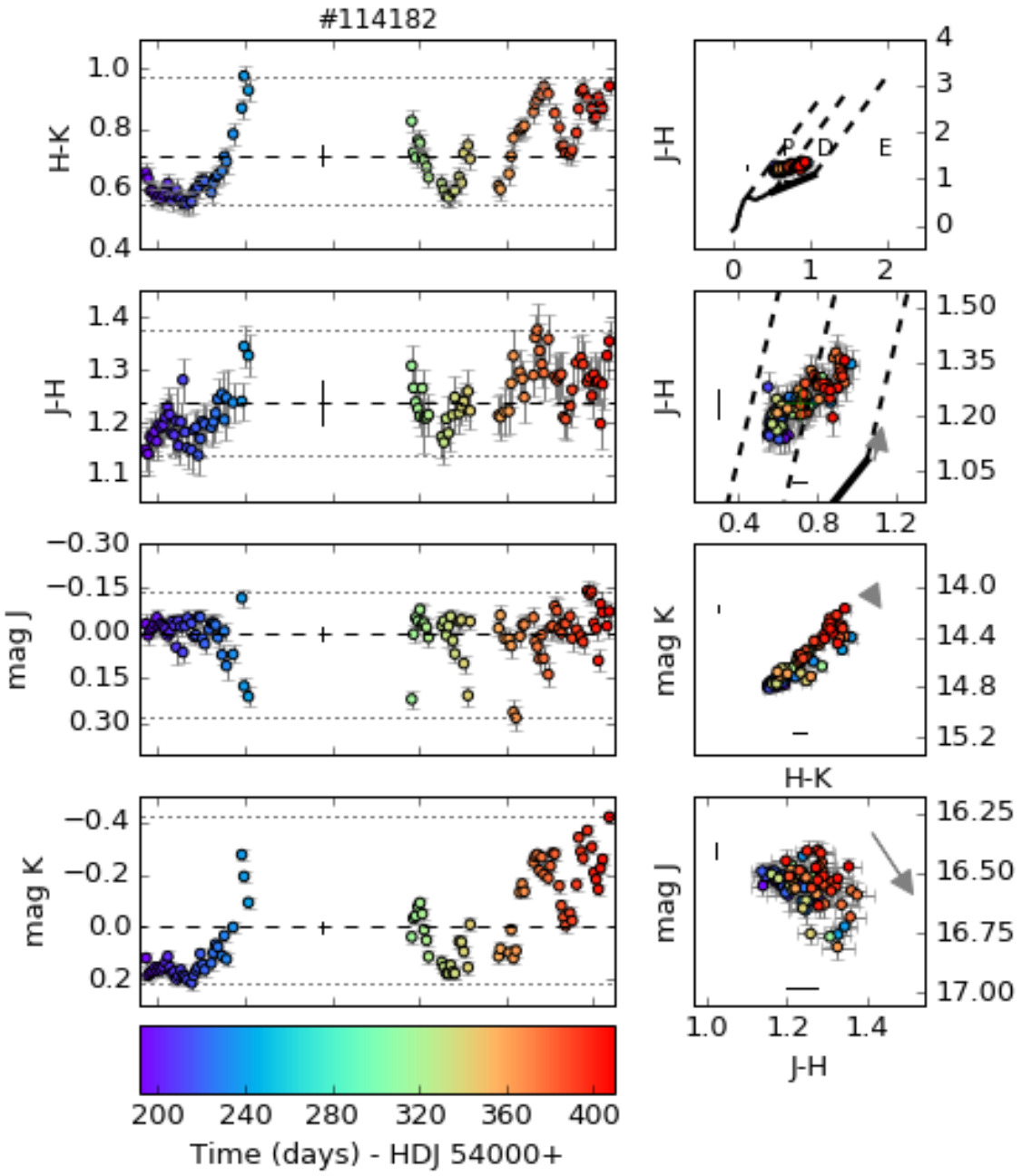

Figure 5.15: Light and colour curves, and colour-colour and colour-magnitude diagrams for the star CygOB2-114182, a non periodic variable star with $S = 1.44$, with transient near-IR excess, and with correlated variability in CC and CM-diagrams (Slopes presented in Table 5.3). The colours and symbols are the same as in Figure 5.6.

While examining the plots for the 8 stars with measured amplitude not listed as disc-bearing stars, we noticed that all of them oscillate between the "P" and "D" regions in the CC-diagram. Also, in some cases the stars had a variability behaviour compatible with variability due to variable accretion rate or changes in the inner disc, but they were not listed as disc-bearing star in the literature. This is the case of the non-periodic variable star CygOB2-114182 (Figure 5.15), which presented slope of 21.04° in the J-H vs. H-K diagram, and -55.09° in the K vs. H-K diagram, but it was not listed as a disc-bearing star.

The existence of non disc-bearing variable stars presenting disc-bearing variability characteristics, as CygOB2-114182, raises the question: how reliable are the disc identification methods based on IR-excess estimated using single epoch photometric surveys?

5.3 Discussion and conclusions

Carpenter et al. (2001) were the first to perform a synoptic study of near-IR variability in young stars. In their study of stars in the ONC, they found variability in 1235 stars (∼45% of their membership candidate sample). They found a mean peak-to peak fluctuation around 0.2 magnitudes with extreme variables having amplitudes up to ∼2 mag. Most of their variables were colourless within their photometric errors, and 77% of them had J-H colour variations smaller than 0.05 mag (their minimum photometric uncertainty was about 0.015). They used an autocorrelation function to establish the time-scales of the photometric fluctuations, and found that it is typically less than a few days. Carpenter et al. (2001) observations were obtained on 29 days over a 36 day time period.

Since then, several authors also contributed to the subject, but if in one hand some studies provided longer baselines, only few studies presented a variable star sample as statistically significant as Carpenter et al. (2001). Carpenter et al. (2002) used 2MASS data to study Chamaleon I, their observations were obtained over 15 nights of observations over 4 months and they identified 95 variable stars. Alves de Oliveira & Casali (2008) used WFCAM/UKIRT data to investigate near-IR variability in stars in the ρ Ophiuchi cluster. Their observations were taken over 14 epochs, and they identified 137 variables in the direction of the cluster, 52 of which were cluster members. Parks et al. (2014) did a high precision, high cadence JHK_s monitoring of ρ Ophiucus stars, using 2MASS Calibration Database, with a temporal baseline of ∼2.5 years, and found 101 variable stars. Rice et al. (2012), Wolk et al. (2013) observed CygOB7 with WFCAM/UKRT in 3 seasons of 26, 71, and 75 days over 1.5 years. They found 25 disc-bearing stars in the association, but only 1.6% of their non disc-bearing stars presented some type of variability. Recently, Rice et al. (2015) presented a WFCAM/UKIRT new near-IR variability survey for stars in the ONC, with a longer time coverage than the one in Carpenter et al. (2001). Their observations were obtained on 120 nights, spanning 894 days, and they identified 1203 variable stars in the ONC, 24% of which were periodic variables.

In the present work, which was based on 115 observed nights over 217 days, we identified 3077 variable stars, 55% of which presented periodic behaviour in their light curves. Periodic behaviour is more common between non disc-bearing stars: while 70% of variable stars without discs show some periodicity in their light curves, only 18% of the variable disc-bearing stars show the same behaviour. Most of the periodic stars are low amplitude variables, 80% had J ptp amplitudes smaller than 0.15 mag. These differences in amplitude are consistent with the physical mechanisms investigated in Section 2.3.4: rotational modulations by cold spot is the most common variability mechanism in stars without discs, and cold spots are expected to produce low amplitude, periodic stars.

We also investigated the trajectories that the physical mechanisms responsible for variability in the near-IR (spots, variable extinction, variable accretion and changes in the inner disc) produce in the colour space.

Using measurements of such trajectories, we identified 178 stars that present one single dominant physical mechanism in action. We identified several compound variable stars in the sense they show more than one type of colour behaviour over the time observed. The existence of such objects highlights the complexity of the near-IR variability.

Out of the 178 stars for which colour slopes were measured, 65.2% presented slopes consistent with spot variability, 11.3% were consistent with variable accretion or changes in the inner disc, 2.5% could be variable extinction or spots, and 21.4% have only $\frac{\Delta J-H}{\Delta(H-K)}$ slopes measured, which was not enough for inferring the most probable physical mechanism.

We caution the reader on the interpretation of the slope distributions. While the study of the trajectories in colour is specially good for selecting high amplitude variable stars with a single dominant physical mechanism producing variability in their light curves, the frequency with which each physical mechanism is observed may not be representative of the reality. For example, Rice et al. (2015) notice that the larger fraction of blueing variables that they found compared to Carpenter et al. (2001) may be a consequence of the different total timespan in each survey that may favour the detection of certain types of variables. For example, surveys developed over a couple of months, as is the case of Carpenter et al. (2001) and of Cody et al. (2014, who surveyed NGC 2264 for variability in the optical and mid-IR) may favour the detection of variable stars such as AA Tauri, which present variability in time-scales of days to weeks. On the other hand, as blueing variability have longer time-scales, surveys as long as Rice et al. (2015, 2.5 years) or Rice et al. (2012, 1.5 years) may favour de detection of this type of variable. We also notice that our dataset is not specially adequate for detecting reddening variables such as AA Tauri stars. The morphology frequently observed in the light curve of such variable stars is similar of what we called 'eclipse-like' in this thesis: the star spend most of the time in a maximum of bright (not necessarily constant), suffering periodic or quasi-periodic minimums of bright, or 'dippers', and due to the nature of this variability (extinction), it gets redder when it fades. As our data cadence is of 1 observation per night, the dippers or eclipses in the eclipse-like variable stars are often composed of one or two data-points, making it difficult to identify the reddening character in their colour curves. Even with this caveat, we composed a list of variable stars that may be of AA Tauri type, and such stars will be analysed individually in the future.

We also note that several stars not listed as disc-bearing stars in the literature presented variability behaviour that makes them alternate between normal photospheric colours, and near-IR excess colours. Some of these stars have variability characteristics that suggest the presence of a disc. Further investigations are needed to complement these results. A next step will be to study the typical time-scales of variability in the whole variable sample. The indications that near-IR variability could be used to complement the disc-bearing star census in the association is specially interesting and further investigations comparing the JHK light curves from the present work with data from GDW13 (in special form the Spitzer Legacy Survey of Cygnus X Region) will be performed.

Chapter 6

Rotational scenario of Cygnus OB2

Given its rich population and the fraction of candidate members with periodic variability, CygOB2 is a valuable target for testing the theory of stellar angular momentum evolution during the PMS. In this Chapter the main characteristics of the periodic star sample, built after the time series analysis described in Chapter 4, will be discussed inside the context of early rotational evolution for low mass stars.

As in Herbst et al. (2002), the definition of rotational regimes is based on values of rotational angular velocity. Given that rotational angular velocity relates to the measured periods as $\omega = \frac{2\pi}{P}$, one may call stars with $\omega \leq 0.5 \frac{\mathrm{rad}}{\mathrm{day}}$ ($P > 12.56$ days) very slow rotators, $0.5 \frac{\mathrm{rad}}{\mathrm{day}} < \omega \leq 1.0 \frac{\mathrm{rad}}{\mathrm{day}}$ ($P > 6.28$ days) slow rotators, stars with rotational angular velocity in the range $1 \frac{\mathrm{rad}}{\mathrm{day}} \leq \omega \leq 2 \frac{\mathrm{rad}}{\mathrm{day}}$ are intermediate rotators, and stars with $\omega > 2 \frac{\mathrm{rad}}{\mathrm{day}}$ ($P <$3.14 days) fast rotators. It is of utmost importance to keep in mind the limitations of the analysed sample. As the fastest rotators ($P < 2$ days) in the sample are strongly contaminated, the discussions here are based on a few fast rotators (with periods in the range 2.0 - 3.14 days), intermediate and slow rotators.

6.1 General properties of the periodic sample

After excluding eclipse-like variables, eclipsing binary candidates and possible visually-selected contaminants, a final list of 1211 candidate members of CygOB2 with periodic variability and periods between 0.86 and 32.49 days was compiled. The period distribution for the 1196 stars with $P < 20$ days is shown in Figure 6.1. Since only 15 stars ($\sim 1\%$ of periodic sample) have periods longer than 20 days, those stars were kept outside the distributions shown in the rest of the present Chapter. Error bars were estimated taking into account the completeness and contamination analysis for periods up to 20 days (Figure 4.21): upper error bars take into account the sample's incompleteness for each magnitude bin (Figure 4.21), and lower error bars take into account the contamination level per magnitude. Even though they were not used in the present analysis, periods shorter than 2 days are shown in red in the distribution in Figure 6.1, and also in the following Figures in this Chapter. Keeping the shortest periods out of the analysis, the mean, standard deviation and median values for the general period distribution are $P(\mu, \sigma, \nu)$= 6.67, 4.18, and 5.92 days.

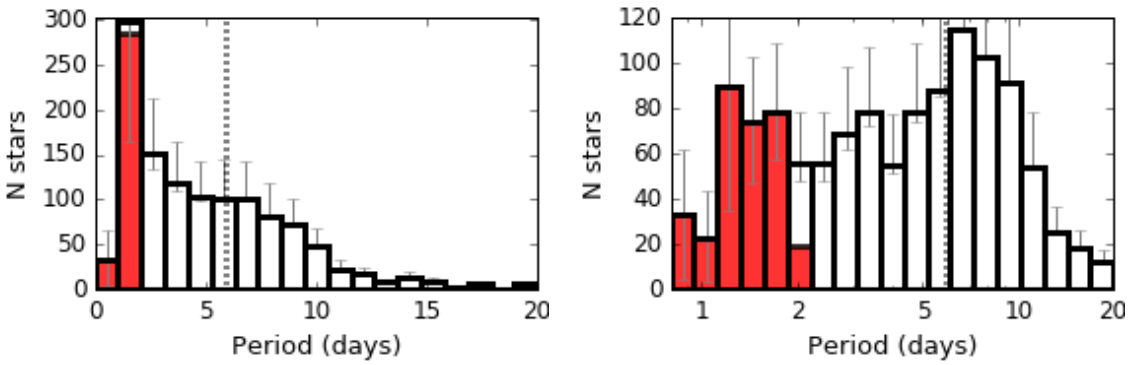

Figure 6.1: Period distributions for the 1196 periodic stars with $P < 20$ days found in the present study in both linear (left) and logarithm (right) scale. The median value for $P \geq 2$ days stars is shown as dotted line. There were 879 stars with $P \geq 2$ days and $P < 20$ days. The red bins show the fast rotators with $P < 2$ days excluded from the analysis.

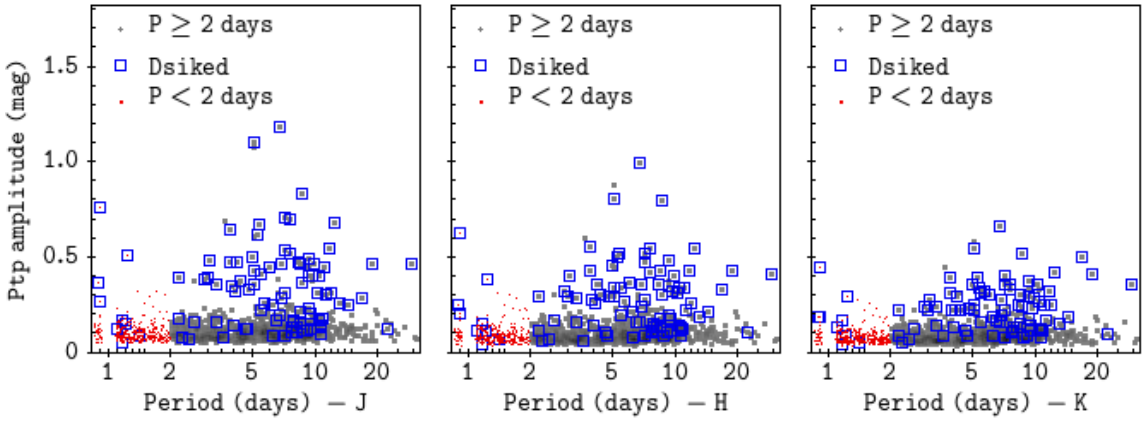

Figure 6.2: Period vs. ptp JHK amplitude for periodic stars. Stars with $P < 2$ days are shown as red dots; Stars with $P \geq 2$ days are shown as grey dots; Disc-bearing periodic stars are shown as blue squares.

The photometric ptp amplitudes for each band are shown as a function of periods in Figure 6.2. The amplitude of 90% of the periodic stars is widely distributed between 0.03 and 0.18 magnitudes; 9% of them exhibit amplitudes between 0.18 and 0.51 magnitudes, and 1% exhibit amplitudes as high as 1 magnitude. Figure 6.3 shows the photometric ptp amplitudes for each band as a function of magnitude. The increase of the lower amplitude envelope with magnitude is due to an observational bias related to the dependence of the minimum photometric errors on the magnitude (cf. Figure 3.5), which makes it increasingly difficult to detect low amplitude variables among fainter stars. On the other hand, the upper envelope of the distribution also shows an increase with amplitude, which can be explained by a larger and/or more uneven spot coverage for fainter (less massive) stars. There are around 60 periodic stars outliers in each band median magnitude vs. ptp amplitude distribution, showing higher amplitude than most of the stars with the same brightness. While around 46% of the disc-bearing stars follow the main distribution, 74% of all the outliers are disc-bearing stars. This is consistent with the idea that most of periodicity observed in the light curves for disc-bearing stars arises mainly from two physical mechanisms: the rotational modulation by hot spots, which are expected to show higher variability amplitudes than cold spots (e.g. Carpenter et al. 2001; Scholz et al. 2009), and by

circumstellar obscuration, which may be the responsible for the higher amplitudes observed (e.g., AA Tauri stars; Bouvier et al. 2003).

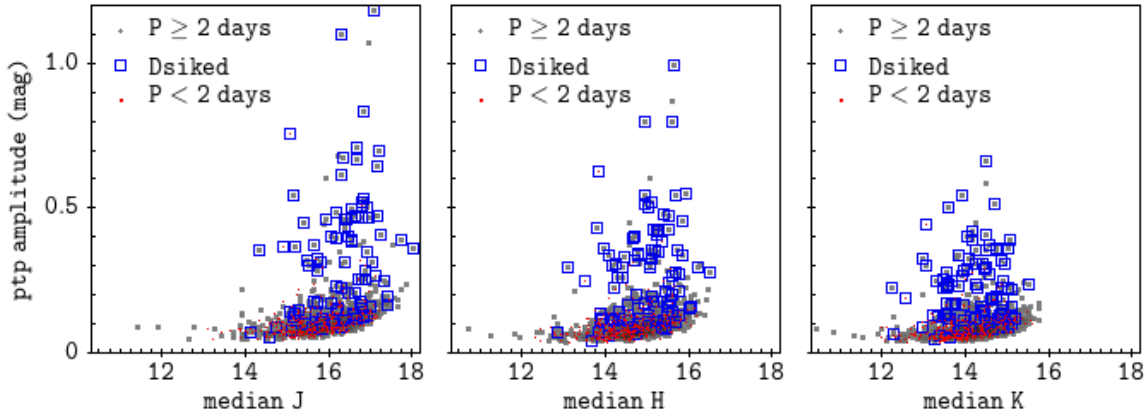

Figure 6.3: Median JHK magnitude vs. ptp amplitude for periodic stars. Stars with $P < 2$ days are shown as red dots; Stars with $P \geq 2$ days are shown as gray dots; Disc-bearing periodic stars are shown as blue squares.

The 894 periodic stars with $P \geq 2$ days are listed in Table C.1 which shows their ID inside our variability survey catalogue, their ID in the catalogues presented by GDW13, and GDW15, their coordinates in the present study; Stetson variability Index (Section 4.2), Period (Section 4.3); Mass, and Av (Section 3.5), median J, H, and K magnitudes, their propagated errors, and their ptp amplitude for each band (Section 4.4.3); their IR-class according to GDW13 (Section 3.6), and a flag indicating the presence of disc, assuming the value 1 for disc-bearing stars, and 0 for non disc-bearing stars. A complete version of Table C.1 is shown in the Appendix C.

6.2 Period distribution and disc presence

To further investigate the nature of the period distribution presented in Figure 6.1, the period distributions of disc-bearing and non disc-bearing stars are compared. As reliable mass accretion rate measurements are not available for Cygnus OB2 low mass stars - only one of the stars with Hα emission information (cf. Section 2.2.1.3) was selected as a periodic star - the X-ray emission and disc diagnosis were used in order to distinguish between CTTs and WTTs samples, and investigate the star/disc connection effect in the period distributions (cf. Section 3.6). The disc-bearing stars in the sample are the disc-bearing stars listed by GDW13. The Non disc-bearing stars in the sample are the X-ray emission sources from Wright et al. (2014) classified as members by Kashyap (2017) without IR-excess.

There were 91 disc-bearing periodic stars, 82 of them with $P \geq 2$ days, and 1120 non disc-bearing periodic stars, 812 of them with $P \geq 2$ days[1]. The period distributions for disc-bearing and non disc-bearing stars are shown in Figure 6.4. A visual inspection of the distributions suggests that the two samples exhibit

[1]Note that these numbers are slightly different from the numbers presented in Figure 6.4. This is because the plot in the refereed Figure presents only stars with $P \leq 20$ days, and there are 3 disc-bearing and 13 non disc-bearing stars with periods larger than that.

Table 6.1: Rotational periods for CygOB2 periodic candidate members. Each column is explained in the text. A complete version of the Table containing the 894 periodic stars is available in the Appendix D.

Id	GDW13	GDW15	RA (h:m:s)	Dec (d:m:s)	Stet	Per (day)	Mass ($M_\odot$)	Av (mag)	mJ (mag)	eJ (mag)	ptpJ (mag)	mH (mag)	eH (mag)	ptpH (mag)	mK (mag)	eK (mag)	ptpK (mag)	Class[1]	Disc[2]
CygOB2-0000004	1047		20:32:04	+41:14:19	0.46	8.35	0.49	4.29	16.61	0.08	0.03	15.35	0.02	0.06	14.78	0.02	0.06		
CygOB2-0000007	1065		20:32:05	+41:17:27	0.52	2.82	0.86	5.13	15.31	0.06	0.02	14.23	0.02	0.05	13.74	0.02	0.06		
CygOB2-0000008	1064		20:32:05	+41:12:48	0.79	3.05	0.79	2.74	15.66	0.08	0.02	14.8	0.02	0.08	14.46	0.02	0.07		
CygOB2-0000010	1070		20:32:05	+41:15:49	0.45	2.62	0.63	5.09	15.55	0.06	0.02	14.34	0.02	0.05	13.79	0.02	0.05		
CygOB2-0000015	1086		20:32:06	+41:06:49	0.92	10.55	0.66	5.91	17.06	0.15	0.04	15.72	0.03	0.13	15.04	0.03	0.12		
CygOB2-0000022	1113		20:32:07	+41:16:01	1.11	2.18	0.6	5.17	15.02	0.1	0.02	13.83	0.02	0.08	13.29	0.02	0.08		
CygOB2-0000035	1159		20:32:10	+41:07:45	0.61	7.55	0.31	4.26	16.59	0.09	0.03	15.28	0.02	0.08	14.62	0.02	0.08		
CygOB2-0000037	5482		20:32:11	+41:18:24	1.24	7.94	0.4	4.26	17.02	0.17	0.04	15.77	0.03	0.14	15.18	0.03	0.13		
CygOB2-0000040	5483		20:32:11	+41:07:52	0.83	7.81	0.36	4.05	17.47	0.15	0.05	16.18	0.03	0.13	15.56	0.03	0.12		
CygOB2-0000041	1175	70438	20:32:11	+41:11:33	2.05	7.1	0.31	4.88	17.03	0.31	0.04	15.71	0.03	0.28	14.88	0.02	0.22	CL2	1
CygOB2-0000044	1187		20:32:12	+41:18:24	0.90	4.9	0.69	4.39	15.99	0.1	0.03	14.84	0.02	0.08	14.32	0.02	0.08		
CygOB2-0000049	1208		20:32:12	+41:16:47	0.75	7.44	0.53	4.24	17.15	0.13	0.04	15.93	0.03	0.12	15.37	0.03	0.12		
CygOB2-0000052	1217		20:32:13	+41:11:45	0.53	19.52	0.52	4.84	15.75	0.06	0.02	14.46	0.02	0.06	13.87	0.02	0.05		
CygOB2-0000060	1229		20:32:14	+41:16:47	0.32	5.17	0.66	3.88	15.59	0.06	0.02	14.5	0.02	0.04	14.02	0.02	0.04		
CygOB2-0000066	1283		20:32:16	+41:15:37	1.27	5.13	0.7	4.13	15.99	0.12	0.03	14.85	0.02	0.11	14.35	0.02	0.09		
CygOB2-0000067	1287		20:32:16	+41:18:28	1.31	9.55	0.63	3.67	16.38	0.13	0.03	15.22	0.02	0.12	14.71	0.02	0.1		
CygOB2-0000070	5267		20:32:16	+41:07:29	2.11	5.81	0.31	4.52	17.1	0.25	0.04	15.78	0.03	0.24	15.06	0.03	0.24		
CygOB2-0000072	1299		20:32:16	+41:14:39	1.78	7.62	0.55	5.0	16.07	0.18	0.03	14.75	0.02	0.17	14.06	0.02	0.16		
CygOB2-0000074	1310		20:32:17	+41:18:49	0.81	6.57	0.41	3.12	17.17	0.13	0.04	16.01	0.03	0.12	15.49	0.03	0.11		
CygOB2-0000078	5485		20:32:17	+41:15:03	0.55	7.16	0.26	3.99	16.92	0.12	0.04	15.7	0.03	0.09	15.07	0.03	0.08		
CygOB2-0000079	1328		20:32:17	+41:17:58	2.09	2.31	0.58	4.1	15.32	0.17	0.02	14.16	0.02	0.16	13.63	0.02	0.15		
CygOB2-0000083	1341		20:32:18	+41:14:04	0.89	5.85	0.42	4.35	16.51	0.11	0.03	15.24	0.02	0.09	14.64	0.02	0.08		
CygOB2-0000086	5269		20:32:19	+41:05:55	1.09	6.13	0.29	4.2	17.23	0.16	0.04	15.89	0.03	0.14	15.23	0.03	0.13		
CygOB2-0000089	1368		20:32:20	+41:12:00	0.38	4.2	0.64	3.74	15.43	0.06	0.02	14.4	0.02	0.04	13.91	0.02	0.04		
CygOB2-0000090	5487		20:32:20	+41:13:33	1.00	3.79			17.43	0.17	0.05	16.1	0.03	0.17	15.44	0.03	0.14		
CygOB2-0000092	5488		20:32:20	+41:13:31	0.79	4.45	0.17	3.66	17.35	0.17	0.05	16.0	0.03	0.13	15.34	0.03	0.11		
CygOB2-0000093	1384		20:32:20	+41:16:54	0.51	8.88	0.31	3.52	16.53	0.07	0.03	15.27	0.02	0.07	14.69	0.02	0.06		
CygOB2-0000102	1427		20:32:22	+41:14:47	0.70	9.02	0.52	4.09	15.76	0.08	0.02	14.48	0.02	0.06	13.92	0.02	0.06		
CygOB2-0000121	1498		20:32:25	+41:17:45	1.01	4.23	0.58	2.99	15.46	0.1	0.02	14.37	0.02	0.08	13.88	0.02	0.07		
CygOB2-0000126	1516		20:32:26	+41:16:44	0.45	6.16	0.61	3.31	15.61	0.05	0.02	14.5	0.02	0.04	14.0	0.02	0.05		
CygOB2-0000131	1520		20:32:27	+41:07:17	1.18	4.63	0.47	5.5	15.74	0.11	0.02	14.28	0.02	0.09	13.53	0.02	0.07		
CygOB2-0000134	1532		20:32:27	+41:12:01	1.05	5.32	0.75	6.21	16.0	0.12	0.03	14.73	0.02	0.1	14.1	0.02	0.08		
CygOB2-0000142	1555		20:32:28	+41:14:39	0.56	4.09	0.68	7.16	16.45	0.09	0.03	14.85	0.02	0.07	13.98	0.02	0.06		
CygOB2-0000143	5280		20:32:28	+41:09:00	0.80	4.96	0.46	6.12	16.85	0.14	0.04	15.39	0.02	0.11	14.65	0.02	0.09		
CygOB2-0000156	1589		20:32:30	+41:16:51	0.48	2.17	0.57	4.91	15.4	0.05	0.02	14.23	0.02	0.05	13.67	0.02	0.05		
CygOB2-0000163	1613		20:32:30	+41:17:45	1.13	8.05	0.8	4.12	15.82	0.12	0.02	14.74	0.02	0.1	14.26	0.02	0.08		
CygOB2-0000165	1615		20:32:31	+41:12:19	0.94	8.27	0.63	5.93	16.76	0.13	0.03	15.4	0.02	0.11	14.76	0.02	0.09		
CygOB2-0000176	1663		20:32:33	+41:09:59	1.00	8.34	0.44	5.1	16.69	0.14	0.03	15.33	0.02	0.11	14.66	0.02	0.09		
CygOB2-0000178	1679		20:32:33	+41:11:33	0.92	6.69	0.69	6.84	16.85	0.14	0.04	15.4	0.02	0.11	14.7	0.02	0.09		

[1]Disc IR evolutionary status from GDW13 attributed by using Wilking et al. (2001) scheme. CL1: Class 1 YSO. CL2: Class 2 YSO. FS: Flat Spectrum. PTD: pre transitional discs. Ha: Hα emitter according to GDW13 or to Vink et al. (2008). BWE: blue stars with excesses candidate stars with discs, but with optical color bluer than the cluster locus). lowmass : low-mass disc with excesses only in [8.0] and [24]. High-incl: highly inclined disc with excesses only in [8.0] and [24] [2]Disc presence: 1 if true.

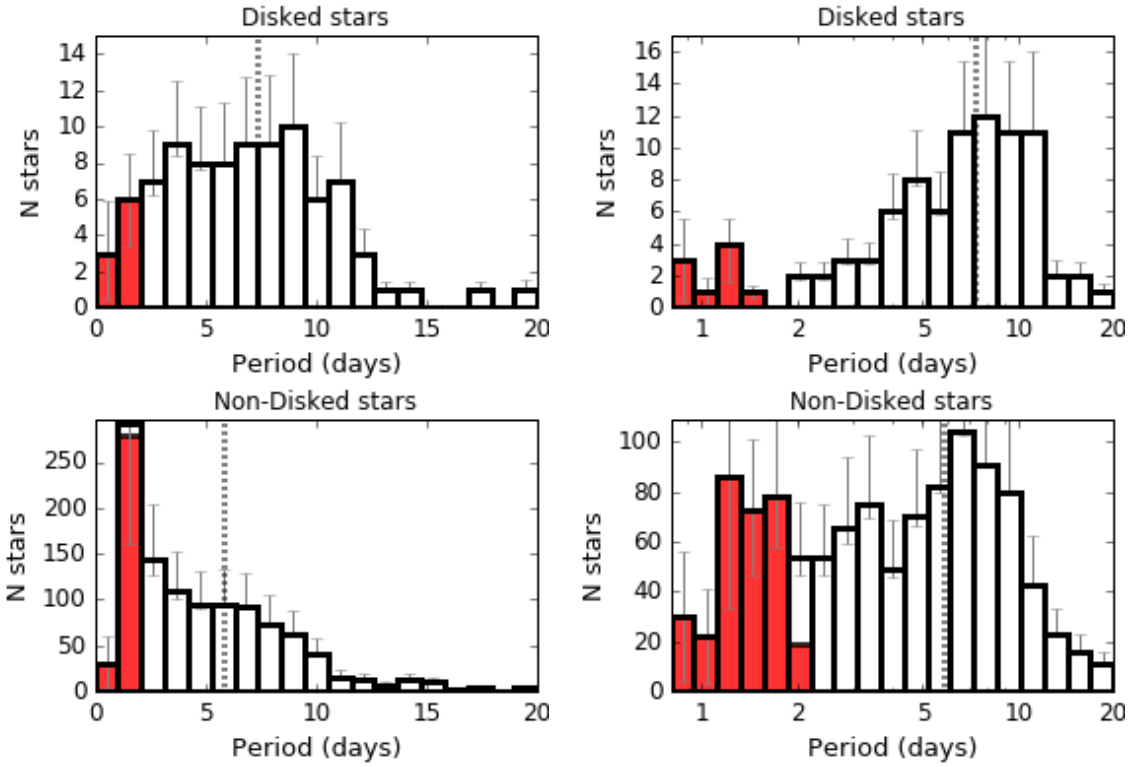

Figure 6.4: Period distributions for periodic disc-bearing stars with $P \leq 20$ days (top) and periodic non disc-bearing stars with $P \leq 20$ days (bottom) for both linear and logarithm distributions. The median value for $P \geq 2$ days stars is shown as dotted line. There were 80 disc-bearing stars, and 799 non disc-bearing stars with with $P \geq 2$ days and $P < 20$ days. The red bins show the fast rotators with $P < 2$ days excluded from the analysis.

different rotational properties, even without taking into account the bins with $P < 2$ days. The disc-bearing stars distribution is quite flat for periods in the range 4 - 11 days, decreasing for periods smaller than 4 days. The non disc-bearing stars distribution is flat for periods between 4 and 7 days, but it decreases for periods larger than that, with a larger fraction of stars with periods smaller than 4 days.

The mean, standard deviation and median values are $P(\mu, \sigma, \nu)$= 7.87, 4.36, and 7.34 days for disc-bearing stars, and $P(\mu, \sigma, \nu)$= 6.55, 4.14, and 5.80 days for non disc-bearing stars. A visual inspection in the distributions of Figure 6.4, and the statistical values for P suggest that although both distributions show a large dispersion, disc-bearing stars are on average rotating slower than non disc-bearing stars. A Kolmogorov-Smirnov (KS) test[2] considering only periods higher than 2 days statistically supports this idea, with a probability of only 0.4% that the two distributions came from the same parent distribution.

6.2.1 Does CygOB2 corroborate the disc-locking scenario?

In Section 6.2 it was considered as CTTS the stars listed by GDW13 as disc-bearing stars, and as WTTS, stars selected as candidate members by having X-ray emission from Kashyap (2017), and not listed as disc-bearing stars. A caveat arises from this selection procedure, since it does not guarantee that the disc-bearing

[2]ks_2samp from Python package scipy.stats

stars are still interacting with their discs, nor account for disc-bearing stars with inclinations that do not produce IR-excess. Nonetheless, using this criterion the disc-fraction in the full candidate member sample is 24%[3], and about 10% among candidate periodic stars. Given that the sample of stars with reliable period measured (with P≥2 days) contains only 82 stars with discs, the disc fraction in this sample is only 7.5%. When looking at the light-curve morphological classification for the non disc-bearing sample: 39.1% of the stars were classified as periodic candidates, 1.1% as eclipse-like, 14.5% as non-periodic variable stars, and 45.3% as non-variable stars. For the disc-bearing stars: 13.8% were periodic candidates, 5.7% were eclipse-like, 59.7% were non-periodic variables, and 10.8% where non-variables. This indicates that data-sampling used here is more efficient for detecting periodicity among non disc-bearing stars, or equivalently, that the sample is biased towards WTTS.

The origin of the bias towards WTTS can be explained by taking into account the different physical mechanisms responsible for variability in CTTS and WTTS (Section 2.3.4). Among WTTS one may expect to detect mainly stars with variability caused by cold spots, which are expected to produce a low amplitude JHK variability (typically smaller than one tenth of magnitude), even for large spot coverages (e.g. Carpenter et al. 2001). For the CTTS the variability scenario may be more complicated. Besides the variability caused by the presence of cold spots, the most common sources of variability in CTTS are: obscuration by circumstellar material, accretion driven variability (like the presence of hot spots and variable mass accretion rates), and instabilities in the accretion disc (e.g. Carpenter et al. 2001; Cody et al. 2014; Stauffer et al. 2014; Rice et al. 2015; McGinnis et al. 2015; Sousa et al. 2016; Roquette 2017, in preparation). While sometimes a single physical process may dominate the stellar light curve, the existence of several concurrent variability sources is often the case. Adding up common limitation in the datasets, as limited time and wavelength coverage, multiple physical process composing a complex light curve may not be distinguishable. Thus, rotational periods in CTTS are often masked by other variability sources in the light curve.

This bias towards WTTS has been reported by other studies in the literature (e.g., Cohen et al. 2004; Herbst & Mundt 2005), and it is assumed to be present in all the studies comparing the rotation of CTTS and WTTS. In the present study, a direct consequence of it is that the size of the CTTS periodic sample is much smaller than the size of the WTTS periodic sample. Consequently the results regarding the rotation of disc-bearing stars are less statistically significant. For this reason, we did not compare CTTS and WTTS separating them by mass ranges. Therefore, we could not verify the statistics correlation of rotational periods with disc-diagnosis for restricted mass ranges, in order to test the evidences that disc-locking acts differently in different mass ranges.

Another bias arising from the use of disc diagnosis based on IR-excess is that a correlation of rotation with disc presence diagnosed via IR-excess can be a secondary effect due to dependence of IR-excess on mass suggested by some authors (e.g., Littlefair et al. 2005). Hillenbrand et al. (1998) showed that the IR-excess produced by the disc is a function of the disc properties, but also of the stellar mass and radius. The contrast between the disc and the stellar photosphere is larger for higher mass stars, so with lower contrast it is more difficult to detect discs of lower mass stars. In regions where lower mass stars rotate

[3]As reference, the disc-fraction of similarly aged Cep OB3b is 33% (Allen et al. 2012)

faster than higher mass stars (e.g. NGC 2362 Irwin et al. 2008), lower mass stars with undetected discs can mimic a correlation between fast rotators and non disc-bearing stars. This effect can be minimized by using longer IR wavelengths to identify stars with IR-excess, and Cieza & Baliber (2007) showed that since the photosphere/disc contrast is higher in the mid-IR, discs can be detected even for lower mass stars by using Spitzer/IRAC colours. The possibility that this thesis sample is being affected by such bias was discarded. The analysis of rotation as a function of mass bin presented in Section 6.3 showed that, contrary to several other young regions studied, lower mass stars in CygOB2 rotate on average slower than higher mass stars. Even if discs around some lower mass stars were undetectable within the limits of the Spitzer data used by GDW13 for evaluating disc-bearing stars, the contamination by those stars would introduce slow rotators to the non disc-bearing sample. This would produce a contamination in the sense of occluding the correlation between IR-excess and slow rotators. Hence the possibility that a correlation between IR-excess and slow rotators in the sample could be mimicked by a secondary effect is ruled out.

Focusing on the whole list of members with periodic variability in CygOB2 (see Section 6.1), and even though the dataset is only complete for rotators with $P \geq 2$ days, the results presented here corroborate the general idea that the star-disc interaction has some influence in the rotational regulation of young stars. Disc-bearing stars in the sample are rotating on average slower than non disc-bearing stars.

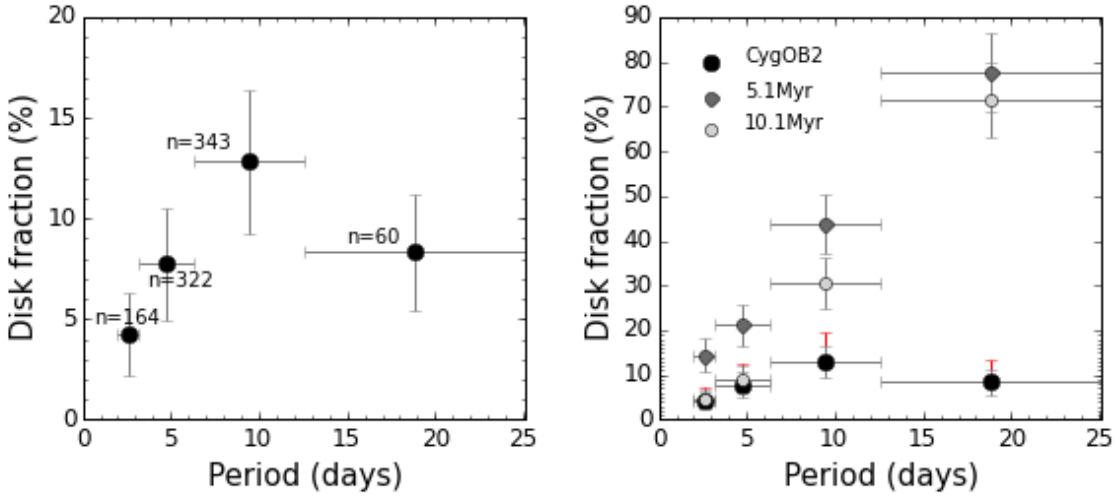

Figure 6.5: Disc fraction as a function of period. In both plots, circles show the centre of each period bin, while horizontal bars indicate the length of each bin. The bins show: fast, intermediate, slow, and very slow rotators. Observational data from the present study are shown as black circles. Left: The number of stars in each bin is shown for each point. Right: disc fractions resulting from M2 simulations from Vasconcelos & Bouvier (2015) for 5.1 Myr, and 10.1 Myr are shown together with the fraction observed in CygOB2. Vertical black bars show the standard Poison errors. The red vertical bars show a tentative correction for the 20% decrease on the disc fractions expected due to environmental conditions (Guarcello et al. 2016).

Next, we applied the Cieza & Baliber (2007) method to look for observational evidences for the disc-locking phenomenon by studying the disc-fraction as a function of period (Section 2.5). A plot of disc-fraction

per period bin is shown in Figure 6.5 (left). The bins were built considering fast rotators, intermediate rotators, slow rotators, and very slow rotators defined as in the beginning of the present Chapter. Even though the disc fraction for periodic stars is low ($\sim$ 9%), the left plot of Figure 6.5 shows that the disc fraction is actually quite dependent on the rotational period, having a maximum value of $\sim$ 13% for stars with rotational periods between 8.4 days, and 12.6 days.

Vasconcelos & Bouvier (2015) also investigated the disc fraction variations as a function of period for simulated coeval populations (Section 1.5.2.3). Figure 7 of their paper is presented in Figure 6.6 and it shows, for their model starting with different period distributions for disc-bearing and non disc-bearing stars, that the disc fraction increases with increasing rotational periods at all ages. Their M2 model has, at age 5.1 Myr, a disc fraction varying from 15% to 77% for periods from 2 days to 18 days, and from 5% to 72% at 10.1 Myr. Their results for 5.1 Myr, and 10.1 Myr are shown in the right plot in Figure 6.5, together with the results for this thesis sample. In both plots in Figure 6.5 vertical bars follow standard errors of a Poisson counting, as the error bars used by Vasconcelos & Bouvier (2015). Results from Guarcello et al. (2016, hereafter GDW16) investigation on the disc-survival in CygOB2 suggest that the environmental feedback on disc evolution for CygOB2 members may be responsible for a decrease of about 20% on the disc fraction. The red vertical error bars in the right plot in Figure 6.5 show a tentative correction for this effect and adds up 20% of each point's disc fraction. Remembering that the disc-bearing periodic sample is biased due the variability mechanisms acting on disc-bearing stars, as described early in the present section, the dataset seems to corroborate the disc-locking results for periods up to 12.6 days, even though the increase of the disc fraction with period occurs in a less accentuate way when compared with Vasconcelos & Bouvier (2015) results. For periods longer than that, *i.e.* for the slowest rotators bin in the plots of Figure 6.5, the disc-fraction decreases, what may indicate that the dataset suffers from contamination from field stars which would cause a underestimated disc-fraction by adding non disc-bearing stars to this bin.

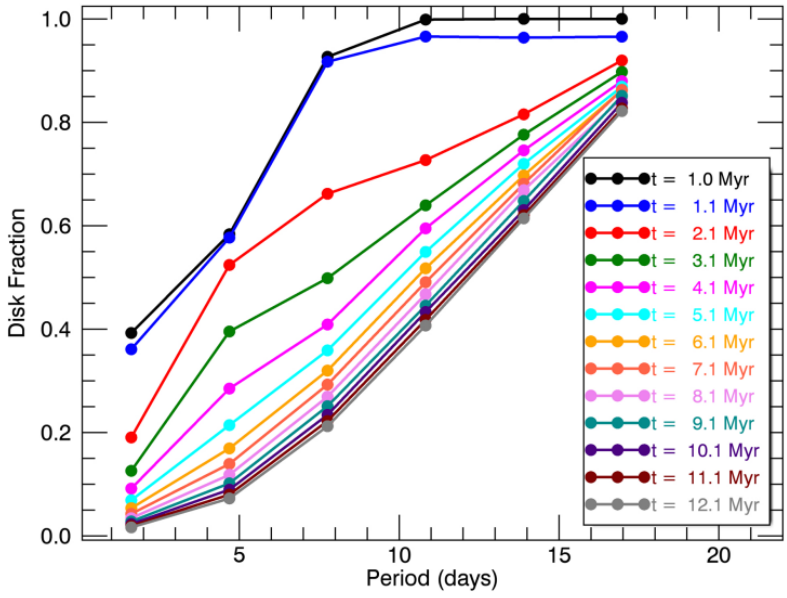

Figure 6.6: Disc fraction as a function of period for different ages for the M2 model from Vasconcelos & Bouvier (2015). This figure was extracted from their paper (Figure 7).

A possible explanation for the lower disc-fraction compared to the models could be a strong premature disc loss due to the high energy radiation coming from the OB stars in the CygOB2 association, and Figure 6.5 (left plot) would be showing signatures of a primordial disc-locking with a reduced disc-fraction due to faster disc dissipation in the association. In this case, the disc lifetime distribution in CygOB2 would be very different from the ones used by Vasconcelos & Bouvier (2015), as they assume in their simulations that most stars are born with discs, and suffer from a smooth decrease on disc-fraction with time. Consequently, a comparison with their results would not be reliable.

Other possible explanations would be that CygOB2 low mass population is a few Myr older than previously thought (to be discussed in Section 6.3.1), or that the environmental conditions in CygOB2 make the disc fraction decrease with time more steeply than considered in Vasconcelos & Bouvier (2015). It seem reasonable that a combination of the two effects could explain the differences between CygOB2 data, and simulated data for the fast, slow, and intermediate rotators points in the right plot of Figure 6.5.

As Figure 6.5 suggests that the very slow rotator sample suffers from strong contamination, the results in Section 6.2 were re-examine by removing stars with $P > 12.56$ days from the analysis. By doing so, it was found that $P(\mu, \sigma, \nu)$= 7.0, 2.7, and 7.1 days for disc-bearing stars, and $P(\mu, \sigma, \nu)$= 5.7, 2.6, and 5.5 days for non disc-bearing stars. A KS-test gives an 0.0001% chance that the two distributions came from the same parent distribution, showing that the results from Section 6.2 hold even when excluding the very slow rotators from the analysis.

6.3 Period distributions in different mass ranges

Mass estimations for PMS stars can be extremely model dependent, but for all models, lower effective temperatures correspond to lower mass stars, and thus the sense of variation of rotation with mass is model independent (Herbst et al. 2001). To test a possible mass-rotation connection in our data, we split the periodic sample into two mass bins according to the convective boundary, *i.e.*, the mass under which all the stars will be fully convective even in the MS. This limit value is around ∼0.3 $M_\odot$ for the model used. On the other hand, all low mass PMS stars are initially fully convective. Gregory et al. (2012) estimated the age at which a PMS star first develops a radiative core for the Pisa models, and according to their estimates a 0.5 $M_\odot$ star develops its radiative core around ∼9.3 Myr, and a 0.4 $M_\odot$ star around ∼15 Myr. As it will be discussed further in the text, CygOB2 low mass stars age estimates are between 2.5 - 6.75 Myr (Wright et al. 2010), but these estimates were based on Siess et al. (2000) models, which, when applied to PMS stars, may result in underestimated ages down to a 1.5 - 2.0 factor. Accounting for this, we split the sample at 0.4 $M_\odot$ as a way to guarantee that the lower mass sample will not be contaminated by stars that are no longer fully convective. Using this limit, the two samples were defined for $M \leq 0.4$ $M_\odot$ (90 stars with $P \geq 2.0$ days), and $M > 0.4$ $M_\odot$ (687 stars with $P \geq 2.0$ days). Histograms showing the period distribution for each of the two mass bins are shown in Figure 6.7. From the distributions, it is evident that the period distribution for medium, and slower rotators present a mass dependence. The period mean, standard deviation and medium values are: $P(\mu, \sigma, \nu)$= 7.0, 2.9, and 6.9 days for the $M \leq 0.4$ $M_\odot$ sample, and $P(\mu, \sigma, \nu)$= 6.5, 4.2, 5.7 days

for the $M > 0.4$ M$_\odot$ sample.

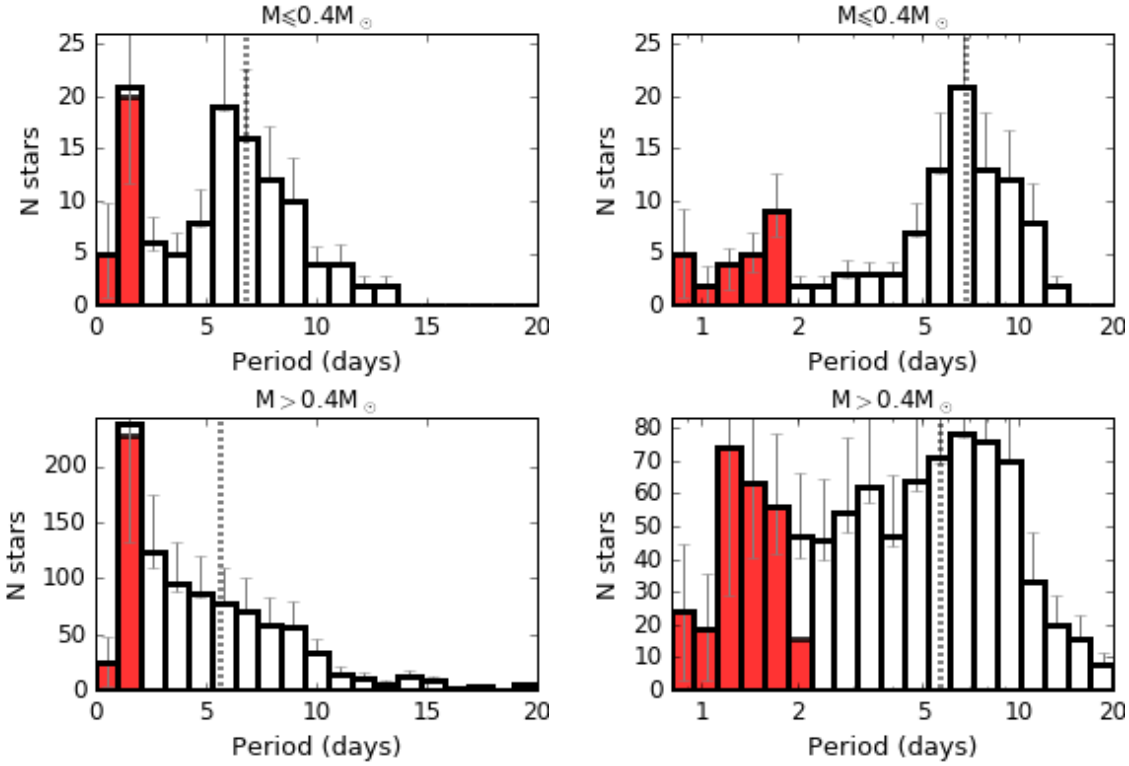

Figure 6.7: Histograms showing period distributions for given mass bins in linear (left) and logarithm scale (right). $M \leq 0.4$ M$_\odot$ (top), and $M > 0.4$ M$_\odot$ (bottom). The median value for $P \geq 2$ days stars is shown as dotted line. There were 90 stars with $P \geq 2.0$ and $M \leq 0.4$ M$_\odot$, and 687 stars with $P \geq 2.0$ days and $M > 0.4$ M$_\odot$.

Figure 6.8 shows the mass vs. rotational period distribution for Cygnus OB2. The blue dashed line marks the limits between the mass bins adopted, and are meant to allow a simple comparison between Figures 6.8 and 6.7. Keeping in mind that CygOB2 data sampling does not allow to completely access the fast rotators population (due to the strong aliasing towards short periods), a lack of periods between 2 and 5 days can be verified for the $M \leq 0.4$ M$_\odot$ mass bin. Both linear and log scaled rotational period distributions are strongly peaked for the lower mass interval, but the peak, around 6.1 days, is more evident in log-scaled distribution. The overall distribution gets broader for the $M > 0.4$ M$_\odot$ mass bin, which is reflected as an increase in the distribution's σ. The peaked distribution verified for lower masses is less evident for the higher mass bin, and an increase in the number of faster and intermediate rotators makes the period distribution flatter.

A KS-test gives a probability of $\sim 0.02\%$ that the distributions for $M \leq$ 0.4M$_\odot$ and $M > 0.4$ M$_\odot$ samples came from the same parent population. The results therefore indicate that for the periodic sample analysed here, the lower mass stars are rotating on average slower than higher mass stars.

Given the model dependence on masses estimated via CM-diagram (Section 3.5), it was checked if the results would hold for masses estimated from different models. Following Section 3.5, masses calculated using Baraffe et al. (1998) models with Bell et al. (2014) empirical corrections, Siess et al. (2000), and Baraffe et al. (2015) were considered. For all models the main result of VLM-stars rotating on average slower than solar-type stars upholds.

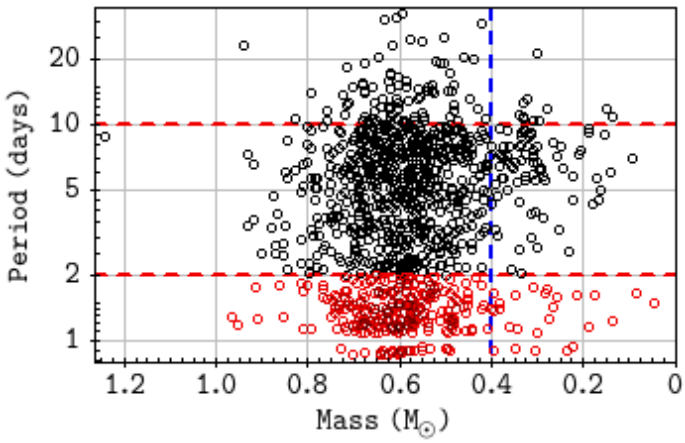

Figure 6.8: Mass vs. period distribution for periodic candidate members of CygOB2. Stars with reliable periods ($P \geq 2$ days) are shown as black circles, and stars with dubious periods ($P < 2$ days) are shown as red circles. Dashed red lines delimit periods equal to 2 and 10 days. The blue dashed line marks the limit between the mass bins analysed in the present section.

6.3.1 CygOB2 inside the picture of PMS rotational evolution

In Figure 2.11 we presented distributions of mass vs. rotational period for several coeval regions. For the purposes of the present Section, the list of clusters previously presented was shortened in order to show only clusters and associations with ages up to 15 Myr and rotational period samples that are numerous enough to be considered statistically significant. The selected regions are: NGC 6530 (Henderson & Stassun 2012), with 244 measured periods in the mass range 0.2 - 2.0 $M_{\odot}$; Orion Nebulae Cluster (ONC, Irwin & Bouvier 2009; Rodríguez-Ledesma et al. 2009), with 528 measured periods in the mass range 0.015 - 1.4 $M_{\odot}$; NGC 2264 (Lamm et al. 2005; Affer et al. 2013; Venuti et al. 2016), with about 581 measured periods in the mass range 0.2 - 3.0 $M_{\odot}$; Cep OB3b (Littlefair et al. 2010) in the mass range 0.1 - 1.3 $M_{\odot}$, with 460 measured periods; NGC 2362 (Irwin et al. 2008), with 271 measured periods in the mass range 0.1 - 1.2 $M_{\odot}$; and h Per (Moraux et al. 2013), with 586 measured periods in the mass range 0.4 - 1.4 $M_{\odot}$.

The panels in Figure 6.9 are presented in order of age. For each cluster, we adopted the most recent age estimation available in the literature: NGC 6530 has ∼2 Myr (Bell et al. 2013), ONC has 2.8 - 5.2 Myr (Naylor 2009), NGC 2264 has 2.4 - 6 Myr (Naylor 2009), Cep OB3b has ∼6 Myr (Bell et al. 2013), NGC 2362 has 9.5-12.6 Myr (Bell et al. 2013), and h Per has 13 Myr (Mayne & Naylor 2008b). Those age estimates partially explain the different rotational scenarios observed in Cep OB3b, and NGC 2362 by Littlefair et al. (2010), since the reviewed ages put the two regions in different evolutionary stages.

In order to make the comparison between the samples presented in Figure 6.9, and CygOB2 sample (Figure 6.10), each sample was filtered for stars with masses larger than 1.4 $M_{\odot}$, and smaller than 0.1 $M_{\odot}$, and periods smaller than 2 days. Stars filtered by this selection rule are shown as light grey circles in the mass vs. period plots in Figure 6.9. Figure 6.10 shows the same plot as in Figure 6.8, but in the same scale as the plots in Figure 6.9. After filtering each sample, their sizes are: 187 stars in NGC 6530 sample; 351 in ONC; 288 in NGC 2264; 342 in Cep OB3b; 198 in NGC 2362; 309 in h Per, and 894 stars in CygOB2.

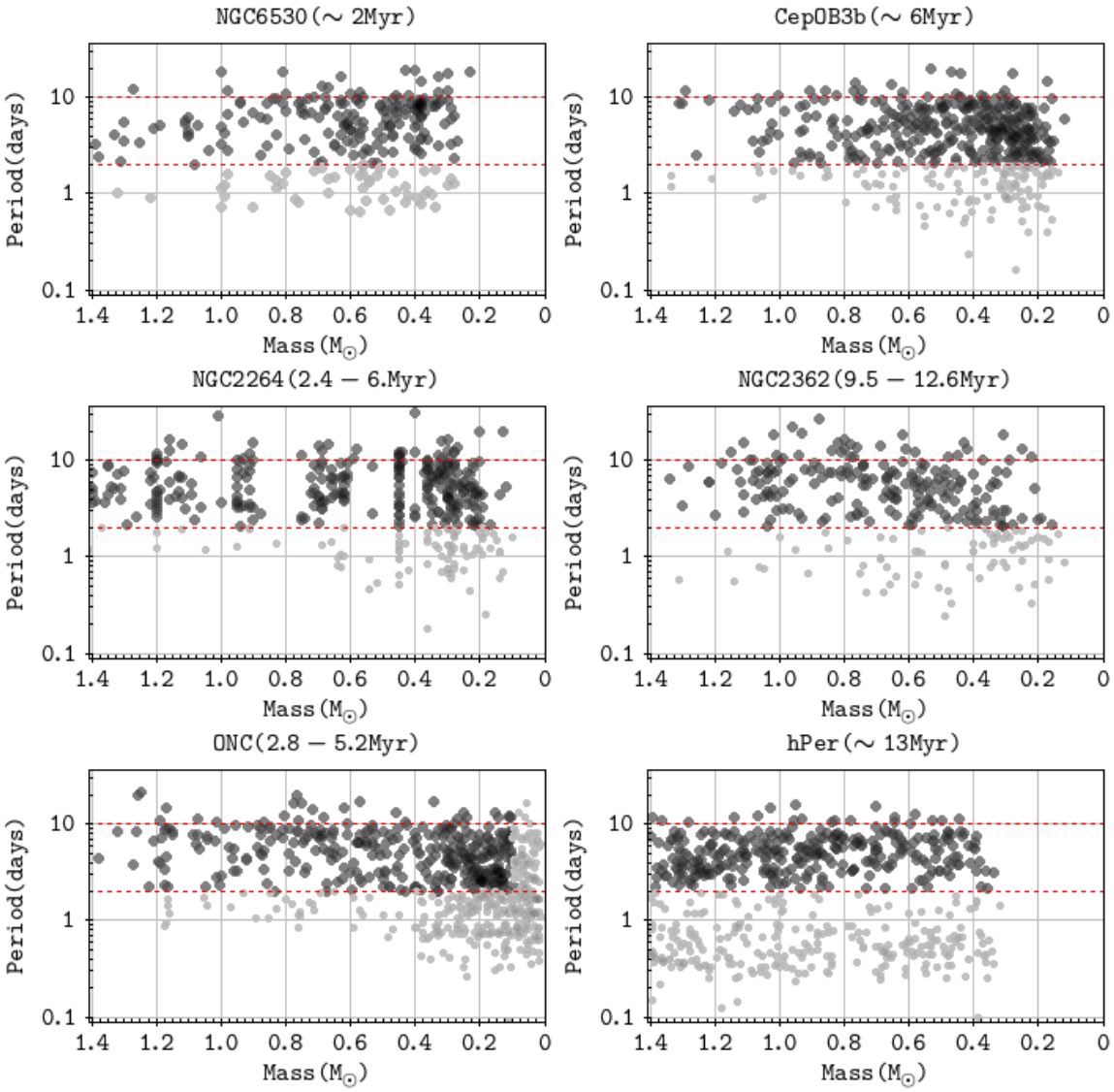

Figure 6.9: Rotational periods as a function of mass for several young regions with ages between 1 - 15 Myr. Dashed red lines delimit the periods between 2 and 10 days. Stars used for comparison with the present study are shown as dark grey.

Wright et al. (2010) derived ages between 2.75 and 6.75 Myr for CygOB2 low mass population, with a median value of 3.5 Myr for the centre field, and 5 Myr for a north-western field. For deriving stellar properties, they used Siess et al. (2000) models converted to 2MASS photometric system using Kenyon & Hartmann (1995). Given that the methods used by Mayne & Naylor (2008b), Naylor (2009), and Bell et al. (2013) for evaluating stellar parameters result in ages 1.5 - 2.0 larger than ages estimated by previous methods, we stress that comparisons with other clusters in the literature using CygOB2 age as a parameter must be done with caution. That being said, using the age range as the unique criterion would place CygOB2 somewhere between ONC, and NGC 2362.

When focusing into the lower masses distribution, CygOB2 may be considered somehow similar to NGC 6530, and to Cep OB3b. In the three regions, there is an accumulation of slow rotators towards lower masses. It was found in Section 6.3 that, similarly to NGC 6530, lower mass stars in CygOB2 also rotate slower than

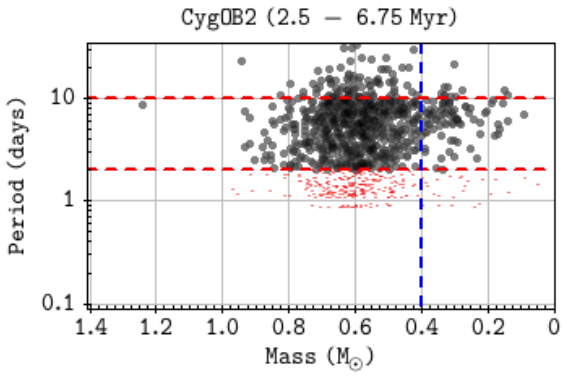

Figure 6.10: Mass vs. period distribution for periodic candidate members of CygOB2. Stars with reliable periods ($P \geq 2$ days) are shown as black circles, and stars with dubious periods ($P < 2$ days) are shown as red circles. Dashed red lines delimit the periods between 2 and 10 days, while blue dashed lines delimits the mass bin analysed in the present section.

higher mass stars. Given the much older age of CygOB2, compared to NGC 6530, and as there are clusters of intermediate age between the two that present a contrary mass rotational connection, it becomes clear that youth (as proposed by Henderson & Stassun 2012) could not explain the observational results of lower mass stars rotating on average slower than higher mass stars in both clusters. An alternative explanation to this inverse period-mass relation for lower mass stars would be the role of environment conditions on regulating the stellar AM.

Inside the context of the mass dependent character of PMS stellar rotational properties, because several studies failed in finding correlations between the disc presence and rotation in the VLM regime, evidences for disc-locking in this regime are still controversial. It is generally suggested that the differences in the internal structure of solar-type stars and VLM-stars would result on different topologies and magnetic fields strengths in each mass regime, and that this would change the star disc interaction (e.g. Cieza & Baliber 2007). However, there is no definitive argument justifying why disc-locking would not occur on VLM-stars. Until the present date, only one PMS VLM-star had its magnetic field topology studied (V2247 Oph, Donati et al. 2010), hence there is a lack of constraints on the subject of magnetic star-disc interaction for VLM regime.

Irwin et al. (2011) argued that disc-locking would be required in a larger time-scale than in the case of solar-type stars, in order to explain the observational results for the evolution of the rotational properties in the VLM regime (Section 1.5.2.2) For their AM evolutionary models to fit the observations (see Figure 1.5), Irwin et al. (2011) found that VLM-stars should remain locked to their discs over $\sim 8 - 16$ Myr. Given that CygOB2 is younger than that, there is the possibility that most of its low mass stars are still locked to their discs. Because the contrast between the disc and the stellar photosphere is lower for lower mass stars, there is the possibility that VLM-stars in CygOB2 do have discs, but the limits in GDW13 observations did not allow the authors to unveil them. Therefore, it remains the possibility that VLM-stars in CygOB2 are slower rotators because they have non detected discs, and they are locked to such discs. This would be, however, a queer explanation if one takes into account the rotational scenario for VLM-stars in other young regions presented in Figure 6.9. Why would disc-locking be more efficient for VLM-stars in a region as hostile to

discs as CygOB2, while no evidence for disc-locking was found for VLM-stars in other similarly aged regions such as NGC 2264, ONC and NGC 2362?

6.3.2 Are the mass vs. periods relations sensitive to the environment?

As mentioned in Section 2.5, a mass-rotation connection was first claimed to explain observations showing that while solar-type stars present a bi-modal distribution of rotational periods, VLM-stars present an uni-modal one. The character of VLM-stars faster or slower rotators than solar-type stars seems to vary from region to region. A role of the environment in determining the mass-rotation relation has been first suggested by Littlefair et al. (2010). They found that even though lower mass stars rotate faster than higher mass stars in Cep OB3b, this difference is less strong than in other clusters, as Cep OB3b has an excess of slowly rotating low mass stars compared to other regions.

As is the case in NGC 6530 (Henderson & Stassun 2012), lower mass stars in CygOB2 rotate on average slower than higher mass stars (Section 6.3) with a median rotational period of 6.9 days for lower mass stars, and 5.7 days for higher mass stars. As the data is incomplete for fast rotators, there is not enough information to discuss the existence of bi-modality in the period distributions, but apart from that, the shape of period distributions for different mass ranges presented on Figure 6.7 shows clear sign of a mass dependence: while the period distribution for higher mass stars ($M \geq 0.4$ M$_\odot$) is quite flat for periods between 2 and 9 days, with a long tail towards slower rotators, it is peaked around slow rotators for the lower mass stars ($M \leq 0.4$ M$_\odot$), and it shows a lack of faster rotators for lower mass stars.

Before putting this results in context, the possibility that a bias due to underestimated extinction could affect the results is examined. An underestimated extinction would cause highly extincted higher mass stars to be considered as low mass stars. As differences in the period distributions for lower and higher mass stars have been repeatedly reported in the literature, including studies for regions with relatively low and homogeneous extinction - as is the case of NGC 2264 ($A_V \sim 0.4$ Dahm 2008), where this contamination effect is probably minimum -, higher mass stars mistaken by lower mass stars would bring contamination to the lower mass period sample. In regions where higher mass stars are slower rotators than lower mass stars, this bias would introduce slow rotators to the lower mass period distributions which was initially composed of faster rotators, biasing the distribution towards slower rotators, and masking the differences between the two mass-regime distributions. In the case of higher mass stars rotating on average faster than lower mass stars, this bias would introduce fast rotators to the lower mass stars distribution and the distribution would be biased towards faster rotators. In both cases, one would expect the period distribution for lower mass stars to be somehow flattened due to the contamination. When comparing CygOB2 Mass vs. Period distributions (Figure 6.10) with the other regions (Figure 6.9), one can see that CygOB2 presents a clear lack of fast and intermediate rotators among its lower mass stars, and therefore the possibility that the result may be mimicked by a contamination due to higher mass stars with underestimated extinction can be ruled out. A third possibility that remains is that the extinction for the stars in our sample is underestimated as whole, and in this case our observations would not reach lower mass at all, and the whole lower mass bin would actually be composed by higher mass stars with underestimated masses. As it was shown in Section 6.3 a

	(μ, σ, ν)		(μ, σ, ν)		KS-test (%)[1]		
	M< 0.4 $M_\odot$ (days)		M≥0.4 $M_\odot$ (days)		between mass ranges		with CygOB2, for M< 0.4 $M_\odot$
Region	All	P≥2 days	All	P≥2 days	All	P≥2 days	P≥2 days
CygOB2	-	**(7.0,2.9,6.8)**	-	(6.5,4.2,5.7)	-	0.02	-
NGC 6530	**(6.5,4.2,6.8)**	**(6.4,3.3,5.6)**	(5.3,3.7,4.7)	(6.5, 3.4, 5.6)	1.4	2.1	0.16
ONC	(3.3,2.8,2.5)	(5.0, 2.7, 4.4)	**(5.7,3.9,5.4)**	**(6.6, 3.6, 6.4)**	10^{-9}	0.0001	10^{-9}
NGC 2264	(4.6,3.7,3.9)	(6.2, 3.4, 5.2)	**(5.4,4.1,4.3)**	**(6.3, 4.0 5.1)**	0.26	74.26	0.02
Cep OB3b	(4.0,2.7,3.5)	(5.1, 2.5, 4.6)	**(4.9,3.5,4.4)**	**(6.0, 3.2, 5.3)**	1.16	1.83	10^{-7}
NGC 2362	(3.0,3.2,1.9)	(5.0, 3.8, 3.0)	**(5.8,4.4,4.9)**	**(6.9, 4.1 ,6.1)**	10^{-8}	0.072	0.002
h Per	(2.0,2.0,1.4)[2]	(4.2, 1.8, 3.3)[3]	**(3.3,3.0,2.7)**	**(5.5, 2.5, 5.1)**	-	-	-

Table 6.2: Period mean, standard deviation, and median values (μ, σ, ν) for each cluster presented in Figure 6.9 for the full, and $P \geq 2$ days samples. For each cluster, the mass regime that rotates slower on average is stressed in bold.
[1]p-value from KS-test between the samples $M < 0.4 M_\odot$, and $M \geq 0.4 M_\odot$, given in percentage, meaning the probability that the two sample were derived from the same parent distribution.
[2]Sample composed with only 25 stars.
[3]Sample composed with only 9 stars.

KS-test between the samples with $M \leq 0.4$ $M_\odot$, and $M \geq 0.4$ $M_\odot$ returned a probability of only ∼0.02% that the two samples came from the same parent population, so the hypothesis that the smaller mass sample could be a sub-sample of higher mass stars with underestimated extinction is also excluded.

A final caveat on interpreting the results arises from the fact that the sample is incomplete for fast rotators with periods under 2 days. To check if the statistical difference between the rotational scenario of different mass regimes holds after removing the fastest rotators from the sample, Table 6.2 presents the mean, standard deviation, and median values (μ, σ, ν) for the period distributions of the young regions in Figure 6.9 for both full, and P≥2 days samples. Each cluster's sample was divided in two mass ranges using $M = 0.4$ $M_\odot$ as a cut. For each cluster, the mass regime that rotates slower on average is stressed in bold. Since h Per sample includes only a few stars with masses $M \leq 0.4$ $M_\odot$, the results for this cluster are presented in Table 6.2, but they were not used in the present investigation. From Table 6.2, one can see that filtering the samples for $P \geq 2$ days does not change qualitatively the rotation-mass connection. Nevertheless, for NGC 2264, KS-tests between the samples of higher and lower mass stars without faster rotators than $P = 2$ days, change significantly and it gives a 74% chance that both samples came from the same parent distribution. For NGC 6530 and Cep OB3b, there is a $\sim 2\%$ chance the two samples came from the same parent distributions, while for the other clusters this chance is negligible. The last column of Table 6.2 shows a KS-test between the lower mass stars from each clusters, with the lower mass stars in CygOB2, and shows that the lower mass end of CygOB2 Mass vs. Period distribution is dissimilar to all the other clusters considered.

The observational results for CygOB2 could be explained if the lower mass stars in the sample remained locked to their discs for a longer time than the higher mass stars in the sample (solar- type). One possible reason why the lower mass star could keep their discs for a longer time is if primordial mass segregation occurs, *i.e.*, very low mass stars are more widely distributed than solar-type stars. They would thus lie further away from the ionizing radiation of central OB stars than the more concentrated solar-type stars. They would as well be in lower stellar density regions, thus avoiding disc-disruptive encounters. However, Wright et al.

(2014), and Wright et al. (2016) found no signal of mass segregation in the association, and additionally GDW16 showed that close encounters in CygOB2 are not important in regulating disc dissipation, so this explanation might not apply.

The present study shows that, like NGC 6530, CygOB2 presents qualitatively a mass-rotation connection in the opposite sense from most other young clusters, with lower mass stars rotating on average slower than higher mass stars. The statistical differences between the distributions from the two regions can be consider as due to different rotational ages, as NGC 6530 is about 2 Myr old, and CygOB2 stars have ages ranging from 2.5 to 6.75 Myr. Also due to this age difference, the explanation given by Henderson & Stassun (2012) based on youth to explain lower mass stars being slower rotators than higher mass stars in that region does not hold for CygOB2. Instead, the hypothesis that environment helps regulating the rotation may be a better explanation.

As both Cep OB3b, and CygOB2 are OB associations with similar ages, it would be reasonable to expect that they would have similar rotational properties. Even though they both present an excess of slow rotators among their lower mass members, their period distributions are statistically different, and their rotational-mass connection is qualitatively inverse. Those differences could be explained by a different concentration of O stars: CygOB2 is a notoriously massive OB association, with more than 160 confirmed OB stars (Wright et al. 2015) among its members, 73 of which are O stars, while Cep OB3b is a small association with a massive population composed by only 3 O stars, and 33 B stars (Blaauw et al. 1959; Blaauw 1964) spread over $\sim$10 pc (Blaauw 1964). On the other hand, NGC 6530 is a core cluster of the Sgr OB1 association and it is located in the eastern part of the very bright Lagoon Nebula (Sung et al. 2000). The open cluster has a modest OB population when compared to CygOB2 as there are around 5 O stars and 60 B stars (Tothill et al. 2008), but these objects are spread over a small 14'$\times$14' region. Additionally, the cluster is in the vicinity of the massive star formation M 8 E. NGC 6530 is also 3 - 4 times richer in OB stars than ONC (Damiani et al. 2004), whose population has similar age.

6.4 Does CygOB2 massive population regulate its low mass star rotation?

GDW16 recently found evidences that discs are more rapidly dissipated in regions of CygOB2 with intense local UV. OB stars can influence their environment due to their strong UV field. Far ultraviolet (FUV) photons (6eV$< h\nu <$13.6 eV) can dissociate H_2 molecules, and extreme ultraviolet (EUV) photons ($h\nu >$13.6 eV) are capable of ionizing hydrogen atoms. Because of that, regions with intense local UV field can be hostile to the evolution of circumstellar discs, and to the processes of star formation (e.g. Johnstone et al. 1998; Adams et al. 2004; Guarcello et al. 2010, 2016).

To test the effect of CygOB2 massive stars on the rotational properties of nearby YSO, we investigated how the rotational period distributions vary as a function of local UV field. To estimate local UV fluxes, the same technique adopted in GDW16 and Guarcello et al. (2007) was used: the FUV and EUV fluxes emitted by each O star were propagated to the position of each periodic stars using 2D projected distances. The

effect of using 2D projected distances instead of real distances is discussed on section 3.1 of GDW16, and it was shown by the authors to have very small impact in the analysis.

The UV flux emitted by each of the 73 O stars, and the 3 Wolf-Rayet (WR) stars in CygOB2 was estimated by GDW16 (Table 1 in their study). Their estimates for FUV flux is presented in terms of Habing flux, G_0=1.6 $\times$ 10^{-3} erg/cm^2/s, and their EUV fluxes (number of ionizing photons with $\lambda < 912$ Å per second per cm^2) are in photons/s/cm^2. For reference: The average UV flux in the spectral range 912-2000 Å in the solar neighbourhood (within 1 kpc) is 1.7 G_0 (Habing 1968). Using their estimates for the UV fluxes of the massive stars, the incident UV flux at the position of each periodic star was estimated. A map for incident FUV and EUV fluxes for CygOB2 candidate member periodic stars is shown in Figure 6.11, together with the position of the O and WR stars used in the calculations. As in GDW16, B stars are omitted because their census is still incomplete and their contribution to the whole UV field in the association is negligible compared to the O and WR stars.

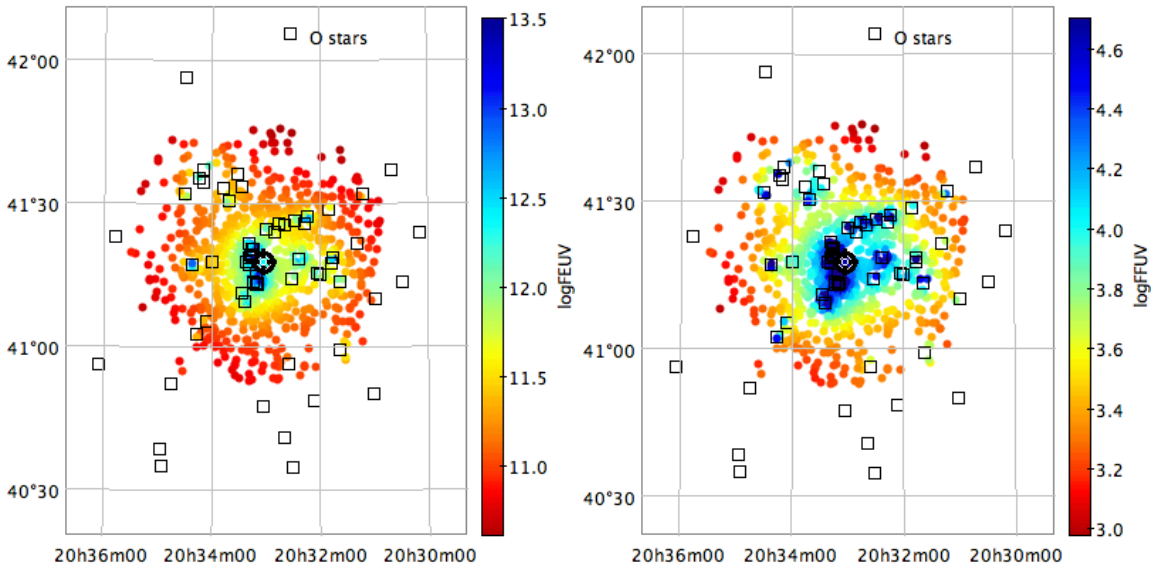

Figure 6.11: Maps of UV incident flux. O and WR stars are shown as black empty squares. The position of each periodic star is shown as a dot, and the colour of each dot indicates the UV incident flux on that position according to the colour bars to the right of each plot. Left plot: the colour bar indicates $\log(F_{FUV})$; right plot: the colour bar indicates $\log(F_{EUV})$.

Using the FUV and EUV local fluxes as criteria, two samples were defined: a sample with low UV incidence for which $\log(F_{FUV}) \leq 3.7\ G_0$ or $\log(F_{EUV}) \leq 11.42$ photons/s/cm^2, and a sample with high UV incidence in which $\log(F_{FUV}) > 3.7\ G_0$ or $\log(F_{EUV}) > 11.42$ photons/s/cm^2. More extreme values, such as $\log(F_{FUV}) = 4.3\ G_0$, and $\log(F_{EUV}) = 12.0$ photons/s/cm^2 were also tested, and it was verified that they yielded the same results qualitatively.

6.4.1 Disc-rotation connection's sensitivity to UV incidence

The disc-rotational connection was re-analysed by taking into account the limits of incident UV defined in the previous Section. Disc fraction as a function of rotational period plots for stars in regions with high and low UV incidence are shown in Figure 6.12, for FUV, and in Figure 6.13, for EUV. From the plots, one

can see that the maximum disc fraction goes from 21% for slow rotators in low FUV incidence regions, to 7.3% for slow rotators in high FUV incidence regions; and from 20.3% for slow rotators in low EUV incidence regions, to 7.1% for intermediate rotators in high EUV incidence regions. Figures 6.12, and 6.13 suggest that high incident UV does yield faster disc dissipation, even though it does not change qualitatively the trend of increasing disc fraction for longer periods.

$\log(F_{FUV}) \leq 3.7\ G_0$ $\log(F_{FUV}) > 3.7\ G_0$

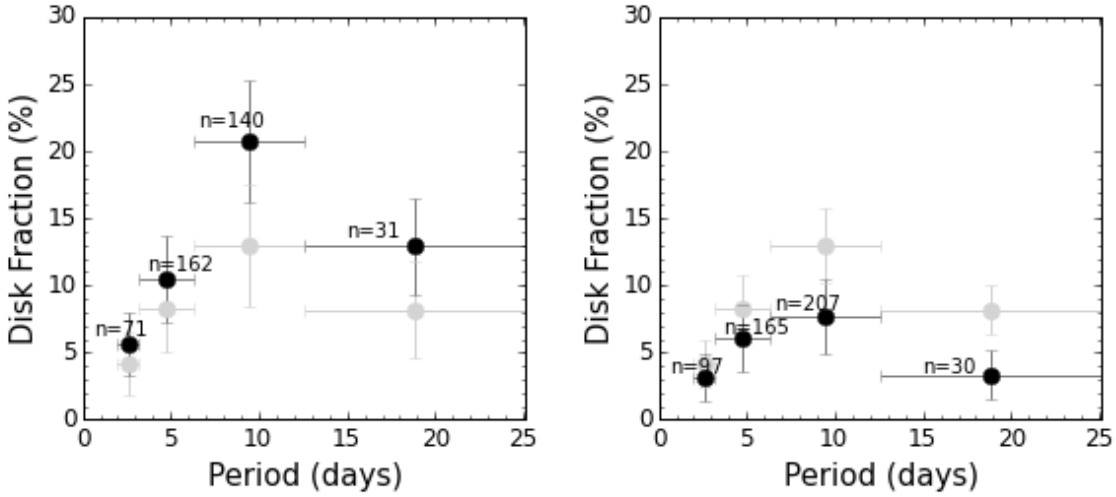

Figure 6.12: Same as Figure 6.5 but for periodic stars with low FUV incident radiation (left) and stars with high FUV incident radiation (right). For reference, the results disc-fractions for the full sample (see Figure 6.5) are also shown in light grey.

	Disc-bearing		Non disc bearing		
FUV	(μ, σ, ν)	N	(μ, σ, ν)	N	KS-test
low UV	(8.0, 4.6, 7.3)	56	(6.4, 4.0, 5.6)	350	0.4%
high UV	(7.3, 3.6, 7.1)	30	(6.6, 4.3, 6.0)	472	42%

Table 6.3: For each FUV flux sample and for samples of disc-bearing and non disc-bearing stars: Mean, standard deviation and median for each period distribution in days. Number of stars in the sample (N), Kolmogorov-Smirnov test between disc-bearing and non disc-bearing stars.

While GDW16 results suggest that regions with high UV incident fields can rapidly erode discs, this thesis results suggest that this can influence the disc-rotation connection. The period distributions for disc-bearing and non disc-bearing stars with low and high FUV and EUV incidence are shown in Figures 6.14 and 6.15 respectively. Tables 6.3 and 6.4 show the (μ, σ, ν) values for each period sample for disc-bearing and non disc-bearing stars in the FUV, and EUV incidence sample. The number of stars in each sample, and a KS-test between samples of disc-bearing and non disc-bearing stars are also included in the Table. From the Table and by comparing the period distributions, one can see that while the disc-bearing and non disc-bearing stars samples are different for regions with low UV incidence (a KS-test gives 0.4% probability they came from the same parent distribution for FUV samples, and 0.05% probability for EUV sample), in

$\log(F_{EUV}) \leq 11.42$ **photons/s/cm**^{2} $\log(F_{EUV}) > 11.42$ **photons/s/cm**^{2}

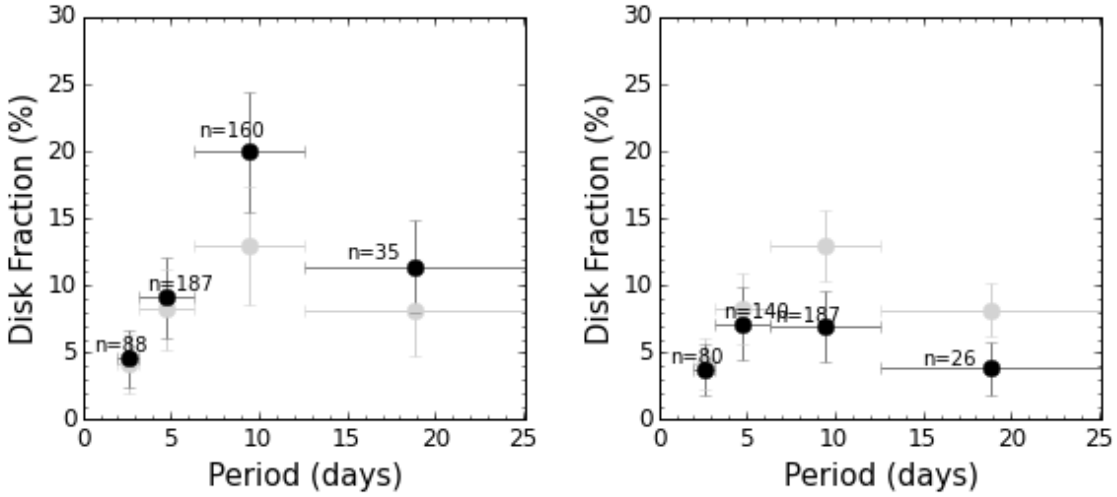

Figure 6.13: Same as Figure 6.5 but for periodic stars with low EUV incident radiation (left) and stars with high EUV incident radiation (right). For reference, the results disc-fractions for the full sample (see Figure 6.5) are also shown in light grey.

	Disc-bearing		Non disc bearing		
EUV	(μ, σ, ν)	N	(μ, σ, ν)	N	KS-test
low UV	(8.0, 4.5, 7.5)	59	(6.4, 4.1, 5.5)	413	0.05%
high UV	(7.2, 3.9, 6.7)	27	(6.7, 4.2, 6.2)	409	71%

Table 6.4: For each EUV flux sample and for samples of disc-bearing and non disc-bearing stars: Mean, standard deviation and median for each period distribution in days. Number of stars in the sample (N), Kolmogorov-Smirnov test between disc-bearing and non disc-bearing stars.

regions with high UV incidence a disc-rotation connection can not be verified and results from KS-test do not discard the possibility that disc-bearing and non disc-bearing period distributions came from the same parent distribution in such samples.

If the impact that the local level of UV radiation has on the disc is capable of changing the star-disc interaction and preventing disc-locking to occur, than stars with and without disc may have a very similar rotational evolution history, and this would explain the similar period distributions for the samples of stars in regions with high local UV levels.

6.4.2 Mass-rotation connection's sensitivity to UV incidence

Next, like in section 6.3, period distributions for different mass ranges for low and high UV incident radiation were built. These distributions are shown in Figure 6.17 for incident FUV, and Figure 6.16 for incident EUV. From the Figures one can verify that the shape of the distributions does not seem to be significantly affected by the amount of UV incident radiation. Both low and high local UV incidence samples show a mass-rotation connection with lower mass stars rotating on average slower than higher mass stars.

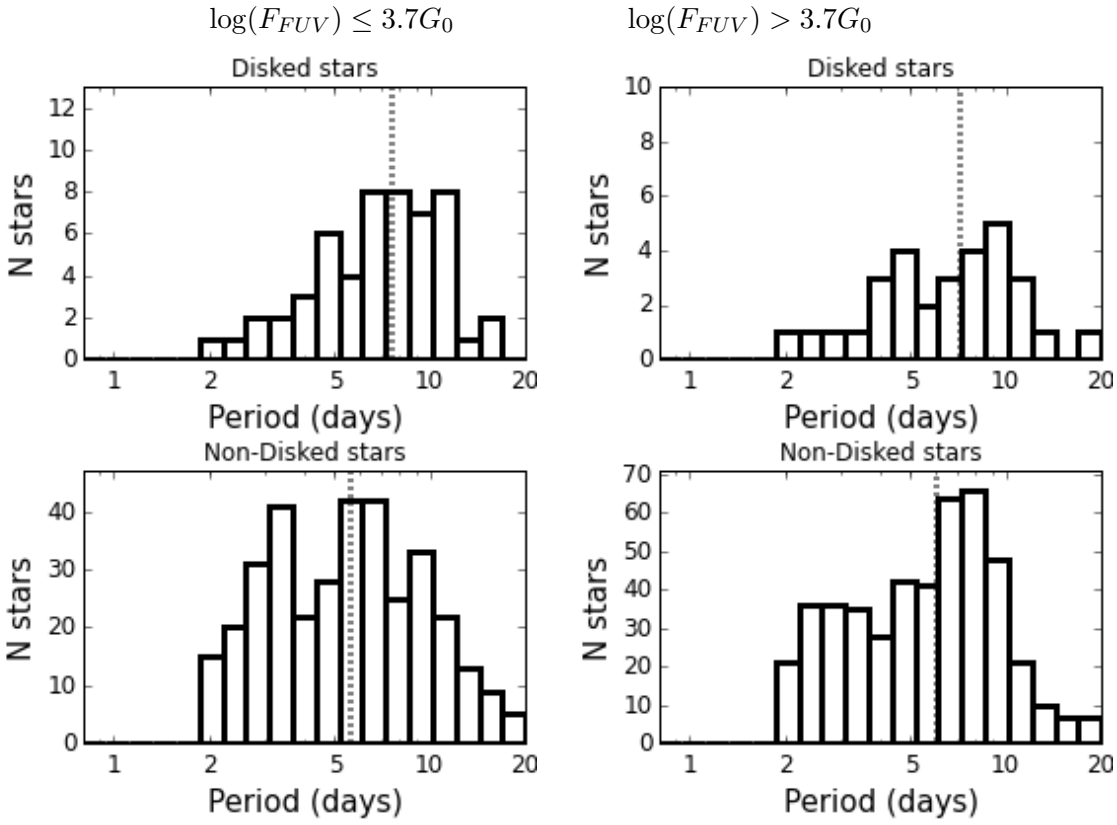

Figure 6.14: Period distributions for stars with (top) and without (bottom) discs for low (left) and high (right) FUV incidence.

Tables 6.5 and 6.6 show the (μ, σ, ν) values for each distribution. The number of stars in each sample, and a KS-test between the two mass ranges for each sub-sample are also shown. KS-tests were performed between each pair of samples for the same mass range and regions with low and high UV incidence, but for all pairs of samples the KS-test yielded that one can not exclude the possibility that the two samples came from the same parent distribution. From Tables 6.5, and 6.6, one can see that KS-tests between period distributions for different mass ranges in samples with high incident UV flux give smaller probabilities that the two samples came from the same parent distribution than regions with low incident UV. This difference, even if less strong than the one found for the case of disc-rotation connection, may hint that UV incident fluxes can also influence the mass-rotation connection.

The magnitude distributions for the samples of high and low UV incidence were analysed as it was done in Section 4.4.5, and the completeness limits found for the two samples were qualitatively the same. The magnitude range in which the two samples can be considered complete is the same as for the full candidate member sample (Figure 3.7), hence we do not consider that completeness issues in the UV-selected samples may be impacting the results. Nevertheless, variability surveys sensitive to fainter stars may improve the size and completeness of the samples towards the fainter stars and help confirming the results presented here.

Further investigations are needed in order to improve these results, in special in order to complete the present analysis for faster rotators and lower masses. But so far, this thesis results suggest that local incident UV radiation may have a relevant role on regulating the rotational properties of YSO. In this sense, evaluating

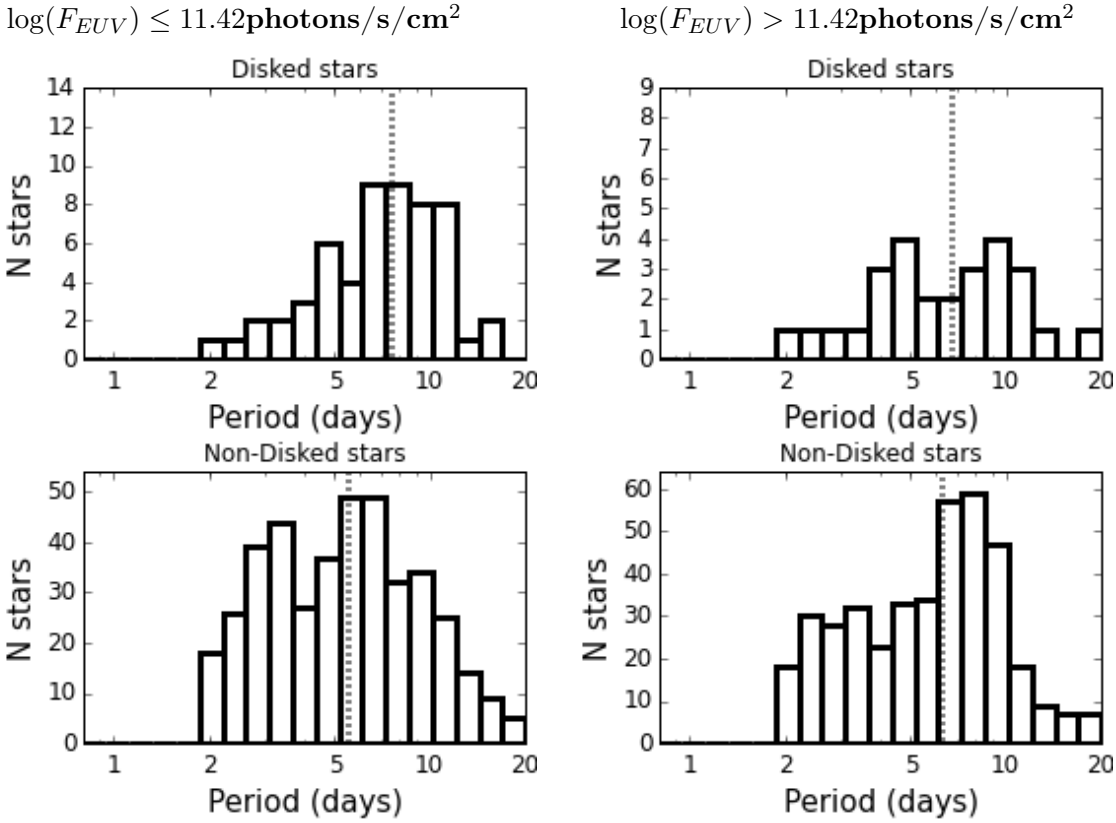

Figure 6.15: Period distributions for stars with (top) and without (bottom) discs for low (left) and high (right) EUV incidence.

the UV radiation arising from massive stars may help explain differences in the rotational properties of low mass stars in young cluster similarly aged presented in the literature.

Table 6.5: For each FUV flux sample and for each mass range considered: Mean, standard deviation and median for each period distribution in days. Number of stars in the sample (N), KS-test between mass-range.

	$M \leq 0.4M_{\odot}$		$M > 0.4M_{\odot}$		
FUV	(μ, σ, ν)	N	(μ, σ, ν)	N	KS-test
low UV	(6.6 2.6, 6.2)	39	(6.5, 4.2, 5.7)	287	3%
high UV	(7.4, 3.0, 7.1)	51	(6.5, 4.2, 5.7)	403	0.2%

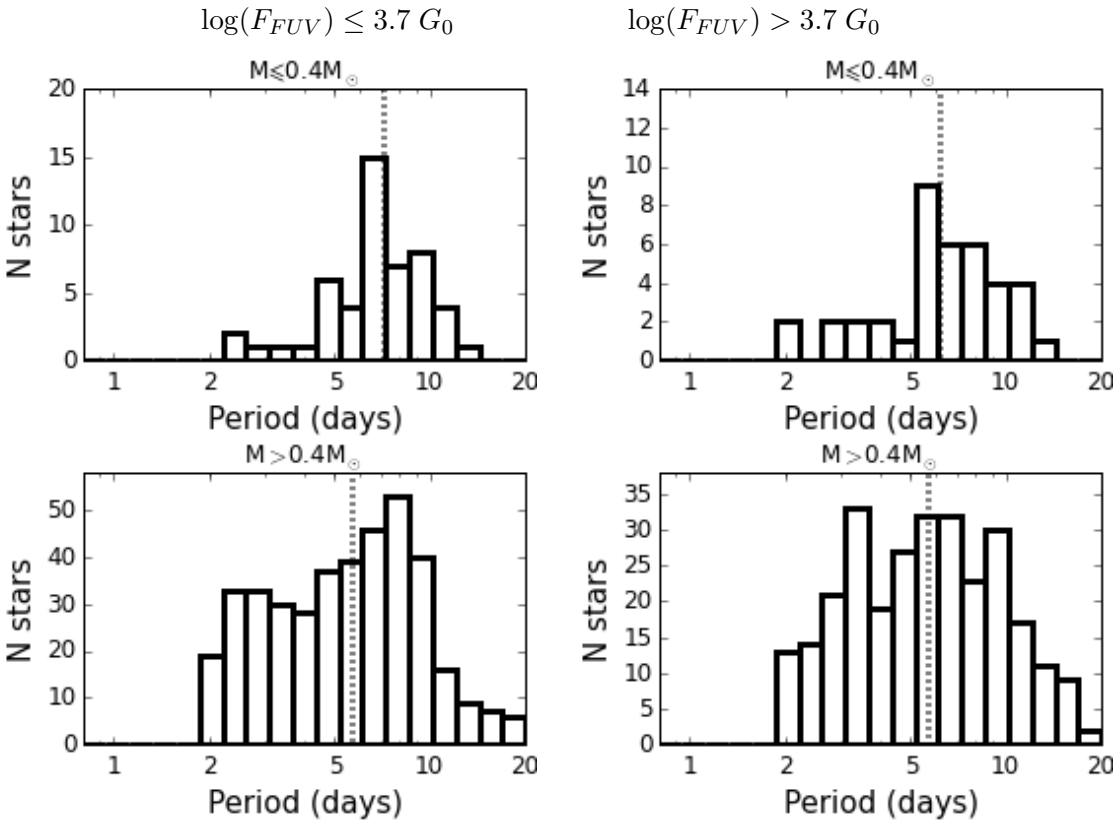

Figure 6.16: Period distributions for stars with $M \leq 0.4$ M$_\odot$(top) and $M > 0.4$ M$_\odot$ (bottom) for low (left) and high (right) EUV incidence.

Table 6.6: For each EUV flux sample and for each mass range considered: Mean, standard deviation and median for each period distribution in days. Number of stars in the sample (N), KS-test between mass-range.

	$M \leq 0.4M_\odot$		$M > 0.4M_\odot$		
EUV	(μ, σ, ν)	N	(μ, σ, ν)	N	KS-test
low UV	(6.9, 3.4, 6.2)	41	(6.5, 4.2, 5.5)	349	0.8%
high UV	(7.1, 2.4, 7.1)	49	(6.6, 4.2, 5.7)	341	0.5%

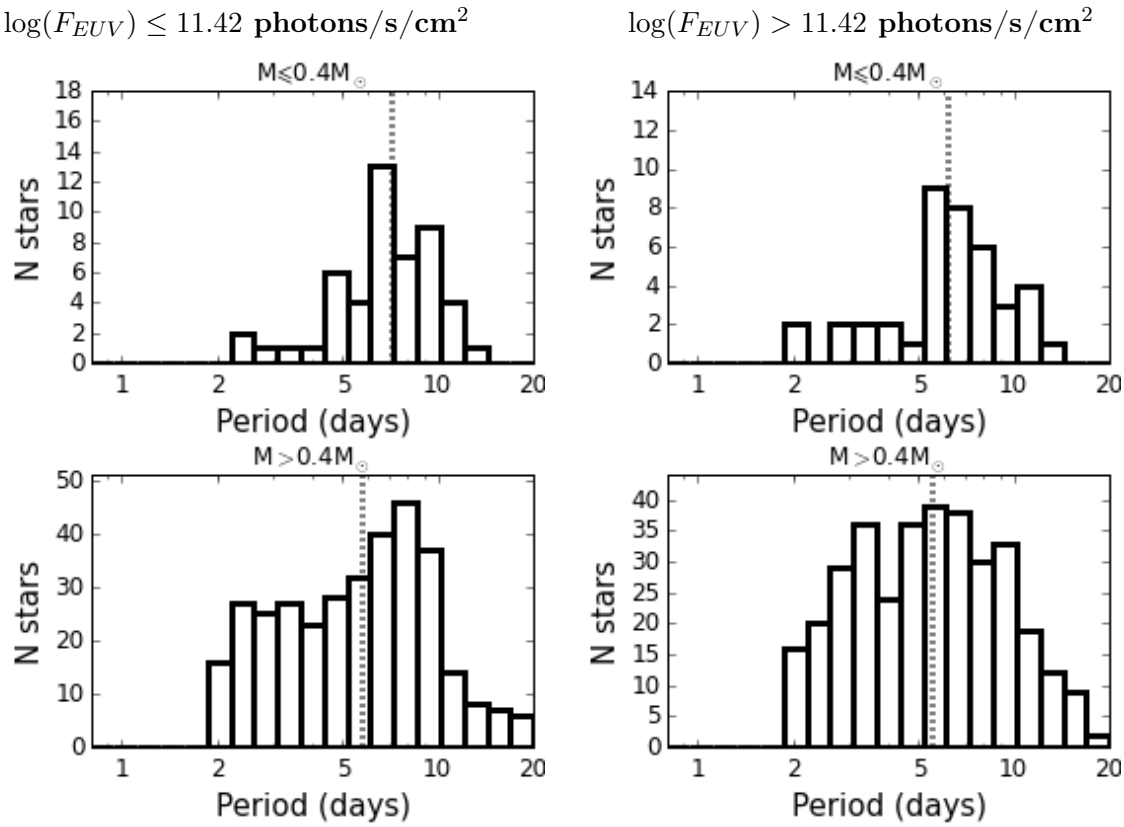

Figure 6.17: Period distributions for stars with $M \leq 0.4$ $M_\odot$ (top) and $M > 0.4$ $M_\odot$ (bottom) for low (left) and high (right) EUV incidence.

Chapter 7

Conclusions and perspectives

The WFCAM/UKIRT JHK survey in the direction of the young Cygnus OB2 association allowed us to investigate the near-IR variability of candidate members in the association. Two mains studies were developed.

The first one focussed in a synoptic investigation of the variable stars in the association. We verified that 80% of the candidate member were variable according to their Stetson variability index, 61% of the same sample showed non stochastic variability in their light curves (periodic or not). These stars were organized in classes according to their light curve morphology. The classes were: Possibly periodic, eclipse-like variables, and non periodic variable stars. After time series analysis, and inspection of the light and colour curves, and of CC and CM-diagrams, the main findings of this study were:

1. We verified that disc-bearing stars are more frequently variable than stars without discs. Disc bearing stars are also more variable than stars without discs in the sense they show higher ptp amplitudes and Stetson index values. This is consistent with the physical processes expected to be producing variability in young stars.

2. We identified 178 stars with correlated variability in colour and magnitude, or in different colours, and measured the slopes of their trajectories in the colour space. The physics behind the near-IR variability in young stars was reviewed. The slopes expected to be produced by the physical mechanisms studied in the colour space were estimated based on physical models. The possible processes producing the trajectories were proposed based on their slopes.

3. We verified that often the light curves are not dominated by a single physical mechanism. The idea of concomitance and switching of multiple physical mechanisms was supported by the identification of some compound variable stars, *i.e.*, stars that change the dominant physical mechanism during the course of time they were observed.

4. We verified that some stars not listed as disc-bearing stars presented transient excess, alternating between phases with normal photospheric colours and near-IR excess colours. Some of these stars showed variability characteristics that could only be explained by the presence of a disc (2.). We

proposed that studying near-IR variability can be used as tool to complement the identification of disc-bearing stars based on single-epoch observations.

The second study presented the first analysis of the rotational properties for low mass stars in the Cygnus OB2 association. We presented results for stars in the mass range 0.1-1.4M$_\odot$. We identified and studied a sample of 1679 stars with signs of periodic variability in their near-IR light curves, out of a sample of 5083 candidate members. After time-series analysis, we confirm periodicity in 1291 stars (25% of total candidate member sample), but after completeness analysis, only 894 of those were considered as reliable period measurements. Since the periodic sample is strongly aliased for periods shorter than about 2 days, most of our analysis was limited to the intermediate (3.14$\leq P \leq$6.28 days) and slow ($P >$6.28 days) rotators, with detected fast rotators only in the range 2-3.14 days. The main findings of this work are:

1. We found periods widely distributed between 0.83 days, and 32.49 days, but due to completeness and contamination issues, we only analysed periods longer than 2 days. The amplitudes of variability for periodic stars were in the range 0.03-1.2 magnitudes; and the masses in the range 0.1-1.4 $M_\odot$.
2. Disc-bearing and non disc-bearing stars are statistically distinct in their rotational properties. Even though there is a significant overlap between their period distributions, disc-bearing stars rotate on average slower (median period 7.34 days) than non disc-bearing stars (median period 5.80 days). Also, period detection is more common among non disc-bearing stars, than among disc-bearing stars.
3. The disc fraction increases as a function of period, except for the very-slow rotator bin ($P >$12.56 days), which has smaller statistics number and seems to suffer from contamination from field stars. The disc fraction varies from $\sim$4% for fast rotators ($P =$2-3.14 days) to $\sim$13% for slow rotators ($P =$6.28-12.56 days). This corroborates the results expected for disc-locking hypothesis, but the variation of disc-fraction as a function of period is shallower than predicted by the simulations of Vasconcelos & Bouvier (2015).
4. A period-mass connection was verified, *i.e.*, statistically distinct properties were found for different mass ranges. A median period of 5.7 days was found for the mass range $M > 0.4M_\odot$,and 6.9 days for $M \leq 0.4M_\odot$. However this mass-rotation connection is different from other regions: As is the case of NGC 6530, lower mass stars in CygOB2 rotate slower than higher mass stars.

We also investigated the possibility of a correlation between the incident UV flux arising from O stars in CygOB2 and the rotational properties of low mass stars described in the previous items.

5. We verified that the distinction in the rotational properties of disc-bearing and non disc-bearing stars is stronger in regions with low UV incidence, while in regions with high UV incidence it is not possible to distinguish between the two samples.
6. The increase of the disc fraction with period is stronger for a sample of stars with low local UV incidence, and it is weaker for a sample of stars with high local UV incidence. A maximum disc fraction of 21%, and 7.3% for slow rotators was found for low and high local UV incidence respectively.
7. Both low and high local UV incidence samples show a mass-rotation connection with lower mass stars rotating on average slower than higher mass stars. For stars with low local UV incidence, a KS-tests

gives that this difference is barely significant, but for stars with high local UV incidence, KS-tests shows stronger evidence that the two mass ranges have different rotational period distributions.

Our results suggest a link between environmental conditions and the rotational evolution of PMS stars. However, it is urgent to complement the sample presented in this study for fast rotators and lower masses, in order to achieve a better understanding of the rotational scenario in the association, and to confirm such suggestions.

The results presented in this thesis have been used as scientific justification in the proposal of two observational follow up campaigns targeting the Cygnus OB2 association, both approved for 2017A: 30h at the WFCAM/UKIRT (P.I. Bo Reipurth, 17A/H05), and 9.6h at the WIRCAM/CFHT (P.I. Julia Roquette, 17AF17). The association will be observed in the K and K_S near-IR bands, and new light curves will be observed by using a time-sampling more adequate to the study of the fast rotators in the sample. The new observations will also complement the sample of very low mass stars, as they were dimensioned to reach fainter stars than the previous campaign.

The access to the properties of very low mass star population is hampered by the completeness of the studies in which membership evaluation was performed. In order to try to unveil such very low mass population, we stacked the WFCAM/UKIRT JHK images used in this thesis, which allowed us to go several orders of magnitude deeper than previous studies. PSF photometry in the stacked images was performed, and this new photometric data is currently been calibrated. The analysis of the new photometric data inside the colour-colour and colour-magnitude diagrams will allow us to evaluate membership for the fainter stars based on their position inside these diagrams and in relation to the cluster locus in such diagrams (As in Section 2.2.1.1). This extra candidate member list will allow us to complement the samples of rotational periods for very low mass stars.

A census of the massive stars contained in the other young clusters, and a revaluation of their rotational properties by considering the levels of incident UV radiation in each cluster should be consider. Such revaluation may bring a better understanding of the environmental influence on regulating the rotational properties of young low mass stars. Moreover, to evaluate the rotational properties of low mass stars in other massive young clusters with similar environmental features to CygOB2 may help us establish how common are rotational properties found in Cygnus. A possible target could be the Eagle Nebulae, also know as NGC 6611, which is a 3Myr young open cluster 1.8 kpc distant from the sun (Bonatto et al. 2006) that has 56 stars earlier than B5 (Hillenbrand et al. 1993). As in CygOB2, Guarcello et al. (2010) found that the disk frequency drops at small distance from the massive stars, where disks are submitted to larger EUV incident fluxes, and one could expect to find a similar correlation between the rotational properties of low mass stars and the UV incidence across the cluster.

Bibliography

Adams, F. C., Hollenbach, D., Laughlin, G., & Gorti, U. 2004, ApJ , 611, 360

Affer, L., Micela, G., Favata, F., Flaccomio, E., & Bouvier, J. 2013, MNRAS , 430, 1433

Aihara, H., Allende Prieto, C., An, D., et al. 2011, ApJS , 193, 29

Allard, F., Homeier, D., & Freytag, B. 2011, in Astronomical Society of the Pacific Conference Series, Vol. 448, 16th Cambridge Workshop on Cool Stars, Stellar Systems, and the Sun, ed. C. Johns-Krull, M. K. Browning, & A. A. West, 91

Allen, T. S., Gutermuth, R. A., Kryukova, E., et al. 2012, ApJ , 750, 125

Alves de Oliveira, C. & Casali, M. 2008, A&A , 485, 155

André, P. 2002, in EAS Publications Series, Vol. 3, EAS Publications Series, ed. J. Bouvier & J.-P. Zahn, 1–38

Andre, P., Ward-Thompson, D., & Barsony, M. 1993, ApJ , 406, 122

Artemenko, S. A., Grankin, K. N., & Petrov, P. P. 2012, Astronomy Letters, 38, 783

Attridge, J. M. & Herbst, W. 1992, ApJ , 398, L61

Baraffe, I., Chabrier, G., Allard, F., & Hauschildt, P. H. 1998, A&A , 337, 403

Baraffe, I., Homeier, D., Allard, F., & Chabrier, G. 2015, A&A , 577, A42

Barentsen, G., Farnhill, H. J., Drew, J. E., et al. 2014, MNRAS , 444, 3230

Barnes, S. A. 2007, ApJ , 669, 1167

Barrado y Navascués, D., Stauffer, J. R., Bouvier, J., Jayawardhana, R., & Cuillandre, J.-C. 2004, ApJ , 610, 1064

Beckwith, S. V. W. & Sargent, A. I. 1991, ApJ , 381, 250

Beerer, I. M., Koenig, X. P., Hora, J. L., et al. 2010, ApJ , 720, 679

Bell, C. P. M., Naylor, T., Mayne, N. J., Jeffries, R. D., & Littlefair, S. P. 2012, MNRAS , 424, 3178

Bell, C. P. M., Naylor, T., Mayne, N. J., Jeffries, R. D., & Littlefair, S. P. 2013, MNRAS , 434, 806

Bell, C. P. M., Rees, J. M., Naylor, T., et al. 2014, MNRAS , 445, 3496

Blaauw, A. 1964, ARA&A, 2, 213

Blaauw, A., Hiltner, W. A., & Johnson, H. L. 1959, ApJ , 130, 69

Bodenheimer, P. 1995, ARA&A, 33, 199

Bonatto, C., Santos, Jr., J. F. C., & Bica, E. 2006, A&A , 445, 567

Bouvier, J. 2013, in EAS Publications Series, Vol. 62, EAS Publications Series, 143–168

Bouvier, J., Alencar, S. H. P., Boutelier, T., et al. 2007, A&A , 463, 1017

Bouvier, J., Bertout, C., Benz, W., & Mayor, M. 1986a, A&A , 165, 110

Bouvier, J., Bertout, C., Benz, W., & Mayor, M. 1986b, A&A , 165, 110

Bouvier, J., Cabrit, S., Fernandez, M., Martin, E. L., & Matthews, J. M. 1993, A&A , 272, 176

Bouvier, J., Grankin, K. N., Alencar, S. H. P., et al. 2003, A&A , 409, 169

Bouvier, J., Matt, S. P., Mohanty, S., et al. 2014, Protostars and Planets VI, 433

Bouy, H., Bertin, E., Moraux, E., et al. 2013, A&A , 554, A101

Cardelli, J. A., Clayton, G. C., & Mathis, J. S. 1989, ApJ , 345, 245

Carpenter, J. M. 2001, AJ , 121, 2851

Carpenter, J. M., Hillenbrand, L. A., & Skrutskie, M. F. 2001, AJ , 121, 3160

Carpenter, J. M., Hillenbrand, L. A., Skrutskie, M. F., & Meyer, M. R. 2002, AJ , 124, 1001

Casagrande, L. & VandenBerg, D. A. 2014, MNRAS , 444, 392

Casali, M., Adamson, A., Alves de Oliveira, C., et al. 2007, A&A , 467, 777

Chen, H., Myers, P. C., Ladd, E. F., & Wood, D. O. S. 1995, ApJ , 445, 377

Cieza, L. & Baliber, N. 2007, ApJ , 671, 605

Claret, A. & Bloemen, S. 2011, A&A , 529, A75

Clarke, C. J., Gendrin, A., & Sotomayor, M. 2001, MNRAS , 328, 485

Clarke, D. 2002, A&A , 386, 763

Cody, A. M. & Hillenbrand, L. A. 2010, ApJS , 191, 389

Cody, A. M., Stauffer, J., Baglin, A., et al. 2014, AJ , 147, 82

Cohen, M. & Kuhi, L. V. 1979, ApJS , 41, 743

Cohen, R. E., Herbst, W., & Williams, E. C. 2004, AJ , 127, 1602

Collier Cameron, A. & Campbell, C. G. 1993, A&A , 274, 309

Comerón, F., Pasquali, A., Rodighiero, G., et al. 2002, A&A , 389, 874

Covey, K. R., Ivezić, Ž., Schlegel, D., et al. 2007, AJ , 134, 2398

Cutri, R. M., Skrutskie, M. F., van Dyk, S., et al. 2003, VizieR Online Data Catalog, 2246, 0

Dahm, S. E. 2008, The Young Cluster and Star Forming Region NGC 2264, ed. B. Reipurth, 966

Damiani, F., Flaccomio, E., Micela, G., et al. 2004, ApJ , 608, 781

Damiani, F., Prisinzano, L., Micela, G., & Sciortino, S. 2006, A&A , 459, 477

de Zeeuw, P. T., Hoogerwerf, R., de Bruijne, J. H. J., Brown, A. G. A., & Blaauw, A. 1999, AJ , 117, 354

Doi, M., Tanaka, M., Fukugita, M., et al. 2010, AJ , 139, 1628

Donati, J.-F. 2011, in IAU Symposium, Vol. 271, IAU Symposium, ed. N. H. Brummell, A. S. Brun, M. S. Miesch, & Y. Ponty, 23–31

Donati, J.-F., Skelly, M. B., Bouvier, J., et al. 2010, MNRAS , 402, 1426

Dotter, A., Chaboyer, B., Jevremović, D., et al. 2008, ApJS , 178, 89

Drew, J. E., Greimel, R., Irwin, M. J., et al. 2005, MNRAS , 362, 753

Drew, J. E., Greimel, R., Irwin, M. J., & Sale, S. E. 2008, MNRAS , 386, 1761

Dullemond, C. P. & Monnier, J. D. 2010, ARA&A, 48, 205

Fang, M., van Boekel, R., Wang, W., et al. 2009, A&A , 504, 461

Favata, F., Flaccomio, E., Reale, F., et al. 2005, ApJS , 160, 469

Fedele, D., van den Ancker, M. E., Henning, T., Jayawardhana, R., & Oliveira, J. M. 2010, A&A , 510, A72

Feigelson, E. D., Gaffney, III, J. A., Garmire, G., Hillenbrand, L. A., & Townsley, L. 2003, ApJ , 584, 911

Ferreira, J., Pelletier, G., & Appl, S. 2000, MNRAS , 312, 387

Froebrich, D., Ray, T. P., Murphy, G. C., & Scholz, A. 2005, A&A , 432, L67

Gallet, F. & Bouvier, J. 2013, A&A , 556, A36

Gallet, F. & Bouvier, J. 2015, A&A , 577, A98

Garcia, P. J. V., Natta, A., & Walmsley, M. 2011, Circumstellar Disks around Young Stars, ed. P. J. V. Garcia, 1–13

Garufi, A., Meeus, G., Benisty, M., et al. 2017, ArXiv e-prints

Ghosh, P. & Lamb, F. K. 1979, ApJ , 234, 296

Gilden, D. L. 1984, ApJ , 283, 679

Gorti, U., Dullemond, C. P., & Hollenbach, D. 2009, ApJ , 705, 1237

Greene, T. P., Wilking, B. A., Andre, P., Young, E. T., & Lada, C. J. 1994, ApJ , 434, 614

Gregory, S. G., Donati, J.-F., Morin, J., et al. 2012, ApJ , 755, 97

Guarcello, M. G., Drake, J. J., Wright, N. J., et al. 2016, ArXiv e-prints

Guarcello, M. G., Drake, J. J., Wright, N. J., et al. 2013, ApJ , 773, 135

Guarcello, M. G., Drake, J. J., Wright, N. J., et al. 2015, ArXiv e-prints

Guarcello, M. G., Micela, G., Damiani, F., et al. 2009, A&A , 496, 453

Guarcello, M. G., Micela, G., Peres, G., Prisinzano, L., & Sciortino, S. 2010, A&A , 521, A61

Guarcello, M. G., Prisinzano, L., Micela, G., et al. 2007, A&A , 462, 245

Guarcello, M. G., Wright, N. J., Drake, J. J., et al. 2012, ApJS , 202, 19

Gutermuth, R. A., Megeath, S. T., Myers, P. C., et al. 2009, ApJS , 184, 18

Habing, H. J. 1968, Bull. Astron. Inst. Netherlands, 19, 421

Haisch, Jr., K. E., Lada, E. A., & Lada, C. J. 2001, ApJ , 553, L153

Hanson, M. M. 2003, ApJ , 597, 957

Hartman, J. D., Gaudi, B. S., Pinsonneault, M. H., et al. 2009, ApJ , 691, 342

Hartmann, L. 1998, Accretion Processes in Star Formation

Hartmann, L. 2009, Accretion Processes in Star Formation: Second Edition (Cambridge University Press)

Hartmann, L. & Stauffer, J. R. 1989, AJ , 97, 873

Harvey, P., Merín, B., Huard, T. L., et al. 2007, ApJ , 663, 1149

Hayashi, C. 1970, Memoires of the Societe Royale des Sciences de Liege, 19, 127

Henderson, C. B., Stanek, K. Z., Pejcha, O., & Prieto, J. L. 2011, ApJS , 194, 27

Henderson, C. B. & Stassun, K. G. 2012, ApJ , 747, 51

Herbst, W., Bailer-Jones, C. A. L., & Mundt, R. 2001, ApJ , 554, L197

Herbst, W., Bailer-Jones, C. A. L., Mundt, R., Meisenheimer, K., & Wackermann, R. 2002, A&A , 396, 513

Herbst, W., Bailer-Jones, C. A. L., Mundt, R., Meisenheimer, K., & Wackermann, R. 2004, in IAU Symposium, Vol. 202, Planetary Systems in the Universe, ed. A. Penny, 341

Herbst, W., Eislöffel, J., Mundt, R., & Scholz, A. 2007, Protostars and Planets V, 297

Herbst, W. & Mundt, R. 2005, ApJ , 633, 967

Hernández, J., Hartmann, L., Megeath, T., et al. 2007, ApJ , 662, 1067

Hertzsprung, E. 1909, Astronomische Nachrichten, 179, 373

Hewett, P. C., Warren, S. J., Leggett, S. K. T. d., & Hodgkin, S. T. 2006, MNRAS , 367, 454

Hillenbrand, L. A., Massey, P., Strom, S. E., & Merrill, K. M. 1993, AJ , 106, 1906

Hillenbrand, L. A., Strom, S. E., Calvet, N., et al. 1998, AJ , 116, 1816

Hodgkin, S. T., Irwin, M. J., Hewett, P. C., & Warren, S. J. 2009, MNRAS , 394, 675

Hollenbach, D. & Gorti, U. 2005, in Protostars and Planets V Posters, Vol. 1286, 8433

Horne, J. H. & Baliunas, S. L. 1986, ApJ , 302, 757

Howell, S. B., Sobeck, C., Haas, M., et al. 2014, PASP , 126, 398

Irwin, J., Berta, Z. K., Burke, C. J., et al. 2011, ApJ , 727, 56

Irwin, J. & Bouvier, J. 2009, in IAU Symposium, Vol. 258, IAU Symposium, ed. E. E. Mamajek, D. R. Soderblom, & R. F. G. Wyse, 363–374

Irwin, J., Hodgkin, S., Aigrain, S., et al. 2008, MNRAS , 384, 675

Jappsen, A.-K. & Klessen, R. S. 2004, A&A , 423, 1

Jeffries, R. D., Jackson, R. J., Cottaar, M., et al. 2014, A&A , 563, A94

Johns-Krull, C. M. 2007, ApJ , 664, 975

Johnson, H. L. & Morgan, W. W. 1953, ApJ , 117, 313

Johnstone, C. P., Jardine, M., Gregory, S. G., Donati, J.-F., & Hussain, G. 2014, MNRAS , 437, 3202

Johnstone, D., Hollenbach, D., & Bally, J. 1998, ApJ , 499, 758

Jones, B. 1997, Mem. Societa Astronomica Italiana, 68, 833

Joy, A. H. 1945, ApJ , 102, 168

Kashyap, V. L. 2017

Kenyon, S. J. & Hartmann, L. 1995, ApJS , 101, 117

Kiminki, D. C., Kobulnicky, H. A., Kinemuchi, K., et al. 2007, ApJ , 664, 1102

Kiminki, D. C., Kobulnicky, H. A., Vargas Álvarez, C. A., Alexander, M. J., & Lundquist, M. J. 2015, ApJ , 811, 85

Knödlseder, J. 2000, A&A , 360, 539

Knödlseder, J. 2003, in IAU Symposium, Vol. 212, A Massive Star Odyssey: From Main Sequence to Supernova, ed. K. van der Hucht, A. Herrero, & C. Esteban, 505

Koenigl, A. 1991a, ApJ , 370, L39

Koenigl, A. 1991b, ApJ , 370, L39

Kraus, A. L. & Hillenbrand, L. A. 2007, AJ , 134, 2340

Krishnamurthi, A., Pinsonneault, M. H., Barnes, S., & Sofia, S. 1997, ApJ , 480, 303

Krumholz, M. R. 2015, Notes on Star Formation

Kuerster, M., Schmitt, J. H. M. M., Cutispoto, G., & Dennerl, K. 1997, A&A , 320, 831

Kurosawa, R., Harries, T. J., & Symington, N. H. 2006, MNRAS , 370, 580

Kurosawa, R. & Romanova, M. M. 2013, MNRAS , 431, 2673

Lada, C. J. 1987, in IAU Symposium, Vol. 115, Star Forming Regions, ed. M. Peimbert & J. Jugaku, 1–17

Lada, C. J. & Lada, E. A. 2003, ARA&A, 41, 57

Lada, C. J., Muench, A. A., Luhman, K. L., et al. 2006, AJ , 131, 1574

Lada, C. J. & Wilking, B. A. 1984, ApJ , 287, 610

Lafler, J. & Kinman, T. D. 1965, ApJS , 11, 216

Lamm, M. H., Mundt, R., Bailer-Jones, C. A. L., & Herbst, W. 2005, A&A , 430, 1005

Larson, R. B. 1969, MNRAS , 145, 271

Larson, R. B. 2003, Reports on Progress in Physics, 66, 1651

Littlefair, S. P., Naylor, T., Burningham, B., & Jeffries, R. D. 2005, MNRAS , 358, 341

Littlefair, S. P., Naylor, T., Mayne, N. J., Saunders, E. S., & Jeffries, R. D. 2010, MNRAS , 403, 545

Lomb, N. R. 1976, Ap&SS , 39, 447

Lovelace, R. V. E. & Romanova, M. M. 2004, in American Institute of Physics Conference Series, Vol. 703, Plasmas in the Laboratory and in the Universe: New Insights and New Challenges, ed. G. Bertin, D. Farina, & R. Pozzoli, 229–237

Lucas, P. W., Hoare, M. G., Longmore, A., et al. 2008, MNRAS , 391, 136

Lynden-Bell, D. & Pringle, J. E. 1974, MNRAS , 168, 603

Maeder, A. 2009, Physics, Formation and Evolution of Rotating Stars

Massey, P. & Thompson, A. B. 1991, AJ , 101, 1408

Mathis, J. S. 1990, ARA&A, 28, 37

Matt, S. & Pudritz, R. E. 2005, ApJ , 632, L135

Matt, S. P., Pinzón, G., de la Reza, R., & Greene, T. P. 2010, ApJ , 714, 989

Matt, S. P., Pinzón, G., Greene, T. P., & Pudritz, R. E. 2012, ApJ , 745, 101

Mayne, N. J. & Naylor, T. 2008a, MNRAS , 386, 261

Mayne, N. J. & Naylor, T. 2008b, MNRAS , 386, 261

McGinnis, P. T., Alencar, S. H. P., Guimarães, M. M., et al. 2015, A&A , 577, A11

McKee, C. F. & Ostriker, E. C. 2007, ARA&A, 45, 565

McKee, C. F., Storey, J. W. V., Watson, D. M., & Green, S. 1982, ApJ , 259, 647

Meibom, S., Barnes, S. A., Latham, D. W., et al. 2011, ApJ , 733, L9

Meibom, S., Mathieu, R. D., & Stassun, K. G. 2009, ApJ , 695, 679

Ménard, F. & Bertout, C. 1999, in NATO Advanced Science Institutes (ASI) Series C, Vol. 540, NATO Advanced Science Institutes (ASI) Series C, ed. C. J. Lada & N. D. Kylafis, 341

Mendes, L. T. S., D'Antona, F., & Mazzitelli, I. 1999, A&A , 341, 174

Meyer, M. R., Calvet, N., & Hillenbrand, L. A. 1997, AJ , 114, 288

Meynet, G. & Maeder, A. 2005, A&A , 429, 581

Miyake, K. & Nakagawa, Y. 1993, Icarus, 106, 20

Mohanty, S. & Shu, F. H. 2008, ApJ , 687, 1323

Moraux, E., Artemenko, S., Bouvier, J., et al. 2013, A&A , 560, A13

Mullan, D. J. & MacDonald, J. 2001, ApJ , 559, 353

Münch, L. & Morgan, W. 1953, ApJ , 118, 161

Najita, J. R., Strom, S. E., & Muzerolle, J. 2007, MNRAS , 378, 369

Naylor, T. 2009, MNRAS , 399, 432

O'Donnell, J. E. 1994, ApJ , 422, 158

Oke, J. B. & Gunn, J. E. 1983, ApJ , 266, 713

Ostriker, E. C. & Shu, F. H. 1995, ApJ , 447, 813

Parks, J. R., Plavchan, P., White, R. J., & Gee, A. H. 2014, ApJS , 211, 3

Pasquali, A., Comerón, F., Gredel, R., Torra, J., & Figueras, F. 2002, A&A , 396, 533

Plavchan, P., Jura, M., Kirkpatrick, J. D., Cutri, R. M., & Gallagher, S. C. 2008, ApJS , 175, 191

Preibisch, T. & Feigelson, E. D. 2005, ApJS , 160, 390

Press, W. H., Flannery, B. P., Teukolsky, S. A., & Veterling, W. T. 1992, Numerical Recipes in C: the art of scientific computing, 2nd edn. (Cambridge: Cambridge University Press)

Rauw, G., Nazé, Y., Wright, N. J., et al. 2015, ApJS , 221, 1

Rebull, L. M., Guieu, S., Stauffer, J. R., et al. 2011, ApJS , 193, 25

Rebull, L. M., Wolff, S. C., & Strom, S. E. 2004, AJ , 127, 1029

Reddish, V., Lawrence, L. C., & Pratt, N. M. 1966, Publications of the Royal Observatory of Edinburgh, 5, 111

Reipurth, B. & Schneider, N. 2008, Star Formation and Young Clusters in Cygnus, ed. B. Reipurth, 36

Rice, T. S., Reipurth, B., Wolk, S. J., Vaz, L. P., & Cross, N. J. G. 2015, AJ , 150, 132

Rice, T. S., Wolk, S. J., & Aspin, C. 2012, ApJ , 755, 65

Ricker, G. R., Winn, J. N., Vanderspek, R., et al. 2014, in Proceedings of the SPIE, Vol. 9143, Space Telescopes and Instrumentation 2014: Optical, Infrared, and Millimeter Wave, 914320

Rodmann, J., Henning, T., Chandler, C. J., Mundy, L. G., & Wilner, D. J. 2006, A&A , 446, 211

Rodríguez-Ledesma, M. V., Mundt, R., & Eislöffel, J. 2009, A&A , 502, 883

Romanova, M. M. & Owocki, S. P. 2016, Accretion, Outflows, and Winds of Magnetized Stars, ed. V. S. Beskin, A. Balogh, M. Falanga, M. Lyutikov, S. Mereghetti, T. Piran, & R. A. Treumann, 347

Romanova, M. M., Ustyugova, G. V., Koldoba, A. V., & Lovelace, R. V. E. 2004, ApJ , 610, 920

Romanova, M. M., Ustyugova, G. V., Koldoba, A. V., & Lovelace, R. V. E. 2009, MNRAS , 399, 1802

Roquette, J. 2017, in preparation

Russell, H. N. 1914, Popular Astronomy, 22, 275

Rygl, K. L. J., Brunthaler, A., Sanna, A., et al. 2012, A&A , 539, A79

Sadavoy, S. I., Stutz, A. M., Schnee, S., et al. 2016, A&A , 588, A30

Sale, S. E., Drew, J. E., Unruh, Y. C., et al. 2009, MNRAS , 392, 497

Saunders, E. S., Naylor, T., & Allan, A. 2006, Astronomische Nachrichten, 327, 783

Scargle, J. D. 1982, ApJ , 263, 835

Schaller, G., Schaerer, D., Meynet, G., & Maeder, A. 1992, A&AS , 96, 269

Schlegel, D. J., Finkbeiner, D. P., & Davis, M. 1998, ApJ , 500, 525

Schneider, N., Simon, R., Bontemps, S., Comerón, F., & Motte, F. 2007, A&A , 474, 873

Scholz, A. & Eislöffel, J. 2004, A&A , 419, 249

Scholz, A., Xu, X., Jayawardhana, R., et al. 2009, MNRAS , 398, 873

Shu, F., Najita, J., Ostriker, E., et al. 1994, ApJ , 429, 781

Siess, L., Dufour, E., & Forestini, M. 2000, A&A , 358, 593

Skumanich, A. 1972, ApJ , 171, 565

Soderblom, D. R. 2010, ARA&A, 48, 581

Sousa, A. P., Alencar, S. H. P., Bouvier, J., et al. 2016, A&A , 586, A47

Stahler, S. W. 1983, ApJ , 274, 822

Stahler, S. W. & Palla, F. 2005, The Formation of Stars, 865

Stahler, S. W., Shu, F. H., & Taam, R. E. 1980a, ApJ , 241, 637

Stahler, S. W., Shu, F. H., & Taam, R. E. 1980b, ApJ , 242, 226

Stahler, S. W., Shu, F. H., & Taam, R. E. 1981, ApJ , 248, 727

Stauffer, J., Cody, A. M., Baglin, A., et al. 2014, AJ , 147, 83

Stetson, P. B. 1996, PASP , 108, 851

Sung, H., Chun, M.-Y., & Bessell, M. S. 2000, AJ , 120, 333

Tambovtseva, L. V. & Grinin, V. P. 2008, Astronomy Letters, 34, 231

Tanner, R. W. 1948, JRASC, 42, 177

Taylor, M. B. 2005, in Astronomical Society of the Pacific Conference Series, Vol. 347, Astronomical Data Analysis Software and Systems XIV, ed. P. Shopbell, M. Britton, & R. Ebert, 29

Tognelli, E., Degl'Innocenti, S., & Prada Moroni, P. G. 2012, Memorie della Societa Astronomica Italiana Supplementi, 22, 225

Tognelli, E., Prada Moroni, P. G., & Degl'Innocenti, S. 2011, A&A , 533, A109

Torres-Dodgen, A., Carroll, M., & Tapia, M. 1991, MNRAS , 249, 1

Tothill, N. F. H., Gagné, M., Stecklum, B., & Kenworthy, M. A. 2008, The Lagoon Nebula and its Vicinity, ed. B. Reipurth, 533

Vasconcelos, M. J. & Bouvier, J. 2015, A&A , 578, A89

Vasconcelos, M. J. & Bouvier, J. 2016, ArXiv e-prints

Venuti, L., Bouvier, J., Cody, A. M., et al. 2016, ArXiv e-prints

Venuti, L., Bouvier, J., Irwin, J., et al. 2015, A&A , 581, A66

Vink, J. S., Drew, J. E., Steeghs, D., et al. 2008, MNRAS , 387, 308

Vogel, S. N. & Kuhi, L. V. 1981, ApJ , 245, 960

Vrba, F. J., Herbst, W., & Booth, J. F. 1988, AJ , 96, 1032

Walborn, N. R., Howarth, I. D., Lennon, D. J., et al. 2002, AJ , 123, 2754

Walter, F. M. 1986, ApJ , 306, 573

White, R. J. & Basri, G. 2003, ApJ , 582, 1109

Wilking, B. A., Bontemps, S., Schuler, R. E., Greene, T. P., & André, P. 2001, ApJ , 551, 357

Williams, J. P., Blitz, L., & McKee, C. F. 2000, Protostars and Planets IV, 97

Williams, J. P. & Cieza, L. A. 2011, ARA&A, 49, 67

Wolk, S. J., Rice, T. S., & Aspin, C. 2013, ApJ , 773, 145

Wright, N. J., Bouy, H., Drew, J. E., et al. 2016, MNRAS , 460, 2593

Wright, N. J. & Drake, J. J. 2009, ApJS , 184, 84

Wright, N. J., Drake, J. J., Drew, J. E., & Vink, J. S. 2010, ApJ , 713, 871

Wright, N. J., Drake, J. J., Guarcello, M. G., et al. 2014, ArXiv e-prints

Wright, N. J., Drew, J. E., & Mohr-Smith, M. 2015, MNRAS , 449, 741

Zanni, C. & Ferreira, J. 2011, ApJ , 727, L22

Zanni, C. & Ferreira, J. 2013, A&A , 550, A99

Zapatero Osorio, M. R., Caballero, J. A., Béjar, V. J. S., & Rebolo, R. 2003, A&A , 408, 663

Appendix A

Description of CASU tables

In this appendix some useful extracts from WFCAM documentation (Cambridge Astronomy Survey Unit: WFCAM for UKIRT[1], Hodgkin et al. 2009) are listed. Table A.1 presents some usefull parameters inside the .fits containing WFCAM processing pipeline output catalogue.

Table A.1: WFCAM pipeline output catalogues parameters and their descriptions

N^o	Name	Description
1	Seq. no.	Running number for ease of reference, in strict order of image detections
3	X coord	Intensity-weighted isophotal centre-of-gravity in X
4	Error in X	Estimate of centroid error
5	Y coord	Intensity-weighted isophotal centre-of-gravity in Y
6	Error in Y	Estimate of centroid error
20	Aperture flux 3	Radii soft-edged apertures fixed to 1.0 arcsec
21	Error in flux 3	Recommended if a single number is required to represent the flux for ALL images
56	Sky level	local interpolated sky level from background tracker
57	Sky rms	local estimate of variation in sky level around image
59	RA	RA and Dec explicitly put in columns for overlay programs that
60	Dec	cannot, in general, understand astrometric solution coefficients - note: r*4 storage precision accurate only to ∼50mas. Astrometry can be derived more precisely from WCS in header and XY in parameters 56
61	Classification Flag	indicating most probable morphological classification: eg. -1 stellar, +1 non-stellar, 0 noise, -2 borderline stellar, -9 saturated

Tables A.2 and A.3 present relevant parameters an photometric information derived by CASU's pipeline and written in the FITS headers. These values are computed per-detector and stored in the headers for each image and catalogue extension.

[1]http://casu.ast.cam.ac.uk/surveys-projects/wfcam

Table A.2: Header items.

Keyword	Description
SKYLEVEL	Median sky brightness (counts/pixel) An automatic 2D background-following algorithm is used to track and "remove" slowly varying background features such as image gradients etc. The default scale size for background tracking (NBSIZE) is currently set to 64 pixels, coupled with a smidge of non-linear filtering this gives a background tracking scale of order 100 pixels. (A bilinear interpolator is used to generate pixel resolution background maps internally).
SKYNOISE	Pixel noise at sky level (counts). Robust MAD estimator for noise scaled to equivalent Gaussian rms value ie. = MAD x 1.48 after removing large scale sky background variations. MAD = Median of the Absolute Deviations about the median
THRESHOLD	Isophotal analysis threshold (counts). User-selectable parameter, the default is to set this to 1.5x skynoise as a compromise between detecting close to the limit of the data and not being swamped by spurious sources. It is possible to push the data limit fainter but at the expense of a large increase in spurious sources. LSBG detection requires a more subtle add-on to the catalogue and could be added given suitable demand.
MINPIX	Minimum size for images (pixels). User-selectable parameter, in conjunction with the threshold above this determines how deep and how small "real" images can be. This default precludes many of the few pixel-hit cosmic rays from being considered since "real" images must have 4 contiguous simply-connected pixels in the union of the detection filter and data domains.
CROWDED	Crowded field analysis flag (0 none, 1 active). User-selectable parameter, detection algorithm tried to disentangle overlapping images or images supperposed on the "slowly" varying background of other large images (default) otherwise just straighforward isophotal detection.
RCORE	Core radius for default profile fit (pixels). User-selectable parameter, aperture flux designed to match median seeing of survey data. It is straighforward to show that if rcore = FWHM then for typical profiles encountered the rcore flux estimate has between 80-90% of the accuracy of an idealised perfectly known PSF model method.
OPTFILT	FWHM of Gaussian detection filter (pixels). User-selectable parameter, should be chosen to match the average FWHM of stellar images in the data. This defines the Gaussian matched detection filter to use.
SEEING	Average FWHM (pixels). An average realistic FWHM estimated directly from the stellar images on the frame. Mutiply by pixel scale size to convert to arcsec (eg. x0.400 WFCAM; x0.333 INT WFC).
ELLIPTIC	Average stellar ellipticity (1-b/a). A direct estimate of the average stellar ellipticity, useful for spotting trailed frames usw.. Should not average much above 0.15 for "normal" frames.
CLASSIFD	Classified (true/false). Has image morphological classifier been run? If so, an object classification flag and a stellarness index is included in the binary table columns.
SATURATE	Average saturation level in frame. An estimate directly from saturated i mages on the frame at what level image saturation occurs, including sky. This varies from detector to detector depending on the relative gains applied to bring them to a uniform flatfield response etc.

Table A.3: Photometric Information inside the Headers.

Keyword	Description
APCORPK	Stellar aperture correction - peak height, core1-7 flux

Table A.3: Continued...

Keyword	Description
APCOR3	Aperture corrections in magnitudes (for flux 3) needed to correct the assorted aperture-like measures produced in the catalogues onto the equivalent of a total flux stellar system. These constitute the components of a curve-of-growth analysis contained within the catalogues with radii defined in the previous table; to be used in the sense that corrected photometry = 2.5xlog10(flux) +apcor.
PERCORR	Sky calibration correction (mags). This is a correction based on the median dark sky recorded in science frames compared to the median for all the detectors and as such is an ancillary correction to the gain correction derived from the flatfield (usually twilight flats) data. This correction is to be used in the samesense as before in that corrected photometry = 2.5xlog10(flux) + apcor + percorr
MAGZPT	Photometric ZP (mags) for default extinction. Derived detector zero-point in the sense of what magnitude object gives a total (corrected) flux of 1 count/s. These ZPs are appropriate for generating magnitudes in the natural detector+filter system based on Vega, see the photometry page for more details on colour equations etc. The ZPs have been derived from a robust average of all photometric standards observed on any particular set of frames, corrected for airmass but assuming the default extinction values listed later. For other airmass or other values of the extinction use ZP -> ZP - [sec(z)-1]x extinct + defaultextinct - extinct You can then make use of any of the assorted flux estimators to produce magnitudes via Mag=ZP-2.5xlog10(flux/exptime)-apcor-percorr. Note that for the so-called total and isophotal flux options it is not possible to have a single-valued aperture correction
MAGZRR	Photometric ZP error (mags). If this was a good photometric night the error in the zero-point will be at the level of a few percent. Values of 0.05 and above indicate correspondingly non-photometric nights and worse.
EXTINCT	Default extinction in passband. For WFCAM these are currently set to a constant clear night level, which within the current measuring erro r is the same for all passbands. Note that the frame-by-frame derived ZP from 2MASS automatically corrects for extinction variations, assuming they are uniform across the field of view. To compute approximate errors in the fluxes you can also use the following: error^2 = flux/gain + npixels x skynoise^2 where npixels is either the effective area ie. $\pi \times rcore^2$ for the "core" measures or the number of pixels above the detection isophote ie. areal profile1; gain is the final overall detector system gain. (see the Science Verification report for values); flux is whichever measure you are using but note that for "total" this formula is not accurate since "total" fluxes are derived using a rather convoluted curve-of-growth technique; average skynoise can be obtained from the catalogue fits header.
NUMZPT	Number of standards used. The actual number of standards used in the photometric calibration for the pointing
NIGHTZPT	Average photometric ZP (mags) for night. A robust estimate of the average ZP in a particualar passband for the night
NIGHTZRR	Photometric ZP sigma for night (mags).A robust estimate of the scatter in this ZPto give an indication of how photometric orotherwise the night was (0.03 or better is good; worse than 0.05 is usually indicative that the majority of the night was non-photometric).

Appendix B

Continuation of the Tables in Chapter 4

Table B.1: Stars with measured slopes in the colour-colour diagram or colour-magnitude diagrams. Median magnitudes and colours. The slopes were presentend in Table B.2.

	median										peak-to-peak				
ID	J	eJ	H	eH	K	eK	J-H	eJ-H	H-K	eH-K	J	H	K	J-H	H-K
CygOB2-000064	15.91	0.03	14.42	0.02	13.27	0.02	1.48	0.03	1.13	0.03	0.73	0.52	0.33	0.23	0.26
CygOB2-000116	13.14	0.02	12.15	0.02	11.41	0.02	0.98	0.03	0.74	0.03	0.17	0.17	0.22	0.09	0.11
CygOB2-000133	16.45	0.03	14.59	0.02	13.13	0.02	1.89	0.04	1.45	0.03	0.62	0.50	0.27	0.20	0.28
CygOB2-000217	16.49	0.03	15.04	0.02	14.14	0.02	1.47	0.04	0.97	0.03	0.48	0.45	0.48	0.18	0.25
CygOB2-000284	16.05	0.03	14.70	0.02	13.82	0.02	1.36	0.03	0.87	0.03	0.40	0.32	0.23	0.13	0.13
CygOB2-000291	13.73	0.02	12.29	0.02	11.23	0.02	1.44	0.03	1.05	0.03	0.35	0.26	0.15	0.11	0.15
CygOB2-000334	16.77	0.04	15.03	0.02	13.81	0.02	1.74	0.04	1.21	0.03	0.69	0.58	0.41	0.18	0.21
CygOB2-000381	16.38	0.03	15.05	0.02	14.35	0.02	1.36	0.04	0.73	0.03	0.76	0.90	0.53	0.23	0.42
CygOB2-000392	16.33	0.03	14.69	0.02	13.59	0.02	1.65	0.04	1.09	0.03	0.65	0.54	0.33	0.15	0.26
CygOB2-000432	16.34	0.03	14.88	0.02	13.87	0.02	1.48	0.04	0.99	0.03	0.94	0.74	0.54	0.25	0.35
CygOB2-000576	16.03	0.03	13.85	0.02	12.14	0.02	2.17	0.03	1.71	0.03	0.75	0.55	0.43	0.21	0.16
CygOB2-000744	13.93	0.02	12.72	0.02	11.96	0.02	1.23	0.03	0.76	0.03	0.14	0.22	0.35	0.10	0.16
CygOB2-000762	17.11	0.05	15.63	0.03	14.51	0.02	1.57	0.05	1.13	0.04	1.18	1.00	0.66	0.40	0.49
CygOB2-000771	15.05	0.02	13.80	0.02	13.06	0.02	1.24	0.03	0.75	0.03	0.76	0.63	0.44	0.19	0.22
CygOB2-000772	15.96	0.03	14.59	0.02	13.80	0.02	1.34	0.03	0.78	0.03	0.60	0.45	0.33	0.18	0.16
CygOB2-000795	14.88	0.02	13.49	0.02	12.58	0.02	1.40	0.03	0.93	0.03	0.37	0.25	0.19	0.16	0.17
CygOB2-000804	15.66	0.02	14.08	0.02	12.73	0.02	1.59	0.03	1.33	0.03	0.56	0.38	0.24	0.22	0.21
CygOB2-000807	16.30	0.03	14.92	0.02	13.89	0.02	1.38	0.04	1.02	0.03	1.10	0.80	0.54	0.31	0.32
CygOB2-000845	16.51	0.03	15.18	0.02	14.46	0.02	1.35	0.04	0.73	0.03	0.22	0.19	0.27	0.13	0.20
CygOB2-000860	16.90	0.04	15.46	0.03	14.60	0.02	1.42	0.04	0.89	0.03	0.63	0.50	0.38	0.21	0.27
CygOB2-000869	17.02	0.04	15.50	0.03	14.47	0.02	1.56	0.05	1.04	0.03	0.72	0.52	0.29	0.28	0.30
CygOB2-000871	16.56	0.03	15.13	0.02	14.34	0.02	1.45	0.04	0.83	0.03	0.57	0.48	0.37	0.17	0.21
CygOB2-000878	16.93	0.04	15.22	0.02	13.98	0.02	1.71	0.05	1.26	0.03	0.60	0.45	0.28	0.19	0.20

Table B.1: Continued.

	median										peak-to-peak				
ID	J	eJ	H	eH	K	eK	J-H	eJ-H	H-K	eH-K	J	H	K	J-H	H-K
CygOB2-000881	16.14	0.03	14.72	0.02	13.86	0.02	1.43	0.03	0.90	0.03	0.21	0.22	0.31	0.10	0.14
CygOB2-000898	15.60	0.02	14.07	0.02	12.84	0.02	1.55	0.03	1.19	0.03	1.14	0.82	0.48	0.38	0.37
CygOB2-000908	17.78	0.07	16.31	0.04	15.24	0.03	1.58	0.08	1.15	0.05	1.02	0.98	0.46	0.36	0.65
CygOB2-000920	16.21	0.03	14.80	0.02	13.94	0.02	1.39	0.04	0.85	0.03	0.71	0.55	0.40	0.19	0.23
CygOB2-010953	16.70	0.04	15.10	0.02	14.02	0.02	1.62	0.04	1.08	0.03	0.71	0.52	0.40	0.26	0.25
CygOB2-011072	13.37	0.02	12.14	0.02	10.96	0.02	1.25	0.03	1.18	0.03	0.34	0.22	0.13	0.16	0.12
CygOB2-011076	15.06	0.02	13.49	0.02	12.22	0.02	1.58	0.03	1.27	0.03	0.93	0.54	0.31	0.42	0.27
CygOB2-011083	17.29	0.05	15.74	0.03	14.82	0.02	1.58	0.06	0.95	0.04	0.94	0.78	0.58	0.27	0.26
CygOB2-011091	16.67	0.03	14.94	0.02	13.84	0.02	1.72	0.04	1.11	0.03	0.67	0.51	0.34	0.18	0.19
CygOB2-011098	16.86	0.04	15.19	0.02	14.09	0.02	1.69	0.04	1.12	0.03	0.37	0.26	0.24	0.20	0.19
CygOB2-021182	16.81	0.04	15.31	0.02	14.29	0.02	1.50	0.04	1.00	0.03	0.85	0.56	0.32	0.32	0.30
CygOB2-021183	16.94	0.04	15.30	0.02	14.22	0.02	1.64	0.04	1.10	0.03	0.51	0.34	0.26	0.22	0.19
CygOB2-021185	17.08	0.04	15.65	0.03	14.78	0.02	1.43	0.05	0.92	0.04	0.81	0.66	0.38	0.30	0.48
CygOB2-021188	16.63	0.03	14.35	0.02	12.70	0.02	2.28	0.04	1.61	0.03	0.41	0.30	0.53	0.32	0.38
CygOB2-021190	16.36	0.03	14.76	0.02	13.67	0.02	1.60	0.04	1.10	0.03	0.43	0.34	0.25	0.16	0.18
CygOB2-031401	17.00	0.04	15.34	0.03	14.10	0.02	1.74	0.05	1.23	0.03	0.82	0.58	0.24	0.38	0.38
CygOB2-041501	15.07	0.02	13.68	0.02	12.75	0.02	1.38	0.03	0.94	0.03	0.31	0.17	0.10	0.16	0.12
CygOB2-041554	13.51	0.02	12.29	0.02	11.30	0.02	1.24	0.03	0.97	0.03	0.50	0.35	0.26	0.17	0.14
CygOB2-041583	15.36	0.02	13.97	0.02	13.21	0.02	1.38	0.03	0.78	0.03	0.54	0.31	0.21	0.22	0.20
CygOB2-041640	15.10	0.02	13.67	0.02	12.64	0.02	1.44	0.03	1.03	0.03	0.40	0.28	0.22	0.17	0.19
CygOB2-041677	15.70	0.02	14.43	0.02	13.60	0.02	1.26	0.03	0.84	0.03	0.28	0.33	0.50	0.12	0.19
CygOB2-041678	15.96	0.03	14.55	0.02	13.58	0.02	1.42	0.03	0.98	0.03	0.34	0.28	0.30	0.13	0.17
CygOB2-041679	15.90	0.03	14.55	0.02	13.59	0.02	1.37	0.03	0.96	0.03	0.55	0.41	0.27	0.18	0.21
CygOB2-041684	15.28	0.02	13.84	0.02	12.61	0.02	1.45	0.03	1.24	0.03	0.54	0.34	0.20	0.24	0.20
CygOB2-041694	15.93	0.03	14.67	0.02	13.94	0.02	1.26	0.03	0.73	0.03	0.58	0.43	0.31	0.17	0.18
CygOB2-041695	15.86	0.03	14.53	0.02	13.73	0.02	1.33	0.03	0.80	0.03	0.64	0.49	0.36	0.16	0.16
CygOB2-041696	15.69	0.02	14.23	0.02	13.29	0.02	1.47	0.03	0.96	0.03	0.28	0.23	0.33	0.15	0.23
CygOB2-041697	16.00	0.03	14.60	0.02	13.80	0.02	1.36	0.03	0.80	0.03	0.71	0.53	0.33	0.19	0.25
CygOB2-041703	16.63	0.03	14.83	0.02	13.56	0.02	1.80	0.04	1.26	0.03	1.09	0.75	0.44	0.40	0.35
CygOB2-041762	17.83	0.06	16.40	0.05	14.77	0.03	2.10	0.07	1.68	0.05	0.82	1.84	1.61	0.23	0.63
CygOB2-041768	17.75	0.06	16.21	0.03	15.31	0.03	1.53	0.07	0.95	0.04	0.68	0.46	0.27	0.34	0.37
CygOB2-041774	14.55	0.02	13.09	0.02	11.95	0.02	1.47	0.03	1.13	0.03	0.31	0.24	0.21	0.12	0.12
CygOB2-051812	15.36	0.02	14.04	0.02	13.29	0.02	1.32	0.03	0.74	0.03	0.45	0.33	0.25	0.15	0.16
CygOB2-051813	14.98	0.02	13.51	0.02	12.48	0.02	1.47	0.03	1.03	0.03	0.42	0.30	0.24	0.16	0.15
CygOB2-051822	15.40	0.02	13.72	0.02	12.68	0.02	1.69	0.03	1.07	0.03	0.36	0.33	0.29	0.10	0.14
CygOB2-051825	16.60	0.03	15.07	0.02	13.98	0.02	1.53	0.04	1.10	0.03	0.50	0.39	0.32	0.20	0.14
CygOB2-051834	17.89	0.07	16.39	0.04	15.03	0.03	1.57	0.08	1.35	0.04	0.88	0.72	0.57	0.37	0.31
CygOB2-072205	15.00	0.02	13.77	0.02	12.90	0.02	1.23	0.03	0.86	0.03	0.34	0.28	0.34	0.14	0.21
CygOB2-072444	17.04	0.04	15.62	0.03	14.53	0.02	1.56	0.05	1.15	0.03	1.07	0.87	0.58	0.35	0.43
CygOB2-072490	16.12	0.03	14.80	0.02	13.80	0.02	1.33	0.04	1.00	0.03	0.42	0.33	0.22	0.16	0.18
CygOB2-072495	15.99	0.03	14.63	0.02	13.68	0.02	1.36	0.04	0.95	0.03	0.49	0.37	0.22	0.18	0.20

Table B.1: Continued.

	median										peak-to-peak				
ID	J	eJ	H	eH	K	eK	J-H	eJ-H	H-K	eH-K	J	H	K	J-H	H-K
CygOB2-072607	15.06	0.02	13.97	0.02	13.21	0.02	1.07	0.03	0.77	0.03	0.55	0.39	0.28	0.19	0.21
CygOB2-072621	14.42	0.02	13.34	0.02	12.65	0.02	1.08	0.03	0.70	0.03	0.46	0.42	0.37	0.16	0.25
CygOB2-072660	13.13	0.02	11.99	0.02	10.87	0.02	1.14	0.03	1.12	0.03	0.36	0.23	0.11	0.15	0.15
CygOB2-072662	15.27	0.02	13.99	0.02	13.10	0.02	1.28	0.03	0.87	0.03	0.66	0.48	0.32	0.21	0.23
CygOB2-072735	15.85	0.03	14.59	0.02	13.78	0.02	1.27	0.03	0.82	0.03	0.31	0.22	0.22	0.16	0.21
CygOB2-072739	16.32	0.03	14.94	0.02	14.16	0.02	1.39	0.04	0.75	0.03	1.22	0.87	0.53	0.46	0.40
CygOB2-072742	13.62	0.02	12.67	0.02	11.93	0.02	0.95	0.03	0.74	0.03	0.47	0.33	0.22	0.20	0.24
CygOB2-072755	15.19	0.02	14.15	0.02	13.59	0.02	1.03	0.03	0.58	0.03	0.37	0.30	0.24	0.09	0.13
CygOB2-072756	16.71	0.04	15.29	0.03	13.94	0.02	1.47	0.04	1.34	0.03	0.77	0.65	0.52	0.31	0.24
CygOB2-072775	16.71	0.04	15.34	0.03	14.13	0.02	1.40	0.05	1.20	0.03	0.96	0.79	0.73	0.31	0.22
CygOB2-072786	16.95	0.04	15.45	0.03	14.38	0.02	1.49	0.05	1.07	0.03	0.99	0.66	0.34	0.39	0.38
CygOB2-072791	16.08	0.03	14.76	0.02	13.82	0.02	1.36	0.04	0.93	0.03	0.58	0.42	0.37	0.22	0.28
CygOB2-072795	15.22	0.02	14.13	0.03	13.33	0.02	1.16	0.03	0.79	0.03	0.91	0.70	0.41	0.27	0.28
CygOB2-082898	16.65	0.03	15.03	0.02	13.90	0.02	1.60	0.04	1.13	0.03	0.81	0.66	0.41	0.26	0.29
CygOB2-082917	15.61	0.02	13.95	0.02	12.74	0.02	1.66	0.03	1.22	0.03	0.33	0.23	0.16	0.14	0.12
CygOB2-082918	16.19	0.03	14.83	0.02	14.07	0.02	1.36	0.04	0.77	0.03	0.50	0.34	0.21	0.20	0.17
CygOB2-082928	17.39	0.05	15.93	0.03	14.89	0.02	1.57	0.06	1.11	0.04	0.89	0.94	0.65	0.30	0.45
CygOB2-092962	15.21	0.02	13.90	0.02	13.10	0.02	1.31	0.03	0.80	0.03	0.13	0.16	0.30	0.09	0.18
CygOB2-092969	14.47	0.02	12.03	0.02	9.99	0.02	2.45	0.03	2.05	0.03	0.15	0.15	0.17	0.12	0.13
CygOB2-092989	15.89	0.03	14.55	0.02	13.67	0.02	1.36	0.03	0.90	0.03	0.38	0.32	0.32	0.12	0.20
CygOB2-093005	14.25	0.02	13.00	0.02	12.21	0.02	1.26	0.03	0.80	0.03	0.21	0.15	0.19	0.11	0.13
CygOB2-093173	15.15	0.02	13.67	0.02	12.54	0.02	1.46	0.03	1.13	0.03	1.79	1.31	0.77	0.53	0.58
CygOB2-093190	14.90	0.02	13.51	0.02	12.49	0.02	1.41	0.03	1.05	0.03	0.77	0.55	0.40	0.23	0.25
CygOB2-093197	14.54	0.02	12.95	0.02	11.75	0.02	1.59	0.03	1.20	0.03	0.35	0.23	0.17	0.16	0.16
CygOB2-093231	15.02	0.02	13.91	0.02	13.19	0.02	1.11	0.03	0.72	0.03	0.22	0.20	0.32	0.16	0.23
CygOB2-093245	15.75	0.02	14.37	0.02	13.51	0.02	1.39	0.03	0.86	0.03	0.31	0.25	0.20	0.09	0.10
CygOB2-093261	16.90	0.04	15.42	0.02	14.45	0.02	1.46	0.05	0.97	0.03	0.63	0.54	0.41	0.20	0.22
CygOB2-093266	16.47	0.03	15.04	0.02	14.05	0.02	1.45	0.04	1.00	0.03	0.67	0.51	0.33	0.23	0.24
CygOB2-103395	16.81	0.04	15.61	0.03	14.93	0.03	1.20	0.05	0.73	0.04	0.83	0.69	0.52	0.27	0.36
CygOB2-103567	16.15	0.03	14.78	0.02	13.82	0.02	1.35	0.03	0.99	0.03	0.23	0.25	0.33	0.13	0.13
CygOB2-103568	15.96	0.03	14.65	0.02	13.84	0.02	1.32	0.03	0.81	0.03	0.46	0.33	0.24	0.19	0.20
CygOB2-103573	14.48	0.02	13.33	0.02	12.48	0.02	1.15	0.03	0.86	0.03	0.18	0.20	0.28	0.11	0.14
CygOB2-103576	15.91	0.03	14.67	0.02	13.85	0.02	1.26	0.03	0.84	0.03	0.67	0.54	0.39	0.17	0.19
CygOB2-103643	14.98	0.02	13.70	0.02	12.86	0.02	1.28	0.03	0.84	0.03	0.41	0.32	0.21	0.12	0.16
CygOB2-103721	15.29	0.02	14.09	0.02	13.33	0.02	1.20	0.03	0.77	0.03	0.40	0.31	0.21	0.11	0.13
CygOB2-103741	15.39	0.02	14.04	0.02	13.09	0.02	1.36	0.03	0.95	0.03	0.15	0.18	0.24	0.07	0.09
CygOB2-103743	15.41	0.02	14.09	0.02	13.27	0.02	1.33	0.03	0.84	0.03	0.33	0.27	0.28	0.15	0.19
CygOB2-103757	15.38	0.02	14.14	0.02	13.38	0.02	1.25	0.03	0.76	0.03	0.32	0.29	0.27	0.11	0.13
CygOB2-103793	15.92	0.03	14.19	0.02	12.81	0.02	1.71	0.03	1.38	0.03	0.71	0.48	0.34	0.29	0.24
CygOB2-103795	13.57	0.02	12.35	0.02	11.10	0.02	1.21	0.03	1.26	0.03	0.25	0.15	0.08	0.11	0.09
CygOB2-103809	17.31	0.05	15.73	0.03	14.60	0.02	1.60	0.06	1.13	0.04	0.76	0.52	0.33	0.33	0.31

Table B.1: Continued.

	median										peak-to-peak				
ID	J	eJ	H	eH	K	eK	J-H	eJ-H	H-K	eH-K	J	H	K	J-H	H-K
CygOB2-103822	16.78	0.03	15.10	0.02	13.77	0.02	1.71	0.04	1.30	0.03	1.07	0.75	0.47	0.36	0.33
CygOB2-113903	15.37	0.02	13.61	0.02	12.32	0.02	1.75	0.03	1.29	0.03	0.64	0.41	0.24	0.25	0.22
CygOB2-113911	14.03	0.02	13.06	0.02	12.14	0.02	0.98	0.03	0.92	0.03	0.16	0.30	0.42	0.15	0.14
CygOB2-113937	15.29	0.02	14.19	0.02	13.41	0.02	1.10	0.03	0.83	0.03	1.00	0.74	0.41	0.31	0.46
CygOB2-114105	15.23	0.02	14.06	0.02	13.10	0.02	1.15	0.03	0.95	0.03	0.34	0.29	0.25	0.10	0.17
CygOB2-114111	15.36	0.02	13.91	0.02	12.84	0.02	1.45	0.03	1.06	0.03	0.46	0.33	0.22	0.16	0.15
CygOB2-114118	15.56	0.02	14.61	0.02	14.05	0.02	0.96	0.03	0.56	0.03	0.15	0.12	0.19	0.07	0.14
CygOB2-114159	16.13	0.03	15.00	0.02	14.25	0.02	1.16	0.04	0.81	0.03	0.68	0.60	0.45	0.15	0.23
CygOB2-114171	15.01	0.02	13.77	0.02	12.64	0.02	1.22	0.03	1.16	0.03	0.45	0.32	0.22	0.16	0.17
CygOB2-114182	16.53	0.03	15.32	0.02	14.66	0.02	1.23	0.04	0.69	0.03	0.20	0.20	0.45	0.16	0.33
CygOB2-114282	15.78	0.03	14.60	0.02	13.89	0.02	1.16	0.03	0.75	0.03	0.60	0.54	0.42	0.11	0.20
CygOB2-114307	16.50	0.03	15.02	0.02	14.15	0.02	1.47	0.04	0.88	0.03	0.53	0.38	0.24	0.18	0.19
CygOB2-124590	15.56	0.02	14.10	0.02	13.19	0.02	1.46	0.03	0.93	0.03	0.36	0.30	0.31	0.19	0.20
CygOB2-124604	14.76	0.02	13.41	0.02	12.49	0.02	1.36	0.03	0.93	0.03	0.33	0.23	0.15	0.11	0.11
CygOB2-124643	14.36	0.02	12.90	0.02	11.54	0.02	1.48	0.03	1.35	0.03	0.61	0.39	0.22	0.25	0.20
CygOB2-124656	13.21	0.02	12.18	0.02	11.37	0.02	1.04	0.03	0.81	0.03	0.43	0.29	0.17	0.15	0.14
CygOB2-124658	15.40	0.02	13.97	0.02	12.94	0.02	1.44	0.03	1.03	0.03	0.59	0.45	0.31	0.18	0.20
CygOB2-124663	16.58	0.03	15.08	0.02	14.06	0.02	1.52	0.04	1.03	0.03	0.47	0.36	0.23	0.18	0.21
CygOB2-124676	16.73	0.03	15.18	0.02	14.14	0.02	1.53	0.04	1.03	0.03	0.61	0.41	0.28	0.19	0.18
CygOB2-124680	15.13	0.02	13.70	0.02	12.52	0.02	1.41	0.03	1.18	0.03	0.64	0.44	0.25	0.25	0.24
CygOB2-124681	17.41	0.05	15.61	0.03	14.30	0.02	1.82	0.06	1.32	0.03	1.09	0.72	0.38	0.43	0.38
CygOB2-124682	15.92	0.03	14.68	0.02	13.95	0.02	1.24	0.03	0.75	0.03	0.46	0.40	0.28	0.12	0.15
CygOB2-124687	16.91	0.04	15.38	0.02	14.21	0.02	1.54	0.04	1.13	0.03	0.64	0.50	0.36	0.19	0.23
CygOB2-134755	14.16	0.02	12.68	0.02	11.55	0.02	1.47	0.03	1.13	0.03	0.41	0.31	0.22	0.16	0.13
CygOB2-134797	16.83	0.04	15.45	0.02	14.53	0.02	1.38	0.05	0.94	0.03	0.62	0.54	0.58	0.23	0.34
CygOB2-134811	16.36	0.03	15.03	0.02	14.14	0.02	1.35	0.04	0.87	0.03	0.40	0.29	0.23	0.17	0.23
CygOB2-134813	15.12	0.02	13.77	0.02	12.96	0.02	1.34	0.03	0.83	0.03	0.54	0.43	0.32	0.14	0.17
CygOB2-134824	16.37	0.03	15.13	0.02	14.36	0.02	1.25	0.04	0.78	0.03	0.65	0.53	0.40	0.18	0.24
CygOB2-134863	15.75	0.02	14.47	0.02	13.65	0.02	1.28	0.03	0.81	0.03	0.43	0.32	0.21	0.14	0.18
CygOB2-134874	15.89	0.03	14.36	0.02	13.27	0.02	1.52	0.03	1.11	0.03	1.05	0.71	0.40	0.35	0.34
CygOB2-134885	16.56	0.03	15.00	0.02	13.99	0.02	1.58	0.04	1.00	0.03	0.25	0.22	0.38	0.16	0.23
CygOB2-134952	16.23	0.03	14.84	0.02	13.92	0.02	1.39	0.04	0.95	0.03	0.62	0.54	0.41	0.15	0.23
CygOB2-134966	16.00	0.03	14.81	0.02	14.14	0.02	1.21	0.03	0.71	0.03	0.31	0.31	0.32	0.11	0.17
CygOB2-135034	15.24	0.02	13.84	0.02	12.86	0.02	1.41	0.03	0.98	0.03	0.37	0.25	0.17	0.16	0.15
CygOB2-135051	15.25	0.02	14.07	0.02	13.23	0.02	1.17	0.03	0.84	0.03	0.20	0.30	0.48	0.14	0.20
CygOB2-135053	14.23	0.02	13.13	0.02	12.57	0.02	1.10	0.03	0.58	0.03	0.20	0.16	0.11	0.06	0.09
CygOB2-135107	12.61	0.02	11.78	0.02	11.25	0.02	0.84	0.03	0.54	0.03	0.21	0.27	0.32	0.06	0.07
CygOB2-135205	16.28	0.03	14.84	0.02	14.03	0.02	1.46	0.04	0.79	0.03	0.79	0.55	0.33	0.28	0.22
CygOB2-135235	14.28	0.02	13.06	0.02	12.21	0.02	1.23	0.03	0.85	0.03	0.36	0.29	0.22	0.10	0.11
CygOB2-135273	14.86	0.02	13.67	0.02	12.89	0.02	1.20	0.03	0.77	0.03	0.23	0.22	0.29	0.13	0.18
CygOB2-135304	15.78	0.03	14.32	0.02	13.47	0.02	1.46	0.03	0.86	0.03	0.78	0.59	0.37	0.23	0.29

Table B.1: Continued.

	median										peak-to-peak				
ID	J	eJ	H	eH	K	eK	J-H	eJ-H	H-K	eH-K	J	H	K	J-H	H-K
CygOB2-135306	17.02	0.04	15.45	0.03	14.44	0.02	1.54	0.05	1.03	0.03	0.97	0.85	0.61	0.23	0.31
CygOB2-135309	15.40	0.02	13.94	0.02	13.06	0.02	1.45	0.03	0.89	0.03	0.45	0.36	0.30	0.11	0.17
CygOB2-135316	16.16	0.03	14.82	0.02	14.03	0.02	1.34	0.04	0.80	0.03	0.24	0.20	0.20	0.08	0.13
CygOB2-135337	15.80	0.03	14.48	0.02	13.63	0.02	1.33	0.03	0.86	0.03	0.67	0.52	0.38	0.19	0.19
CygOB2-135339	15.56	0.02	14.32	0.02	13.60	0.02	1.28	0.03	0.73	0.03	0.33	0.27	0.27	0.14	0.23
CygOB2-135341	15.71	0.03	14.36	0.02	13.54	0.02	1.36	0.03	0.85	0.03	0.50	0.38	0.28	0.14	0.16
CygOB2-135342	16.47	0.03	15.18	0.02	14.41	0.02	1.31	0.04	0.80	0.03	0.53	0.43	0.31	0.17	0.19
CygOB2-135350	16.12	0.03	14.74	0.02	13.80	0.02	1.38	0.04	0.94	0.03	0.56	0.43	0.28	0.18	0.19
CygOB2-135351	15.00	0.02	13.57	0.02	12.64	0.02	1.43	0.03	0.94	0.03	0.32	0.23	0.15	0.11	0.10
CygOB2-135356	15.80	0.03	14.49	0.02	13.69	0.02	1.32	0.03	0.80	0.03	0.22	0.21	0.29	0.10	0.15
CygOB2-135362	16.85	0.04	15.46	0.03	14.51	0.02	1.40	0.05	0.96	0.03	0.73	0.55	0.40	0.27	0.39
CygOB2-135364	17.11	0.04	15.27	0.02	13.88	0.02	1.83	0.05	1.39	0.03	0.95	0.68	0.45	0.34	0.29
CygOB2-135366	16.19	0.03	14.31	0.02	12.94	0.02	1.89	0.04	1.38	0.03	0.39	0.27	0.19	0.15	0.13
CygOB2-135377	16.42	0.03	14.73	0.02	13.51	0.02	1.69	0.04	1.21	0.03	0.77	0.61	0.42	0.20	0.23
CygOB2-135385	16.30	0.03	14.66	0.02	13.55	0.02	1.65	0.04	1.13	0.03	0.80	0.46	0.22	0.37	0.33
CygOB2-135393	16.10	0.03	14.71	0.02	13.74	0.02	1.38	0.03	0.97	0.03	0.68	0.51	0.31	0.21	0.26
CygOB2-135404	16.59	0.03	15.08	0.02	14.01	0.02	1.52	0.04	1.08	0.03	0.47	0.35	0.29	0.17	0.16
CygOB2-135408	18.26	0.08	16.57	0.04	15.06	0.03	1.80	0.09	1.51	0.05	0.70	0.66	0.54	0.40	0.35
CygOB2-135431	16.35	0.03	14.92	0.02	14.13	0.02	1.44	0.04	0.78	0.03	0.68	0.54	0.42	0.15	0.15
CygOB2-135432	16.09	0.03	14.50	0.02	13.35	0.02	1.58	0.04	1.18	0.03	0.62	0.44	0.27	0.24	0.23
CygOB2-145446	15.27	0.02	14.19	0.02	13.57	0.02	1.09	0.03	0.65	0.03	0.41	0.30	0.27	0.17	0.20
CygOB2-155488	14.83	0.02	13.60	0.02	12.70	0.02	1.24	0.03	0.91	0.03	0.39	0.32	0.29	0.13	0.16
CygOB2-145614	14.99	0.02	13.72	0.02	12.54	0.02	1.29	0.03	1.13	0.03	0.37	0.26	0.21	0.17	0.13
CygOB2-145627	16.47	0.03	15.15	0.02	14.21	0.02	1.33	0.04	0.92	0.03	0.61	0.49	0.39	0.20	0.22
CygOB2-145633	16.98	0.04	15.26	0.02	13.90	0.02	1.75	0.04	1.35	0.03	0.72	0.60	0.42	0.31	0.29
CygOB2-145642	12.88	0.02	12.04	0.02	11.27	0.02	0.86	0.03	0.78	0.03	0.21	0.18	0.16	0.08	0.11

Table B.2: . Stars with measured slopes in the colour-colour diagram or colour-magnitude diagrams. The table shows their coordinates, slopes of variability and informationa about their variability. Stars with valid GDW13 ID were disc-bearing stars.

								Slopes (°)					
ID	RA (h:m:s)	Dec (d:m:s)	GDW13	GWD15	Type[1]	Per?[2]	Stetson	$\frac{\Delta J-H}{\Delta(H-K)}$	err	$\frac{\Delta K}{\Delta(H-K)}$	err	$\frac{\Delta J}{\Delta(J-H)}$	err
CygOB2-000064	20:32:15	+41:11:10	11704	1269	2		5.79	42.61	0.05			73.11	0.14
CygOB2-000116	20:32:25	+41:17:22	29903	1482	2		2.04	41.23	0.1				
CygOB2-000133	20:32:27	+41:15:16	67478	1531	2		4.52	35.51	0.05			73.74	0.19
CygOB2-000217	20:32:38	+41:12:01	308405	1822	2		4.1	32.72	0.06				
CygOB2-000284	20:32:46	+41:16:47	31382	2006	1	1	3.33	44.49	0.15			75.75	0.47
CygOB2-000291	20:32:46	+41:10:42	10284	2016	2		2.97	35.67	0.05			74.25	0.19
CygOB2-000334	20:32:50	+41:14:59	67108	2124	2		5.91	38.93	0.09	65.6	0.26	77.32	1.24
CygOB2-000381	20:32:54	+41:10:07	73793	2249	2		5.48	31.61	0.05			73.41	0.27

Table B.2: Continued...

ID	RA (h:m:s)	Dec (d:m:s)	GDW13	GWD15	Type[1]	Per?[2]	Stetson	$\frac{\Delta J-H}{\Delta(H-K)}$	err	$\frac{\Delta K}{\Delta(H-K)}$	err	$\frac{\Delta J}{\Delta(J-H)}$	err
CygOB2-000392	20:32:55	+41:09:02	73721	2266	2		4.97	26.8	0.04			80.01	0.65
CygOB2-000432	20:32:58	+41:17:35		2355	2		7.8	34.5	0.04			77.12	0.89
CygOB2-000576	20:33:06	+41:16:35	66361	2652	2		7.12	49.37	0.16			77.32	1.0
CygOB2-000744	20:33:13	+41:11:33	312145	2972	1		3.02	31.46	0.04	-67.83	0.13		
CygOB2-000762	20:33:14	+41:13:46	65768	3009	1	1	7.91	36.69	0.08			77.79	4.82
CygOB2-000771	20:33:14	+41:12:22	292858	3029	1	1	7.65	40.88	0.06	70.78	0.25	78.06	11.98
CygOB2-000772	20:33:14	+41:12:24		3032	1	1	5.65	47.42	0.17			74.77	0.2
CygOB2-000795	20:33:16	+41:08:28	72761	3083	1	1	2.53	43.23	0.07			69.2	0.17
CygOB2-000804	20:32:06	+41:12:24	10595		2		3.82	46.61	0.08			70.21	0.16
CygOB2-000807	20:32:14	+41:16:05	11995		1	1	8.75	41.38	0.06	63.73	0.35	75.99	0.26
CygOB2-000845	20:32:07	+41:18:14	68446		2		1.51	27.13	0.05	-60.66	0.72		
CygOB2-000860	20:33:07	+41:07:51	73267		2		4.04	35.37	0.07			74.76	0.38
CygOB2-000869	20:32:49	+41:10:32	73827		2		3.76	43.24	0.08			70.32	0.15
CygOB2-000871	20:32:38	+41:06:00	73946		3		4.1	34.26	0.06				
CygOB2-000878	20:32:41	+41:09:47	74085		2		5.17	43.81	0.1	58.44	1.72	74.36	0.18
CygOB2-000881	20:32:35	+41:06:36	74147		2		2.36	31.24	0.05	-69.66	0.25		
CygOB2-000898	20:33:14	+41:13:04	101288		2		10.19	44.48	0.13	55.71	0.92	74.18	0.25
CygOB2-000908	20:32:52	+41:17:42	112350		2		4.66	28.76	0.07			72.03	0.25
CygOB2-000920	20:33:12	+41:11:40	312016		3		5.89	38.09	0.06			77.73	2.3
CygOB2-010953	20:34:34	+41:15:41	92649	4831	1	1	4.46	45.59	0.11			73.14	0.29
CygOB2-011072	20:34:27	+41:11:31	16491		2		2.52	54.91	0.49			67.19	0.16
CygOB2-011076	20:34:52	+41:14:07	18989		2		7.07	57.55	16.44			66.5	0.08
CygOB2-011083	20:34:28	+41:17:36	63764		1		7.1	46.44	0.18	69.35	0.18	76.33	0.39
CygOB2-011091	20:35:03	+41:10:01	98617		1	1	5.39	42.76	0.08	62.07	0.29	75.48	0.23
CygOB2-011098	20:34:59	+41:12:02	102105		2		1.84	42.34	0.11				
CygOB2-021182	20:34:47	+41:41:59	93709		1		5.87	44.12	0.1			71.78	0.15
CygOB2-021183	20:35:24	+41:34:38	94590		2		2.63	45.14	0.17			70.9	0.32
CygOB2-021185	20:34:53	+41:40:18	95624		2		3.82	32.04	0.05			70.56	0.11
CygOB2-021188	20:35:06	+41:39:32	96834		2		0.99	38.16	0.06	-55.69	0.92		
CygOB2-021190	20:35:14	+41:34:00	97877		1	1	3.24	33.94	0.09				
CygOB2-031401	20:32:15	+41:36:36	11488		2		3.69	50.36	0.24			65.32	0.18
CygOB2-041501	20:32:33	+41:03:05	10555	1676	2		1.97					64.29	0.18
CygOB2-041554	20:32:51	+40:59:43	21399	2137	2		5.02	52.02	0.18			72.68	0.16
CygOB2-041583	20:32:58	+41:03:47	32121	2344	3		3.37	46.07	0.12			65.81	0.17
CygOB2-041640	20:33:10	+40:59:08	32879	5514	2		2.73	40.86	0.08			71.01	0.23
CygOB2-041677	20:32:17	+40:56:02	7586		1	1	4.24	28.84	0.05	-71.78	0.19		
CygOB2-041678	20:32:21	+41:01:34	8131		3		2.9	34.65	0.07				
CygOB2-041679	20:32:24	+41:01:46	8206		3		4.45	38.12	0.06			73.8	0.14
CygOB2-041684	20:32:04	+40:59:24	9710		2		3.32	48.49	0.14			63.65	0.27
CygOB2-041694	20:32:50	+40:58:56	22214		3		4.72	42.13	0.11			75.54	0.3
CygOB2-041695	20:33:02	+41:02:33	22861		3		5.75	44.12	0.1	70.91	0.26	77.31	0.81
CygOB2-041696	20:33:02	+41:03:28	23012		2		2.13	32.8	0.04	-60.8	0.69		

Table B.2: Continued...

ID	RA (h:m:s)	Dec (d:m:s)	GDW13	GWD15	Type[1]	Per?[2]	Stetson	$\frac{\Delta J-H}{\Delta(H-K)}$	err	$\frac{\Delta K}{\Delta(H-K)}$	err	$\frac{\Delta J}{\Delta(J-H)}$	err
CygOB2-041697	20:33:07	+41:01:44	24989		2		5.74	36.49	0.04			75.96	0.28
CygOB2-041703	20:32:25	+41:05:24	74316		2		7.65	47.79	0.16	55.13	0.86	71.37	0.13
CygOB2-041762	20:32:43	+40:53:05	89816		2		10.42	35.71	0.11	63.14	0.33	76.18	0.73
CygOB2-041768	20:32:56	+41:01:53	107307		2		1.92	39.29	0.11			62.82	0.31
CygOB2-041774	20:32:38	+41:03:46	308366		2		2.58	45.65	0.11				
CygOB2-051812	20:34:32	+40:54:38	15614		1	1	3.68	31.58	0.04				
CygOB2-051813	20:35:14	+40:57:34	17119		2		3.35	47.9	0.16			71.93	0.18
CygOB2-051822	20:35:34	+41:01:20	91831		2		3.68	30.71	0.06				
CygOB2-051825	20:34:40	+40:54:51	92082		2		3.4	49.02	0.26			73.93	0.41
CygOB2-051834	20:34:40	+41:04:32	109965		2		4.97	48.65	0.3			74.68	0.57
CygOB2-072205	20:32:20	+41:20:13	62679	1374	1		3.36	26.18	0.06				
CygOB2-072444	20:32:45	+41:20:17	62285	1992	1	1	7.39	39.73	0.13			72.59	0.2
CygOB2-072490	20:32:51	+41:23:35	57153	2143	2		2.93	39.77	0.1				
CygOB2-072495	20:32:52	+41:20:38	22521	2160	2		3.66	45.9	0.13			72.53	0.18
CygOB2-072607	20:33:05	+41:24:16	55994	2603	3		4.18	40.91	0.07			72.86	0.21
CygOB2-072621	20:33:05	+41:21:39	32560	2636	3		4.09	27.82	0.05				
CygOB2-072660	20:33:09	+41:19:15	32794	2796	2		2.46					68.43	0.11
CygOB2-072662	20:33:09	+41:21:10	32802	2799	3		5.29	42.03	0.1			74.0	0.21
CygOB2-072735	20:32:05	+41:20:55	12792		1		1.6	33.45	0.07			67.23	0.28
CygOB2-072739	20:32:19	+41:20:23	29561		2		7.75	49.31	0.23	54.62	0.74	70.18	0.11
CygOB2-072742	20:32:24	+41:21:00	29804		2		3.16	37.09	0.05			71.01	0.15
CygOB2-072755	20:32:55	+41:27:51	31895		1	1	3.49	35.88	0.08			78.84	1.05
CygOB2-072756	20:33:04	+41:25:45	32455		2		5.98	52.59	0.45				
CygOB2-072775	20:32:36	+41:25:41	57441		2		7.79	54.41	0.66				
CygOB2-072786	20:33:03	+41:20:38	62091		2		5.03	45.64	0.12			69.77	0.13
CygOB2-072791	20:32:54	+41:20:28	85047		3		3.59	37.93	0.08			71.91	0.32
CygOB2-072795	20:32:57	+41:27:52	101388		2		8.48	42.59	0.07	60.13	0.94	75.15	0.19
CygOB2-082898	20:32:02	+41:01:56	82822	1012	1		6.25	43.9	0.08	64.09	0.35	75.32	0.32
CygOB2-082917	20:31:58	+41:00:23	5617		2		2.38	51.18	0.26			69.95	0.21
CygOB2-082918	20:31:56	+41:00:34	5618		2		3.74	52.64	0.27			68.79	0.08
CygOB2-082928	20:32:00	+40:59:17	82650		2		6.0	34.76	0.07				
CygOB2-092962	20:33:16	+40:58:47	80010	3106	2		1.79	23.85	0.03	-60.44	0.39		
CygOB2-092969	20:33:18	+40:59:17	91633		2		1.01	38.75	0.13				
CygOB2-092989	20:33:20	+41:04:04	76293	3279	1		3.3	26.63	0.04				
CygOB2-093005	20:33:23	+41:04:03	25003	3389	2		1.39	36.39	0.06				
CygOB2-093173	20:34:07	+41:02:13	13214	4444	2		15.64	42.87	0.03	55.39	0.55	74.15	0.09
CygOB2-093190	20:34:09	+41:00:03	16736	4492	3		7.0	41.93	0.07			75.96	0.41
CygOB2-093197	20:34:12	+40:59:35	13692	4528	3		2.21	46.32	0.11			67.5	0.18
CygOB2-093231	20:34:08	+40:54:17	13506		2		1.36	33.84	0.03				
CygOB2-093245	20:34:07	+41:04:33	76032		2		2.8	35.39	0.08			78.33	3.35
CygOB2-093261	20:33:54	+41:02:08	78739		2		5.06	35.47	0.08				
CygOB2-093266	20:33:25	+40:58:35	79430		2		4.54	44.09	0.09			73.0	0.25

Table B.2: Continued...

ID	RA (h:m:s)	Dec (d:m:s)	GDW13	GWD15	Type[1]	Per?[2]	Stetson	$\frac{\Delta J-H}{\Delta(H-K)}$	err	$\frac{\Delta K}{\Delta(H-K)}$	err	$\frac{\Delta J}{\Delta(J-H)}$	err
CygOB2-103395	20:33:25	+41:20:01		3455	3		5.26	27.81	0.06				
CygOB2-103567	20:33:44	+41:20:55	34327	3985	2		2.63	32.53	0.08				
CygOB2-103568	20:33:44	+41:19:40	34338	3988	3		3.29	36.12	0.08			73.41	0.29
CygOB2-103573	20:33:45	+41:21:33	34374	4006	2		2.25	36.79	0.06				
CygOB2-103576	20:33:45	+41:28:50	14164	4010	3		6.69	38.11	0.07	65.37	0.24	77.74	1.81
CygOB2-103643	20:33:55	+41:20:01	34705	4234	2		3.68	39.49	0.08			75.23	0.27
CygOB2-103721	20:34:10	+41:20:07	20586	4499	2		3.8	37.15	0.06			76.94	0.58
CygOB2-103741	20:34:16	+41:22:08	25803	4584	2		2.45	29.81	0.07	-73.96	0.26		
CygOB2-103743	20:34:16	+41:26:26	25858	4588	3		2.69	35.1	0.06				
CygOB2-103757	20:34:20	+41:30:47	15967	4644	2		3.16	34.99	0.07				
CygOB2-103793	20:33:53	+41:31:24	24723		1		5.19	50.29	0.16			70.69	0.17
CygOB2-103795	20:33:30	+41:18:46	33817		2		2.0					67.69	0.1
CygOB2-103809	20:33:50	+41:30:37	38176		2		3.57	43.78	0.14			69.27	0.18
CygOB2-103822	20:33:26	+41:26:44	54486		2		7.48	48.77	0.1	60.83	0.73	71.5	0.09
CygOB2-113903	20:31:09	+41:19:05	13040	221	2		5.2	49.68	0.16			69.43	0.11
CygOB2-113911	20:31:11	+41:21:56	13016	237	2		3.67	47.87	0.13	-73.41	0.12	-47.62	0.16
CygOB2-113937	20:31:17	+41:30:01	27853	296	2		7.98	33.36	0.03			73.85	0.14
CygOB2-114105	20:31:46	+41:28:14	301855	692	2		3.23	29.45	0.04				
CygOB2-114111	20:31:46	+41:19:50	12303	704	2		3.87	46.7	0.12			73.53	0.22
CygOB2-114118	20:31:48	+41:24:28	5076	723	2		1.07	24.85	0.05	-58.55	2.24		
CygOB2-114159	20:31:52	+41:26:10		807	1	1	6.4	35.34	0.07			79.69	0.64
CygOB2-114171	20:31:54	+41:25:34	8795	834	3		3.6	44.48	0.07			72.52	0.23
CygOB2-114182	20:31:55	+41:24:33		852	2		1.44	21.04	0.03	-55.09	0.42		
CygOB2-114282	20:31:56	+41:27:36	5725		3	1	5.99	25.55	0.04			82.2	1.42
CygOB2-114307	20:31:26	+41:19:19	63083		2		3.43	40.36	0.12			71.39	0.21
CygOB2-124590	20:31:53	+41:14:30	6853	827	1		2.99	41.31	0.11			76.3	0.57
CygOB2-124604	20:31:56	+41:15:07	6744	890	3		2.92	45.84	0.13			73.65	0.22
CygOB2-124643	20:31:43	+41:06:19	3196		2		5.06	51.9	0.18	51.4	0.32	68.89	0.12
CygOB2-124656	20:31:23	+41:14:58	13161		2		3.59	47.58	0.15			70.76	0.13
CygOB2-124658	20:31:54	+41:17:36	28500		3	1	5.04	42.85	0.09				
CygOB2-124663	20:31:56	+41:14:07	68618		2		3.06	43.56	0.1			71.99	0.2
CygOB2-124676	20:31:50	+41:08:20	74910		2		4.11	43.26	0.11			74.4	0.24
CygOB2-124680	20:31:54	+41:09:29	85665		2		4.59	45.68	0.08			70.35	0.14
CygOB2-124681	20:31:07	+41:08:17	85875		2		5.67	47.81	0.11	48.79	0.22	69.28	0.08
CygOB2-124682	20:31:13	+41:12:29	85886		1	1	4.35	33.57	0.07			78.48	2.05
CygOB2-124687	20:31:15	+41:15:28	89096		2		4.78	38.08	0.08			76.2	0.49
CygOB2-134755	20:33:19	+41:14:37	66061	3224	2		3.37	50.86	0.19			71.69	0.19
CygOB2-134797	20:33:21	+41:12:08	69819	3318	2		4.15	30.98	0.04				
CygOB2-134811	20:33:22	+41:14:24	65530	3347	2		2.06	33.06	0.06			71.66	0.26
CygOB2-134813	20:33:22	+41:09:45	24875	3353	1	1	5.8	38.69	0.05			78.12	7.59
CygOB2-134824	20:33:22	+41:17:37	33537	3371	2		4.92	30.85	0.06				
CygOB2-134863	20:33:26	+41:13:33	65505	3482	3		3.29	36.75	0.07			73.6	0.25

Table B.2: Continued...

ID	RA (h:m:s)	Dec (d:m:s)	GDW13	GWD15	Type[1]	Per?[2]	Stetson	$\frac{\Delta J-H}{\Delta(H-K)}$	err	$\frac{\Delta K}{\Delta(H-K)}$	err	$\frac{\Delta J}{\Delta(J-H)}$	err
CygOB2-134874	20:33:27	+41:15:04	65557	3500	1		8.16	46.11	0.05	51.59	0.29	71.36	0.07
CygOB2-134885	20:33:27	+41:13:20	65499	3514	2		1.82	29.65	0.04	-61.41	0.44		
CygOB2-134952	20:33:33	+41:12:52	23815	3675	3		5.46	33.36	0.04			79.25	0.86
CygOB2-134966	20:33:35	+41:17:20		3723	1	1	3.14	28.26	0.05				
CygOB2-135034	20:33:42	+41:13:23	315413	3909	2		2.7	41.07	0.06			71.14	0.16
CygOB2-135051	20:33:44	+41:11:01	23068	3971	2		3.8	33.98	0.06	-67.42	0.12		
CygOB2-135053	20:33:44	+41:09:19	13615	3982	2		1.66					76.41	0.61
CygOB2-135107	20:33:49	+41:14:09		4106	3		3.85	41.06	0.11	-79.67	0.53	-77.24	1.44
CygOB2-135205	20:34:06	+41:07:27	71757	4423	2		5.66	51.07	0.26	60.22	0.57	74.27	0.31
CygOB2-135235	20:34:11	+41:08:15	16692	4511	1	1	3.63	39.17	0.08			77.93	9.01
CygOB2-135273	20:34:18	+41:09:14	35196	4608	2		1.86	34.01	0.05				
CygOB2-135304	20:34:22	+41:10:01		4676	1		5.9	37.35	0.05			74.85	0.29
CygOB2-135306	20:34:22	+41:15:18	63724	4683	2		7.37	35.9	0.06			78.57	1.12
CygOB2-135309	20:34:22	+41:06:52	35272	4686	1	1	4.51	38.87	0.09			78.17	5.41
CygOB2-135316	20:34:23	+41:11:54	15335	4704	1		2.27	28.85	0.06				
CygOB2-135337	20:34:18	+41:11:47	20941		1		5.62	44.64	0.1			75.6	0.3
CygOB2-135339	20:33:39	+41:06:49	21010		2		2.53	29.3	0.04				
CygOB2-135341	20:34:03	+41:12:14	22550		3		4.38	40.7	0.07			76.74	0.74
CygOB2-135342	20:33:44	+41:16:36	22710		3	1	4.15	39.02	0.09			75.1	0.42
CygOB2-135350	20:33:58	+41:16:56	34787		1		4.77	41.2	0.1			75.01	0.27
CygOB2-135351	20:34:04	+41:07:02	34960		2		2.78	48.43	0.18			72.86	0.18
CygOB2-135356	20:34:17	+41:15:51	64015		2		2.0	29.1	0.04				
CygOB2-135362	20:34:00	+41:14:53	64465		2		3.88	34.14	0.05			72.29	0.23
CygOB2-135364	20:33:41	+41:14:40	64666		2		6.24	48.32	0.14	61.11	0.62	71.81	0.15
CygOB2-135366	20:33:41	+41:15:13	64711		2		3.0	49.31	0.17			71.35	0.17
CygOB2-135377	20:33:17	+41:15:38	65887		2		6.62	39.83	0.08	64.26	0.27	77.26	0.91
CygOB2-135385	20:34:14	+41:09:46	71357		2		4.63	48.43	0.08			65.83	0.1
CygOB2-135393	20:33:45	+41:08:32	72295		2		4.89	37.52	0.06			74.43	0.22
CygOB2-135404	20:33:20	+41:08:09	72749		1	1	3.71	45.02	0.13				
CygOB2-135408	20:33:38	+41:14:27	93574		2		3.75	44.81	0.24			68.09	0.59
CygOB2-135431	20:33:35	+41:08:01	292890		1	1	6.08	44.89	0.13	74.8	0.34	79.1	0.62
CygOB2-135432	20:34:11	+41:17:06	293225		2		4.78	47.17	0.1			70.84	0.13
CygOB2-145446	20:33:17	+41:33:44	293356	3132	3	1	3.04	28.19	0.06				
CygOB2-155488	20:31:56	+41:43:15	7003		3		3.62	34.25	0.08				
CygOB2-145614	20:34:06	+41:37:31	14240		2		2.87	51.29	0.18			69.34	0.24
CygOB2-145627	20:34:20	+41:41:44	15379	5557	3	1	4.63	44.03	0.14			76.1	0.62
CygOB2-145633	20:33:48	+41:33:38	38415		1		4.87	47.23	0.19			70.76	0.26
CygOB2-145642	20:34:22	+41:35:44	16165		2		1.71	32.35	0.07				

[1]Per? equal to 1 means the star had reliable period measured.

[2]Variability type according to the morphological of the light curves. 1- Possibly Periodic; 2- Other type of variables; 3- Eclipse-like variables.

Appendix C

Periodic stars parameters

The 894 periodic stars with $P \geq 2$ days are listed in Table C.1 which shows their ID inside our variability survey catalogue, their ID in the catalogues presented by GDW13, and GDW15, their coordinates in the present study; Stetson variability Index (Section 4.2), Period (Section 4.3); Mass, and Av (Section 3.5), median J, H, and K magnitudes, their propagated errors, and their ptp amplitude for each band (Section 4.4.3); their IR-class according to GDW13 (Sections 3.6, and 6.2), and a flag indicating the presence of disc, assuming the value 1 for disc-bearing stars, and 0 for non disc-bearing stars.

Table C.1: Rotational periods for CygOB2 periodic candidate members.

Id	GDW13	GDW15	RA	Dec	Stet	Per	Mass	Av	mJ	eJ	ptpJ	mH	eH	ptpH	mK	eK	ptpK	Class[1]	Disc[2]
(CysOB2-)			(h:m:s)	(d:m:s)		(day)	($M_\odot$)	(mag)	(mag)	(mag)	(mag)	(mag)	(mag)	(mag)	(mag)	(mag)	(mag)		
0000191	1726		20:32:35	+41:11:43	0.79	5.17	0.5	4.84	14.8	0.1	0.02	13.6	0.02	0.07	13.0	0.02	0.06		
0000193	1730		20:32:35	+41:08:01	0.92	4.25	0.63	5.86	16.23	0.09	0.03	14.89	0.02	0.09	14.22	0.02	0.07		
0000194	1734		20:32:36	+41:16:25	0.63	3.13	0.62	5.02	16.34	0.1	0.03	14.95	0.02	0.06	14.24	0.02	0.06		
0000197	1748		20:32:36	+41:12:48	0.77	3.37			17.64	0.18	0.06	16.23	0.03	0.18	15.5	0.03	0.14		
0000206	1781		20:32:37	+41:06:05	1.13	15.16	0.68	6.07	16.43	0.13	0.03	15.14	0.02	0.11	14.52	0.02	0.09		
0000208	1790		20:32:38	+41:17:12	0.87	3.21	0.47	4.75	17.28	0.19	0.05	15.99	0.03	0.14	15.36	0.03	0.12		
0000213	1809	10731	20:32:38	+41:08:32	1.25	8.22	0.54	5.29	15.46	0.1	0.02	14.21	0.02	0.11	13.53	0.02	0.13	CL2	1
0000215	1812		20:32:38	+41:14:42	0.50	3.34	0.63	3.77	12.65	0.05	0.02	11.97	0.02	0.05	11.55	0.02	0.05		
0000216	1816		20:32:38	+41:11:42	0.57	2.6	0.34	4.24	15.92	0.07	0.03	14.55	0.02	0.06	13.9	0.02	0.06		
0000226	1860		20:32:40	+41:13:48	0.49	8.93	0.49	4.26	16.5	0.09	0.03	15.21	0.02	0.07	14.62	0.02	0.06		
0000231	1872		20:32:40	+41:17:41	0.54	2.1	0.53	4.05	15.54	0.07	0.02	14.32	0.02	0.06	13.74	0.02	0.05		
0000244	1908		20:32:42	+41:15:56	1.10	2.09	0.55	4.03	16.13	0.11	0.03	14.9	0.02	0.1	14.31	0.02	0.09		
0000247	1916		20:32:42	+41:17:12	1.73	11.69	0.43	3.53	16.63	0.21	0.03	15.39	0.02	0.19	14.81	0.02	0.16		
0000251	1927	74025	20:32:43	+41:07:57	1.10	10.37	0.54	5.45	16.79	0.16	0.04	15.49	0.02	0.13	14.84	0.02	0.13	CL2	1
0000254	1937		20:32:43	+41:13:59	0.91	7.04	0.47	4.11	15.14	0.08	0.02	13.94	0.02	0.07	13.36	0.02	0.07		
0000255	1938		20:32:43	+41:17:42	0.85	7.29	0.63	3.49	15.92	0.11	0.03	14.82	0.02	0.08	14.31	0.02	0.07		
0000258	1944		20:32:43	+41:15:14	2.94	6.63			16.3	0.31	0.03	15.07	0.02	0.3	14.49	0.02	0.23		
0000259	1946		20:32:43	+41:11:03	1.11	8.25			16.22	0.12	0.03	14.92	0.02	0.11	14.3	0.02	0.11		
0000261	1953		20:32:44	+41:05:54	0.46	3.37	0.64	4.72	15.32	0.06	0.02	14.18	0.02	0.05	13.66	0.02	0.05		
0000262	1954	73882	20:32:44	+41:05:35	1.26	4.05	0.57	5.45	15.68	0.14	0.02	14.32	0.02	0.14	13.54	0.02	0.13	CL2_PTD	
0000273	1984		20:32:45	+41:08:58	1.45	6.62	0.63	5.39	16.03	0.13	0.03	14.79	0.02	0.12	14.19	0.02	0.11		
0000275	1991		20:32:45	+41:17:26	0.30	6.52	0.57	5.21	16.35	0.07	0.03	15.16	0.02	0.05	14.58	0.02	0.05		
0000281	2004		20:32:46	+41:14:41	0.51	9.65	0.63	5.03	16.38	0.1	0.03	15.13	0.02	0.07	14.58	0.02	0.07		
0000282	2003		20:32:46	+41:06:39	0.47	5.72	0.58	4.88	14.59	0.06	0.02	13.41	0.02	0.04	12.86	0.02	0.05		
0000283	2005		20:32:46	+41:16:59	0.79	9.08	0.19	2.08	16.94	0.15	0.04	15.71	0.03	0.12	15.15	0.03	0.11		
0000284	2006	31382	20:32:46	+41:16:47	3.33	9.62	0.68	4.88	16.07	0.4	0.03	14.72	0.02	0.32	13.83	0.02	0.23	CL2	1
0000287	2012		20:32:46	+41:17:58	1.03	3.28	0.7	4.37	16.18	0.12	0.03	15.0	0.02	0.1	14.48	0.02	0.08		
0000292	2021		20:32:46	+41:08:10	0.43	12.62	0.6	4.64	16.78	0.1	0.03	15.55	0.03	0.07	14.98	0.02	0.06		
0000295	2024		20:32:46	+41:07:14	0.40	9.86	0.63	4.57	14.58	0.06	0.02	13.5	0.02	0.04	13.0	0.02	0.04		

Table C.1: Continued.

Id	GDW13	GDW15	RA	Dec	Stet	Per	Mass	Av	mJ	eJ	ptpJ	mH	eH	ptpH	mK	eK	ptpK	Class	Disk
0000303	2055		20:32:47	+41:05:54	0.39	8.74	0.55	4.74	15.32	0.06	0.02	14.08	0.02	0.05	13.51	0.02	0.05		
0000313	2076		20:32:48	+41:14:40	1.52	5.09	0.49	5.04	15.87	0.12	0.02	14.61	0.02	0.12	13.99	0.02	0.1		
0000315	2080		20:32:49	+41:08:50	0.60	3.34	0.6	5.53	16.69	0.11	0.03	15.41	0.02	0.07	14.79	0.02	0.06		
0000316	2079		20:32:49	+41:08:12	1.13	2.24	0.64	4.81	15.29	0.1	0.02	14.11	0.02	0.09	13.56	0.02	0.08		
0000317	2081		20:32:49	+41:07:15	0.65	9.42	0.63	4.72	16.02	0.09	0.03	14.79	0.02	0.06	14.22	0.02	0.06		
0000318	2086		20:32:49	+41:09:28	0.66	3.47	0.6	5.23	15.49	0.08	0.02	14.27	0.02	0.06	13.69	0.02	0.05		
0000319	2087		20:32:49	+41:15:41	0.61	8.9	0.52	4.2	16.64	0.11	0.03	15.42	0.02	0.09	14.9	0.02	0.07		
0000321	2091		20:32:49	+41:07:46	0.67	2.89	0.64	4.89	15.9	0.08	0.03	14.67	0.02	0.07	14.11	0.02	0.06		
0000323	2099		20:32:49	+41:16:55	0.56	2.2	0.71	4.2	16.07	0.09	0.03	14.96	0.02	0.06	14.44	0.02	0.06		
0000325	2103		20:32:49	+41:16:07	0.69	9.23	0.46	4.88	16.79	0.12	0.03	15.51	0.02	0.09	14.88	0.02	0.09		
0000326	2102		20:32:49	+41:12:31	1.05	3.79	0.44	5.32	16.31	0.12	0.03	14.99	0.02	0.11	14.35	0.02	0.09		
0000328	2111		20:32:50	+41:06:17	0.63	3.72	0.57	4.32	14.6	0.07	0.02	13.48	0.02	0.05	12.97	0.02	0.05		
0000336	2129		20:32:50	+41:10:38	0.72	8.96	0.6	4.79	16.37	0.09	0.03	15.1	0.02	0.08	14.54	0.02	0.07		
0000338	2132		20:32:50	+41:17:50	0.78	2.74	0.5	4.52	14.89	0.08	0.02	13.64	0.02	0.07	13.06	0.02	0.06		
0000348	2154		20:32:51	+41:12:38	1.62	5.11	0.65	4.85	15.46	0.13	0.02	14.28	0.02	0.12	13.74	0.02	0.11		
0000349	2156		20:32:51	+41:11:24	1.71	6.84	0.5	5.1	16.97	0.19	0.04	15.72	0.03	0.18	15.13	0.03	0.16		
0000355	2172		20:32:52	+41:16:01	0.62	8.18			17.59	0.19	0.06	16.26	0.03	0.13	15.62	0.03	0.12		
0000356	2177		20:32:52	+41:13:14	1.94	20.2	0.46	6.2	16.93	0.2	0.04	15.55	0.03	0.19	14.85	0.02	0.16		
0000360	2187		20:32:53	+41:17:37	0.33	10.38	0.31	4.22	17.16	0.14	0.04	15.9	0.03	0.07	15.28	0.03	0.08		
0000361	2190		20:32:53	+41:10:19	0.51	5.81	0.73	4.36	13.96	0.06	0.02	12.86	0.02	0.05	12.36	0.02	0.04		
0000371	2226		20:32:54	+41:10:22	0.94	2.38	0.64	4.04	15.73	0.11	0.02	14.62	0.02	0.08	14.11	0.02	0.07		
0000378	2234		20:32:54	+41:13:08	0.60	3.45	0.53	5.56	16.14	0.07	0.03	14.85	0.02	0.06	14.23	0.02	0.07		
0000380	2247		20:32:54	+41:15:50	0.55	10.35	0.59	4.1	16.19	0.09	0.03	14.96	0.02	0.06	14.43	0.02	0.07		
0000386	2260	66618	20:32:55	+41:14:40	0.79	7.69	0.47	4.53	16.58	0.13	0.03	15.24	0.02	0.1	14.57	0.02	0.11	CL2	1
0000394	2270		20:32:55	+41:16:52	0.85	4.5	0.22	3.43	17.34	0.17	0.05	16.09	0.03	0.17	15.51	0.03	0.14		
0000395	2272		20:32:55	+41:08:32	1.41	7.18	0.63	5.03	15.98	0.13	0.03	14.7	0.02	0.11	14.11	0.02	0.1		
0000399	2279		20:32:55	+41:09:32	2.31	19.83	0.44	4.8	16.51	0.22	0.03	15.15	0.02	0.21	14.53	0.02	0.18		
0000406	2297		20:32:56	+41:13:18	2.36	3.09	0.48	5.39	16.26	0.18	0.03	15.01	0.02	0.2	14.38	0.02	0.17		
0000407	2298		20:32:56	+41:14:37	0.64	8.17	0.65	4.44	15.28	0.07	0.02	14.16	0.02	0.05	13.67	0.02	0.05		
0000412	2304		20:32:57	+41:10:45	0.82	7.29	0.64	4.77	16.84	0.12	0.04	15.57	0.03	0.1	15.01	0.02	0.09		
0000416	2311		20:32:57	+41:07:40	0.90	4.19	0.56	4.34	16.01	0.1	0.03	14.78	0.02	0.08	14.23	0.02	0.07		
0000420	2328		20:32:57	+41:13:33	2.05	3.46	0.63	5.06	15.27	0.16	0.02	14.09	0.02	0.14	13.55	0.02	0.13		
0000423	2335		20:32:58	+41:12:35	0.75	3.26	0.67	4.66	15.29	0.08	0.02	14.14	0.02	0.07	13.63	0.02	0.06		
0000430	2353		20:32:58	+41:10:58	0.70	2.86			15.12	0.07	0.02	13.95	0.02	0.06	13.4	0.02	0.06		
0000433	2366		20:32:58	+41:16:18	0.52	2.61	0.49	4.37	16.14	0.08	0.03	14.91	0.02	0.06	14.35	0.02	0.06		
0000435	2359		20:32:58	+41:12:51	0.99	4.72	0.57	4.56	16.9	0.14	0.04	15.64	0.03	0.13	15.09	0.03	0.11		
0000438	2374		20:32:59	+41:11:39	0.61	3.28	0.39	4.68	15.99	0.07	0.03	14.65	0.02	0.06	14.04	0.02	0.06		
0000443	2381		20:32:59	+41:11:10	0.96	5.62	0.63	4.3	16.15	0.1	0.03	14.9	0.02	0.09	14.37	0.02	0.1		
0000452	2406		20:32:59	+41:10:38	0.65	5.92	0.71	5.51	16.3	0.08	0.03	15.0	0.02	0.07	14.42	0.02	0.07		
0000457	2410		20:33:00	+41:06:22	0.60	6.2	0.55	4.82	15.33	0.06	0.02	14.12	0.02	0.06	13.57	0.02	0.05		
0000465	2433		20:33:00	+41:08:49	0.86	8.53			16.22	0.09	0.03	14.87	0.02	0.09	14.23	0.02	0.08		
0000472	2449		20:33:00	+41:16:52	0.71	6.15	0.3	4.24	16.56	0.1	0.03	15.24	0.02	0.09	14.62	0.02	0.07		
0000477	2458		20:33:01	+41:06:21	0.36	24.1	0.55	4.44	15.9	0.05	0.03	14.65	0.02	0.05	14.1	0.02	0.05		
0000479	2459		20:33:01	+41:06:16	0.42	3.79	0.73	4.05	15.6	0.06	0.02	14.6	0.02	0.05	14.15	0.02	0.04		
0000481	2467		20:33:01	+41:16:28	0.66	4.58	0.58	4.76	15.51	0.07	0.02	14.27	0.02	0.06	13.71	0.02	0.06		
0000483	2472		20:33:01	+41:17:37	0.64	7.11	0.62	4.72	15.84	0.08	0.02	14.6	0.02	0.07	14.03	0.02	0.06		
0000488	2487	70008	20:33:01	+41:11:53	3.84	18.96	0.5	5.51	16.98	0.46	0.04	15.54	0.03	0.42	14.51	0.02	0.41	CL2	1
0000496	2494		20:33:01	+41:13:32	0.81	11.83	0.28	4.43	17.17	0.14	0.04	15.88	0.03	0.13	15.27	0.03	0.11		
0000502	2504		20:33:02	+41:17:51	0.67	4.64	0.65	4.15	14.6	0.07	0.02	13.51	0.02	0.06	13.05	0.02	0.05		
0000507	2509		20:33:02	+41:11:04	1.09	7.29	0.59	4.29	16.09	0.11	0.03	14.85	0.02	0.09	14.28	0.02	0.08		
0000510	2516		20:33:02	+41:10:59	1.69	27.03			15.38	0.13	0.02	14.11	0.02	0.15	13.54	0.02	0.16		
0000520	2537		20:33:03	+41:13:56	0.39	9.59	0.67	5.36	16.5	0.07	0.03	15.23	0.02	0.06	14.67	0.02	0.07		
0000525	2552		20:33:03	+41:08:11	0.68	7.05	0.56	5.07	15.36	0.07	0.02	14.14	0.02	0.06	13.57	0.02	0.06		
0000526	2555		20:33:03	+41:16:30	2.20	8.92	0.42	2.15	15.63	0.22	0.02	14.7	0.02	0.2	14.26	0.02	0.19		
0000527	2556		20:33:03	+41:16:57	0.56	11.87	0.15	2.93	17.46	0.18	0.05	16.21	0.03	0.13	15.65	0.03	0.11		
0000531	2571		20:33:04	+41:12:37	1.04	5.16	0.55	5.91	17.34	0.19	0.05	16.06	0.03	0.17	15.43	0.03	0.15		
0000537	2582		20:33:04	+41:12:21	0.56	23.28	0.61	4.88	17.01	0.14	0.04	15.69	0.03	0.09	15.13	0.03	0.08		

Table C.1: Continued.

Id	GDW13	GDW15	RA	Dec	Stet	Per	Mass	Av	mJ	eJ	ptpJ	mH	eH	ptpH	mK	eK	ptpK	Class	Disk
0000542	2593		20:33:04	+41:06:51	1.01	3.39	0.44	4.57	13.89	0.09	0.02	12.8	0.02	0.07	12.3	0.02	0.07		
0000543	2592		20:33:04	+41:12:55	1.11	2.18	0.63	5.03	15.06	0.09	0.02	13.85	0.02	0.08	13.33	0.02	0.08		
0000544	2595		20:33:04	+41:16:14	1.01	9.67	0.58	4.9	15.94	0.11	0.03	14.66	0.02	0.11	13.99	0.02	0.11		
0000547	2598		20:33:04	+41:14:06	0.95	7.16	0.59	5.32	15.92	0.09	0.03	14.63	0.02	0.08	14.04	0.02	0.08		
0000549	2600		20:33:04	+41:18:31	0.45	2.72	0.76	3.75	13.92	0.06	0.02	12.96	0.02	0.04	12.52	0.02	0.04		
0000555	2615		20:33:05	+41:16:51	0.56	30.53	0.63	5.05	15.87	0.08	0.03	14.51	0.02	0.06	13.92	0.02	0.05		
0000556	2617		20:33:05	+41:13:13	0.39	3.63	0.71	5.06	15.77	0.06	0.02	14.56	0.02	0.05	14.02	0.02	0.04		
0000562	2625	66584	20:33:05	+41:14:22	3.62	4.37	0.57	5.26	15.66	0.37	0.02	14.25	0.02	0.3	13.46	0.02	0.22	CL2	1
0000564	2631		20:33:05	+41:12:33	1.00	9.53	0.59	5.18	15.64	0.09	0.02	14.35	0.02	0.09	13.78	0.02	0.08		
0000569	2643		20:33:05	+41:11:54	1.24	4.59	0.6	5.15	15.15	0.11	0.02	13.9	0.02	0.09	13.34	0.02	0.08		
0000571	2648		20:33:06	+41:07:33	0.67	5.67	0.63	4.44	16.62	0.1	0.03	15.4	0.02	0.08	14.87	0.02	0.07		
0000572	2647		20:33:06	+41:07:46	0.42	4.12	0.58	4.36	14.77	0.05	0.02	13.63	0.02	0.05	13.11	0.02	0.04		
0000574	2650		20:33:06	+41:14:53	0.47	7.74	0.61	4.49	16.71	0.1	0.03	15.47	0.02	0.08	14.93	0.02	0.07		
0000586	2674		20:33:06	+41:17:16	0.72	7.89	0.25	2.91	16.71	0.12	0.03	15.54	0.02	0.1	14.99	0.02	0.09		
0000592	2686		20:33:06	+41:13:31	0.49	17.04	0.62	5.11	14.92	0.06	0.02	13.73	0.02	0.05	13.2	0.02	0.05		
0000594	2689		20:33:06	+41:11:24	0.89	4.49	0.42	4.96	16.25	0.1	0.03	14.91	0.02	0.08	14.26	0.02	0.08		
0000595	2691		20:33:06	+41:12:07	0.37	2.93	0.81	4.75	13.99	0.05	0.02	12.95	0.02	0.04	12.48	0.02	0.04		
0000597	2701		20:33:07	+41:17:28	1.70	3.97	0.69	3.61	15.52	0.12	0.02	14.41	0.02	0.12	13.95	0.02	0.1		
0000598	2703		20:33:07	+41:12:25	0.53	3.84	0.56	5.56	15.89	0.07	0.03	14.53	0.02	0.06	13.9	0.02	0.05		
0000601	2709		20:33:07	+41:18:59	0.80	3.52			15.17	0.08	0.02	14.07	0.02	0.07	13.61	0.02	0.06		
0000604	2711		20:33:07	+41:11:40	0.51	4.94	0.54	5.32	15.84	0.08	0.02	14.52	0.02	0.06	13.9	0.02	0.05		
0000607	2717		20:33:07	+41:17:30	0.48	7.5	0.51	3.72	17.0	0.11	0.04	15.83	0.03	0.09	15.3	0.03	0.08		
0000609	2723	69995	20:33:07	+41:11:42	0.90	9.12	0.67	5.6	16.36	0.11	0.03	15.01	0.02	0.11	14.36	0.02	0.08	CL2	1
0000618	2747		20:33:08	+41:19:04	1.23	7.41			17.35	0.24	0.05	16.13	0.03	0.2	15.58	0.03	0.16		
0000620	2751		20:33:08	+41:10:48	1.02	2.15	0.64	5.13	16.28	0.12	0.03	15.0	0.02	0.1	14.42	0.02	0.09		
0000621	2750		20:33:08	+41:13:01	0.55	2.52	0.87	5.01	13.95	0.06	0.02	12.86	0.02	0.05	12.36	0.02	0.04		
0000632	2768		20:33:08	+41:13:01	1.00	3.63	0.64	5.37	15.02	0.09	0.02	13.82	0.02	0.08	13.27	0.02	0.08		
0000634	2771		20:33:08	+41:16:43	1.26	9.54			16.56	0.16	0.03	15.3	0.02	0.15	14.72	0.02	0.11		
0000638	2775		20:33:08	+41:15:27	1.19	5.03	0.68	4.7	16.44	0.14	0.03	15.24	0.02	0.12	14.74	0.02	0.1		
0000646	2787		20:33:08	+41:14:21	1.02	7.48	0.64	5.21	15.53	0.1	0.02	14.29	0.02	0.08	13.75	0.02	0.08		
0000648	5317		20:33:08	+41:12:26	2.36	5.12			16.78	0.24	0.04	15.36	0.02	0.22	14.68	0.02	0.19		
0000653	2802		20:33:09	+41:12:58	0.81	3.46			14.09	0.11	0.02	13.01	0.02	0.06	12.54	0.02	0.06		
0000654	2804		20:33:09	+41:12:15	1.59	17.64			16.51	0.14	0.03	15.11	0.02	0.14	14.47	0.02	0.12		
0000657	2810		20:33:09	+41:11:02	1.14	4.13			15.86	0.1	0.03	14.6	0.02	0.11	14.03	0.02	0.09		
0000671	2833		20:33:10	+41:09:13	1.69	2.72	0.53	5.48	15.23	0.15	0.02	13.91	0.02	0.13	13.27	0.02	0.11		
0000676	2839		20:33:10	+41:09:03	1.52	5.68	0.64	4.85	15.66	0.13	0.02	14.44	0.02	0.11	13.9	0.02	0.1		
0000680	2845		20:33:10	+41:11:39	1.41	3.28	0.52	4.65	17.18	0.18	0.04	15.87	0.03	0.17	15.28	0.03	0.15		
0000689	2865		20:33:10	+41:13:40	0.95	2.95	0.61	4.58	14.63	0.1	0.02	13.51	0.02	0.07	13.02	0.02	0.07		
0000690	2864		20:33:10	+41:15:46	0.51	2.17	0.42	4.3	14.01	0.06	0.02	12.9	0.02	0.05	12.41	0.02	0.05		
0000691	2871	21578	20:33:10	+41:05:29	1.81	10.76	0.57	4.94	15.08	0.14	0.02	13.9	0.02	0.13	13.35	0.02	0.12	CL2	1
0000694	2875		20:33:10	+41:11:56	0.38	6.46	0.7	4.87	15.67	0.05	0.02	14.46	0.02	0.04	13.94	0.02	0.05		
0000698	2886		20:33:11	+41:13:29	1.16	8.31	0.69	4.96	14.64	0.11	0.02	13.52	0.02	0.08	13.03	0.02	0.08		
0000700	2888		20:33:11	+41:13:24	0.77	2.3			15.35	0.09	0.02	14.13	0.02	0.08	13.6	0.02	0.07		
0000703	2890		20:33:11	+41:18:15	1.30	13.29	0.56	3.71	16.45	0.14	0.03	15.31	0.03	0.15	14.84	0.02	0.14		
0000704	2901		20:33:11	+41:12:57	1.20	6.2	0.67	5.32	15.65	0.11	0.02	14.42	0.02	0.1	13.85	0.02	0.09		
0000708	2905		20:33:11	+41:09:54	1.16	5.4	0.66	5.28	16.25	0.12	0.03	14.94	0.02	0.1	14.36	0.02	0.09		
0000713	2915		20:33:11	+41:06:48	0.88	2.4	0.6	3.9	16.28	0.1	0.03	15.11	0.02	0.09	14.63	0.02	0.09		
0000717	2921		20:33:11	+41:09:30	1.00	3.09	0.62	5.12	16.21	0.1	0.03	14.89	0.02	0.09	14.28	0.02	0.08		
0000720	2923		20:33:11	+41:17:29	0.84	3.3	0.66	3.99	15.23	0.09	0.02	14.13	0.02	0.07	13.67	0.02	0.07		
0000722	2927		20:33:11	+41:12:57	1.65	5.59	0.59	4.7	14.82	0.13	0.02	13.66	0.02	0.11	13.16	0.02	0.1		
0000723	2928		20:33:11	+41:13:48	3.11	7.23	0.66	5.77	15.92	0.25	0.03	14.63	0.02	0.23	14.05	0.02	0.2		
0000726	2930		20:33:12	+41:07:20	3.13	7.68	0.76	4.04	15.64	0.25	0.02	14.56	0.02	0.22	14.11	0.02	0.2		
0000729	2935		20:33:12	+41:08:59	0.34	6.34	0.61	6.85	14.55	0.05	0.02	13.07	0.02	0.03	12.37	0.02	0.04		
0000730	2938		20:33:12	+41:16:47	0.92	7.01	0.66	4.22	14.91	0.09	0.02	13.81	0.02	0.07	13.35	0.02	0.06		
0000731	2942		20:33:12	+41:12:59	0.79	14.09			16.58	0.13	0.03	15.37	0.03	0.09	14.83	0.02	0.08		
0000735	2946		20:33:12	+41:12:14	1.13	5.59	0.66	4.46	14.98	0.1	0.02	13.85	0.02	0.08	13.37	0.02	0.08		
0000741	2966		20:33:13	+41:14:53	4.22	9.33	0.69	5.31	15.89	0.44	0.03	14.59	0.02	0.37	13.78	0.02	0.32		

Table C.1: Continued.

Id	GDW13	GDW15	RA	Dec	Stet	Per	Mass	Av	mJ	eJ	ptpJ	mH	eH	ptpH	mK	eK	ptpK	Class	Disk
0000745	2973		20:33:13	+41:14:40	1.37	2.14	0.59	5.09	15.78	0.14	0.02	14.55	0.02	0.12	13.97	0.02	0.11		
0000747	2979		20:33:13	+41:15:39	0.51	2.37	0.63	4.76	15.35	0.07	0.02	14.13	0.02	0.06	13.59	0.02	0.04		
0000748	2981		20:33:13	+41:10:31	0.90	7.03	0.61	4.86	16.34	0.11	0.03	15.09	0.02	0.1	14.5	0.02	0.08		
0000750	2982		20:33:13	+41:13:39	0.86	5.65	0.84	6.13	15.54	0.11	0.02	14.24	0.02	0.07	13.66	0.02	0.07		
0000752	2990		20:33:13	+41:07:26	1.38	4.21	0.69	4.28	15.5	0.12	0.02	14.4	0.02	0.11	13.93	0.02	0.1		
0000754	2993		20:33:13	+41:11:11	0.83	4.54			16.18	0.09	0.03	14.98	0.02	0.08	14.44	0.02	0.08		
0000757	2995		20:33:14	+41:11:58	0.81	7.08	0.36	3.73	16.78	0.13	0.03	15.49	0.02	0.1	14.93	0.02	0.09		
0000762	3009	65768	20:33:14	+41:13:46	7.91	6.72	0.52	5.38	17.09	1.18	0.05	15.63	0.03	1.0	14.5	0.02	0.66	CL2	1
0000764	3015		20:33:14	+41:09:26	0.58	2.04	0.68	4.7	15.78	0.08	0.02	14.62	0.02	0.06	14.1	0.02	0.05		
0000767	3024		20:33:14	+41:08:53	0.52	2.33	0.66	4.73	16.7	0.1	0.03	15.5	0.02	0.08	15.0	0.02	0.07		
0000772	3032		20:33:14	+41:12:24	5.65	5.07	0.68	4.46	15.93	0.6	0.03	14.59	0.02	0.45	13.81	0.02	0.33		
0000776	3039		20:33:15	+41:12:54	1.01	11.49	0.76	4.83	15.74	0.1	0.02	14.54	0.02	0.09	14.02	0.02	0.08		
0000778	3046		20:33:15	+41:09:45	0.48	7.37	0.6	5.21	16.12	0.07	0.03	14.86	0.02	0.05	14.28	0.02	0.05		
0000779	3044		20:33:15	+41:16:19	1.52	6.13	0.58	5.16	16.73	0.16	0.03	15.41	0.02	0.15	14.8	0.02	0.13		
0000783	3055	65929	20:33:15	+41:15:57	2.64	11.36	0.55	4.68	15.53	0.3	0.02	14.22	0.02	0.22	13.54	0.02	0.17	CL2	1
0000791	3076		20:33:15	+41:18:16	1.04	7.34	0.68	3.58	15.64	0.11	0.02	14.55	0.02	0.1	14.1	0.02	0.08		
0000793	3074		20:33:15	+41:13:30	1.20	5.27	0.61	5.0	16.45	0.14	0.03	15.22	0.02	0.14	14.64	0.02	0.12		
0000796	3080		20:33:16	+41:06:32	1.04	8.12	0.73	3.93	15.87	0.11	0.03	14.75	0.02	0.09	14.29	0.02	0.11		
0000807		11995	20:32:14	+41:16:05	8.75	5.04	0.78	4.68	16.29	1.1	0.03	14.96	0.02	0.8	13.93	0.02	0.54	CL2	1
0000859		73260	20:33:01	+41:07:45	1.76	3.34	0.45	5.77	18.02	0.36	0.07	16.51	0.04	0.28	15.54	0.03	0.24	CL2	1
0000883		74190	20:32:33	+41:05:51	0.79	8.83	0.51	5.16	16.68	0.11	0.03	15.35	0.02	0.09	14.66	0.02	0.08	CL2	1
0000884		74252	20:32:31	+41:09:19	1.48	14.36	0.54	5.53	17.31	0.25	0.05	15.78	0.03	0.21	14.91	0.02	0.18	CL2_BWE	1
0100922	4721		20:34:24	+41:15:05	0.59	3.27	0.49	4.64	14.78	0.1	0.02	13.53	0.02	0.06	12.94	0.02	0.06		
0100924	5559		20:34:25	+41:12:03	0.96	5.92	0.71	5.84	16.2	0.1	0.03	14.96	0.02	0.09	14.36	0.02	0.08		
0100925	4733	63758	20:34:25	+41:14:37	0.98	7.84	0.3	3.63	16.99	0.15	0.04	15.75	0.03	0.13	15.12	0.03	0.13	CL2	1
0100941	4794		20:34:30	+41:17:44	0.77	9.36	0.36	2.5	15.96	0.09	0.03	14.73	0.02	0.08	14.19	0.02	0.07		
0100953	4831	92649	20:34:34	+41:15:41	4.46	7.12	0.75	7.14	16.69	0.71	0.04	15.12	0.02	0.52	14.04	0.02	0.4	CL2	1
0100979	4895		20:34:40	+41:07:44	0.52	4.39			14.59	0.06	0.02	13.51	0.02	0.04	13.02	0.02	0.04		
0100980	4901		20:34:41	+41:06:53	0.50	2.8			14.45	0.06	0.02	13.65	0.02	0.05	13.35	0.02	0.04		
0100981	5411		20:34:41	+41:16:31	0.47	8.88	0.15	4.67	16.76	0.09	0.04	15.45	0.02	0.08	14.64	0.02	0.07		
0100988	4921		20:34:43	+41:18:24	3.01	9.66	0.51	5.57	16.76	0.37	0.04	15.29	0.02	0.31	14.44	0.02	0.26		
0100990	4924		20:34:43	+41:11:51	1.44	2.94	0.6	4.67	15.0	0.12	0.02	13.81	0.02	0.11	13.26	0.02	0.09		
0100996	4951		20:34:45	+41:10:10	0.47	8.08			16.36	0.09	0.03	15.04	0.02	0.06	14.44	0.02	0.05		
0101005	4993		20:34:51	+41:09:30	0.82	6.76	0.48	3.04	13.29	0.08	0.02	12.35	0.02	0.07	11.93	0.02	0.07		
0101008	5012		20:34:54	+41:13:19	0.54	2.2	0.51	5.08	15.17	0.06	0.02	13.85	0.02	0.04	13.24	0.02	0.05		
0101016	5040	101728	20:34:57	+41:16:13	1.49	10.81			15.64	0.17	0.02	14.34	0.02	0.12	13.62	0.02	0.11	CL2	1
0101026	5073		20:35:01	+41:11:26	2.36	3.95			16.49	0.22	0.03	14.97	0.02	0.19	14.25	0.02	0.17		
0101027	5077		20:35:02	+41:14:01	0.62	16.24			16.08	0.08	0.03	14.65	0.02	0.06	14.0	0.02	0.06		
0101046	5120		20:35:11	+41:16:53	0.71	7.09			16.63	0.11	0.03	15.48	0.03	0.09	14.95	0.02	0.08		
0101054	5133		20:35:17	+41:08:00	0.45	3.32	0.57	5.48	15.58	0.07	0.02	14.31	0.02	0.05	13.72	0.02	0.06		
0101079		63570	20:34:30	+41:14:17	0.80	10.71	0.33	4.54	16.12	0.1	0.03	14.66	0.02	0.08	13.9	0.02	0.08	CL2	1
0101091		98617	20:35:03	+41:10:01	5.39	5.41			16.66	0.67	0.03	14.96	0.02	0.51	13.86	0.02	0.34	CL2	1
0101094		99455	20:35:07	+41:18:54	3.04	3.04			16.54	0.39	0.03	15.09	0.02	0.29	14.28	0.02	0.22	FS	1
0101107		320645	20:34:31	+41:07:54	1.70	9.56	0.38	4.63	16.63	0.21	0.03	15.24	0.02	0.18	14.48	0.02	0.14	CL2	1
0201116	4753		20:34:27	+41:39:48	0.54	7.22			17.26	0.14	0.04	16.09	0.03	0.1	15.54	0.03	0.1		
0201119	4797		20:34:31	+41:34:34	0.50	3.41	0.74	3.76	15.8	0.07	0.02	14.77	0.02	0.05	14.31	0.02	0.06		
0201124	4811		20:34:32	+41:42:13	0.71	4.83	0.82	5.58	16.5	0.09	0.03	15.35	0.02	0.08	14.8	0.02	0.07		
0201125	4813		20:34:32	+41:39:14	0.49	2.27	0.8	3.89	14.76	0.07	0.02	13.79	0.02	0.05	13.34	0.02	0.04		
0201126	4816		20:34:32	+41:35:59	0.34	3.1	0.55	1.59	15.88	0.07	0.02	14.87	0.02	0.05	14.42	0.02	0.05		
0201128	4836		20:34:35	+41:31:51	0.80	3.6	0.55	4.62	15.37	0.11	0.02	14.22	0.02	0.08	13.65	0.02	0.07		
0201129	4842		20:34:35	+41:34:23	0.96	15.35	0.68	3.9	15.55	0.1	0.02	14.47	0.02	0.08	13.99	0.02	0.07		
0201130	4856		20:34:36	+41:32:24	2.34	2.31	0.49	5.51	15.8	0.18	0.02	14.48	0.02	0.18	13.83	0.02	0.15		
0201136	4878		20:34:39	+41:34:59	0.49	3.17	0.68	3.98	15.8	0.07	0.02	14.72	0.02	0.06	14.24	0.02	0.05		
0201148	4942		20:34:45	+41:43:02	1.65	2.78			15.54	0.16	0.02	14.43	0.02	0.13	13.92	0.02	0.11		
0201160	5008		20:34:53	+41:34:20	0.68	6.29			16.62	0.11	0.03	15.21	0.02	0.08	14.53	0.02	0.07		
0201165	5057		20:34:59	+41:39:05	0.57	2.63	0.7	4.08	15.68	0.09	0.02	14.61	0.02	0.06	14.12	0.02	0.05		
0201166	5058		20:34:59	+41:38:33	1.00	2.14	0.77	3.66	14.34	0.08	0.02	13.5	0.02	0.09	13.03	0.02	0.08		

Table C.1: Continued.

Id	GDW13	GDW15	RA	Dec	Stet	Per	Mass	Av	mJ	eJ	ptpJ	mH	eH	ptpH	mK	eK	ptpK	Class	Disk
0201190		97877	20:35:14	+41:34:00	3.24	5.1			16.36	0.43	0.03	14.78	0.02	0.34	13.67	0.02	0.25	CL2	1
0301218	1188		20:32:12	+41:33:51	1.06	14.1	0.68	3.15	16.06	0.12	0.03	15.0	0.02	0.11	14.55	0.02	0.1		
0301220	1212		20:32:13	+41:32:15	0.72	4.61	0.87	3.45	15.24	0.09	0.02	14.28	0.02	0.07	13.86	0.02	0.09		
0301226	1249		20:32:14	+41:36:02	0.71	6.55			15.09	0.09	0.02	14.14	0.02	0.07	13.73	0.02	0.05		
0301239	1345		20:32:19	+41:34:02	0.44	9.25	0.79	3.03	15.61	0.07	0.02	14.62	0.02	0.06	14.22	0.02	0.06		
0301254	1420		20:32:22	+41:36:43	0.94	2.43			16.57	0.15	0.03	15.46	0.03	0.11	14.9	0.02	0.12		
0301265	1507		20:32:26	+41:33:28	0.88	3.59	0.62	3.86	15.45	0.1	0.02	14.37	0.02	0.09	13.85	0.02	0.07		
0301267	1524		20:32:27	+41:34:49	0.48	5.66	0.78	3.8	15.25	0.06	0.02	14.24	0.02	0.05	13.78	0.02	0.05		
0301275	1608		20:32:30	+41:44:39	2.91	3.43	0.78	2.07	13.93	0.22	0.02	13.27	0.02	0.21	13.0	0.02	0.2		
0301284	1677		20:32:33	+41:40:42	1.83	2.96			16.01	0.17	0.03	15.0	0.02	0.17	14.44	0.02	0.14		
0301291	1746		20:32:36	+41:42:31	1.28	17.41			13.94	0.13	0.02	12.85	0.02	0.1	12.39	0.02	0.09		
0301294	1785		20:32:37	+41:32:42	0.70	9.39	0.56	4.13	16.37	0.13	0.03	15.17	0.02	0.09	14.63	0.02	0.09		
0301303	1933		20:32:43	+41:45:32	1.48	3.22	0.56	3.28	15.09	0.15	0.02	14.04	0.02	0.14	13.59	0.02	0.13		
0301304	1935		20:32:43	+41:35:00	1.24	2.54			16.44	0.15	0.03	15.32	0.02	0.12	14.84	0.02	0.11		
0301316	2090		20:32:49	+41:42:26	1.09	3.28			15.95	0.13	0.03	14.96	0.02	0.1	14.52	0.02	0.08		
0301317	2094		20:32:49	+41:40:43	0.93	3.51			16.88	0.17	0.04	15.8	0.03	0.11	15.33	0.03	0.12		
0301318	2098		20:32:49	+41:35:18	0.28	8.85			15.7	0.05	0.02	14.6	0.02	0.04	14.16	0.02	0.04		
0301323	2183		20:32:52	+41:34:45	0.55	5.83	0.58	3.85	16.26	0.09	0.03	15.13	0.02	0.07	14.62	0.02	0.07		
0301324	2200		20:32:53	+41:42:37	0.73	3.62			15.6	0.08	0.02	14.58	0.02	0.07	14.15	0.02	0.06		
0301325	2206		20:32:53	+41:43:59	0.48	3.3			15.6	0.07	0.02	14.62	0.02	0.05	14.21	0.02	0.05		
0301329	2246		20:32:54	+41:32:50	1.71	6.32	0.36	4.41	16.21	0.19	0.03	14.94	0.02	0.19	14.23	0.02	0.15		
0301331	2271		20:32:55	+41:44:43	0.34	4.38	0.72	3.66	15.7	0.05	0.02	14.63	0.02	0.05	14.18	0.02	0.05		
0301334	2296		20:32:56	+41:34:25	0.68	2.43	0.69	4.2	15.63	0.09	0.02	14.52	0.02	0.07	14.02	0.02	0.06		
0301337	2319		20:32:57	+41:37:03	0.82	11.66			15.33	0.08	0.02	14.17	0.02	0.08	13.64	0.02	0.07		
0301356	2536		20:33:03	+41:42:19	0.37	6.45			15.6	0.06	0.02	14.64	0.02	0.05	14.24	0.02	0.04		
0301375	2792		20:33:09	+41:36:03	0.51	4.45	0.62	4.37	15.72	0.09	0.03	14.56	0.02	0.07	13.97	0.02	0.06		
0301383	2951		20:33:12	+41:38:59	0.62	7.19			15.41	0.08	0.02	14.32	0.02	0.06	13.86	0.02	0.05		
0301386	2991		20:33:13	+41:37:20	2.09	12.14			15.98	0.17	0.03	14.84	0.02	0.17	14.32	0.02	0.15		
0301388	3021		20:33:14	+41:40:34	0.50	4.55	0.7	3.4	16.08	0.07	0.03	15.08	0.02	0.07	14.64	0.02	0.06		
0301395	3070		20:33:15	+41:34:15	0.96	3.77	0.69	4.65	16.01	0.12	0.03	14.87	0.02	0.11	14.33	0.02	0.09		
0301404		21892	20:33:01	+41:32:00	3.88	8.44	0.53	4.27	16.43	0.46	0.03	15.17	0.02	0.42	14.43	0.02	0.3	CL2	1
0301406		29902	20:32:25	+41:36:31	1.46	5.42			16.32	0.22	0.03	15.11	0.02	0.19	14.36	0.02	0.16	CL2	1
0301410		33126	20:33:14	+41:45:13	0.57	3.59			15.87	0.08	0.03	14.76	0.02	0.06	14.26	0.02	0.08	CL2	1
0401424	1037		20:32:03	+40:55:45	1.40	5.49	0.52	4.51	16.6	0.21	0.03	15.39	0.03	0.17	14.84	0.02	0.14		
0401443	1178		20:32:12	+41:04:47	1.10	7.75	0.56	5.57	17.11	0.14	0.04	15.66	0.03	0.13	14.92	0.02	0.11		
0401445	1190		20:32:12	+40:59:35	2.32	2.52	0.51	5.46	16.11	0.2	0.03	14.79	0.02	0.18	14.12	0.02	0.16		
0401447	1223		20:32:13	+41:05:21	1.05	5.3	0.56	4.64	16.93	0.14	0.04	15.65	0.03	0.13	15.04	0.03	0.12		
0401452	1275		20:32:15	+41:03:46	0.52	12.0			16.33	0.08	0.03	15.06	0.02	0.06	14.46	0.02	0.06		
0401458	1301		20:32:17	+41:04:40	1.89	3.89	0.61	4.51	15.65	0.16	0.02	14.42	0.02	0.14	13.83	0.02	0.13		
0401460	1307		20:32:17	+41:03:38	0.65	8.03	0.64	3.8	16.11	0.08	0.03	14.96	0.02	0.07	14.46	0.02	0.07		
0401462	1316		20:32:17	+41:02:46	0.74	7.72	0.51	4.12	17.02	0.13	0.04	15.75	0.03	0.1	15.17	0.03	0.09		
0401466	1323		20:32:17	+40:55:46	0.52	5.78	0.58	3.25	14.83	0.07	0.02	13.84	0.02	0.05	13.37	0.02	0.05		
0401477	1417	8001	20:32:22	+40:53:52	1.05	4.6	0.69	3.88	15.86	0.12	0.03	14.77	0.02	0.1	14.24	0.02	0.12	CL2	1
0401486	1536		20:32:27	+41:04:06	1.45	5.95	0.61	4.46	15.83	0.13	0.03	14.58	0.02	0.12	14.0	0.02	0.11		
0401507	1732		20:32:35	+40:57:36	1.33	3.54	0.53	4.21	15.37	0.12	0.02	14.22	0.02	0.11	13.67	0.02	0.09		
0401514	1766		20:32:37	+41:03:33	0.89	5.49	0.31	5.13	17.37	0.17	0.05	16.02	0.03	0.13	15.35	0.03	0.12		
0401529	1914		20:32:42	+40:59:31	1.71	12.46	0.66	4.6	16.06	0.13	0.03	14.85	0.02	0.13	14.31	0.02	0.13		
0401538	1976		20:32:45	+40:55:42	1.14	3.93	0.42	4.29	16.76	0.15	0.03	15.49	0.02	0.13	14.87	0.02	0.11		
0401541	1995		20:32:45	+40:53:15	0.73	9.55	0.58	4.14	14.16	0.08	0.02	13.03	0.02	0.06	12.49	0.02	0.06		
0401543	2050		20:32:47	+40:52:51	0.33	3.35	0.7	4.63	14.96	0.05	0.02	13.94	0.02	0.04	13.46	0.02	0.04		
0401545	2059		20:32:47	+41:01:13	1.04	2.02	0.72	5.11	14.41	0.09	0.02	13.31	0.02	0.09	12.75	0.02	0.08		
0401549	2095		20:32:49	+40:55:51	0.93	2.16	0.48	4.25	15.65	0.1	0.02	14.43	0.02	0.08	13.85	0.02	0.07		
0401556	2150		20:32:51	+40:53:19	0.63	3.75	0.74	5.11	15.92	0.09	0.03	14.74	0.02	0.06	14.18	0.02	0.06		
0401571	2277		20:32:55	+40:59:10	0.81	5.6	0.64	4.48	15.6	0.09	0.02	14.41	0.02	0.07	13.86	0.02	0.07		
0401572	2280		20:32:56	+41:02:28	0.65	8.57	0.63	4.18	16.03	0.09	0.03	14.86	0.02	0.07	14.35	0.02	0.07		
0401578	2324		20:32:57	+41:05:04	0.96	2.92	0.62	3.74	14.87	0.1	0.02	13.89	0.02	0.08	13.45	0.02	0.08		
0401582	2341		20:32:58	+41:03:41	2.62	2.26	0.63	5.81	16.06	0.22	0.03	14.76	0.02	0.2	14.15	0.02	0.17		

Table C.1: Continued.

Id	GDW13	GDW15	RA	Dec	Stet	Per	Mass	Av	mJ	eJ	ptpJ	mH	eH	ptpH	mK	eK	ptpK	Class	Disk
0401598	2486		20:33:01	+41:04:02	0.56	9.67	0.62	4.96	15.57	0.07	0.02	14.37	0.02	0.06	13.83	0.02	0.04		
0401603	2522		20:33:02	+40:56:05	1.09	6.23	0.56	4.73	16.01	0.12	0.03	14.75	0.02	0.11	14.18	0.02	0.09		
0401607	2562		20:33:03	+40:54:46	1.25	2.28			16.91	0.15	0.04	15.6	0.03	0.13	15.02	0.02	0.12		
0401609	2577		20:33:04	+41:04:25	0.75	2.52	0.48	4.42	17.32	0.17	0.05	16.01	0.03	0.13	15.43	0.03	0.11		
0401611	2580		20:33:04	+41:02:55	0.57	2.81			14.54	0.05	0.02	13.21	0.02	0.06	12.59	0.02	0.05		
0401641	2850		20:33:10	+41:02:14	0.51	18.95			16.5	0.1	0.03	15.26	0.02	0.06	14.74	0.02	0.06		
0401658	2944		20:33:12	+40:56:47	0.47	4.89	0.6	4.64	16.75	0.1	0.03	15.46	0.02	0.07	14.89	0.02	0.06		
0401659	2950		20:33:12	+40:58:16	0.39	3.52	0.47	5.12	16.79	0.08	0.04	15.51	0.03	0.07	14.9	0.02	0.06		
0401661	2957		20:33:12	+41:00:08	0.70	30.96	0.61	5.16	14.52	0.06	0.02	13.25	0.02	0.06	12.71	0.02	0.07		
0401662	2974		20:33:13	+41:04:03	0.78	5.52	0.46	3.99	16.11	0.1	0.03	14.85	0.02	0.09	14.32	0.02	0.07		
0401668	3035		20:33:14	+40:56:31	0.97	8.04			17.41	0.18	0.05	16.12	0.03	0.15	15.51	0.03	0.13		
0401669	3038		20:33:15	+41:05:04	1.07	3.69	0.74	3.72	14.79	0.09	0.02	13.79	0.02	0.09	13.38	0.02	0.08		
0401672	3064		20:33:15	+40:53:08	0.71	2.67			16.95	0.12	0.04	15.65	0.03	0.11	15.02	0.03	0.1		
0401677		7586	20:32:17	+40:56:02	4.24	16.87	0.62	4.29	15.71	0.28	0.02	14.44	0.02	0.33	13.6	0.02	0.5	CL2	1
0401692		12272	20:32:48	+40:58:39	4.52	29.23	0.42	4.35	16.55	0.46	0.03	15.24	0.02	0.41	14.52	0.02	0.35	CL2	1
0401708		76481	20:32:59	+41:03:20	3.54	10.53	0.61	5.95	16.16	0.4	0.03	14.78	0.02	0.34	13.94	0.02	0.26	CL2	1
0401716		76664	20:32:38	+41:04:04	2.88	2.92	0.52	5.65	16.56	0.38	0.03	15.11	0.02	0.32	14.25	0.02	0.24	CL2	1
0401742		81042	20:32:44	+40:56:36	1.87	6.19	0.29	4.63	16.71	0.25	0.03	15.44	0.02	0.21	14.6	0.02	0.19	CL2	1
0401744		81147	20:32:47	+40:57:28	3.59	3.88	0.31	4.71	16.78	0.47	0.03	15.28	0.02	0.43	14.27	0.02	0.31	CL2	1
0501797	4889		20:34:39	+41:05:24	0.66	3.18	0.56	3.74	16.41	0.11	0.03	15.26	0.02	0.07	14.74	0.02	0.08		
0501801	4843		20:34:35	+40:56:43	0.80	2.82	0.61	3.98	12.79	0.09	0.02	11.82	0.02	0.06	11.35	0.02	0.06		
0501812		15614	20:34:32	+40:54:38	3.68	11.12	0.72	5.6	15.4	0.45	0.02	14.07	0.02	0.33	13.31	0.02	0.25	CL2	1
0601845	4740		20:34:26	+41:19:43	0.63	9.67	0.63	4.33	15.35	0.09	0.02	14.19	0.02	0.07	13.65	0.02	0.06		
0601848	4751		20:34:27	+41:21:54	0.52	7.25	0.71	4.24	16.02	0.08	0.03	14.88	0.02	0.06	14.36	0.02	0.06		
0601855	4763		20:34:28	+41:31:16	0.98	7.21	0.53	4.91	16.77	0.13	0.03	15.51	0.03	0.12	14.93	0.02	0.1		
0601856	4765		20:34:28	+41:20:41	0.63	4.45	0.58	4.51	15.05	0.08	0.02	13.87	0.02	0.06	13.32	0.02	0.06		
0601858	4768		20:34:28	+41:21:57	2.31	14.99	0.66	4.62	15.74	0.19	0.02	14.55	0.02	0.17	13.99	0.02	0.16		
0601860	4772		20:34:28	+41:31:10	0.47	4.55	0.64	4.53	16.31	0.06	0.03	15.11	0.02	0.06	14.58	0.02	0.06		
0601864	4780	52548	20:34:29	+41:23:29	1.40	13.09	0.56	3.97	16.8	0.25	0.03	15.58	0.03	0.18	14.93	0.02	0.15	CL2	1
0601882	4829		20:34:34	+41:28:53	2.15	5.93	0.54	4.79	16.46	0.19	0.03	15.25	0.02	0.18	14.64	0.02	0.16		
0601883	4830		20:34:34	+41:28:19	0.50	2.95	0.67	4.16	15.45	0.08	0.02	14.42	0.02	0.06	13.91	0.02	0.05		
0601886	4840		20:34:35	+41:26:01	0.44	3.56	0.75	3.76	15.5	0.06	0.02	14.46	0.02	0.05	13.96	0.02	0.04		
0601892	4858		20:34:36	+41:20:34	0.55	11.8	0.62	4.53	16.2	0.09	0.03	14.92	0.02	0.07	14.34	0.02	0.07		
0601893	4859		20:34:36	+41:23:25	0.33	6.17	0.65	3.78	16.58	0.08	0.03	15.45	0.03	0.06	14.94	0.02	0.06		
0601895	4863		20:34:37	+41:27:45	1.10	5.93	0.54	4.28	16.42	0.12	0.03	15.2	0.02	0.11	14.6	0.02	0.1		
0601943	4954		20:34:46	+41:22:45	0.36	11.99			15.99	0.06	0.03	14.81	0.02	0.05	14.22	0.02	0.05		
0601958	4983		20:34:50	+41:28:45	0.60	10.39			16.34	0.09	0.03	15.09	0.02	0.07	14.5	0.02	0.07		
0601960	4987		20:34:51	+41:20:41	0.58	4.21			16.3	0.09	0.03	15.07	0.02	0.07	14.51	0.02	0.06		
0601981	5028		20:34:55	+41:26:56	0.44	2.7			16.94	0.12	0.04	15.68	0.03	0.08	15.07	0.03	0.07		
0602027	5143		20:35:20	+41:24:21	0.37	5.77	0.69	1.69	15.13	0.06	0.02	14.32	0.02	0.04	14.04	0.02	0.05		
0602031	5577		20:35:25	+41:19:16	0.49	4.65	0.73	6.11	16.58	0.1	0.03	15.24	0.02	0.07	14.66	0.02	0.07		
0602061		105687	20:35:29	+41:19:37	1.83	2.19			17.72	0.39	0.06	16.23	0.03	0.3	15.11	0.03	0.22	FS	1
0702081	1060		20:32:05	+41:30:43	0.84	2.47	0.85	2.95	15.66	0.1	0.02	14.79	0.02	0.08	14.43	0.02	0.08		
0702084	1067		20:32:05	+41:27:15	0.97	7.95	0.54	3.14	16.45	0.12	0.03	15.41	0.03	0.13	14.94	0.03	0.12		
0702087	1080		20:32:06	+41:24:13	1.23	6.43	0.72	3.48	16.01	0.13	0.03	14.96	0.02	0.12	14.5	0.02	0.11		
0702092	1097		20:32:06	+41:25:38	0.59	9.37	0.73	3.26	15.52	0.08	0.02	14.52	0.02	0.07	14.08	0.02	0.06		
0702113	1142		20:32:09	+41:22:42	0.49	6.23	0.29	2.53	17.05	0.13	0.04	15.94	0.03	0.11	15.43	0.03	0.1		
0702118	1151		20:32:10	+41:25:56	0.41	15.69	0.63	3.13	16.09	0.09	0.03	14.99	0.02	0.07	14.54	0.02	0.06		
0702124	1164		20:32:11	+41:26:22	1.89	3.64	0.63	3.2	16.02	0.18	0.03	14.97	0.02	0.19	14.5	0.02	0.19		
0702129	1172		20:32:11	+41:20:55	0.85	9.61	0.57	3.46	16.18	0.1	0.03	15.03	0.02	0.09	14.52	0.02	0.09		
0702140	1205		20:32:12	+41:26:49	1.04	6.15	0.83	2.66	15.34	0.11	0.02	14.46	0.02	0.09	14.08	0.02	0.09		
0702142	1209		20:32:13	+41:28:26	0.67	13.99	0.79	3.81	15.46	0.08	0.02	14.45	0.02	0.06	14.02	0.02	0.06		
0702145	1215		20:32:13	+41:29:51	0.57	3.41	0.85	3.58	15.45	0.08	0.02	14.48	0.02	0.07	14.07	0.02	0.06		
0702159	1250		20:32:14	+41:26:51	0.58	2.04	0.6	2.79	15.85	0.09	0.03	14.82	0.02	0.07	14.38	0.02	0.06		
0702167	1259		20:32:15	+41:26:57	0.82	7.57			16.86	0.14	0.04	15.83	0.03	0.13	15.34	0.03	0.11		
0702177	1284		20:32:16	+41:20:56	0.77	10.74	0.68	4.29	16.49	0.11	0.03	15.37	0.03	0.11	14.85	0.02	0.11		
0702178	1291		20:32:16	+41:23:28	1.23	12.01	0.62	3.27	15.96	0.13	0.03	14.9	0.02	0.12	14.42	0.02	0.11		

Table C.1: Continued.

Id	GDW13	GDW15	RA	Dec	Stet	Per	Mass	Av	mJ	eJ	ptpJ	mH	eH	ptpH	mK	eK	ptpK	Class	Disk
0702186	1329		20:32:17	+41:27:35	0.64	4.54	0.62	2.74	16.32	0.09	0.03	15.29	0.03	0.09	14.86	0.02	0.07		
0702192	1340		20:32:18	+41:19:25	0.64	8.75	0.6	3.54	15.41	0.08	0.02	14.33	0.02	0.08	13.83	0.02	0.09		
0702193	1342		20:32:18	+41:21:22	1.61	9.38	0.68	3.52	15.67	0.15	0.02	14.61	0.02	0.13	14.13	0.02	0.13		
0702199	1365		20:32:20	+41:30:09	0.76	7.43	0.51	3.21	16.29	0.1	0.03	15.15	0.02	0.09	14.67	0.02	0.08		
0702202	1371		20:32:20	+41:20:15	1.01	5.67	0.79	3.87	15.33	0.1	0.02	14.29	0.02	0.1	13.8	0.02	0.1		
0702203	1370		20:32:20	+41:24:03	0.83	7.73	0.73	3.1	15.48	0.1	0.02	14.5	0.02	0.08	14.05	0.02	0.08		
0702212	1387		20:32:21	+41:31:36	1.45	5.54	0.62	3.12	16.45	0.17	0.03	15.39	0.03	0.16	14.95	0.03	0.14		
0702219	1414		20:32:22	+41:28:03	0.59	9.27	0.62	2.73	15.58	0.08	0.02	14.58	0.02	0.06	14.15	0.02	0.06		
0702221	1421		20:32:22	+41:24:55	0.98	4.45	0.46	2.29	16.15	0.13	0.03	15.09	0.02	0.12	14.61	0.02	0.1		
0702223	1423		20:32:22	+41:23:37	1.07	8.07	0.62	3.24	16.38	0.14	0.03	15.31	0.03	0.12	14.83	0.02	0.1		
0702231	1444		20:32:23	+41:23:05	0.72	6.44	0.75	4.15	15.99	0.09	0.03	14.9	0.02	0.08	14.42	0.02	0.07		
0702233	1448		20:32:23	+41:23:00	1.56	7.45	0.75	3.54	15.66	0.15	0.02	14.61	0.02	0.12	14.16	0.02	0.11		
0702234	1450		20:32:23	+41:28:28	0.55	6.25	0.66	2.77	16.22	0.09	0.03	15.22	0.02	0.07	14.83	0.02	0.07		
0702235	1451		20:32:23	+41:28:53	0.55	2.67	0.52	2.63	16.85	0.11	0.04	15.85	0.03	0.09	15.42	0.03	0.09		
0702238	1457		20:32:24	+41:29:30	0.74	14.54	0.62	2.84	16.35	0.1	0.03	15.32	0.02	0.11	14.89	0.03	0.09		
0702242	1463		20:32:24	+41:27:24	0.84	3.71	0.74	2.77	15.57	0.1	0.02	14.61	0.02	0.08	14.21	0.02	0.07		
0702249	1476		20:32:25	+41:26:47	0.80	3.26	0.6	2.9	15.98	0.09	0.03	14.97	0.02	0.09	14.53	0.02	0.08		
0702254	1499		20:32:25	+41:21:11	0.65	2.28	0.82	3.5	14.59	0.08	0.02	13.66	0.02	0.07	13.24	0.02	0.07		
0702258	1504	58635	20:32:26	+41:25:54	5.38	8.61	0.55	3.73	16.85	0.83	0.04	15.62	0.03	0.8	14.71	0.02	0.51	CL2	1
0702265	1515		20:32:26	+41:24:10	0.56	9.82	0.77	3.35	14.46	0.07	0.02	13.54	0.02	0.06	13.12	0.02	0.05		
0702266	1519		20:32:27	+41:26:39	0.86	7.79	0.79	2.67	15.46	0.09	0.02	14.52	0.02	0.08	14.14	0.02	0.07		
0702270	1527		20:32:27	+41:28:52	1.24	10.72			15.83	0.19	0.03	14.89	0.02	0.14	14.52	0.02	0.12		
0702271	1528		20:32:27	+41:21:41	1.96	2.62	0.65	3.81	16.38	0.19	0.03	15.27	0.02	0.17	14.77	0.02	0.16		
0702276	1552		20:32:28	+41:28:29	0.58	4.21	0.65	3.02	14.82	0.06	0.02	13.87	0.02	0.06	13.47	0.02	0.06		
0702284	1567		20:32:29	+41:19:17	0.80	7.01	0.51	3.5	17.02	0.18	0.04	15.84	0.03	0.13	15.31	0.03	0.14		
0702285	1569		20:32:29	+41:22:37	1.07	7.47	0.62	4.08	16.17	0.12	0.03	15.03	0.02	0.11	14.51	0.02	0.1		
0702293	1587		20:32:29	+41:28:57	0.75	2.9	0.58	2.95	15.7	0.09	0.03	14.72	0.02	0.08	14.28	0.02	0.08		
0702300	1606		20:32:30	+41:23:49	1.34	7.71	0.46	3.38	16.56	0.15	0.03	15.42	0.03	0.15	14.89	0.03	0.12		
0702310	1630		20:32:31	+41:20:39	0.65	9.83	0.5	3.33	16.42	0.1	0.03	15.32	0.02	0.09	14.82	0.02	0.09		
0702324	1668		20:32:33	+41:28:13	1.49	11.03	0.62	3.29	16.12	0.15	0.03	15.07	0.02	0.14	14.63	0.02	0.11		
0702325	1669		20:32:33	+41:29:29	0.59	6.85	0.33	2.28	16.81	0.1	0.04	15.77	0.03	0.1	15.31	0.03	0.1		
0702326	1674		20:32:33	+41:30:24	0.57	6.09	0.7	3.08	15.86	0.09	0.03	14.83	0.02	0.06	14.41	0.02	0.05		
0702346	1733		20:32:35	+41:24:09	0.49	9.11	0.64	3.55	16.16	0.09	0.03	15.06	0.02	0.07	14.59	0.02	0.06		
0702357	5583		20:32:37	+41:25:40	1.77	2.59	0.23	3.57	17.52	0.37	0.06	16.26	0.04	0.3	15.27	0.03	0.22		
0702362	1775		20:32:37	+41:19:45	2.19	5.44	0.59	3.32	15.31	0.17	0.02	14.21	0.02	0.16	13.71	0.02	0.15		
0702363	1776		20:32:37	+41:21:46	1.51	7.28	0.33	3.25	16.66	0.18	0.04	15.6	0.03	0.2	15.05	0.03	0.17		
0702364	1780		20:32:37	+41:24:56	0.62	2.3	0.54	3.45	15.43	0.09	0.02	14.34	0.02	0.07	13.84	0.02	0.06		
0702365	1777		20:32:37	+41:24:30	0.63	3.29	0.58	3.36	15.22	0.07	0.02	14.14	0.02	0.06	13.66	0.02	0.06		
0702367	1783		20:32:37	+41:28:11	0.93	2.12	0.84	4.05	15.65	0.1	0.02	14.62	0.02	0.08	14.18	0.02	0.08		
0702370	1786		20:32:37	+41:23:37	0.75	5.66	0.57	3.57	16.73	0.12	0.04	15.59	0.03	0.11	15.08	0.03	0.1		
0702374	1798		20:32:38	+41:31:50	1.08	8.07	0.54	4.25	16.2	0.11	0.03	15.03	0.02	0.1	14.49	0.02	0.11		
0702380	1814		20:32:38	+41:27:47	1.41	8.69	0.55	3.63	16.47	0.15	0.03	15.4	0.02	0.14	14.94	0.03	0.12		
0702390	1839		20:32:39	+41:26:51	0.52	9.21	0.73	2.95	15.42	0.07	0.02	14.45	0.02	0.06	14.03	0.02	0.05		
0702396	1857		20:32:40	+41:22:40	0.73	7.08	0.4	3.53	16.32	0.1	0.03	15.17	0.02	0.1	14.63	0.02	0.09		
0702400	1862		20:32:40	+41:22:02	1.19	2.39	0.57	3.57	15.84	0.11	0.03	14.76	0.02	0.1	14.26	0.02	0.09		
0702414	1903		20:32:42	+41:30:52	0.90	6.22	0.63	5.63	17.18	0.16	0.05	16.06	0.03	0.14	15.5	0.03	0.12		
0702421	1924		20:32:43	+41:25:15	0.95	6.01	0.85	2.93	15.32	0.09	0.02	14.36	0.02	0.08	13.97	0.02	0.07		
0702426	1932		20:32:43	+41:23:11	0.49	7.15	0.68	3.47	14.83	0.06	0.02	13.77	0.02	0.05	13.32	0.02	0.04		
0702428	1949		20:32:44	+41:26:32	0.73	8.51	0.68	3.21	15.88	0.08	0.03	14.84	0.02	0.08	14.41	0.02	0.08		
0702434	1964		20:32:44	+41:24:29	0.77	9.45	0.65	3.51	16.31	0.1	0.03	15.2	0.02	0.11	14.73	0.02	0.08		
0702444	1992		20:32:45	+41:20:17	7.39	5.03	0.45	3.93	16.97	1.07	0.04	15.59	0.03	0.87	14.51	0.02	0.58		
0702446	1993		20:32:45	+41:26:17	0.81	8.59	0.68	3.18	15.82	0.09	0.03	14.79	0.02	0.08	14.35	0.02	0.07		
0702449	2013		20:32:46	+41:26:05	1.51	6.84	0.57	3.33	16.3	0.16	0.03	15.2	0.02	0.15	14.72	0.02	0.13		
0702451	2019		20:32:46	+41:28:30	0.47	4.83	0.41	3.26	16.8	0.1	0.04	15.72	0.03	0.08	15.25	0.03	0.08		
0702453	2028		20:32:46	+41:27:43	0.75	5.2	0.68	3.53	16.5	0.11	0.03	15.42	0.03	0.08	14.98	0.03	0.09		
0702470	2073		20:32:48	+41:27:45	0.79	12.62	0.71	3.78	16.09	0.09	0.03	15.07	0.02	0.09	14.62	0.02	0.08		
0702473	2085		20:32:49	+41:20:02	0.93	10.2	0.59	3.55	16.16	0.11	0.03	15.04	0.02	0.1	14.51	0.02	0.09		

Table C.1: Continued.

Id	GDW13	GDW15	RA	Dec	Stet	Per	Mass	Av	mJ	eJ	ptpJ	mH	eH	ptpH	mK	eK	ptpK	Class	Disk
0702474	2084		20:32:49	+41:29:09	2.42	7.31	0.71	3.65	16.07	0.21	0.03	15.04	0.02	0.2	14.61	0.02	0.18		
0702481	2105		20:32:49	+41:25:18	0.54	6.4	0.75	2.74	15.47	0.06	0.02	14.46	0.02	0.06	14.06	0.02	0.06		
0702502	2184		20:32:52	+41:31:45	1.08	10.34	0.68	4.18	15.89	0.11	0.03	14.75	0.02	0.1	14.25	0.02	0.09		
0702504	2195		20:32:53	+41:25:48	0.55	6.58	0.57	2.83	16.14	0.08	0.03	15.07	0.02	0.08	14.63	0.02	0.07		
0702509	2204		20:32:53	+41:24:11	0.80	9.25	0.68	3.36	15.86	0.09	0.03	14.83	0.02	0.07	14.36	0.02	0.07		
0702519	2232		20:32:54	+41:29:16	0.41	5.46	0.72	3.66	15.38	0.06	0.02	14.36	0.02	0.05	13.93	0.02	0.04		
0702520	2238		20:32:54	+41:23:34	0.99	6.88	0.69	3.29	15.56	0.09	0.02	14.49	0.02	0.08	14.02	0.02	0.07		
0702531	2284		20:32:56	+41:22:48	1.85	2.73	0.59	3.57	15.65	0.18	0.02	14.58	0.02	0.16	14.03	0.02	0.13		
0702532	2287		20:32:56	+41:29:36	1.28	14.96	0.7	3.66	16.2	0.13	0.03	15.17	0.02	0.13	14.73	0.02	0.1		
0702534	2306		20:32:57	+41:28:58	1.01	3.41	0.93	4.0	15.19	0.09	0.02	14.21	0.02	0.08	13.8	0.02	0.08		
0702539	2333		20:32:58	+41:29:49	1.40	3.37			15.71	0.11	0.02	14.72	0.02	0.11	14.29	0.02	0.11		
0702549	2358		20:32:58	+41:21:47	1.06	5.52	0.44	2.82	15.86	0.1	0.03	14.77	0.02	0.1	14.25	0.02	0.09		
0702553	2378		20:32:59	+41:24:44	0.47	18.36	0.71	2.84	13.72	0.06	0.02	12.78	0.02	0.05	12.38	0.02	0.05		
0702573	2446		20:33:00	+41:22:14	0.82	2.16	0.56	2.93	15.26	0.08	0.02	14.19	0.02	0.07	13.69	0.02	0.06		
0702578	2470		20:33:01	+41:21:34	0.83	6.31	0.35	3.02	16.51	0.12	0.03	15.27	0.02	0.1	14.69	0.02	0.09		
0702584	2510		20:33:02	+41:22:27	0.72	4.39	0.58	2.61	15.75	0.09	0.03	14.71	0.02	0.07	14.23	0.02	0.06		
0702585	2512		20:33:02	+41:21:17	0.62	4.94	0.37	2.53	16.5	0.1	0.03	15.36	0.03	0.09	14.83	0.02	0.08		
0702588	2534		20:33:03	+41:27:27	0.91	8.32	0.57	3.7	14.72	0.09	0.02	13.64	0.02	0.07	13.15	0.02	0.07		
0702600	2576		20:33:04	+41:27:36	0.77	3.66	0.76	3.07	15.0	0.09	0.02	14.11	0.02	0.06	13.73	0.02	0.06		
0702610	2609		20:33:05	+41:30:53	1.98	3.08	0.79	3.99	14.91	0.16	0.02	13.92	0.02	0.14	13.47	0.02	0.13		
0702615	2620		20:33:05	+41:22:10	0.68	10.4	0.3	2.62	16.24	0.09	0.03	15.08	0.02	0.08	14.53	0.02	0.07		
0702619	2630		20:33:05	+41:29:04	0.80	17.05	0.49	3.52	15.1	0.07	0.02	13.93	0.02	0.07	13.4	0.02	0.07		
0702620	2627		20:33:05	+41:26:31	0.63	10.34	0.57	3.38	15.14	0.07	0.02	14.07	0.02	0.07	13.59	0.02	0.07		
0702633	2673		20:33:06	+41:22:14	1.14	9.3	0.49	2.82	16.25	0.12	0.03	15.11	0.02	0.11	14.6	0.02	0.1		
0702636	2680		20:33:06	+41:29:29	0.97	5.63	0.59	4.23	15.15	0.09	0.02	14.0	0.02	0.07	13.48	0.02	0.07		
0702643	2716		20:33:07	+41:20:07	0.62	6.87	0.47	2.63	14.19	0.07	0.02	13.12	0.02	0.06	12.63	0.02	0.06		
0702646	2727		20:33:07	+41:29:04	0.46	6.65	0.69	3.9	15.15	0.06	0.02	14.1	0.02	0.05	13.63	0.02	0.05		
0702648	2732		20:33:07	+41:25:18	1.32	2.23	0.63	3.05	14.98	0.13	0.02	13.95	0.02	0.11	13.49	0.02	0.09		
0702650	2740		20:33:07	+41:22:45	0.99	5.48	0.52	3.29	16.4	0.12	0.03	15.24	0.02	0.1	14.72	0.02	0.09		
0702653	2744		20:33:07	+41:20:32	0.85	9.59	0.19	2.49	16.91	0.17	0.04	15.68	0.03	0.12	15.11	0.03	0.1		
0702658	2773		20:33:08	+41:27:47	0.60	5.86	0.66	3.36	15.55	0.07	0.02	14.51	0.02	0.06	14.06	0.02	0.06		
0702661	2797		20:33:09	+41:25:35	0.35	3.39	0.67	2.8	16.16	0.07	0.03	15.14	0.02	0.05	14.71	0.02	0.06		
0702666	2818	55506	20:33:09	+41:25:26	0.55	2.28	0.59	2.98	15.12	0.07	0.02	14.1	0.02	0.06	13.64	0.02	0.05	CL2	1
0702673	2844		20:33:10	+41:25:14	0.65	6.75	0.37	2.48	15.84	0.08	0.03	14.7	0.02	0.07	14.19	0.02	0.06		
0702677	2863		20:33:10	+41:23:53	0.93	6.71	0.46	3.1	15.5	0.09	0.02	14.38	0.02	0.09	13.86	0.02	0.07		
0702678	2866		20:33:10	+41:25:30	0.87	5.57	0.37	2.88	16.61	0.13	0.03	15.49	0.03	0.1	14.98	0.03	0.1		
0702688	2940		20:33:12	+41:28:10	0.63	5.18	0.71	3.18	15.93	0.07	0.03	14.91	0.02	0.06	14.49	0.02	0.06		
0702700	2977		20:33:13	+41:21:17	1.01	6.62	0.54	3.0	15.9	0.11	0.03	14.76	0.02	0.1	14.24	0.02	0.09		
0702711	3013		20:33:14	+41:28:57	1.78	4.62	0.65	4.18	15.27	0.14	0.02	14.15	0.02	0.13	13.64	0.02	0.12		
0702713	3018		20:33:14	+41:20:55	1.33	3.43			16.32	0.17	0.03	15.19	0.02	0.15	14.57	0.02	0.13		
0702723	3082		20:33:16	+41:24:34	2.38	8.61	0.5	3.61	16.33	0.23	0.03	15.22	0.02	0.23	14.65	0.02	0.2		
0702727	3088		20:33:16	+41:21:15	1.17	8.91			16.31	0.14	0.03	15.13	0.02	0.12	14.62	0.02	0.1		
0702736		21845	20:32:54	+41:31:43	1.19	8.43	0.68	4.1	16.17	0.15	0.03	15.02	0.02	0.13	14.47	0.02	0.13	CL2	1
0702755		31895	20:32:55	+41:27:51	3.49	8.68	1.24	5.74	15.2	0.37	0.02	14.17	0.02	0.3	13.6	0.02	0.24	CL2	1
0702771		56783	20:32:51	+41:25:30	0.69	4.68	0.39	2.6	16.58	0.13	0.03	15.44	0.03	0.09	14.91	0.03	0.09	CL2	1
0702779		58027	20:32:33	+41:25:10	3.60	3.85	0.43	3.35	17.15	0.64	0.05	15.92	0.03	0.55	15.06	0.03	0.39	CL2	1
0702780		58239	20:32:33	+41:25:49	5.49	5.29	0.39	3.9	16.28	0.61	0.03	15.02	0.02	0.5	14.17	0.02	0.39	CL2	1
0702792		86159	20:32:16	+41:23:11	3.45	4.94	0.16	2.77	16.91	0.5	0.04	15.83	0.03	0.45	15.02	0.03	0.36	CL2	1
0802815	253		20:31:12	+41:00:56	0.45	4.66	0.58	5.21	16.49	0.07	0.03	15.23	0.02	0.07	14.58	0.02	0.06		
0802820	332		20:31:20	+41:04:03	0.87	10.88	0.49	4.34	16.52	0.1	0.03	15.25	0.02	0.09	14.63	0.02	0.08		
0802824	384		20:31:24	+41:05:04	0.54	2.91	0.55	3.73	15.31	0.07	0.02	14.2	0.02	0.05	13.64	0.02	0.05		
0802828	417		20:31:27	+41:05:03	0.99	3.04	0.55	3.74	14.22	0.1	0.02	13.17	0.02	0.08	12.64	0.02	0.08		
0802831	436		20:31:29	+41:02:21	0.66	3.94	0.51	5.14	15.59	0.07	0.02	14.28	0.02	0.07	13.63	0.02	0.06		
0802835	444		20:31:30	+41:00:29	0.88	6.07	0.53	3.78	14.85	0.1	0.02	13.8	0.02	0.07	13.28	0.02	0.07		
0802837	472		20:31:33	+41:00:52	0.50	5.5	0.58	4.27	15.89	0.07	0.03	14.72	0.02	0.06	14.17	0.02	0.06		
0802838	495		20:31:34	+41:05:08	0.95	2.35	0.58	5.9	17.22	0.16	0.04	15.93	0.03	0.15	15.25	0.03	0.14		
0802849	598		20:31:40	+41:05:11	0.80	10.19	0.58	4.71	16.69	0.13	0.03	15.34	0.02	0.08	14.7	0.02	0.09		

Table C.1: Continued.

Id	GDW13	GDW15	RA	Dec	Stet	Per	Mass	Av	mJ	eJ	ptpJ	mH	eH	ptpH	mK	eK	ptpK	Class	Disk
0802857	5467		20:31:41	+41:05:42	0.65	3.45	0.49	6.01	16.08	0.09	0.03	14.57	0.02	0.07	13.79	0.02	0.06		
0802861	647		20:31:43	+41:03:28	0.68	8.83	0.43	1.9	15.96	0.08	0.03	15.05	0.02	0.08	14.65	0.02	0.07		
0802913		3727	20:31:31	+40:57:08	3.90	9.4	0.42	3.71	16.47	0.4	0.03	15.26	0.02	0.35	14.5	0.02	0.29	CL2	1
0802914		3728	20:31:32	+40:57:40	2.90	4.07	0.56	3.61	15.49	0.32	0.02	14.31	0.02	0.26	13.57	0.02	0.22	CL2	1
0802927		77153	20:31:20	+41:03:59	4.37	7.52	0.58	5.36	17.19	0.7	0.05	15.71	0.03	0.54	14.75	0.02	0.35	CL2	1
0902964	3121	80044	20:33:17	+40:59:58	0.69	2.46			14.12	0.07	0.02	12.87	0.02	0.07	12.28	0.02	0.06	CL2_low	1mass
0902968	3162		20:33:17	+40:52:44	0.54	3.91			16.13	0.08	0.03	14.91	0.02	0.07	14.33	0.02	0.07		
0902973	3172		20:33:18	+40:54:08	0.40	6.24	0.64	4.96	16.08	0.08	0.03	14.87	0.02	0.05	14.29	0.02	0.05		
0902978	3202		20:33:18	+40:59:18	0.81	4.84			16.19	0.11	0.03	15.04	0.02	0.08	14.48	0.02	0.07		
0902985	5330		20:33:19	+41:01:12	0.52	2.96			17.0	0.13	0.04	15.66	0.03	0.09	14.99	0.03	0.08		
0902986	3269		20:33:20	+40:59:45	0.42	6.32	0.42	3.91	13.71	0.05	0.02	12.64	0.02	0.04	12.12	0.02	0.04		
0902988	3275		20:33:20	+41:05:19	0.42	4.38	0.61	3.65	16.61	0.1	0.03	15.44	0.02	0.07	14.93	0.02	0.06		
0902991	3289		20:33:20	+40:59:01	0.58	3.13	0.7	3.85	15.68	0.07	0.02	14.62	0.02	0.06	14.12	0.02	0.06		
0902995	3315		20:33:21	+41:01:19	0.33	2.49	0.53	5.02	15.17	0.05	0.02	13.86	0.02	0.04	13.25	0.02	0.04		
0903011	3425		20:33:24	+41:04:35	0.93	2.47	0.62	3.98	16.38	0.1	0.03	15.21	0.02	0.1	14.65	0.02	0.09		
0903014	3461		20:33:25	+41:03:21	0.59	4.38	0.34	4.03	16.63	0.08	0.03	15.37	0.02	0.08	14.77	0.02	0.08		
0903015	3467		20:33:25	+40:59:08	0.56	5.51	0.69	3.7	15.42	0.07	0.02	14.38	0.02	0.06	13.89	0.02	0.05		
0903027	3554	102253	20:33:28	+40:53:11	1.73	2.6			16.2	0.15	0.03	14.95	0.02	0.17	14.14	0.02	0.12	CL2	1
0903037	3648		20:33:32	+40:57:05	0.73	3.42	0.59	4.44	15.89	0.08	0.03	14.65	0.02	0.07	14.07	0.02	0.06		
0903040	3671	314445	20:33:33	+41:01:42	1.60	3.34	0.41	4.54	16.81	0.15	0.03	15.52	0.03	0.16	14.88	0.02	0.14	CL2	1
0903049	3709		20:33:34	+40:55:52	1.31	10.87	0.14	2.53	16.89	0.15	0.04	15.61	0.03	0.14	15.0	0.03	0.13		
0903051	3711		20:33:34	+40:54:01	0.30	5.92			17.05	0.11	0.04	15.8	0.03	0.08	15.19	0.03	0.07		
0903052	3716		20:33:34	+40:56:13	0.88	2.2	0.56	4.4	16.43	0.11	0.03	15.19	0.02	0.09	14.61	0.02	0.08		
0903054	3724		20:33:35	+41:05:07	0.49	13.85	0.52	3.74	15.61	0.08	0.02	14.42	0.02	0.05	13.88	0.02	0.04		
0903059	3769		20:33:37	+40:55:06	0.28	10.16			17.08	0.13	0.04	15.96	0.03	0.09	15.42	0.03	0.08		
0903067	3811		20:33:38	+41:05:10	1.12	8.08	0.55	3.82	15.76	0.1	0.02	14.56	0.02	0.1	14.02	0.02	0.09		
0903076	3916		20:33:42	+41:02:57	1.10	6.56			15.93	0.11	0.03	14.58	0.02	0.1	13.93	0.02	0.09		
0903085	3984		20:33:44	+41:00:53	0.70	5.94	0.58	4.45	15.23	0.07	0.02	14.1	0.02	0.06	13.56	0.02	0.06		
0903086	3986		20:33:44	+40:57:46	0.78	6.36	0.5	4.55	15.71	0.09	0.02	14.53	0.02	0.08	13.96	0.02	0.07		
0903091	4027		20:33:46	+40:58:59	0.60	6.28	0.56	4.08	15.31	0.06	0.02	14.15	0.02	0.05	13.63	0.02	0.05		
0903102	4073		20:33:48	+41:02:36	2.19	3.19	0.63	5.28	16.07	0.19	0.03	14.79	0.02	0.17	14.19	0.02	0.16		
0903113	4146		20:33:51	+40:59:59	1.22	9.41	0.49	4.39	16.45	0.12	0.03	15.22	0.02	0.12	14.62	0.02	0.12		
0903117	4173		20:33:53	+40:56:36	0.49	3.07	0.42	4.01	16.45	0.07	0.03	15.23	0.02	0.07	14.64	0.02	0.06		
0903124	4202		20:33:54	+41:01:43	0.56	5.42	0.34	3.84	16.69	0.1	0.03	15.47	0.03	0.08	14.88	0.02	0.08		
0903128	4227		20:33:55	+41:00:10	0.54	2.7	0.52	4.62	15.18	0.06	0.02	13.99	0.02	0.05	13.44	0.02	0.05		
0903129	4243		20:33:56	+41:03:15	0.42	2.95	0.31	3.18	15.56	0.05	0.02	14.25	0.02	0.04	13.7	0.02	0.04		
0903135	4265		20:33:57	+40:59:56	0.52	5.2	0.52	4.11	16.27	0.09	0.03	15.05	0.02	0.07	14.48	0.02	0.06		
0903139	4273		20:33:57	+41:04:03	1.07	5.45	0.54	3.49	15.14	0.1	0.02	14.02	0.02	0.08	13.52	0.02	0.07		
0903140	4279		20:33:57	+41:05:36	0.78	4.35			15.05	0.08	0.02	13.95	0.02	0.07	13.45	0.02	0.06		
0903142	4287		20:33:58	+41:02:15	0.44	8.81	0.61	4.92	16.97	0.11	0.04	15.73	0.03	0.08	15.17	0.03	0.06		
0903153	4361		20:34:02	+41:01:46	0.70	3.04	0.62	4.11	16.4	0.1	0.03	15.27	0.02	0.07	14.77	0.02	0.07		
0903157	4385		20:34:03	+41:01:09	1.21	7.04	0.49	4.69	14.93	0.1	0.02	13.73	0.02	0.09	13.16	0.02	0.08		
0903168	4419		20:34:05	+41:03:43	2.38	5.22	0.53	3.89	15.85	0.18	0.03	14.69	0.02	0.19	14.14	0.02	0.16		
0903169	4435		20:34:06	+41:01:16	0.54	10.43	0.62	3.77	16.54	0.11	0.03	15.39	0.02	0.08	14.89	0.02	0.07		
0903174	4448		20:34:07	+41:03:54	0.33	3.51	0.55	3.85	16.22	0.07	0.03	15.04	0.02	0.05	14.5	0.02	0.05		
0903177	4460		20:34:08	+41:05:20	1.86	2.01	0.59	4.57	15.96	0.15	0.03	14.8	0.02	0.15	14.25	0.02	0.12		
0903185	4482		20:34:09	+41:00:02	0.72	13.07	0.64	3.89	15.8	0.08	0.02	14.65	0.02	0.07	14.14	0.02	0.06		
0903198	4529		20:34:12	+41:02:53	0.49	3.96	0.55	3.36	14.63	0.06	0.02	13.65	0.02	0.04	13.19	0.02	0.04		
0903200	4535		20:34:13	+41:02:10	0.83	5.24	0.65	3.43	15.31	0.08	0.02	14.3	0.02	0.07	13.85	0.02	0.07		
0903207	4592		20:34:16	+41:01:59	0.65	4.82	0.56	4.79	15.53	0.07	0.02	14.31	0.02	0.06	13.7	0.02	0.06		
0903208	4594		20:34:16	+40:59:53	0.58	7.42	0.53	4.8	15.09	0.06	0.02	13.79	0.02	0.06	13.17	0.02	0.06		
0903241		70845	20:34:22	+41:05:10	3.63	7.59	0.2	4.23	16.78	0.52	0.04	15.24	0.02	0.42	14.07	0.02	0.33	CL2	1
0903267		79467	20:33:39	+40:59:40	2.21	6.84	0.45	5.13	16.88	0.28	0.04	15.53	0.03	0.24	14.76	0.02	0.19	CL2	1
0903277		88025	20:33:58	+41:03:05	1.01	9.52			16.62	0.12	0.03	15.38	0.02	0.11	14.8	0.02	0.12	CL2	1
1003308	3160		20:33:18	+41:20:42	0.72	10.7	0.41	4.36	16.14	0.1	0.03	14.96	0.02	0.09	14.32	0.02	0.07		
1003309	3169		20:33:18	+41:20:22	0.65	14.8	0.59	3.57	15.64	0.1	0.02	14.62	0.02	0.08	14.11	0.02	0.08		
1003313	3186		20:33:18	+41:31:09	0.28	5.08	0.62	2.9	13.97	0.05	0.02	13.01	0.02	0.04	12.57	0.02	0.04		

Table C.1: Continued.

Id	GDW13	GDW15	RA	Dec	Stet	Per	Mass	Av	mJ	eJ	ptpJ	mH	eH	ptpH	mK	eK	ptpK	Class	Disk
1003322	3219		20:33:19	+41:21:31	1.12	7.88	0.58	3.62	15.47	0.11	0.02	14.38	0.02	0.1	13.86	0.02	0.09		
1003323	3223		20:33:19	+41:21:18	2.19	2.24	0.67	3.87	15.54	0.18	0.02	14.46	0.02	0.16	13.93	0.02	0.14		
1003325	3241		20:33:19	+41:19:07	1.34	10.44			16.54	0.17	0.03	15.43	0.02	0.16	14.92	0.02	0.14		
1003331	3260		20:33:20	+41:21:27	1.39	8.13	0.57	4.07	14.99	0.13	0.02	13.84	0.02	0.11	13.22	0.02	0.1		
1003334	3278		20:33:20	+41:20:12	1.23	7.31	0.67	3.99	15.59	0.1	0.02	14.51	0.02	0.11	13.99	0.02	0.08		
1003335	3282		20:33:20	+41:19:43	0.86	2.05	0.65	3.21	13.89	0.08	0.02	12.91	0.02	0.07	12.45	0.02	0.06		
1003336	3286		20:33:20	+41:21:15	0.49	2.3	0.57	3.98	15.14	0.06	0.02	14.05	0.02	0.06	13.49	0.02	0.05		
1003344	3308		20:33:21	+41:26:57	0.79	2.48	0.55	3.67	14.46	0.07	0.02	13.39	0.02	0.06	12.86	0.02	0.06		
1003345	3319		20:33:21	+41:19:46	0.44	2.25	0.7	3.02	16.01	0.08	0.03	15.08	0.02	0.07	14.64	0.02	0.05		
1003346	3320	55249	20:33:21	+41:26:06	1.63	8.53	0.41	4.11	16.45	0.21	0.03	15.15	0.02	0.17	14.41	0.02	0.15	CL2	1
1003361	3366		20:33:22	+41:23:51	0.44	2.49	0.7	3.14	14.81	0.06	0.02	13.89	0.02	0.05	13.45	0.02	0.05		
1003365	3380		20:33:23	+41:19:00	1.18	3.21			15.3	0.12	0.02	14.23	0.02	0.1	13.73	0.02	0.09		
1003367	3386		20:33:23	+41:31:03	0.41	2.42	0.73	2.82	15.56	0.06	0.02	14.64	0.02	0.05	14.19	0.02	0.05		
1003372	3401		20:33:24	+41:30:49	0.47	4.26	0.57	3.23	16.13	0.07	0.03	15.01	0.02	0.06	14.5	0.02	0.06		
1003376	3406		20:33:24	+41:28:59	0.40	4.45	0.47	3.22	14.86	0.05	0.02	13.72	0.02	0.04	13.16	0.02	0.04		
1003384	3422		20:33:24	+41:29:11	1.26	11.14	0.34	2.79	16.61	0.12	0.03	15.46	0.02	0.12	14.88	0.02	0.12		
1003389	3436		20:33:24	+41:26:55	1.42	6.93	0.61	4.19	16.12	0.13	0.03	14.92	0.02	0.13	14.32	0.02	0.13		
1003390	3438		20:33:25	+41:20:26	0.47	8.79	0.7	3.22	15.84	0.07	0.02	14.79	0.02	0.08	14.32	0.02	0.06		
1003396	3454		20:33:25	+41:31:52	1.00	2.65	0.48	3.78	16.49	0.11	0.03	15.31	0.02	0.1	14.76	0.02	0.09		
1003405	3481		20:33:26	+41:18:54	0.57	10.25			15.28	0.09	0.02	14.23	0.02	0.07	13.76	0.02	0.06		
1003410	3499		20:33:27	+41:31:09	0.48	10.25	0.59	3.59	14.73	0.05	0.02	13.68	0.02	0.05	13.19	0.02	0.05		
1003412	3505		20:33:27	+41:20:47	0.61	8.32	0.7	3.39	15.81	0.08	0.02	14.77	0.02	0.07	14.3	0.02	0.06		
1003415	3525		20:33:27	+41:31:11	0.82	4.56	0.52	3.76	16.27	0.11	0.03	15.1	0.02	0.09	14.54	0.02	0.08		
1003419	3544		20:33:28	+41:31:33	1.08	6.03	0.67	4.01	16.09	0.1	0.03	14.96	0.02	0.09	14.44	0.02	0.09		
1003420	3547		20:33:28	+41:21:29	0.51	9.42	0.33	2.98	16.73	0.08	0.03	15.67	0.03	0.08	15.13	0.03	0.07		
1003422	3560		20:33:28	+41:19:37	0.34	4.27	0.68	3.15	13.92	0.05	0.02	13.03	0.02	0.04	12.59	0.02	0.04		
1003435	3591		20:33:30	+41:22:45	0.84	8.93	0.52	2.98	16.34	0.1	0.03	15.27	0.02	0.09	14.78	0.02	0.09		
1003437	3600		20:33:30	+41:18:38	0.80	8.32	0.7	4.99	16.06	0.1	0.03	14.87	0.02	0.08	14.28	0.02	0.08		
1003438	3605		20:33:30	+41:27:30	0.73	4.7	0.54	2.75	15.36	0.07	0.02	14.28	0.02	0.06	13.77	0.02	0.06		
1003445	3629		20:33:31	+41:20:26	0.42	5.65	0.69	3.17	15.03	0.06	0.02	14.04	0.02	0.05	13.6	0.02	0.04		
1003447	3643		20:33:31	+41:25:00	0.57	8.1	0.46	3.66	15.36	0.06	0.02	14.23	0.02	0.06	13.66	0.02	0.06		
1003451	3650		20:33:32	+41:31:38	0.67	2.56	0.51	4.49	15.96	0.08	0.03	14.77	0.02	0.07	14.18	0.02	0.07		
1003461	3680		20:33:33	+41:23:08	0.51	2.16	0.65	3.29	14.02	0.06	0.02	13.02	0.02	0.05	12.55	0.02	0.05		
1003475	3706		20:33:34	+41:25:26	2.56	12.14	0.64	3.52	15.62	0.21	0.02	14.54	0.02	0.19	14.02	0.02	0.17		
1003477	3712		20:33:34	+41:18:52	0.55	8.38	0.42	4.2	16.89	0.11	0.03	15.62	0.03	0.09	15.08	0.03	0.1		
1003480	3727		20:33:35	+41:20:50	0.41	5.93	0.14	2.16	16.65	0.08	0.03	15.56	0.03	0.09	14.97	0.02	0.07		
1003485	3751		20:33:36	+41:25:44	0.59	4.55	0.65	3.09	14.7	0.06	0.02	13.76	0.02	0.05	13.3	0.02	0.05		
1003492	3765		20:33:36	+41:30:00	0.61	2.86	0.51	4.28	15.93	0.08	0.03	14.81	0.02	0.08	14.22	0.02	0.08		
1003493	3767		20:33:36	+41:25:55	0.79	2.17	0.61	4.25	15.62	0.09	0.02	14.61	0.02	0.08	14.02	0.02	0.08		
1003495	3768		20:33:37	+41:26:18	0.51	2.14	0.59	2.88	14.32	0.05	0.02	13.38	0.02	0.05	12.93	0.02	0.05		
1003504	3799		20:33:38	+41:23:16	0.40	19.04	0.51	2.74	15.6	0.08	0.02	14.56	0.02	0.05	14.06	0.02	0.05		
1003508	3804		20:33:38	+41:21:53	1.00	5.43	0.55	3.13	16.14	0.1	0.03	15.07	0.02	0.09	14.57	0.02	0.1		
1003511	3813		20:33:39	+41:26:51	1.70	2.03	0.34	2.71	15.4	0.14	0.02	14.31	0.02	0.14	13.7	0.02	0.12		
1003519	3830		20:33:39	+41:24:27	0.62	7.35	0.59	2.48	15.95	0.09	0.03	14.94	0.02	0.07	14.48	0.02	0.07		
1003525	3853		20:33:39	+41:25:47	1.17	13.22	0.45	2.43	15.84	0.12	0.02	14.76	0.02	0.1	14.24	0.02	0.09		
1003526	3857		20:33:40	+41:18:59	0.73	6.91			16.5	0.1	0.03	15.4	0.02	0.1	14.9	0.02	0.1		
1003528	3867		20:33:40	+41:31:52	1.60	3.57	0.92	2.52	14.76	0.12	0.02	13.97	0.02	0.11	13.64	0.02	0.11		
1003529	3868		20:33:40	+41:21:18	0.42	4.06	0.64	3.98	15.46	0.07	0.02	14.34	0.02	0.05	13.82	0.02	0.05		
1003533	3872		20:33:40	+41:31:09	0.61	2.53	0.9	5.91	15.81	0.07	0.02	14.63	0.02	0.07	14.07	0.02	0.07		
1003550	3926		20:33:42	+41:28:46	0.73	21.08	0.3	3.59	16.46	0.1	0.03	15.28	0.02	0.11	14.68	0.02	0.08		
1003554	3948		20:33:43	+41:25:14	1.90	6.66			16.24	0.16	0.03	15.18	0.02	0.18	14.61	0.02	0.16		
1003555	3952		20:33:43	+41:30:01	0.92	23.37	0.94	1.77	11.43	0.09	0.02	10.73	0.02	0.08	10.45	0.02	0.08		
1003561	3966		20:33:43	+41:20:31	1.06	8.33	0.62	4.11	16.56	0.13	0.03	15.43	0.02	0.13	14.9	0.02	0.12		
1003562	3968		20:33:43	+41:23:06	0.38	7.75	0.54	3.58	16.24	0.07	0.03	15.15	0.02	0.06	14.57	0.02	0.06		
1003572	4003		20:33:45	+41:21:55	0.61	3.23	0.79	3.71	15.73	0.07	0.02	14.72	0.02	0.06	14.24	0.02	0.07		
1003588	4061		20:33:47	+41:20:06	2.11	6.91	0.63	3.72	16.4	0.22	0.03	15.24	0.02	0.2	14.73	0.02	0.18		
1003589	4063		20:33:47	+41:24:00	2.06	3.33	0.72	3.62	15.7	0.16	0.02	14.66	0.02	0.16	14.18	0.02	0.15		

Table C.1: Continued.

Id	GDW13	GDW15	RA	Dec	Stet	Per	Mass	Av	mJ	eJ	ptpJ	mH	eH	ptpH	mK	eK	ptpK	Class	Disk
1003595	4077		20:33:48	+41:19:11	1.50	8.85			15.39	0.13	0.02	14.25	0.02	0.13	13.72	0.02	0.12		
1003597	4086		20:33:48	+41:18:40	0.94	8.81	0.56	2.84	15.67	0.1	0.02	14.57	0.02	0.1	14.07	0.02	0.09		
1003603	4114		20:33:49	+41:22:30	1.05	15.12	0.48	3.42	16.57	0.14	0.03	15.44	0.02	0.12	14.89	0.02	0.11		
1003615	4144		20:33:51	+41:20:29	0.44	4.26	0.75	3.27	15.48	0.07	0.02	14.49	0.02	0.05	14.04	0.02	0.05		
1003623	4167		20:33:53	+41:23:16	1.19	6.09	0.72	3.77	15.35	0.11	0.02	14.31	0.02	0.09	13.83	0.02	0.09		
1003627	4179		20:33:53	+41:30:21	0.86	5.82	0.66	4.8	16.06	0.09	0.03	14.82	0.02	0.09	14.24	0.02	0.08		
1003635	4211		20:33:54	+41:19:34	0.89	8.36	0.6	3.35	14.83	0.08	0.02	13.78	0.02	0.07	13.3	0.02	0.06		
1003637	4218		20:33:55	+41:31:43	1.48	8.57	0.67	4.89	16.26	0.16	0.03	15.05	0.02	0.13	14.5	0.02	0.12		
1003641	5603		20:33:55	+41:31:30	0.53	4.85	0.55	4.6	16.98	0.11	0.04	15.71	0.03	0.09	15.11	0.03	0.09		
1003646	4241		20:33:56	+41:23:03	1.58	3.81	0.72	4.72	16.28	0.15	0.03	15.17	0.02	0.16	14.35	0.02	0.16		
1003654	4262		20:33:56	+41:28:40	0.46	3.15	0.56	4.21	14.68	0.07	0.02	13.61	0.02	0.05	13.08	0.02	0.04		
1003655	4264		20:33:56	+41:24:10	1.16	5.6	0.38	3.79	16.79	0.16	0.03	15.61	0.03	0.15	15.03	0.03	0.13		
1003657	4266		20:33:57	+41:18:51	1.36	5.57	0.17	2.89	17.0	0.2	0.04	15.89	0.03	0.18	15.24	0.03	0.15		
1003659	4268		20:33:57	+41:29:16	1.66	3.16	0.42	4.55	16.84	0.17	0.04	15.62	0.03	0.19	15.01	0.03	0.15		
1003664	4301		20:33:59	+41:27:07	0.74	3.18	0.71	3.67	14.07	0.07	0.02	13.09	0.02	0.06	12.61	0.02	0.05		
1003674	4339		20:34:01	+41:20:35	0.49	2.06	0.8	2.67	15.34	0.07	0.02	14.5	0.02	0.05	14.13	0.02	0.06		
1003683	4376		20:34:03	+41:20:03	1.15	10.64	0.33	3.11	16.07	0.12	0.03	14.96	0.02	0.13	14.42	0.02	0.1		
1003685	4380		20:34:03	+41:25:55	0.52	2.83	0.46	4.11	16.42	0.08	0.03	15.17	0.02	0.09	14.58	0.02	0.1		
1003706	4446		20:34:07	+41:20:14	0.79	5.74	0.56	4.35	16.87	0.12	0.03	15.68	0.03	0.11	15.11	0.03	0.09		
1003710	4466		20:34:08	+41:21:42	0.82	10.09	0.65	4.88	16.0	0.09	0.03	14.69	0.02	0.08	14.06	0.02	0.08		
1003713	4473		20:34:08	+41:25:31	0.65	2.33	0.73	3.7	15.88	0.09	0.03	14.89	0.02	0.08	14.43	0.02	0.08		
1003715	4481		20:34:09	+41:28:22	0.31	6.27	0.56	4.7	14.91	0.05	0.02	13.79	0.02	0.04	13.26	0.02	0.04		
1003720	4489		20:34:10	+41:26:25	0.74	17.52			16.15	0.09	0.03	14.86	0.02	0.08	14.22	0.02	0.07		
1003722	4506		20:34:11	+41:20:04	0.51	2.45	0.78	3.12	15.1	0.07	0.02	14.24	0.02	0.05	13.84	0.02	0.06		
1003726	4534		20:34:12	+41:27:54	0.67	9.41	0.52	4.45	16.69	0.11	0.03	15.46	0.02	0.1	14.9	0.02	0.09		
1003731	4554		20:34:14	+41:25:05	0.96	3.74	0.69	4.53	16.1	0.12	0.03	14.94	0.02	0.1	14.41	0.02	0.1		
1003740	5551		20:34:15	+41:28:53	0.93	4.19	0.53	4.51	16.6	0.14	0.03	15.38	0.02	0.12	14.84	0.02	0.11		
1003744	4590		20:34:16	+41:26:14	0.97	7.05	0.57	4.59	16.4	0.14	0.03	15.14	0.02	0.11	14.57	0.02	0.1		
1003748	4600		20:34:17	+41:23:59	0.43	2.18	0.46	4.94	16.71	0.09	0.03	15.36	0.02	0.08	14.73	0.02	0.07		
1003759	4652		20:34:21	+41:21:19	0.68	3.87	0.48	3.6	13.45	0.06	0.02	12.51	0.02	0.07	11.99	0.02	0.08		
1003767	4690		20:34:23	+41:22:19	1.12	24.45	0.58	4.6	15.94	0.12	0.03	14.72	0.02	0.11	14.16	0.02	0.09		
1003815		53145	20:34:02	+41:25:45	1.90	9.41	0.48	4.53	16.18	0.23	0.03	14.74	0.02	0.2	13.75	0.02	0.17	CL2	1
1003823		54491	20:33:35	+41:26:52	4.27	9.38	0.46	3.43	16.54	0.49	0.03	15.41	0.02	0.48	14.59	0.02	0.37	CL2	1
1003826		61305	20:34:21	+41:19:26	2.54	5.5	0.28	4.18	17.25	0.41	0.05	15.86	0.03	0.34	14.94	0.02	0.31	CL2	1
1003842		54992	20:33:24	+41:25:39	4.68	7.16	0.51	3.89	16.85	0.53	0.04	15.54	0.03	0.47	14.75	0.02	0.36	CL2	1
1103848	125		20:30:54	+41:23:51	0.92	3.06			15.73	0.12	0.02	14.61	0.02	0.1	14.06	0.02	0.08		
1103850	127		20:30:54	+41:25:36	0.70	6.62	0.67	2.5	16.08	0.1	0.03	15.23	0.02	0.08	14.85	0.02	0.09		
1103851	128	1872	20:30:54	+41:30:17	1.15	7.69	0.47	3.62	15.8	0.11	0.03	14.58	0.02	0.11	13.95	0.02	0.11	CL2	1
1103855	135	102637	20:30:56	+41:20:15	2.77	10.27			16.39	0.31	0.03	15.06	0.02	0.31	14.24	0.02	0.36	CL2	1
1103857	140		20:30:56	+41:25:40	0.90	15.69			16.32	0.12	0.03	15.12	0.02	0.1	14.55	0.02	0.09		
1103873	168		20:31:02	+41:22:06	0.78	7.45	0.58	2.3	15.61	0.08	0.02	14.75	0.02	0.08	14.32	0.02	0.07		
1103875	172	27624	20:31:02	+41:30:06	0.48	6.22			16.29	0.08	0.03	15.45	0.03	0.08	15.03	0.03	0.09	CL2	1
1103876	176		20:31:03	+41:22:15	0.83	5.83	0.63	4.59	15.9	0.11	0.03	14.72	0.02	0.08	14.14	0.02	0.07		
1103883	191		20:31:05	+41:20:26	0.55	2.12	0.61	3.61	14.36	0.07	0.02	13.41	0.02	0.06	12.92	0.02	0.05		
1103887	198		20:31:06	+41:25:38	0.48	4.9	0.69	4.14	15.15	0.06	0.02	14.12	0.02	0.05	13.63	0.02	0.05		
1103888	199		20:31:06	+41:28:53	0.35	10.42	0.48	3.38	16.5	0.09	0.03	15.32	0.02	0.06	14.77	0.02	0.07		
1103918	254		20:31:12	+41:31:20	1.09	7.22	0.44	2.74	16.45	0.13	0.03	15.38	0.03	0.12	14.92	0.03	0.11		
1103922	260		20:31:13	+41:21:57	0.35	7.1	0.63	4.15	14.04	0.05	0.02	12.9	0.02	0.05	12.37	0.02	0.05		
1103933	290		20:31:16	+41:26:32	0.90	5.26	0.57	4.02	15.36	0.1	0.02	14.19	0.02	0.09	13.64	0.02	0.07		
1103938	295		20:31:17	+41:31:29	0.75	6.64	0.31	2.89	16.79	0.13	0.04	15.72	0.03	0.12	15.23	0.03	0.1		
1103942	303		20:31:17	+41:23:54	0.62	2.69	0.61	4.42	16.84	0.13	0.04	15.64	0.03	0.09	15.07	0.03	0.09		
1103945	311		20:31:18	+41:30:10	2.38	9.61	0.64	2.78	15.84	0.2	0.03	14.83	0.02	0.18	14.39	0.02	0.17		
1103947	318		20:31:19	+41:19:23	1.42	10.24	0.67	4.48	15.55	0.13	0.02	14.35	0.02	0.12	13.78	0.02	0.11		
1103958	347		20:31:21	+41:29:04	0.84	3.28	0.25	3.25	16.77	0.13	0.04	15.64	0.03	0.12	15.04	0.03	0.09		
1103962	362		20:31:23	+41:23:47	1.77	8.82	0.45	3.94	16.63	0.17	0.03	15.43	0.03	0.18	14.87	0.02	0.15		
1103974	381		20:31:24	+41:31:08	0.56	7.71	0.44	2.66	16.48	0.09	0.03	15.45	0.03	0.08	15.0	0.03	0.08		
1103976	383		20:31:25	+41:27:34	1.06	5.79	0.22	2.31	16.79	0.14	0.04	15.66	0.03	0.14	15.12	0.03	0.11		

Table C.1: Continued.

Id	GDW13	GDW15	RA	Dec	Stet	Per	Mass	Av	mJ	eJ	ptpJ	mH	eH	ptpH	mK	eK	ptpK	Class	Disk
1103987	407		20:31:26	+41:32:10	1.41	6.13	0.41	2.81	16.56	0.15	0.03	15.51	0.03	0.15	15.04	0.03	0.14		
1103989	5217		20:31:27	+41:19:26	0.56	9.34	0.33	4.47	16.97	0.15	0.04	15.63	0.03	0.1	14.98	0.03	0.1		
1103993	419		20:31:27	+41:24:59	0.57	8.91	0.68	3.8	15.16	0.07	0.02	14.1	0.02	0.05	13.62	0.02	0.05		
1104007	452		20:31:30	+41:28:19	1.05	2.12	0.36	3.39	16.83	0.14	0.04	15.71	0.03	0.15	15.17	0.03	0.13		
1104026	491		20:31:34	+41:29:52	1.41	15.32	0.53	3.86	16.31	0.12	0.03	15.28	0.02	0.13	14.76	0.02	0.11		
1104030	502		20:31:35	+41:31:21	0.46	4.46	0.78	3.55	14.63	0.06	0.02	13.71	0.02	0.05	13.29	0.02	0.04		
1104037	514		20:31:36	+41:26:37	0.63	2.05	0.66	3.29	15.98	0.09	0.03	14.93	0.02	0.07	14.44	0.02	0.07		
1104042	523		20:31:36	+41:21:22	0.45	4.62	0.6	4.26	15.79	0.06	0.03	14.59	0.02	0.05	14.02	0.02	0.05		
1104048	535		20:31:37	+41:25:20	0.75	3.55	0.67	3.52	15.44	0.07	0.02	14.36	0.02	0.07	13.88	0.02	0.06		
1104051	538		20:31:37	+41:25:33	0.59	8.13	0.66	3.0	14.72	0.07	0.02	13.81	0.02	0.05	13.39	0.02	0.05		
1104055	547		20:31:38	+41:19:00	0.83	2.47			16.24	0.11	0.03	14.91	0.02	0.1	14.25	0.02	0.08		
1104057	553		20:31:38	+41:20:48	0.69	6.12	0.55	4.3	15.96	0.08	0.03	14.73	0.02	0.07	14.14	0.02	0.06		
1104092	648		20:31:43	+41:20:09	0.61	4.52	0.69	4.54	15.83	0.09	0.03	14.6	0.02	0.07	14.04	0.02	0.06		
1104097	662		20:31:44	+41:31:10	1.57	3.05	0.78	3.4	15.52	0.13	0.02	14.53	0.02	0.14	14.1	0.02	0.12		
1104099	664		20:31:45	+41:24:54	0.42	19.0	0.68	3.57	15.57	0.06	0.02	14.5	0.02	0.04	14.0	0.02	0.04		
1104101	679		20:31:45	+41:25:13	0.73	10.91	0.62	3.8	16.0	0.09	0.03	14.86	0.02	0.08	14.32	0.02	0.07		
1104107	695		20:31:46	+41:31:21	1.07	3.19	0.55	3.38	15.67	0.1	0.02	14.62	0.02	0.09	14.14	0.02	0.09		
1104109	700		20:31:46	+41:22:28	0.98	7.79	0.48	3.68	16.14	0.11	0.03	14.97	0.02	0.09	14.4	0.02	0.08		
1104116	717		20:31:47	+41:19:41	0.51	7.5	0.56	3.95	16.84	0.12	0.04	15.57	0.03	0.09	15.0	0.03	0.08		
1104124	738		20:31:48	+41:29:02	0.81	7.08	0.38	2.46	15.48	0.07	0.02	14.45	0.02	0.07	13.97	0.02	0.07		
1104129	746		20:31:49	+41:25:19	0.65	4.92	0.48	3.49	16.98	0.13	0.04	15.83	0.03	0.09	15.27	0.03	0.09		
1104146	784		20:31:51	+41:26:55	1.53	13.71	0.72	3.96	16.13	0.15	0.03	15.07	0.02	0.13	14.58	0.02	0.11		
1104151	790		20:31:51	+41:26:39	0.81	4.63	0.43	2.42	15.62	0.08	0.02	14.58	0.02	0.08	14.1	0.02	0.07		
1104153	795		20:31:52	+41:22:20	0.32	3.66	0.67	4.73	16.66	0.09	0.03	15.55	0.03	0.07	15.0	0.03	0.07		
1104154	799		20:31:52	+41:25:23	0.37	7.54	0.47	4.3	16.3	0.07	0.03	15.2	0.02	0.05	14.62	0.02	0.06		
1104159	807		20:31:52	+41:26:10	6.40	3.67	0.75	4.11	16.21	0.68	0.03	15.07	0.02	0.6	14.26	0.02	0.45		
1104176	842		20:31:54	+41:30:51	0.41	9.41	0.59	3.17	16.46	0.08	0.03	15.39	0.03	0.06	14.92	0.03	0.06		
1104184	854		20:31:55	+41:21:51	0.58	2.53	0.68	3.99	14.23	0.07	0.02	13.21	0.02	0.05	12.75	0.02	0.05		
1104185	855		20:31:55	+41:31:25	0.81	5.83	0.59	3.02	16.01	0.08	0.03	14.97	0.02	0.08	14.51	0.02	0.08		
1104189	867		20:31:55	+41:19:48	1.10	4.63	0.61	4.5	15.55	0.11	0.02	14.38	0.02	0.1	13.83	0.02	0.08		
1104190	873		20:31:55	+41:20:56	0.65	3.16	0.56	3.65	14.69	0.08	0.02	13.64	0.02	0.07	13.14	0.02	0.06		
1104193	878		20:31:56	+41:26:07	0.57	11.54	0.65	3.46	16.05	0.07	0.03	15.01	0.02	0.07	14.55	0.02	0.06		
1104199	889		20:31:56	+41:30:00	0.33	6.18	0.24	2.41	16.28	0.07	0.03	15.29	0.02	0.06	14.76	0.02	0.06		
1104207	911		20:31:57	+41:27:01	0.76	5.72	0.33	2.78	16.86	0.14	0.04	15.78	0.03	0.11	15.24	0.03	0.1		
1104216	935		20:31:59	+41:27:36	0.92	2.75	0.87	3.49	15.44	0.09	0.02	14.47	0.02	0.07	14.03	0.02	0.07		
1104221	940		20:31:59	+41:25:45	0.91	10.84	0.54	3.31	16.87	0.16	0.04	15.73	0.03	0.12	15.23	0.03	0.11		
1104226	950		20:31:59	+41:29:03	0.46	8.86	0.46	2.84	16.56	0.08	0.03	15.55	0.03	0.08	15.08	0.03	0.07		
1104227	949		20:31:59	+41:31:25	0.66	5.2	0.59	3.14	16.29	0.1	0.03	15.24	0.02	0.08	14.78	0.02	0.08		
1104239	976		20:32:01	+41:22:09	1.28	5.89	0.75	3.73	15.5	0.11	0.02	14.47	0.02	0.11	13.98	0.02	0.09		
1104240	979		20:32:01	+41:22:46	0.70	6.12	0.72	3.75	15.81	0.08	0.03	14.76	0.02	0.08	14.28	0.02	0.07		
1104242	984	303795	20:32:01	+41:31:14	1.27	10.65	0.83	3.54	15.21	0.13	0.02	14.18	0.02	0.11	13.6	0.02	0.11	CL2_Ha	1
1104243	987		20:32:01	+41:29:29	0.58	13.91	0.68	3.2	15.72	0.07	0.02	14.74	0.02	0.06	14.28	0.02	0.06		
1104249	1006		20:32:02	+41:26:44	0.60	7.14	0.46	3.23	16.11	0.08	0.03	15.0	0.02	0.07	14.49	0.02	0.07		
1104250	1004		20:32:02	+41:31:07	0.82	8.03	0.45	2.87	16.4	0.11	0.03	15.38	0.02	0.1	14.89	0.02	0.11		
1104254	1009		20:32:02	+41:31:37	1.16	3.71	0.78	2.9	14.52	0.11	0.02	13.63	0.02	0.1	13.24	0.02	0.11		
1104259	1028		20:32:03	+41:25:14	0.75	2.62	0.77	3.26	15.46	0.09	0.02	14.53	0.02	0.06	14.09	0.02	0.06		
1104284		5749	20:32:01	+41:29:51	2.03	3.93	0.3	2.33	16.92	0.35	0.04	15.77	0.03	0.27	15.05	0.03	0.22	CL2	1
1104285		6721	20:31:57	+41:22:30	1.70	6.53	0.81	4.72	15.75	0.17	0.03	14.52	0.02	0.16	13.69	0.02	0.16	CL2	1
1104286		9259	20:31:35	+41:25:45	3.33	6.89	0.6	3.59	16.37	0.46	0.03	15.21	0.02	0.35	14.58	0.02	0.27	CL2_high-incl	1
1204346	153		20:30:59	+41:17:29	0.60	7.46			16.12	0.08	0.03	14.75	0.02	0.07	14.04	0.02	0.07		
1204353	174		20:31:02	+41:15:19	1.13	9.77			16.66	0.13	0.03	15.36	0.02	0.11	14.74	0.02	0.11		
1204367	212		20:31:08	+41:10:58	0.61	3.03	0.39	3.52	13.72	0.07	0.02	12.71	0.02	0.06	12.17	0.02	0.05		
1204371	225		20:31:09	+41:15:04	0.93	6.26	0.44	4.08	15.71	0.1	0.02	14.49	0.02	0.08	13.88	0.02	0.07		
1204376	244		20:31:12	+41:18:36	1.14	2.31			16.01	0.12	0.03	14.79	0.02	0.11	14.17	0.02	0.1		
1204380	258		20:31:13	+41:14:31	0.78	3.31	0.67	4.61	15.76	0.11	0.02	14.6	0.02	0.09	14.06	0.02	0.09		
1204387	270		20:31:14	+41:15:26	2.19	5.19			17.01	0.23	0.04	15.82	0.03	0.23	15.24	0.03	0.21		

Table C.1: Continued.

Id	GDW13	GDW15	RA	Dec	Stet	Per	Mass	Av	mJ	eJ	ptpJ	mH	eH	ptpH	mK	eK	ptpK	Class	Disk
1204392	278		20:31:15	+41:06:42	0.41	9.15	0.62	3.66	15.65	0.06	0.02	14.55	0.02	0.05	14.02	0.02	0.05		
1204397	288		20:31:16	+41:10:05	0.50	8.36	0.57	3.62	15.53	0.06	0.02	14.39	0.02	0.05	13.83	0.02	0.05		
1204419	341		20:31:21	+41:09:00	0.72	4.72	0.51	3.54	14.78	0.07	0.02	13.61	0.02	0.06	13.07	0.02	0.05		
1204423	352		20:31:22	+41:14:50	0.95	8.66			15.67	0.11	0.02	14.48	0.02	0.09	13.88	0.02	0.09		
1204431	366		20:31:23	+41:15:19	1.39	9.7	0.56	6.92	17.32	0.19	0.05	16.04	0.03	0.19	15.4	0.03	0.16		
1204435	5216		20:31:25	+41:17:30	0.36	8.05	0.6	6.73	16.88	0.1	0.04	15.53	0.02	0.06	14.84	0.02	0.06		
1204437	388		20:31:25	+41:10:37	1.37	14.64	0.56	3.88	16.26	0.13	0.03	15.06	0.02	0.12	14.5	0.02	0.11		
1204439	393		20:31:26	+41:08:00	0.40	6.75	0.55	1.42	15.78	0.06	0.02	14.92	0.02	0.05	14.54	0.02	0.05		
1204441	401		20:31:26	+41:07:47	0.57	6.68	0.62	3.78	15.05	0.06	0.02	13.96	0.02	0.06	13.45	0.02	0.05		
1204442	410		20:31:26	+41:18:19	0.62	8.62	0.66	6.02	16.57	0.09	0.03	15.22	0.02	0.08	14.55	0.02	0.07		
1204448	428	6968	20:31:28	+41:17:11	3.40	4.81	0.72	5.95	15.72	0.32	0.02	14.41	0.02	0.3	13.57	0.02	0.23	CL2	1
1204455	446		20:31:30	+41:15:26	0.60	2.32	0.71	5.58	15.98	0.08	0.03	14.73	0.02	0.06	14.12	0.02	0.06		
1204468	479		20:31:33	+41:10:25	1.55	3.9	0.46	2.87	16.81	0.16	0.03	15.63	0.03	0.15	15.08	0.03	0.14		
1204469	482	69058	20:31:33	+41:14:01	4.14	3.06	0.65	5.97	16.17	0.48	0.03	14.68	0.02	0.4	13.56	0.02	0.28	CL2	1
1204477	496		20:31:34	+41:17:45	0.99	7.57			17.85	0.24	0.06	16.48	0.04	0.22	15.79	0.03	0.17		
1204479	503		20:31:35	+41:10:27	0.89	6.71	0.3	3.95	17.31	0.14	0.05	16.12	0.03	0.15	15.51	0.03	0.13		
1204491	540		20:31:37	+41:11:40	0.46	13.07	0.32	4.04	17.2	0.12	0.04	16.0	0.03	0.09	15.38	0.03	0.09		
1204499	563		20:31:39	+41:11:26	0.81	15.89	0.59	5.02	15.8	0.09	0.02	14.56	0.02	0.08	13.96	0.02	0.06		
1204506	573		20:31:39	+41:07:53	0.90	7.32	0.93	3.39	11.9	0.09	0.02	11.25	0.02	0.06	10.85	0.02	0.07		
1204512	584		20:31:40	+41:11:47	0.82	2.68	0.3	4.36	16.82	0.11	0.03	15.56	0.02	0.11	14.93	0.02	0.09		
1204514	593		20:31:40	+41:11:26	1.04	5.92	0.49	4.59	16.75	0.14	0.03	15.52	0.02	0.12	14.94	0.02	0.1		
1204517	601		20:31:40	+41:14:05	0.54	32.49	0.6	4.35	14.93	0.06	0.02	13.77	0.02	0.05	13.25	0.02	0.05		
1204522	616		20:31:41	+41:11:01	0.59	3.37	0.67	4.46	15.66	0.08	0.02	14.53	0.02	0.06	14.0	0.02	0.05		
1204526	627		20:31:42	+41:08:05	0.62	4.11	0.73	4.28	15.9	0.08	0.03	14.8	0.02	0.06	14.3	0.02	0.05		
1204542	669		20:31:45	+41:10:40	0.63	7.37	0.67	4.16	15.14	0.07	0.02	14.06	0.02	0.06	13.56	0.02	0.06		
1204545	678		20:31:45	+41:18:33	1.04	2.09			14.36	0.15	0.02	13.33	0.02	0.09	12.83	0.02	0.07		
1204547	681		20:31:45	+41:10:54	0.43	2.34	0.68	5.35	16.14	0.06	0.03	14.93	0.02	0.05	14.32	0.02	0.05		
1204551	697		20:31:46	+41:18:04	1.01	6.26	0.74	5.56	16.63	0.13	0.03	15.41	0.02	0.1	14.87	0.02	0.1		
1204552	698		20:31:46	+41:11:12	0.37	5.12	0.81	6.33	15.83	0.06	0.02	14.57	0.02	0.04	13.97	0.02	0.04		
1204567	747		20:31:49	+41:13:53	1.00	2.59	0.75	6.52	17.01	0.14	0.04	15.7	0.03	0.12	15.1	0.03	0.1		
1204576	774		20:31:51	+41:15:20	1.30	9.8	0.62	6.05	16.79	0.13	0.03	15.44	0.02	0.14	14.81	0.02	0.12		
1204579	777	68798	20:31:51	+41:15:42	1.18	8.11			16.93	0.13	0.04	15.59	0.03	0.14	14.89	0.02	0.13	CL2	1
1204581	785		20:31:51	+41:08:33	0.54	4.07	0.49	4.24	16.59	0.11	0.03	15.34	0.02	0.07	14.75	0.02	0.06		
1204585	812		20:31:53	+41:14:19	0.40	3.83	0.87	5.45	15.75	0.06	0.02	14.6	0.02	0.04	14.08	0.02	0.05		
1204586	816		20:31:53	+41:09:11	0.91	6.44	0.67	5.37	16.47	0.11	0.03	15.15	0.02	0.1	14.52	0.02	0.09		
1204588	821		20:31:53	+41:17:10	0.80	5.57	0.78	5.07	15.68	0.09	0.02	14.54	0.02	0.07	14.02	0.02	0.06		
1204589	824	68803	20:31:53	+41:15:20	2.31	5.73	0.63	5.32	16.9	0.25	0.04	15.6	0.03	0.26	14.89	0.02	0.32	CL2	1
1204600	864		20:31:55	+41:14:42	0.74	14.09	0.53	4.27	16.22	0.09	0.03	15.04	0.02	0.09	14.51	0.02	0.07		
1204606	899		20:31:57	+41:06:41	0.93	20.21	0.64	6.03	16.96	0.13	0.04	15.54	0.02	0.12	14.89	0.02	0.11		
1204682		85886	20:31:13	+41:12:29	4.35	9.87			15.95	0.46	0.03	14.72	0.02	0.4	13.97	0.02	0.28	CL2	1
1204684		86423	20:31:03	+41:15:50	0.86	6.77			17.41	0.19	0.05	16.05	0.03	0.16	15.12	0.03	0.16	CL2	1
1204691		106264	20:31:03	+41:09:39	0.98	7.86			17.42	0.16	0.05	16.0	0.03	0.15	15.18	0.03	0.12	CL2	1
1304722	3139		20:33:17	+41:06:32	1.20	4.54			14.79	0.11	0.02	13.7	0.02	0.09	13.19	0.02	0.09		
1304725	3141		20:33:17	+41:15:07	4.37	4.3	0.58	4.56	16.27	0.35	0.03	15.02	0.02	0.36	14.42	0.02	0.31		
1304730	3159		20:33:17	+41:07:24	1.13	3.19	0.48	4.62	16.75	0.13	0.03	15.55	0.03	0.12	14.93	0.02	0.11		
1304739	3188		20:33:18	+41:07:50	1.21	7.01	0.37	4.06	16.52	0.13	0.03	15.31	0.02	0.13	14.71	0.02	0.11		
1304744	3192		20:33:18	+41:11:01	0.83	7.32			16.45	0.09	0.03	15.18	0.02	0.09	14.57	0.02	0.09		
1304748	3206		20:33:18	+41:12:41	0.67	6.93	0.09	2.06	17.09	0.13	0.04	15.79	0.03	0.12	15.16	0.03	0.1		
1304749	3210		20:33:18	+41:11:19	0.76	3.07	0.61	4.24	15.66	0.08	0.02	14.48	0.02	0.07	13.9	0.02	0.08		
1304752	3215		20:33:19	+41:17:24	0.40	6.78	0.53	4.85	16.44	0.08	0.03	15.07	0.02	0.06	14.42	0.02	0.05		
1304753	3221		20:33:19	+41:17:04	0.70	4.27	0.18	2.35	16.22	0.08	0.03	15.07	0.02	0.08	14.5	0.02	0.07		
1304756	3225		20:33:19	+41:13:33	0.32	2.9	0.6	4.1	15.85	0.05	0.03	14.63	0.02	0.04	14.08	0.02	0.04		
1304757	3226		20:33:19	+41:13:19	0.57	9.39	0.42	3.61	17.24	0.15	0.05	16.0	0.03	0.11	15.42	0.03	0.1		
1304759	3232		20:33:19	+41:09:56	2.76	5.89	0.67	5.45	16.2	0.21	0.03	14.92	0.02	0.21	14.3	0.02	0.18		
1304762	3234		20:33:19	+41:13:54	0.56	8.66	0.62	4.18	15.64	0.07	0.02	14.46	0.02	0.06	13.89	0.02	0.06		
1304764	3240		20:33:19	+41:11:56	2.24	6.6	0.35	3.59	16.84	0.38	0.04	15.47	0.02	0.28	14.68	0.02	0.24		
1304766	3244		20:33:19	+41:17:02	0.61	7.18	0.38	2.62	15.27	0.08	0.02	14.12	0.02	0.06	13.56	0.02	0.05		

Table C.1: Continued.

Id	GDW13	GDW15	RA	Dec	Stet	Per	Mass	Av	mJ	eJ	ptpJ	mH	eH	ptpH	mK	eK	ptpK	Class	Disk
1304770	3249	65563	20:33:19	+41:15:18	3.42	11.91	0.62	4.75	15.8	0.31	0.03	14.4	0.02	0.26	13.46	0.02	0.25	CL2	1
1304774	3257		20:33:20	+41:10:43	0.50	15.18	0.6	3.57	14.77	0.06	0.02	13.74	0.02	0.04	13.26	0.02	0.04		
1304775	3261		20:33:20	+41:09:57	0.84	2.57	0.69	4.96	15.98	0.09	0.03	14.77	0.02	0.08	14.19	0.02	0.07		
1304787	3287		20:33:20	+41:14:32	1.95	5.57	0.6	4.01	15.21	0.15	0.02	14.08	0.02	0.14	13.55	0.02	0.12		
1304788	3290		20:33:20	+41:16:48	0.98	9.12	0.32	3.55	16.39	0.11	0.03	15.17	0.02	0.11	14.57	0.02	0.09		
1304798	3322		20:33:21	+41:17:09	1.87	8.13	0.45	3.37	17.1	0.21	0.04	15.92	0.03	0.22	15.38	0.03	0.19		
1304803	3331		20:33:21	+41:08:57	0.89	14.7	0.54	5.2	16.63	0.12	0.03	15.23	0.02	0.09	14.6	0.02	0.08		
1304806	3332		20:33:21	+41:18:46	1.91	7.14			15.84	0.15	0.02	14.76	0.02	0.14	14.28	0.02	0.12		
1304807	3334		20:33:21	+41:06:33	0.94	6.35	0.41	4.16	16.82	0.15	0.04	15.55	0.03	0.12	14.97	0.03	0.11		
1304813	3353	24875	20:33:22	+41:09:45	5.80	11.83	0.6	4.7	15.16	0.54	0.02	13.82	0.02	0.43	12.98	0.02	0.32	CL2	1
1304817	3359		20:33:22	+41:12:18	0.83	2.93	0.5	4.01	15.01	0.07	0.02	13.88	0.02	0.07	13.31	0.02	0.07		
1304818	3360		20:33:22	+41:10:04	0.93	5.69	0.43	4.0	16.71	0.11	0.03	15.46	0.03	0.11	14.86	0.02	0.13		
1304819	3363		20:33:22	+41:12:45	0.69	2.22	0.51	3.53	15.27	0.07	0.02	14.1	0.02	0.06	13.55	0.02	0.06		
1304823	3369		20:33:22	+41:15:52	0.60	8.85	0.34	3.84	16.16	0.07	0.03	14.9	0.02	0.06	14.29	0.02	0.06		
1304825	3375		20:33:23	+41:13:40	2.05	5.26	0.57	4.02	15.81	0.18	0.02	14.58	0.02	0.17	13.99	0.02	0.14		
1304839	3432		20:33:24	+41:08:13	0.95	4.61	0.49	4.98	15.56	0.08	0.02	14.27	0.02	0.08	13.64	0.02	0.08		
1304843	3445		20:33:25	+41:15:54	1.01	2.65	0.44	4.32	16.63	0.12	0.03	15.37	0.02	0.11	14.75	0.02	0.1		
1304844	3447		20:33:25	+41:11:00	0.66	6.22			15.95	0.08	0.03	14.72	0.02	0.06	14.14	0.02	0.07		
1304852	3460		20:33:25	+41:15:37	0.72	4.94	0.42	3.69	15.82	0.07	0.02	14.58	0.02	0.07	13.98	0.02	0.07		
1304853	3464		20:33:25	+41:10:51	1.11	14.13	0.49	4.1	16.47	0.11	0.03	15.21	0.02	0.11	14.59	0.02	0.1		
1304856	5527		20:33:25	+41:09:18	1.04	21.92			17.2	0.16	0.05	15.94	0.03	0.15	15.24	0.03	0.14		
1304864	3485		20:33:26	+41:13:17	0.73	7.21	0.21	2.46	17.25	0.15	0.05	16.0	0.03	0.13	15.43	0.03	0.11		
1304865	3486		20:33:26	+41:17:19	0.85	4.27	0.4	3.1	16.55	0.11	0.03	15.31	0.02	0.09	14.77	0.02	0.08		
1304866	3483		20:33:26	+41:13:22	1.21	2.28	0.58	3.38	15.05	0.1	0.02	13.94	0.02	0.09	13.43	0.02	0.09		
1304870	3495		20:33:26	+41:12:39	0.62	2.72	0.51	2.9	14.37	0.07	0.02	13.38	0.02	0.05	12.91	0.02	0.05		
1304876	3502		20:33:27	+41:09:26	0.65	9.05	0.34	3.84	16.94	0.12	0.04	15.61	0.03	0.1	15.01	0.03	0.08		
1304877	3506		20:33:27	+41:15:56	0.46	6.32	0.38	3.65	16.67	0.09	0.03	15.4	0.02	0.07	14.82	0.02	0.07		
1304881	3510		20:33:27	+41:12:18	1.13	2.28	0.55	3.17	15.38	0.09	0.02	14.22	0.02	0.09	13.68	0.02	0.08		
1304889	3532		20:33:27	+41:07:54	1.07	11.54	0.48	4.09	16.57	0.12	0.03	15.33	0.02	0.11	14.73	0.02	0.1		
1304890	3531		20:33:27	+41:15:26	0.93	6.52			16.41	0.1	0.03	15.15	0.02	0.1	14.51	0.02	0.08		
1304898	3545		20:33:28	+41:15:10	1.10	6.59	0.8	4.84	15.92	0.11	0.03	14.79	0.02	0.09	14.28	0.02	0.08		
1304902	3558		20:33:28	+41:15:02	0.85	3.68	0.67	5.24	15.53	0.08	0.02	14.35	0.02	0.08	13.77	0.02	0.07		
1304904	3565		20:33:29	+41:14:06	0.86	4.86	0.59	5.37	17.03	0.16	0.04	15.75	0.03	0.11	15.14	0.03	0.1		
1304907	3572		20:33:29	+41:15:35	1.98	4.81	0.75	5.33	16.05	0.18	0.03	14.78	0.02	0.16	13.96	0.02	0.17		
1304909	3578		20:33:29	+41:16:06	0.39	4.37	0.47	4.59	16.34	0.07	0.03	15.15	0.02	0.05	14.56	0.02	0.05		
1304910	3579		20:33:29	+41:15:07	1.41	4.19	0.47	4.83	16.4	0.13	0.03	15.28	0.02	0.13	14.71	0.02	0.12		
1304911	3581		20:33:29	+41:09:25	1.01	8.12	0.33	3.57	16.99	0.14	0.04	15.75	0.03	0.13	15.15	0.03	0.12		
1304922	3604		20:33:30	+41:09:37	0.36	4.13	0.62	3.53	14.85	0.05	0.02	13.89	0.02	0.04	13.41	0.02	0.04		
1304926	3616		20:33:31	+41:10:12	0.93	2.31	0.56	4.05	15.23	0.07	0.02	14.06	0.02	0.09	13.51	0.02	0.1		
1304928	5343		20:33:31	+41:13:29	0.40	8.4			17.67	0.16	0.06	16.38	0.04	0.13	15.76	0.03	0.11		
1304930	3622		20:33:31	+41:13:41	0.67	3.47	0.57	4.81	15.91	0.11	0.03	14.65	0.02	0.08	14.06	0.02	0.08		
1304941	3645		20:33:32	+41:14:45	0.86	5.07	0.55	5.09	17.36	0.16	0.05	16.11	0.03	0.14	15.48	0.03	0.12		
1304957	3686		20:33:33	+41:17:30	0.57	12.17	0.72	4.32	15.6	0.07	0.02	14.49	0.02	0.06	13.99	0.02	0.05		
1304959	3690		20:33:33	+41:08:03	1.66	2.35	0.58	4.1	15.32	0.13	0.02	14.12	0.02	0.12	13.56	0.02	0.11		
1304961	3705		20:33:34	+41:11:29	1.05	10.46	0.65	4.4	16.33	0.12	0.03	15.11	0.02	0.11	14.53	0.02	0.11		
1304966	3723		20:33:35	+41:17:20	3.14	10.42	0.67	4.01	16.02	0.31	0.03	14.82	0.02	0.31	14.12	0.02	0.32		
1304971	3729		20:33:35	+41:16:13	2.20	7.48	0.68	5.72	17.14	0.23	0.04	15.97	0.03	0.26	15.39	0.03	0.24		
1304975	3735		20:33:35	+41:18:22	1.35	2.32	0.58	4.08	16.29	0.14	0.03	15.16	0.02	0.15	14.61	0.02	0.13		
1304978	3741		20:33:36	+41:15:56	0.68	2.18	0.6	4.5	16.31	0.09	0.03	15.13	0.02	0.07	14.57	0.02	0.07		
1304979	3746		20:33:36	+41:12:07	0.63	7.83	0.34	3.77	16.81	0.1	0.04	15.6	0.03	0.09	15.03	0.03	0.08		
1304981	3750		20:33:36	+41:15:19	0.72	16.62	0.6	5.45	17.02	0.12	0.04	15.69	0.03	0.09	15.06	0.03	0.1		
1304982	5353		20:33:36	+41:08:30	0.93	7.8	0.37	4.59	17.72	0.22	0.06	16.42	0.04	0.18	15.77	0.03	0.15		
1304989	3776		20:33:37	+41:07:07	0.49	8.1	0.51	4.13	15.92	0.07	0.03	14.65	0.02	0.06	14.06	0.02	0.06		
1304994	3797		20:33:38	+41:14:57	2.67	2.94	0.52	4.87	16.52	0.23	0.03	15.21	0.02	0.24	14.56	0.02	0.2		
1305004	3831		20:33:39	+41:14:36	0.82	2.65	0.61	4.77	15.34	0.08	0.02	14.14	0.02	0.07	13.57	0.02	0.06		
1305005	3839		20:33:39	+41:12:01	0.56	8.24	0.27	3.31	17.03	0.12	0.04	15.84	0.03	0.11	15.25	0.03	0.09		
1305008	3847		20:33:39	+41:06:47	0.67	4.84	0.46	4.16	15.02	0.07	0.02	13.78	0.02	0.06	13.21	0.02	0.06		

Table C.1: Continued.

Id	GDW13	GDW15	RA	Dec	Stet	Per	Mass	Av	mJ	eJ	ptpJ	mH	eH	ptpH	mK	eK	ptpK	Class	Disk
1305009	3849		20:33:39	+41:07:08	0.44	7.48	0.5	3.97	16.14	0.07	0.03	14.93	0.02	0.06	14.37	0.02	0.06		
1305013	3860		20:33:40	+41:15:26	1.42	8.8	0.32	4.92	17.06	0.17	0.04	15.75	0.03	0.17	15.06	0.03	0.14		
1305014	3863		20:33:40	+41:07:25	0.51	2.79	0.7	3.61	15.84	0.08	0.03	14.8	0.02	0.06	14.31	0.02	0.05		
1305035	3911		20:33:42	+41:12:35	1.03	4.11	0.67	3.5	15.2	0.12	0.02	14.18	0.02	0.09	13.7	0.02	0.08		
1305038	3919		20:33:42	+41:10:20	1.77	2.18	0.78	4.47	13.91	0.13	0.02	12.79	0.02	0.12	12.27	0.02	0.12		
1305041	3925		20:33:42	+41:10:55	1.73	8.44	0.65	4.19	16.53	0.17	0.03	15.33	0.02	0.17	14.77	0.02	0.15		
1305050	3973		20:33:43	+41:17:19	1.70	2.81	0.44	3.72	15.7	0.13	0.02	14.49	0.02	0.14	13.94	0.02	0.11		
1305064	4002		20:33:45	+41:13:32	0.65	3.26	0.54	3.67	14.55	0.06	0.02	13.49	0.02	0.05	12.99	0.02	0.05		
1305066	4007		20:33:45	+41:10:51	0.92	6.27	0.66	4.17	15.39	0.08	0.02	14.23	0.02	0.07	13.7	0.02	0.06		
1305097	4076		20:33:48	+41:15:38	0.64	8.32	0.66	3.49	15.4	0.07	0.02	14.32	0.02	0.06	13.84	0.02	0.05		
1305104	4095		20:33:49	+41:07:54	0.79	14.09	0.49	3.37	16.45	0.1	0.03	15.25	0.02	0.09	14.75	0.02	0.08		
1305111	4115		20:33:49	+41:11:48	0.57	2.62	0.58	3.78	15.96	0.08	0.03	14.79	0.02	0.06	14.23	0.02	0.06		
1305112	4120		20:33:50	+41:17:10	0.59	2.65	0.54	3.89	16.29	0.09	0.03	15.12	0.02	0.08	14.55	0.02	0.07		
1305120	4138		20:33:51	+41:08:57	0.95	9.17	0.56	4.21	16.25	0.11	0.03	15.05	0.02	0.1	14.47	0.02	0.08		
1305123	4145		20:33:51	+41:16:36	1.62	10.64			16.36	0.16	0.03	15.23	0.02	0.14	14.74	0.02	0.13		
1305125	4147		20:33:51	+41:06:42	1.11	12.82	0.58	3.91	16.21	0.12	0.03	15.03	0.02	0.1	14.52	0.02	0.09		
1305129	4158	13713	20:33:52	+41:07:45	0.77	7.13	0.45	4.21	15.59	0.08	0.02	14.3	0.02	0.09	13.59	0.02	0.08	CL2	1
1305132	4165		20:33:52	+41:07:44	1.63	2.14	0.57	3.83	16.26	0.16	0.03	15.08	0.02	0.15	14.54	0.02	0.14		
1305133	4170		20:33:53	+41:15:59	0.79	8.44	0.85	4.57	15.9	0.08	0.03	14.84	0.02	0.08	14.37	0.02	0.07		
1305138	4187		20:33:54	+41:09:52	1.08	3.67	0.29	3.5	16.42	0.13	0.03	15.17	0.02	0.11	14.55	0.02	0.1		
1305143	4212		20:33:54	+41:13:40	0.90	2.92	0.58	5.22	15.55	0.1	0.02	14.29	0.02	0.09	13.69	0.02	0.07		
1305150	4230		20:33:55	+41:16:57	1.35	4.54	0.68	3.87	16.17	0.13	0.03	15.07	0.02	0.12	14.59	0.02	0.1		
1305151	4231		20:33:55	+41:07:09	1.44	2.35	0.62	3.48	15.49	0.13	0.02	14.38	0.02	0.11	13.89	0.02	0.09		
1305153	4233		20:33:55	+41:10:43	2.31	3.29	0.55	4.35	16.28	0.21	0.03	14.99	0.02	0.18	14.38	0.02	0.16		
1305162	4276		20:33:57	+41:07:04	0.45	5.5	0.32	3.28	16.74	0.1	0.03	15.53	0.03	0.08	14.98	0.03	0.07		
1305164	4278		20:33:57	+41:18:21	0.62	3.33	0.88	3.49	15.41	0.07	0.02	14.49	0.02	0.06	14.09	0.02	0.06		
1305165	4286		20:33:58	+41:15:31	0.77	2.26	0.8	2.92	15.35	0.08	0.02	14.48	0.02	0.07	14.09	0.02	0.07		
1305166	4294		20:33:58	+41:06:52	0.86	11.07			16.87	0.13	0.04	15.64	0.03	0.11	15.07	0.03	0.1		
1305172	4321		20:34:00	+41:15:35	0.58	2.77	0.59	3.96	14.55	0.06	0.02	13.5	0.02	0.05	13.01	0.02	0.04		
1305173	4322		20:34:00	+41:07:12	1.45	5.77	0.29	3.66	16.68	0.15	0.03	15.45	0.02	0.15	14.87	0.02	0.13		
1305178	4333		20:34:00	+41:06:14	0.48	4.69	0.48	3.68	16.44	0.08	0.03	15.28	0.02	0.07	14.76	0.02	0.07		
1305182	4343		20:34:01	+41:07:13	0.65	5.05	0.61	3.55	14.9	0.08	0.02	13.85	0.02	0.06	13.39	0.02	0.06		
1305188	4366		20:34:02	+41:14:25	1.81	9.36	0.48	4.48	16.51	0.17	0.03	15.21	0.02	0.17	14.58	0.02	0.14		
1305190	4370		20:34:02	+41:15:49	1.30	8.56	0.57	4.11	16.73	0.15	0.03	15.49	0.02	0.14	14.93	0.02	0.13		
1305194	4390		20:34:03	+41:07:54	0.60	7.17	0.62	3.88	14.76	0.06	0.02	13.68	0.02	0.06	13.18	0.02	0.05		
1305195	4395		20:34:04	+41:08:14	0.92	7.08	0.57	3.74	14.76	0.09	0.02	13.67	0.02	0.08	13.17	0.02	0.07		
1305200	4404		20:34:04	+41:16:38	1.20	4.24	0.52	4.0	15.69	0.1	0.02	14.48	0.02	0.1	13.92	0.02	0.08		
1305202	4407		20:34:05	+41:17:52	0.56	6.49	0.66	3.7	15.41	0.06	0.02	14.32	0.02	0.05	13.84	0.02	0.05		
1305217	4459		20:34:08	+41:09:26	0.77	4.23	0.5	4.69	15.79	0.08	0.02	14.53	0.02	0.08	13.94	0.02	0.07		
1305220	4470		20:34:08	+41:15:40	1.01	12.68	0.33	4.08	16.5	0.12	0.03	15.2	0.02	0.11	14.58	0.02	0.09		
1305235	4511	16692	20:34:11	+41:08:15	3.63	5.06	0.52	4.29	14.32	0.36	0.02	13.09	0.02	0.29	12.23	0.02	0.22	CL2	1
1305238	4517		20:34:11	+41:07:34	1.08	2.01	0.5	4.64	16.0	0.12	0.03	14.71	0.02	0.09	14.1	0.02	0.09		
1305246	4541		20:34:13	+41:07:59	0.60	9.57	0.5	4.14	15.86	0.07	0.03	14.63	0.02	0.07	14.05	0.02	0.07		
1305250	4553		20:34:14	+41:18:22	1.55	7.7	0.49	3.5	15.53	0.13	0.02	14.43	0.02	0.14	13.91	0.02	0.13		
1305251	4550		20:34:14	+41:15:42	1.04	9.01	0.55	4.49	16.47	0.11	0.03	15.19	0.02	0.1	14.62	0.02	0.09		
1305252	4555		20:34:14	+41:13:08	1.95	10.39	0.76	4.66	15.9	0.15	0.03	14.76	0.02	0.14	14.26	0.02	0.13		
1305257	4558		20:34:14	+41:16:11	1.97	9.82			15.74	0.17	0.02	14.6	0.02	0.16	14.0	0.02	0.14		
1305266	4585		20:34:16	+41:10:54	1.51	5.22	0.57	4.5	15.7	0.13	0.02	14.44	0.02	0.12	13.85	0.02	0.11		
1305282	4628		20:34:19	+41:14:50	0.93	5.05	0.79	5.87	16.2	0.11	0.03	15.08	0.02	0.1	14.52	0.02	0.1		
1305297	4658		20:34:21	+41:14:23	0.54	6.49	0.7	4.15	15.86	0.07	0.03	14.74	0.02	0.06	14.25	0.02	0.06		
1305302	4678		20:34:22	+41:17:18	1.43	2.86	0.56	3.48	15.29	0.13	0.02	14.16	0.02	0.12	13.63	0.02	0.11		
1305303	4677		20:34:22	+41:16:30	1.29	3.47	0.65	4.8	16.06	0.12	0.03	14.84	0.02	0.12	14.26	0.02	0.11		
1305309	4686	35272	20:34:22	+41:06:52	4.51	6.06	0.54	5.07	15.39	0.45	0.02	13.95	0.02	0.36	13.07	0.02	0.3	CL2	1
1305381		69536	20:33:55	+41:12:18	3.06	8.24	0.27	4.45	17.16	0.47	0.05	15.73	0.03	0.35	14.89	0.02	0.25	CL2	1
1305404		72749	20:33:20	+41:08:09	3.71	4.15	0.55	5.14	16.61	0.47	0.03	15.1	0.02	0.35	14.03	0.02	0.29	CL2	1
1305412		97309	20:33:39	+41:11:05	1.09	2.21			16.75	0.18	0.04	15.04	0.02	0.12	13.98	0.02	0.09	CL1	1
1305431		292890	20:33:35	+41:08:01	6.08	12.38	0.48	4.32	16.35	0.68	0.03	14.94	0.02	0.54	14.15	0.02	0.42	CL2	1

Table C.1: Continued.

Id	GDW13	GDW15	RA	Dec	Stet	Per	Mass	Av	mJ	eJ	ptpJ	mH	eH	ptpH	mK	eK	ptpK	Class	Disk
1405476	3559		20:33:28	+41:32:30	0.87	25.02	0.5	3.92	15.94	0.09	0.03	14.79	0.02	0.09	14.24	0.02	0.08		
1405481	3612		20:33:31	+41:42:17	0.67	3.52			15.95	0.09	0.03	14.9	0.02	0.07	14.4	0.02	0.06		
1405490	3678		20:33:33	+41:32:25	1.21	5.52	0.61	4.53	16.25	0.12	0.03	15.05	0.02	0.13	14.49	0.02	0.11		
1405502	3740		20:33:35	+41:32:44	0.51	7.52	0.62	4.49	15.96	0.07	0.03	14.79	0.02	0.06	14.23	0.02	0.05		
1405503	3744		20:33:36	+41:36:47	0.44	4.42	0.53	4.11	15.57	0.06	0.02	14.38	0.02	0.05	13.8	0.02	0.05		
1405504	3755		20:33:36	+41:33:45	1.00	6.09	0.52	4.83	16.49	0.11	0.03	15.28	0.02	0.11	14.69	0.02	0.09		
1405507	5536		20:33:37	+41:34:10	1.40	7.46	0.56	5.49	17.24	0.18	0.04	15.97	0.03	0.17	15.34	0.03	0.14		
1405508	3786		20:33:37	+41:39:21	0.53	14.06			17.16	0.14	0.04	15.95	0.03	0.1	15.37	0.03	0.1		
1405520	3939		20:33:42	+41:38:02	0.71	6.51	0.92	5.34	15.64	0.08	0.02	14.51	0.02	0.07	13.98	0.02	0.07		
1405521	3947		20:33:43	+41:41:49	1.07	3.62			17.01	0.2	0.04	15.77	0.03	0.15	15.18	0.03	0.13		
1405526	3981		20:33:44	+41:35:59	1.04	4.23	0.64	4.84	15.51	0.1	0.02	14.35	0.02	0.1	13.8	0.02	0.1		
1405527	3983		20:33:44	+41:39:38	0.57	13.07	0.61	3.92	16.52	0.09	0.03	15.34	0.02	0.07	14.79	0.02	0.06		
1405539	4072		20:33:48	+41:41:39	0.52	10.23			16.83	0.11	0.03	15.61	0.03	0.09	15.03	0.03	0.09		
1405547	4101		20:33:49	+41:41:04	0.62	7.71			16.99	0.1	0.04	15.75	0.03	0.1	15.08	0.03	0.1		
1405560	4219		20:33:55	+41:38:19	0.94	2.77			15.76	0.11	0.02	14.65	0.02	0.09	14.13	0.02	0.08		
1405565	4242		20:33:56	+41:40:25	0.65	6.38			15.94	0.08	0.03	14.77	0.02	0.07	14.2	0.02	0.06		
1405605	4559		20:34:14	+41:35:33	1.04	2.06			15.15	0.09	0.02	14.05	0.02	0.09	13.57	0.02	0.08		
1405625	4636		20:34:20	+41:42:30	0.92	3.01			16.48	0.13	0.03	15.38	0.02	0.1	14.89	0.02	0.11		
1405641	4722		20:34:25	+41:36:26	0.98	9.72	0.8	3.95	15.22	0.09	0.02	14.19	0.02	0.08	13.76	0.02	0.08		
1502023	307		20:31:18	+41:35:29	0.91	3.45	0.67	3.45	15.35	0.1	0.02	14.36	0.02	0.08	13.91	0.02	0.08		
1502189	317		20:31:19	+41:34:55	2.28	3.09	0.68	3.54	15.32	0.19	0.02	14.3	0.02	0.15	13.82	0.02	0.14		
1503778	500		20:31:35	+41:39:02	1.09	2.83	0.69	3.35	15.35	0.1	0.02	14.35	0.02	0.1	13.9	0.02	0.09		
1503779	508		20:31:35	+41:32:48	0.93	3.1	0.74	3.42	15.86	0.11	0.03	14.86	0.02	0.1	14.42	0.02	0.09		
1504269	660		20:31:44	+41:34:44	0.66	6.57	0.63	3.39	15.32	0.08	0.02	14.23	0.02	0.06	13.74	0.02	0.06		
1504601	863		20:31:55	+41:33:50	0.39	7.82	0.32	2.64	16.76	0.11	0.04	15.6	0.03	0.08	15.09	0.03	0.08		
1505192	745		20:31:49	+41:33:58	0.59	6.83	0.71	3.27	15.82	0.09	0.03	14.75	0.02	0.07	14.27	0.02	0.07		
1505328	283		20:31:16	+41:34:23	0.71	3.09	0.51	3.79	15.79	0.1	0.03	14.63	0.02	0.08	14.07	0.02	0.08		
1505610		106742	20:31:57	+41:39:38	0.59	22.38			16.81	0.12	0.04	15.69	0.03	0.1	15.1	0.03	0.1	CL2	1

[1]Disc IR evolutionary status from GDW13 attributed by using Wilking et al. (2001) scheme. CL1: Class 1 YSO. CL2: Class 2 YSO. FS: Flat Spectrum. PTD: pre transitional discs. Ha: Hα emitter according to GDW13 or to Vink et al. (2008). BWE: blue stars with excesses candidate stars with discs, but with optical color bluer than the cluster locus). lowmass : low-mass disc with excesses only in [8.0] and [24]. high-incl: highly inclined disc with excesses only in [8.0] and [24]

[2]Disc presence: 1 if true.

Appendix D

Folded Light Curves

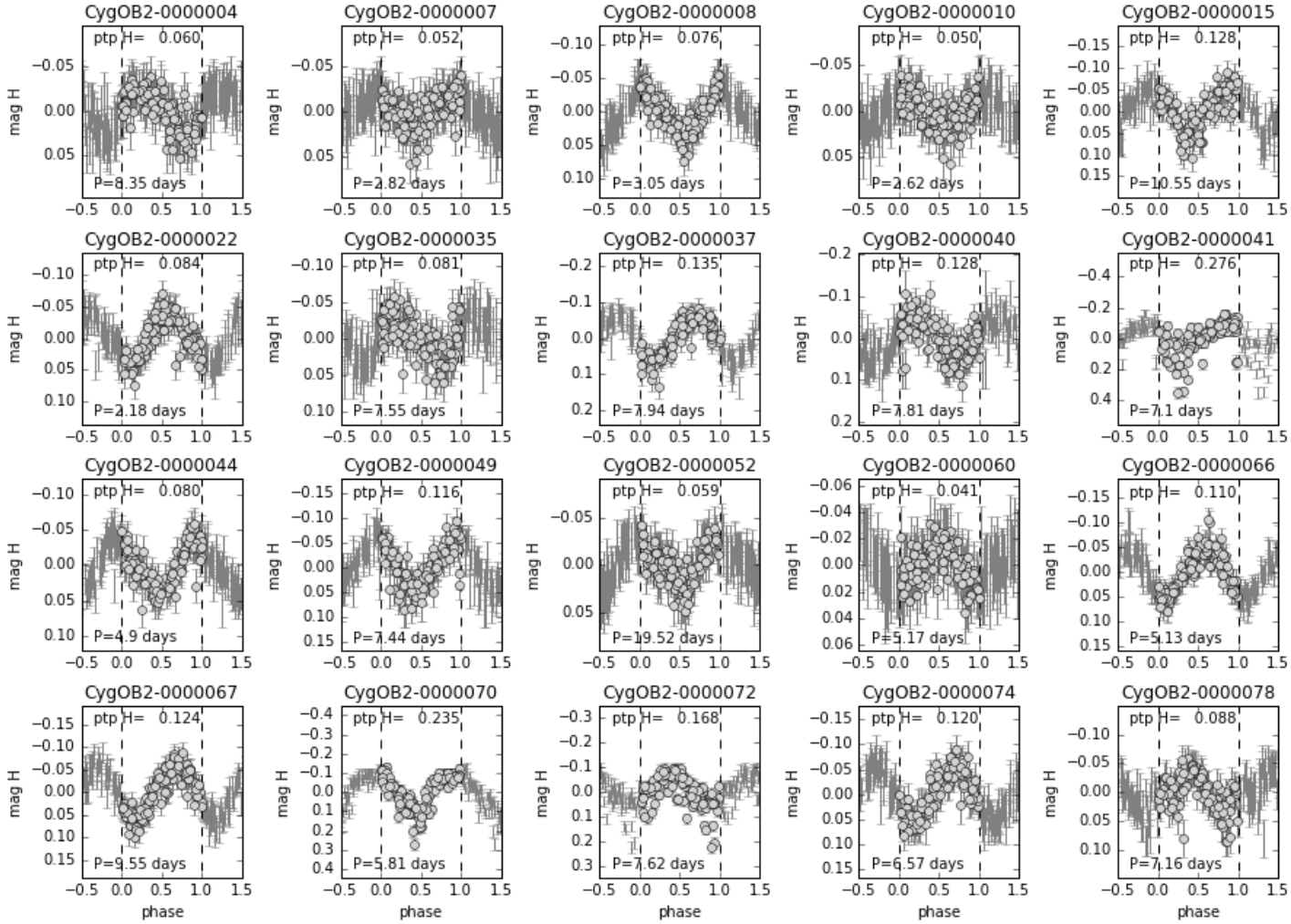

Figure D.1: Phased light curves of periodic CygOB2 candidate members for H filter. The name of the object is given in the top of each panel. The periods and peak to peak amplitude are given inside the plots.

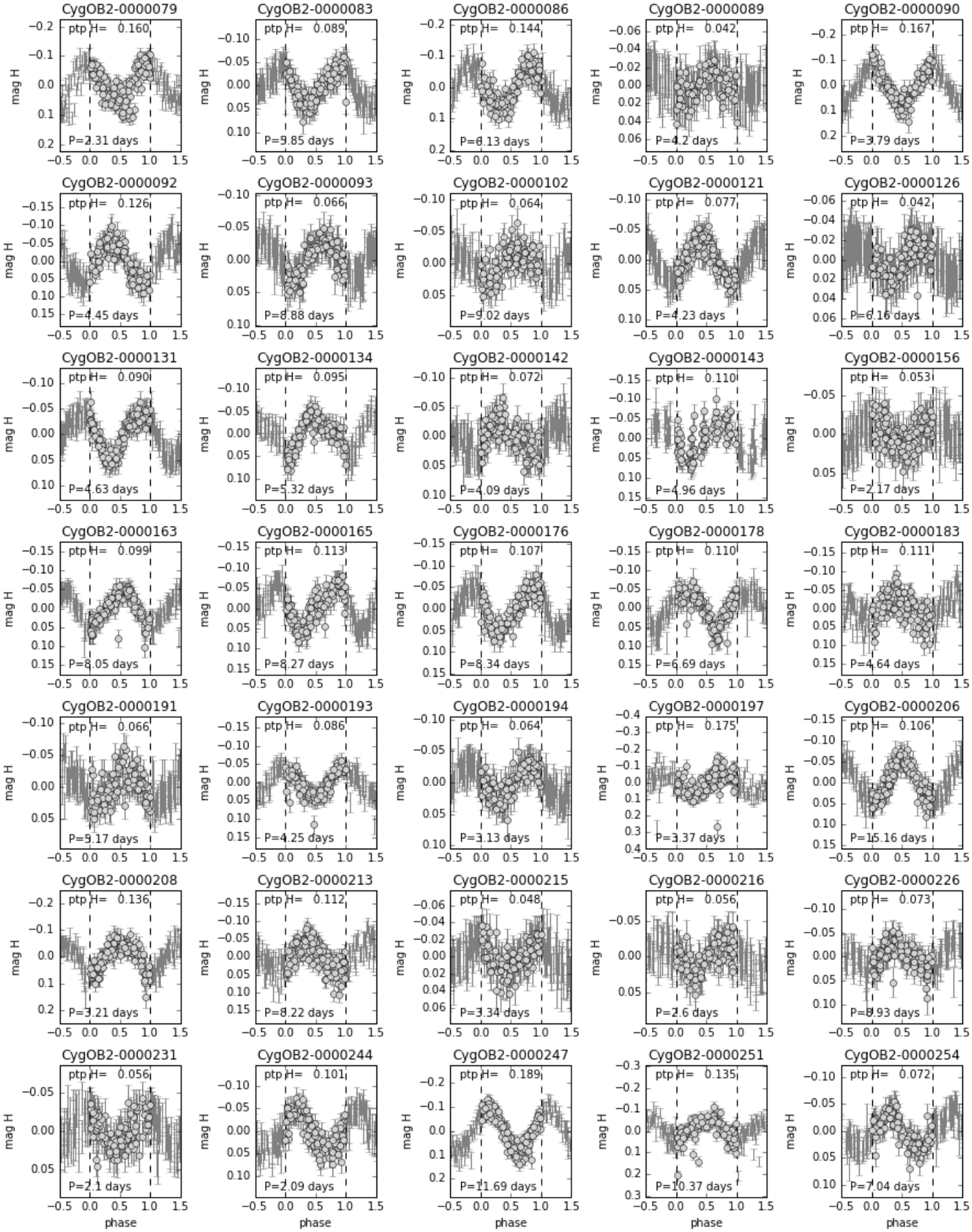
CygOB2-0000079
ptp H= 0.160
P=2.31 days
CygOB2-0000083
ptp H= 0.089
P=9.85 days
CygOB2-0000086
ptp H= 0.144
P=6.13 days
CygOB2-0000089
ptp H= 0.042
P=4.2 days
CygOB2-0000090
ptp H= 0.167
P=3.79 days
CygOB2-0000092
ptp H= 0.126
P=4.45 days
CygOB2-0000093
ptp H= 0.066
P=8.88 days
CygOB2-0000102
ptp H= 0.064
P=9.02 days
CygOB2-0000121
ptp H= 0.077
P=4.23 days
CygOB2-0000126
ptp H= 0.042
P=6.16 days
CygOB2-0000131
ptp H= 0.090
P=4.63 days
CygOB2-0000134
ptp H= 0.095
P=5.32 days
CygOB2-0000142
ptp H= 0.072
P=4.09 days
CygOB2-0000143
ptp H= 0.110
P=4.96 days
CygOB2-0000156
ptp H= 0.053
P=2.17 days
CygOB2-0000163
ptp H= 0.099
P=8.05 days
CygOB2-0000165
ptp H= 0.113
P=8.27 days
CygOB2-0000176
ptp H= 0.107
P=8.34 days
CygOB2-0000178
ptp H= 0.110
P=6.69 days
CygOB2-0000183
ptp H= 0.111
P=4.64 days
CygOB2-0000191
ptp H= 0.066
P=5.17 days
CygOB2-0000193
ptp H= 0.086
P=4.25 days
CygOB2-0000194
ptp H= 0.064
P=3.13 days
CygOB2-0000197
ptp H= 0.175
P=3.37 days
CygOB2-0000206
ptp H= 0.106
P=15.16 days
CygOB2-0000208
ptp H= 0.136
P=3.21 days
CygOB2-0000213
ptp H= 0.112
P=8.22 days
CygOB2-0000215
ptp H= 0.048
P=3.34 days
CygOB2-0000216
ptp H= 0.056
P=2.6 days
CygOB2-0000226
ptp H= 0.073
P=8.93 days
CygOB2-0000231
ptp H= 0.056
P=2.1 days
CygOB2-0000244
ptp H= 0.101
P=2.09 days
CygOB2-0000247
ptp H= 0.189
P=11.69 days
CygOB2-0000251
ptp H= 0.135
P=10.37 days
CygOB2-0000254
ptp H= 0.072
P=7.04 days
mag H
phase

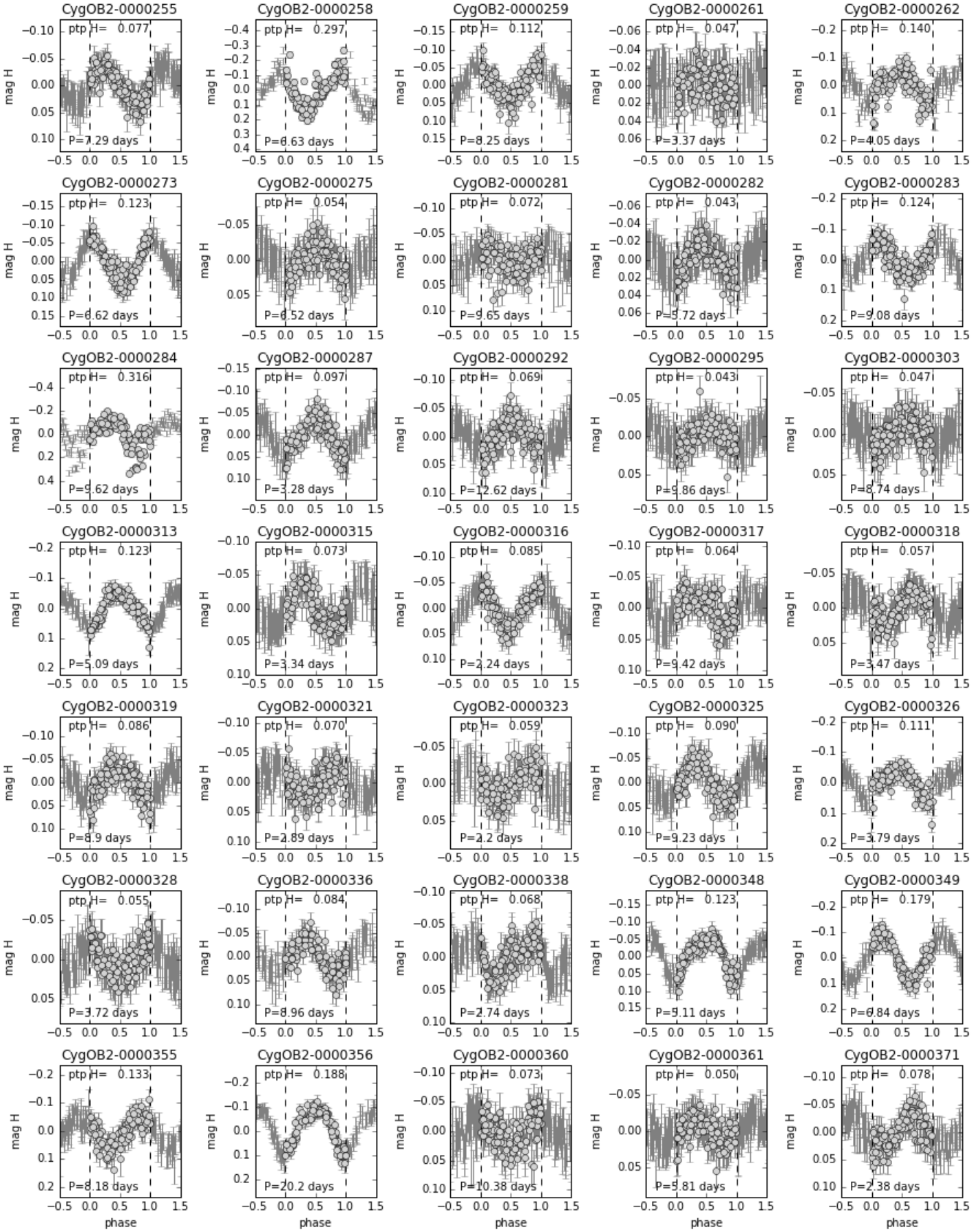
CygOB2-0000255
ptp H= 0.077
P=7.29 days
CygOB2-0000258
ptp H= 0.297
P=6.63 days
CygOB2-0000259
ptp H= 0.112
P=8.25 days
CygOB2-0000261
ptp H= 0.047
P=3.37 days
CygOB2-0000262
ptp H= 0.140
P=4.05 days
CygOB2-0000273
ptp H= 0.123
P=6.62 days
CygOB2-0000275
ptp H= 0.054
P=6.52 days
CygOB2-0000281
ptp H= 0.072
P=9.65 days
CygOB2-0000282
ptp H= 0.043
P=5.72 days
CygOB2-0000283
ptp H= 0.124
P=9.08 days
CygOB2-0000284
ptp H= 0.316
P=9.62 days
CygOB2-0000287
ptp H= 0.097
P=3.28 days
CygOB2-0000292
ptp H= 0.069
P=12.62 days
CygOB2-0000295
ptp H= 0.043
P=9.86 days
CygOB2-0000303
ptp H= 0.047
P=8.74 days
CygOB2-0000313
ptp H= 0.123
P=5.09 days
CygOB2-0000315
ptp H= 0.073
P=3.34 days
CygOB2-0000316
ptp H= 0.085
P=2.24 days
CygOB2-0000317
ptp H= 0.064
P=9.42 days
CygOB2-0000318
ptp H= 0.057
P=3.47 days
CygOB2-0000319
ptp H= 0.086
P=8.9 days
CygOB2-0000321
ptp H= 0.070
P=2.89 days
CygOB2-0000323
ptp H= 0.059
P=2.2 days
CygOB2-0000325
ptp H= 0.090
P=9.23 days
CygOB2-0000326
ptp H= 0.111
P=3.79 days
CygOB2-0000328
ptp H= 0.055
P=3.72 days
CygOB2-0000336
ptp H= 0.084
P=8.96 days
CygOB2-0000338
ptp H= 0.068
P=2.74 days
CygOB2-0000348
ptp H= 0.123
P=5.11 days
CygOB2-0000349
ptp H= 0.179
P=6.84 days
CygOB2-0000355
ptp H= 0.133
P=8.18 days
CygOB2-0000356
ptp H= 0.188
P=20.2 days
CygOB2-0000360
ptp H= 0.073
P=10.38 days
CygOB2-0000361
ptp H= 0.050
P=5.81 days
CygOB2-0000371
ptp H= 0.078
P=2.38 days
mag H
phase

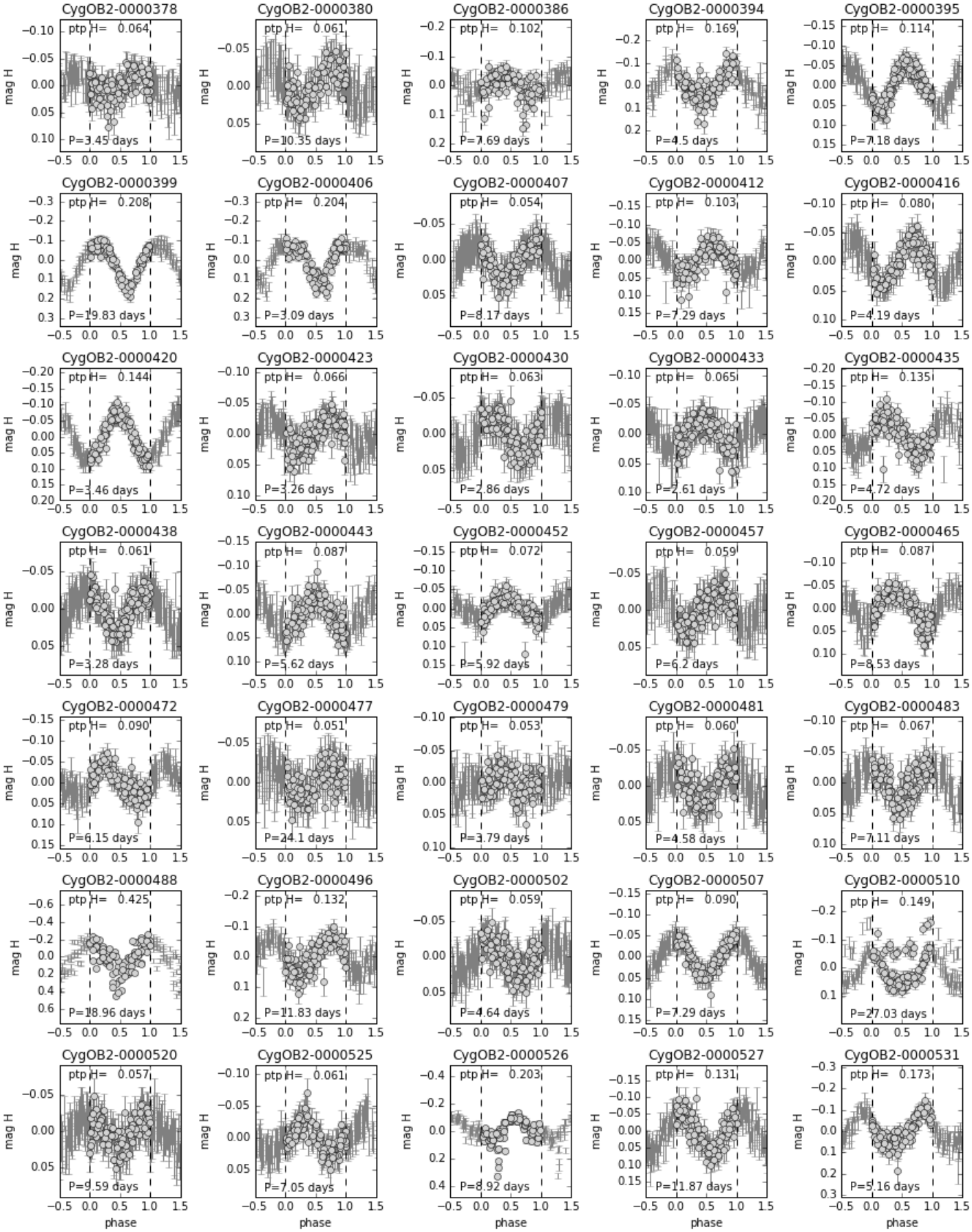
CygOB2-0000378
ptp H= 0.064
P=3.45 days
CygOB2-0000380
ptp H= 0.061
P=10.35 days
CygOB2-0000386
ptp H= 0.102
P=7.69 days
CygOB2-0000394
ptp H= 0.169
P=4.5 days
CygOB2-0000395
ptp H= 0.114
P=7.18 days
CygOB2-0000399
ptp H= 0.208
P=19.83 days
CygOB2-0000406
ptp H= 0.204
P=3.09 days
CygOB2-0000407
ptp H= 0.054
P=8.17 days
CygOB2-0000412
ptp H= 0.103
P=7.29 days
CygOB2-0000416
ptp H= 0.080
P=4.19 days
CygOB2-0000420
ptp H= 0.144
P=3.46 days
CygOB2-0000423
ptp H= 0.066
P=3.26 days
CygOB2-0000430
ptp H= 0.063
P=2.86 days
CygOB2-0000433
ptp H= 0.065
P=2.61 days
CygOB2-0000435
ptp H= 0.135
P=4.72 days
CygOB2-0000438
ptp H= 0.061
P=3.28 days
CygOB2-0000443
ptp H= 0.087
P=5.62 days
CygOB2-0000452
ptp H= 0.072
P=5.92 days
CygOB2-0000457
ptp H= 0.059
P=6.2 days
CygOB2-0000465
ptp H= 0.087
P=8.53 days
CygOB2-0000472
ptp H= 0.090
P=6.15 days
CygOB2-0000477
ptp H= 0.051
P=24.1 days
CygOB2-0000479
ptp H= 0.053
P=3.79 days
CygOB2-0000481
ptp H= 0.060
P=4.58 days
CygOB2-0000483
ptp H= 0.067
P=7.11 days
CygOB2-0000488
ptp H= 0.425
P=18.96 days
CygOB2-0000496
ptp H= 0.132
P=11.83 days
CygOB2-0000502
ptp H= 0.059
P=4.64 days
CygOB2-0000507
ptp H= 0.090
P=7.29 days
CygOB2-0000510
ptp H= 0.149
P=27.03 days
CygOB2-0000520
ptp H= 0.057
P=9.59 days
CygOB2-0000525
ptp H= 0.061
P=7.05 days
CygOB2-0000526
ptp H= 0.203
P=8.92 days
CygOB2-0000527
ptp H= 0.131
P=11.87 days
CygOB2-0000531
ptp H= 0.173
P=5.16 days
mag H
phase

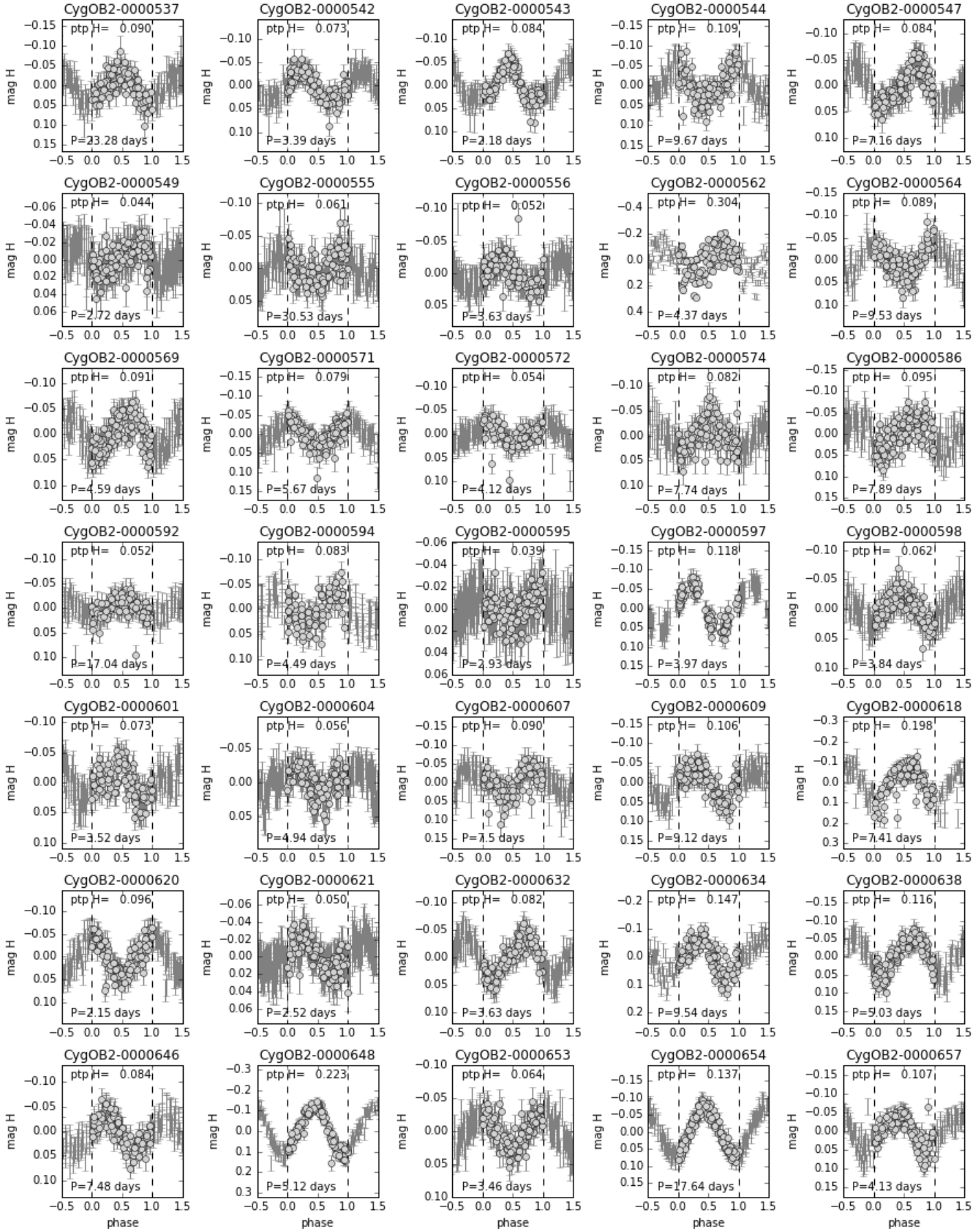
CygOB2-0000537
ptp H= 0.090
P=23.28 days
CygOB2-0000542
ptp H= 0.073
P=3.39 days
CygOB2-0000543
ptp H= 0.084
P=2.18 days
CygOB2-0000544
ptp H= 0.109
P=9.67 days
CygOB2-0000547
ptp H= 0.084
P=7.16 days
CygOB2-0000549
ptp H= 0.044
P=2.72 days
CygOB2-0000555
ptp H= 0.061
P=30.53 days
CygOB2-0000556
ptp H= 0.052
P=3.63 days
CygOB2-0000562
ptp H= 0.304
P=4.37 days
CygOB2-0000564
ptp H= 0.089
P=9.53 days
CygOB2-0000569
ptp H= 0.091
P=4.59 days
CygOB2-0000571
ptp H= 0.079
P=5.67 days
CygOB2-0000572
ptp H= 0.054
P=4.12 days
CygOB2-0000574
ptp H= 0.082
P=7.74 days
CygOB2-0000586
ptp H= 0.095
P=7.89 days
CygOB2-0000592
ptp H= 0.052
P=17.04 days
CygOB2-0000594
ptp H= 0.083
P=4.49 days
CygOB2-0000595
ptp H= 0.039
P=2.93 days
CygOB2-0000597
ptp H= 0.118
P=3.97 days
CygOB2-0000598
ptp H= 0.062
P=3.84 days
CygOB2-0000601
ptp H= 0.073
P=3.52 days
CygOB2-0000604
ptp H= 0.056
P=4.94 days
CygOB2-0000607
ptp H= 0.090
P=7.5 days
CygOB2-0000609
ptp H= 0.106
P=9.12 days
CygOB2-0000618
ptp H= 0.198
P=7.41 days
CygOB2-0000620
ptp H= 0.096
P=2.15 days
CygOB2-0000621
ptp H= 0.050
P=2.52 days
CygOB2-0000632
ptp H= 0.082
P=3.63 days
CygOB2-0000634
ptp H= 0.147
P=9.54 days
CygOB2-0000638
ptp H= 0.116
P=5.03 days
CygOB2-0000646
ptp H= 0.084
P=7.48 days
CygOB2-0000648
ptp H= 0.223
P=5.12 days
CygOB2-0000653
ptp H= 0.064
P=3.46 days
CygOB2-0000654
ptp H= 0.137
P=17.64 days
CygOB2-0000657
ptp H= 0.107
P=4.13 days
mag H
phase

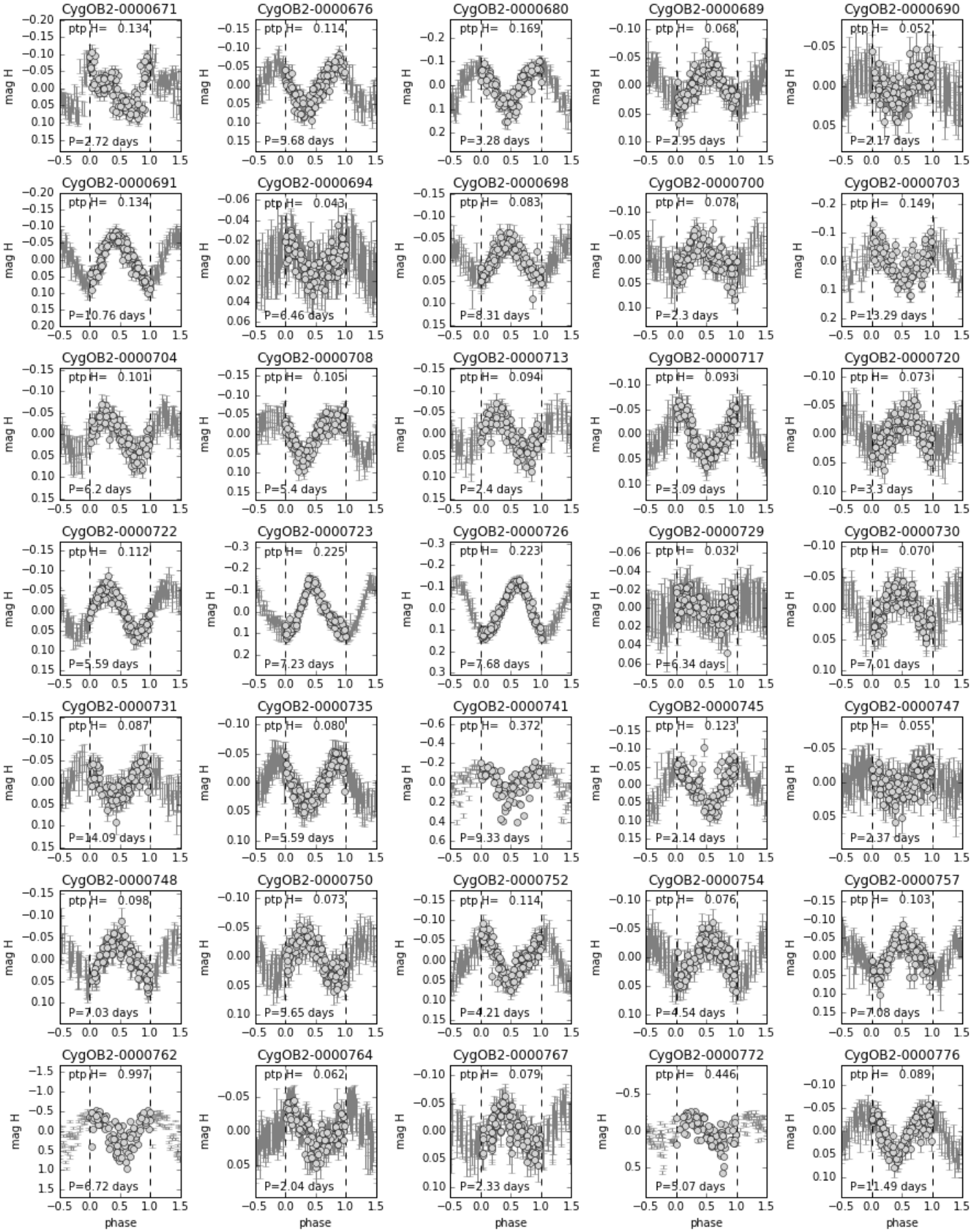
CygOB2-0000671
ptp H= 0.134
P=2.72 days
CygOB2-0000676
ptp H= 0.114
P=5.68 days
CygOB2-0000680
ptp H= 0.169
P=3.28 days
CygOB2-0000689
ptp H= 0.068
P=2.95 days
CygOB2-0000690
ptp H= 0.052
P=2.17 days
CygOB2-0000691
ptp H= 0.134
P=10.76 days
CygOB2-0000694
ptp H= 0.043
P=6.46 days
CygOB2-0000698
ptp H= 0.083
P=8.31 days
CygOB2-0000700
ptp H= 0.078
P=2.3 days
CygOB2-0000703
ptp H= 0.149
P=13.29 days
CygOB2-0000704
ptp H= 0.101
P=6.2 days
CygOB2-0000708
ptp H= 0.105
P=5.4 days
CygOB2-0000713
ptp H= 0.094
P=2.4 days
CygOB2-0000717
ptp H= 0.093
P=3.09 days
CygOB2-0000720
ptp H= 0.073
P=3.3 days
CygOB2-0000722
ptp H= 0.112
P=5.59 days
CygOB2-0000723
ptp H= 0.225
P=7.23 days
CygOB2-0000726
ptp H= 0.223
P=7.68 days
CygOB2-0000729
ptp H= 0.032
P=6.34 days
CygOB2-0000730
ptp H= 0.070
P=7.01 days
CygOB2-0000731
ptp H= 0.087
P=14.09 days
CygOB2-0000735
ptp H= 0.080
P=5.59 days
CygOB2-0000741
ptp H= 0.372
P=9.33 days
CygOB2-0000745
ptp H= 0.123
P=2.14 days
CygOB2-0000747
ptp H= 0.055
P=2.37 days
CygOB2-0000748
ptp H= 0.098
P=7.03 days
CygOB2-0000750
ptp H= 0.073
P=5.65 days
CygOB2-0000752
ptp H= 0.114
P=4.21 days
CygOB2-0000754
ptp H= 0.076
P=4.54 days
CygOB2-0000757
ptp H= 0.103
P=7.08 days
CygOB2-0000762
ptp H= 0.997
P=6.72 days
CygOB2-0000764
ptp H= 0.062
P=2.04 days
CygOB2-0000767
ptp H= 0.079
P=2.33 days
CygOB2-0000772
ptp H= 0.446
P=5.07 days
CygOB2-0000776
ptp H= 0.089
P=11.49 days
mag H
phase

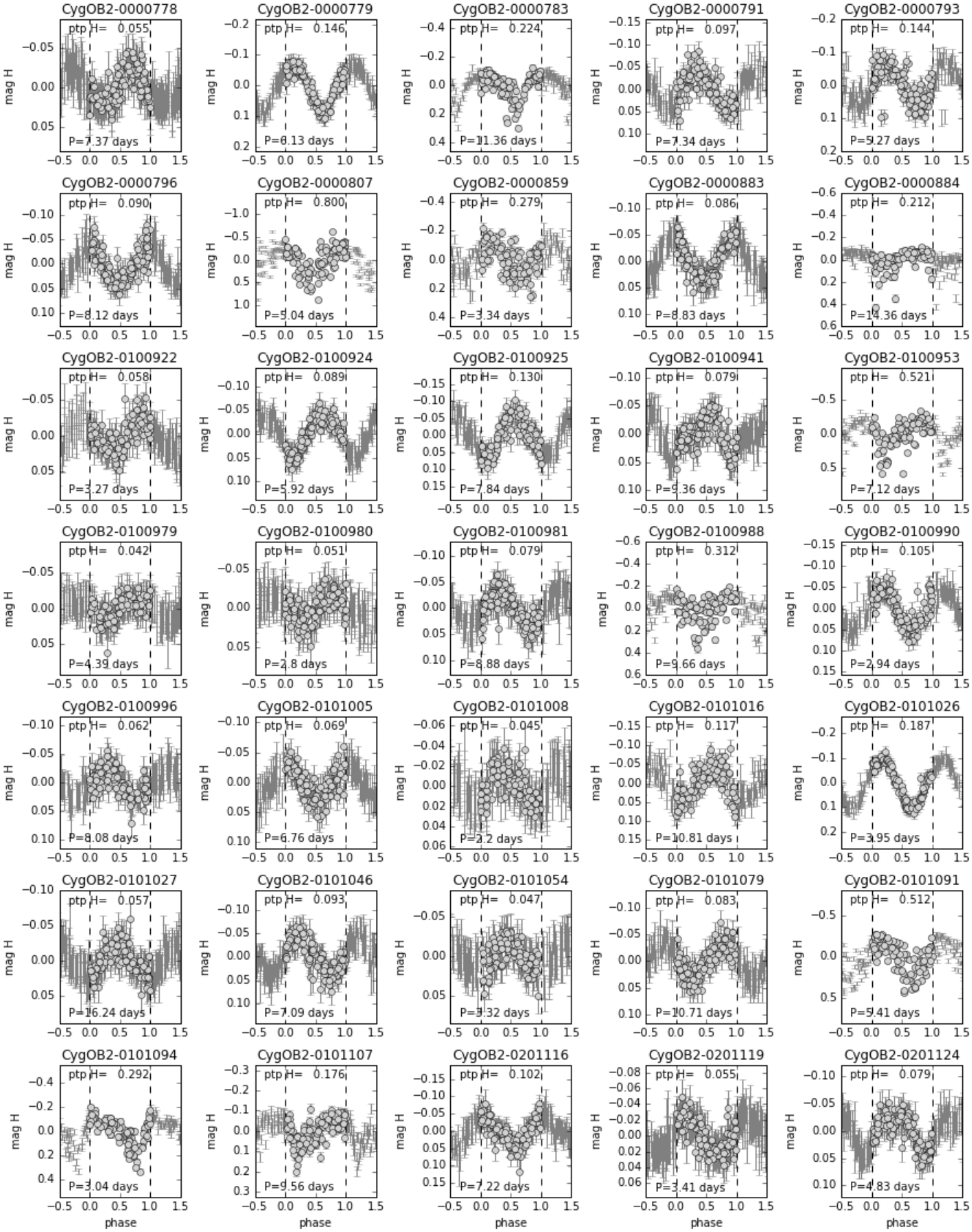
CygOB2-0000778
ptp H= 0.055
P=7.37 days
CygOB2-0000779
ptp H= 0.146
P=6.13 days
CygOB2-0000783
ptp H= 0.224
P=11.36 days
CygOB2-0000791
ptp H= 0.097
P=7.34 days
CygOB2-0000793
ptp H= 0.144
P=9.27 days
CygOB2-0000796
ptp H= 0.090
P=8.12 days
CygOB2-0000807
ptp H= 0.800
P=5.04 days
CygOB2-0000859
ptp H= 0.279
P=3.34 days
CygOB2-0000883
ptp H= 0.086
P=8.83 days
CygOB2-0000884
ptp H= 0.212
P=14.36 days
CygOB2-0100922
ptp H= 0.058
P=3.27 days
CygOB2-0100924
ptp H= 0.089
P=5.92 days
CygOB2-0100925
ptp H= 0.130
P=7.84 days
CygOB2-0100941
ptp H= 0.079
P=9.36 days
CygOB2-0100953
ptp H= 0.521
P=7.12 days
CygOB2-0100979
ptp H= 0.042
P=4.39 days
CygOB2-0100980
ptp H= 0.051
P=2.8 days
CygOB2-0100981
ptp H= 0.079
P=8.88 days
CygOB2-0100988
ptp H= 0.312
P=9.66 days
CygOB2-0100990
ptp H= 0.105
P=2.94 days
CygOB2-0100996
ptp H= 0.062
P=8.08 days
CygOB2-0101005
ptp H= 0.069
P=6.76 days
CygOB2-0101008
ptp H= 0.045
P=2.2 days
CygOB2-0101016
ptp H= 0.117
P=10.81 days
CygOB2-0101026
ptp H= 0.187
P=3.95 days
CygOB2-0101027
ptp H= 0.057
P=16.24 days
CygOB2-0101046
ptp H= 0.093
P=7.09 days
CygOB2-0101054
ptp H= 0.047
P=3.32 days
CygOB2-0101079
ptp H= 0.083
P=10.71 days
CygOB2-0101091
ptp H= 0.512
P=5.41 days
CygOB2-0101094
ptp H= 0.292
P=3.04 days
CygOB2-0101107
ptp H= 0.176
P=9.56 days
CygOB2-0201116
ptp H= 0.102
P=7.22 days
CygOB2-0201119
ptp H= 0.055
P=3.41 days
CygOB2-0201124
ptp H= 0.079
P=4.83 days
mag H
phase

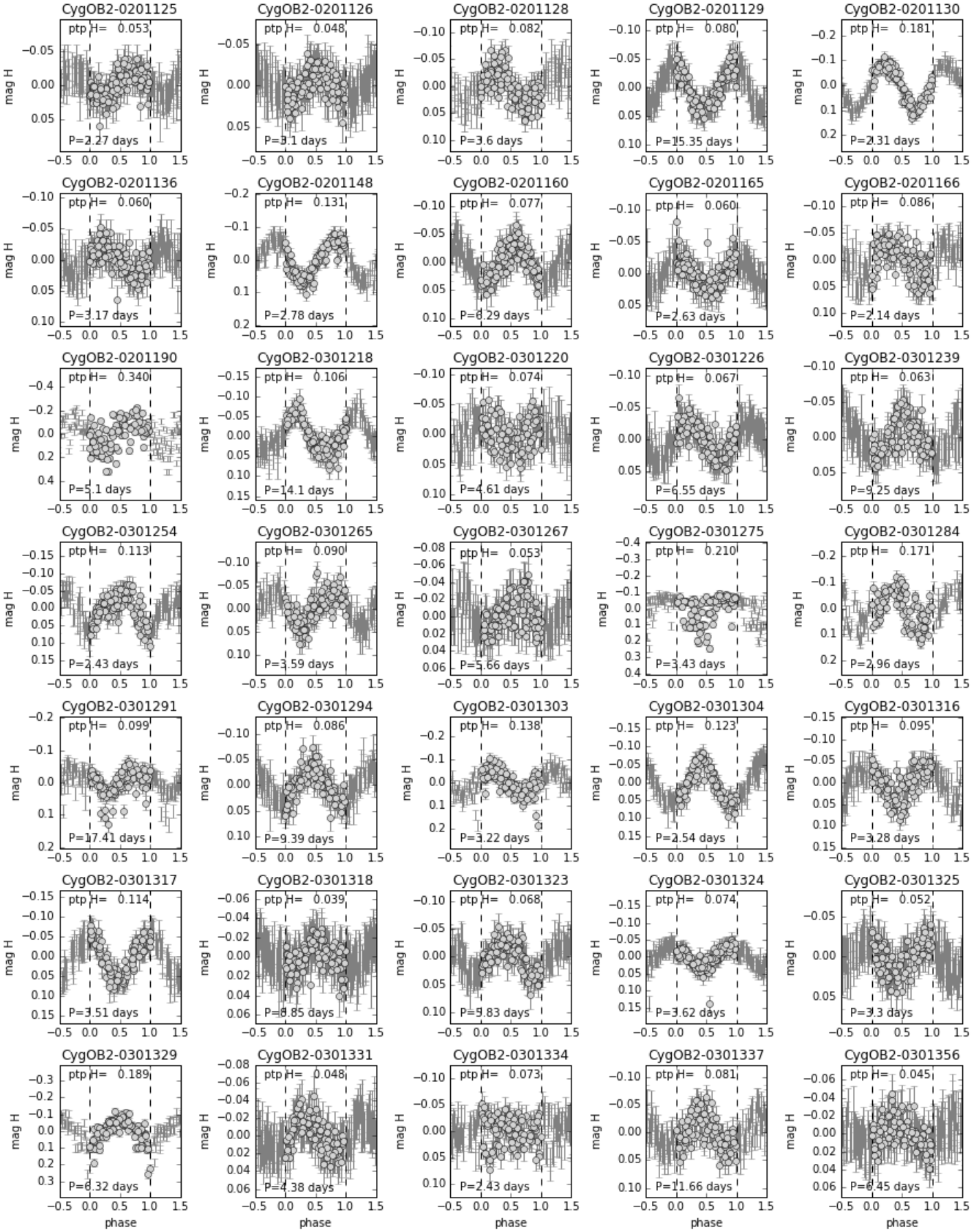
CygOB2-0201125
ptp H= 0.053
P=2.27 days
CygOB2-0201126
ptp H= 0.048
P=3.1 days
CygOB2-0201128
ptp H= 0.082
P=3.6 days
CygOB2-0201129
ptp H= 0.080
P=15.35 days
CygOB2-0201130
ptp H= 0.181
P=2.31 days
CygOB2-0201136
ptp H= 0.060
P=3.17 days
CygOB2-0201148
ptp H= 0.131
P=2.78 days
CygOB2-0201160
ptp H= 0.077
P=6.29 days
CygOB2-0201165
ptp H= 0.060
P=2.63 days
CygOB2-0201166
ptp H= 0.086
P=2.14 days
CygOB2-0201190
ptp H= 0.340
P=5.1 days
CygOB2-0301218
ptp H= 0.106
P=14.1 days
CygOB2-0301220
ptp H= 0.074
P=4.61 days
CygOB2-0301226
ptp H= 0.067
P=6.55 days
CygOB2-0301239
ptp H= 0.063
P=9.25 days
CygOB2-0301254
ptp H= 0.113
P=2.43 days
CygOB2-0301265
ptp H= 0.090
P=3.59 days
CygOB2-0301267
ptp H= 0.053
P=5.66 days
CygOB2-0301275
ptp H= 0.210
P=3.43 days
CygOB2-0301284
ptp H= 0.171
P=2.96 days
CygOB2-0301291
ptp H= 0.099
P=17.41 days
CygOB2-0301294
ptp H= 0.086
P=9.39 days
CygOB2-0301303
ptp H= 0.138
P=3.22 days
CygOB2-0301304
ptp H= 0.123
P=2.54 days
CygOB2-0301316
ptp H= 0.095
P=3.28 days
CygOB2-0301317
ptp H= 0.114
P=3.51 days
CygOB2-0301318
ptp H= 0.039
P=8.85 days
CygOB2-0301323
ptp H= 0.068
P=5.83 days
CygOB2-0301324
ptp H= 0.074
P=3.62 days
CygOB2-0301325
ptp H= 0.052
P=3.3 days
CygOB2-0301329
ptp H= 0.189
P=6.32 days
CygOB2-0301331
ptp H= 0.048
P=4.38 days
CygOB2-0301334
ptp H= 0.073
P=2.43 days
CygOB2-0301337
ptp H= 0.081
P=11.66 days
CygOB2-0301356
ptp H= 0.045
P=6.45 days
mag H
phase

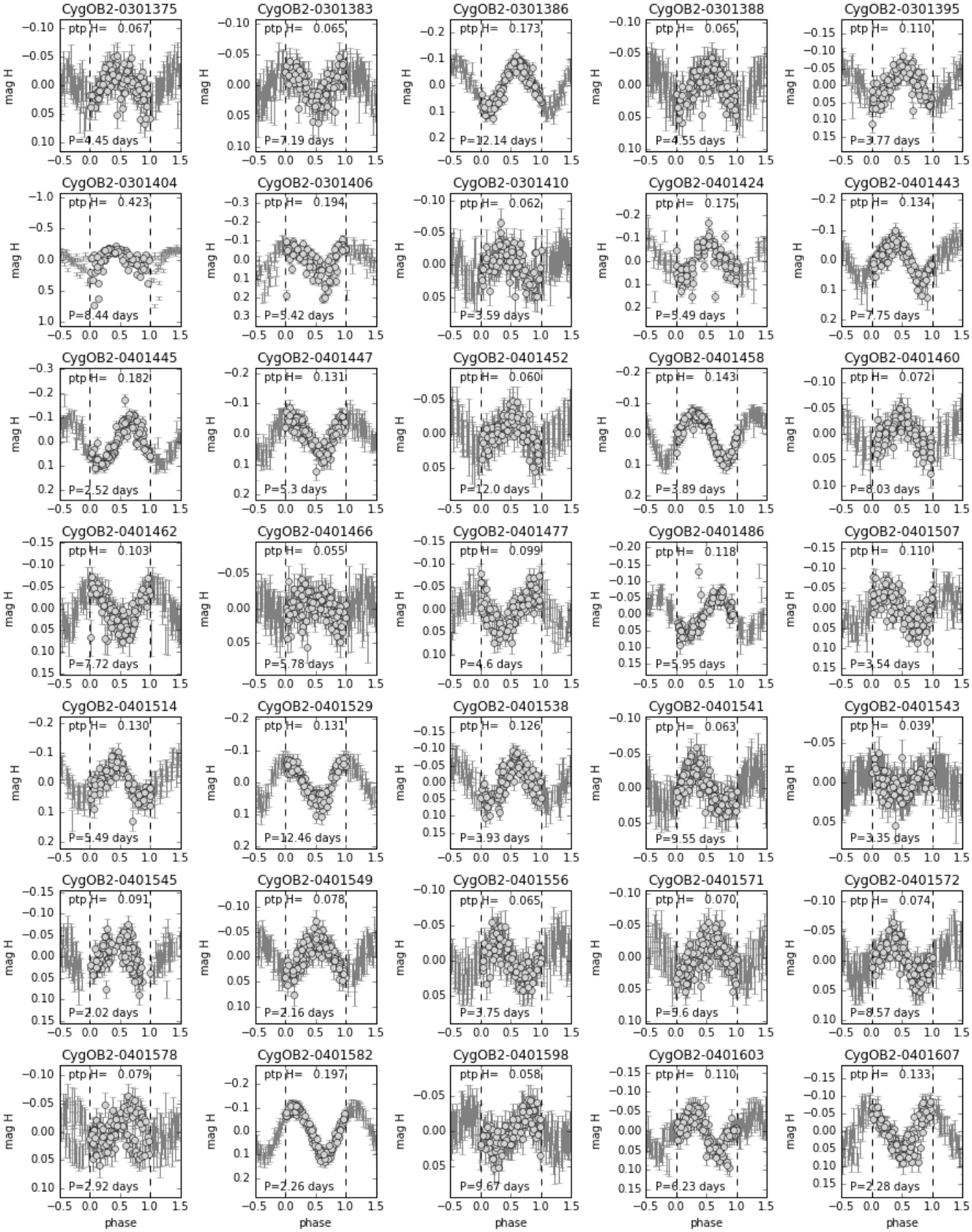
CygOB2-0301375
ptp H= 0.067
P=4.45 days
CygOB2-0301383
ptp H= 0.065
P=7.19 days
CygOB2-0301386
ptp H= 0.173
P=12.14 days
CygOB2-0301388
ptp H= 0.065
P=4.55 days
CygOB2-0301395
ptp H= 0.110
P=3.77 days
CygOB2-0301404
ptp H= 0.423
P=8.44 days
CygOB2-0301406
ptp H= 0.194
P=5.42 days
CygOB2-0301410
ptp H= 0.062
P=3.59 days
CygOB2-0401424
ptp H= 0.175
P=5.49 days
CygOB2-0401443
ptp H= 0.134
P=7.75 days
CygOB2-0401445
ptp H= 0.182
P=2.52 days
CygOB2-0401447
ptp H= 0.131
P=5.3 days
CygOB2-0401452
ptp H= 0.060
P=12.0 days
CygOB2-0401458
ptp H= 0.143
P=3.89 days
CygOB2-0401460
ptp H= 0.072
P=8.03 days
CygOB2-0401462
ptp H= 0.103
P=7.72 days
CygOB2-0401466
ptp H= 0.055
P=5.78 days
CygOB2-0401477
ptp H= 0.099
P=4.6 days
CygOB2-0401486
ptp H= 0.118
P=5.95 days
CygOB2-0401507
ptp H= 0.110
P=3.54 days
CygOB2-0401514
ptp H= 0.130
P=5.49 days
CygOB2-0401529
ptp H= 0.131
P=12.46 days
CygOB2-0401538
ptp H= 0.126
P=3.93 days
CygOB2-0401541
ptp H= 0.063
P=9.55 days
CygOB2-0401543
ptp H= 0.039
P=3.35 days
CygOB2-0401545
ptp H= 0.091
P=2.02 days
CygOB2-0401549
ptp H= 0.078
P=2.16 days
CygOB2-0401556
ptp H= 0.065
P=3.75 days
CygOB2-0401571
ptp H= 0.070
P=5.6 days
CygOB2-0401572
ptp H= 0.074
P=8.57 days
CygOB2-0401578
ptp H= 0.079
P=2.92 days
CygOB2-0401582
ptp H= 0.197
P=2.26 days
CygOB2-0401598
ptp H= 0.058
P=9.67 days
CygOB2-0401603
ptp H= 0.110
P=8.23 days
CygOB2-0401607
ptp H= 0.133
P=2.28 days
mag H
phase

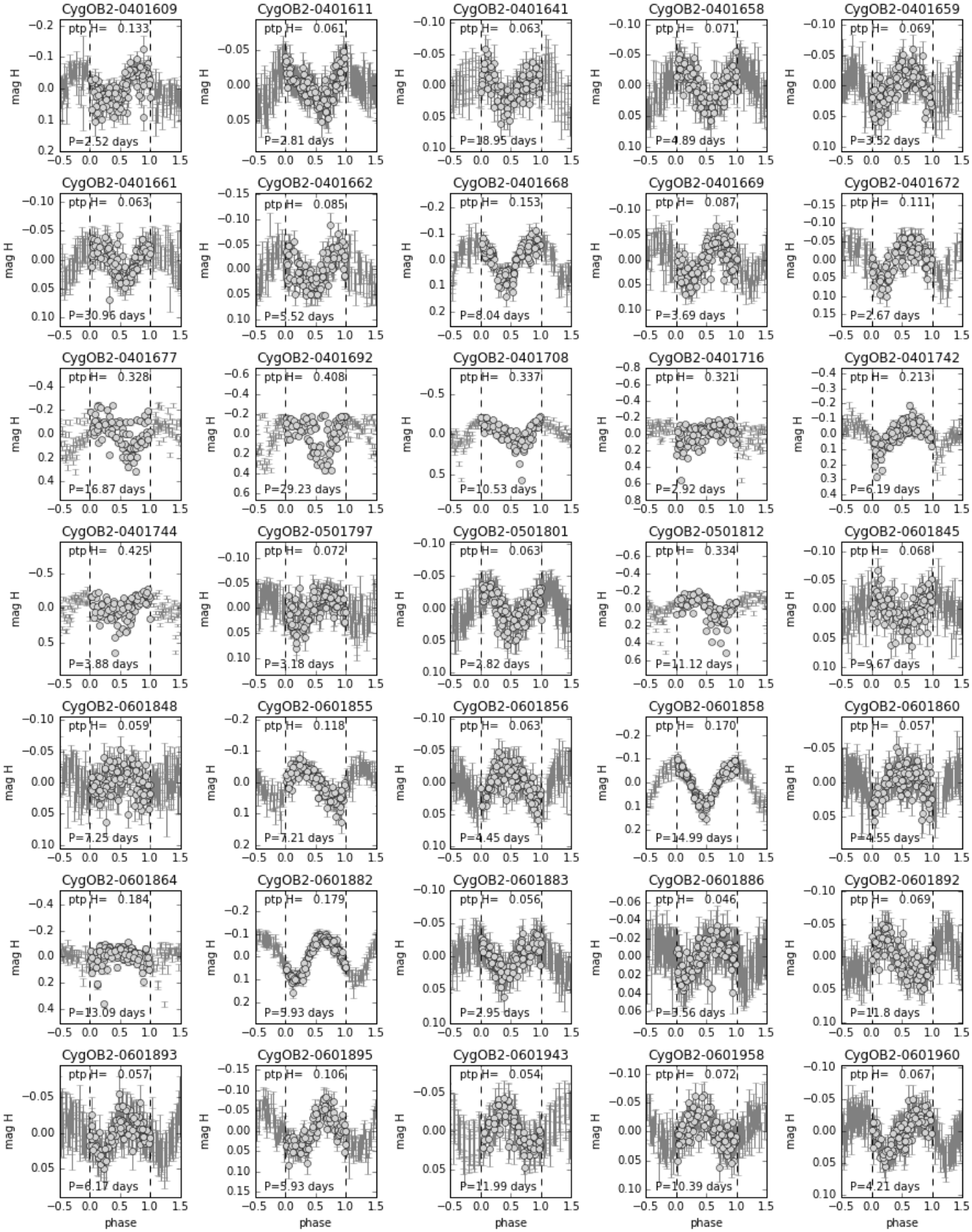
CygOB2-0401609
ptp H= 0.133
P=2.52 days
CygOB2-0401611
ptp H= 0.061
P=2.81 days
CygOB2-0401641
ptp H= 0.063
P=18.95 days
CygOB2-0401658
ptp H= 0.071
P=4.89 days
CygOB2-0401659
ptp H= 0.069
P=3.52 days
CygOB2-0401661
ptp H= 0.063
P=30.96 days
CygOB2-0401662
ptp H= 0.085
P=5.52 days
CygOB2-0401668
ptp H= 0.153
P=8.04 days
CygOB2-0401669
ptp H= 0.087
P=3.69 days
CygOB2-0401672
ptp H= 0.111
P=2.67 days
CygOB2-0401677
ptp H= 0.328
P=16.87 days
CygOB2-0401692
ptp H= 0.408
P=29.23 days
CygOB2-0401708
ptp H= 0.337
P=10.53 days
CygOB2-0401716
ptp H= 0.321
P=2.92 days
CygOB2-0401742
ptp H= 0.213
P=6.19 days
CygOB2-0401744
ptp H= 0.425
P=3.88 days
CygOB2-0501797
ptp H= 0.072
P=3.18 days
CygOB2-0501801
ptp H= 0.063
P=2.82 days
CygOB2-0501812
ptp H= 0.334
P=11.12 days
CygOB2-0601845
ptp H= 0.068
P=9.67 days
CygOB2-0601848
ptp H= 0.059
P=7.25 days
CygOB2-0601855
ptp H= 0.118
P=7.21 days
CygOB2-0601856
ptp H= 0.063
P=4.45 days
CygOB2-0601858
ptp H= 0.170
P=14.99 days
CygOB2-0601860
ptp H= 0.057
P=4.55 days
CygOB2-0601864
ptp H= 0.184
P=13.09 days
CygOB2-0601882
ptp H= 0.179
P=5.93 days
CygOB2-0601883
ptp H= 0.056
P=2.95 days
CygOB2-0601886
ptp H= 0.046
P=3.56 days
CygOB2-0601892
ptp H= 0.069
P=11.8 days
CygOB2-0601893
ptp H= 0.057
P=6.17 days
CygOB2-0601895
ptp H= 0.106
P=5.93 days
CygOB2-0601943
ptp H= 0.054
P=11.99 days
CygOB2-0601958
ptp H= 0.072
P=10.39 days
CygOB2-0601960
ptp H= 0.067
P=4.21 days
mag H
phase

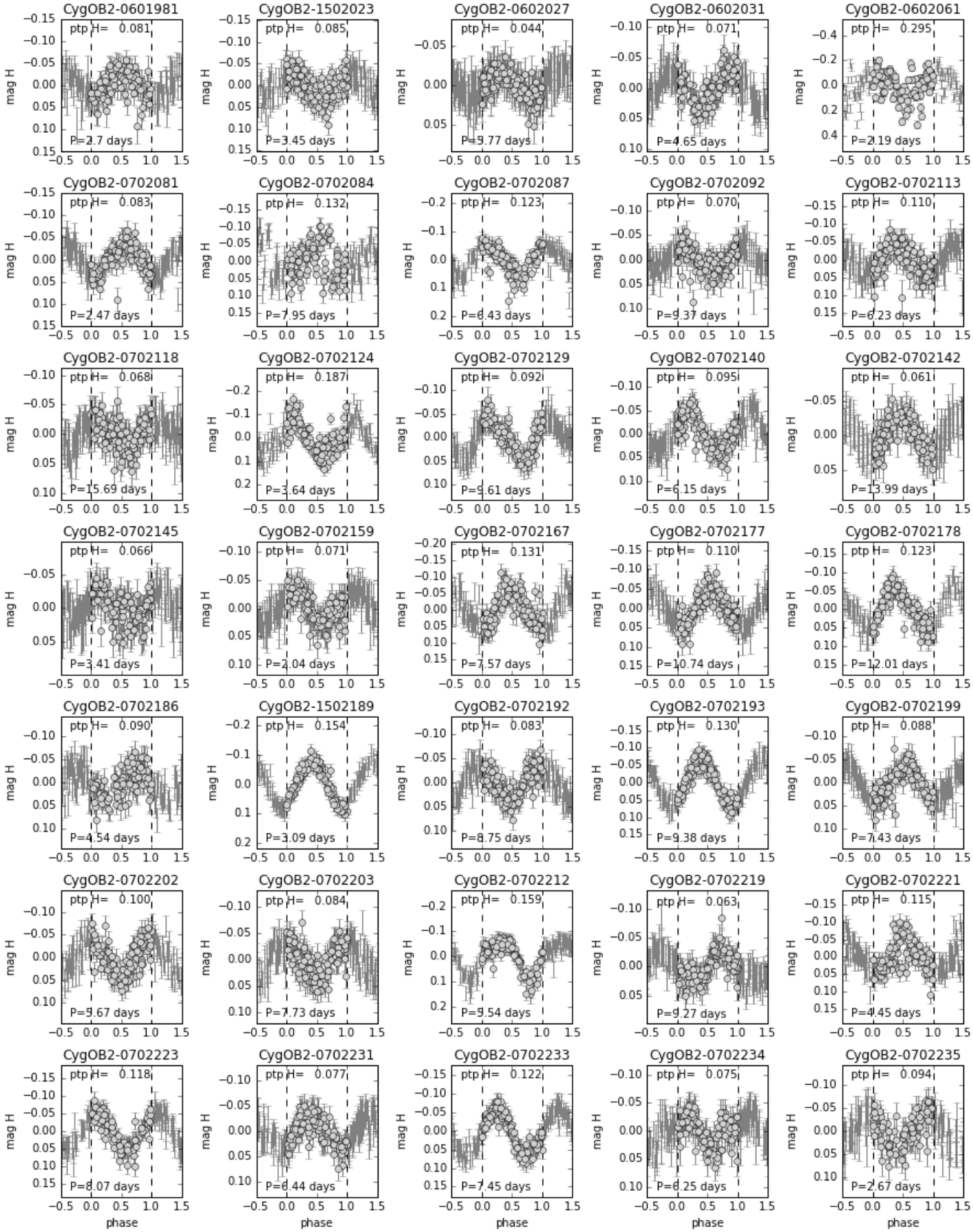
CygOB2-0601981
ptp H= 0.081
P=2.7 days
CygOB2-1502023
ptp H= 0.085
P=3.45 days
CygOB2-0602027
ptp H= 0.044
P=9.77 days
CygOB2-0602031
ptp H= 0.071
P=4.65 days
CygOB2-0602061
ptp H= 0.295
P=2.19 days
CygOB2-0702081
ptp H= 0.083
P=2.47 days
CygOB2-0702084
ptp H= 0.132
P=7.95 days
CygOB2-0702087
ptp H= 0.123
P=6.43 days
CygOB2-0702092
ptp H= 0.070
P=9.37 days
CygOB2-0702113
ptp H= 0.110
P=6.23 days
CygOB2-0702118
ptp H= 0.068
P=15.69 days
CygOB2-0702124
ptp H= 0.187
P=3.64 days
CygOB2-0702129
ptp H= 0.092
P=9.61 days
CygOB2-0702140
ptp H= 0.095
P=6.15 days
CygOB2-0702142
ptp H= 0.061
P=13.99 days
CygOB2-0702145
ptp H= 0.066
P=3.41 days
CygOB2-0702159
ptp H= 0.071
P=2.04 days
CygOB2-0702167
ptp H= 0.131
P=7.57 days
CygOB2-0702177
ptp H= 0.110
P=10.74 days
CygOB2-0702178
ptp H= 0.123
P=12.01 days
CygOB2-0702186
ptp H= 0.090
P=4.54 days
CygOB2-1502189
ptp H= 0.154
P=3.09 days
CygOB2-0702192
ptp H= 0.083
P=8.75 days
CygOB2-0702193
ptp H= 0.130
P=9.38 days
CygOB2-0702199
ptp H= 0.088
P=7.43 days
CygOB2-0702202
ptp H= 0.100
P=5.67 days
CygOB2-0702203
ptp H= 0.084
P=7.73 days
CygOB2-0702212
ptp H= 0.159
P=5.54 days
CygOB2-0702219
ptp H= 0.063
P=9.27 days
CygOB2-0702221
ptp H= 0.115
P=4.45 days
CygOB2-0702223
ptp H= 0.118
P=8.07 days
CygOB2-0702231
ptp H= 0.077
P=6.44 days
CygOB2-0702233
ptp H= 0.122
P=7.45 days
CygOB2-0702234
ptp H= 0.075
P=6.25 days
CygOB2-0702235
ptp H= 0.094
P=2.67 days
mag H
phase

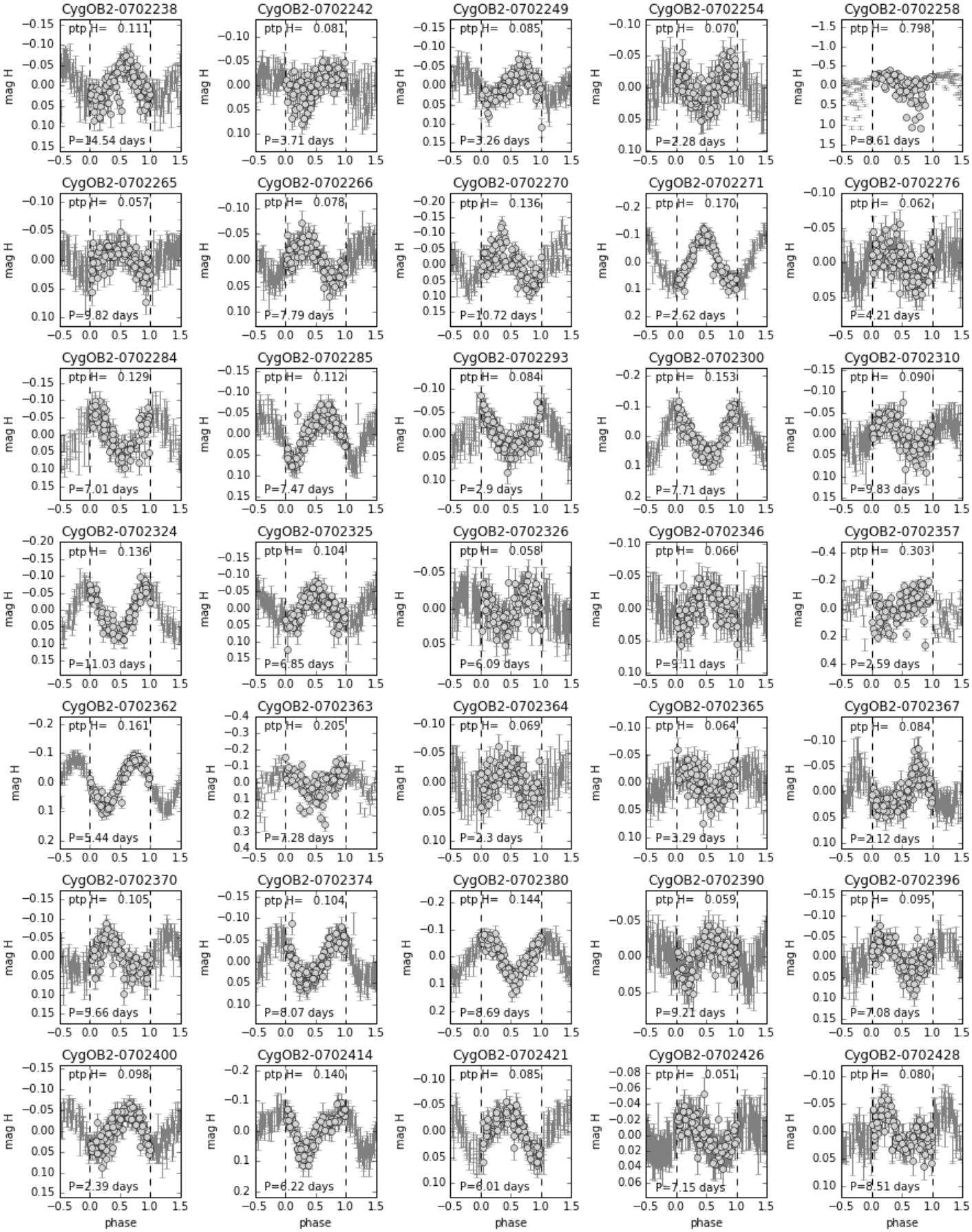
CygOB2-0702238
ptp H= 0.111
P=14.54 days
CygOB2-0702242
ptp H= 0.081
P=3.71 days
CygOB2-0702249
ptp H= 0.085
P=3.26 days
CygOB2-0702254
ptp H= 0.070
P=2.28 days
CygOB2-0702258
ptp H= 0.798
P=8.61 days
CygOB2-0702265
ptp H= 0.057
P=9.82 days
CygOB2-0702266
ptp H= 0.078
P=7.79 days
CygOB2-0702270
ptp H= 0.136
P=10.72 days
CygOB2-0702271
ptp H= 0.170
P=2.62 days
CygOB2-0702276
ptp H= 0.062
P=4.21 days
CygOB2-0702284
ptp H= 0.129
P=7.01 days
CygOB2-0702285
ptp H= 0.112
P=7.47 days
CygOB2-0702293
ptp H= 0.084
P=2.9 days
CygOB2-0702300
ptp H= 0.153
P=7.71 days
CygOB2-0702310
ptp H= 0.090
P=9.83 days
CygOB2-0702324
ptp H= 0.136
P=11.03 days
CygOB2-0702325
ptp H= 0.104
P=6.85 days
CygOB2-0702326
ptp H= 0.058
P=6.09 days
CygOB2-0702346
ptp H= 0.066
P=9.11 days
CygOB2-0702357
ptp H= 0.303
P=2.59 days
CygOB2-0702362
ptp H= 0.161
P=5.44 days
CygOB2-0702363
ptp H= 0.205
P=7.28 days
CygOB2-0702364
ptp H= 0.069
P=2.3 days
CygOB2-0702365
ptp H= 0.064
P=3.29 days
CygOB2-0702367
ptp H= 0.084
P=2.12 days
CygOB2-0702370
ptp H= 0.105
P=5.66 days
CygOB2-0702374
ptp H= 0.104
P=8.07 days
CygOB2-0702380
ptp H= 0.144
P=8.69 days
CygOB2-0702390
ptp H= 0.059
P=9.21 days
CygOB2-0702396
ptp H= 0.095
P=7.08 days
CygOB2-0702400
ptp H= 0.098
P=2.39 days
CygOB2-0702414
ptp H= 0.140
P=6.22 days
CygOB2-0702421
ptp H= 0.085
P=6.01 days
CygOB2-0702426
ptp H= 0.051
P=7.15 days
CygOB2-0702428
ptp H= 0.080
P=8.51 days
mag H
phase

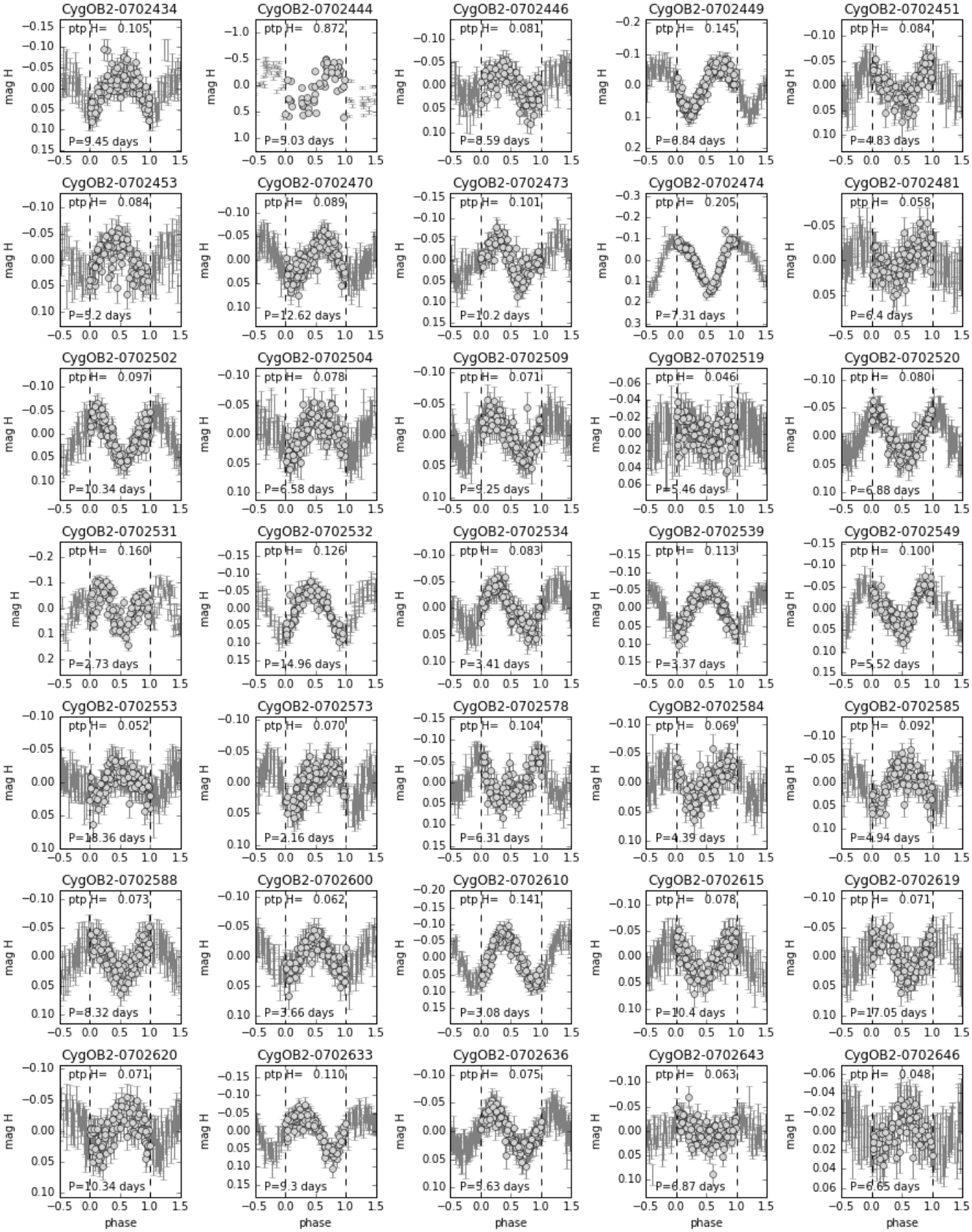
CygOB2-0702434
ptp H= 0.105
P=9.45 days
CygOB2-0702444
ptp H= 0.872
P=5.03 days
CygOB2-0702446
ptp H= 0.081
P=8.59 days
CygOB2-0702449
ptp H= 0.145
P=6.84 days
CygOB2-0702451
ptp H= 0.084
P=4.83 days
CygOB2-0702453
ptp H= 0.084
P=5.2 days
CygOB2-0702470
ptp H= 0.089
P=12.62 days
CygOB2-0702473
ptp H= 0.101
P=10.2 days
CygOB2-0702474
ptp H= 0.205
P=7.31 days
CygOB2-0702481
ptp H= 0.058
P=6.4 days
CygOB2-0702502
ptp H= 0.097
P=10.34 days
CygOB2-0702504
ptp H= 0.078
P=6.58 days
CygOB2-0702509
ptp H= 0.071
P=9.25 days
CygOB2-0702519
ptp H= 0.046
P=5.46 days
CygOB2-0702520
ptp H= 0.080
P=6.88 days
CygOB2-0702531
ptp H= 0.160
P=2.73 days
CygOB2-0702532
ptp H= 0.126
P=14.96 days
CygOB2-0702534
ptp H= 0.083
P=3.41 days
CygOB2-0702539
ptp H= 0.113
P=3.37 days
CygOB2-0702549
ptp H= 0.100
P=5.52 days
CygOB2-0702553
ptp H= 0.052
P=18.36 days
CygOB2-0702573
ptp H= 0.070
P=2.16 days
CygOB2-0702578
ptp H= 0.104
P=6.31 days
CygOB2-0702584
ptp H= 0.069
P=4.39 days
CygOB2-0702585
ptp H= 0.092
P=4.94 days
CygOB2-0702588
ptp H= 0.073
P=8.32 days
CygOB2-0702600
ptp H= 0.062
P=3.66 days
CygOB2-0702610
ptp H= 0.141
P=3.08 days
CygOB2-0702615
ptp H= 0.078
P=10.4 days
CygOB2-0702619
ptp H= 0.071
P=17.05 days
CygOB2-0702620
ptp H= 0.071
P=10.34 days
CygOB2-0702633
ptp H= 0.110
P=9.3 days
CygOB2-0702636
ptp H= 0.075
P=5.63 days
CygOB2-0702643
ptp H= 0.063
P=6.87 days
CygOB2-0702646
ptp H= 0.048
P=6.65 days
mag H
phase

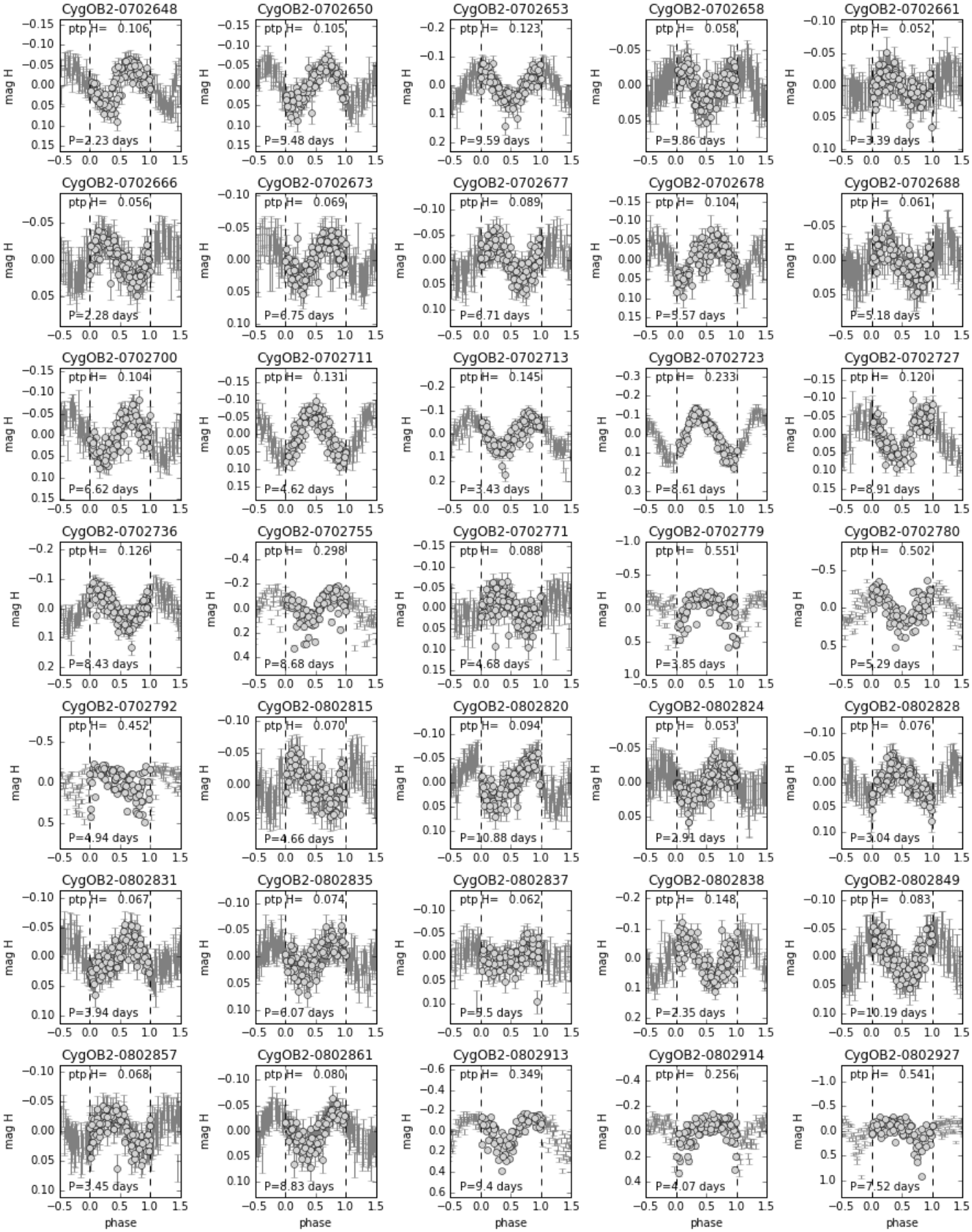
CygOB2-0702648
ptp H= 0.106
P=2.23 days
CygOB2-0702650
ptp H= 0.105
P=5.48 days
CygOB2-0702653
ptp H= 0.123
P=9.59 days
CygOB2-0702658
ptp H= 0.058
P=9.86 days
CygOB2-0702661
ptp H= 0.052
P=3.39 days
CygOB2-0702666
ptp H= 0.056
P=2.28 days
CygOB2-0702673
ptp H= 0.069
P=6.75 days
CygOB2-0702677
ptp H= 0.089
P=6.71 days
CygOB2-0702678
ptp H= 0.104
P=5.57 days
CygOB2-0702688
ptp H= 0.061
P=5.18 days
CygOB2-0702700
ptp H= 0.104
P=6.62 days
CygOB2-0702711
ptp H= 0.131
P=4.62 days
CygOB2-0702713
ptp H= 0.145
P=3.43 days
CygOB2-0702723
ptp H= 0.233
P=8.61 days
CygOB2-0702727
ptp H= 0.120
P=8.91 days
CygOB2-0702736
ptp H= 0.126
P=8.43 days
CygOB2-0702755
ptp H= 0.298
P=8.68 days
CygOB2-0702771
ptp H= 0.088
P=4.68 days
CygOB2-0702779
ptp H= 0.551
P=3.85 days
CygOB2-0702780
ptp H= 0.502
P=5.29 days
CygOB2-0702792
ptp H= 0.452
P=4.94 days
CygOB2-0802815
ptp H= 0.070
P=4.66 days
CygOB2-0802820
ptp H= 0.094
P=10.88 days
CygOB2-0802824
ptp H= 0.053
P=2.91 days
CygOB2-0802828
ptp H= 0.076
P=3.04 days
CygOB2-0802831
ptp H= 0.067
P=3.94 days
CygOB2-0802835
ptp H= 0.074
P=6.07 days
CygOB2-0802837
ptp H= 0.062
P=9.5 days
CygOB2-0802838
ptp H= 0.148
P=2.35 days
CygOB2-0802849
ptp H= 0.083
P=10.19 days
CygOB2-0802857
ptp H= 0.068
P=3.45 days
CygOB2-0802861
ptp H= 0.080
P=8.83 days
CygOB2-0802913
ptp H= 0.349
P=9.4 days
CygOB2-0802914
ptp H= 0.256
P=4.07 days
CygOB2-0802927
ptp H= 0.541
P=7.52 days
mag H
phase

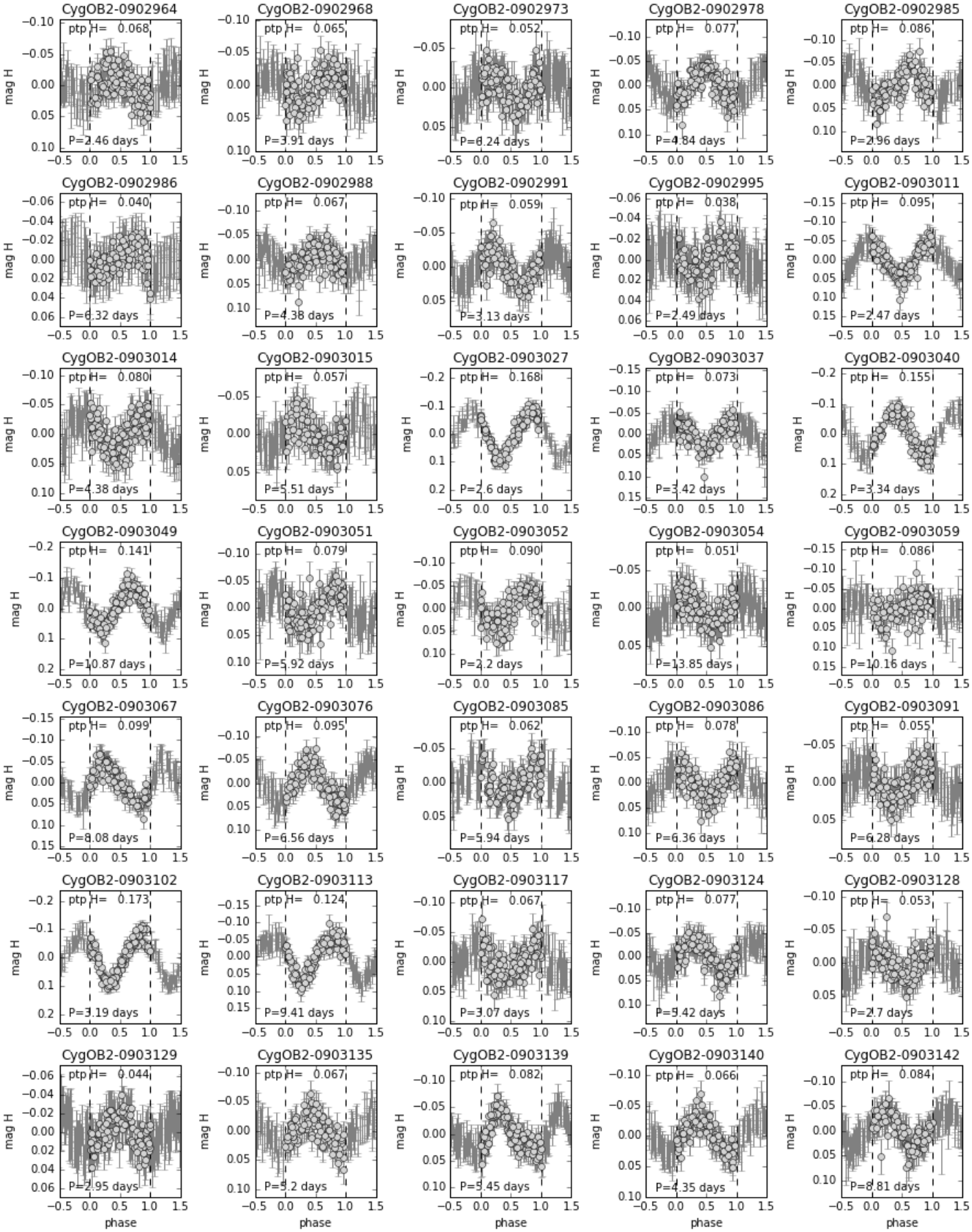
CygOB2-0902964
ptp H= 0.068
P=2.46 days
CygOB2-0902968
ptp H= 0.065
P=3.91 days
CygOB2-0902973
ptp H= 0.052
P=6.24 days
CygOB2-0902978
ptp H= 0.077
P=4.84 days
CygOB2-0902985
ptp H= 0.086
P=2.96 days
CygOB2-0902986
ptp H= 0.040
P=6.32 days
CygOB2-0902988
ptp H= 0.067
P=4.38 days
CygOB2-0902991
ptp H= 0.059
P=3.13 days
CygOB2-0902995
ptp H= 0.038
P=2.49 days
CygOB2-0903011
ptp H= 0.095
P=2.47 days
CygOB2-0903014
ptp H= 0.080
P=4.38 days
CygOB2-0903015
ptp H= 0.057
P=5.51 days
CygOB2-0903027
ptp H= 0.168
P=2.6 days
CygOB2-0903037
ptp H= 0.073
P=3.42 days
CygOB2-0903040
ptp H= 0.155
P=3.34 days
CygOB2-0903049
ptp H= 0.141
P=10.87 days
CygOB2-0903051
ptp H= 0.079
P=5.92 days
CygOB2-0903052
ptp H= 0.090
P=2.2 days
CygOB2-0903054
ptp H= 0.051
P=13.85 days
CygOB2-0903059
ptp H= 0.086
P=10.16 days
CygOB2-0903067
ptp H= 0.099
P=8.08 days
CygOB2-0903076
ptp H= 0.095
P=6.56 days
CygOB2-0903085
ptp H= 0.062
P=5.94 days
CygOB2-0903086
ptp H= 0.078
P=6.36 days
CygOB2-0903091
ptp H= 0.055
P=6.28 days
CygOB2-0903102
ptp H= 0.173
P=3.19 days
CygOB2-0903113
ptp H= 0.124
P=9.41 days
CygOB2-0903117
ptp H= 0.067
P=3.07 days
CygOB2-0903124
ptp H= 0.077
P=5.42 days
CygOB2-0903128
ptp H= 0.053
P=2.7 days
CygOB2-0903129
ptp H= 0.044
P=2.95 days
CygOB2-0903135
ptp H= 0.067
P=5.2 days
CygOB2-0903139
ptp H= 0.082
P=5.45 days
CygOB2-0903140
ptp H= 0.066
P=4.35 days
CygOB2-0903142
ptp H= 0.084
P=8.81 days
mag H
phase

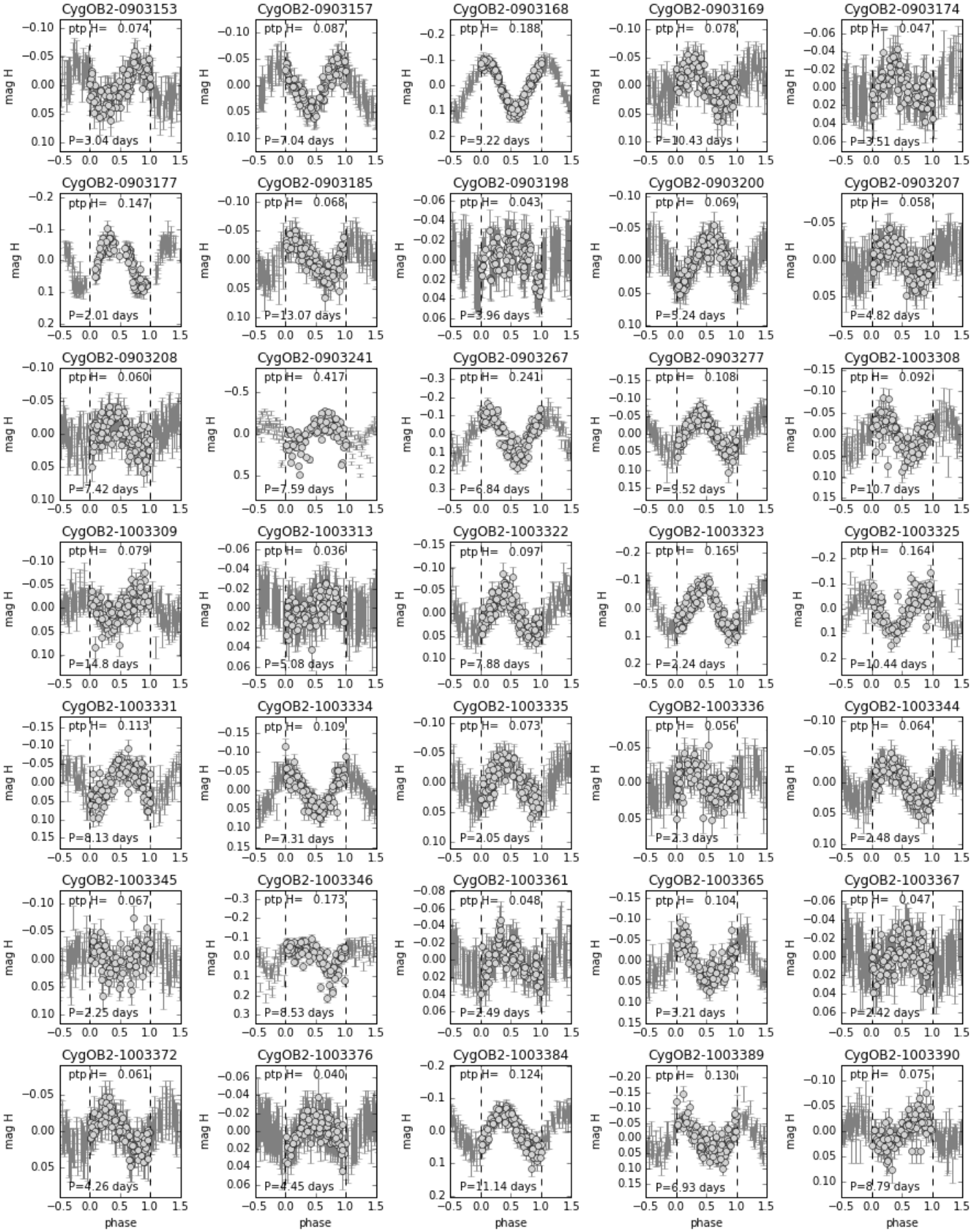
CygOB2-0903153
ptp H= 0.074
P=3.04 days
CygOB2-0903157
ptp H= 0.087
P=7.04 days
CygOB2-0903168
ptp H= 0.188
P=9.22 days
CygOB2-0903169
ptp H= 0.078
P=10.43 days
CygOB2-0903174
ptp H= 0.047
P=3.51 days
CygOB2-0903177
ptp H= 0.147
P=2.01 days
CygOB2-0903185
ptp H= 0.068
P=13.07 days
CygOB2-0903198
ptp H= 0.043
P=3.96 days
CygOB2-0903200
ptp H= 0.069
P=5.24 days
CygOB2-0903207
ptp H= 0.058
P=4.82 days
CygOB2-0903208
ptp H= 0.060
P=7.42 days
CygOB2-0903241
ptp H= 0.417
P=7.59 days
CygOB2-0903267
ptp H= 0.241
P=6.84 days
CygOB2-0903277
ptp H= 0.108
P=9.52 days
CygOB2-1003308
ptp H= 0.092
P=10.7 days
CygOB2-1003309
ptp H= 0.079
P=14.8 days
CygOB2-1003313
ptp H= 0.036
P=5.08 days
CygOB2-1003322
ptp H= 0.097
P=7.88 days
CygOB2-1003323
ptp H= 0.165
P=2.24 days
CygOB2-1003325
ptp H= 0.164
P=10.44 days
CygOB2-1003331
ptp H= 0.113
P=8.13 days
CygOB2-1003334
ptp H= 0.109
P=7.31 days
CygOB2-1003335
ptp H= 0.073
P=2.05 days
CygOB2-1003336
ptp H= 0.056
P=2.3 days
CygOB2-1003344
ptp H= 0.064
P=2.48 days
CygOB2-1003345
ptp H= 0.067
P=2.25 days
CygOB2-1003346
ptp H= 0.173
P=8.53 days
CygOB2-1003361
ptp H= 0.048
P=2.49 days
CygOB2-1003365
ptp H= 0.104
P=3.21 days
CygOB2-1003367
ptp H= 0.047
P=2.42 days
CygOB2-1003372
ptp H= 0.061
P=4.26 days
CygOB2-1003376
ptp H= 0.040
P=4.45 days
CygOB2-1003384
ptp H= 0.124
P=11.14 days
CygOB2-1003389
ptp H= 0.130
P=6.93 days
CygOB2-1003390
ptp H= 0.075
P=8.79 days
mag H
phase

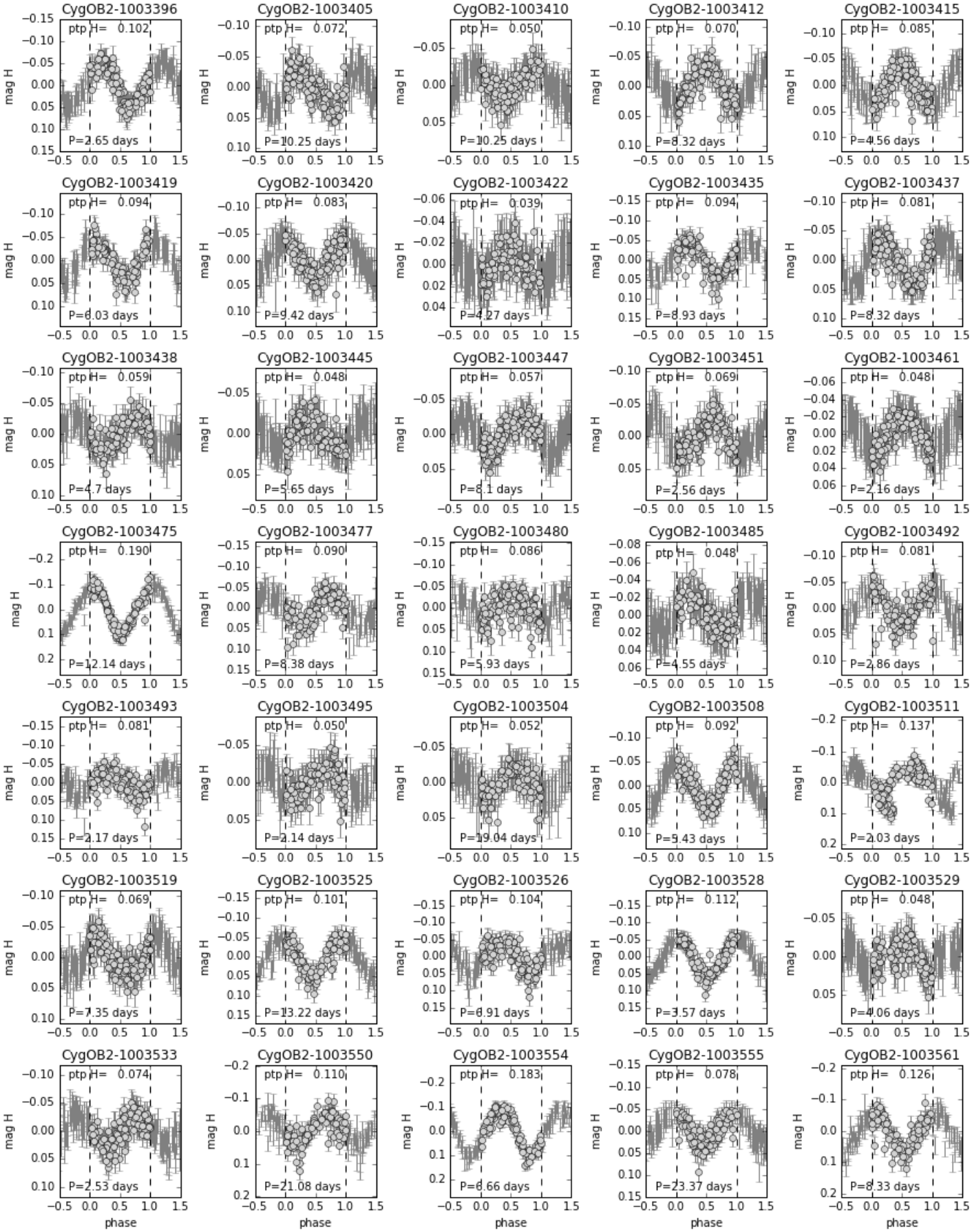
CygOB2-1003396
ptp H= 0.102
P=2.65 days
CygOB2-1003405
ptp H= 0.072
P=10.25 days
CygOB2-1003410
ptp H= 0.050
P=10.25 days
CygOB2-1003412
ptp H= 0.070
P=8.32 days
CygOB2-1003415
ptp H= 0.085
P=4.56 days
CygOB2-1003419
ptp H= 0.094
P=8.03 days
CygOB2-1003420
ptp H= 0.083
P=9.42 days
CygOB2-1003422
ptp H= 0.039
P=4.27 days
CygOB2-1003435
ptp H= 0.094
P=8.93 days
CygOB2-1003437
ptp H= 0.081
P=8.32 days
CygOB2-1003438
ptp H= 0.059
P=4.7 days
CygOB2-1003445
ptp H= 0.048
P=5.65 days
CygOB2-1003447
ptp H= 0.057
P=8.1 days
CygOB2-1003451
ptp H= 0.069
P=2.56 days
CygOB2-1003461
ptp H= 0.048
P=2.16 days
CygOB2-1003475
ptp H= 0.190
P=12.14 days
CygOB2-1003477
ptp H= 0.090
P=8.38 days
CygOB2-1003480
ptp H= 0.086
P=5.93 days
CygOB2-1003485
ptp H= 0.048
P=4.55 days
CygOB2-1003492
ptp H= 0.081
P=2.86 days
CygOB2-1003493
ptp H= 0.081
P=2.17 days
CygOB2-1003495
ptp H= 0.050
P=2.14 days
CygOB2-1003504
ptp H= 0.052
P=19.04 days
CygOB2-1003508
ptp H= 0.092
P=5.43 days
CygOB2-1003511
ptp H= 0.137
P=2.03 days
CygOB2-1003519
ptp H= 0.069
P=7.35 days
CygOB2-1003525
ptp H= 0.101
P=13.22 days
CygOB2-1003526
ptp H= 0.104
P=6.91 days
CygOB2-1003528
ptp H= 0.112
P=3.57 days
CygOB2-1003529
ptp H= 0.048
P=4.06 days
CygOB2-1003533
ptp H= 0.074
P=2.53 days
CygOB2-1003550
ptp H= 0.110
P=21.08 days
CygOB2-1003554
ptp H= 0.183
P=6.66 days
CygOB2-1003555
ptp H= 0.078
P=23.37 days
CygOB2-1003561
ptp H= 0.126
P=8.33 days
mag H
phase

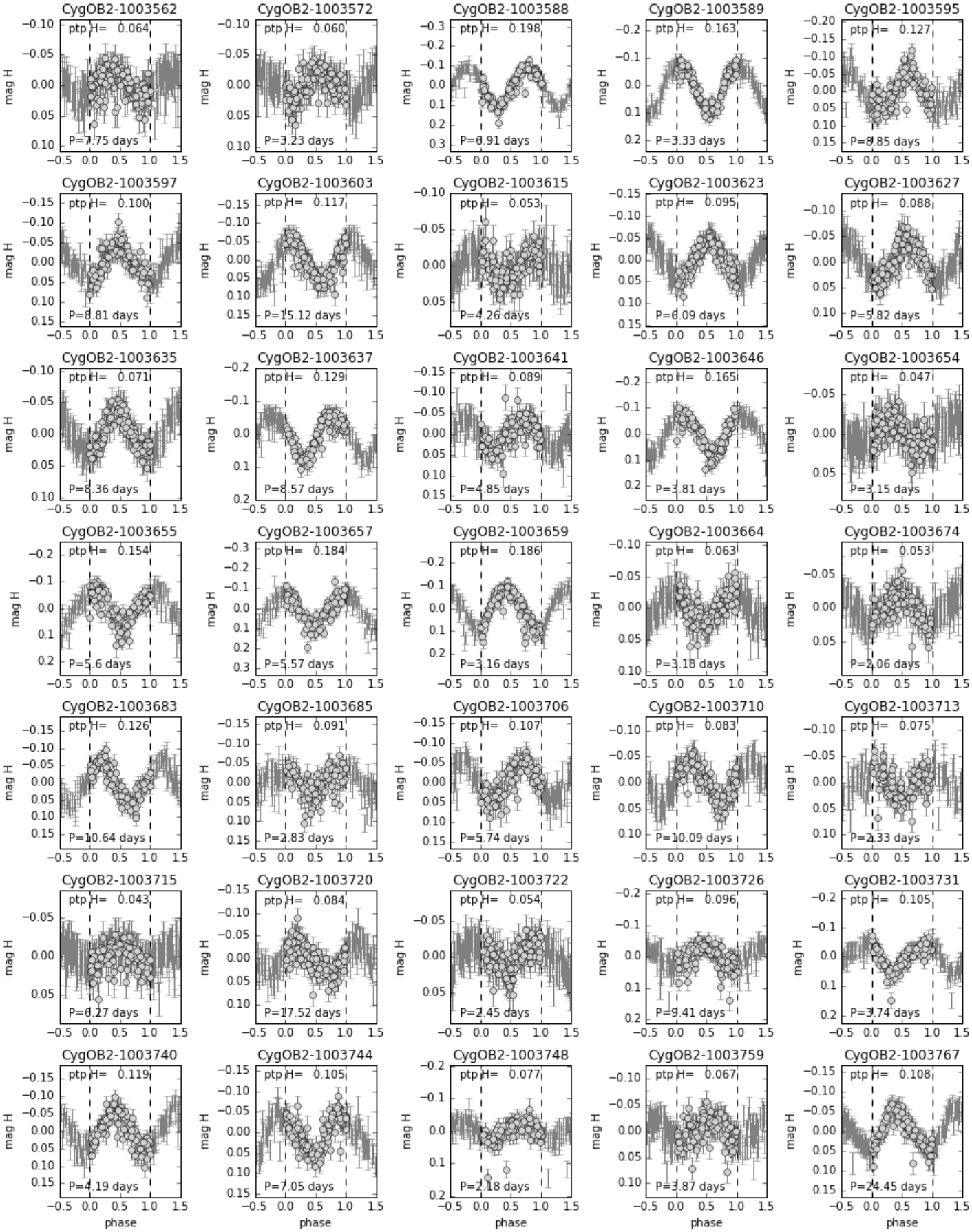
CygOB2-1003562
ptp H= 0.064
P=7.75 days
CygOB2-1003572
ptp H= 0.060
P=3.23 days
CygOB2-1003588
ptp H= 0.198
P=6.91 days
CygOB2-1003589
ptp H= 0.163
P=3.33 days
CygOB2-1003595
ptp H= 0.127
P=8.85 days
CygOB2-1003597
ptp H= 0.100
P=8.81 days
CygOB2-1003603
ptp H= 0.117
P=15.12 days
CygOB2-1003615
ptp H= 0.053
P=4.26 days
CygOB2-1003623
ptp H= 0.095
P=6.09 days
CygOB2-1003627
ptp H= 0.088
P=5.82 days
CygOB2-1003635
ptp H= 0.071
P=8.36 days
CygOB2-1003637
ptp H= 0.129
P=8.57 days
CygOB2-1003641
ptp H= 0.089
P=4.85 days
CygOB2-1003646
ptp H= 0.165
P=3.81 days
CygOB2-1003654
ptp H= 0.047
P=3.15 days
CygOB2-1003655
ptp H= 0.154
P=5.6 days
CygOB2-1003657
ptp H= 0.184
P=5.57 days
CygOB2-1003659
ptp H= 0.186
P=3.16 days
CygOB2-1003664
ptp H= 0.063
P=3.18 days
CygOB2-1003674
ptp H= 0.053
P=2.06 days
CygOB2-1003683
ptp H= 0.126
P=10.64 days
CygOB2-1003685
ptp H= 0.091
P=2.83 days
CygOB2-1003706
ptp H= 0.107
P=5.74 days
CygOB2-1003710
ptp H= 0.083
P=10.09 days
CygOB2-1003713
ptp H= 0.075
P=2.33 days
CygOB2-1003715
ptp H= 0.043
P=6.27 days
CygOB2-1003720
ptp H= 0.084
P=17.52 days
CygOB2-1003722
ptp H= 0.054
P=2.45 days
CygOB2-1003726
ptp H= 0.096
P=9.41 days
CygOB2-1003731
ptp H= 0.105
P=3.74 days
CygOB2-1003740
ptp H= 0.119
P=4.19 days
CygOB2-1003744
ptp H= 0.105
P=7.05 days
CygOB2-1003748
ptp H= 0.077
P=2.18 days
CygOB2-1003759
ptp H= 0.067
P=3.87 days
CygOB2-1003767
ptp H= 0.108
P=24.45 days
mag H
phase

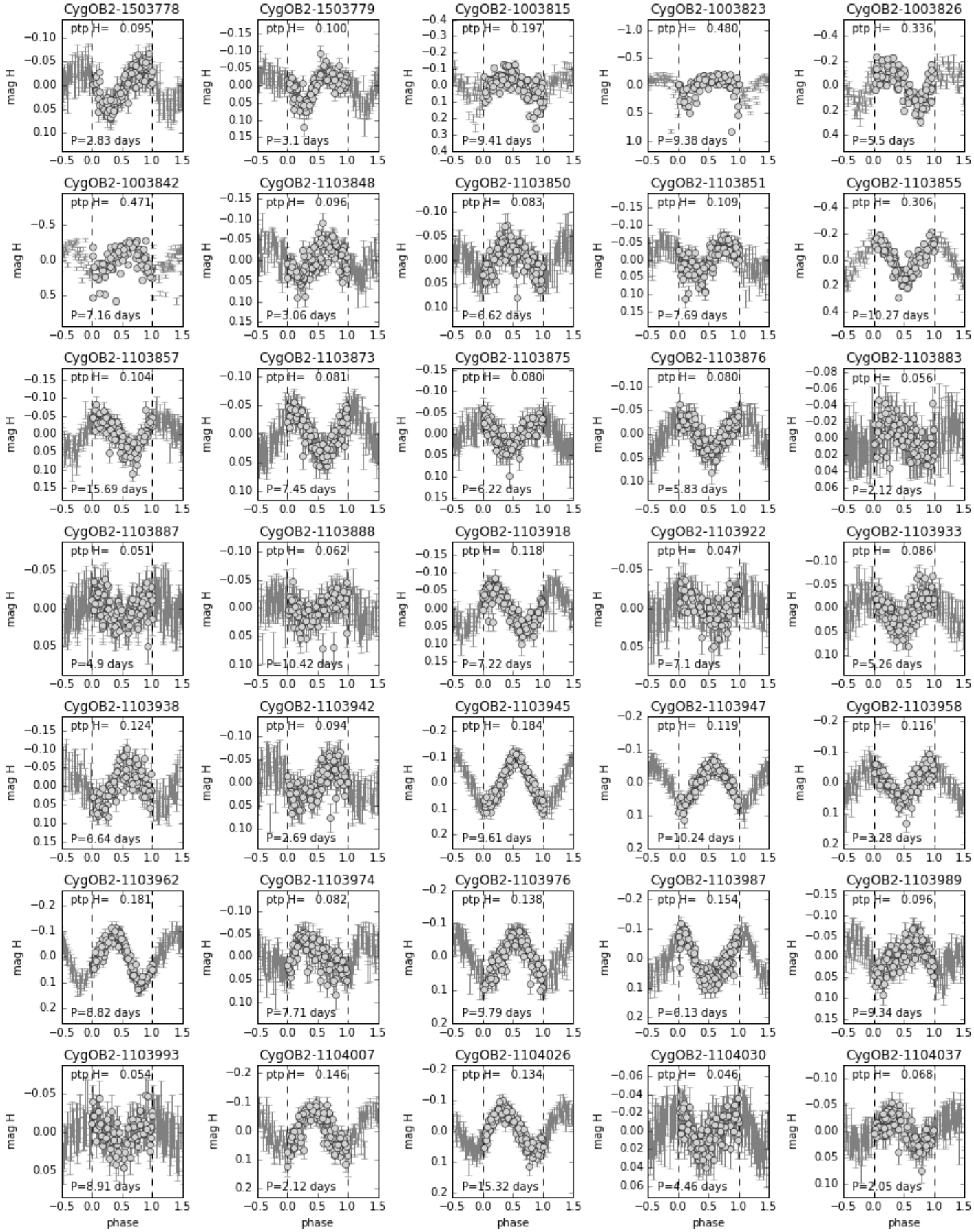
CygOB2-1503778
ptp H= 0.095
P=2.83 days
CygOB2-1503779
ptp H= 0.100
P=3.1 days
CygOB2-1003815
ptp H= 0.197
P=9.41 days
CygOB2-1003823
ptp H= 0.480
P=9.38 days
CygOB2-1003826
ptp H= 0.336
P=5.5 days
CygOB2-1003842
ptp H= 0.471
P=7.16 days
CygOB2-1103848
ptp H= 0.096
P=3.06 days
CygOB2-1103850
ptp H= 0.083
P=6.62 days
CygOB2-1103851
ptp H= 0.109
P=7.69 days
CygOB2-1103855
ptp H= 0.306
P=10.27 days
CygOB2-1103857
ptp H= 0.104
P=15.69 days
CygOB2-1103873
ptp H= 0.081
P=7.45 days
CygOB2-1103875
ptp H= 0.080
P=6.22 days
CygOB2-1103876
ptp H= 0.080
P=5.83 days
CygOB2-1103883
ptp H= 0.056
P=2.12 days
CygOB2-1103887
ptp H= 0.051
P=4.9 days
CygOB2-1103888
ptp H= 0.062
P=10.42 days
CygOB2-1103918
ptp H= 0.118
P=7.22 days
CygOB2-1103922
ptp H= 0.047
P=7.1 days
CygOB2-1103933
ptp H= 0.086
P=5.26 days
CygOB2-1103938
ptp H= 0.124
P=6.64 days
CygOB2-1103942
ptp H= 0.094
P=2.69 days
CygOB2-1103945
ptp H= 0.184
P=9.61 days
CygOB2-1103947
ptp H= 0.119
P=10.24 days
CygOB2-1103958
ptp H= 0.116
P=3.28 days
CygOB2-1103962
ptp H= 0.181
P=8.82 days
CygOB2-1103974
ptp H= 0.082
P=7.71 days
CygOB2-1103976
ptp H= 0.138
P=5.79 days
CygOB2-1103987
ptp H= 0.154
P=6.13 days
CygOB2-1103989
ptp H= 0.096
P=9.34 days
CygOB2-1103993
ptp H= 0.054
P=8.91 days
CygOB2-1104007
ptp H= 0.146
P=2.12 days
CygOB2-1104026
ptp H= 0.134
P=15.32 days
CygOB2-1104030
ptp H= 0.046
P=4.46 days
CygOB2-1104037
ptp H= 0.068
P=2.05 days
mag H
phase

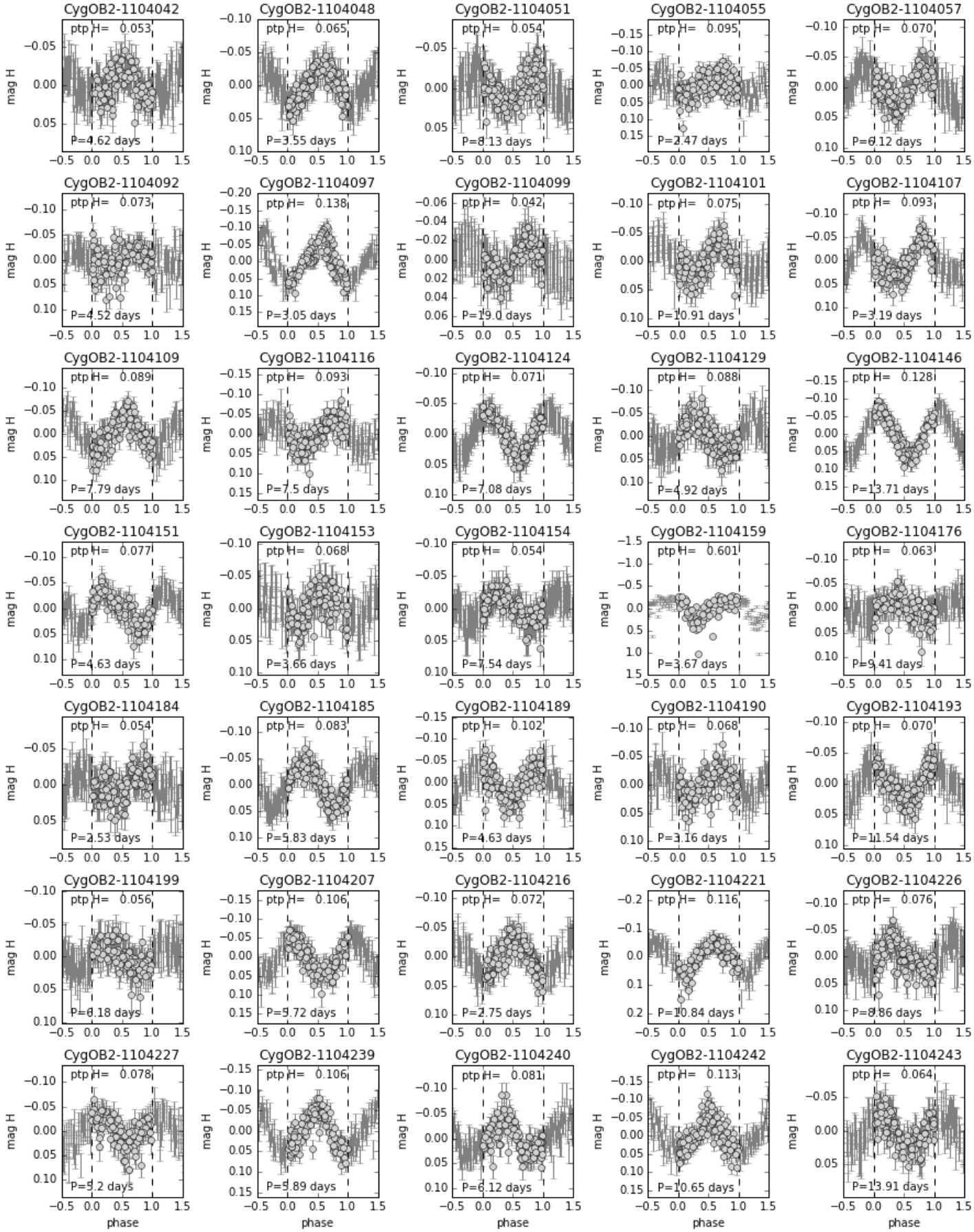
CygOB2-1104042
ptp H= 0.053
P=4.62 days
CygOB2-1104048
ptp H= 0.065
P=3.55 days
CygOB2-1104051
ptp H= 0.054
P=8.13 days
CygOB2-1104055
ptp H= 0.095
P=2.47 days
CygOB2-1104057
ptp H= 0.070
P=6.12 days
CygOB2-1104092
ptp H= 0.073
P=4.52 days
CygOB2-1104097
ptp H= 0.138
P=3.05 days
CygOB2-1104099
ptp H= 0.042
P=19.0 days
CygOB2-1104101
ptp H= 0.075
P=10.91 days
CygOB2-1104107
ptp H= 0.093
P=3.19 days
CygOB2-1104109
ptp H= 0.089
P=7.79 days
CygOB2-1104116
ptp H= 0.093
P=7.5 days
CygOB2-1104124
ptp H= 0.071
P=7.08 days
CygOB2-1104129
ptp H= 0.088
P=4.92 days
CygOB2-1104146
ptp H= 0.128
P=13.71 days
CygOB2-1104151
ptp H= 0.077
P=4.63 days
CygOB2-1104153
ptp H= 0.068
P=3.66 days
CygOB2-1104154
ptp H= 0.054
P=7.54 days
CygOB2-1104159
ptp H= 0.601
P=3.67 days
CygOB2-1104176
ptp H= 0.063
P=9.41 days
CygOB2-1104184
ptp H= 0.054
P=2.53 days
CygOB2-1104185
ptp H= 0.083
P=5.83 days
CygOB2-1104189
ptp H= 0.102
P=4.63 days
CygOB2-1104190
ptp H= 0.068
P=3.16 days
CygOB2-1104193
ptp H= 0.070
P=11.54 days
CygOB2-1104199
ptp H= 0.056
P=6.18 days
CygOB2-1104207
ptp H= 0.106
P=9.72 days
CygOB2-1104216
ptp H= 0.072
P=2.75 days
CygOB2-1104221
ptp H= 0.116
P=10.84 days
CygOB2-1104226
ptp H= 0.076
P=8.86 days
CygOB2-1104227
ptp H= 0.078
P=5.2 days
CygOB2-1104239
ptp H= 0.106
P=9.89 days
CygOB2-1104240
ptp H= 0.081
P=6.12 days
CygOB2-1104242
ptp H= 0.113
P=10.65 days
CygOB2-1104243
ptp H= 0.064
P=13.91 days
mag H
phase

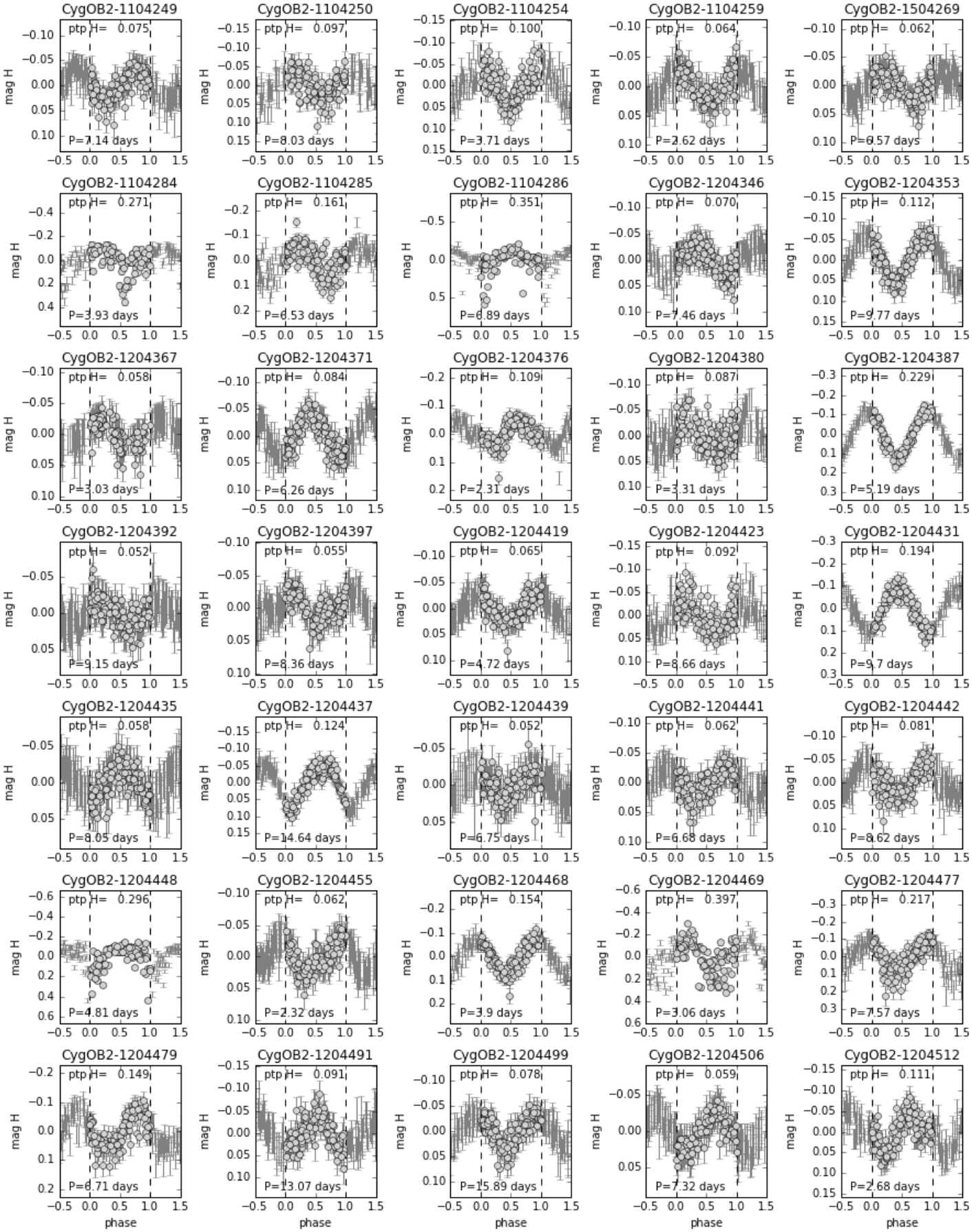
CygOB2-1104249
ptp H= 0.075
P=7.14 days
CygOB2-1104250
ptp H= 0.097
P=8.03 days
CygOB2-1104254
ptp H= 0.100
P=3.71 days
CygOB2-1104259
ptp H= 0.064
P=2.62 days
CygOB2-1504269
ptp H= 0.062
P=6.57 days
CygOB2-1104284
ptp H= 0.271
P=3.93 days
CygOB2-1104285
ptp H= 0.161
P=6.53 days
CygOB2-1104286
ptp H= 0.351
P=6.89 days
CygOB2-1204346
ptp H= 0.070
P=7.46 days
CygOB2-1204353
ptp H= 0.112
P=9.77 days
CygOB2-1204367
ptp H= 0.058
P=3.03 days
CygOB2-1204371
ptp H= 0.084
P=6.26 days
CygOB2-1204376
ptp H= 0.109
P=2.31 days
CygOB2-1204380
ptp H= 0.087
P=3.31 days
CygOB2-1204387
ptp H= 0.229
P=5.19 days
CygOB2-1204392
ptp H= 0.052
P=9.15 days
CygOB2-1204397
ptp H= 0.055
P=8.36 days
CygOB2-1204419
ptp H= 0.065
P=4.72 days
CygOB2-1204423
ptp H= 0.092
P=8.66 days
CygOB2-1204431
ptp H= 0.194
P=9.7 days
CygOB2-1204435
ptp H= 0.058
P=8.05 days
CygOB2-1204437
ptp H= 0.124
P=14.64 days
CygOB2-1204439
ptp H= 0.052
P=6.75 days
CygOB2-1204441
ptp H= 0.062
P=6.68 days
CygOB2-1204442
ptp H= 0.081
P=8.62 days
CygOB2-1204448
ptp H= 0.296
P=4.81 days
CygOB2-1204455
ptp H= 0.062
P=2.32 days
CygOB2-1204468
ptp H= 0.154
P=3.9 days
CygOB2-1204469
ptp H= 0.397
P=3.06 days
CygOB2-1204477
ptp H= 0.217
P=7.57 days
CygOB2-1204479
ptp H= 0.149
P=6.71 days
CygOB2-1204491
ptp H= 0.091
P=13.07 days
CygOB2-1204499
ptp H= 0.078
P=15.89 days
CygOB2-1204506
ptp H= 0.059
P=7.32 days
CygOB2-1204512
ptp H= 0.111
P=2.68 days
mag H
phase

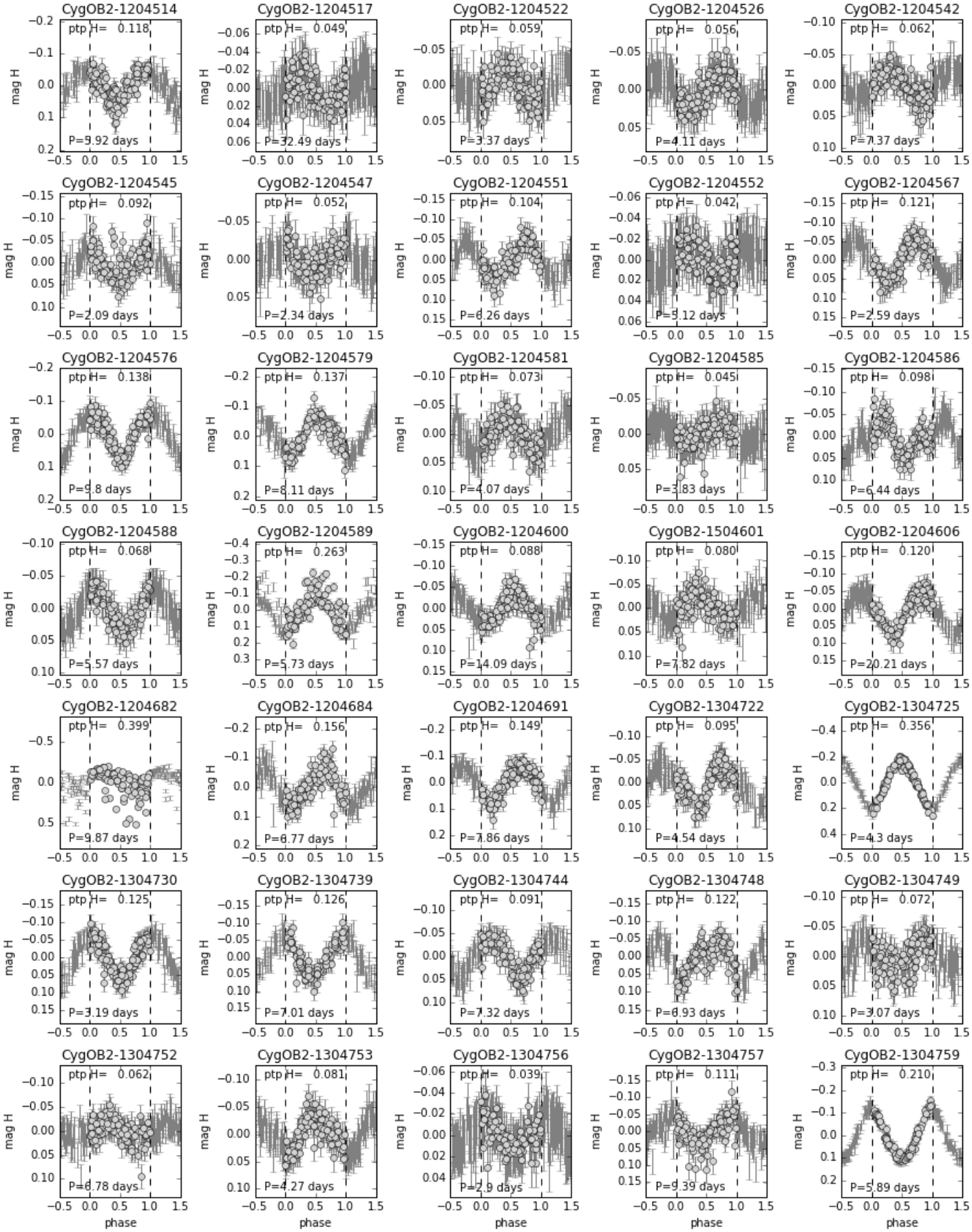
CygOB2-1204514
ptp H= 0.118
P=9.92 days
CygOB2-1204517
ptp H= 0.049
P=32.49 days
CygOB2-1204522
ptp H= 0.059
P=3.37 days
CygOB2-1204526
ptp H= 0.056
P=4.11 days
CygOB2-1204542
ptp H= 0.062
P=7.37 days
CygOB2-1204545
ptp H= 0.092
P=2.09 days
CygOB2-1204547
ptp H= 0.052
P=2.34 days
CygOB2-1204551
ptp H= 0.104
P=6.26 days
CygOB2-1204552
ptp H= 0.042
P=3.12 days
CygOB2-1204567
ptp H= 0.121
P=2.59 days
CygOB2-1204576
ptp H= 0.138
P=9.8 days
CygOB2-1204579
ptp H= 0.137
P=8.11 days
CygOB2-1204581
ptp H= 0.073
P=4.07 days
CygOB2-1204585
ptp H= 0.045
P=3.83 days
CygOB2-1204586
ptp H= 0.098
P=6.44 days
CygOB2-1204588
ptp H= 0.068
P=5.57 days
CygOB2-1204589
ptp H= 0.263
P=5.73 days
CygOB2-1204600
ptp H= 0.088
P=14.09 days
CygOB2-1504601
ptp H= 0.080
P=7.82 days
CygOB2-1204606
ptp H= 0.120
P=20.21 days
CygOB2-1204682
ptp H= 0.399
P=9.87 days
CygOB2-1204684
ptp H= 0.156
P=6.77 days
CygOB2-1204691
ptp H= 0.149
P=7.86 days
CygOB2-1304722
ptp H= 0.095
P=4.54 days
CygOB2-1304725
ptp H= 0.356
P=4.3 days
CygOB2-1304730
ptp H= 0.125
P=3.19 days
CygOB2-1304739
ptp H= 0.126
P=7.01 days
CygOB2-1304744
ptp H= 0.091
P=7.32 days
CygOB2-1304748
ptp H= 0.122
P=6.93 days
CygOB2-1304749
ptp H= 0.072
P=3.07 days
CygOB2-1304752
ptp H= 0.062
P=6.78 days
CygOB2-1304753
ptp H= 0.081
P=4.27 days
CygOB2-1304756
ptp H= 0.039
P=2.9 days
CygOB2-1304757
ptp H= 0.111
P=9.39 days
CygOB2-1304759
ptp H= 0.210
P=5.89 days
mag H
phase

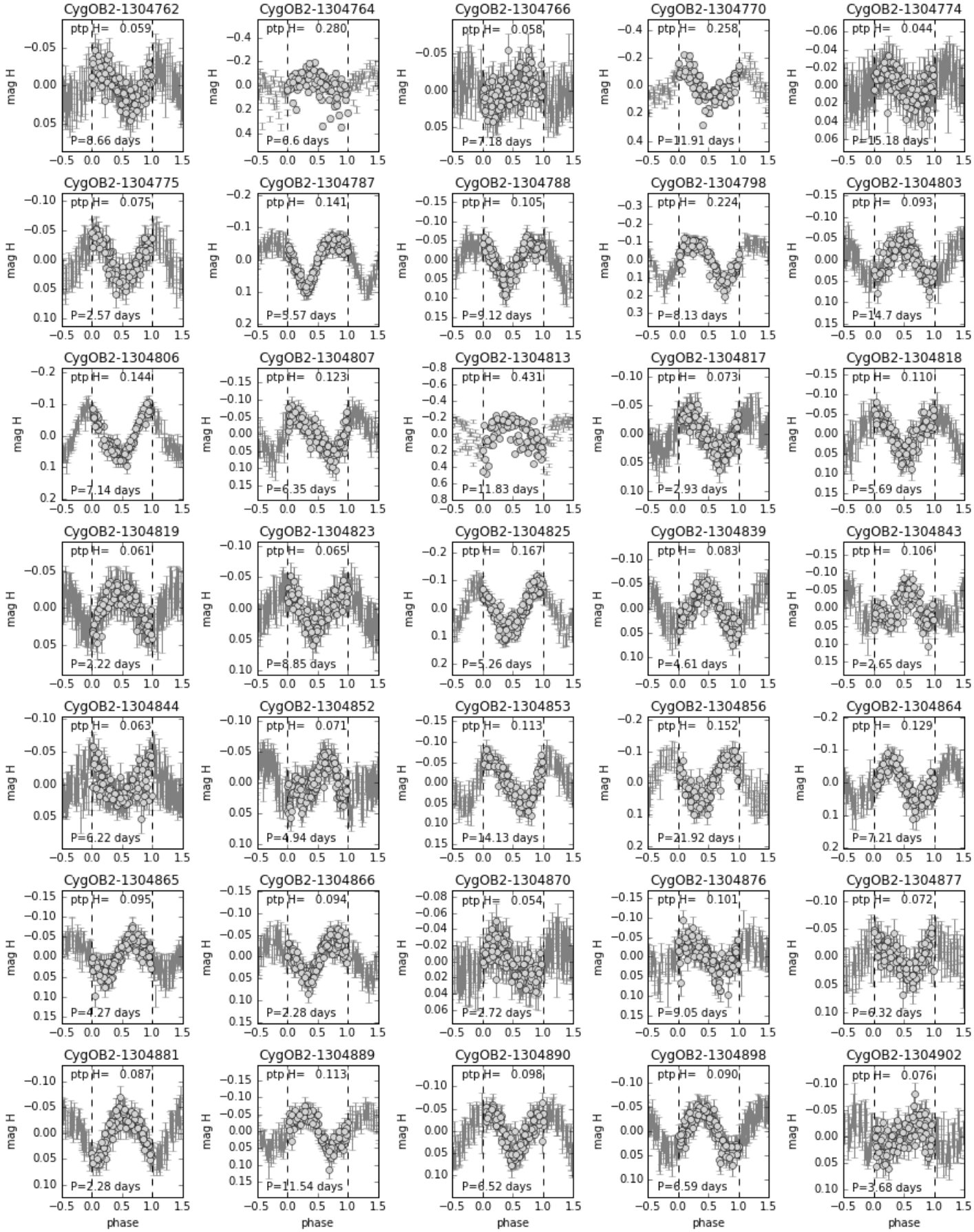
CygOB2-1304762
ptp H= 0.059
P=8.66 days
CygOB2-1304764
ptp H= 0.280
P=6.6 days
CygOB2-1304766
ptp H= 0.058
P=7.18 days
CygOB2-1304770
ptp H= 0.258
P=11.91 days
CygOB2-1304774
ptp H= 0.044
P=15.18 days
CygOB2-1304775
ptp H= 0.075
P=2.57 days
CygOB2-1304787
ptp H= 0.141
P=5.57 days
CygOB2-1304788
ptp H= 0.105
P=9.12 days
CygOB2-1304798
ptp H= 0.224
P=8.13 days
CygOB2-1304803
ptp H= 0.093
P=14.7 days
CygOB2-1304806
ptp H= 0.144
P=7.14 days
CygOB2-1304807
ptp H= 0.123
P=6.35 days
CygOB2-1304813
ptp H= 0.431
P=11.83 days
CygOB2-1304817
ptp H= 0.073
P=2.93 days
CygOB2-1304818
ptp H= 0.110
P=5.69 days
CygOB2-1304819
ptp H= 0.061
P=2.22 days
CygOB2-1304823
ptp H= 0.065
P=8.85 days
CygOB2-1304825
ptp H= 0.167
P=5.26 days
CygOB2-1304839
ptp H= 0.083
P=4.61 days
CygOB2-1304843
ptp H= 0.106
P=2.65 days
CygOB2-1304844
ptp H= 0.063
P=6.22 days
CygOB2-1304852
ptp H= 0.071
P=4.94 days
CygOB2-1304853
ptp H= 0.113
P=14.13 days
CygOB2-1304856
ptp H= 0.152
P=21.92 days
CygOB2-1304864
ptp H= 0.129
P=7.21 days
CygOB2-1304865
ptp H= 0.095
P=4.27 days
CygOB2-1304866
ptp H= 0.094
P=2.28 days
CygOB2-1304870
ptp H= 0.054
P=2.72 days
CygOB2-1304876
ptp H= 0.101
P=9.05 days
CygOB2-1304877
ptp H= 0.072
P=6.32 days
CygOB2-1304881
ptp H= 0.087
P=2.28 days
CygOB2-1304889
ptp H= 0.113
P=11.54 days
CygOB2-1304890
ptp H= 0.098
P=6.52 days
CygOB2-1304898
ptp H= 0.090
P=6.59 days
CygOB2-1304902
ptp H= 0.076
P=3.68 days
mag H
phase

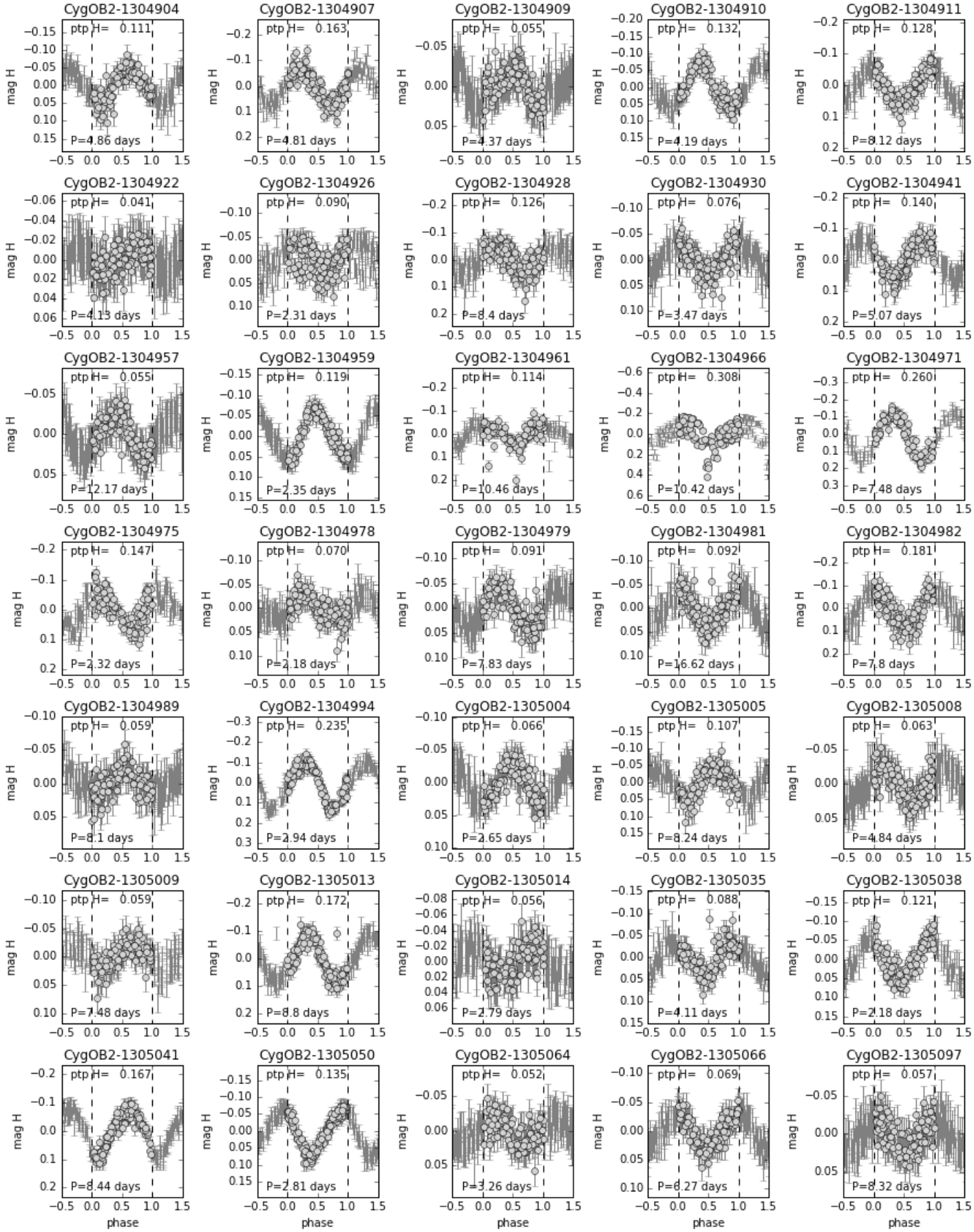
CygOB2-1304904
ptp H= 0.111
P=4.86 days
CygOB2-1304907
ptp H= 0.163
P=4.81 days
CygOB2-1304909
ptp H= 0.055
P=4.37 days
CygOB2-1304910
ptp H= 0.132
P=4.19 days
CygOB2-1304911
ptp H= 0.128
P=8.12 days
CygOB2-1304922
ptp H= 0.041
P=4.13 days
CygOB2-1304926
ptp H= 0.090
P=2.31 days
CygOB2-1304928
ptp H= 0.126
P=8.4 days
CygOB2-1304930
ptp H= 0.076
P=3.47 days
CygOB2-1304941
ptp H= 0.140
P=5.07 days
CygOB2-1304957
ptp H= 0.055
P=12.17 days
CygOB2-1304959
ptp H= 0.119
P=2.35 days
CygOB2-1304961
ptp H= 0.114
P=10.46 days
CygOB2-1304966
ptp H= 0.308
P=10.42 days
CygOB2-1304971
ptp H= 0.260
P=7.48 days
CygOB2-1304975
ptp H= 0.147
P=2.32 days
CygOB2-1304978
ptp H= 0.070
P=2.18 days
CygOB2-1304979
ptp H= 0.091
P=7.83 days
CygOB2-1304981
ptp H= 0.092
P=16.62 days
CygOB2-1304982
ptp H= 0.181
P=7.8 days
CygOB2-1304989
ptp H= 0.059
P=8.1 days
CygOB2-1304994
ptp H= 0.235
P=2.94 days
CygOB2-1305004
ptp H= 0.066
P=2.65 days
CygOB2-1305005
ptp H= 0.107
P=8.24 days
CygOB2-1305008
ptp H= 0.063
P=4.84 days
CygOB2-1305009
ptp H= 0.059
P=7.48 days
CygOB2-1305013
ptp H= 0.172
P=8.8 days
CygOB2-1305014
ptp H= 0.056
P=2.79 days
CygOB2-1305035
ptp H= 0.088
P=4.11 days
CygOB2-1305038
ptp H= 0.121
P=2.18 days
CygOB2-1305041
ptp H= 0.167
P=8.44 days
CygOB2-1305050
ptp H= 0.135
P=2.81 days
CygOB2-1305064
ptp H= 0.052
P=3.26 days
CygOB2-1305066
ptp H= 0.069
P=6.27 days
CygOB2-1305097
ptp H= 0.057
P=8.32 days
mag H
phase

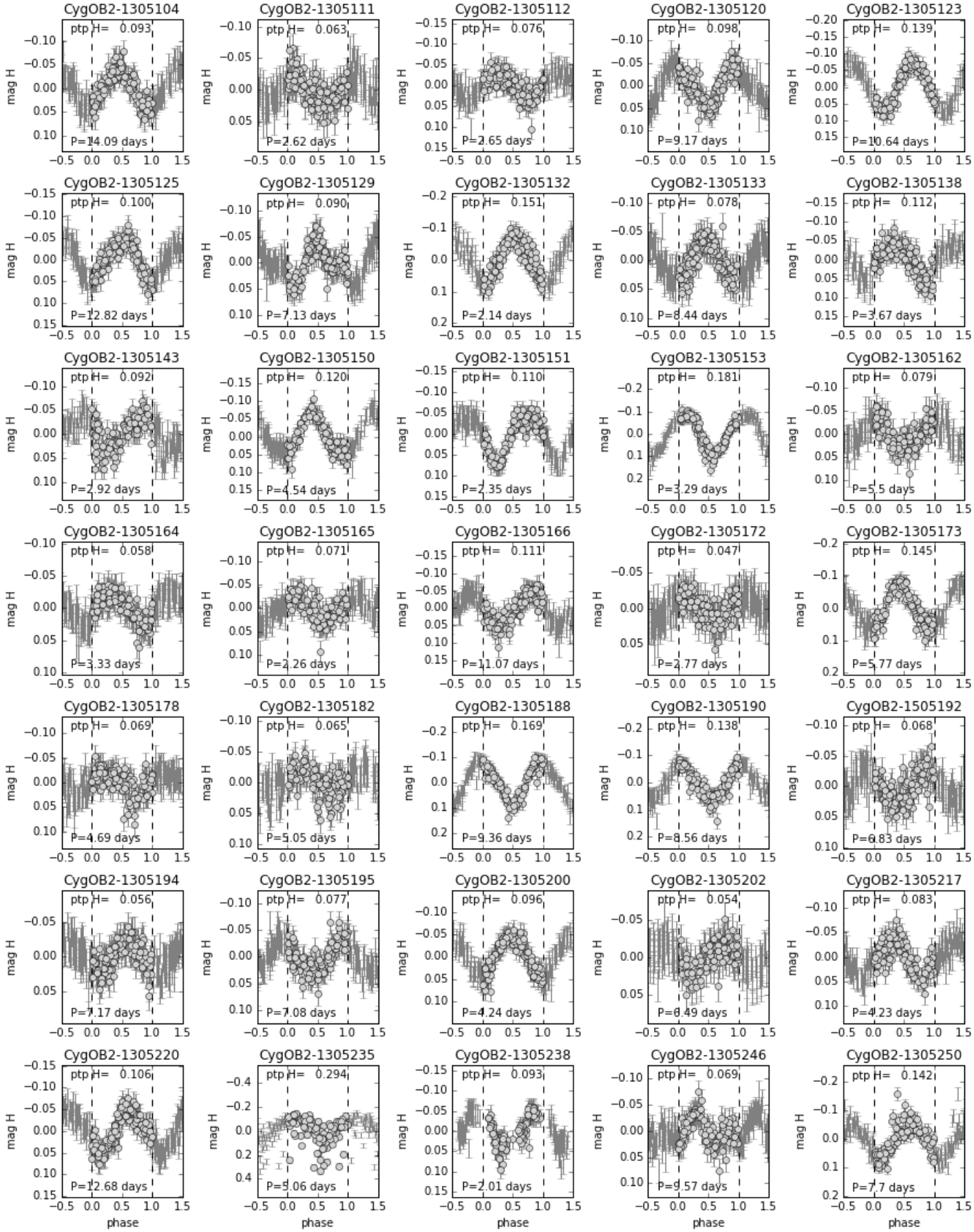
CygOB2-1305104
ptp H= 0.093
P=14.09 days
CygOB2-1305111
ptp H= 0.063
P=2.62 days
CygOB2-1305112
ptp H= 0.076
P=2.65 days
CygOB2-1305120
ptp H= 0.098
P=9.17 days
CygOB2-1305123
ptp H= 0.139
P=10.64 days
CygOB2-1305125
ptp H= 0.100
P=12.82 days
CygOB2-1305129
ptp H= 0.090
P=7.13 days
CygOB2-1305132
ptp H= 0.151
P=2.14 days
CygOB2-1305133
ptp H= 0.078
P=8.44 days
CygOB2-1305138
ptp H= 0.112
P=3.67 days
CygOB2-1305143
ptp H= 0.092
P=2.92 days
CygOB2-1305150
ptp H= 0.120
P=4.54 days
CygOB2-1305151
ptp H= 0.110
P=2.35 days
CygOB2-1305153
ptp H= 0.181
P=3.29 days
CygOB2-1305162
ptp H= 0.079
P=5.5 days
CygOB2-1305164
ptp H= 0.058
P=3.33 days
CygOB2-1305165
ptp H= 0.071
P=2.26 days
CygOB2-1305166
ptp H= 0.111
P=11.07 days
CygOB2-1305172
ptp H= 0.047
P=2.77 days
CygOB2-1305173
ptp H= 0.145
P=5.77 days
CygOB2-1305178
ptp H= 0.069
P=4.69 days
CygOB2-1305182
ptp H= 0.065
P=5.05 days
CygOB2-1305188
ptp H= 0.169
P=9.36 days
CygOB2-1305190
ptp H= 0.138
P=8.56 days
CygOB2-1505192
ptp H= 0.068
P=6.83 days
CygOB2-1305194
ptp H= 0.056
P=7.17 days
CygOB2-1305195
ptp H= 0.077
P=7.08 days
CygOB2-1305200
ptp H= 0.096
P=4.24 days
CygOB2-1305202
ptp H= 0.054
P=6.49 days
CygOB2-1305217
ptp H= 0.083
P=4.23 days
CygOB2-1305220
ptp H= 0.106
P=12.68 days
CygOB2-1305235
ptp H= 0.294
P=5.06 days
CygOB2-1305238
ptp H= 0.093
P=2.01 days
CygOB2-1305246
ptp H= 0.069
P=9.57 days
CygOB2-1305250
ptp H= 0.142
P=7.7 days
mag H
phase

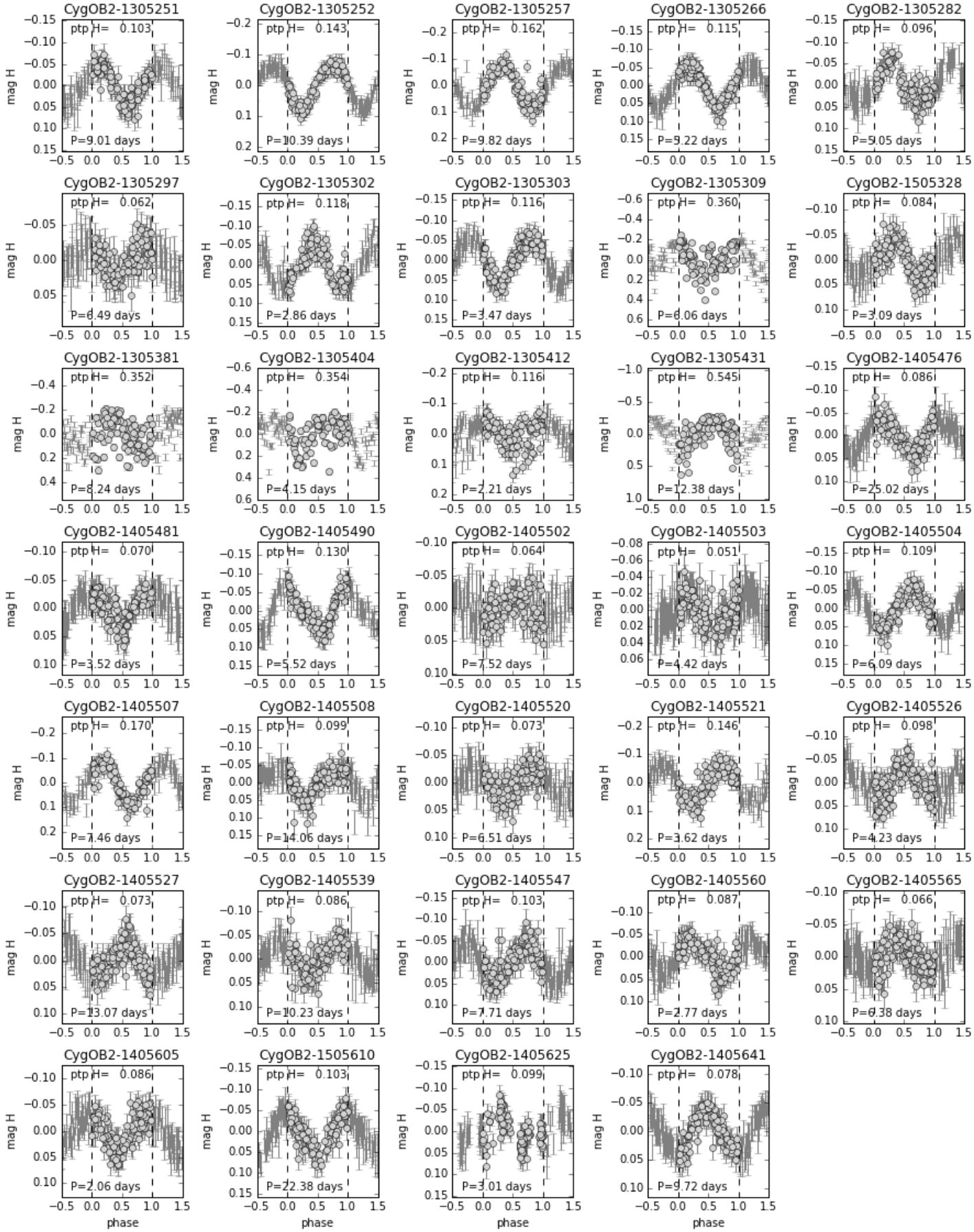
CygOB2-1305251
ptp H= 0.103
P=9.01 days
CygOB2-1305252
ptp H= 0.143
P=10.39 days
CygOB2-1305257
ptp H= 0.162
P=9.82 days
CygOB2-1305266
ptp H= 0.115
P=9.22 days
CygOB2-1305282
ptp H= 0.096
P=9.05 days
CygOB2-1305297
ptp H= 0.062
P=6.49 days
CygOB2-1305302
ptp H= 0.118
P=2.86 days
CygOB2-1305303
ptp H= 0.116
P=3.47 days
CygOB2-1305309
ptp H= 0.360
P=6.06 days
CygOB2-1505328
ptp H= 0.084
P=3.09 days
CygOB2-1305381
ptp H= 0.352
P=8.24 days
CygOB2-1305404
ptp H= 0.354
P=4.15 days
CygOB2-1305412
ptp H= 0.116
P=2.21 days
CygOB2-1305431
ptp H= 0.545
P=12.38 days
CygOB2-1405476
ptp H= 0.086
P=25.02 days
CygOB2-1405481
ptp H= 0.070
P=3.52 days
CygOB2-1405490
ptp H= 0.130
P=5.52 days
CygOB2-1405502
ptp H= 0.064
P=7.52 days
CygOB2-1405503
ptp H= 0.051
P=4.42 days
CygOB2-1405504
ptp H= 0.109
P=6.09 days
CygOB2-1405507
ptp H= 0.170
P=7.46 days
CygOB2-1405508
ptp H= 0.099
P=14.06 days
CygOB2-1405520
ptp H= 0.073
P=6.51 days
CygOB2-1405521
ptp H= 0.146
P=3.62 days
CygOB2-1405526
ptp H= 0.098
P=4.23 days
CygOB2-1405527
ptp H= 0.073
P=13.07 days
CygOB2-1405539
ptp H= 0.086
P=10.23 days
CygOB2-1405547
ptp H= 0.103
P=7.71 days
CygOB2-1405560
ptp H= 0.087
P=2.77 days
CygOB2-1405565
ptp H= 0.066
P=6.38 days
CygOB2-1405605
ptp H= 0.086
P=2.06 days
CygOB2-1505610
ptp H= 0.103
P=22.38 days
CygOB2-1405625
ptp H= 0.099
P=3.01 days
CygOB2-1405641
ptp H= 0.078
P=9.72 days
mag H
phase